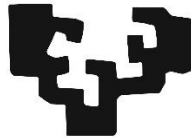eman ta zabal zazu

Universidad   Euskal Herriko
del País Vasco   Unibertsitatea

METAL-ORGANIC FRAMEWORKS AND THEIR COMPOSITES FOR WATER REMEDIATION
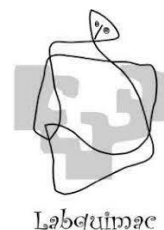
Ainara Valverde de Mingo

2022

Supervisors:

Dr. Roberto Fernández de Luis

Dr. José Manuel Laza Terroba

Agradecimientos

Desde que tenía 14 años sabía que quería estudiar algo relacionado con la ciencia, y trabajar en un laboratorio, pero creo que ni siquiera mientras cursaba la carrera de química me imaginé que llegaría a ser doctora algún día. Ha sido un viaje largo y he disfrutado cada momento, pero sé a ciencia cierta que no podría haberlo conseguido si no llega a ser por las muchas personas que me han acompañado durante este camino, y es por eso que quiero agradecérselo a todos de corazón.

En primer lugar, quiero darles las gracias a mis directores. A Roberto, por ayudarme desde el principio del camino y hasta el último momento, por invertir el tiempo en formarme y convertirme en mejor investigadora, creo que es poco probable que vuelva a encontrarme con tan buen jefe a lo largo de mi carrera. A Manu, por la cercanía y la ayuda prestada siempre que la he necesitado, y por su infinita paciencia.

Quiero agradecer a toda la gente que me ha ayudado a llevar a cabo este trabajo. A los SGIker de la UPV/EHU por su apoyo técnico y humano, en especial a Juan Carlos Raposo, Maribel Collado, Javier Sanguesa y Alex Diaz. A Luis por su ayuda con las medidas de EPR y las incontables dudas de papeleo que he tenido estos cuatro años. Gracias también a Mónica por todo el apoyo con las medidas de scattering inelástico de neutrones, por la paciencia y por resolvernos todas las dudas que nos han ido surgiendo. A Pedro y Carlos por estar siempre dispuestos a ayudar con lo que haga falta.

Agradecer también a toda la gente del laboratorio de Quimica Macromolecular (Labquimac) de la facultad de ciencia y tecnología de la UPV/EHU, pues es ahí donde di mis primeros pasos como investigadora. A Leyre y a Vilas por darme la oportunidad de empezar ahí mi carrera científica, y en especial a Sheila, Julia, Alazne y Manu, por animarme siempre y estar ahí para lo que necesitaba.

Gracias también a Senentxu y al BCMaterials por darme la oportunidad de hacer esta tesis con ellos, por el uso de las instalaciones y por haber sido mi hogar durante estos 4 años. En un doctorado surgen retos constantemente, y llevarlo a cabo en un centro como el BCMaterials, rodeados de muchos otros estudiantes de doctorado que ya han pasado por lo que estás pasando tú, no tiene precio. Gracias a todos por la

ayuda, en especial a Paula, Ander, Cristian, David, Mikel y Bruno, que allanaron el camino del doctorado antes que yo. A Arkaitz, por toda la ayuda brindada, especialmente los primeros años cuando más que una persona parecía un saco de preguntas. A Txema y a Viktor, por enseñarme y guiarme durante estos años en todo lo relacionado con los neutrones, llegué sin saber nada y no sé lo que hubiera hecho sin vosotros. A Stefan por el apoyo y los ánimos cuando más falta hacían. A Juan Ignacio por toda la ayuda brindada, especialmente estos últimos meses. A Natalia, Dani, Leire, Joseba, Maitane, Lorea, Marcos, Amaia, Paula, Nagore... y a todos los compañeros que, aunque no haya mencionado, quiero agradecer por el apoyo y la amistad de estos años, no puedo imaginarme un sitio mejor para haber hecho este camino.

No quiero olvidarme de agradecer a Guille, Gabriel, Ayelen, Juan Manuel y el resto de compañeros de la Universidad de Buenos Aires por acogerme como si fuera una más durante mi estancia en Argentina, fue una experiencia que siempre llevaré conmigo.

Y fuera del ámbito científico, a mi kuadrilla, que han sido desde siempre los que saben hacerme desconectar, que cualquier problema me parezca de pronto pequeño y que consiguen sacarme una sonrisa en un mal momento sin siquiera saberlo. A mis amigos del Burgo de Osma, por todos los momentos que me han dado y porque nunca hubiera llegado a ser quien soy hoy si no los hubiese conocido.

Quiero agradecer también a toda mi familia, especialmente a mi ama y a mi aita, por inculcarme desde pequeña la importancia de los estudios, por apoyarme siempre, y por darlo todo sin esperar nada a cambio. A mi tía Nieves, por estar siempre dispuesta a ayudar con cualquier cosa, y a mi hermano Unai por saber sacar siempre lo mejor de las personas.

Y por último a Ibai, por acompañarme en cada paso, apoyarme en los malos momentos y compartir los buenos, y por saber siempre sacarme una sonrisa cuando más lo necesito.

Table of contents

Chapter 3: MOFs as photoreductive materials for Cr^{VI} remediation in wastewater..105

Abstract

As the number and type of chemicals, drugs and materials increases due to the techno-economic advance of the modern XXI society, they enter increasingly in contact with water sources, and hence, with the full trophic chain. Consequently, the water quality is affected both by traditional pollutants, like toxic metals and inorganic compounds, and by emerging ones, like pharmaceuticals and endocrine disruptors. Among this wide variety, heavy metal ions and phenolic compounds are two of the most dangerous pollutants, since they combine a high chemical stability with a high impact in the ecosystems.

Today, several water remediation strategies are applied to detoxify the waters from heavy metals and persistent pollutants, but they still show important drawbacks such as being chemically, energetically and operationally intensive. Moreover, they rely on large installations that require a considerable infusion of capital, engineering expertise and infrastructure. Because of this, there is an urgent need of developing cost-effective technologies for water remediation. Among the different water remediation strategies that are being studied nowadays, adsorption and photocatalysis have attracted considerable attention due to their simplicity, cost-efficiency, easy portability and the needless of addition of harmful secondary products.

In this regard, Metal-Organic Frameworks (MOFs) show an outstanding chemical versatility that enables merging adsorption and photocatalysis functions in the same material thanks to their intrinsic porosity and semiconductivity. These physicochemical features arise from the ordered arrangement of their fundamental building units; metal ions or clusters connected by organic linkers, into extended and highly porous robust networks. In addition to the plenty of design opportunities coming from the reticular chemistry to engineer MOFs with varied characteristics, these materials can be pre or post-synthetically encoded to further expand their functionality and efficiency towards an specific application.

Among the myriad of reticular materials that have been reported up to date, M^{III} and M^{IV} based MOFs have been widely studied for water remediation because of the

chemical robustness coming from the strong bridges formed by the acid metals and the carboxylate type linker. However, most of these MOFs show small selectivity to adsorb most of the cationic metals. Thus, different functionalization strategies must be performed in them to improve their affinity and achieve more specific heavy metal adsorption.

This thesis is focused on the exploration of the synthesis and functionalization pathways of archetypal Zr-based (UiO-66 and MOF-808) and Ti-based (MIL-125) MOFs, in order to improve their adsorption and photocatalytic functionalities to capture, degrade and/or separate metals and phenolic pollutants. Moreover, the inclusion of MOFs in two different polymeric matrixes (poly(vinylidene fluoride-co-hexafluoropropylene) (PVDF-HFP) and chitin) has been studied in order to engineer composite membrane technologies easy to recover after the metal adsorption.

Chapter 1 of this thesis gives a general introduction to Metal-Organic Frameworks, as well as to the requirements they should have for their use in water remediation. Moreover, the strategies that can be applied to enhance their adsorption and photocatalytic functions are presented. In parallel, a brief state of art of polymer@MOF composites that have been employed for water remediation purposes is developed, specially focusing in the polymeric materials investigated in this work.

In Chapter 2, the chemicals and general experimental procedures that have been systematically applied in the thesis are described. In parallel, a brief introduction to the fundamental basis, the experimental conditions and the equipment employed during the work has been developed.

Chapter 3 focuses on the synthesis and chemical encoding of MOFs photocatalysts and sorbents for the Cr^{VI} remediation. Cr^{VI} is a highly concerning pollutant but also an economically appealing ion. Therefore, its recovery coupled to its photoreduction to the less toxic and mobile Cr^{III} is of high economic interest. The chapter is divided in two sections. In the first section the combined photoreduction and adsorption capacity of Ti-based MIL-125 and Zr-based UiO-66 towards Cr^{VI} has been explored, identifying the parameters (*i.e.* defect chemistry, particle size…) that play a key role to tune their adsorptive and photocatalytic functions. In this regard, the decrease of the particle size of MIL-125 has shown to be highly beneficial to increase the

photoreduction capacity. On the other hand, the incorporation of –NH$_2$ groups into the UiO-66 framework has shown to endow the material with higher photoreduction capacity in both UV and visible light. The defect chemistry has shown to be detrimental for Cr^{VI} photoreduction, as the semiconductor nature of the framework is decreased due to a decrease of the linkers. However, it is beneficial for the adsorption of Cr^{VI}, since it is an anionic specie that can link to the defective points of the cluster. In the second section of the chapter, the potentials of multivariate (MTV) functionalization of UiO-66 with –NH$_2$, –(OH)$_2$ and –NO$_2$ functions has been explored. The integral functionalization of UiO-66 has led to a synergistic enhancement of the band gap, photoconduction and photocatalytic efficiency of the multivariate frameworks, which exceed properties of the single functionalized materials. The trifunctional UiO-66-NH$_2$-(OH)$_2$-NO$_2$ has exhibited outstanding Cr^{VI} to Cr^{III} photoreduction and a great capacity to retain the phototransformed Cr^{III} ions, with only negligible amounts of the highly reactive and hazardous Cr^{V} intermediate specie after operation.

Chapter 4 explores the post-synthetic modification of MOF-808 with amino acids and natural acids as a tool to tune its adsorption affinity and selectivity towards metal ions. In parallel, the immobilization of metal ions into pore environments decorated with biological functionalities as amino acids has opened the perspective to engineer biomimetic catalytic systems. The chapter is divided in two sections. The first one is focused in the functionalization process of the MOF-808, creating a metal-chelator like trap. More concretely, the impact of the chemical modifications to modulate its adsorption affinity in static and dynamic conditions over various metal ions of different acidities has been studied. The immobilization of these molecules have drastically changed the affinity that the material shows towards metal ions, showing higher affinities for soft or hard metal acids depending on the inserted functionality. Once the capacity of the functionalized materials to adsorb heavy metals was tested, a chromatographic column working in continuous flux was successfully designed to separate metal ions of a multielement solution. The second section of the chapter studies the immobilization of copper ions within the MOF-808@(amino) acid systems. The coordination of copper *via* single or cooperative metal-binding modes gives rise to the stabilization of isolated, clustered and even partially reduced metal-

species. Moreover, copper doped MOF-808@(amino) acids have shown to have a catalytic activity similar to some metalloenzymes for the phenolic compounds wet oxidation. The catalytic activity and selectivity of the system has shown to depend on the amino acid and acid residues coordinating the copper metal sites, as well as on the clustering degree of the copper catalytic centers. Inelastic neutron scattering has helped to elucidate the amino acid anchoring process and the metal immobilization into the framework.

Even if the studied MOFs have shown to be highly efficient sorbents to recover metal ions from wastewater, there are still some drawbacks that hinders the MOF's applicability as heavy metal remediation systems. The first one is related to their powder nature, which makes their recovery from water time and energy consuming. Second, MOFs exhibit limited processability to shape them as millimeter to micrometer size objects like filters or membranes.

Because of this, Chapter 5 focuses in the development of polymer@MOF composites. This chapter explores in its first section how the introduction of three different MOFs (MIL-125, UiO-66-NH$_2$, and MOF-808) alters the structure of the PVDF-HFP@MOF membranes obtained by phase inversion techniques (thermally induced phase separation (TIPS) and non-solvent induced phase separation (NIPS)). The micro to nanostructure of the composites has been studied through a combination of different techniques, including small angle neutron scattering, unravelling specific features of this complex systems not reported before. As a small drawback, the combination of the experimental techniques applied in this study does not allow to quantify to which extent the MOF particles included within the system are active for adsorption. To this end, comparative Cr^{VI} adsorption experiments have allowed estimating the accessibility degree of the MOF particles in the composites, comparting the adsorption capacities of the MOF in the membrane with the capacity of the powdered MOF in a solution. This experiments pointed out that the accessibility of the MOFs installed into TIPS membranes is higher than the one observed for NIPS homologues. In order to improve the capacity of the more eco-friendly and with quicker preparation time NIPS membranes, the *in-situ* functionalization of the composites with cysteine has been successfully performed. This strategy has been

fully effective to modulate the adsorption affinity of the system towards cationic soft species such as Hg^{II}. In the second section of the Chapter 5, the chemical, structural and functional characteristics of Chitin@MOF-808 composites to function as wide range adsorbents have been researched. Thanks to their micro, meso and macroporous structure, the Chitin@MOF-808 composites have shown to be able to work efficiently for the adsorption of a large variety of pollutants ranging from small ions and molecules to large proteins or nanoparticles. Furthermore, Chitin@MOF-808 composites have shown to exhibit the chemical affinity of their separate components, but in some cases, the material benefits from the synergistic interactions of its components, outperforming both MOF-808 and chitin efficiencies.

Finally, Chapter 6 summarizes the main conclusions derived from this investigation, as well as the future trends in which it would be interesting to focus in forthcoming investigations. In general, the potentials for water remediation of chemically robust MOFs and their composites has been assessed. Moreover, the pros and cons of the functionalization strategies that can be applied to water stable MOFs for the capture, separation and degradation of specific pollutants such as heavy metals and phenolic compounds has been determined.

List of abbreviations

Asp	L-asparagine
BET	Brunauer-Emmet-Teller
BDC	1,4-Benzenedicarboxylic acid, Terephthalic acid
BDC-NH$_2$	Aminoterephthalic acid
BDC-(OH)$_2$	2,5-Dihydroxyterephthalic acid
BDC-NO$_2$	Nitroterephthalic acid
BTC	1,3,5-Benzenetricarboxylic acid, Trimesic acid
Cit	Citric acid
CH	Chitin
Cys	L-cysteine
DMF	Dimethylformamide
DSC	Differential Scanning Calorimetry
EDX	Energy Dispersive X-rays
EPR	Electron Paramagnetic Resonance
Fum	Fumaric acid
His	L-histidine
^{1}H-NMR	Proton Nuclear Magnetic Resonance
HPLC	High Performance Liquid Chromatography
ICP-AES	Inductively Coupled Plasma Atomic Emission Spectroscopy
ICP-MS	Inductively Coupled Plasma Mass Spectometer
INS	Inelastic Neutron Scattering
IR	Infrared
Mal	Malic acid
MMF	Mixed Matrix Filtering

MMM	Mixed Matrix Membrane
MOF	Metal-Organic Framework
Msc	Mercaptosuccinic acid
MTV-MOF	Multivariate Metal-Organic Framework
NIPS	Non-solvent Induced Phase Separation
PVDF	Poly(vinylidene fluoride)
PVDF-HFP	Poly(vinylidene fluoride-co-hexafluoropropylene)
REE	Rare Earth Element
ROS	Reactive Oxygen Specie
SALE	Solvent Assisted Ligand Exchange
SALI	Solvent Assisted Ligand Incorporation
SANS	Small Angle Neutron Scattering
SAXS	Small Angle X-ray Scattering
SEM	Scanning Electron Microscopy
SBU	Secondary Building Unit
Suc	Succinic acid
TDX	Temperature-Dependent X-ray diffraction
TEM	Transmission Electron Microscopy
TGA	Thermogravimetric Analysis
TIPS	Thermally Induced Phase Separation
UV-VIS	Ultraviolet-Visible
XPS	X-ray Photoelectron Spectroscopy
XRD	X-ray Diffraction
XRF	X-ray Fluorescence
WHO	World Health Organization

Chapter 1

Chapter 1
Introduction

1.1. WATER QUALITY

The incredibly fast development of technology during the XX and XXI centuries is directly related to the pollution of the environment, including the water sources.[1] Jointly, industrial revolution, fossil fuel accelerated consumption, mining activities, intensive agriculture, exponential increase of chemicals development, and even natural events as volcanic eruptions or the weathering of natural rock-beds have all contributed to an alarming increase of toxic pollutants in the ecosystems in general, and in drinking water sources in particular (Figure 1.1). If this scenario requires itself urgent solutions, it will become even more dramatic in the coming future, as the global warming will drastically reduce the abundance and quality of drinking, industrial and irrigation water sources.[2] Simultaneously, the demand for accessible water is raising caused by population growth in developing countries, a situation that adds even more pressure to the global water sources.

Furthermore, as the number and type of chemicals, drugs and materials increases due to the techno-economic advance of the modern XXI society, they enter increasingly in contact with water sources, and hence, with the full trophic chain. Today, the water quality is affected both by traditional pollutants like heavy metals and inorganic compounds and/or by emerging pollutants like pharmaceuticals and endocrine disruptors. Both types of pollutants have a great impact of the ecosystems and human health, even when they are present at microgram per litre concentration. Needless to say that the cocktail effect of the combined action of different kind of chemicals can even worsen the impact of the water pollution.

The effects of water pollution impact more acutely to developing countries, where water and sanitation services are still severely limited to the central cities. This situation leads to the lack of safe drinking water for more than a third of the population of the world. As a result, millions suffer from preventable illnesses and die every

year.[3] Even in developed countries, where water and sanitation services are nearly universal, the technologies are revealing inefficient to fully remove persistent organic chemicals, endocrine disruptors or even daily used drugs as ibuprofen. In it important to note, that anthropogenic and natural pollution does not only affects drinking water, but have an important impact on the water used for energy and food production and industrial manufacturing. All in all, the quality of our environment is steadily affecting the health and economies of both developing and industrialized nations.[4]
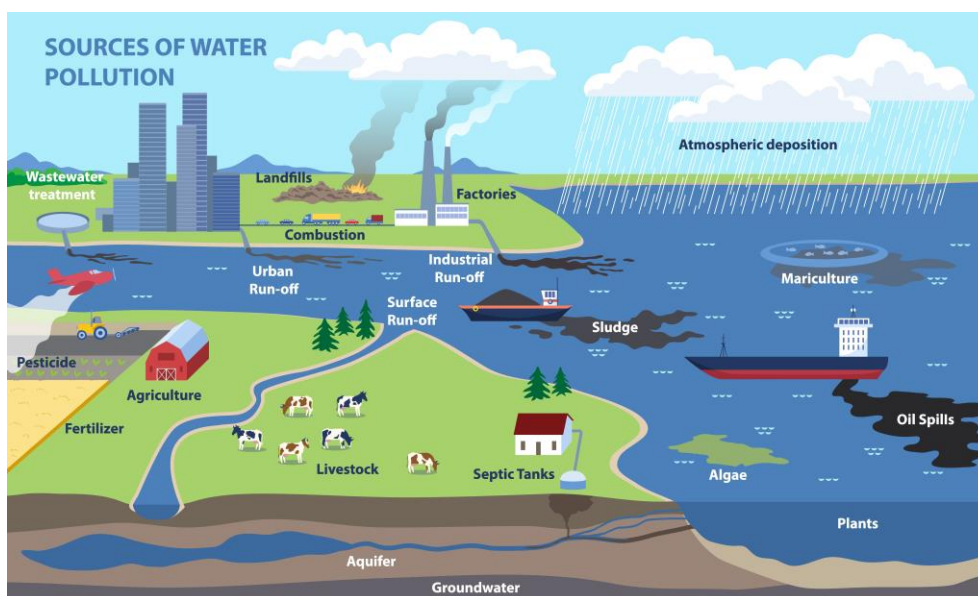
Figure 1.1. Water pollution sources.

From the chemical point of view, four are the major physical and chemical properties that make a pollutant of high risk and concern:

- Chemical stability (being able to remain intact for long periods of time in the environment).
- High transportability and distribution (being prone to long-range transport and distribution in the environment).
- High bioaccumulation potential in the fatty tissue of living organisms (often found at higher concentration levels in the food chain).
- Potential toxicity to both humans and wildlife. However, some pollutants that are chemically labile and with a short half-life time, can also be dangerous due to continuous chronic exposure to non-lethal levels.

Among the broad scope of chemicals that could drastically affect the water-quality, heavy metal ions and phenolic compounds combine a high chemical stability with a high impact in the ecosystems' health, even when present at very low-doses.

1.1.1. TOXIC METAL IONS

Most of the heavy metals introduced into the environment are found at low concentration, usually between milligram and microgram per litre. Nevertheless, toxic heavy metal cations and oxyanions remain to be a significant threat to environmental and public health due to their capacity to be bioaccumulated during long-term exposures[5]. This situation does not only dangers the ecosystems in general, but threaten human health in particular, since heavy metals are increasingly concentrated along the entire food chain.[6] Compared with organic pollutants, heavy metals, such as Pb^{2+}, Cd^{2+}, Hg^{2+}, $Cr_2O_7^{2-}$ and AsO_4^{2-}, are not degradable into eco-friendly substances,[7] and their bioaccumulation induces notorious toxicity, teratogenicity and carcinogenicity in living organisms.[8]

These contaminants are released to the water mainly through human activities such as steel factories and paper and pulp mills (Cr^{VI}), refineries (Hg^{II}), wood industries (Cu^{II}), or the corrosion of pipes (Pb^{II}).[9] This scenario becomes even more concerning when metal-ion are accidentally released from nuclear power plants, giving rise to a long-term radioactive contamination of natural waters by highly persistent radioisotopes. Even the decontamination of toxic and radioactive metal ions of the waters employed to refrigerate radioactive fuels remains to be a serious challenge for public health and environmental protection.[10] Nonetheless, the natural pollution of water sources may as well occur *via* the natural weathering of bedrocks with heavy-metals rich compositions. This is the case of high arsenic concentrations found many rivers of Chile,[11] United States,[12] India[13] or Indonesia,[14] just to mention some of the many examples that can be found in literature.

In this regard, the selective adsorption of metal ions from aqueous solutions has become a pivotal process for environmental remediation,[15] but it is as well a technology of paramount importance for metal recovery and separation purposes.[16,17] It is increasingly clear that the recovery and purification of metal ions from polluted

water sources are gaining importance within the concept of a closed-loop circular economy.[18] That is, anthropogenic heavy metals water pollution is usually accompanied of high-concentration levels of techno-economic critical elements. In this sense, adsorption technologies could play an interesting role to face the selective recovery of specific metal ions from complex matrixes. Just to mention few examples, the recovery and separation of critical raw materials from acid waters derived from mining activities,[19] rare-earth elements (REEs) uptake from water streams arising from phosphor-gypsum deposits,[20] or the precious metals recovery from radioactive wastewaters,[21–24] are some of the relevant application-areas where intensive research is in place to develop a greener and more efficient capture and separation technologies.

1.1.2. PHENOLS AND PHENOLIC COMPOUNDS

Contrary to heavy metals, organic pollutants can be degraded and mineralized to non-hazardous components. However, their diversity, high environmental-impact at very low doses, and in some cases, their bio-persistence, make organic-contaminants a priority concern when facing the water decontamination.[25–27]

Phenol and phenolic compounds are one of the families of highly persistent organics that have important industrial implications, but in parallel, they generate huge environmental issues.[28,29] They are used as chemicals for wood preservation, agriculture, and drug synthesis, among others.[30] As a consequence, phenolic compounds are usually found in the wastewater of various industries, such as refineries, coal processing or petrochemical plants. What is more, they can also be found in pharmaceuticals, plastics, wood products, and paint and paper industries.[31] Their dangerousness is related to the high solubility they show, combined with their rapid absorption through contact with the skin and eyes, inhalation and ingestion.[31] In addition, they are resistant to biodegradation and persist in the environment for long periods,[32,33] and thus, may interfere with the ecosystem equilibrium and affect biogeochemical pathways of organic matter and nutrient recycling.[34]

Besides their capture through adsorption, an intense research has been devoted to find an efficient, economical, and environmentally friendly chemical degradation process for these persistent organic chemicals.[35,36] Among the multiple alternatives

explored up to date, catalytic wet oxidation or biocatalytic oxidation paths are between the technical alternatives that have attracted considerable attention due to their simplicity and environmental friendliness.[37]

1.2. WATER REMEDIATION

Considering the current and future pressures on water supply, the development of low-cost and high-efficiency means of water purification for a variety of pollution-sources will be key to restore the quality of our natural resources.

Conventional and advanced waste water treatment plants can address the water disinfection and decontamination on most of the inorganic and organic pollutants with high efficiency. However, these treatments are often chemically, energetically and operationally intensive, and they rely on large installations. In addition, waste water treatment plants require a considerable infusion of capital, engineering expertise and infrastructure, all of which precludes their use in developing or isolated areas around the world.[4] Although their high rate of water detoxification, some inorganic and organic persistent pollutants scape to conventional water treatment protocols. This is the case of phenols or phenolic endocrine disruptor molecules as paracetamol. Therefore, developing cost-effective technologies for the remediation of water pollution is urgently needed. In this regard, adsorption and photocatalysis have attracted considerable attention due to their simplicity, low cost, easy portability and the needless of addition of harmful secondary products.[38–41]

Adsorption can be classified into physical adsorption (physisorption) and chemical adsorption (chemisorption). Physisorption is governed by intramolecular Van der Waals or electrostatic forces. In this process, a multilayer is formed on the adsorbent surface. As a consequence of the weakness of the sorbent-adsorbate interaction, physisorption is an easily reversible process. On the other hand, chemisorption is defined as the adhering and mass transfer to the surface of the adsorbent, by the formation of covalent bonds, involving a monolayer. As a result, the bonding energy is higher, and the process requires significant energy input to reverse it.

Independently on the adsorption mechanisms, four are the main characteristics that shape the adsorption capacity, kinetics and affinity of a porous material: (i) the pore structure, (ii) the surface area, (iii) the nature of the functional groups installed at the pore space, and finally, (iv) the density of adsorption sites. Today, the potential of classic ordered sorbents as zeolites as cation and anion exchanger are duly proved. [42,43] Nevertheless, the narrow pore-structure and limited surface area of classic sorbents limit the diffusion rates of the pollutants within their crystal structure. In addition, zeolites have limited access to capture organic pollutants due to their small pore-window apertures. Amorphous or highly disordered sorbents as clays[44] or activated carbons[45] have great potential for water remediation because they combine low costs, rich surface chemistry with large surface areas. Nevertheless, they suffer from low adsorption capacity[46] and selectivity due to their limited chemical tailorability. This handicap is especially limiting when trying to remove inorganic oxyanions or specific persistent organics. All in all, the development of advanced porous materials is highly desirable to achieve a combination of an effective, efficient and selective adsorption. Here is where the reticular chemistry, and specially the robust Metal-Organic Frameworks (MOFs) employed in this work could make the difference in comparison to classic sorbents, as it will be explained in the following sections.

Complementary to adsorption, photocatalysis has been deeply investigated during the last decades for water detoxification. Driven by solar light, it could induce the full mineralization of organics, the fixation of inorganic pollutants, or the change in the oxidation state of heavy metals in order to decrease their toxicity and carcinogenicity (e.g. Cr^{VI} to Cr^{III} photoreduction). This process refers to a light-driven photoreaction accelerated by the presence of photocatalysts, which can absorb light in appropriate range of wavelengths depending on its bands structure. Photocatalysis has been recognized for its low cost, low energy consumption, easy installation, and the possibility of working at room temperature. The ultimate photocatalyst function is the generation of reactive oxygen species (ROSs) able to degrade efficiently some kind of organics, as well as, to work as disinfection agents to kill microorganisms, or reduce toxic inorganic species to less hazardous ones.

Photocatalysis is based on the initial excitation of electrons (e$^-$) from the valence band to the conduction band, leaving a positive charge (h$^+$) in the valence band. This process happens when a semiconductor is irradiated with a light source of an energy at least equal to its optical band gap (Figure 1.2a). The photogenerated charge carriers diffuse through the solid crystalline structure to the inner or external surface (Figure 1.2b). Finally, the electron – hole pairs actively participate in varied redox reactions for the formation of ROSs, which are the responsible of the oxidative and reductive degradation of the pollutants (Figure 1.2c). Thus, considering all the photocatalysis processes in perspective, the main descriptors of the efficiency of a photocatalyst are (i) its capacity to harvest light (optical band-gap) (Figure 1.2a), (ii) the efficiency to generate excitons during illumination, separate their electron and holes components and transport them through the crystal lattice preventing their recombination (photoconduction) (Figure 1.2b), and (iii) the easy generation of radicals at the photocatalysts-water interphase, which in the end, are the ones that drive the oxidative and reductive degradation of pollutants (Figure 1.2c).

In parallel, the oxidative or reductive power of the hydroxyl (•OH), superoxide anion (O$_2$•$^-$), hydrogen peroxide (H$_2$O$_2$), singlet oxygen (^{1}O$_2$) or electron radicals generated at the photocatalysts-aqueous interphase, are as well responsible of the degradation or transformation of inorganic and organic chemicals.[47] For instance, in photocatalytic reactions for environmental remediation, numerous oxidizable compounds such as common organic pollutants or trivalent arsenic species are known.[48–51] In contrast, the reducible compounds are limited to alkyl halides, halogen oxoacids or the case of hexavalent chromium explored in this thesis.[52–56]

Considering the current state of the art of photocatalysts, up to date, the most efficient class of materials are metal oxide semiconductors,[57,58] chalcogenides[59,60] and carbon nitrides.[61] In perspective, current challenges of photocatalysts for water remediation purposes are (i) widening the bandgap to make them functional under visible light illumination, (ii) circumventing the carrier recombination while boosting their separation, and (iii) increase their mobility through the photocatalyst's crystalline framework.[62,63] Consequently, the intrinsic non-porous nature of inorganic photocatalysts has strongly limited their ability to efficiently capture both

the substrates and their oxidized or reduced products of the photocatalytic reaction. This bottleneck is especially important by applying a photocatalyst for the Cr^{VI} detoxification of water. For instance, when working at acidic conditions, it is well-known that conventional photocatalysts lack the capacity to capture through adsorption the photo transformed Cr^{III} species that remain soluble in the water media.
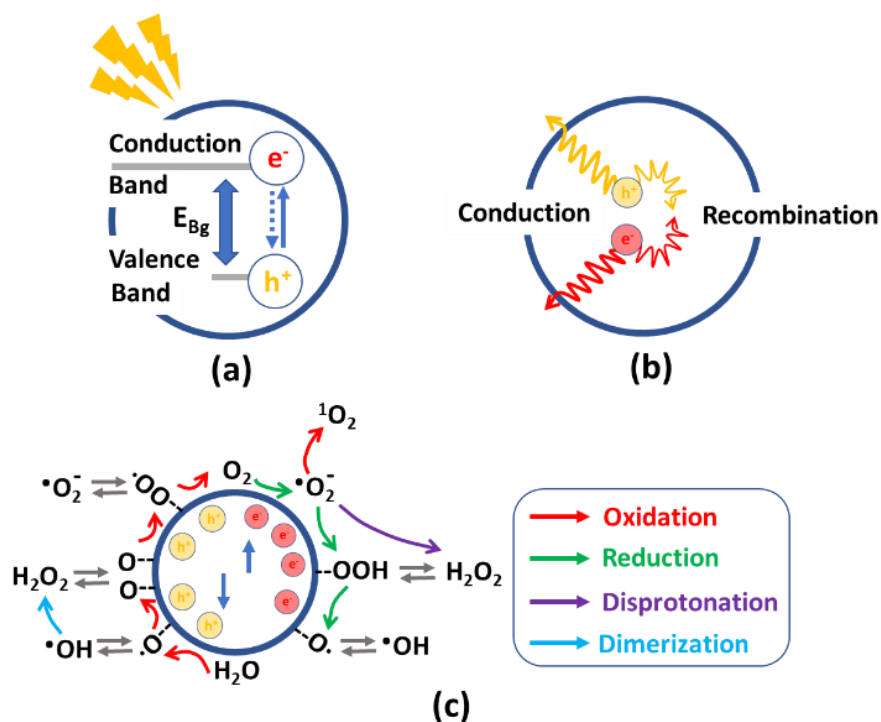
Figure 1.2. Scheme of photocatalytic process on semiconductors. (a) Illustration of the optical Band Gap (E_{Bg}) of a semiconductor and the separation of electrons and holes during illumination. (b) Transport and recombination of electron and hole pairs in photocatalysts. (c) Oxygen reactive species generated due to the oxidation, reduction, deprotonation and dimerization reactions at the surface of the photocatalysts. Adapted with permissions from Nosaka *et al.*[47]

Here, Metal-Organic Frameworks can make the difference, since in addition to their semiconductor nature and porous structure, they have plenty of opportunities to improve these functions *via* the chemical encoding of their frameworks. This is especially beneficial for heavy metal photoreduction, as they are able to meet both adsorption and reduction capacity in the same material.

1.3. METAL-ORGANIC FRAMEWORKS

Metal-Organic Frameworks (MOFs) are crystalline solids built from metal ions or clusters connected by organic linkers into extended, ordered, and highly porous networks (Figure 1.3).[64–72] Since the beginning of the reticular chemistry up to date, MOFs have been assembled from a variety of metal ions including almost all the transition metals, alkaline and alkaline-earths, lanthanides, and even actinide elements. In parallel, the chemistry of the organic linkers has been expanded from the initial carboxylic and imidazole, to sulfonates, phosphonate or tetrazole-linkers, among others, being the carboxyl ones the most used (Figure 1.4).
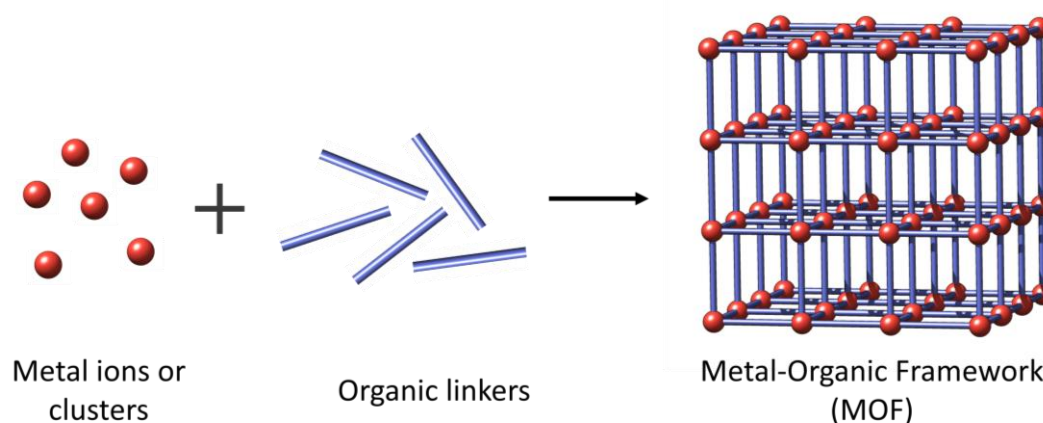
Figure 1.3. Schematic representation of Metal-Organic Frameworks (MOFs).

The coordination of the metal-ions and organic linkers under certain synthetic conditions has generated wide variety of broadly recognizable metal-organic porous structures. In fact, given the connectivity and geometries of the inorganic and organic building blocks, the topology guided design of the reticular materials has been broadly developed during the last two decades. As a given example, the widely employed 2,4-benzenedicarboxylic acid linker can led to different MOF topologies if the connectivity and geometry of the metal cluster is varied (Figure 1.5). The opposite strategy is as well possible, by fixing the inorganic building block and varying the connectivity of the organic linker, a myriad of MOFs with varied topologies can be accessed.
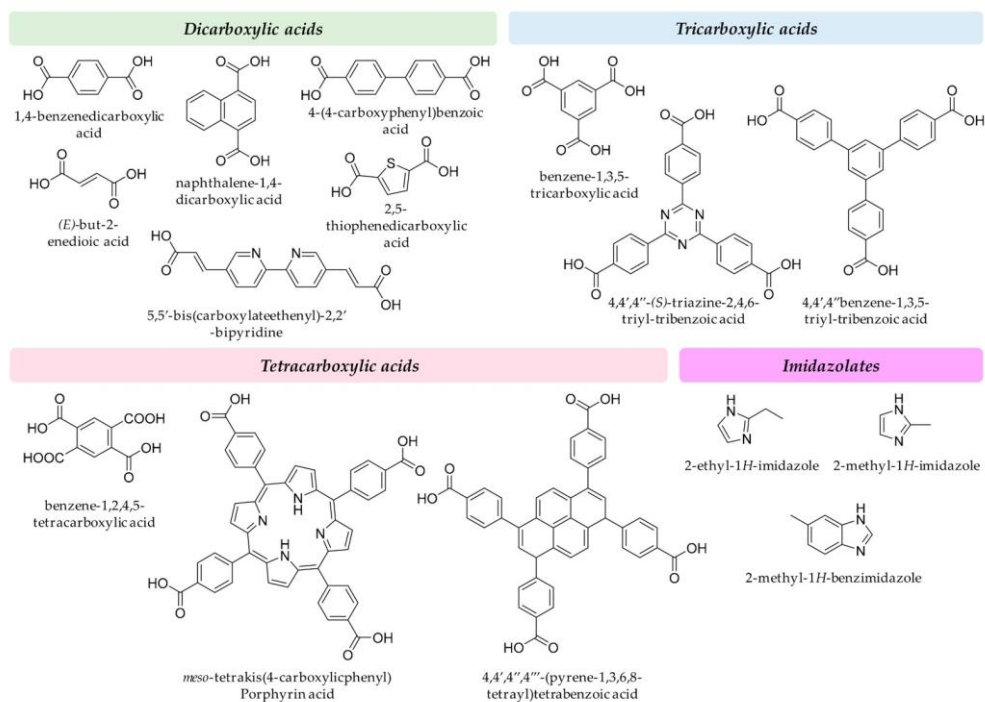
Figure 1.4. Representative examples of organic ligands used in MOF synthesis. Reproduced with permission from Rocío-Bautista *et al.*[73]
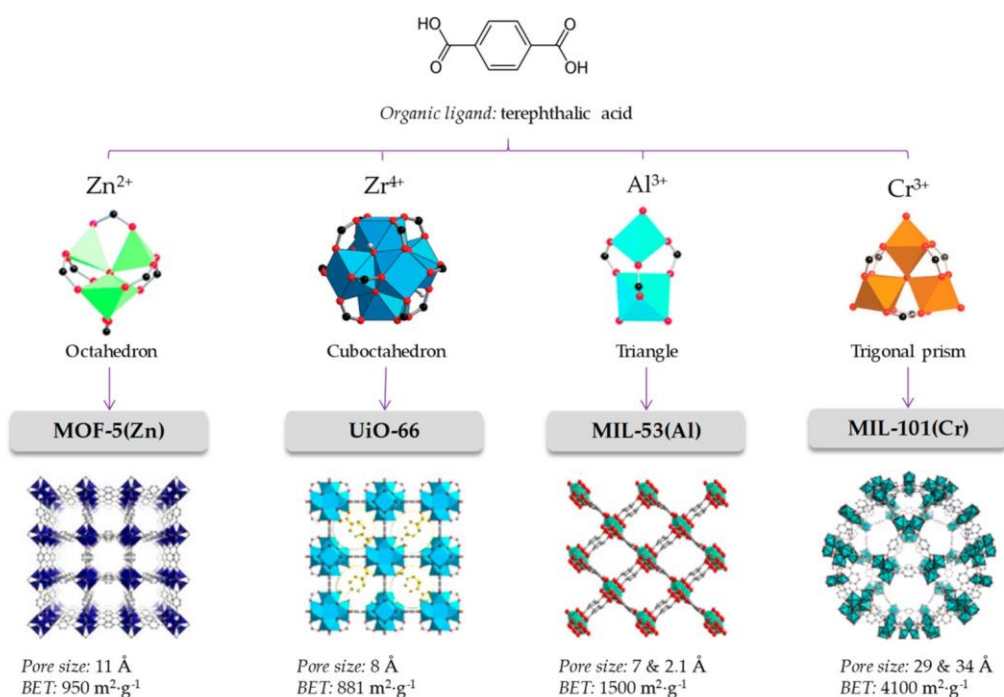
Figure 1.5. The node-and-connector approach to prepare MOFs. The adequate selection of the organic linker (linear in the case of terephthalic acid) and connection geometry of the metal cluster lead to the desired topology. Each framework topology has its characteristic pore size and available surface. Reproduced with permission from Rocío-Bautista *et al.*[73]

The methodology to synthetize MOFs usually involves the mixture of the metal salt and an organic linker in a solvent, which can be chosen because of its reactivity, solubility, redox potential, etc. Solid-based synthesis have also been studied in the last years because they are able to guide quicker and easier reactions. In contrast, they usually face difficulties obtaining single crystals, and thus, determining the product structure.[74]

Among the different liquid-phase synthesis methods (Figure 1.6), solvothermal synthesis stands out as the most used one. In this methodology, reactions are carried out in closed vessels under autogenous pressure.[74] The most common solvents used in this synthesis method are organic linkers with high-boiling points, such as dimethyl formamide, diethyl formamide, acetonitrile, etc.

Once a new MOF with a specific topology or connectivity is developed; the expanded or chemically functionalized versions of the same topology network can be easily obtained following the same guides. In addition, MOFs offer uncountable opportunities even to functionalize their frameworks post-synthetically, once the materials have been already assembled.
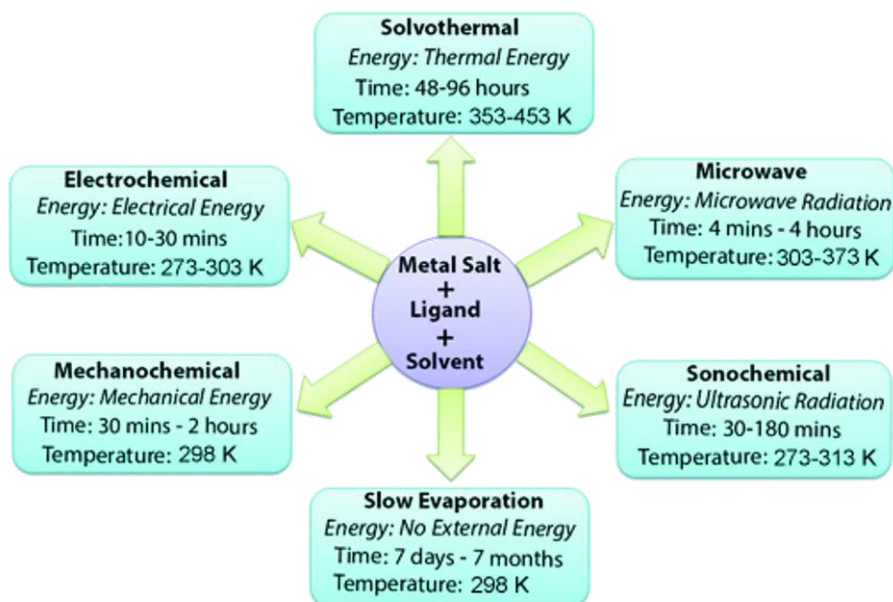
Figure 1.6. Synthesis conditions commonly used for MOF preparation. Adapted with permission from Dey *et al.*[74]

Overall, and independently on the type of MOF, they share an emerging research interest resulting from the simultaneous occurrence of key characteristics such as:

- Crystallinity (i.e. ordered assembly).
- Their tuneable porosity.
- High surface area (MOF materials have so far, the highest surface area of all porous materials).
- The existence of strong metal-ligand interactions.
- The structural diversity and versatility that allows to precisely design materials for a particular application.

As a consequence, since their discovery by Omar Yaghi at the University of Michigan in 1995,[75] and immediate further development by the research teams of Gerard Férey[76] and Susumo Kitagawa,[77] MOFs have become a rapidly evolving research field welcomed by many researchers worldwide. In fact, the number of publications regarding the term "Metal-Organic Frameworks" has grown exponentially to reach more than 14000 publications in 2021. This statement is especially true for MOFs based on carboxylate linkers. Since their discovery, carboxylate-based MOFs have been the flagship of reticular chemistry, opening the room to novel designs, disruptive properties and advanced applications, including the water remediation ones studied in this work. Indeed, archetypal MOFs have shown outstanding performance over metal ion recovery from different aqueous media just because of their intrinsic interconnected porosity and high surface area.[78–81]

In addition, once the main modification paths of MOFs to tune their host-guest chemistry to capture target gases and organic vapours more effectively were established; it was a natural step for the scientific community working on MOFs to apply this knowledge to the adsorption of metal-ions from water. As the MOF chemistry was steadily understood in more detail, the mechanisms governing the hydrolytic instability of these type of materials started to be discovered. That is, the outstanding performance of some of the studied divalent and trivalent metal-based MOFs does not prevent their mid to long term degradation upon exposure to water.[82,83]

Later on, once the chemical robustness of some trivalent and tetravalent metal-based MOFs was proved, the chemical lability and plasticity to modify their inorganic and organic components enabled to include increasingly complex metal trap-chelating motifs inside their pore structure. In addition to water remediation, MOFs have been applied successfully in more stringent and complex media, in terms of acidity, ionic strength, multicomponent metal ions mixture, or even radioactivity. Depending on the application scenario, MOFs have shown their feasibility to recover and separate metal ions of different natures and charges from acid waters,[84] multi-element metal leachates, seawater[85] or radioactive aqueous waste[21,23,86], just to mention the most relevant application areas. In addition to high capacities and relatively fast kinetics, MOFs have demonstrated that their pore chemistry can be modified to: (i) enhance their adsorption specificity towards low concentrated ions in the presence of high concentrated competitor species, (ii) work in a repeatable manner; and (iii) with enough chemical stability, at least to be used in proof of concept studies without a dramatic loss of their performance over cycling.

1.3.1. REQUIREMENTS OF MOF MATERIALS FOR METAL ION RECOVERY

Applicability of MOFs for metal ion recovery/separation in different scenarios requires several characteristics that the adsorbent needs to accomplish, the most important being:

- Long-term chemical stability during operation.
- High adsorption capacity.
- Fast kinetics.
- High selectivity over target metals, even in the presence of competitor ions.
- Easy reactivation and reusability.

Chemical stability

The water and chemical stability of MOFs mainly depends on the degree of hydrolysis of the metal-ligand bonds during the operation conditions.[87] Generally, when the metal-ligand binding energy is higher than the metal-water binding energy,

MOF's structure can resist hydrolysis and are stable against water. [82,88,89] The strength of the metal-ligand bond is directly related to the acidity of the metal at the inorganic clusters, and the basicity of the chelating groups at the organic linkers. As a general rule, the higher the charge density (Z/r^2) of the metal ions at the inorganic clusters (e.g. elements with small radii but high valences such as Zr^{IV}, Ti^{IV}, Cr^{III} or Al^{III}) the better the chemical resistance to water of the Metal-Organic Frameworks.[90]

The chemistry of the organic linkers, their geometry and connection points to the inorganic building units also affect the chemical resistance of the MOFs. Therefore, organic bridges with higher anchoring points usually generate MOFs with a wider chemical applicability window.[91] In addition, the same inorganic and organic building blocks can be arranged in different manners when MOFs crystallize as varied polymorphic forms. Overall, the combination of all these features condition the chemical resistance of the material, which need to be deeply studied to determine the applicability range of the material.

What is more, MOFs formed from strong and rigid moieties, such as benzene-bearing linkers, exhibit higher chemical resistance than aliphatic chain-based ones. The decorative motifs of the linkers also influence the MOFs' stability, even if the connectivity and topology of the MOFs' net are the same. One of the most clarifying examples in that regard is the varied chemical resistance shown by the derivatives of the UiO-66 framework obtained with $-NH_2$, $-NO_2$, $-(OH)_2$, $-(SH)_2$ functions. Furthermore, the length of the linkers also affects the stability of the MOFs. This is the case of some of the compounds of the UiO family. UiO-66 (Figure 1.7a), formed by a Zr_6 oxocluster linked through benzenedicarboxylic acid (BDC) linkers, shows outstanding stability in water media, even in acidic conditions.[92] However, its upper analogues, UiO-67 and UiO-68 (Figure 1.7b and c), have shown to be unstable in the same conditions.[93]
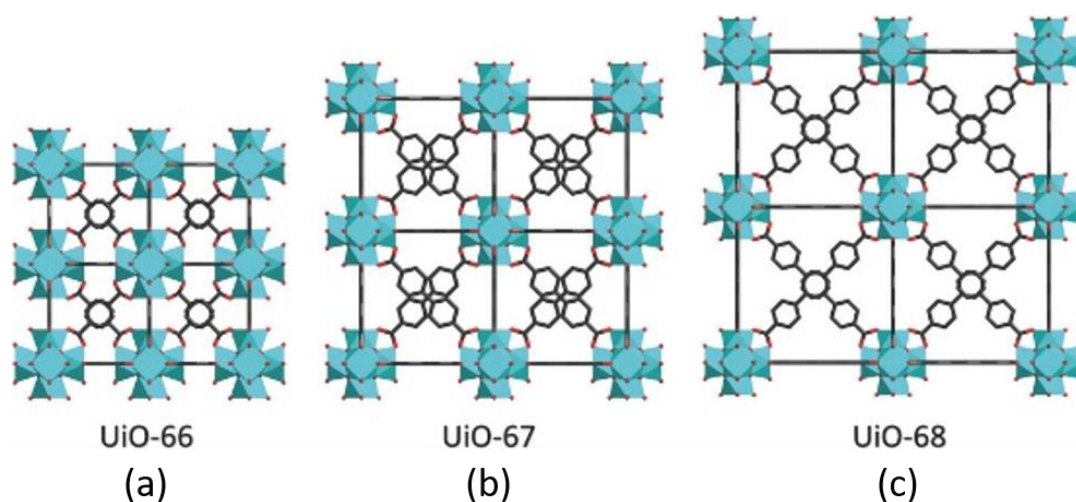
Figure 1.7. Schematic representation of (a) UiO-66, (b) UiO-67 and (c) UiO-68 structures. Reproduced with permission from Yuan *et al.*[94]

Adsorption capacity

The maximum adsorption capacity, metal ions mobility from the solution to the solid, and metal ion affinity degree of the MOFs towards inorganic or organic pollutants can be determined from the fitting of adsorption isotherms to different models. Usually, adsorption isotherms are obtained from batch experiments where a known amount of MOF material is immersed in model single-element solutions of increasing concentrations.

From the fundamental point of view, the adsorption isotherms allow quantifying the thermodynamics of the adsorbate and adsorbent interactions, the maximum adsorption capacity of the material, and its affinity to capture the studied ions from the solution. Among the numerous adsorption isotherm models applied to simulate the experimental data, usually Langmuir and Freundlich fit well the metal adsorption isotherms obtained from MOFs, suggesting that the metal ion uptake is well described by a monolayer adsorption mechanism.[95,96]

Therefore, the adsorption capacity of MOFs is not directly ascribed to their surface area, but to the density of adsorption points at the surface of the pores within their internal structure. This is a key criterion when selecting or modifying the MOF chemistry for a specific application. As stated before, it is worth keeping in mind that

the importance of maximum adsorption capacity and adsorbent-metal ion affinity is relative, and depends on the target application.

Fast kinetics

When talking about metal ion adsorption for water remediation, adsorption kinetics is one of the most important parameters to evaluate. Kinetic analyses give information about the time required to complete the adsorption process, and are simulated based on different models (e.g., pseudo first order, pseudo-second order, intraparticle diffusion, Lagergrenn, Zeldowitsh and Elovich Kinetic), which reveal the nature of the adsorbate migration within the pores or/and surface of the particles.[97]

Surface area, pore window aperture, and the presence of preferential adsorption sites within the MOF structure are some of the characteristics that shape their metal ions' adsorption kinetics profile. The higher the pore window aperture, the more favourable the metal ion migration paths through the pores to the preferential adsorption points, and hence, the faster the adsorption kinetics. In addition, the existence of preferential chemisorption/adsorption points within the MOF assures that the metal ion-adsorbent interaction is strong enough to prevent their posterior release to the media.

It is worthy to mention that the adsorption kinetic parameters, obtained from the fitting of the experimental data, depend on many experimental parameters that need to be carefully selected considering the target application; such as the metal ion concentration, adsorbent dosage, stirring conditions or temperature, just to mention some of the most relevant ones. Indeed, one needs to be careful when comparing directly the kinetic parameters obtained from works applying different experimental conditions, since it could induce misleading conclusions.

High selectivity

Depending on the specific application, the selectivity degree that the MOF adsorbent needs to accomplish is quite different. For instance, a decontamination process of polluted water only needs for an efficient removal of the target heavy metal from the matrix, being secondary if the competitor species with similar characteristics are also co-adsorbed during the process. Nevertheless, separation and purification of valuable metal ions from acid leachates (e.g., REE recovery from permanent magnets, electronic scratch, phosphorous lamps, batteries…), requires a higher degree of selectivity as possible for the target ions, even in the presence of similar species in terms of chemical and physical behaviour.

Here the development of adsorption experiments in multielement matrixes is highly relevant to unravel if co-adsorption takes place during the metal-recover, and in order to evaluate the separation factor between metals when applying a specific MOF for their capture, separation and purification.

Reusability

After the saturation of the adsorbent, it is necessary to activate the material eluting the adsorbed metal without altering or destroying the MOF or the functionalization motifs included within it. This will depend both on the adsorbent chemical stability window as well as on the nature of metal ions. Usually acid solutions with varying concentrations or specific metal chelator solutions are applied to elute efficiently the adsorbates.

Again, the evaluation of the chemical stability of the MOFs during and after each elution cycle is key to understand the efficiency decay, especially in these metal-organic frameworks decorated with organic pedant motifs that could be detached during the sorbent re-activation process.

1.3.2. FUNCTIONALIZATION STRATEGIES TO IMPROVE METAL ADSORPTION

The overall performance of MOFs to capture metal-ions, including their adsorption kinetics, adsorption capacity, adsorption thermodynamics, selectivity, stability, and recyclability, are controlled by the geometric features of their highly-ordered framework, its hydrophilicity, surface area, functionality, and their pore size, interconnection and distribution. In this regard, the tunability of MOFs opens the perspective to improve their specific characteristics that affect their adsorption performance *via* different strategies. These can be divided into five categories that are represented in Figure 1.8:
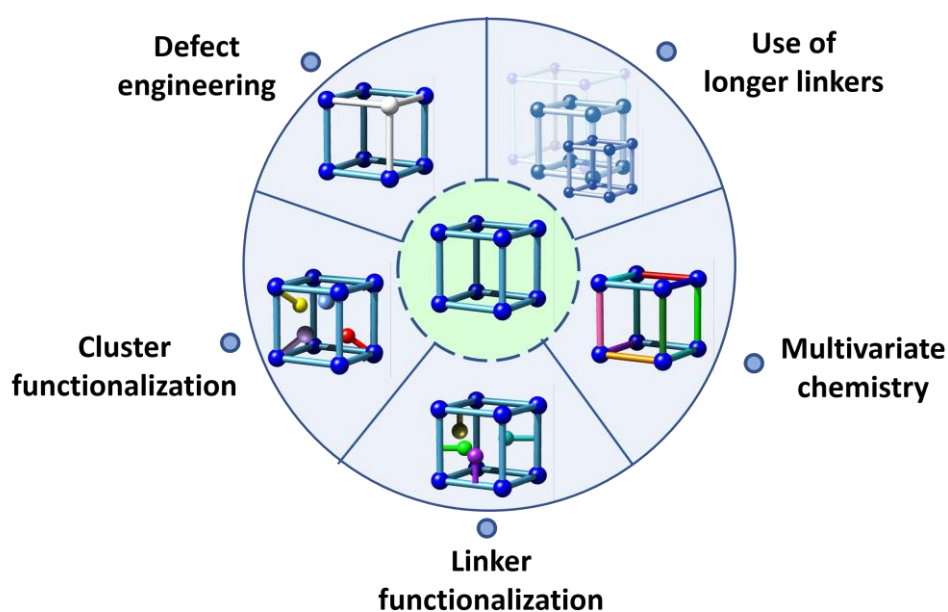
Figure 1.8. Graphical representation of MOFs and strategies for boosting the adsorption performance of MOFs.

Longer organic linkers

The expansion of the pore-aperture and surface area of MOFs by the crystallization of a material with the same topology and connectivity but expanding the length of the organic linkers is a very powerful tool to facilitate the diffusion of metal ions through the MOF's pore space.[98] As a given example, the porosity of UiO-66 can be enlarged using longer organic linkers (i.e. UiO-67 and UiO-68) (Figure 1.7). However, it is

important to balance the gains on the kinetics of adsorption with the possible loss of chemical stability when expanding the porosity of the MOFs.

Defect engineering

The controlled incorporation of structural defects in a MOF to modify its properties or, called defect engineering, is a relatively new research area within the reticular materials development that is rapidly gaining popularity.[99–103] The creation of defects into the MOF structure is directly related to the enlarging of their pore size and introduction of extra adsorption sites in the framework.[18] Defective chemistry of MOFs is closely related with (i) the synthesis conditions, (ii) the addition of monodentate modulators that can compete with the organic linkers that participate in the formation of the ordered framework, or (iii) a design of a network *via* multivariate chemistry able to introduce inorganic clusters and/or organic linkers vacancies into the structure. In general terms, defect engineering is about creating vacancies distributed in ordered or disordered fashions within the crystal structure of the MOF. For example, MOF-808 framework exhibits six linker-vacant ordered positions, usually occupied by monocarboxylate molecules. This does not preclude to induce additional disorder vacancies of the synthesis conditions are tuned properly. For example, among others, Basu *et al.*[104], created a different number of defects per formula unit in the Zr-based MOF-808 by increasing the concentration of formic acid, which acted as a modulator linked to the Zr_6 cluster, but also as a displacer of trimesic acids in the structure (Figure 1.9).

Expanding this approach, Cai *et al.*[105] developed hierarchically porous MOFs (HP-MOFs) by reacting metal precursors and insufficient amounts of linkers, in the presence of monocarboxylic acids with long alkyl chains as a modulator. The modulator plays a dual role: the carboxylic acid coordinates to the metal ion for the formation of metal–oxo clusters, while the alkyl chain creates structural defects and additional pore space (Figure 1.10a-c). These modulators can be then eliminated from the structure *via* an activation process. Depending on the length and concentration of the modulator, different pore diameters could be obtained (Figure 1.10d-f).
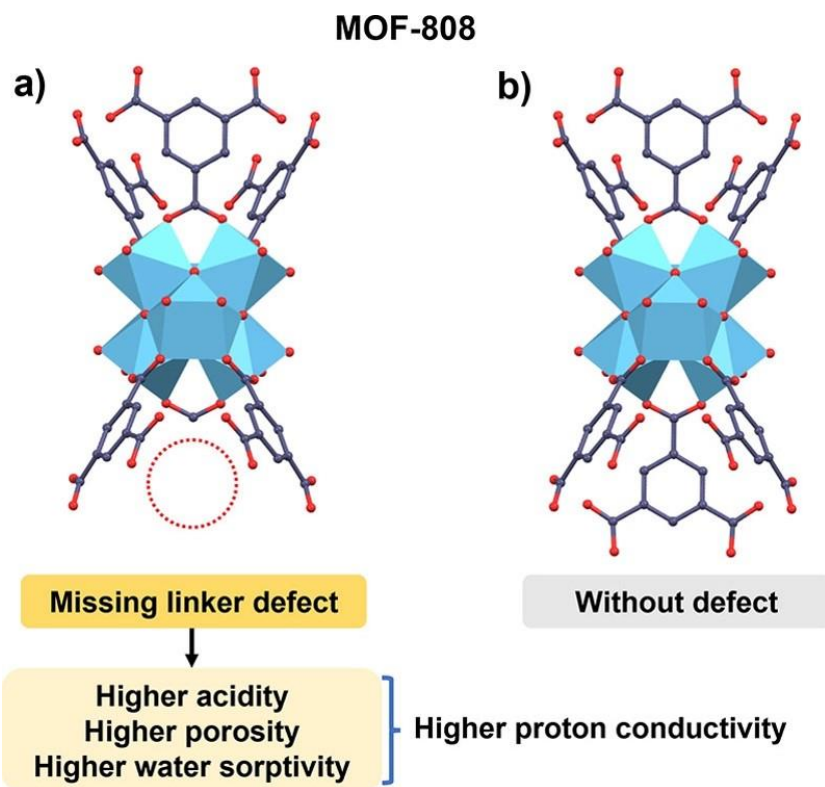
MOF-808

Figure 1.9. Illustration of the MOF-808 structure (a) with and (b) without linker defects. Reproduced with permission from Basu *et al.*[104]
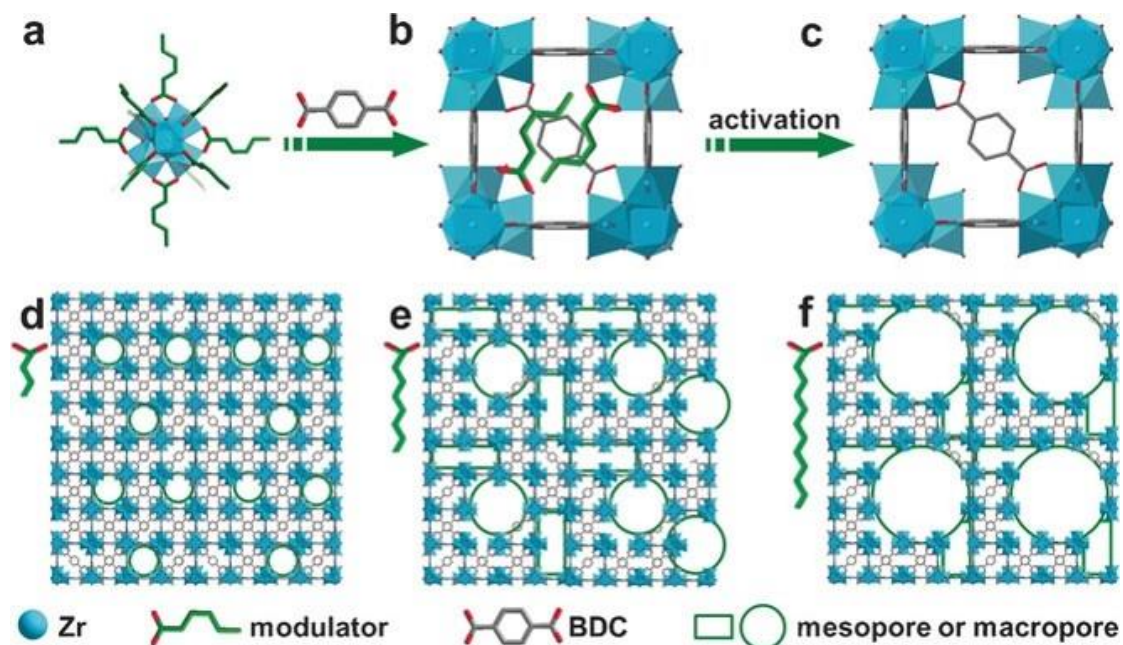
Figure 1.10. Schematic illustration of the synthesis of HP-MOFs with adjustable porosity using UiO-66 as an example. Reproduced with permission from Cai *et al.*[105]

As a drawback, the excess of defects in the structure can lead to a lower chemical and thermal stability of the material, making the structure collapse earlier than its ideal non-defective material,[103] so this approach must be applied carefully.

Linker functionalization

Under traditional synthetic conditions, functional groups can be introduced into MOFs' structure by using an organic linker resembling that of the parent material, but with additional pendant functional groups.[106–108] Thanks to this, additional adsorption sites are provided in the structure. An illustrative example is the UiO-66-SH variant assembled by Yee *et al.*[108], which was applied for Hg^{II} removal from water media. The material resembles the UiO-66 structure, but decorated with –SH groups in the BDC linkers that improve by far the Hg^{II} adsorption kinetics and capacity of the parent material. It is important to note that the incorporation of organic linkers with some functional groups such as –SH into a known MOF may complicate the synthesis process, since they can participate in the coordination process of metal ions that leads to the formation of the MOF. In fact, there are several metal ions that strongly interact with –SH groups (e.g. Zn^{II} or Cu^{II}), disrupting the crystallization of the desired MOF. To suppress the thiol-metal interaction, it is helpful to choose chemically hard metal ions that more selectively bind to the carboxyl groups, such as Al^{III}, Cr^{III}, Eu^{III} or Zr^{IV}, or follow up post-synthetic cluster functionalization protocols to introduce these kinds of functional groups once the MOF is synthetized.

Cluster functionalization

Inorganic cluster decoration is a widely employed strategy to introduce different functional groups into the MOFs' structure in an easy and low-cost way. However, it depends on the crystal structure of the MOF and the cluster themselves. This modification strategy is only possible when the presence of intentionally engineered defects or open positions within the inorganic building blocks are available.

One of the most employed strategies is that called solvent-assisted ligand exchange (SALE),[109] which involves replacing structural linkers coordinated to the clusters

with alternative linkers.[110] On the other hand, solvent-assisted ligand incorporation (SALI) involves replacing labile, non-structural inorganic linkers with functional organic or inorganic functions.[110]

These strategies have emerged as a very facile and versatile experimental protocols to anchor metal-chelating motifs into the clusters of Zr-based MOFs in order to tune their affinity towards specific metal ions or organic molecules. This is the widely explored example of MOF-808. This material is built up by the archetypal Zr^{IV} hexanuclear clusters, which are connected through six trimesic acid molecules. In addition, the Zr^{IV} hexanuclear clusters exhibit six labile formate linkers coordinated to their equatorial plane. SALI has allowed anchoring of different molecules into the cluster by replacing the formates. Just as a relevant example, Y. Peng *et al.*[38] have successfully installed the well-known ethylenediaminetetraacetic acid (EDTA) metal-chelator into the MOF-808 structure endowing the material with impressive adsorption capacity towards a broad scope of metal-ions with varied acidities (Figure 1.11)
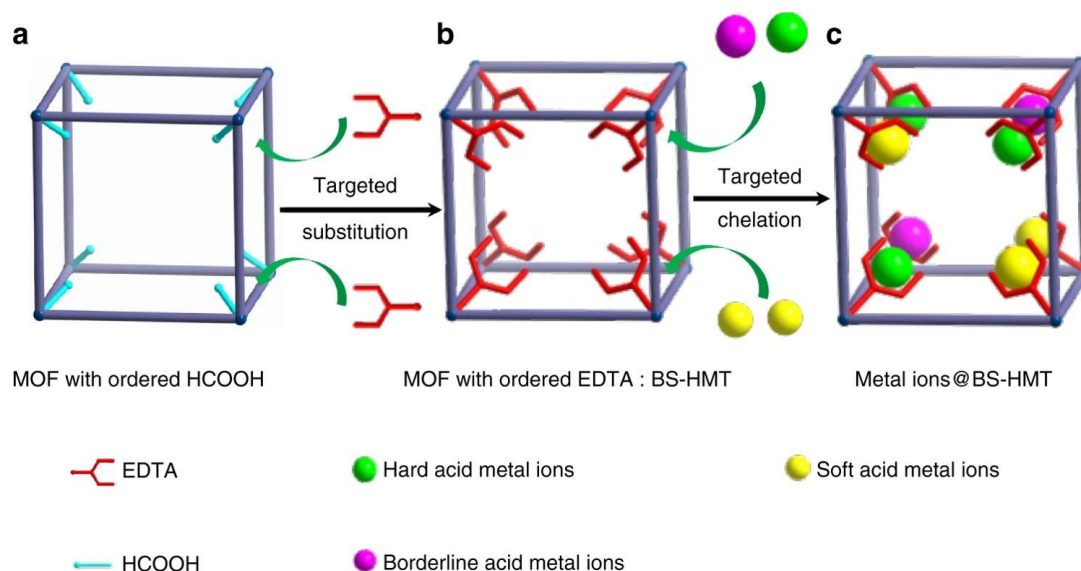
Figure 1.11. Schematic representation of the SALI in MOF-808. (a) The ordered HCOOH in MOF-808 can be substituted by EDTA to form (b) MOF-808 with ordered EDTA, which can be used as a (c) trap for metal ion capture. Reproduced with permission from Peng *et al.*[38]

Multivariate chemistry

During the last years, it has been duly proved that the chemical variance introduced by the multivariate encoding of the organic linkers or inorganic units within the ordered MOFs structure, can lead to cooperative or coupled functionalities. Multivariate MOFs (MTV-MOFs) possess more than two functionalities randomly distributed within the framework that work together in a cooperative or coupled fashions, outperforming their homogenous and periodic counterparts.[111–114]

MTV-MOFs must not be mixed up with multicomponent MOFs, where the multiple linkers are topologically different from one another in terms on length and connectivity, and thus, can be distinguished individually in a crystalline lattice.[66] Indeed, the fundamental criteria of MTV-MOFs are specific functionalities occupying a similar location in the framework and a changeable percentage of each functionality.[111] This way, the introduction of varied functional groups can be achieved without altering the underlying backbone of their structure, obtaining a "heterogeneity within the order".[66]

In 2010, Omar Yaghi's group achieved to build a multivariate MOF-5 combining up to 5 different linkers in the same structure.[115] Thanks to this, they obtained up to a 400% better selectivity for carbon dioxide over carbon monoxide compared with its best same-link counterparts. In the field of heavy metal adsorption, Mon *et al.*[116] succeeded to synthetize a MTV-MOF that could adsorb both inorganic and organic contaminants thanks to the multivariate functions installed within the framework. These findings demonstrate that the properties of MTV-MOFs are not simple linear combinations of their constituents, supporting the notion that the sequence of functionalities within MTV-MOF may be very useful as code to enhance a specific property or to achieve a new property.

1.3.3. PHOTOREDUCTION PROPERTIES IN MOFs

Some pollutants, such as hexavalent chromium, suffer a drastic decrease of their toxicity and carcinogenicity when their oxidation state changes. In the specific case of Cr^{VI}, it becomes less toxic and mobile when it is reduced to Cr^{III}, and thus, less dangerous.

One of the most appealing approaches to combine the concurrent phototransformation and adsorption of chromium species is the development of dual-function sorbent/photocatalysts.[117] Among the porous materials that can fulfil this duality, metal-organic frameworks (MOFs) stand out by their intrinsic high porosity, semiconductor nature and their high degree of structural and functional tuneability.[71,118–121] This photoreduction capacity is due to the interfacial charge transfer properties that MOFs show, which awards them the character of a porous semiconductor under light irradiation.[121–123] More specifically, the photocatalytic functionalities of MOFs arise from their versatility at compositional, chemical and porous structural levels.[124–126] The versatility to decorate the chemical structure of the linkers with electron donor or withdrawing groups, or to design the linker itself as an antenna or chromophore to capture certain UV-Vis radiation, have been of paramount importance to tuning the light harvesting and carriers separation and transport in MOFs.[127–130] In the specific case of Cr^{VI} photoreduction, the chemical structure and functional groups installed into the organic linkers serve to modulate the adsorption affinity of MOFs over hexavalent and trivalent chromium species, but also to tune their light harvesting and photoconduction efficiency.[18,131]

In this regard, multivariate reticular chemistry has emerged as a promising strategy to tailor and balance the light-harvesting, photoconduction capacity and oxygen radicals' generation to achieve a fast and efficient chromium photoreduction. This variance of the different functional groups encoded within the ordered pore space of MOFs, opens the avenue to obtain synergistic effects.

As a clarifying example, multivariate reticular chemistry offers interesting advantages to combining electron donor or withdrawing functions able to expand the band gap to the visible range, and enhance the photoconduction of the MOFs' three-

dimensional scaffolds.[132] Even if this strategy has been rarely studied for Cr^{VI} photoreduction, the initial results seed the light to a promising perspective to further implement the MOF potentials in this research area.

Although less explored for chromium photoreduction, the defect chemistry of MOFs, as well as their porosity metrics, have a great impact on the Cr^{VI} adsorption capacity and kinetics. In addition, the local chemistry of linker defective positions at the clusters can endow the material with Lewis and/or Brønsted sites and those sites can be systematically varied in order to tune the catalytic activity.[63]

Overall, the versatility of reticular materials offers multiple ways to tune the light harvesting, charge mobility and transfer. Further, the ability to generate reactive oxygen species as a photocatalyst, opening the possibility to couple them with the pore space that can be specifically designed to adsorb the substrates and the products of the photocatalytic processes.

1.3.4. MOFs SELECTED FOR THIS THESIS

As mentioned previously, hydrolytic stability and functionalization versatility are two of the cornerstones for the application of MOFs in water remediation. Therefore, the ones obtained from the combination of tetravalent ions as Zr^{IV} and Ti^{IV} with carboxylic linkers such as 1,4-benzenedicarboxylic acid (BDC) or 1,3,5-benzenetricarboxilic acid (trimesic acid, BTC) are certainly appealing to be explored as sorbents and photocatalysts for water remediation, both for their chemical stability and impressive porosity metrics.

Among the wide variety of structures developed by Yaghi *et al.*[133–135] (named MOF-n (n=2, 3, 4, 5…)), the combination of zirconium ions with trimesate linkers in the proper reaction conditions has given rise to the crystallization of one of the most investigated mesoporous metal-organic materials: the MOF-808. This ordered sorbent, which was first reported in 2014,[83] features large cavities (diameter of 18.4 Å) and high Brunauer-Emmet-Teller (BET) surface areas exceeding 2000 $m^2 \cdot g^{-1}$.[136] Similarly than other Zr^{IV} MOFs, it has a secondary building unit (SBU) that consists

of a hexanuclear zirconium node ($[Zr_6(\mu_3\text{-}O)_4(\mu_3\text{-}OH)_4]^{12+}$) connected to six tridentate ligands (BTC) in an spn topology and a cubic Fd-3m symmetry (Figure 1.12).

The high oxidation state of Zr^{IV} in the inorganic SBU results in high charge density and bond polarization leading to a strong coordination bond between Zr and O atoms belonging to the BTC linkers, a feature that endows MOF-808 with remarkable stability in hydrothermal and acidic environments.[136] This MOF has a lower six node-linker connectivity compared to most of the other hexanuclear zirconium node-based MOFs (e.g. 12-connected UiO-66[137] or 8-connected DUT-67,[138] just to mention a couple of relevant examples). The low connectivity of the framework leaves some BTC-uncoordinated positions within the Zirconium hexanuclear clusters (located in the equatorial plane of the cluster) to be occupied by six additional monodentate ligands (HCOO$^-$ and H$_2$O/OH$^-$) per SBU. These labile uncoordinated sites provide the structure with two important advantages: (i) they can be easily replaced by other functionalities and thus, act as anionic metal adsorption sites for molecules such as chromate or arsenate, and (ii) they make it possible to introduce different functionalities by SALI, as it was demonstrated by Aunan *et al.*[139] These authors introduced benzoate, formate or acetate functionalities in those positions by post-synthetic modification in order to tune the chemical properties of MOF-808. Since the pioneer work of these authors, the encoding of MOF-808 *via* SALI has been extended to other carboxyl-based functionalities as amino acids, and even to more acidic sulfonates and phosphonates.[140] What is more, these open metal sites can be increased to more than six positions by introducing linker defects into the structure (Figure 1.9), as it was proved by Basu *et al.*[104]

Other archetypal MOF group based on Zr^{IV} ions belong to the called UiO-n (Universitetet i Oslo). One of the most remarkable materials of this MOF series is UiO-66. Due to its exceptional chemical and thermal stability, UiO-66 has become one of the most studied MOFs since its invention by Lillerud's group in 2008.[141–143] This MOF is constructed from 12-connected hexanuclear zirconium oxoclusters ($[Zr_6(\mu_3\text{-}O)_4(\mu_3\text{-}OH)_4]^{12+}$) and BDC linkers. It crystallizes as a face-centred-cubic structure of F m-3m symmetry with a lattice parameter of 20.7 Å. (Figure 1.12) The fcu topology generated from the connectivity between the inorganic and organic SBUs

gives rise to the generation of two types of pore-cages with tetrahedron and octahedron geometries of 7.5 Å, and 12 Å, respectively.

Similarly than other Zr^{IV} MOFs, UiO-66 can show linker and cluster defective sites that may reduce the average connectivity of the inorganic clusters down to 8. In contrast to MOF-808, these defective sites are randomly distributed along the ordered network, and act as preferential adsorption sites for negative species as chromate or arsenate oxyanions. What is more, functional groups can be easily introduced in its structure by selecting linkers with the same topology but including amino, nitro, hydroxy or thiol groups, among others (*i.e.* aminoterephtalate, nitroterephtalate or dihydroxyterephtalate linkers). These functionalities can serve as well as anchoring points for further functionalization of the framework through "click" chemistry.[144] Overall, the chemical encoding UiO-66 can endow the framework with different functions such as selective adsorption or improved photoreduction capacity. Just to mention an illustrating example, Shen *et al.*[145] tuned the Cr^{VI} to Cr^{III} photoreduction efficiency of UiO-66 by encoding amino groups into its framework (*i.e.* UiO-66-NH$_2$). Due to the typical yellow color of the amino-terephthalic acid, and of the UiO-66-NH$_2$ sample, the band-gap energy was shifted to the visible light region unlocking the capacity of the material to drive the hexavalent chromium photoreduction under sunlight illumination.

Finally, within the MIL-n (Materials of Institute Lavoisier) materials developed by Férey *et al.*[146,147], the titanium terephthalate MIL-125 stands out as the titanium homologue of the UiO-66 framework (Figure 1.12).[148] Ti-MIL-125 and Ti-MIL-125-NH$_2$ homologues have attracted lots of attention due to their strong photocatalytic activity and redox capability. Ti-MIL-125 shares the same topology and connectivity of their inorganic and organic building units with UiO-66. Therefore, similar tetrahedral and octahedral cages and surface areas have been reported for this compound as well.[143,148] The main difference between the Zr^{IV} and Ti^{IV} homologues lies in the characteristics of their inorganic nodes. MIL-125 is built up from a pseudo cubic arrangement of octameric wheels, built up from edge- or corner-sharing titanium octahedra, and terephthalate dianions leading to a three-dimensional periodic array of two types of hybrid cages with accessible pore diameters of 6.13 and

12.55 Å (Figure 1.12).[148] Overall, the connectivity of the Ti-oxo clusters (12-connected) and the organic linkers (2-connected) give rise to a fcu topology with a slightly distorted tetragonal I4/mmm symmetry in comparison to the cubic Fm-3m one of UiO-66.
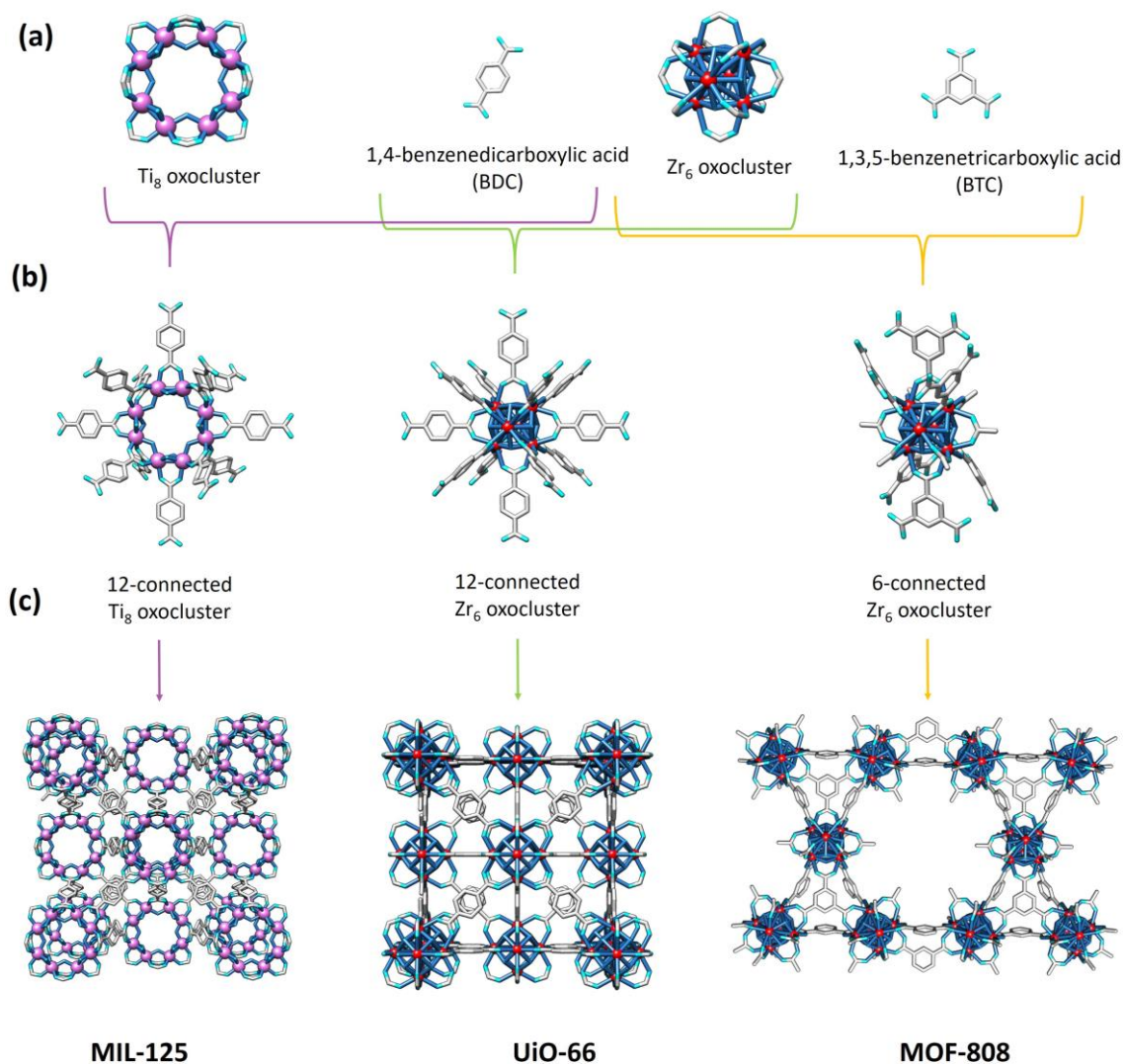
Figure 1.12. Schematic representation of (a) BDC, Zr hexanuclear cluster and BTC, (b) Cluster-linker connection in UiO-66 and MOF-808 and (c) Crystal structure of UiO-66 and MOF-808.

1.4. POLYMER@MOF COMPOSITES

Even given the structural, chemical and functional versatility of MOFs, their powdered nature is a handicap when exploring their potentials for water remediation. First, the recovery of a powder suspended in a water solution is time and energy consuming, and second, shaping and processing a powder to incorporate it in a final device is always a challenge. This is one of the main reasons that has boosted the research on the hybridization of MOF with magnetic nanoparticles, layered carbon-based materials (e.g. graphene, carbon nanotubes…), metal-oxide semiconductors (e.g. TiO$_2$), but specially, with polymeric materials.

Polymers are easy to process as membranes, filters, or spheres with controlled macro to mesoporous structures. So, the incorporation of MOFs into these polymeric matrixes opens the room to the engineering of micro to mesoporous materials combining the intrinsic versatility of MOFs, with the easy processability of polymers. All in all, polymer@MOF composites offer a functional solution for an easy recovery and activation of the MOF, but also the possibility to modify the polymeric matrix to make it functional during the adsorption and photocatalysis process. Nevertheless, the combination of these two materials is not straightforward, since their structuration need to be done in order to achieve the minimum inactivation of the MOF, while maintaining the overall properties of the polymeric host.

Therefore, immobilization in cost-effective polymeric membranes allows an easy application and recovery from liquid media for heterogeneous phase adsorption. The processing and operation technology of polymers as membranes or filters is fairly mature in the industry due to the advantages of high processability, economic feasibility, and low energy consumption these polymeric devices show.[149] However, the existing polymeric materials are far from being optimal: improvement in permeability is always at the expense of selectivity, and vice versa.

The processing versatility of polymer@MOF composites makes possible to shape them as Mixed Matrix Membrane (MMMs),[150–153] formed from an intimate and homogeneous dispersion of filler particles in a polymeric matrix. The polymer and filler properties affect the morphology, adsorptive or separation performance of these

composite materials.[154] Similarly than for classic membrane technologies, MMM can be classified according to their size selectivity as microfiltration (100 nm – 10 μm), ultrafiltration (2- 100 nm), nanofiltration (1-2 nm) or reverse osmosis (0.1 – 1 nm) devices. As the size selectivity of the membrane decreases, its permeation decreases and the operation costs increases. In contrast to an MMM like operation, where a flux of water is forced to cross membrane, polymer@MOF composites can be as well applied as a filtering technology that is able to extract the pollutant from the water media in static or dynamic conditions. This is the strategy that have been followed to remove or degrade inorganic metal ions or organic pollutants from water media in this thesis.

Regardless of whether polymer@MOF composites are ultimately intended for use as membranes or as filters, their processing strategies are similar. First, some of the most important variables to consider regarding the filler are its chemical structure, surface chemistry, particle size distribution and aspect ratio. Indeed, poor filler-polymer compatibilities and filler segregation or blocking of its porosity by the polymer are the main reasons why traditional zeolites-, silica- or activated carbons-polymer based membrane or filter technologies hardly achieve the final steps towards industrial implementation.[155] Fortunately, the use of MOFs in composite polymeric materials offers potential advantages because the control of the polymer-MOF interface interaction is easier to achieve than with classic materials. For instance, MOF's organic linkers can be chosen aiming to achieve an optimal affinity for the polymer chains, which is not possible or simple for other inorganic fillers[155]. In addition, the size, shape and chemical functionalities of their cavities can be easily adjusted by choosing the appropriate linkers in the synthesis[156] or by post-synthetic functionalization in order to tune the adsorption properties of the filler.[157]

The synthesis method of MOF containing polymeric membranes of filters has proved to be an easy and cheap procedure. Depending on the MOF and the polymer characteristics, and on the processing protocol, the polymer@MOF composite membranes or filters can be processed with precise macro to microporous interconnected structures able to selectively trap or separate certain ions or pollutants from the water media.

1.4.1. POLYMER@MOF COMPOSITES FOR HEAVY METAL ADSORPTION

In the last years, polymer@MOF composites have attracted considerable attention for heavy metal remediation. Both if the MOF is integrated within the polymer just by a process involving the physical mixture of two components, or chemical bonding between the MOF and the polymeric host is induced through a polymerization process, the performance of the composite systems has overcome the one obtained by the parent polymeric membranes or filters.[158–160]

As a given example, Gnanasekaran *et al.*[161] incorporated MOF-5 into three different polymeric membranes: polyether sulfone (PES); cellulose acetate (CA) and poly(vinylidene fluoride) (PVDF). The hydrophilic properties and performance of the composite membranes were enhanced by their hybridization with MOF-5, and the porosity and surface mean pore size was influenced too. Moreover, all the composites showed higher rejection efficiency of Cu^{II} and Co^{II} ions compared to neat polymeric membranes, which allowed to filtrate water without these heavy metals. Valadi *et al.*[162] also endowed chitosan natural polysaccharide with MOF-808, and they prove that the insertion of the MOF could significantly affect the adsorption behaviour of chitosan.

Other interesting example of MOF-based membrane technology for chromium separation was reported by M. Kalaj *et al.*[163] The copolymerization of a modified UiO-66-NH$_2$ MOF growing on polyamide fiber during an interfacial polymerization led to interesting hybrid materials.[150] The hybrid material demonstrated nearly an order of magnitude higher catalytic activity compared to MOFs that are physically entrapped, non-covalently, in nylon, thus highlighting the importance of MOF–polymer hybridization. Also, through photoinduced post-synthetic polymerization, UiO-66-NH$_2$ can be functionalized with polymerizable functional groups, and its subsequent copolymerization with monomers is easily induced by UV light under solvent-free and mild conditions. Because of the improved interaction between MOF particles and polymer chains, the resulting stand-alone and elastic MOF-based PSP-derived membranes possess crack-free and uniform structures and outstanding separation capabilities for Cr^{VI} ions from water.[164] Moreover, Miao *et al.*[165] developed a Fe-based polyacrylonitrile@MOF, immobilizing the MOF in nanofibers

by electrospinning. These composites succeeded in adsorbing Cr^{VI} in water and reducing it to Cr^{III}.

The MOF chemistry has been expanded exponentially during the last two decades, while the research background on polymeric materials give access to uncountable types of polymers to engineer MOF-composite materials. From synthetic to natural-based, a broad scope of polymers has been synthesized, functionalized, processed and applied for water remediation with outstanding success.[166–168] Indeed, most of the water filtering and membrane commercial technologies are based on polymeric materials. In this work, we have selected two archetypal polymers to develop MOF-composite devices, the poly(vinylidene fluoride) (PVDF) synthetic homologue and the natural derived chitin (CH) polysaccharide.

Poly(vinylidene fluoride)

Poly(vinylidene fluoride) (PVDF) is a thermoplastic fluoropolymer produced from the polymerization of vinylidene fluoride, with the chemical formula $-CH_2-CF_2-$ (Figure 1.13a). It has been known since the 1960s for its outstanding mechanical properties, which has extended its use to many research areas and industrial uses.[169]

PVDF and its copolymers have received great attention as a membrane material for water remediation applications, thanks to their chemical, thermal and mechanical stability, wide processing temperature and its aging resistance. What is more, these polymer shows a controlled porosity and pore size depending on its processing conditions, which has allowed the production of materials with different morphologies.[170–173]

However, PVDF is a hydrophobic material, and thus, the selection of a proper membrane preparation technique is of paramount importance. Of the several preparation methodologies that can be used to process PVDF membranes,[173] phase inversion ones are the most employed for water remediation applications. In fact, method generates PVDF-membranes with high porosities and suitable permeabilities. This PVDF phase separation processing can be induced thermally (TIPS) and using a non-solvent (NIPS).

In the last decades, various PVDF copolymers have been developed to improve certain properties and make this material more suitable for specific applications. Among others, poly(vinylidene fluoride-co-chlorotrifluoroethylene) (PVDF-CTFE), poly(vinylidene fluoride-trifluoroethylene) (PVDF-TrFE), and poly(vinylidene fluoride-co-hexafluoropropylene) (PVDF-HFP) have gained considerable attention due to their improved properties. PVDF-HFP (Figure 1.13b) is especially interesting because of its higher mechanical strength, increased free volume and lower crystallinity. As a consequence, it has been widely studied as a matrix to hold different nanoparticles.[174–177] Thanks to the structuration of the PVDF-HFP composites, they are able to immobilize varied nanoparticulated materials without leading to a fade of their efficiency to capture and separate both inorganic and organic pollutants.
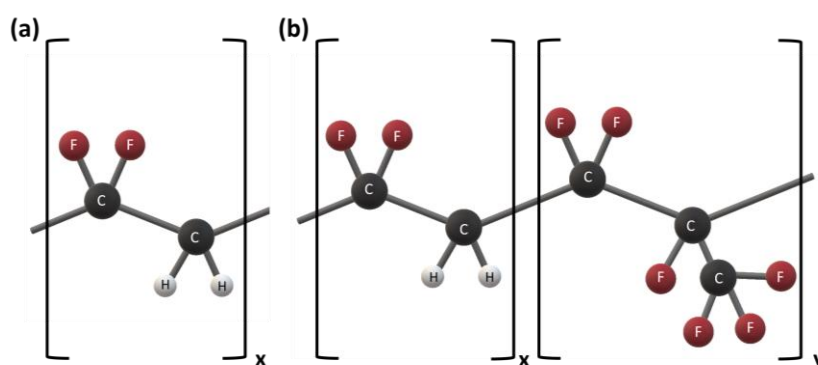
Figure 1.13. Schematic representation of the chain conformation of (a) PVDF and (b) PVDF-HFP.

Among others, Salazar *et al.*[174] developed nanocomposite membranes using PVDF-HFP as the matrix and Fe_3O_4 and $Y_2(CO_3)_3$ as fillers. The prepared nanocomposite membranes proved to be suitable for the removal from contaminated water of the most common and toxic forms of arsenic (As^{III} and As^V) in a wide range of concentrations and natural conditions. Moreover, Martins *et al.*[176] developed PVDF-HFP membranes with Au functionalized TiO_2 nanoparticles, which showed photocatalytic and adsorptive efficiency tested in norfloxacin and arsenic removal.

Metal-Organic Frameworks have also been introduced into PVDF-HFP matrixes for heavy metal remediation. As a given example, Queirós *et al.*[175] introduced MIL-88-B(Fe) and UiO-66-NH$_2$ into PVDF-HFP polymeric matrixes to develop composite systems able to function in close to real-conditions. They obtained membranes with well-defined and interconnected micrometric porous structures, which led to an efficient Cr^{VI} adsorption. Among the studied composites, the membranes containing UiO-66-NH$_2$ maintained the dual adsorption and reduction capacity of hexavalent chromium shown by the MOF material itself.

Chitin

Natural polymers, such as polysaccharides, proteins, and nucleic acids, show important advantages compared to synthetic polymers. These materials can be produced from renewable raw materials, are usually non-toxic and ideally biodegradable. Among these, chitin (CH) stands out for being the second most abundant natural biopolymer, only after cellulose.[178] It is obtained from marine media and especially from the exoskeleton of crustaceans or cartilage of molluscs.[179] It is formed by polymeric chains of N-acetyl glucosamine units (Figure 1.14), and it has an extremely chemical resistance, dissolving only under very harsh conditions,[180] which makes it ideal material for using it as polymeric matrix in water remediation membranes. What is more, the presence of acetamido and hydroxyl groups at the CH's molecular chains makes this natural polymer highly effective in interacting with organic pollutants.[181,182]
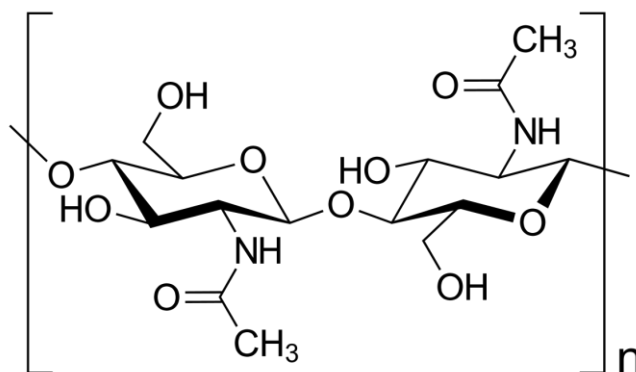
Figure 1.14. Schematic representation of the chain conformation of chitin.

CH@MOF composites have been fairly explored, with only one example reported in bibliography up to date. In this case, the copper-trimesate MOF (HKUST-1) was directly crystallized in the macro-mesoporous structure of the CH to generate a composite system able to trap ammonia efficiently from air both in static and dynamic conditions.[183] MOF hybridization of other polysaccharide far from CH have been revealed as a really interesting strategy to face water remediations, since the composite systems combine both the porosity and chemistry of both systems to trap organic and inorganic pollutants. Just to show some illustrating examples in this line, Ma *et al.*[184] directly growth the tetrahedral imidazolate framework TIF-A1 into chitosan matrix for Pb^{II} adsorption, and Ashour *et al.*[185] immobilized MIL-100(Fe) onto bacterial cellulose nanofibers to efficiently separate arsenic and Rhodamine B from aqueous solutions.

1.5. OBJECTIVES AND STRUCTURE OF THE THESIS

This thesis aims to explore the different functionalization strategies that can be applied to water stable Metal-Organic Frameworks, and their integration into final polymeric filtering devices, to face an efficient recovery, separation and photoreduction of heavy metals and phenolic pollutants from water. Within this general aim, four are the intermediate objectives of the work:

- To identify the best pre- and post-synthetic functionalization strategies of Zr^{VI} benchmark MOFs in order to improve the specific functions to adsorb and photo-reduce Cr^{VI} to Cr^{III}, or to selectively separate ions with different characteristics from complex multielement mixtures.

- To explore the oxidative enzymatic-like functionality of the MOFs to degrade organic persistent chemicals once specific metal ions have been immobilized with their pore space.

- To study the polymer@MOF composites, identifying how the insertion of the particles affects to the nano to microstructure of the composite and also to the adsorptive properties of the MOFs once immobilized in the polymeric matrix.

- To apply neutron scattering techniques to fully understand the underpinning structural and chemical characteristics of our MOF and polymer@MOF systems when applied for water remediation purposes.

To achieve these objectives, this thesis has been structured in six chapters. In Chapter 1, a general introduction to Metal-Organic Frameworks, together with the requirements they should have for their use in metal adsorption, separation and photoreduction processes is explained. What is more, different strategies to boost these functions are presented. In parallel, the general state of art in polymer@MOF composites for water remediation, specially focused on the polymeric materials studied in this thesis project is summarized.

In Chapter 2, the materials, reagents and general experimental procedures that have been systematically used in this work are described. In parallel, a brief description of

the fundamental basis, experimental conditions and equipment of the characterization methods and the experimental protocols have been summarized.

Chapter 3 explores the dual photoreductive and adsorptive capacity of different MOFs for Cr^{VI} remediation. This chapter is divided in two sections. In section 3.1, the functionality of UiO-66(-NH$_2$) and MIL-125 materials for this end is fully investigated. To this end, the effect of the defect chemistry of the UiO-66 materials and the particle size of MIL-125 on their adsorptive and photoreduction efficiencies has been studied. Section 3.2 focuses in the Multivariate Functionalization of UiO-66, combining linkers with –NH$_2$, -(OH)$_2$ and –NO$_2$ functionalities within its framework. We have unravelled the synergic effects of MTV chemistry for Cr^{VI} adsorption and photoreduction, but also, on the variation of the chemical stability of the framework.

Chapter 4 explores the post-synthetic modification of MOF-808 to improve its adsorption affinity towards anionic, and especially cationic ions with a broad variety of acidities. Once achieved the metal-immobilization, the capacity of the material to work as a bioinspired catalyst has been studied. It is also divided in two sections. In section 4.1, the incorporation of amino acids and natural acids to the pore space of MOF-808 *via* solvent assisted ligand incorporation (SALI) is explored. The impact of the chemical modifications to modulate the adsorption affinity over various metal cations and anions is studied. In section 4.2, the catalytic activity of copper-doped MOF-808@(amino) acid materials for phenolic compounds wet oxidation has been assessed. The impact of the coordination and clustering of copper ions installed in our biomimetic system into its catalytic efficiency has been investigated. Inelastic neutron scattering has helped to elucidate the amino acid anchoring process and the metal immobilization into the framework.

Chapter 5 is focused in the development of polymer@MOF composites. In section 5.1, PVDF-HPF@MOF membranes are developed, using two different phase inversion techniques (thermally induced phase separation (TIPS) and non-solvent induced phase separation (NIPS)) and inserting three different MOFs (MIL-125, UiO-66-NH$_2$, and MOF-808). The micro to nanostructure of the composites has been studied through different techniques, including small angle neutron scattering. The

adsorption capacities towards Cr^{VI} of the composite systems are studied and compared to the ones obtained for the MOF materials. What is more, the *in-situ* functionalization of PVDF-HPF@MOF-808 membranes with cysteine is explored, and their capacity to adsorb Hg^{II} has been determined. In section 5.2 the natural polymer chitin is used as matrix, and a material that can adsorb from heavy metal ions to large proteins or nanoparticles is developed.

The last chapter of this thesis, Chapter 6, is dedicated to the general conclusions derived from this work, together with the open perspectives to develop in the future.

1.6. REFERENCES

1   Barakat MA. New trends in removing heavy metals from industrial wastewater. *Arabian Journal of Chemistry* 2011; **4**: 361–377. [DOI: 10.1016/j.arabjc.2010.07.019]

2   Schindler DW. The Cumulative Effects of Climate Warming and Other Human Stresses on Canadian Freshwaters in the New Millennium. In: *Waters in Peril*. Springer, Boston, MA, 2001: 165–186.

3   Smith DW. Water and sanitation in developing countries: including health in the equation. *Environ Sci Technol* 2007; **41**: 17–24.

4   Bohn PW, Elimelech M, Georgiadis JG, Mariñas BJ, Mayes AM, Mayes AM. Science and technology for water purification in the coming decades. *Nanoscience and Technology: A Collection of Reviews from Nature Journals* 2009; **452**: 337–346. [DOI: 10.1142/9789814287005_0035]

5   Wang C, Tao S, Wei W, Meng C, Liu F, Han M. Multifunctional mesoporous material for detection, adsorption and removal of Hg2+ in aqueous solution. *J Mater Chem* 2010; **20**: 4635–4641. [DOI: 10.1039/c000315h]

6   Bolisetty S, Peydayesh M, Mezzenga R. Sustainable technologies for water purification from heavy metals: review and analysis. Chem Soc Rev. 2019; **48**: 463–487.

7   Zou Y, Wang X, Khan A, Wang P, Liu Y, Alsaedi A, Hayat T, Wang X. Environmental Remediation and Application of Nanoscale Zero-Valent Iron and Its Composites for the Removal of Heavy Metal Ions: A Review. *Environ Sci Technol* 2016; **50**: 7290–7304. [PMID: 27331413 DOI: 10.1021/acs.est.6b01897]

8   Li J, Fan Q, Wu Y, Wang X, Chen C, Tang Z, Wang X. Magnetic polydopamine decorated with Mg-Al LDH nanoflakes as a novel bio-based adsorbent for simultaneous removal of potentially toxic metals and anionic dyes. *J Mater Chem A Mater* 2016; **4**: 1737–1746. [DOI: 10.1039/c5ta09132b]

9   Srivastav AL, Ranjan M. Chapter 1 - Inorganic water pollutants. In: Devi P, Singh P, Kansal SK, editors. *Inorganic Pollutants in Water*. Elsevier, 2020: 1–15.

10   Li J, Wang X, Power E, Zhao G, Chai Z, Chen C, Alsaedi A, Hayat T, Wang X. Metal–organic framework-based materials: superior adsorbents for the capture of toxic and radioactive metal ions. *Chem Soc Rev* 2018; **47**: 2322. [DOI: 10.1039/c7cs00543a]

11   Smith AH, Goycolea M, Haque R, Biggs M lou. Marked Increase in Bladder and Lung Cancer Mortality in a Region of Northern Chile Due to Arsenic in

Drinking Water. *Am J Epidemiol* 1998; **147**: 660–669. [PMID: 9554605 DOI: 10.1093/OXFORDJOURNALS.AJE.A009507]

12   Mayer JE, Goldman RH. Arsenic and skin cancer in the USA: the current evidence regarding arsenic-contaminated drinking water. *Int J Dermatol* 2016; **55**: e585–e591. [PMID: 27420023 DOI: 10.1111/IJD.13318]

13   Rahman MM, Chowdhury UK, Mukherjee SC, Mondal BK, Paul K, Lodh D, Biswas BK, Chanda CR, Basu GK, Saha KC, Roy S, Das R, Palit SK, Quamruzzaman Q, Chakraborti D. Chronic Arsenic Toxicity in Bangladesh and West Bengal, India—A Review and Commentary. *J Toxicol Clin Toxicol* 2001; **39**: 683–700. [PMID: 11778666 DOI: 10.1081/CLT-100108509]

14   Winkel L, Berg M, Stengel C, Rosenberg T. Hydrogeological survey assessing arsenic and other groundwater contaminants in the lowlands of Sumatra, Indonesia. *Applied Geochemistry* 2008; **23**: 3019–3028. [DOI: 10.1016/J.APGEOCHEM.2008.06.021]

15   Tchounwou PB, Yedjou CG, Patlolla AK, Sutton DJ. Heavy Metal Toxicity and the Environment. In: *Molecular, Clinical and Envirnmental Toxicology*.2012: 133–164.

16   Lee YR, Yu K, Ravi S, Ahn WS. Selective Adsorption of Rare Earth Elements over Functionalized Cr-MIL-101. *ACS Appl Mater Interfaces* 2018; **10**: 23918–23927. [DOI: 10.1021/acsami.8b07130]

17   de Decker J, de Clercq J, Vermeir P, van der Voort P. Functionalized metal-organic-framework CMPO@MIL-101(Cr) as a stable and selective rare earth adsorbent. *J Mater Sci* 2016; **51**: 5019–5026. [DOI: 10.1007/s10853-016-9807-9]

18   G. Saiz P, Valverde A, Gonzalez-Navarrete B, Rosales M, Quintero YM, Fidalgo-Marijuan A, Orive J, Reizabal A, Larrea ES, Arriortua MI, Lanceros-Méndez S, García A, Fernández de Luis R. Modulation of the Bifunctional CrVI to CrIII Photoreduction and Adsorption Capacity in ZrIV and TiIV Benchmark Metal-Organic Frameworks. Catalysts. 2021; **11**: 51–60.

19   Naidu G, Ryu S, Thiruvenkatachari R, Choi Y, Jeong S, Vigneswaran S. A critical review on remediation, reuse, and resource recovery from acid mine drainage. *Environmental Pollution* 2019; **247**: 1110–1124. [PMID: 30823340 DOI: 10.1016/j.envpol.2019.01.085]

20   León R, Macías F, R. Cánovas C, Pérez-López R, Ayora C, Nieto JM, Olías M. Mine waters as a secondary source of rare earth elements worldwide: The case of the Iberian Pyrite Belt. *J Geochem Explor* 2021; **224**. [DOI: 10.1016/j.gexplo.2021.106742]

21   Peng Y, Huang H, Liu D, Zhong C. Radioactive Barium Ion Trap Based on Metal-Organic Framework for Efficient and Irreversible Removal of Barium

from Nuclear Wastewater. *ACS Appl Mater Interfaces* 2016; **8**: 8527–8535. [DOI: 10.1021/acsami.6b00900]

22 Lin S, Zhao Y, Bediako JK, Cho C, Sarkar AK, Lim C, Yun Y. Structure-controlled recovery of palladium (II) from acidic aqueous solution using metal-organic frameworks of MOF-802 , UiO-66 and MOF-808. *Chemical Engineering Journal* (e-pub ahead of print 2019; doi:10.1016/j.cej.2019.01.044).

23 Zha M, Liu J, Wong YL, Xu Z. Extraction of palladium from nuclear waste-like acidic solutions by a metal-organic framework with sulfur and alkene functions. *J Mater Chem A Mater* 2015; **3**: 3928–3934. [DOI: 10.1039/c4ta06678b]

24 Sun DT, Gasilova N, Yang S, Oveisi E, Queen WL. Rapid, Selective Extraction of Trace Amounts of Gold from Complex Water Mixtures with a Metal-Organic Framework (MOF)/Polymer Composite. *J Am Chem Soc* 2018; **140**: 16697–16703. [PMID: 30395464 DOI: 10.1021/jacs.8b09555]

25 Gonsioroski A, Mourikes VE, Flaws JA. Endocrine Disruptors in Water and Their Effects on the Reproductive System. *International Journal of Molecular Sciences 2020, Vol 21, Page 1929* 2020; **21**: 1929. [PMID: 32178293 DOI: 10.3390/IJMS21061929]

26 Loos R, Locoro G, Comero S, Contini S, Schwesig D, Werres F, Balsaa P, Gans O, Weiss S, Blaha L, Bolchi M, Gawlik BM. Pan-European survey on the occurrence of selected polar organic persistent pollutants in ground water. *Water Res* 2010; **44**: 4115–4126. [PMID: 20554303 DOI: 10.1016/J.WATRES.2010.05.032]

27 Jepson PD, Law RJ. Persistent pollutants, persistent threats Perspectives: Polychlorinated biphenyls remain a major threat to marine apex predators such as orcas. *Science (1979)* 2016; **352**: 1388–1389. [PMID: 27313021 DOI: 10.1126/SCIENCE.AAF9075/ASSET/06A63BB5-73F8-4E8B-829B-552CDA4E31C4/ASSETS/GRAPHIC/352_1388_F1.JPEG]

28 Li C, Yu S, Gu L, Han J, Dong H, Wang Y, Chen G. A New Graphitic Carbon Nitride/Horseradish Peroxidase Hybrid Nano–Bio Artificial Catalytic System for Unselective Degradation of Persistent Phenolic Pollutants. *Adv Mater Interfaces* 2018; **5**: 1801297. [DOI: 10.1002/ADMI.201801297]

29 Deng N, Li M, Zhao L, Lu C, de Rooy SL, Warner IM. Highly efficient extraction of phenolic compounds by use of magnetic room temperature ionic liquids for environmental remediation. *J Hazard Mater* 2011; **192**: 1350–1357. [PMID: 21783320 DOI: 10.1016/J.JHAZMAT.2011.06.053]

30 Chen GC, Shan XQ, Wang YS, Wen B, Pei ZG, Xie YN, Liu T, Pignatello JJ. Adsorption of 2,4,6-trichlorophenol by multi-walled carbon nanotubes as

affected by Cu(II). *Water Res* 2009; **43**: 2409–2418. [PMID: 19324390 DOI: 10.1016/J.WATRES.2009.03.002]

31   Mohammadi S, Kargari A, Sanaeepur H, Abbassian K, Najafi A, Mofarrah E. Phenol removal from industrial wastewaters: a short review. *Desalination Water Treat* 2015; **53**: 2215–2234. [DOI: 10.1080/19443994.2014.883327]

32   Pera-Titus M, García-Molina V, Baños MA, Giménez J, Esplugas S. Degradation of chlorophenols by means of advanced oxidation processes: A general review. *Appl Catal B* 2004; **47**: 219–256. [DOI: 10.1016/J.APCATB.2003.09.010]

33   Sabhi S, Kiwi J. Degradation of 2,4-dichlorophenol by immobilized iron catalysts. *Water Res* 2001; **35**: 1994–2002. [PMID: 11337846 DOI: 10.1016/S0043-1354(00)00460-7]

34   Cordova-Rosa SM, Dams RI, Cordova-Rosa E v., Radetski MR, Corrêa AXR, Radetski CM. Remediation of phenol-contaminated soil by a bacterial consortium and Acinetobacter calcoaceticus isolated from an industrial wastewater treatment plant. *J Hazard Mater* 2009; **164**: 61–66. [PMID: 18774223 DOI: 10.1016/J.JHAZMAT.2008.07.120]

35   Araña J, Tello-Rendón E, Doña-Rodríguez JM, Valdés Do Campo C, Herrera-Melidán JA, González-Díz O, Pérez-Peña J. Highly concentrated phenolic wastewater treatment by heterogeneous and homogeneous photocatalysis: mechanism study by FTIR-ATR. *Water Science and Technology* 2001; **44**: 229–236. [PMID: 11695463 DOI: 10.2166/WST.2001.0292]

36   sen Gupta S, Stadler M, Noser CA, Ghosh A, Steinhoff B, Lenoir D, Horwitz CP, Schramm KW, Collins TJ. Rapid total destruction of chlorophenols by activated hydrogen peroxide. *Science (1979)* 2002; **296**: 326–328. [PMID: 11951040 DOI: 10.1126/SCIENCE.1069297/ASSET/448C26EF-C511-4E8F-8930-1C6B2C6E6049/ASSETS/GRAPHIC/SE1420366003.JPEG]

37   Chaliha S, Bhattacharyya KG. Catalytic wet oxidation of 2-chlorophenol, 2,4-dichlorophenol and 2,4,6-trichlorophenol in water with Mn(II)-MCM41. *Chemical Engineering Journal* 2008; **139**: 575–588. [DOI: 10.1016/J.CEJ.2007.09.006]

38   Peng Y, Huang H, Zhang Y, Kang C, Chen S, Song L, Liu D, Zhong C. A versatile MOF-based trap for heavy metal ion capture and dispersion. *Nat Commun* 2018; **9**. [DOI: 10.1038/s41467-017-02600-2]

39   Huang N, Zhai L, Xu H, Jiang D. Stable Covalent Organic Frameworks for Exceptional Mercury Removal from Aqueous Solutions. *J Am Chem Soc* 2017; **139**: 2428–2434. [PMID: 28121142 DOI: 10.1021/jacs.6b12328]

40   Vilela D, Parmar J, Zeng Y, Zhao Y, Sánchez S. Graphene-Based Microbots for Toxic Heavy Metal Removal and Recovery from Water. *Nano Lett* 2016; **16**: 2860–2866. [PMID: 26998896 DOI: 10.1021/acs.nanolett.6b00768]

41   Li B, Zhang Y, Ma D, Shi Z, Ma S. Mercury nano-trap for effective and efficient removal of mercury(II) from aqueous solution. *Nat Commun* 2014; **5**. [PMID: 25410491 DOI: 10.1038/ncomms6537]

42   Lu X, Wang F, Li X, Shih K, Zeng EY. Adsorption and Thermal Stabilization of Pb 2+ and Cu 2+ by Zeolite. *Ind Eng Chem Res* 2016; **55**: 8767–8773. [DOI: 10.1021/acs.iecr.6b00896]

43   Liu B, Jian M, Liu R, Yao J, Zhang X. Highly efficient removal of arsenic(III) from aqueous solution by zeolitic imidazolate frameworks with different morphology. *Colloids Surf A Physicochem Eng Asp* 2015; **481**: 358–366. [DOI: 10.1016/j.colsurfa.2015.06.009]

44   Seliman AF, Lasheen YF, Youssief MAE, Shehata FA. Removal of some radionuclides from contaminated solution using natural clay: bentonite. *J Radioanal Nucl Chem* 2014; **300**: 969–979. [DOI: 10.1007/s10967-014-3027-z]

45   Krukowska J, Thomas P, Kołodyn D. Comparison of sorption and desorption studies of heavy metal ions from biochar and commercial active carbon. *Chemical Engeneering Journal* 2017; **307**: 353–363. [DOI: 10.1016/j.cej.2016.08.088]

46   Li J, Wang X, Power E, Zhao G, Chai Z, Chen C, Alsaedi A, Hayat T, Wang X. Metal–organic framework-based materials: superior adsorbents for the capture of toxic and radioactive metal ions. *Chem Soc Rev* 2018; **47**: 2322. [DOI: 10.1039/c7cs00543a]

47   Nosaka Y, Nosaka AY. Generation and Detection of Reactive Oxygen Species in Photocatalysis. *Chem Rev* 2017; **117**: 11302–11336. [PMID: 28777548 DOI: 10.1021/acs.chemrev.7b00161]

48   Martínez-Huitle CA, Ferro S. Electrochemical oxidation of organic pollutants for the wastewater treatment: direct and indirect processes. *Chem Soc Rev* 2006; **35**: 1324–1340. [DOI: 10.1039/b517632h]

49   Martínez-Huitle CA, Panizza M. Electrochemical oxidation of organic pollutants for wastewater treatment. *Curr Opin Electrochem* 2018; **11**: 62–71. [DOI: 10.1016/J.COELEC.2018.07.010]

50   Xu J, Li J, Wu F, Zhang Y. Rapid Photooxidation of As(III) through Surface Complexation with Nascent Colloidal Ferric Hydroxide. *Environ Sci Technol* 2014; **48**: 272–278. [DOI: 10.1021/es403667b]

51   Ding W, Wang Y, Yu Y, Zhang X, Li J, Wu F. Photooxidation of arsenic(III) to arsenic(V) on the surface of kaolinite clay. *J Environ Sci (China)* 2015; **36**: 29–37. [PMID: 26456603 DOI: 10.1016/J.JES.2015.03.017]

52   Ueng S-H, Fensterbank L, Lacôte E, Malacria M, Curran DP. Organic & Biomolecular Chemistry Radical reductions of alkyl halides bearing electron withdrawing groups with N-heterocyclic carbene boranes. *Org Biomol Chem* 2011; **9**: 3415–3420. [DOI: 10.1039/c0ob01075h]

53   Haibach MC, Stoltz BM, Grubbs RH. Catalytic Reduction of Alkyl and Aryl Bromides Using Propan-2-ol. *Angewandte Chemie Interanational Edition* 2017; **56**: 15123–15126. [DOI: 10.1002/ange.201708800]

54   Costa IGF, Terra NM, Cardoso VL, Batista FRX, Reis MHM. Photoreduction of chromium(VI) in microstructured ceramic hollow fibers impregnated with titanium dioxide and coated with green algae Chlorella vulgaris. *J Hazard Mater* 2019; **379**: 120837. [DOI: 10.1016/j.jhazmat.2019.120837]

55   Barrera-Díaz CE, Lugo-Lugo V, Bilyeu B. A review of chemical, electrochemical and biological methods for aqueous Cr(VI) reduction. *J Hazard Mater* 2012; **223–224**: 1–12. [PMID: 22608208 DOI: 10.1016/j.jhazmat.2012.04.054]

56   Wang CC, Du XD, Li J, Guo XX, Wang P, Zhang J. Photocatalytic Cr(VI) reduction in metal-organic frameworks: A mini-review. *Appl Catal B* 2016; **193**: 198–216. [DOI: 10.1016/j.apcatb.2016.04.030]

57   Serpone N, Emeline AV. Semiconductor Photocatalysis □ Past, Present, and Future Outlook. *J Phys Chem Lett* 2012; **3**: 673–677. [DOI: 10.1021/jz300071j]

58   Ramchiary A. Metal-oxide semiconductor photocatalysts for the degradation of organic contaminants. In: *Handbook of Smart Photocatalytic Materials*. Elsevier, 2020: 23–38.

59   Ates M, Yılmaz E, Tanaydın MK. Challenges, novel applications, and future prospects of chalcogenides and chalcogenide-based nanomaterials for photocatalysis. In: *Chalcogenide-Based Nanomaterials as Photocatalysts*. Elsevier, 2021: 307–337.

60   Silva-Gaspar B, Martinez-Franco R, Pirngruber G, Fécant A, Diaz U, Corma A. Open-Framework Chalcogenide Materials - from isolated clusters to highly ordered structures - and their photocalytic applications. *Coord Chem Rev* 2022; **453**: 214243. [DOI: 10.1016/J.CCR.2021.214243]

61   Schwinghammer K, Tuffy B, Mesch MB, Wirnhier E, Martineau C, Taulelle F, Schnick W, Senker J, Lotsch B v, Schwinghammer K, Tuffy B, Lotsch B v, Wirnhier E, Schnick W, Mesch MB, Senker J, Martineau C, Taulelle F. Triazine-based Carbon Nitrides for Visible-Light-Driven Hydrogen Evolution.

Angewandte Chemie International Edition 2013; **52**: 2435–2439. [DOI: 10.1002/ANIE.201206817]

62   Jeon J-P, Kweon H, Jang J, Ju MJ, Baek J-B, Jeon J-P, Kweon DH, Jang BJ, Ju MJ, Baek J-B. Enhancing the Photocatalytic Activity of TiO2 Catalysts. *Adv Sustain Syst* 2020; **4**: 2000197. [DOI: 10.1002/ADSU.202000197]

63   Bavykina A, Kolobov N, Khan S, Bau JA, Ramirez A, Gascon J. Metal−Organic Frameworks in Heterogeneous Catalysis: Recent Progress, New Trends, and Future Perspectives. *Chem Rev* 2020; **120**: 8468–8535. [DOI: 10.1021/acs.chemrev.9b00685]

64   Ji Z, Wang H, Canossa S, Wuttke S, Yaghi OM. Pore Chemistry of Metal–Organic Frameworks. *Adv Funct Mater* 2020; **30**: 2000238. [DOI: https://doi.org/10.1002/adfm.202000238]

65   Larrea ES, Fernández De Luis R, Orive J, Iglesias M, Arriortua MI. Mixed Metal-Organic Framework as a Heterogeneous Catalyst. *Eur J Inorg Chem* 2015; **2015**. [DOI: 10.1002/ejic.201500431]

66   Freund R, Canossa S, Cohen SM, Yan W, Deng H, Guillerm V, Eddaoudi M, Madden DG, Fairen-Jimenez D, Lyu H, Macreadie LK, Ji Z, Zhang Y, Wang B, Haase F, Wöll C, Zaremba O, Andreo J, Wuttke S, Diercks CS. 25 years of Reticular Chemistry. *Angewandte Chemie International Edition* 2021; **60**: 23946–23974. [DOI: 10.1002/anie.202101644]

67   Valverde A, Gonçalves R, Silva MM, Wuttke S, Fidalgo-Marijuan A, Costa CM, Vilas-Vilela JL, Laza JM, Arriortua MI, Lanceros-Méndez S, Fernández de Luis R. Metal–Organic Framework Based PVDF Separators for High Rate Cycling Lithium-Ion Batteries. *ACS Appl Energy Mater* 2020; **3**: 11907–11919. [DOI: 10.3390/catal11010051]

68   Assi H, Mouchaham G, Steunou N, Devic T, Serre C. Titanium coordination compounds: From discrete metal complexes to metal-organic frameworks. *Chem Soc Rev* 2017; **46**: 3431–3452. [PMID: 28537319 DOI: 10.1039/c7cs00001d]

69   Mouchaham G, Wang S, Serre C. The Stability of Metal-Organic Frameworks. *Metal-Organic Frameworks* 2018; : 1–28. [DOI: 10.1002/9783527809097.ch1]

70   Lin KA, Chen S, Jochems AP. Zirconium-based metal organic frameworks : Highly selective adsorbents for removal of phosphate from water and urine. *Mater Chem Phys* 2015; : 1–9. [DOI: 10.1016/j.matchemphys.2015.04.021]

71   Freund R, Zaremba O, Arnauts G, Ameloot R, Skorupskii G, Dincă M, Bavykina A, Gascon J, Ejsmont A, Gościańska J, Kalmutzki M, Lächelt U, Ploetz E, Diercks C, Wuttke S. The Current Status of MOF and COF Applications. *Angewandte Chemie International Edition* 2021; **60**: 23975–24001. [DOI: 10.1002/anie.202106259]

72   Gropp C, Canossa S, Wuttke S, Gándara F, Li Q, Gagliardi L, Yaghi OM. Standard Practices of Reticular Chemistry. *ACS Cent Sci* 2020; **6**: 1255–1273. [DOI: 10.1021/acscentsci.0c00592]

73   Rocío-Bautista P, Taima-Mancera I, Pasán J, Pino V. Metal-Organic Frameworks in Green Analytical Chemistry. *Separations* 2019; **6**. [DOI: 10.3390/separations6030033]

74   Dey C, Kundu T, Biswal BP, Mallick A, Banerjee R. Crystalline metal-organic frameworks (MOFs): synthesis, structure and function. *Acta Crystallogr B Struct Sci Cryst Eng Mater* 2014; **70**: 3–10. [DOI: 10.1107/s2052520613029557]

75   Yaghi OM, Li G, Li H. Selective binding and removal of guests in a microporous metal-organic framework. *Nature* 1995; **378**: 703–706.

76   Férey C, Mellot-Draznieks C, Serre C, Millange F, Dutour J, Surblé S, Margiolaki I. Chemistry: A chromium terephthalate-based solid with unusually large pore volumes and surface area. *Science (1979)* 2005; **309**: 2040–2042. [PMID: 16179475 DOI: 10.1126/SCIENCE.1116275/SUPPL_FILE/FEREY-SOM.PDF]

77   Su Y, Otake K-I, Zheng J-J, Horike S, Kitagawa S, Cheng Gu ✉ &. Separating water isotopologues using diffusion-regulatory porous materials. *Nature* 2022; **611**: 289–294. [PMID: 36352136 DOI: 10.1038/s41586-022-05310-y]

78   Feng M, Zhang P, Zhou HC, Sharma VK. Water-stable metal-organic frameworks for aqueous removal of heavy metals and radionuclides: A review. *Chemosphere* 2018; **209**: 783–800. [PMID: 29960946 DOI: 10.1016/J.CHEMOSPHERE.2018.06.114]

79   Kobielska PA, Howarth AJ, Farha OK, Nayak S. Metal–organic frameworks for heavy metal removal from water. *Coord Chem Rev* 2018; **358**: 92–107. [DOI: 10.1016/J.CCR.2017.12.010]

80   Ahmadijokani F, Tajahmadi S, Bahi A, Molavi H, Rezakazemi M, Ko F, Aminabhavi TM, Arjmand M. Ethylenediamine-functionalized Zr-based MOF for efficient removal of heavy metal ions from water. *Chemosphere* 2021; **264**. [PMID: 33065327 DOI: 10.1016/J.CHEMOSPHERE.2020.128466]

81   Manousi N, Giannakoudakis DA, Rosenberg E, Zachariadis GA, Samanidou V, Deliyanni E. Extraction of Metal Ions with Metal-Organic Frameworks. *Molecules* 2019; **24**: 4605. [DOI: 10.3390/molecules24244605]

82   Burtch NC, Jasuja H, Walton KS. Water stability and adsorption in metal-organic frameworks. *Chem Rev* 2014; **114**: 10575–10612. [PMID: 25264821 DOI: 10.1021/cr5002589]

83   Furukawa H, Gándara F, Zhang YB, Jiang J, Queen WL, Hudson MR, Yaghi OM. Water adsorption in porous metal-organic frameworks and related materials. *J Am Chem Soc* 2014; **136**: 4369–4381. [DOI: 10.1021/ja500330a]

84   Sarker M, Song JY, Jhung SH. Adsorption of organic arsenic acids from water over functionalized metal-organic frameworks. *J Hazard Mater* 2017; **335**: 162–169. [DOI: 10.1016/j.jhazmat.2017.04.044]

85   Chen L, Bai Z, Zhu L, Zhang L, Cai Y, Li Y, Liu W, Wang Y, Chen L, Diwu J, Wang J, Chai Z, Wang S. Ultrafast and Efficient Extraction of Uranium from Seawater Using an Amidoxime Appended Metal − Organic Framework. *ACS Appl Energy Mater* 2017; **9**: 32446–32451. [DOI: 10.1021/acsami.7b12396]

86   Demir S, Brune NK, Van Humbeck JF, Mason JA, Plakhova T V., Wang S, Tian G, Minasian SG, Tyliszczak T, Yaita T, Kobayashi T, Kalmykov SN, Shiwaku H, Shuh DK, Long JR. Extraction of lanthanide and actinide ions from aqueous mixtures using a carboxylic acid-functionalized porous aromatic framework. *ACS Cent Sci* 2016; **2**: 253–265. [DOI: 10.1021/acscentsci.6b00066]

87   Wang C, Liu X, Keser Demir N, Chen JP, Li K. Applications of water stable metal-organic frameworks. *Chem Soc Rev* 2016; **45**: 5107–5134. [DOI: 10.1039/c6cs00362a]

88   Bai Y, Dou Y, Xie LH, Rutledge W, Li JR, Zhou HC. Zr-based metal-organic frameworks: Design, synthesis, structure, and applications. *Chem Soc Rev* 2016; **45**: 2327–2367. [PMID: 26886869 DOI: 10.1039/c5cs00837a]

89   Lee YJ, Chang YJ, Lee DJ, Hsu JP. Water stable metal-organic framework as adsorbent from aqueous solution: A mini-review. *J Taiwan Inst Chem Eng* 2018; **93**: 176–183. [DOI: 10.1016/J.JTICE.2018.06.035]

90   Yuan S, Qin JS, Lollar CT, Zhou HC. Stable Metal-Organic Frameworks with Group 4 Metals: Current Status and Trends. *ACS Cent Sci* 2018; **4**: 440–450. [PMID: 29721526 DOI: 10.1021/acscentsci.8b00073]

91   Mouchaham G, Wang S, Serre C. The Stability of Metal–Organic Frameworks. In: Garcia H, Navalón S, editors. *Metal-Organic Frameworks: Applications in Separations and Catalysis, First Edition*. Wiley, 2018: 1.

92   Valenzano L, Civalleri B, Chavan S, Bordiga S, Nilsen MH, Jakobsen S, Lillerud KP, Lamberti C. Disclosing the complex structure of UiO-66 metal organic framework: A synergic combination of experiment and theory. *Chemistry of Materials* 2011; **23**: 1700–1718. [DOI: 10.1021/cm1022882]

93   Mondloch JE, Katz MJ, Planas N, Semrouni D, Gagliardi L, Hupp JT, Farha OK. Are Zr 6-based MOFs water stable? Linker hydrolysis vs. capillary-force-driven channel collapse †. *Chem Commun* 2014; **50**: 8944. [DOI: 10.1039/c4cc02401j]

94   Yuan S, Feng L, Wang K, Pang J, Bosch M, Lollar C, Sun Y, Qin J, Yang X, Zhang P, Wang Q, Zou L, Zhang Y, Zhang L, Fang Y, Li J, Zhou H-C, Yuan S, Feng L, Wang K, Pang J, Bosch M, Lollar C, Sun Y, Qin J, Yang X, Zhang P, Wang Q, Zou L, Zhang Y, Zhang L, Fang Y, Li J, Zhou H. Stable Metal-Organic Frameworks: Design, Synthesis, and Applications. *Advanced Materials* 2018; **30**: 704303–704338. [DOI: 10.1002/adma.201704303]

95   Chowdhury S, Mishra R, Saha P, Kushwaha P. Adsorption thermodynamics, kinetics and isosteric heat of adsorption of malachite green onto chemically modified rice husk. *Desalination* 2011; **265**: 159–168. [DOI: 10.1016/J.DESAL.2010.07.047]

96   Allen SJ, Mckay G, Porter JF. Adsorption isotherm models for basic dye adsorption by peat in single and binary component systems. *J Colloid Interface Sci* 2004; **280**: 322–333. [DOI: 10.1016/j.jcis.2004.08.078]

97   sen Gupta S, Bhattacharyya KG. Kinetics of adsorption of metal ions on inorganic materials: A review. *Adv Colloid Interface Sci* 2011; **162**: 39–58. [DOI: 10.1016/J.CIS.2010.12.004]

98   Howarth AJ, Katz MJ, Wang TC, Platero-Prats AE, Chapman KW, Hupp JT, Farha OK. High Efficiency Adsorption and Removal of Selenate and Selenite from Water Using Metal-Organic Frameworks. *J Am Chem Soc* 2015; **137**: 7488–7494. [PMID: 26000611 DOI: 10.1021/jacs.5b03904]

99   Zhang N, Gao C, Xiong Y. Defect engineering: A versatile tool for tuning the activation of key molecules in photocatalytic reactions. *Journal of Energy Chemistry* 2019; **37**: 43–57. [DOI: 10.1016/J.JECHEM.2018.09.010]

100   Sholl DS, Lively RP. Defects in Metal−Organic Frameworks: Challenge or Opportunity? *J Phys Chem Lett* 2015; **6**: 3437–3444. [DOI: 10.1021/acs.jpclett.5b01135]

101   Xiang W, Zhang Y, Chen Y, Liu C-J, Tu X. Synthesis, characterization and application of defective metal-organic frameworks: current status and perspectives. *J Mater Chem A Mater* 2020; **8**: 21526–21546. [DOI: 10.1039/d0ta08009h]

102   Platero-Prats AE, Mavrandonakis A, Gallington LC, Liu Y, Hupp JT, Farha OK, Cramer CJ, Chapman KW. Structural Transitions of the Metal-Oxide Nodes within Metal-Organic Frameworks: On the Local Structures of NU-1000 and UiO-66. *J Am Chem Soc* 2016; **138**: 4178–4185. [DOI: 10.1021/JACS.6B00069/SUPPL_FILE/JA6B00069_SI_002.CIF]

103   Shearer GC, Chavan S, Ethiraj J, Vitillo JG, Svelle S, Olsbye U, Lamberti C, Bordiga S, Lillerud KP. Tuned to perfection: Ironing out the defects in metal-organic framework UiO-66. *Chemistry of Materials* 2014; **26**: 4068–4071. [DOI: 10.1021/cm501859p]

104 Basu O, Mukhopadhyay S, Laha S, Das SK. Defect Engineering in a Metal − Organic Framework System to Achieve Super-Protonic Conductivity. *Chemistry of Materials* 2022; **34**: 6734–6734. [DOI: 10.1021/acs.chemmater.2c00654]

105 Cai G, Jiang H-L, Cai] G, Jiang H-L. Hierarchically Porous MOFs A Modulator-Induced Defect-Formation Strategy to Hierarchically Porous Metal-Organic Frameworks with High Stability. *Angew Chem Int Ed* 2017; **56**: 563–567. [DOI: 10.1002/ange.201610914]

106 Mu X, Jiang J, Chao F, Lou Y, Chen J. Ligand modification of UiO-66 with an unusual visible light photocatalytic behavior for RhB degradation. *Dalton Transactions* 2018; **47**: 1895–1902. [PMID: 29340397 DOI: 10.1039/c7dt04477a]

107 Musho T, Li J, Wu N. Band gap modulation of functionalized metal-organic frameworks. *Phys Chem Chem Phys* 2364; **16**: 23646–23653. [DOI: 10.1039/c4cp03110e]

108 Yee K-K, Reimer N, Liu J, Cheng S-Y, Yiu S-M, Weber J, Stock N, Xu Z. Effective Mercury Sorption by Thiol-Laced Metal−Organic Frameworks: in Strong Acid and the Vapor Phase. *J Am Chem Soc* 2013; **135**: 47. [DOI: 10.1021/ja400212k]

109 Karagiaridi O, Bury W, Mondloch JE, Hupp JT, Farha OK. Solvent-assisted linker exchange: An alternative to the de novo synthesis of unattainable metal-organic frameworks. *Angewandte Chemie - International Edition* 2014; **53**: 4530–4540. [DOI: 10.1002/anie.201306923]

110 Islamoglu T, Goswami S, Li Z, Howarth AJ, Farha OK, Hupp JT. Postsynthetic Tuning of Metal−Organic Frameworks for Targeted Applications. *Acc Chem Res* 2017; **50**: 805–813. [DOI: 10.1021/acs.accounts.6b00577]

111 Patial S, Raizada P, Hasija V, Singh P, Thakur VK, Nguyen V-H. Recent advances in photocatalytic multivariate metal organic frameworks-based nanostructures toward renewable energy and the removal of environmental pollutants. *Mater Today Energy* 2021; **19**: 100589. [DOI: https://doi.org/10.1016/j.mtener.2020.100589]

112 Luo TY, Liu C, Gan XY, Muldoon PF, Diemler NA, Millstone JE, Rosi NL. Multivariate Stratified Metal-Organic Frameworks: Diversification Using Domain Building Blocks. *J Am Chem Soc* 2019; **141**: 2161–2168. [PMID: 30636428 DOI: 10.1021/jacs.8b13502]

113 Dong Z, Sun Y, Chu J, Zhang X, Deng H. Multivariate Metal-Organic Frameworks for Dialing-in the Binding and Programming the Release of Drug Molecules. *J Am Chem Soc* 2017; **139**: 14209–14216. [PMID: 28898070 DOI: 10.1021/jacs.7b07392]

114 Osborn Popp TM, Yaghi OM. Sequence-dependent materials. *Acc Chem Res* 2017; **50**: 532–534. [PMID: 28945416 DOI: 10.1021/acs.accounts.6b00529]

115 Deng H, Doonan CJ, Furukawa H, Ferreira RB, Towne J, Knobler CB, Wang B, Yaghi OM. Multiple functional groups of varying ratios in metal-organic frameworks. *Science (1979)* 2010; **327**: 846–850. [PMID: 20150497 DOI: 10.1126/science.1181761]

116 Mon M, Bruno R, Tiburcio E, Viciano-Chumillas M, Kalinke LHG, Ferrando-Soria J, Armentano D, Pardo E. Multivariate Metal–Organic Frameworks for the Simultaneous Capture of Organic and Inorganic Contaminants from Water. *J Am Chem Soc* 2019; **141**: 13601–13609. [DOI: 10.1021/jacs.9b06250]

117 Wang T, Tian B, Han B, Ma D, Sun M, Hanif A, Xia D, Shang J. Recent Advances on Porous Materials for Synergetic Adsorption and Photocatalysis. *Energy & Environmental Materials* 2022; **5**: 711–730. [DOI: 10.1002/eem2.12229]

118 Zhang X, Tong S, Huang D, Liu Z, Shao B, Liang Q, Wu T, Pan Y, Huang J, Liu Y, Cheng M, Chen M. Recent advances of Zr based metal organic frameworks photocatalysis: Energy production and environmental remediation. *Coord Chem Rev* 2021; **448**. [DOI: 10.1016/J.CCR.2021.214177]

119 Azimi A, Azari A, Rezakazemi M, Ansarpour M. Removal of Heavy Metals from Industrial Wastewaters: A Review. *ChemBioEng Reviews* 2017; **4**: 37–59. [DOI: 10.1002/cben.201600010]

120 Joseph L, Jun BM, Flora JRV, Park CM, Yoon Y. Removal of heavy metals from water sources in the developing world using low-cost materials: A review. *Chemosphere* 2019; **229**: 142–159. [PMID: 31078029 DOI: 10.1016/J.CHEMOSPHERE.2019.04.198]

121 Tachikawa T, Choi JR, Fujitsuka M, Majima T. Photoinduced Charge-Transfer Processes on MOF-5 Nanoparticles: Elucidating Differences between Metal-Organic Frameworks and Semiconductor Metal Oxides. *The Journal of Physical Chemistry C* 2008; **112**: 14090–14101. [DOI: 10.1021/jp803620v]

122 Guo X, Liu L, Xiao Y, Qi Y, Duan C, Zhang F. Band gap engineering of metal-organic frameworks for solar fuel productions. *Coord Chem Rev* 2021; **435**. [DOI: 10.1016/J.CCR.2021.213785]

123 Alvaro M, Carbonell E, Ferrer B, Llabrøs I Xamena FX, Garcia H. Semiconductor Behavior of a Metal-Organic Framework (MOF). *Chemistry A European Journal* 2007; **13**: 5106–5112. [DOI: 10.1002/chem.200601003]

124 Fuchs A, Mannhardt P, Hirschle P, Wang H, Zaytseva I, Ji Z, Yaghi O, Wuttke S, Ploetz E, Fuchs A, Mannhardt P, Hirschle P, Zaytseva I, Wuttke S, Ploetz E, Wang H, Ji Z, Yaghi O. Single Crystals Heterogeneity Impacts the Intrinsic and

Extrinsic Properties of Metal-Organic Frameworks. *Advaned Materials* 2022; **34**: 2104530. [DOI: 10.1002/adma.202104530]

125 Shen Y, Pan T, Wang L, Ren Z, Zhang W, Huo F, Shen Y, Pan T, Wang L, Ren Z, Zhang W, Huo F. Programmable Logic in Metal–Organic Frameworks for Catalysis. *Advanced Materials* 2021; **33**: 2007442. [PMID: 34050572 DOI: 10.1002/ADMA.202007442]

126 Li Z, Wang L, Qin L, Lai C, Wang Z, Zhou M, Xiao L, Liu S, Zhang M. Recent advances in the application of water-stable metal-organic frameworks: Adsorption and photocatalytic reduction of heavy metal in water. *Chemosphere* 2021; **285**. [PMID: 34273693 DOI: 10.1016/J.CHEMOSPHERE.2021.131432]

127 Schrimpf W, Jiang J, Ji Z, Hirschle P, Lamb DC, Yaghi OM, Wuttke S. Chemical diversity in a metal-organic framework revealed by fluorescence lifetime imaging. *Nat Commun* 2018; **9**: 1647. [DOI: 10.1038/s41467-018-04050-w]

128 al Danaf N, Schrimpf W, Hirschle P, Lamb DC, Ji Z, Wuttke S. Linker Exchange via Migration along the Backbone in Metal− Organic Frameworks. *Cite This: J Am Chem Soc* 2021; **143**: 10541–10546. [DOI: 10.1021/jacs.1c04804]

129 Mandal S, Natarajan S, Mani P, Pankajakshan A, Mandal S, Mani P, Pankajakshan A, Natarajan S. Post-Synthetic Modification of Metal-Organic Frameworks Toward Applications. *Adv Funct Mater* 2021; **31**: 2006291. [DOI: 10.1002/adfm.202006291]

130 Hao J, Xu X, Fei H, Li L, Yan B, Hao J, Xu X, Fei H, Li L, Yan B. Functionalization of Metal-Organic Frameworks for Photoactive Materials. *Advanced Materials* 2018; **30**: 1705634-. [DOI: 10.1002/adma.201705634]

131 G. Saiz, P., Iglesias, N., Gonzalez-Navarrete, B., Rosales, M., Quintero, Y. M., Reizabal, A., Orive, J., Fidalgo-Marijuan, A., Lanceros-Mendez, S., Arriortua, M. I.,& Fernandez de Luis R. Chromium speciation in zirconium-based metal – organic frameworks for environmental remediation. *Chemistry—A European Journal* 2020; **26**: 1–13. [DOI: 10.1002/chem.202001435]

132 Ji Z, Freund R, Diercks CS, Hirschle P, Yaghi OM, Wuttke S, Ji Z, Diercks CS, Yaghi OM, Freund R, Hirschle P, Wuttke S. From Molecules to Frameworks to Superframework Crystals. *Advanced Materials* 2021; **33**: 2103808. [DOI: 10.1002/adma.202103808]

133 Eddaoudi M, Li H, Yaghi OM. Highly Porous and Stable Metal-Organic Frameworks: Structure Design and Sorption Properties. *J Am Chem Soc* 2000; **122**: 1391–1397. [DOI: 10.1021/ja9933386]

134 Li H, Eddaoudi M, O'Keeffe M, Yaghi OM. Design and synthesis of an exceptionally stable and highly porous metal-organic framework. *Nature* 1999; **402**: 276–279.

135 Kim J, Chen B, Reineke TM, Li H, Eddaoudi M, Moler DB, O'Keeffe M, Yaghi OM. Assembly of metal-organic frameworks from large organic and inorganic secondary building units: New examples and simplifying principles for complex structures. *J Am Chem Soc* 2001; **123**: 8239–8247. [PMID: 11516275 DOI: 10.1021/ja010825o]

136 Liang W, Chevreau H, Ragon F, Southon PD, Peterson VK, D DM. Tuning pore size in a zirconium–tricarboxylatemetal–organic framework. *CrystEngComm* 2014; **16**: 6530–6533. [DOI: 10.1039/c4ce01031k]

137 Kandiah M, Nilsen MH, Usseglio S, Jakobsen S, Olsbye U, Tilset M, Larabi C, Quadrelli EA, Bonino F, Lillerud KP. Synthesis and stability of tagged UiO-66 Zr-MOFs. *Chemistry of Materials* 2010; **22**: 6632–6640. [DOI: 10.1021/cm102601v]

138 Chen S, Feng F, Li S, Li X, Shu L. Metal-organic framework DUT-67 (Zr) for adsorptive removal of trace Hg and CH 3 Hg in water. *Chemical Speciation & Bioavailability* 2018; **00**: 1–8. [DOI: 10.1080/09542299.2018.1509020]

139 Aunan E, Affolter CW, Olsbye U, Lillerud KP. Modulation of the Thermochemical Stability and Adsorptive Properties of MOF-808 by the Selection of Non-structural Ligands. *Cite This: Chem Mater* 2021; **33**: 1471–1476. [DOI: 10.1021/acs.chemmater.0c04823]

140 Zhang W, Bu A, Ji Q, Min L, Zhao S, Wang Y, Chen J. pKa-directed incorporation of phosphonates into mof-808 via ligand exchange: Stability and adsorption properties for uranium. *ACS Appl Mater Interfaces* 2019; **11**: 33931–33940. [PMID: 31409065 DOI: 10.1021/acsami.9b10920]

141 Destefano MR, Islamoglu T, Garibay SJ, Hupp JT, Farha OK. Room-Temperature Synthesis of UiO-66 and Thermal Modulation of Densities of Defect Sites. *Chemistry of Materials* 2017; **29**: 1357–1361. [DOI: 10.1021/acs.chemmater.6b05115]

142 Garibay SJ, Cohen SM. Isoreticular synthesis and modification of frameworks with the UiO-66 topologyw. *Chemical Communications* 2010; **46**: 7700–7702. [DOI: 10.1039/c0cc02990d]

143 Cavka JH, Jakobsen S, Olsbye U, Guillou N, Lamberti C, Bordiga S, Lillerud KP. A new zirconium inorganic building brick forming metal organic frameworks with exceptional stability. *J Am Chem Soc* 2008; **130**: 13850–13851.

144 Zou XN, Zhang D, Xie Y, Luan TX, Li W, Li L, Li PZ. High Enhancement in Proton Conductivity by Incorporating Sulfonic Acids into a Zirconium-Based

Metal-Organic Framework via 'click' Reaction. *Inorg Chem* 2021; **60**: 10089–10094. [PMID: 34180672 DOI: 10.1021/ACS.INORGCHEM.1C01191/ASSET/IMAGES/LARGE/IC1C01191_0004.JPEG]

145   Shen L, Liang S, Wu W, Liang R, Wu L. Multifunctional NH2-mediated zirconium metal-organic framework as an efficient visible-light-driven photocatalyst for selective oxidation of alcohols and reduction of aqueous Cr(vi). *Dalton Transactions* 2013; **42**: 13649–13657. [PMID: 23903996 DOI: 10.1039/c3dt51479j]

146   Serre C, Millange F, Thouvenot C, Gardant N, Pellé F, Férey G. Synthesis, characterisation and luminescent properties of a new three-dimensional lanthanide trimesate: M((C 6 H 3)-(CO 2) 3) (M ~ Y, Ln) or MIL-78. *J Mater Chem* 2004; **14**: 1540–1543. [DOI: 10.1039/b312425h]

147   Millange F, Serre C, Férey G. Synthesis, structure determination and properties of MIL-53as and MIL-53ht: the first CrIII hybrid inorganic-organic microporous solids: CrIII (OH)·{O 2 C-C 6 H 4-CO 2 }·{HO 2 C-C 6 H 4-CO 2 H} x †. *Chemical Communications* 2002; : 822–823. [DOI: 10.1039/b201381a]

148   Dan-hardi, M., & Serre C. A new photoactive crystalline highly porous titanium (IV) dicarboxylate. *J Am Chem Soc* 2009; **131**: 10857–10859. [DOI: 10.1021/ja903726m]

149   Ulbricht M. Advanced functional polymer membranes. *Polymer (Guildf)* 2006; **47**: 2217–2262. [DOI: 10.1016/j.polymer.2006.01.084]

150   Gutiérrez-Serpa A, Kundu T, Pasán J, Jiménez-Abizanda AI, Kaskel S, Senkovska I, Pino V. Zirconium-Based Metal–Organic Framework Mixed-Matrix Membranes as Analytical Devices for the Trace Analysis of Complex Cosmetic Samples in the Assessment of Their Personal Care Product Content. *ACS Appl Mater Interfaces* 2022; **14**: 4510–4521. [PMID: 35006682 DOI: 10.1021/ACSAMI.1C21284/ASSET/IMAGES/MEDIUM/AM1C21284_M010.GIF]

151   Carja ID, Tavares SR, Shekhah O, Ozcan A, Semino R, Kale VS, Eddaoudi M, Maurin G. Insights into the Enhancement of MOF/Polymer Adhesion in Mixed-Matrix Membranes via Polymer Functionalization. *ACS Appl Mater Interfaces* 2021; **13**: 29041–29047. [PMID: 34105948 DOI: 10.1021/ACSAMI.1C03859/ASSET/IMAGES/LARGE/AM1C03859_0005.JPEG]

152   Lu Y, Zhang H, Chan JY, Ou R, Zhu H, Forsyth M, Marijanovic EM, Doherty CM, Marriott PJ, Holl MMB, Wang H. Homochiral MOF–Polymer Mixed Matrix Membranes for Efficient Separation of Chiral Molecules. *Angewandte Chemie* 2019; **131**: 17084–17091. [DOI: 10.1002/ANGE.201910408]

153   El-Mehalmey WA, Safwat Y, Bassyouni M, Alkordi MH. Strong Interplay between Polymer Surface Charge and MOF Cage Chemistry in Mixed-Matrix Membrane for Water Treatment Applications. *ACS Appl Mater Interfaces* 2020; **12**: 27625–27631. [PMID: 32496035 DOI: 10.1021/ACSAMI.0C06399/SUPPL_FILE/AM0C06399_SI_002.MP4]

154   Chung TS, Jiang LY, Li Y, Kulprathipanja S. Mixed matrix membranes (MMMs) comprising organic polymers with dispersed inorganic fillers for gas separation. *Progress in Polymer Science (Oxford)* 2007; **32**: 483–507. [DOI: 10.1016/j.progpolymsci.2007.01.008]

155   Zornoza B, Tellez C, Coronas J, Gascon J, Kapteijn F. Metal organic framework based mixed matrix membranes: An increasingly important field of research with a large application potential. *Microporous and Mesoporous Materials* 2013; **166**: 67–78. [DOI: 10.1016/j.micromeso.2012.03.012]

156   Gascon J, Aktay U, Hernandez-Alonso MD, van Klink GPM, Kapteijn F. Amino-based metal-organic frameworks as stable, highly active basic catalysts. *J Catal* 2009; **261**: 75–87. [DOI: 10.1016/j.jcat.2008.11.010]

157   Wang Z, Cohen SM. Postsynthetic modification of metal–organic frameworks. *Chem Soc Rev* 2009; **38**: 1315–1329. [DOI: 10.1039/b802258p]

158   Le T, Chen X, Dong H, Tarpeh W, Perea-Cachero A, Coronas J, Martin SM, Mohammad M, Razmjou A, Esfahani AR, Koutahzadeh N, Cheng P, Kidambi PR, Esfahani MR. An Evolving Insight into Metal Organic Framework-Functionalized Membranes for Water and Wastewater Treatment and Resource Recovery. *Ind Eng Chem Res* 2021; **60**: 6869–6907. [DOI: 10.1021/ACS.IECR.1C00543/ASSET/IMAGES/LARGE/IE1C00543_0019.JPEG]

159   Li J, Wang H, Yuan X, Zhang J, Chew JW. Metal-organic framework membranes for wastewater treatment and water regeneration. *Coord Chem Rev* 2020; **404**: 213116. [DOI: 10.1016/J.CCR.2019.213116]

160   Jun BM, Al-Hamadani YAJ, Son A, Park CM, Jang M, Jang A, Kim NC, Yoon Y. Applications of metal-organic framework based membranes in water purification: A review. *Sep Purif Technol* 2020; **247**: 116947. [DOI: 10.1016/J.SEPPUR.2020.116947]

161   Gnanasekaran G, Balaguru S, Arthanareeswaran G, Das DB. Removal of hazardous material from wastewater by using metal organic framework (MOF) embedded polymeric membranes. *Sep Sci Technol* 2018; **54**: 434–446. [DOI: 10.1080/01496395.2018.1508232]

162   Valadi FM, Shahsavari S, Akbarzadeh E, Gholami MR. Preparation of new MOF-808/chitosan composite for Cr(VI) adsorption from aqueous solution: Experimental and DFT study. *Carbohydr Polym* 2022; **288**: 119383. [PMID: 35450645 DOI: 10.1016/J.CARBPOL.2022.119383]

163   Kalaj M, Denny MS, Bentz KC, Palomba JM, Cohen SM. Nylon–MOF Composites through Postsynthetic Polymerization. *Angewandte Chemie - International Edition* 2019; **58**: 2336–2340. [PMID: 30511412 DOI: 10.1002/anie.201812655]

164   Zhang Y, Feng X, Li H, Chen Y, Zhao J, Wang S, Wang L, Wang B. Photoinduced Postsynthetic Polymerization of a Metal-Organic Framework toward a Flexible Stand-Alone Membrane. *Angewandte Chemie* 2015; **127**: 4333–4337. [DOI: 10.1002/ange.201500207]

165   Miao S, Guo J, Deng Z, Yu J, Dai Y. Adsorption and reduction of Cr(VI) in water by iron-based metal-organic frameworks (Fe-MOFs) composite electrospun nanofibrous membranes. *J Clean Prod* 2022; **370**: 133566. [DOI: 10.1016/J.JCLEPRO.2022.133566]

166   Dongre RS, Sadasivuni KK, Deshmukh K, Mehta A, Basu S, Meshram JS, Al-Maadeed MAA, Karim A. Natural polymer based composite membranes for water purification: a review. *https://doi.org/101080/2574088120181563116* 2019; **58**: 1295–1310. [DOI: 10.1080/25740881.2018.1563116]

167   Qi D, Liu Y, Liu Y, Liu Z, Luo Y, Xu H, Zhou X, Zhang J, Yang H, Wang W, Chen X, Qi D, Liu Y, Xu H, Zhou X, Zhang J, Wang W, Liu Z, Luo Y, Yang H, Chen X. Polymeric Membranes with Selective Solution-Diffusion for Intercepting Volatile Organic Compounds during Solar-Driven Water Remediation. *Advanced Materials* 2020; **32**: 2004401. [PMID: 33169447 DOI: 10.1002/ADMA.202004401]

168   Cova TF, Murtinho D, Aguado R, Pais AACC, Valente AJM. Cyclodextrin Polymers and Cyclodextrin-Containing Polysaccharides for Water Remediation. *Polysaccharides 2021, Vol 2, Pages 16-38* 2021; **2**: 16–38. [DOI: 10.3390/POLYSACCHARIDES2010002]

169   Seiler DA. PVDF in the chemical process industry. In: Scheirs J, editor. *Modern Fluoropolymers*. New York: Wiley, 1997: 487–506.

170   Liu F, Hashim NA, Liu Y, Abed MRM, Li K. Progress in the production and modification of PVDF membranes. *J Memb Sci* 2011; **375**: 1–27. [DOI: 10.1016/j.memsci.2011.03.014]

171   Kang G dong, Cao Y ming. Application and modification of poly(vinylidene fluoride) (PVDF) membranes - A review. *J Memb Sci* 2014; **463**: 145–165. [DOI: 10.1016/j.memsci.2014.03.055]

172   Saxena P, Shukla P. A comprehensive review on fundamental properties and applications of poly(vinylidene fluoride) (PVDF). *Adv Compos Hybrid Mater* 2021; **4**: 8–26. [DOI: 10.1007/S42114-021-00217-0/FIGURES/10]

173   Ribeiro C, Costa CM, Correia DM, Nunes-Pereira J, Oliveira J, Martins P, Gonçalves R, Cardoso VF, Lanceros-Méndez S. Electroactive poly(vinylidene

fluoride)-based structures for advanced applications. *Nat Protoc* 2018; **13**: 681–704. [DOI: 10.1038/nprot.2017.157]

174   Salazar H, Martins PM, Valverde A, Fernández De Luis R, Luis Vilas-Vilela J, Ferdov S, Botelho G, Lanceros-Mendez S. Reusable Nanocomposite Membranes for Highly Efficient Arsenite and Arsenate Dual Removal from Water. *Adv Mater Interfaces* 2021; **9**: 2101419. [DOI: 10.1002/admi.202101419]

175   Queirós JM, Salazar H, Valverde A, Botelho G, Fernández de Luis R, Teixeira J, Martins PM, Lanceros-Mendez S. Reusable composite membranes for highly efficient chromium removal from real water matrixes. *Chemosphere* 2022; **307**. [PMID: 35940413 DOI: 10.1016/J.CHEMOSPHERE.2022.135922]

176   Martins PM, Santos B, Salazar H, Carabineiro SAC, Botelho G, Tavares CJ, Lanceros-Mendez S. Multifunctional hybrid membranes for photocatalytic and adsorptive removal of water contaminants of emerging concern. *Chemosphere* 2022; **293**. [PMID: 34999100 DOI: 10.1016/J.CHEMOSPHERE.2022.133548]

177   Zheng F, Martins PM, Queirós JM, Tavares CJ, Vilas-Vilela JL, Lanceros-Méndez S, Reguera J. Size Effect in Hybrid TiO2:Au Nanostars for Photocatalytic Water Remediation Applications. *International Journal of Molecular Sciences 2022, Vol 23, Page 13741* 2022; **23**: 13741. [DOI: 10.3390/IJMS232213741]

178   Younes I, Rinaudo M, Harding D, Sashiwa H. Chitin and Chitosan Preparation from Marine Sources. Structure, Properties and Applications. *Mar Drugs* 2015; **13**: 1133–1174. [DOI: 10.3390/md13031133]

179   Tovar-Jimenez GI, Hirsch DB, Villanueva ME, Urtasun N, Wolman FJ, Copello GJ. Chitin blends, interpenetrating polymer networks, gels, composites, and nanocomposites for adsorption systems: environmental remediation and protein purification. In: *Handbook of Chitin and Chitosan.* Elsevier, 2020: 135–175.

180   Rinaudo M. Chitin and chitosan: Properties and applications. *Prog Polym Sci* 2006; **31**: 603–632. [DOI: 10.1016/J.PROGPOLYMSCI.2006.06.001]

181   Zhou D, Zhang L, Zhou J, Guo S. Cellulose/chitin beads for adsorption of heavy metals in aqueous solution. *Water Res* 2004; **38**: 2643–2650. [DOI: 10.1016/j.watres.2004.03.026]

182   Torres DI, Lazaro-Martínez JM, Copello GJ, dall Orto VC. Single step synthesis of a polyhydroxy ether and its optimization to adsorption of a textile dye. *J Environ Chem Eng* 2019; : 103416. [DOI: 10.1016/j.jece.2019.103416]

183   Wisser D, Wisser FM, Raschke S, Klein N, Leistner M, Grothe J, Brunner E, Kaskel S. Biological Chitin–MOF Composites with Hierarchical Pore Systems

for Air-Filtration Applications. *Angewandte Chemie International Edition* 2015; **54**: 12588–12591. [PMID: 26314273 DOI: 10.1002/ANIE.201504572]

184   Ma Y, You D, Fang Y, Luo J, Pan Q, Liu Y, Wang F, Yang W. Confined growth of MOF in chitosan matrix for removal of trace Pb(II) from reclaimed water. *Sep Purif Technol* 2022; **294**: 121223. [DOI: 10.1016/J.SEPPUR.2022.121223]

185   Ashour RM, Abdel-Magied AF, Wu Q, Olsson RT, Forsberg K. Green Synthesis of Metal-Organic Framework Bacterial Cellulose Nanocomposites for Separation Applications. *Polymers 2020, Vol 12, Page 1104* 2020; **12**: 1104. [DOI: 10.3390/POLYM12051104]
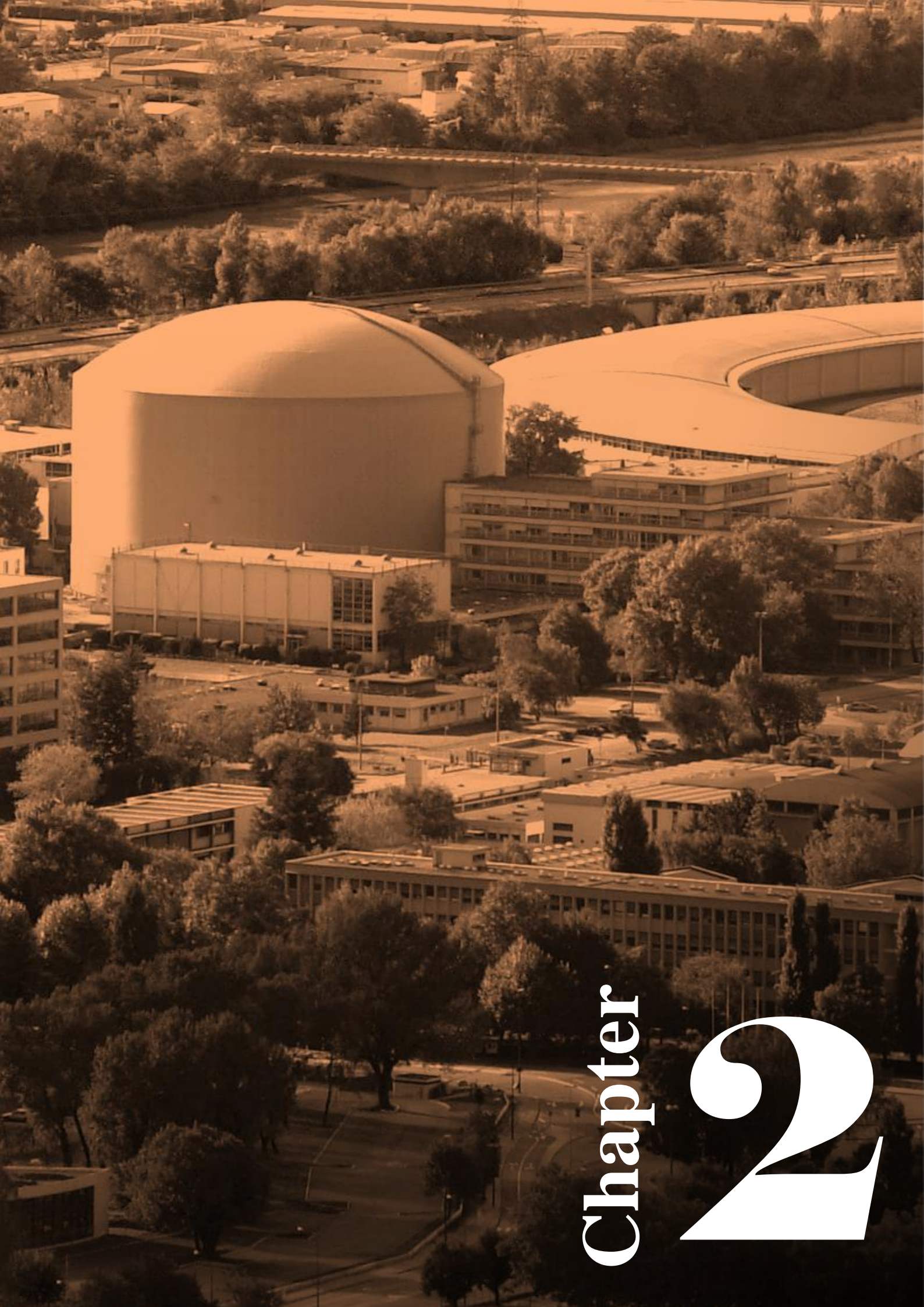
Chapter 2

Chapter 2
Experimental techniques

In this chapter, the most general materials, reagents and procedures that have been systematically used in this work will be described to avoid unnecessary repetitions throughout the document. In parallel, a brief description of the fundamental basis, experimental conditions and equipment of the most used characterization methods and the experimental protocols have been summarized.

2.1. CHEMICALS

Tables 2.1, to 2.5 gather the reactants, chemical formula, commercial supplier (CS), assay (AS) and Chemical Abstracts Service number (CAS) of the chemicals used in this thesis.

Table 2.1. Chemicals and solvents used for MOF synthesis and cleaning.

Name	Formula	CS	AS	CAS
Zirconium (IV) chloride	$ZrCl_4$	Alfa Aesar	98%	10026-11-6
Titanium (IV) isopropoxide	$Ti[OCH(CH_3)_2]_4$	Sigma Aldrich	97%	546-68-9
Zirconium dichloride oxide octahydrate	$ZrOCl_2 \cdot 8H_2O$	Alfa Aesar	98%	13520-92-8
Terephthalic acid	$C_8H_6O_4$	Sigma Aldrich	97%	100-21-0
2-aminoterephthalic acid	$C_8H_7NO_4$	Sigma Aldrich	97%	10312-55-7
2,5-dihydroxyterephthalic acid	$C_8H_6O_6$	Sigma Aldrich	97%	610-92-4
2-nitroterephthalic acid	$C_8H_5NO_6$	Sigma Aldrich	97%	610-29-7
Trimesic acid	$C_9H_6O_6$	Alfa Aesar	98%	554-95-0
N,N-Dimethylformamide	$HCON(CH_3)_2$	Labkem	99.8%	68-12-2
Formic acid	H_2CO_2	Labkem	99%	64-18-6
Acetone	C_3H_6O	Scharlau	99.5%	67-64-1
Ethanol	C_2H_6O	Labkem	99%	64-17-5
Methanol	CH_4O	Alfa Aesar	99%	67-56-1

Table 2.2. Amino acids and natural acids used for post-synthetic functionalization of MOFs..

Name	Formula	CS	AS	CAS
L-(+)-Asparagine	$C_4H_8N_2O_3$	Alfa Aesar	99%	70-47-3
L-Histidine	$C_6H_9N_3O_2$	TCI Chemicals	99%	71-00-1
L-Cysteine	$C_3H_7NO_2S$	Sigma Aldrich	97%	52-90-4
Mercaptosuccinic acid	$C_4H_6O_4S$	Alfa Aesar	98%	70-49-5
Succinic acid	$C_4H_6O_4$	Alfa Aesar	99%	110-15-6
Fumaric acid	$C_4H_4O_4$	Sigma Aldrich	99%	110-17-8
Malic acid	$C_4H_6O_5$	Alfa Aesar	97%	97-67-6
Citric acid monohydrate	$C_6H_8O_7.H_2O$	Labkem	99%	5949-29-1

Table 2.3. Metals salts employed to obtain the solutions used in the adsorption tests.

Name	Formula	CS	AS	CAS
Mercury (II) chloride	$HgCl_2$	Sigma Aldrich	99.5%	7487-94-7
Nickel (II) chloride	$NiCl_2$	Sigma Aldrich	98%	7718-54-9
Chromium (III) chloride hexahydrate	$CrCl_3.6H_2O$	Sigma Aldrich	96%	10060-12-5
Cadmium (II) nitrate tetrahydrate	$Cd(NO_3)_2.4H_2O$	Sigma Aldrich	98%	10022-68-1
Lead (II) nitrate	$Pb(NO_3)_2$	Labkem	99%	10099-74-8
Lanthanum (III) nitrate hexahydrate	$La(NO_3)_3.6H_2O$	Sigma Aldrich	99.99%	10277-43-7
Yttrium (III) chloride	YCl_3	Abcr	99.9%	10361-92-9
Europium (III) nitrate	$Eu(NO_3)_3.6H_2O$	Alfa Aesar	99.9%	10031-53-5
Potassium dichromate	$K_2Cr_2O_7$	Sigma Aldrich	99%	7778-50-9
Copper (II) chloride dihydrate	$CuCl_2.2H_2O$	Acros Organics	99%	10125-13-0
Sodium arsenate dibasic heptahydrate	$Na_2HAsO_4 \cdot 7H_2O$	Sigma Aldrich	98%	10048-95-0

Table 2.4. Reagents used for the catalytic acitivity tests.

Name	Formula	CS	AS	CAS
Phenol	C_6H_6O	TCI Chemicals	99.5%	108-95-2
Catechol	$C_6H_6O_2$	TCI Chemicals	99%	120-80-9
2,4-dichlorophenol	$C_6H_4OCl_2$	TCI Chemicals	98%	120-83-2
Hydroquinone	$C_6H_6O_2$	Sigma Aldrich	99%	123-31-9
Paracetamol	$C_8H_9NO_2$	Sigma Aldrich	99%	103-90-2
4-aminoantyprine	$C_{11}H_{13}N_3O$	Alfa Aesar	97%	83-07-8
Hydrogen peroxide	H_2O_2	Panreac	30% w/w in water	7722-84-1

Table 2.5. Other reagents used along the thesis.

Name	Formula	CS	AS	CAS
PVDF-HFP	$(C_2H_2F_2)_x(C_3F_6)_y$	Solvay	88% PVDF 12% HFP	9011-17-0
Chitin	$(C_8H_{13}O_5N)_x$	Sigma Aldrich	99%	1398-61-4
Calcium chloride	$CaCl_2$	Panreac	99.99%	10043-52-4
Erythrosine B	$C_{20}H_6I_4Na_2O_5$	Sigma Aldrich	95%	16423-68-0
Methylene blue	$C_{16}H_{18}ClN_3S$	Sigma Aldrich	98%	61-73-4
Methyl orange	$C_{14}H_{14}N_3NaO_3S$	Sigma Aldrich	85%	547-58-0
Polymyxin B sulfate	$C_{48}H_{84}N_{16}O_{17}S$	Sigma Aldrich	-	1405-20-5
Lysozyme	-	Sigma Aldrich	90%	12650-88-3
Gold (III) chloride	$HAuCl_4$	Sigma Aldrich	99%	13453-07-1
1,5-Diphenylcarbazide	$C_{13}H_{14}N_4O$	Sigma Aldrich	99%	140-22-7
Sulphuric acid	H_2SO_4	Labkem	97%	7664-93-9
Potassium permanganate	$KMnO_4$	Sigma Aldrich	99%	7722-64-7
Sodium azide	NaN_3	Sigma Aldrich	99.5%	26628-22-8
4-aminoantipyrine	$C_{11}H_{13}N_3O$	Alfa Aesar	97%	83-07-8
Hydrochloric acid	HCl	Sigma Aldrich	30%	7647-01-0
Sodium hydroxide	$NaOH$	Alfa Aesar	97%	1310-73-2

2.2. CHARACTERIZATION METHODS

2.2.1. X-RAY SCATTERING TECHNIQUES

X-rays are electromagnetic radiation with a wavelength, λ, which magnitude is of the same order as the one of the atomic ordered planes of the crystalline structures. When X-ray radiation with a given wavelength hits the valence electrons of these atoms, it gets diffracted from the different atomic layers.[1] The radiation emitted by each atom expands as a wave and interferes with that created by the surrounding atoms. These interferences can be destructive or constructive. The constructive ones occur at certain angles (θ) that satisfy Bragg's law[2] (Equation 2.1).

$$\lambda = 2\, d_{hkl}\, sen\, \theta \qquad (2.1)$$

where λ is the wavelength of the X-rays, θ is the incident angle of the radiation and d_{hkl} the is spacing between two consecutive planes defined as a vector of the hkl components. A schematic representation of the X-ray diffraction process can be found in Figure 2.1.
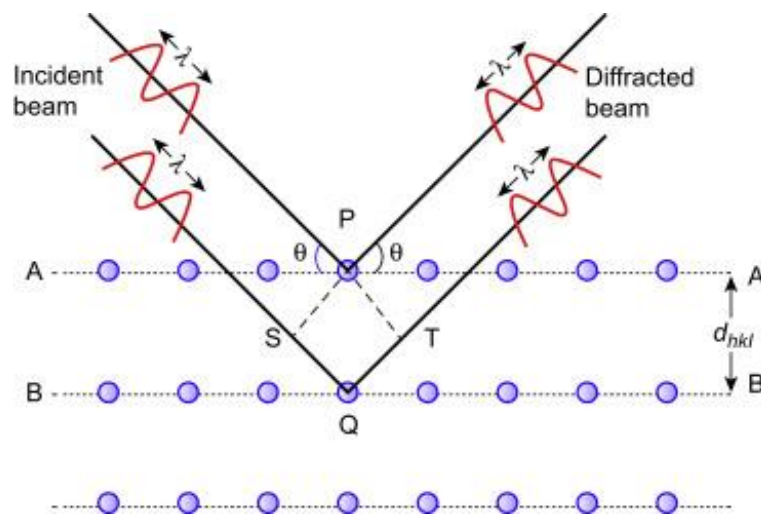
Figure 2.1. Schematic representation of the X-ray diffraction by a set of ordered planes of atoms. Reproduced with permission from U. Gawas *et al.*[3]

Powder X–ray Diffraction

Powder X-ray Diffraction (PXRD) has been applied in this thesis to confirm the presence of the desired phase after the synthesis, as well as to discard the co-crystallization of secondary compounds while assessing the crystallinity of the materials before and after operation. A polycrystalline material is made up of a large number of tiny crystals arranged randomly with respect to one another. A sample with these characteristics, when irradiated with an X-ray beam of a specific wavelength, will always present a certain number of crystallites that, due to their orientation, satisfy Bragg's law. As the diffraction signature is given by the internal ordered disposition of the atoms within the crystal structure of the materials, the X-ray diffraction pattern mainly depends on the spacing of the planes and the electron density of the atoms within the planes in the studied material, as well as on the characteristics of the diffractometer and of the experiment. Therefore, each material has its characteristic X-ray diffraction signature that can be calculated from its structural model and the experimental conditions used in the experiment.

As the average structure of all the materials that have been synthesized in this work is already known, their structural models have been obtained from the Cambridge Structural Database.[4,5] In parallel, in this work, two different spectrometers have been used to characterize the samples.

For the vast majority of the samples, a Panalytical X´pert CuK_α ($K_{\alpha1}$=1.540560, $K_{\alpha2}$=1.544390) diffractometer in the following conditions: 2θ range = 5 – 70°, step size = 0.05°, exposure time = 10 s per step at room temperature was used. Panalytical X´pert is a polycrystalline sample diffractometer with theta-theta geometry, a programmable slit, secondary graphite monochromator adjusted to a copper radiation ($K_{\alpha1}$=1.540560, $K_{\alpha2}$=1.544390) and fast solid state PixCel detector adjusted to a 3.347º active length in 2θ(°). The equipment allows performing high-quality measurements for the subsequent data processing, at the level of full profile adjustments without/with a structural model.

Furthermore, temperature-dependent X-ray diffraction (TDX) analysis were performed in order to study the thermal stability of the samples with a Bruker D8

Advance Vantec diffractometer (CuK$_\alpha$ radiation, K$_{\alpha 1}$=1.540560, K$_{\alpha 2}$=1.544390), equipped with a variable-temperature stage HTK2000 for the measurements performed in the 30 to 500 °C temperature range. Patterns were registered each 10 °C (2θ range= 5-40°, step size= 0.01°, exposure time = 0.5 s per step). Both diffractometers belong to the General Research Services (SGIker) of the UPV/EHU.

The X-ray diffraction results are collected on a diffractogram representing the intensity of the diffracted radiation that reaches the detector as a function of the 2θ angle. In this diffractogram, a series of peaks that occur for those values of θ that comply with Bragg's law (Equation 2.1) could be observed. Each crystalline solid presents a characteristic diffractogram as if it were its fingerprint. To obtain information from the diffractograms, it is necessary to make an analysis of them taking into account the position of the diffraction maxima, their profile and their intensity. Among the information that can be obtained from the X-ray diffractograms are the space group and the network parameters or the average size of the particles.

To obtain those parameters the results are commonly analysed by using different programs, such as FullProf[6,7] or TOPAS,[8] and are compared with those present in a database in order to study their crystalline structure by using a refinement method, such as the Rietveld method. The Rietveld method consists of a theoretical least square´ adjustment of the full diffraction pattern to a profile calculated for a structural model in order to refine the crystal structures and obtain the structural and profile parameters. Along this thesis, full peak fit profile matching of the samples has been performed in order to confirm the absence of impurities and analyse the structure of the samples.

Small Angle X-ray Scattering

Small-angle X-ray scattering (SAXS) is a powerful analysis tool, capable of selectively resolving structures of the order 1 nm to over 100 nm.[9] This means that it can determine nanoparticle size distributions, resolve the size and shape of (monodisperse) macromolecules, determine pore sizes, characteristic distances of partially ordered materials, and much more. If the scattering object is bigger than

several tenths to hundreds of nanometers, SAXS gives information about the interfaces within the scattering object. This is achieved by analysing the elastic scattering behaviour of X-rays when traveling through the material, recording their scattering at small angles (typically 0.1 – 10°, hence the "Small-angle" in its name). It belongs to the family of small-angle scattering (SAS) techniques along with small-angle neutron scattering, and is typically done using hard X-rays with a wavelength of 0.07 – 0.2 nm.

SAXS measurements of this work were carried out using a Cu K_α radiation SAXS point 2.0 instrument (Anton Paar, Austria) with a hybrid photon-counting 2D EIGER R series detector. The measurements covered a q-range of 0.07-5 nm^{-1} with q-resolution $\delta q < 0.003$ nm^{-1}. The measurements were carried out on samples in solution at room temperature using a special quartz capillary of 1 mm in diameter or a special plate for solid films and powdered samples.

2.2.2. NEUTRON SCATTERING TECHNIQUES

Neutron scattering techniques are widely used in materials science due to their multiple advantages. Thanks to their neutral nature (they have no charge), they are non-destructive and highly penetrating in the matter. The basis of neutron scattering is similar to X-ray scattering, but unlike X-rays, neutrons interact with atoms *via* nuclei forces rather than electrical forces, making it possible to scatter light elements and distinguish isotopes and elements with similar atomic numbers (Z).[10]

One of the remarkable consequences of quantum mechanics is that matter has both particle- and wave-like nature.[11] The neutron is no exception from this. To be more specific on the wave nature of matter, a particle moving with constant velocity, v, can be ascribed a corresponding (de-Broglie) wavelength, given by Equation 2.2.

$$\lambda = \frac{2\pi\hbar}{mv} \qquad (2.2)$$

where λ is the wavelength, m the mass of the neutron, v the velocity of the neutron and $\hbar$ reduced plank constant.

Thanks to this, neutrons can have similar wavelengths than X-rays ($\lambda \approx 0.1$ nm), but with much smaller energies (X-rays have energies in the range of keV, while neutrons work in ranges of meV for the same wavelength), which is an enormous advantage when we want to study dynamic processes, as small energies are needed (1-100 meV) to see small changes in energies.

Neutron facilities can be classified into two main groups: fission reactors and spallation sources. In reactors, the most commonly used element for fission is the ^{235}U isotope. This reaction can be made self-sustaining because it is exothermal and releases more neutrons per fission process than are needed to initiate the process (Figure 2.2a). In these facilities, a high continuous flux of neutrons is produced in the core of a conventional fission reactor. Because of this continuous flux, in fission reactors, a monochromator is normally used to determine the incoming neutron wavelength. Institute Laue-Langevin (ILL), located in Grenoble (France) is an example of this type of facility. For instance, the Inelastic Neutron Scattering data analysed in this work have been obtained in the IN1-Lagrange beamline of this strategic installation.

On the contrary, in a spallation facility a pulsed production of neutrons is generated by bombarding a target of heavy elements with high-energy particles, typically accelerated protons (Figure 2.2b). As an advantage of having a pulsed neutron flux instead than a continuous one, the incoming neutron wavelength can be determined by the time the neutrons need to reach the detector (Time-of-flight methodology), without the need for a monochromator. An example of a spallation facility is the ISIS Neutron and Muon Source, located in Oxfordshire (United Kingdom), where Small-Angle Scattering experiments shown in this thesis have been developed.

On the other hand, neutron scattering techniques can also be classified into two large groups: (i) elastic scattering, used to study the structure of the materials and (ii) inelastic scattering, also known as spectroscopy, which is used to study the lattice dynamics.
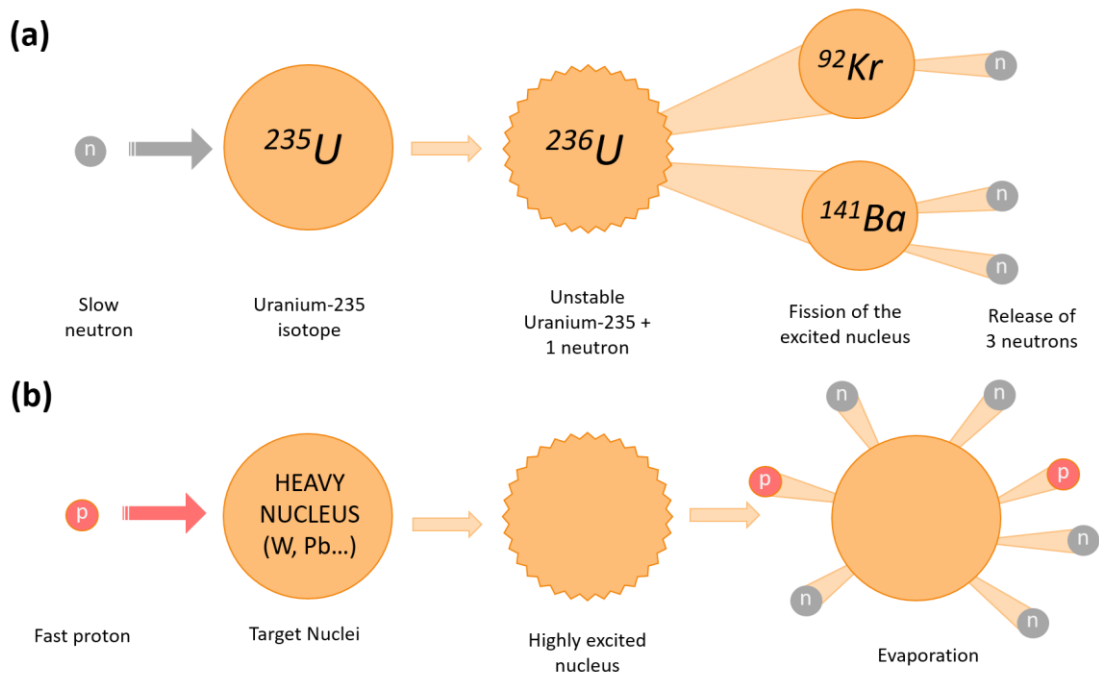
Figure 2.2. The two main methods of neutron production. (a) Fission of ^{235}U nucleus in a traditional nuclear reactor. (b) Spallation process: protons accelerated into the GeV regime can split heavy nuclei with a large neutron surplus, creating free neutrons among the reaction products.

Small Angle Neutron Scattering

Small Angle Neutron Scattering (SANS) follows the same basics as Small Angle X-ray Scattering, but it is based on the elastic scattering of neutrons instead of X-rays. Besides the general advantages of neutron methods, such as non-destructivity, isotopic substitution, sensitivity to the magnetic structure etc., SANS shows several special advantages:

- Gives average information about the entire volume of the sample placed into the neutron beam (not only about its surface).
- Needs no sample preparation, therefore sample-preparing artefacts can be avoided.
- Makes possible the in-situ following of various processes in function of physical or chemical parameters, such as temperature, concentration, annealing, enlightening, strain or stress etc.

Comparing it to the small angle X-ray scattering (SAXS), because of the difference between the X-rays' and neutrons' interaction with the matter, SANS and SAXS usually provide different information; often the neutron and X-ray small angle scattering are used as complementary methods.

SANS measurements were performed on the SANS2D instrument[12] at the ISIS Pulsed Neutron and Muon Source (Oxfordshire, UK). This versatile instrument combines time-of-flight techniques with a 'white' beam of neutrons and two, large, independently-moveable, two-dimensional detectors to provide a very wide, but adjustable, dynamic range in scattering vector, q (=$4 \cdot \pi \cdot \sin\theta/\lambda$, where 2q is the scattering angle and λ is the neutron wavelength). For this experiment, the instrument was operated at 10 Hz with a wavelength band of $1.75 \leq \lambda$ (Å) ≤ 12.5 and the detectors were situated at 5 m and 12 m from the sample (with the rear detector also offset vertically by 75 mm and horizontally by 100 mm) to provide a simultaneous q-range of $0.0015 \leq \lambda$ (Å^{-1}) ≤ 1.0. The incident neutron beam was collimated to 8 mm in diameter. The samples were contained in thin aluminium foil 'envelopes' and attached to an enclosed computer-controlled, multi-position, sample changer thermo-stated by a circulating fluid bath. Measurements were performed at 25 °C. Independent measurements of the scattering pattern and the neutron transmission were performed on each sample for ~30 min and ~10 min, respectively. The 'raw' neutron data were corrected for the efficiency and spatial linearity of the detectors, the neutron absorption and illuminated volume of the sample, the background scattering from an empty foil envelope and the instrument itself using the Mantid framework, and radially averaged to yield the coherent elastic differential scattering cross-section, hereafter denoted as 'intensity', I, in absolute units, as a function of q. These data were then placed on an absolute scale by reference to the scattering from a partially-deuterated polystyrene polymer blend of known molecular weight measured with the same instrument configuration.[13]

Inelastic Neutron Scattering

Inelastic neutron scattering (INS) is a spectroscopy technique based on the energy analysis of neutrons after they have been scattered by a sample. A detected energy transfer can be related to the physical interaction of the corresponding atoms with their environment. This energy transfer, located in the range of meV, typically arises from vibrations of atoms or molecules.

INS can be used to characterize chemical bonds both in the bulk as well as on the surface.[14] The method exploits the slightly different behaviour between bound and free atoms during the scattering process and uses the difference in energy and momentum transfer to construct the vibrational states of the system, and thus, gives complementary data to Infrared or Raman spectroscopies.

The Inelastic Neutron Scattering (INS) spectra of Chapter 4 were measured at 10 K in the range of energy transfers from ~ 8 to 3600 cm^{-1} (that corresponds to ~ 1 to 438 meV) with an energy resolution of $\Delta E/ \Delta E$ ~ 2 % using the IN1-Lagrange neutron spectrometer installed at the hot source of the high-flux reactor at the Institute Laue-Langevin (Grenoble, France).[15] This energy range was obtained by using different monochromators: Si(111) monochromator for energies from 8 to 113 cm^{-1}, Si(311) for energies from 97 to 193 cm^{-1} and Cu(220) monochromator for energies from 173 to 3576 cm^{-1}. The background spectrum from the cryostat and an empty sample holder was measured separately and then subtracted from the raw INS spectrum of the sample. To the extent that k_f is much smaller than k_i (and therefore high Q), the observed intensity is directly proportional to the generalized density of states (GDOS), which is the hydrogen partial density of states in the case of hydrogenated materials. Data sets were then normalized for monitor counts and corrected for empty cells.

2.2.3. INFRARED SPECTROSCOPY

Infrared spectroscopy (IR) is a highly useful technique to identify specific functional groups or organic molecules present in solid, liquid or gases. In this technique, the sample is irradiated with infrared radiation, which is not very energetic,

and thus, it is not capable to produce electronic transitions. The absorption of radiation is limited to molecular species for which there are small energy differences induced by the vibrational states of the molecules.

To absorb in the infrared range, a molecule must undergo a change in the dipole moment as a consequence of its vibrating or rotating movement. This way, the radiation can interact with the molecule and cause changes in the amplitude of some of its movements. If the frequency of the radiation matches the natural vibration frequency of the molecule, a net transfer of energy takes place, causing a change in the amplitude of the molecular vibration and the infrared absorption as a consequence.

Two basic categories of vibrations can be distinguished: stretching and bending. Stretching vibrations are changes in the interatomic distance along the axis of the bond between two atoms, while bending vibrations are caused by changes in the angle between two bonds. Figure 2.3 shows the schematic representation of these vibrations.
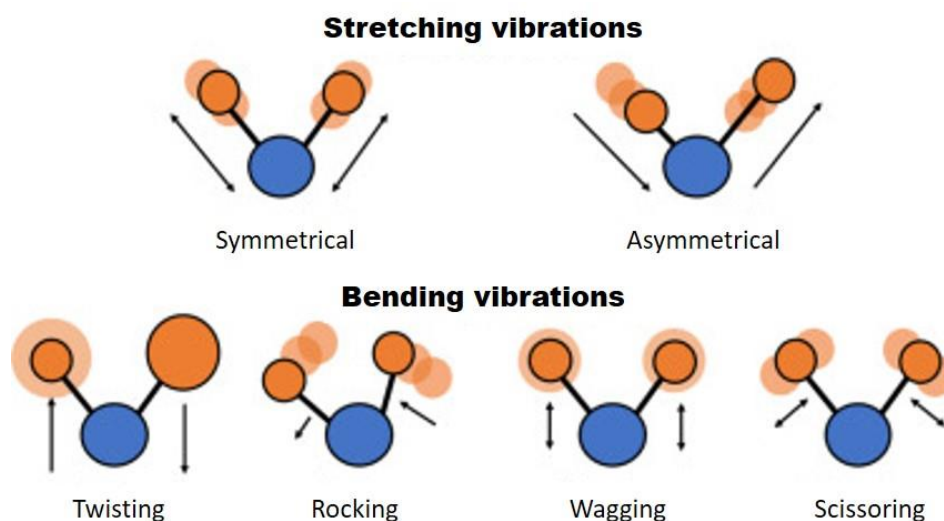
Figure 2.3. Schematic representation of molecular vibrations. Reproduced with permission from J. M. Cameron *et al*.[16]

The signal resulting from the Infrared Spectroscopy measurement is a spectrum that represents the molecular "footprint" of the sample, which is characteristic of its chemical structure. In this thesis, the infrared spectra have been obtained in a spectrophotometer with Fourier transform JASCO FT/IR-6100 in Attenuated Total

Reflectance mode (FTIR-ATR). Fourier transform instruments have a better signal/noise ratio than most instruments operating in the infrared spectral range. They are also characterized by their high resolutions and by their high accuracy and reproducibility in the determination of frequencies. This is due to the fact that their optics allow the arrival of a higher intensity of radiation at the detector. On the other hand, ATR is an infrared sampling technique that has allowed to eliminate in many cases the need for sample preparation, improving sample-to-sample reproducibility and minimizing user-to-user spectral variation. An ATR accessory works by measuring the changes that occur in a total internal reflected infrared beam when the beam comes into contact with a sample. An infrared beam is directed onto an optically dense crystal with a high refractive index at a certain angle. This internal reflectance creates an evanescent wave that extends beyond the surface of the crystal into the sample held in contact with the crystal.

Infrared spectroscopy has allowed characterizing several materials synthetized in this work, as it is a powerful tool to identify functional groups incorporated into the organic linkers of the MOFs during the synthesis (Chapter 3), or the amino-acid functionalities introduced in the framework (Chapter 4) after the synthesis of the ordered porous materials. In addition, IR spectroscopy allows monitoring any change in the vibrational fingerprint of the materials after adsorption or photocatalysis.

2.2.4. RAMAN SPECTROSCOPY

Raman spectroscopy is a high-resolution photonic technique that provides chemical and structural information on almost any organic and/or inorganic material or compound in a few seconds, allowing its identification. Raman spectroscopy analysis is based on the examination of light scattered by a material when a monochromatic light beam is incident on it. A small portion of the light is inelastically scattered, undergoing slight changes in frequency that are characteristic of the analyzed material, and independent of the frequency of the incident light. It is an analysis technique that is performed directly on the material to be analysed without the need for any special preparation.

Raman spectra of Chapters 4 and 5 were obtained on a Renishaw InVia Raman from the SGIker with an excitation laser beam of 785 cm^{-1} and 75mV laser power. For that, a few milligrams of MOF nanoparticles or CH/MOF-808 composites were placed at the sample holder and measured for 5 scans of 20 s in the 150-3200 cm^{-1} wavenumber range.

2.2.5. ELECTRON PARAMAGNETIC RESONANCE

Electron paramagnetic resonance (EPR) is a widely used spectroscopic technique for the characterization of materials containing metal ions or organic radicals with single unpaired electrons. Moreover, EPR analysis provides information about the electronic configuration, distortion of the coordination environment of paramagnetic ions, as well as on the existence of possible magnetic interactions between them.

This technique describes the case of resonance of an atomic particle as a result of high-frequency electromagnetic radiation absorption in the presence of an external magnetic field, and it is based on the fact that the spin of an electron can adopt two orientations along the direction defined by the applied magnetic field H. This breaking of the spin degeneracy gives rise to an energy difference (ΔE) between the m_s=+1/2 and -1/2 states (Zeeman states) (Figure 2.4) being its value defined by Equation 2.3.

$$\Delta E = g\mu_B H \qquad\qquad (2.3)$$

where μ_B is Bohr electronic magneton, *H* is the external magnetic field and g is Lande's factor. This factor is a characteristic constant for each substance. For instance, for an electron g_e = 2.0023. The symbol *g* is used when the electrons interact with other particles, in which case g $\neq$ g$_e$.
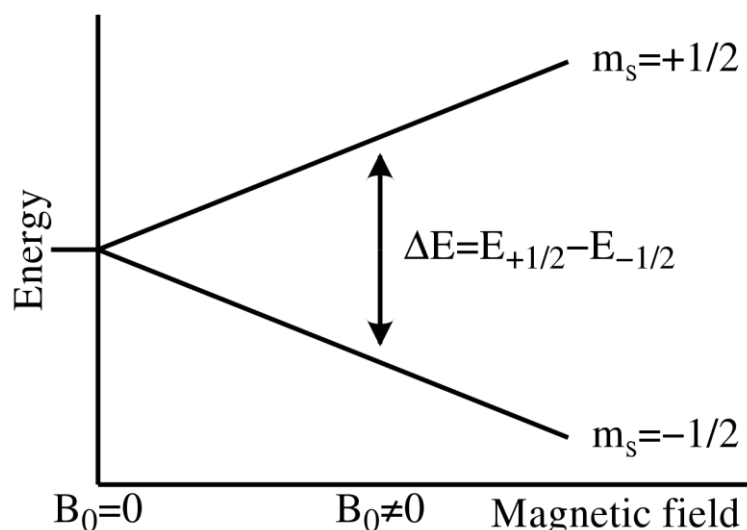
Figure 2.4 Schematic representation of the splitting of electron spin states.

In EPR spectroscopy, the radiation used is in the gigahertz range. Unlike most traditional spectroscopy techniques, in most EPR equipment, the frequency of the radiation (which is usually in the range of microwaves) is held constant while the magnetic field is varied, and thus, the energy difference between the two spin states too (Figure 2.4).

When the energy difference between the two spin states matches the incident photon energy, some electrons are excited in the upper energy level and flip their spin direction. After a time (t_1), the relaxation time, excited electrons return to their original state emitting photons whose energy is equal to ΔE.

In Chapter 3, EPR analysis allowed to study the Cr^{VI} reduction process, as the EPR signature of the samples (more extensively explained in Chapter 3.2), allows identifying Cr^V species, as well as both clustered and isolated Cr^{III} species. In Chapter 4, EPR analysis allowed to obtain substantial information about the electronic structure and the nature of the coordination environment of several EPR-active metal ions adsorbed into amino acid-modified MOF-808.

EPR spectra were recorded at room temperature using a Bruker ELEXSYS 500 spectrometer (X band). The spectrometer was equipped with a super high-Q resonator ER-4123-SHQ and the samples were placed in quartz tubes. In order to establish a

qualitative comparison, approximately the same amount of sample and packing degree within the quartz tubes was used in all cases. The magnetic field was calibrated by a S4 nuclear magnetic resonance (NMR) probe and the frequency inside the cavity (~9.395 GHz) was determined with an integrated microwave frequency.

2.2.6. PROTON NUCLEAR MAGNETIC RESONANCE

Nuclear magnetic resonance (NMR) is a physical phenomenon in which nuclei in a strong constant magnetic field are perturbed by a weak oscillating magnetic field and respond by producing an electromagnetic signal with a frequency characteristic of the magnetic field at the nucleus. As it happens in EPR, NMR analysis describes the case of resonance of an atomic particle as a result of high-frequency electromagnetic radiation absorption in the presence of an external magnetic field. The main difference is that NMR is related to the nucleus, while EPR is related to the unpaired electron.

Among the huge variety of nuclei that can be analysed with this technique, proton nuclear magnetic resonance (^{1}H-NMR) is an especially useful technique for MOF characterization. ^{1}H-NMR analyses of the thesis were performed in a Bruker AVANCE 500 at 500 Hz, from the SGIker. To this end, the MOF samples were digested in a NaOH 1 M D_2O-based solution.

Afterwards, by integrating and comparing the proton signals associated with the organic linkers, a molar ratio of the linker in multivariate UiO-66-R (R= NH_2, $(OH)_2$, NO_2, NH_2-$(OH)_2$, NH_2-NO_2, $(OH)_2$-NO_2 and NH_2-$(OH)_2$-NO_2) materials was obtained in Chapter 3.2. Similarly, the amino acid molecules installed per formula unit of MOF-808 were quantified by ^{1}H-NMR in Chapter 4. The integration of the NMR signals was performed with the MestReNova software, by selecting the signals easier to isolate in the cases where there was more than a signal for the same molecule.

2.2.7. ULTRAVIOLET-VISIBLE SPECTROSCOPY

Ultraviolet-Visible (UV-Vis) spectroscopy for liquid and solid samples is a widely employed characterization technique to quantify the presence of certain substances in solution, or to identify/quantify the presence of certain functional groups or metals that exhibit electronic transitions that occur within the energy range of the UV-Vis wavelengths. This technique consists of measuring the light that a sample absorbs at different wavelengths within the UV-Vis range, as a consequence of an electron moving from a lower energy level to a higher energy level after adsorbing a photon of a concrete wavelength. This absorption depends on the molecules' or metals' electronic structures and is characteristic of the substance/coordination complex.

What is more, the optical band gap of a semiconductor can be also determined thanks to UV-Vis spectroscopy. The term "band gap" refers to the energy difference between the top and bottom of the valence and conduction bands in a semiconductor. The electronic structure of semiconductor materials determines the energy barrier between the conduction and balance bands, which is related to the energy input that is necessary for an electron to jump between them. In the specific case of photocatalytic processes, the band gap determines the energy of the phonons (wavelength of the light source) that is needed to trigger the exciton generation through the electron transfer from the balance to conduction bands.

In Chapter 3.2, laser absorptivity of the powder samples was measured using diffuse reflectance spectroscopy (DRS) to determine the optical band gap of the samples, as well as to monitor the Cr^{VI} and Cr^{III} immobilization in the MOF after adsorption and photoreduction processes. In Chapter 4.2, the same technique was employed to study the UV-Vis signature of Cu^{II} ions immobilized in (amino)acid functionalizes MOF-808 samples.

DRS was recorded in the 200-2200 nm wavelength range with 1 nm spectral resolution using an ultraviolet-visible-near infrared (UV-Vis-NIR) V-770 Jasco spectrophotometer equipped with a 150 mm diameter integrating sphere coated with Spectralon from the SGIker. A Spectralon reference was used to measure the 100% reflectance and internal attenuators were used to determine zero reflectance to remove

background and noise. The powders were placed in a quartz cuvette, sealed, and mounted on a Teflon sample holder for the DRS measurement. The measured reflectance spectra were subsequently converted to Kubelka-Munk (K-M) absorption factors to evaluate the absorption spectra of the powders. This conversion was performed using the K-M equation (Equation 2.4).

$$f(R) = \frac{(1R^2)}{2R} \tag{2.4}$$

where R is the measured reflectivity of the samples.

On the other hand, liquid UV-Vis spectroscopy was especially useful to develop the stability tests performed in Chapter 3.2. UV-Vis was used to quantify the linker concentration leached from the MOFs after immersing them in solutions of different acidities. In addition, UV-Vis spectroscopy was also used for Cr^{VI} quantification in the photoreduction experiments, following a simplified methodology based on a previously reported one for 1,5-Diphenylcarbazide,[17,18] which is described in detail in section 2.3.3 of this chapter. These spectra were recorded using a Spectronic 20 Genesys spectrophotometer.

Finally, the determination of the concentrations of the different organic and inorganic pollutants of Chapter 5.2 were also recorded using a Spectronic 20 Genesys spectrophotometer.

2.2.8. X-RAY PHOTOELECTRON SPECTROSCOPY

X-ray photoelectron spectroscopy (XPS) is a non-destructive technique that provides information on the elements present on the surface, as well as on their oxidation state and/or coordination environment. In this technique, a photon of *hv* energy attacks the atoms located on the surface and as a consequence of the photoelectric effect, photoelectrons are emitted with the energy based on Equation 2.5:

$$EB = h\upsilon - EK - W \tag{2.5}$$

where *hv* is the energy of the photons, Ek the energy of the created photoelectron, W the work function of the spectrophotometer and EB the binding energy (a parameter that identifies the electron in a specific way).

XPS measurements were acquired using a SPECS spectrometer (Berlin, Germany) equipped with a Phoibos 150 1D-DLD analyser and monochromatic Al Kα radiation (h·v=1486.6 eV). XPS survey scans (step energy 1 eV, dwell time 0.1 s, pass energy 80 eV) were acquired. The spectrometer was previously calibrated with Ag (Ag $3d_{5/2}$, 368.26 eV). Selected energy ranges were studies for specific elements recording higher energy resolution scans of the appropriate peaks (step energy 0.08 eV, dwell time 0.1 s, pass energy 30 eV) with an electron take-off angle of 90°. The binding energies (BEs) were calibrated against the surface carbon contamination at 284.6 eV. The spectra were fitted by CasaXPS 2.3.16 software, modelling properly weighted sum of Gaussian and Lorentzian component curves, after background subtraction according to Shirley.

2.2.9. GAS ADSORPTION/DESORPTION ISOTHERMS

Gas adsorption isotherms measurement is one of the most important techniques for the characterization of porous materials since it offers information about the surface area and the pore distribution (pores size and volume).[19] These measurements are based on the analysis of the amount of gas physically adsorbed in the material surface and how it adsorbs it.

The uptake of gas can be expressed as an equivalent volume at standard pressure, as a true volume or mass, or as moles per gram. This is plotted against the equilibrium pressure (p/p_0) at a constant temperature, and the plot is an isotherm of the adsorbate uptake. Figure 2.5 shows the different types of adsorption isotherms which complete the IUPAC classification.

Type I isotherms, also known as Langmuir isotherms, are the simplest ones, characteristic of a chemisorption process in microporous materials. There is an initial step where a monolayer is deposited inside the micropores, and once they are filled, the isotherm reaches a saturation value quickly. In type II and IV isotherms, a

monolayer is created at low pressures, then there is a plateau when all energetically favorable sites have been occupied, and multilayers are created at high pressures. Porous materials show the hysteresis effect of type IV isotherms, due to the different energetics of condensation on the surface and evaporation away from the pore (as a consequence of a surface with different curvatures in the forward and reverse direction). Type III and V isotherms correspond to physical adsorption in multilayers where the equilibrium constant for the formation of the first layer is the same as for the following ones (no difference is observed between the filling of the first layer and the rest). These isotherms are characteristic of macro-porous or non-porous materials with a weak interaction between the adsorbate and the adsorbent. Type VI isotherms result from distinct monolayers being built up on a surface, which means, that only when a layer is completed, another one can be formed. This happens in materials with a very uniform surface and no preferential adsorbent sites.
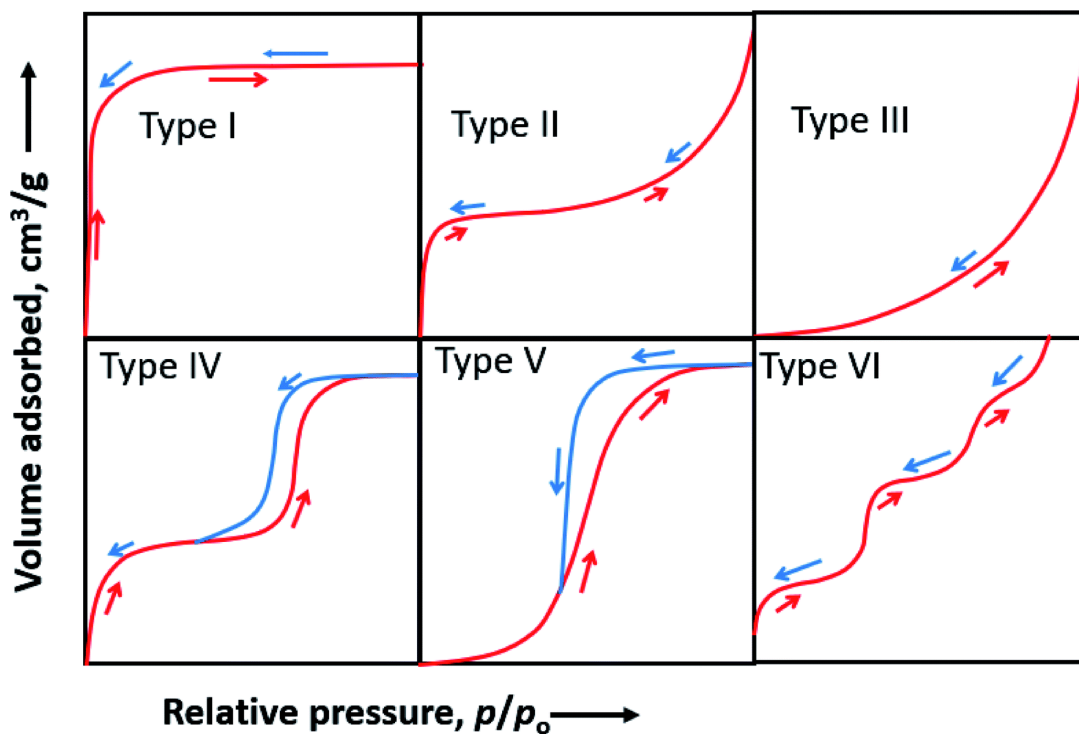
Figure 2.5. Different types of adsorption isotherms as classified by IUPAC. Reproduced with permission from Kumar *et al.*[20]

Type I, II and IV isotherms are the ones usually found in MOF materials. By analysing the monolayer adsorption zone (low-pressure zone) the Brunauer-Emmet-Teller (BET) surface area of the samples can be obtained. This is an extension of the Langmuir theory (a theory for monolayer molecular adsorption) to multilayer adsorption with the following hypotheses:

- Gas molecules physically adsorb on a solid in layers infinitely.
- Gas molecules only interact with adjacent layers.
- The Langmuir theory can be applied to each layer.
- The enthalpy of adsorption for the first layer is constant and greater than the second (and higher).
- The enthalpy of adsorption for the second (and higher) layers is the same as the enthalpy of liquefaction.

For Chapters 3.1 and 5 of the thesis, CO_2 sorption isotherms were measured at 273 K using a Quantachrome ISorb instrument. Approximately 10-20 mg of the MOF particles were degassed at 120 °C in a high vacuum for at least 12 h before the measurement. The surface area value was obtained by fitting the adsorption data to a linearized form of the Brunauer–Emmett–Teller (BET) equation[21]. For Chapters 3.2 and 4 of the thesis, the porosity was studied by means of N_2 adsorption isotherms at 77 K using a Quantachrome Autosorb-iQ-MP analyser. The samples were activated at 120 ºC for 12 h. The surface area values were obtained by the fittings of the adsorption data to the BET equation.

2.2.10. MERCURY INTRUSION POROSIMETRY

Mercury intrusion porosimetry (MIP) is a powerful technique utilized for the evaluation of porosity, pore size distribution, and pore volume (among others) of a wide variety of solid and powder macro to mesoporous materials. The instrument, known as mercury porosimeter, is a device that is capable of generating suitably high pressures, measuring simultaneously both the pressure and volume of mercury taken up by a porous material.[22] As pressure is applied, mercury fills the larger pores first.

As pressure increases, the filling expands to smaller and smaller pores.[23] MIP is capable of analysing a very broad range of pore sizes reaching from 3 nm up to 950 µm. This covers the macropore region as well as almost the complete region of mesopores as well. Both the inter-particle pores (between the individual particles) and the intra-particle pores (within the particle itself) can be characterized using this technique. Mercury porosimetry is especially useful to determine the macro to mesoporosity of polymeric material when processed as porous films or membranes, as the PVDF/MOF composites developed within this work.

To this end, a Quantachrome Instruments Poremaster-60 GT operating in the pressure range from vacuum (10^{-4} MPa) to 414 MPa was used. Samples were degassed *in situ* at 110 ºC for 12 h before the measurement. A contact angle of 140º and surface tension of 480 dyn·cm^{-1} for mercury and a pressure equilibration time of 11 s were used. Before the measurement of MIP, the He density for all the samples was measured in a Quantachrome Instruments automatic Micro Ultrapycnometer.

2.2.11. THERMOGRAVIMETRIC ANALYSIS

Thermogravimetric analysis (TGA) is a technique by which the variation of the mass of a substance is recorded as a function of time or temperature in a specific atmosphere, heating at a controlled rate. The change in mass of the sample as a function of the time or the temperature is reflected in a curve called a thermogram or thermogravimetric curve, which provides information on the thermal stability and composition of the initial sample, as well as on the residue and the volatile products that may be generated. The information provided by thermogravimetry is limited to the processes that produce a change in the mass of the analysed compound, which are: decomposition reactions, oxidations and processes such as vaporization, sublimation and desorption.

In this work, two different pieces of equipment have been used to obtain the TGA data. For Chapter 3.1, TGAs were performed under synthetic air (25 mL·min^{-1}) with a NETZSCH STA 449F3 DSC–TGA thermo-balance instrument. An alumina crucible containing 25 mg of the sample was heated at 5 °C min^{-1} in the temperature range of

30–700 °C. For Chapters 3.2, 4 and 5, TGAs were performed in a Shimadzu thermo-balance, model DTG-60, under a dynamic air atmosphere (20 mL·min^{-1}), at a heating rate of 5 °C ·min^{-1} over the temperature range 30 to 800 °C. Both types of equipment allow adjusting the heating rate, controlling the measurement atmosphere and selecting the temperature program.

Thermogravimetric analysis has been especially useful in this work, as it can be employed to (i) determine the thermal degradation processes, (ii) quantify the linker defect degree per formula unit within the MOFs, or (iii) to semi-quantify the functionalization degree achieved when solvent assisted linker exchange is applied to encode the MOFs. As explained in detail by G. C. Shearer and co-workers,[24] the average of the linker-defect positions per formula can be estimated from the weight loss associated with the organic linker calcination step. In Chapter 3.1, where the impact of the linker defects in the UiO-66-NH$_2$ structure for Cr^{VI} adsorption and photoreduction is studied, the defect degree of each sample was estimated from the weight loss associated with the organic linker calcination step occurring above ~300 °C[25]. The TGA curves exhibit three important weight loss steps for this material. The first one (in the temperature range between 30 to 100 °C) is related to the release of the solvent trapped within the porous framework. The second one (from 100 to 300 °C) is associated with the de-hydroxylation and de-hydration of the Zr-hexanuclear clusters. Finally, the third step is ascribed to the previously mentioned calcination of the organic linkers, which induces the collapse of the crystal framework.[26,27]

Assuming that the complete dehydration of the zirconium hexanuclear clusters of the MOFs occurs before the organic linker calcination step (~300 °C), the theoretical weight loss associated with the linker release can be calculated based on Equation 2.6.

$$Zr_6O_{6+x}(Linker)_{6-x} \rightarrow Zr_6O_{12} \tag{2.6}$$
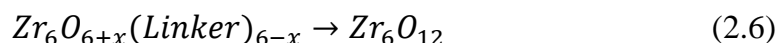
where x is the defect degree.

The theoretically calculated data (Table 2.6) can be fitted to a linear equation (Figure 2.6b) that has been used to determine the experimental defects per formula from experimental weight loss obtained from the thermogravimetric curves.

Table 2.6. Theoretical weight loss assigned to the organic linker calcination in UiO-66 and UiO-66-NH₂ samples calculated for different defect degrees.

	Defects degree	Formula	Molecular Weight Formula	Weight Difference*	% Diff
UiO-66	0	$Zr_6O_{6.0}(BDC)_{6.0}$	1628.03	888.69	54.59
	0.5	$Zr_6O_{6.5}(BDC)_{5.5}$	1553.97	814.63	52.42
	1	$Zr_6O_{7.0}(BDC)_{5.0}$	1479.91	740.57	50.04
	1.5	$Zr_6O_{7.5}(BDC)_{4.5}$	1405.85	666.52	47.41
	2	$Zr_6O_{8.0}(BDC)_{4.0}$	1331.79	592.46	44.48
UiO-66-NH₂	0	$Zr_6O_{6.0}(BDC-NH_2)_{6.0}$	1699.98	960.64	56.51
	0.5	$Zr_6O_{6.5}(BDC-NH_2)_{5.5}$	1619.92	880.58	54.36
	1	$Zr_6O_{7.0}(BDC-NH_2)_{5.0}$	1539.86	800.52	51.99
	1.5	$Zr_6O_{7.5}(BDC-NH_2)_{4.5}$	1459.81	720.47	49.35
	2	$Zr_6O_{8.0}(BDC-NH_2)_{4.0}$	1379.76	640.42	46.42

*The weight difference was calculated taking into account a molecular weight of 739.34 g·mol⁻¹ for the Zr_6O_{12} residue expected after the calcination.
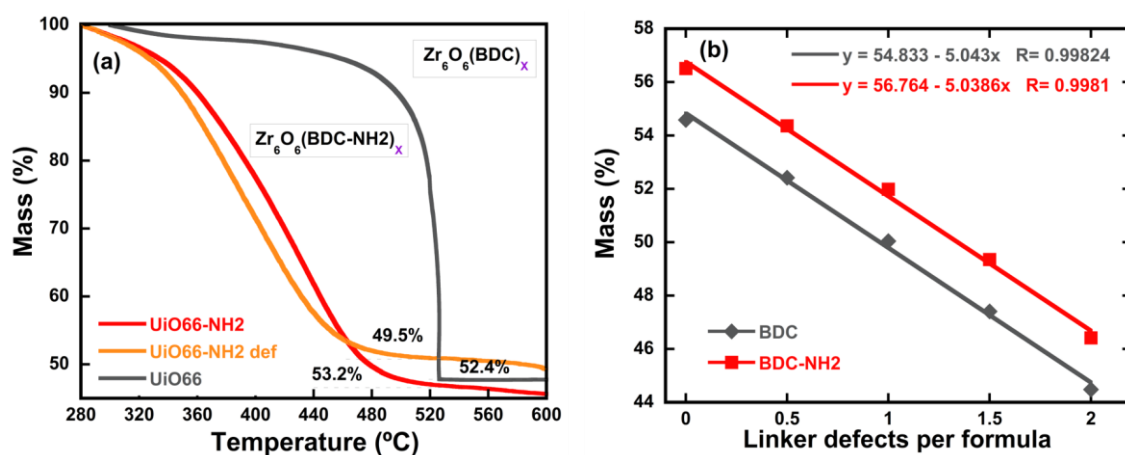
Figure 2.6. (a) Normalized TGA curves from 280 °C for the UiO-66 samples. (b) Theoretically calculated weight loss associated with linker defects in UiO-66-R (R = -H and NH2) compounds.

A similar approach has been followed to calculate the linker defect degree of MOF-808 in Chapter 4. Calculation of the BTC-linker defects was done by taking into account the chemical formula of the dehydroxylated MOF-808 and the molecular weights of the dehydroxylated MOF-808 and the ZrO_2 residue after the calcination (Table 2.7 and Figure 2.7).
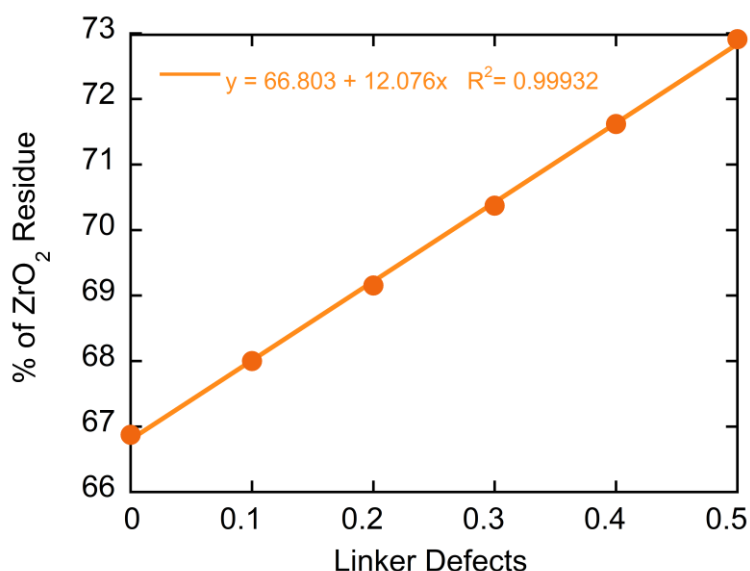
Figure 2.7. ZrO_2 residue percentage depending on the linker defects.

Table 2.7. Molecular weights of the dehydroxylated MOF-808 depending on the defect degree.

Formula at 350ºC	Molecular Weight	% of ZrO_2 residue
$Zr_6O_9(C_9H_3O_6)_2$	1105.57	66.9
$Zr_6O_{9.15}(C_9H_3O_6)_{1.9}$	1087.26	68.0
$Zr_6O_{9.30}(C_9H_3O_6)_{1.8}$	1068.95	69.2
$Zr_6O_{9.45}(C_9H_3O_6)_{1.7}$	1050.64	70.4
$Zr_6O_{9.6}(C_9H_3O_6)_{1.6}$	1032.32	71.6
$Zr_6O_{9.75}(C_9H_3O_6)_{1.5}$	1014.01	72.9

The experimental weight of the ZrO_2 residue when the weight loss data is normalized to 100% at 400 ºC (Figure 2.8), allows estimating the linker defect range by applying the equation of the fitting obtained in Figure 2.7.
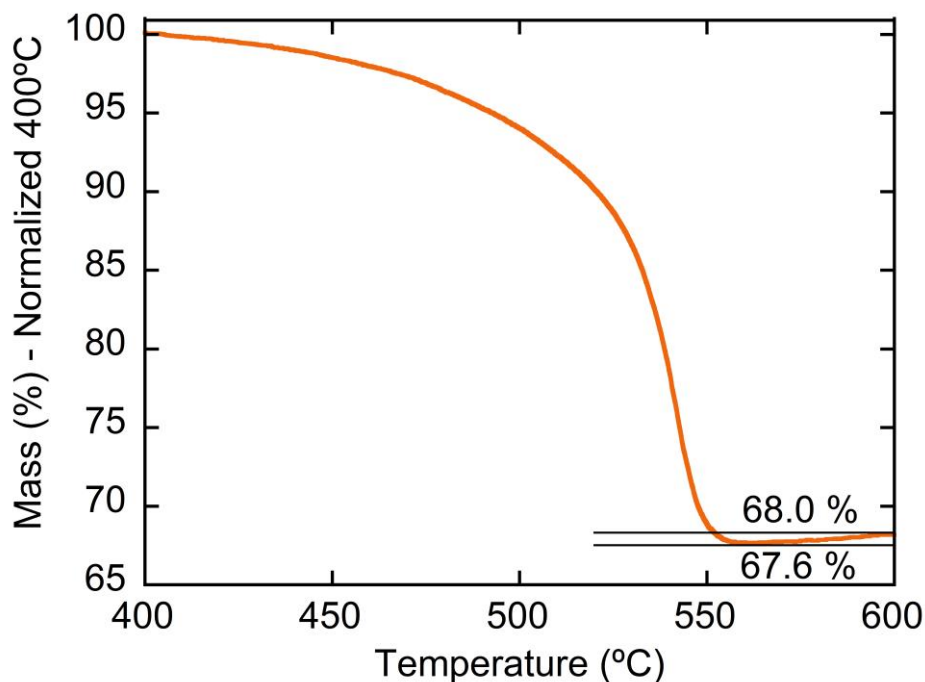
Figure 2.8. ZrO_2 residue percentage depending on the linker defects.

What is more, in Chapter 4, by taking into account the weight loss observed between 150 and 300 ºC, a rough estimation of the amino acid functionalization degree of the MOF-808 was obtained. Later on, more accurate data was obtained by ^{1}H-NMR.

2.2.12. DIFFERENTIAL SCANNING CALORIMETRY

Differential Scanning Calorimetry (DSC) is a thermal analysis technique that allows the study of those processes in which an enthalpy variation occurs. The technique usually consists of making a continuous record of the temperature difference between the analyzed sample and an inert reference material when both are subjected to a controlled temperature program (heating or cooling). When the sample undergoes some exothermic or endothermic phenomenon, a temperature variation is recorded between the sample (T_s) and the reference (T_r), ($\Delta T=T_s-T_r$). This way, the DSC can to provide important information such as the glass transition temperature, the melting point, the crystallization temperature, the percentage of crystallinity, the specific heat and the thermal stability, among others.

DSC analyses of Chapter 5 were performed on Mettler-Toledo DSC 822[e] under heating-cooling-heating cycles from -100 to 200 ºC, down to -100 ºC and finally back up to 200 ºC again. Measurements were performed under a N_2 atmosphere (flow rate 50 mL/min) in aluminium pans with a sample weight of approx. 7 to 10 mg. The measurements were recorded with heating and cooling rates of 10 ºC·min^{-1} and 20 ºC·min^{-1}, respectively.

2.2.13. SCANNING AND TRANSMISSION ELECTRON MICROSCOPIES

Electron microscopies are based on the use of an electron beam instead of a light beam to form an image.[28] In these techniques, a beam of electrons is produced at the top of the microscope by an electron gun. The electron beam follows a vertical path through the microscope, which is held within a vacuum. The beam travels through electromagnetic fields and lenses, which focus the beam down toward the sample. The electrons in the beam interact with the sample, producing various signals that can be used to obtain information. In scanning electron microscopy (SEM), secondary and backscattered electrons are analyzed, while in transmission electron microscopy (TEM), scattered electrons transmitted through the sample (usually a thin film or a suspension on a grid) are analysed. In addition, these devices usually include an energy dispersive X-rays (EDX) detector, which allows analysing the sample composition.

Both techniques have been used to study the morphology and composition of the MOFs used in this work as well as the MOF@polymer composites. The transmission electron employed has been a Philips Supertwin CM200 TEM, from the SGIker. This TEM operates at 200 kV and is equipped with a LaB_6 filament and EDAX-DX-4 microanalysis system. The equipment incorporates a double tilting sample holder, a Megaview III rapid acquisition camera, and a high resolution (4k x 4k) and high sensitivity digital camera.

On the other hand, two different scanning electron microscopes have been used: For all the MOF particles and PVDF-HFP@MOF membranes, (Chapter 3, 4 and 5.1) a HITACHI S-4800 with Field Emission Gun (FEG) cold cathode (0.5-30 kV) from

the SGIker was employed. The samples were dispersed in methanol under ultrasonication, and afterwards a drop was deposited in the copper sample holder and metalized with a gold conductive layer. For the SEM images including EDX mapping of Chapter 5.2, a Carl-Zeiss EVO-40 Electronic Scanning Microscopy equipment from SGIker was used, whereby both images in high vacuum mode (with metallization of the samples) and in extended pressure or low vacuum and wet sample mode (without the need to metalize the samples) can be employed. The equipment features a secondary electron detector (SIM) and a retro-scattered electron detector, together with an EDX elementary analyser, that allows performing both punctual and mapping analyses of the samples.

2.2.14. INDUCTIVELY COUPLED PLASMA ATOMIC EMISSION SPECTROSCOPY AND INDUCTIVELY COUPLED PLASMA MASS SPECTROMETRY

Inductively coupled plasma atomic emission spectroscopy (ICP-AES) is a type of emission spectroscopy based on the employment of inductively coupled plasma to excite atoms and ions which emit electromagnetic radiation at characteristic wavelengths of the element. The plasma is a high-temperature source of an ionized source gas (often argon) and it is sustained and maintained by inductive coupling from cooled electrical coils at megahertz frequencies. The source temperature is in the range of 6000 to 10,000 K, and the intensity of the emissions from various wavelengths of light is proportional to the concentrations of the elements within the sample.

A Horiba Yobin Yvon Activa atomic emission spectrometer with inductively-coupled plasma (ICP-AES) from the SGIker was used to quantify different metal concentrations during this work. The system is equipped with a glass and Teflon nebulizer system, which enables samples from acidic digestion to be determined using hydrofluoric acid. The equipment is controlled by a computer with Activa Analyst 5.4 software. It allows sequential multi-elemental analysis as well as numerous analytical requirements to be met due to the large linear interval that characterizes this technique, which in turn facilitates the analysis of majority and minority elements. For the

adsorption assays, samples were diluted until the detection limits of the equipment, performing triplicate measurements for each solution.

When higher sensitivity was needed (for example, metal adsorption efficiencies in natural conditions (1 ppm) in Chapter 4.1), an Agilent 7700 Mass spectrometer with inductively-coupled plasma (ICP-MS) from the SGIker was used. In this technique, an inductively coupled plasma is used to ionize the sample, but then it is analysed through a mass spectrometer.

2.2.15. X-RAY FLUORESCENCE

X-ray fluorescence (XRF) is based on the emission that occurs in a sample when it is irradiated with X-radiation. The most common method uses X-ray tubes to excite the samples, which, by absorbing the primary beam, emit their characteristic X-rays. This method is one of the most widely used for the qualitative identification of elements with atomic numbers greater than 8. It is also often used for semi-quantitative and quantitative analysis. One of the main advantages of this method is that it is not destructive like most elemental analysis techniques.

Each element has electronic orbitals of characteristic energy. When the sample is irradiated with X-radiation, an inner electron can be ejected, and when this happens, electrons in higher orbitals can "fall" into the lower orbital to fill the hole left behind (Figure 2.9). In this falling, energy is released in the form of a photon, the energy is equal to the energy difference between the two orbitals involved. Thus, the material emits radiation, which has energy characteristic of the atoms present.
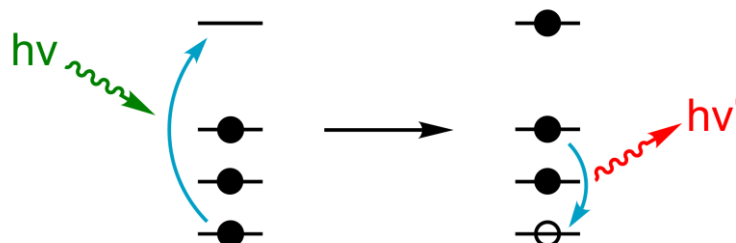
Figure 2.9. Schematic representation of the physics of X-ray fluorescence.

The X-ray fluorescence measurements on the compounds included in this thesis have been carried out in an FRX AXIOS spectrometer. The samples were homogeneously dispersed and slightly pressed between two polymeric films. The contribution of the sample holder and of the polymeric films were subtracted from the final measurement before the quantification of the samples.

2.2.16. PHOTOCONDUCTIVITY AND MOTT-SCHOTTKY MEASUREMENTS

The determination of the optical band gap is the first characterization step to understanding the optical properties of photocatalysts, information that afterwards will aid to adapt the source of illumination (i.e. wavelength equal or below to the optical band gap energy) during the photocatalytic experiments. But before to this stage, Mott-Schottky and photocurrent experiments give access to understanding the nature of the semiconducting process, and its efficiency to separate and transport the electron and hole pairs. To this end, the photocatalyst is usually integrated into an electron conductive transparent electrode (most usually Indium tin oxide coated glass slide). The system is connected in a three-electrode configuration (working electrode, Ag/AgCl reference electrode, and Pt counter electrode) while immersed in a liquid electrolyte. For n-type semiconductors, Mott-Schottky plots exhibit a positive and linear slope which is related to the flat band potential versus the reference electrode. The flat band potential of an n-type semiconductor (intercept value at the *x*-axis) can be used to estimate the conduction band (CB) of the semiconductor. By comparing the potential of the conduction band, it can be estimated to which extent it is more negative than the redox potential for a given reaction, such as the generation of radical oxygen species through the oxygen reduction (e.g. $O_2 \rightarrow \cdot O_2^-$ -0.13 V *vs.* Ag/AgCl)[29] or the Cr(VI) to Cr(III) transformation (+1.15 V *vs.* Ag/AgCl).[30]

Photocurrent experiments are performed with the same three-electrode configuration used to measure the Mott- Schottky curves, but instead of scanning the variation of the capacitance *vs.* the potential, the photocurrent response of the material in dark and illumination conditions is measured in an open circuit configuration mode. The absolute value of the photoconduction (always normalized to the area of the working electrode), is related to the capacity of the material to generate excitons and

separate their electron and hole components efficiently. In parallel, the profile of every single pulse (i.e. dark-illumination-dark cycle) in photocurrent experiments offers also information about how fast the material is able to respond to the illumination to generate and release the hole/electron pairs.

In Chapter 3.2, photoconductivity and Mott-Schottky measurements were acquired using a Biologic impedance analyser, in a standard three-electrode configuration with the sample as the working electrode, Ag/AgCl in 3 M KCl as reference electrode, a Pt sheet as the counter electrode, and a 0.2 M Na_2SO_4 aqueous solution, with a pH of 7, as the electrolyte. The samples consist of thin films of the UiO-66-R variants deposited on a transparent and conductive $F:SnO_2$ (FTO) coated glass. The samples were prepared by spin coating. First, the FTO-coated glass was sequentially cleaned by 10 minutes of ultrasonication in hellmanex solution, acetone, isopropanol and distilled water separately. The powdered materials were dispersed in methanol up to a 10 mg·mL^{-1} concentration dispersion. 50 µL of each dispersion was spun coated on a different FTO coated glass at 1000 rpm for 30 s, delimiting an active area of 1.5 cm^2. For the photoconductivity measurements, the system was maintained under short-circuit (0 V *vs.* Ag/AgCl), and the samples were submitted to illumination – dark cycles of 30 s, using a 150 W halogen lamp. Mott-Schottky measurements were taken under dark, using a 20 mV AC perturbation at 1000 Hz in a range of voltage from -1.0 to 1.0 V *vs.* Ag/AgCl. The range of voltage where the recombination in the depletion region dominates is used to fit the flat band potential.

2.2.17. CYCLIC VOLTAMMETRY

Cyclic Voltammetry (CV) is a technique of great importance in the field of electrochemistry, especially for studies of redox processes, reaction mechanisms or electrocatalytic properties. In a CV experiment, a potential is applied to the working electrode and ramped linearly versus time, and after the set potential is reached, it is ramped in the opposite direction to return to the initial potential. This way, the redox process of a substrate can be studied by measuring the received current. What is more, it also allows to study electron transfer-initiated chemical reactions, which includes catalysis.[31]

Cyclic voltammetry has allowed to study the redox capacity of MOFs in Chapter 4.2. The experiments were carried out at potentials between -900 and +800 mV at a scan rate of 50 mV in a 3M KNO_3 solution. To this end, active MOF materials were deposited at the working electrode just dispersing the 10 mg of the MOF powder in 1 mL of ethanol. 100 µL of the dispersion were successively deposited drop by drop on the working electrode, drying it at 80 ºC between the successive additions of the dispersion. In all cases, the open circuit potential (OCP) was determined prior to the start of the cyclic voltammetry. The starting potential was then selected within 50 mV of the OCP to ensure a near zero starting current. All measurements were carried out at room temperature. Cyclic voltammetry experiments were carried out using a SPELEC UV-Vis spectroelectrochemistry instrument (Metrohm-Dropsens, ES) controlled by DropView SPELEC software (version 3.0), installed on a PC running Windows 10. Unless otherwise stated, all spectra reported were collected using the reflectance cell, and all potentials are reported versus Ag. Electrodes were discarded after a single use.

2.2.18. DIELECTRIC SPECTROSCOPY

Dielectric spectroscopy (sometimes called impedance spectroscopy) measures the dielectric properties of a medium as a function of frequency. It is based on the interaction of an external field with the electric dipole moment of the sample, often expressed as permittivity. It is a powerful tool for the electrical characterization of nonconducting or semiconducting materials in relation to their structure, as it is sensitive to dipolar species and localized charges in a material, determining their strength, their kinetics and their interactions.

Dielectric spectroscopy has allowed to study the relaxation dynamics of the chitin before and after the insertion of MOF-808 in Chapter 5.2. The spectra were acquired using a Palm Sense 4 electrochemical workstation (Netherlands). Measurements were carried out in the frequency range 0.01 Hz-1 MHz at room temperature. Glassy carbon (diameter: 3mm) and graphite electrodes were employed as the working and the counter electrode respectively. CH and CH@MOF-808 hydrogels with a swelled thickness of 0.55 mm were used as test pieces.

2.2.19. HIGH PERMORMANCE LIQUID CHROMATOGRAFY

High Performance Liquid Chromatrography (HPLC) is a technique that allows to separate a sample into its individual components, thanks to the interactions of the sample with the mobile and stationary phases. Indeed, if the components are of different polarities, when the mobile phase goes through the column, one component will migrate through the column faster than the other. After going through the column, the presence of each component is usually monitored by other instrumental analysis such as UV-Vis spectroscopy.

The formation of the reaction byproducts in Chapter 4.2 was monitored by HPLC with an Agilent 1200 chromatographer and a ZORBAX SB-C18 (3.0 mm x 150 mm x 3.5 μm) column in reverse phase. Water was employed as the mobile phase. The measurements were carried out with a 0.4 mL·min^{-1} flux rate, column temperature of 30 ºC and 10 μL injection. A UV-Vis detector at 210 nm was used to monitor the byproducts of the reaction. Calibration curves for phenol, catechol and hydroquinone molecules were obtained with solutions of 0, 20, 50, 100, 250 and 500 mg·L^{-1} prepared from a parent solution at a concentration of 1g·L^{-1}. The measurements were done by triplicate for each of the solutions.

2.3. GENERAL MODELS AND EXPERIMENTAL PROTOCOLS

In the following, the isotherm and kinetic models applied to fit the experimental data of metal-adsorption and photoreduction experiments performed in the Thesis are detailed. Finally, the colorimetric protocol applied to quantify the concentration of Cr^{VI} ions in solution is described as well.

2.3.1. ISOTHERM MODELS

The Langmuir (Equation 2.7) and Freundlich (Equation 2.8) models, have been the two theoretical approximations applied to fit the experimental metal-ions adsorption isotherms.[32,33]

Langmuir model is defined as,

$$q_e = q_m K_L \frac{C_e}{1 + K_L C_e} \tag{2.7}$$

where q_e is the adsorption capacity (mg·g^{-1}) at equilibrium conditions, q_m is the maximum adsorption capacity, C_e is the equilibrium concentration and K_L is the Langmuir constant.

Freundlich model is described as,

$$q_e = K_F C_e^{1/n} \tag{2.8}$$

where q_e is the adsorption capacity at equilibrium conditions, q_m is the maximum adsorption capacity, C_e is the equilibrium concentration and K_F and n are constants for a given adsorbate and adsorbent at a particular temperature.

2.3.2. KINETIC MODELS

Metal ion adsorption tests

Bangham (Equation 2.9)[34], Pseudo-first order (Equation 2.10)[35], Pseudo-second order (Equation 2.12)[35] and Elovich (Equation 2.14)[36] models described below were employed to fit the metal-ions adsorption kinetic curves of this work.

Bangham kinetic model is defined as:

$$q_t = k_t \cdot t^{1/m} \tag{2.9}$$

where q_t is the amount of adsorbate adsorbed at a time t, 1/m provides an idea of the kinetics order of the system and k_t is the constant rate of the adsorption process.

Pseudo-first order kinetic model is defined as:

$$q_t = q_e(1 - e^{-k_1 t}) \tag{2.10}$$

This equation can also be displayed in a linearized form, shown in Equation 2.11.

$$\ln(q_e - q_t) = \ln q_e - k_1 t \tag{2.11}$$

where k_1 is the pseudo-first order constant rate, q_t is the amount of adsorbate adsorbed at a time t and q_e the equilibrium adsorption capacity.

Pseudo-second order kinetic model is defined as

$$q_t = \frac{q_e^2 k_2 t}{1 + q_e k_2 t} \qquad (2.12)$$

This equation can also be displayed in a linear form (Equation 2.13).

$$\frac{t}{q_t} = \frac{1}{q_e^2 k_2} + \frac{t}{q_e} \qquad (2.13)$$

where k_2 is the pseudo-second order constant rate, q_t is the amount of adsorbate adsorbed at a time t and q_e the equilibrium adsorption capacity.

Elovicth model is defined as

$$q_t = \left(\frac{1}{\beta}\right) \ln(\alpha\beta) + \left(\frac{1}{\beta}\right) lnt \qquad (2.14)$$

where q_t is the adsorption capacity at a certain time, α is the initial adsorption rate and β the Elovich constant.

Photocatalysis experiments

Langmuir-Hinshelwood model (Equation 2.15)[37] has been used to fit the photocatalysis experiments in Chapter 3. This equation is commonly used to describe surface catalysed reactions.

$$Ln\left(\frac{C}{C_0}\right) = -kt \qquad (2.15)$$

where k is the constant of reaction rate, C the ion concentration and C_0 the initial ion concentration.

Continuous flux columns

Thomas model (Equation 2.16)[38,39] has been used to fit the data obtained in the continuous flux Cr^{VI} adsorption in a column in Chapter 3, and the continuous flux metal separation in a column in Chapter 4. Mathematical models such as Thomas are used to describe the dynamic behaviour of the pollutants captured in a fixed-bed column assuming negligible external and internal diffusion limitations.

$$\frac{C_t}{C_o} = \frac{1}{1+\exp\left[\frac{k_{Th}q_0 m}{Q}-k_{Th}C_0 t\right]} \tag{2.16}$$

where q_0 is the equilibrium adsorption capacity, C_0 and C_t are the original and instant ion concentration, k_{Th} is the Thomas constant rate, m is the mass of the adsorbent and Q is the flow rate.

Catalytic Wet Peroxide Oxidation (CWPO)

First order kinetic model (Equation 2.17) has been used to fit the data of the Catalytic Wet Peroxide Oxidation in Chapter 4.2, and is described as:

$$\ln q_t = ln q_e - k_1 t \tag{2.17}$$

where q_t is the capacity at a certain moment, q_e the equilibrium capacity, and k_1 the first-order rate constant.

Michaelis-Menten fit (Equation 2.18) has been used to fit the CWPO performed at different concentrations, and is described as:

$$V_0 = V_{max}\frac{[S]}{K_M+[S]} \tag{2.18}$$

where V_0 is the apparent initial catalytic rate, K_M is the apparent Michaelis-Menten constant, V_{max} is the maximum apparent initial reaction rate and $[S]$ is the substrate concentration.

2.3.3. COLORIMETRIC METHOD FOR Cr^{VI} DETERMINATION

Quantification of Cr^{VI} was performed inspired by the previously reported 1,5-Diphenylcarbazide colorimetric methodology.[40,41] First, a highly concentrated Cr^{VI} stock solution was prepared with distilled water. Several solutions of lower concentrations were prepared to obtain the calibration curve. The 1,5-diphenylcarbazide protocol was applied to each of the solutions to obtain a linear correlation of the Cr^{VI} concentration and the absorbance value at $\lambda_{max} = 540$ nm. To this end, 10 µL H_2SO_4 10% (v/v) and 100 µL of a 1,5-diphenylcarbazide solution (5 mg·mL^{-1} in acetone) were added to 5 mL of the chromium solution. The mixture was stirred for 10 minutes and then the absorbance was measured at 540 nm. Once the calibration curve was obtained, the 1,5-diphenylcarbazide protocol is applied to the solutions generated during the photocatalysis experiments. Once the absorbance of the solutions at 540 nm was recorded, their Cr^{VI} concentration can be obtained from the previously obtained calibration curve. The overall chromium concentration (Cr^{III} + Cr^{VI}) was determined as well by the 1,5-diphenylcarbacide protocol but with an additional oxidative step for the samples' preparation. Cr^{III} was oxidized to Cr^{VI} by adding 500 µL of a 1 N H_2SO_4 solution and 250 µL of a $KMnO_4$ solution (1.6 M $KMnO_4$ in H_2SO_4 1 N) to a 5 mL of the chromium solution. The mixture was heated at 100 °C for 20 min and then cool down to room temperature in a water bath. Afterwards, 50 µL of a NaN_3 solution (0.05 g NaN_3 in 1.25 mL of water) was added to the mixture until the purple colour of the potassium permanganate disappears from the solution. Finally, the 1,5-diphenylcarbazide colorimetric methodology was used to quantify the chromium content. The Cr^{III} concentration was calculated by subtracting the Cr^{VI} concentration from the overall chromium concentration of the solutions.

2.4. REFERENCES

1   Subudhi S, Tripathy SP, Parida K. Highlights of the characterization techniques on inorganic, organic (COF) and hybrid (MOF) photocatalytic semiconductors. *Catal Sci Technol* 2021; **11**: 392–415. [DOI: 10.1039/d0cy02034f]

2   Guinier A. X-ray diffraction in crystals, imperfect crystals and amorphous bodies. Courier Corporation

3   Gawas UB, Mandrekar VK, Majik MS. Structural analysis of proteins using X-ray diffraction technique. In: *Advances in Biological Science Research: A Practical Approach*. Elsevier Inc., 2019: 69–84.

4   Groom CR, Allen FH. The Cambridge Structural Database in Retrospect and Prospect. *Angewandte Chemie International Edition* 2014; **53**: 662–671. [DOI: 10.1002/ANIE.201306438]

5   Allen FH. The Cambridge Structural Database: A quarter of a million crystal structures and rising. *Acta Crystallogr B* 2002; **58**: 380–388. [PMID: 12037359 DOI: 10.1107/S0108768102003890/HTTPS://JOURNALS.IUCR.ORG/SERVICES /TERMSOFUSE.HTML]

6   Frontera C, Rodríguez-Carvajal J. FullProf as a new tool for flipping ratio analysis. *Physica B Condens Matter* 2003; **335**: 219–222. [DOI: 10.1016/S0921-4526(03)00241-2]

7   Bindzus N, Iversen BB. Maximum-entropy-method charge densities based on structure-factor extraction with the commonly used Rietveld refinement programs GSAS, FullProf and Jana2006. *Acta Crystallogr A* 2012; **68**: 750–762. [DOI: 10.1107/S0108767312037269/WL5161SUP1.PDF]

8   Perl J, Shin J, Schümann J, Faddegon B, Paganetti H. TOPAS: An innovative proton Monte Carlo platform for research and clinical applications. *Med Phys* 2012; **39**: 6818–6837. [PMID: 23127075 DOI: 10.1118/1.4758060]

9   Hollamby MJ. Practical applications of small-angle neutron scattering. *Physical Chemistry Chemical Physics* 2013; **15**: 10566–10579. [DOI: 10.1039/c3cp50293g]

10   Río-lópez NA, Lázpita P, Salazar D, Petrenko VI, Plazaola F, Chernenko V, Porro JM. Neutron scattering as a powerful tool to investigate magnetic shape memory alloys: A review. *Metals (Basel)* 2021; **11**: 1–21. [DOI: 10.3390/met11050829]

11   Feynman RP. Quantum mechanics, vol. 3. In: *Lectures on Physics*. Addison Wesley Longman, 1970

12   Heenan RK, Rogers SE, Turner D, Terry AE, Treadgold J, King SM. Small Angle Neutron Scattering Using Sans2d. *Neutron News* 2011; **22**: 19–21.

13   Wignall GD, Bates FS. Absolute calibration of small-angle neutron scattering data. *J Appl Crystallogr* 1987; **20**: 28–40. [DOI: 10.1107/S0021889887087181]

14   Mitchell PCH, Parker SF, Ramirez-Cuesta AJ, Tomkinson J. Vibrational spectroscopy with neutrons: with applications in chemistry, biology, materials science and catalysis. World Scientific

15   Ivanov A, Jimenéz-Ruiz M, Kulda J. IN1-Lagrange-the new ILL instrument to explore vibration dynamics of complex materials. *J Phys Conf Ser* 2014; **554**. [DOI: 10.1088/1742-6596/554/1/012001]

16   Cameron JM, Bruno C, Parachalil DR, Baker MJ, Bonnier F, Butler HJ, Byrne HJ. Vibrational spectroscopic analysis and quantification of proteins in human blood plasma and serum. In: *Purified Proteins to Aggregates and Assemblies*.2020: 269–314.

17   Sereshti H, Vasheghani Farahani M, Baghdadi M. Trace determination of chromium(VI) in environmental water samples using innovative thermally reduced graphene (TRG) modified SiO2 adsorbent for solid phase extraction and UV-vis spectrophotometry. *Talanta* 2016; **146**: 662–669. [PMID: 26695315 DOI: 10.1016/j.talanta.2015.06.051]

18   Rai D, Sass BM, Moore DA. Chromium(III) hydrolysis constants and solubility of chromium(III) hydroxide. *Inorg Chem* 1987; **26**: 345–349. [DOI: 10.1021/ic00250a002]

19   Sing K. The use of nitrogen adsorption for the characterisation of porous materials. *Colloids Surf A Physicochem Eng Asp* 2001; **187–188**: 3–9. [DOI: 10.1016/S0927-7757(01)00612-4]

20   Kumar KV, Gadipelli S, Wood B, Ramisetty KA, Stewart AA, Howard CA, Brett DJL, Rodriguez-Reinoso F. Characterization of the adsorption site energies and heterogeneous surfaces of porous materials. *J Mater Chem A Mater* 2019; **7**: 10104–10137. [DOI: 10.1039/c9ta00287a]

21   Chul K, Yoon T, Bae Y. Applicability of using CO2 adsorption isotherms to determine BET surface areas of microporous materials. *Microporous and Mesoporous Materials* 2016; **224**: 294–301. [DOI: 10.1016/j.micromeso.2016.01.003]

22   Gregg SJ, Sing, W. KS, Salzberg HW. Adsorption Surface Area and Porosity. *J Electrochem Soc* 1967; **114**: 279C.

23   Brabazon D. Nanocharacterization Techniques for Dental Implant Development. In: *Emerging Nanotechnologies in Dentistry*. First Edit. Elsevier Inc., 2012: 307–331.

24 Shearer GC, Chavan S, Ethiraj J, Vitillo JG, Svelle S, Olsbye U, Lamberti C, Bordiga S, Lillerud KP. AAAAAAAAAAAAAAAAAAAA. *Chemistry of Materials* 2014; **26**: 4068–4071. [DOI: 10.1021/cm501859p]

25 Audu CO, Nguyen HGT, Chang CY, Katz MJ, Mao L, Farha OK, Hupp JT, Nguyen ST. The dual capture of AsV and AsIII by UiO-66 and analogues. *Chem Sci* 2016; **7**: 6492–6498. [DOI: 10.1039/c6sc00490c]

26 Chavan S, Vitillo JG, Uddin MJ, Bonino F, Lamberti C, Groppo E, Lillerud KP, Bordiga S. Functionalization of UiO-66 metal-organic framework and highly cross-linked polystyrene with Cr(CO)3: In situ formation, stability, and photoreactivity. *Chemistry of Materials* 2010; **22**: 4602–4611. [DOI: 10.1021/cm1005899]

27 Valenzano L, Civalleri B, Chavan S, Bordiga S, Nilsen MH, Jakobsen S, Lillerud KP, Lamberti C. Disclosing the complex structure of UiO-66 metal organic framework: A synergic combination of experiment and theory. *Chemistry of Materials* 2011; **23**: 1700–1718. [DOI: 10.1021/cm1022882]

28 Egerton RF. Physical Principles of Electron Microscopy. Springer

29 Liang Q, Cui S, Liu C, Xu S, Yao C, Li Z. Construction of CdS@UIO-66-NH2 core-shell nanorods for enhanced photocatalytic activity with excellent photostability. *J Colloid Interface Sci* 2018; **524**: 379–387. [PMID: 29660625 DOI: 10.1016/j.jcis.2018.03.114]

30 Shen L, Liang S, Wu W, Liang R, Wu L. Multifunctional NH2-mediated zirconium metal-organic framework as an efficient visible-light-driven photocatalyst for selective oxidation of alcohols and reduction of aqueous Cr(vi). *Dalton Transactions* 2013; **42**: 13649–13657. [PMID: 23903996 DOI: 10.1039/c3dt51479j]

31 Elgrishi N, Rountree KJ, McCarthy BD, Rountree ES, Eisenhart TT, Dempsey JL. A Practical Beginner's Guide to Cyclic Voltammetry. *J Chem Educ* 2018; **95**: 197–206. [DOI: 10.1021/ACS.JCHEMED.7B00361/SUPPL_FILE/ED7B00361_SI_002.DOCX]

32 Demir S, Brune NK, Van Humbeck JF, Mason JA, Plakhova T V., Wang S, Tian G, Minasian SG, Tyliszczak T, Yaita T, Kobayashi T, Kalmykov SN, Shiwaku H, Shuh DK, Long JR. Extraction of lanthanide and actinide ions from aqueous mixtures using a carboxylic acid-functionalized porous aromatic framework. *ACS Cent Sci* 2016; **2**: 253–265. [DOI: 10.1021/acscentsci.6b00066]

33 G. Saiz, P., Iglesias, N., Gonzalez-Navarrete, B., Rosales, M., Quintero, Y. M., Reizabal, A., Orive, J., Fidalgo-Marijuan, A., Lanceros-Mendez, S., Arriortua, M. I.,& Fernandez de Luis R. Chromium speciation in zirconium-based metal

– organic frameworks for environmental remediation. *Chemistry—A European Journal* 2020; **26**: 1–13. [DOI: 10.1002/chem.202001435]

34   Rodriguez A, Ovejero G, Mestanza M, García J. Removal of Dyes from Wastewaters by Adsorption on Sepiolite and Pansil. *Ind Eng Chem Res* 2010; **49**: 3207–3216.

35   Gil A, Assis FCC, Albeniz S, Korili SA. Removal of dyes from wastewaters by adsorption on pillared clays. *Chemical Engineering Journal* 2011; **168**: 1032–1040. [DOI: 10.1016/j.cej.2011.01.078]

36   Wu FC, Tseng RL, Juang RS. Characteristics of Elovich equation used for the analysis of adsorption kinetics in dye-chitosan systems. *Chemical Engineering Journal* 2009; **150**: 366–373. [DOI: 10.1016/J.CEJ.2009.01.014]

37   Zoltan T, Rosales MC, Yadarola C. Reactive oxygen species quantification and their correlation with the photocatalytic activity of TiO2 (anatase and rutile) sensitized with asymmetric porphyrins. *J Environ Chem Eng* 2016; **4**: 3967–3980. [DOI: 10.1016/j.jece.2016.09.008]

38   Abdi J, Abedini H. MOF-based polymeric nanocomposite beads as an efficient adsorbent for wastewater treatment in batch and continuous systems: Modelling and experiment. *Chemical Engineering Journal* 2020; **400**: 125862. [DOI: 10.1016/J.CEJ.2020.125862]

39   Han R, Wang Y, Zhao X, Wang Y, Xie F, Cheng J, Tang M. Adsorption of methylene blue by phoenix tree leaf powder in a fixed-bed column: experiments and prediction of breakthrough curves. *Desalination* 2009; **245**: 284–297. [DOI: 10.1016/J.DESAL.2008.07.013]

40   Sereshti H, Vasheghani Farahani M, Baghdadi M. Trace determination of chromium(VI) in environmental water samples using innovative thermally reduced graphene (TRG) modified SiO2 adsorbent for solid phase extraction and UV-vis spectrophotometry. *Talanta* 2016; **146**: 662–669. [PMID: 26695315 DOI: 10.1016/j.talanta.2015.06.051]

41   Rai D, Sass BM, Moore DA. Chromium(III) hydrolysis constants and solubility of chromium(III) hydroxide. *Inorg Chem* 1987; **26**: 345–349. [DOI: 10.1021/ic00250a002]

Chapter 3
MOFs as photoreductive materials for Cr^{VI} remediation in wastewater

Among the heavy metal ions, hexavalent chromium (Cr^{VI}) is particularly dangerous due to its carcinogenicity, teratogenicity, and acute toxicity,[1–3] but in parallel, it plays a pivotal role in metal plating, metallurgy, tanning and textile industries,[4] causing substantial industrial water pollution worldwide. Cr^{VI} is typically found in water media in the form of chromate oxyanions (such as $(H_xCrO_4)^{2-x}$ or $Cr_2O_7^{2-}$). With a net negative charge, high solubility and mobility, hexavalent chromium is difficult to remove from water media if it is not reduced to its less soluble and toxic trivalent form.[2,5]

Several technologies, including precipitation-coagulation, ion exchange[6], membrane separation[7] or adsorption[8] are currently applied to remove Cr^{VI} from waste and industrial water effluents. Unfortunately, except adsorption, most of the processes are energy intensive (e.g. membrane separation[9]) or require the addition of co-chemicals/products to achieve an efficient chromium removal (e.g. coagulation, chemical reduction). Therefore, in the last decades, photocatalytic reduction of Cr^{VI} to the less toxic and mobile Cr^{III} has gained a great deal of attention due to its effectiveness, low-cost, no addition of co-reagents, and absence of generation of secondary hazardous chemicals[10–12]. However, the scientific community has paid less attention to assess whether the photocatalysts are able to immobilize or adsorb the trivalent chromium cations[13] at the same time that hexavalent species are photoreduced.[14,15]

When approaching water remediation from a circular economy point of view, the conjunction of photocatalysis and adsorption functionalities in the same material is of paramount importance. For instance, as shown in the Pourbaix diagram of Figure 3.1, above a critical pH threshold, the photoreduced Cr^{III} ions usually precipitate as Cr(OH)$_3$ solid, making it easy to recover after operation.[2,16,17] Nonetheless, under this critical pH frontier, the Cr^{III} species generated during the Cr^{VI} photoreduction remain

soluble.[18] At these acidic solutions, an additional immobilization step is necessary to extract Cr^{III} ions from the aqueous media. Here, the importance of bifunctional photocatalysts that are able to transform and retain chromium species is revealed, since they open the possibility to couple environmental detoxification of polluted water sources (photocatalysis) to the recovery of critical raw elements such as chromium (adsorption).[1]
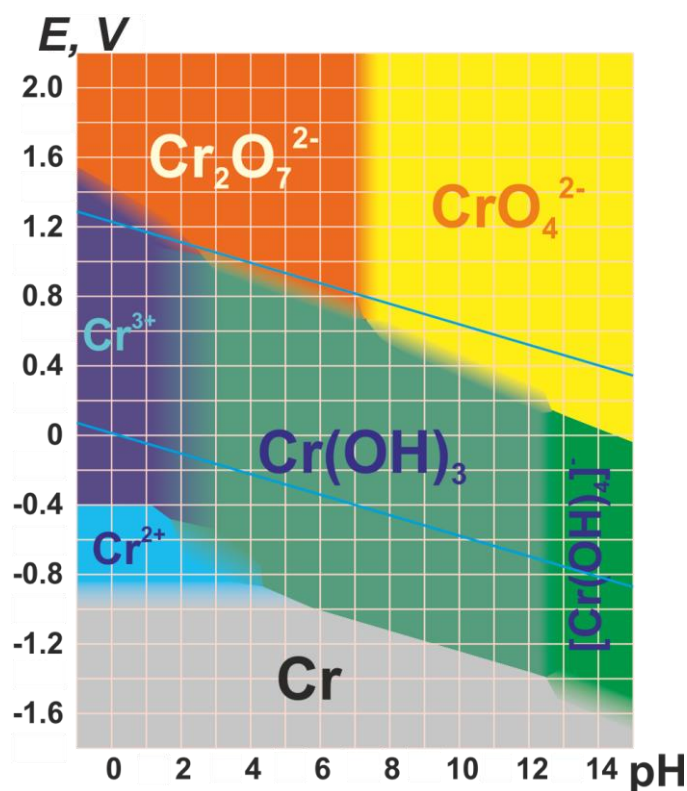
Figure 3.1. Pourbaix diagram of Cr. Reproduced from Denis Zihilin. Copyright <u>CC BY-SA 3.0</u> License: <u>https://creativecommons.org/licenses/by-sa/3.0/legalcode</u>

It is important to note that chromium is currently located at the borderline of the European raw materials map because of its economic importance.[19,20] Indeed, the circular water remediation concept gains even more relevance if it is applied in highly concentrated and acidic water effluents arising from industrial (e.g., plating, alloying, tanning, textile dyes, pigments…) and mining activities (e.g., acidic water streams)[21]. Chromium recovery from these media becomes economically appealing to reduce the costs associated with the water treatment.[22] The challenge to manage acid rising waters derived from industrial platting or tanning activities is even more challenging

than the revalorization of exhausted electrolytic baths or highly concentrated solutions applied in industrial manufacturing processes. In this case, chromium is highly diluted in large volumes of water, and its recovery by the technologies usually applied to concentrated industrial solutions (e.g., as liquid-liquid extraction, ion exchange and/or electrochemical separation[23] or precipitation, acid leaching, and subsequent precipitation[24]) is neither efficient nor economically appealing to revalorize the chromium ions. Diluted hexavalent chromium solutions require high-cost chemicals for their reduction to Cr^{III} until the legal thresholds for Cr^{VI} (groundwater = 0.1 ppm, drinking water = 0.05 ppm)[8] are accomplished. This scenario is where bifunctional photocatalyst sorbents could play a key role to couple the water treatment with the chromium recovery.

At the materials design level, a bi-functional photocatalyst applied for chromium recovery needs to be specifically tailored to (i) harvest light, (ii) induce hole-electron pairs separation, (iii) transport them avoiding their recombination, and (iv) generate reactive oxygen radicals. At the same time, these bi-functional materials need to (v) adsorb the chemical species transformed during photocatalysis, which in the specific case studied in this chapter are the Cr^{III} ions, but also the Cr^{V} pentavalent transient species generated during the Cr^{VI} to Cr^{III} photoreduction. Therefore, efficient light harvesting[25], semiconducting nature[26], porosity[27–29], and chemical affinity to capture the transformed species are some of the key characteristics that need to be specifically encoded within the desired bi-functional catalyst.[30]

Classic metal-oxide photocatalysts exhibit excellent photodegradation activities over a variety of pollutants, but their capacity to adsorb or retain the photodegradation intermediates and products is limited by their reduced porosity and surface areas [31–34]. In this context, Metal-Organic Frameworks (MOFs) stand out as highly porous materials able to meet photoactivity and porosity. MOFs can be formed from semiconductor metal-oxide clusters, and efficient light-harvesting organic linkers; which are assembled in extended and ordered porous structures.[35,36] The combination of these two characteristics, together with the possibility to further decorate or engineer their structures, both pre and post-synthetically, make MOFs the ideal candidates to combine photoreduction and adsorption properties.[37–40]

3.1. BI-FUNCTIONAL PHOTOCATALYSTS: ARCHETYPICAL Zr-TEREPHTHALATE AND Ti-TEREPHTHALATE MOFs

Metal-Organic Frameworks have been widely applied for chromium adsorption, photoreduction and detection purposes,[5,8,16,41] but their combined capacity to photoreduce and at the same time adsorb the phototransformed trivalent chromium ions has been rarely explored.[4] In the last years, the photocatalytic activity of UiO-66-NH$_2$ and MIL-125 to transform Cr^{VI} to Cr^{III} has been proved under varied experimental conditions (e.g. chromate concentration, photocatalyst loading, source of illumination, pH of the media, presence of competitor species, electron and holes scavengers...). In parallel, several studies point out that UiO-66-NH$_2$ is able to sorb quite efficiently both hexavalent and trivalent species from solution, exhibiting also a moderate capacity to chemically reduce the Cr^{VI} to Cr^{III} under dark conditions.[42,43] What is more, the chromium speciation within the Zr-MOF sorbents and photocatalysts has been successfully determined in a previous research by our group by applying a combination of UV-Vis and electron paramagnetic resonance (EPR) spectroscopies.[3] These findings confirmed that Cr^{VI} to Cr^{III} chemical and photoreduction processes are driven by the intermediate generation of transient pentavalent chromium, that later on are stabilized upon further reduction as trivalent isolated or clustered ions inside UiO-66-based materials.[3] Nevertheless, this research did not unravel the fate of trivalent chromium phototransformed species in solution, that is, whether Cr^{III} is stabilized into the MOF porous photocatalysts or if it migrates to the aqueous surrounding media, especially when the experiments are carried out at acidic conditions where Cr^{III} ions are soluble. This experimental gap, that is, the lack of monitoring of the concentration of hexavalent and trivalent chromium in solution during photocatalysis, is common for most of the investigations carried out in Cr^{VI} to Cr^{III} photoreduction experiments. Most typically, during photocatalysis, the concentration of the hexavalent chromium is experimentally determined by UV-Vis or Inductively Coupled Plasma (ICP) analysis, overriding the monitoring of the trivalent chromium ions that could be still present in the solution after the photoreduction. In this work, we have fulfilled this gap, researching whether the photoactive MOFs can also act as efficient sorbents of the photoreduced Cr^{III} ions.

The photoreduction and adsorptive capacities of two iconic photoactive water-stable zirconium and titanium-based MOFs, UiO-66 and MIL-125, have been addressed. For both materials, the experimental monitoring of Cr^{VI} and Cr^{III} in solution during and after the operation has been determined. Going a step forward, photoactive chromatographic columns based on UiO-66-NH$_2$ have been assembled to perform Cr^{VI} adsorption in a continuous flux mode. Our conclusions clearly point out that the studied bifunctional MOFs are able to completely photoreduce Cr^{VI} to Cr^{III} and at the same time partially immobilize reduced Cr^{III} species.

3.1.1. EXPERIMENTAL PROCEDURE

Synthesis of Materials

UiO-66, UiO-66-NH$_2$, and UiO-66-NH$_2$-def (-def stands for the linker defective sample) were prepared through a slightly modified solvothermal synthesis previously reported by Øien *et al.*[44] First, zirconium chloride (ZrCl$_4$, 0.5418 g) was dissolved in 60 mL of dimethylformamide (DMF) under stirring in a Pyrex® autoclave. Afterwards, terephthalic acid (BDC, 0.3801 g) or aminoterephthalic acid (BDC-NH$_2$, 0.4185 g) and distilled water (1.5 mL) were added to the ZrCl$_4$ solution under continuous stirring in order to obtain the UiO-66 and UiO-66-NH$_2$ samples. The synthesis of the UiO-66-NH$_2$-def sample requires the addition of 1 mL of HCl (37%) solution to the ZrCl$_4$, BDC-NH$_2$ acid and DMF mixture. Once a clear solution is obtained, the Pyrex® reactor was closed and placed in a preheated oven (80 °C for 24 h). After that, the sample was recovered by centrifugation and washed three times with methanol. Finally, the compound was dried at 80 °C for 12 h.

MIL-125 samples were prepared through two different synthesis methods. First, MIL125-R was synthetized by reflux adapting the protocol described by Wang *et al.*[45] BDC (7.70 g) was dissolved in 100 mL of DMF under reflux and continuous stirring at 100 °C for 1 h. Then, 28 mL of methanol was added to the solution and further stirred for 1 h. Afterwards, 8.4 mL of Titanium isopropoxide (Ti(iPrO)$_4$) was added drop by drop to prevent the formation of agglomerates. The reaction was refluxed for three days, recovered by centrifugation, and thoroughly washed with

DMF (100 mL, three times) and methanol (100 mL, three times) over the period of three days to remove the non-reacted reagents. Finally, it was dried at 80°C during one day. On the other hand, MIL-125-H was synthetized by a hydrothermal protocol described by Dan-Hardi *et al.*[46] First 0.5 g of BDC and 0.6 mL of Ti(iPrO)$_4$ were introduced in a solution of DMF (9 mL) and methanol (1 mL). The mixture was stirred for 5 minutes and then introduced into a 40 mL Teflon® Lined autoclave reactor. The Teflon® container was introduced into a metallic PAAR digestion bomb at 150ºC for 15 hours. After the system was cooled at room conditions, the solid was recovered by filtration, washed twice with acetone and dried under air at room temperature. All the materials were finally activated at 200 °C overnight for 12 hours.

Adsorption Kinetics

Cr^{VI} and Cr^{III} adsorption kinetics were conducted in the same conditions as those of the photoreduction experiments described in the following section (5 ppm Cr^{VI} or Cr^{III} solution, 0.25 g·L^{-1} of adsorbent) but in the absence of light. 5 mL aliquots were taken from the solution at different time intervals until adsorption equilibrium was reached. The liquid samples were filtrated with a hydrophilic 0.20 µm filter, acidified for its stabilization, and finally analysed by means of ICP-AES (see section 2.2.10). The adsorption capacity of the materials at different equilibrium times was calculated considering the initial and equilibrium concentrations of chromium, the volume of the solution, and the mass of the sorbent material. The data was plotted as adsorption capacity (mg Cr adsorbed per grams of sorbent) versus the equilibrium time. The kinetic curves were fitted to Bangham (Equation 2.8) and Pseudo-second order (Equation 2.11) kinetic models.[47,48]

Photocatalytic Reduction of Cr^{VI} to Cr^{III}

Photocatalysis experiments were conducted in a 5 ppm Cr^{VI} solution using 0.25 g·L^{-1} photocatalyst loading illuminated under UV and Vis light sources. First, 50 mg of the photocatalyst was immersed in 200 mL of Cr^{VI} 5 ppm solution under stirring in the dark. Once the adsorption equilibrium was achieved, 5 mL aliquots were taken at

different times under illumination conditions. The experiments were performed in a LuzChem LZC-4V photoreactor equipped with 14 lamps emitting in the ultraviolet range. Additional experiments were performed using visible lamps and also reducing the catalyst's loading down to a concentration of 0.35 g·L^{-1}.

The quantification of Cr^{VI} was performed inspired on the previously reported diphenyl carbazide colorimetric methodology,[49,50] which can be found in section 2.3.3. Photoreduction processes were fitted with the Langmuir-Hinshelwood model (Equation 2.13).[51]

Continuous Flux Adsorption Experiments

Open chromatographic columns of 1% weight of UiO-66-NH$_2$ (0.0125 g) in sand (1.25 g) were assembled as illustrated in Figure 3.2. A continuous flux of 1 mL·min^{-1} of a chromium solution of 2.5 ppm concentration was passed through the column, and the Cr^{VI} concentration was monitored during the process. A similar experiment was conducted with 2.5, 30 and 50 ppm chromium solutions but configuring the system to work in a closed loop. The chromium concentration was monitored until the MOF has reached its saturation point, that is, when the concentration of the input and output solutions is equal when the system is run in an open configuration, or, at the moment that the Cr^{VI} concentration is stabilized when the experiment is carried out in a closed loop.

Figure 3.2. Image of the UiO-66-NH$_2$/sand column experiment in closed circuit mode.

3.1.2. RESULTS AND DISCUSSION

<u>Metal-Organic Framework Selection, Synthesis and Characterization</u>

Among the MOFs that could potentially exhibit bi-functional photocatalytic and adsorption activities, zirconium aminoterephthalate (UiO-66-NH$_2$) and titanium terephthalate (MIL-125) compounds have been selected as benchmark materials to conduct this section. As explained in detail in the introduction, both MOFs exhibit a fcu topology arising from the connectivity between the inorganic hexanuclear clusters through twelve terephthalate-type organic linkers.[46,52] In the specific case of UiO-66-NH$_2$, it exhibits a cubic symmetry; which is slightly distorted to a pseudo-cubic orthorhombic group for the MIL-125 material.

Further, the effect on the photocatalytic and adsorptive properties of (i) the particle size of MIL-125 material and (ii) the organic linker defect density of UiO-66-NH$_2$ have been studied. MIL-125 has been synthesized as micron-size particles applying hydrothermal synthesis (here and after denoted as MIL-125-H) and as nanoparticles (100-400 nm) under reflux conditions (here and after identified as MIL-125-R). Despite the bulk to surface proton-coupled transfer has been confirmed to be highly independent of the particle size for MIL-125[53], the Cr^{VI} to Cr^{III} photoreduction kinetics are greatly affected by this parameter. In parallel, the density of the organic linker defects in UiO-66-NH$_2$ has been modulated by the addition of hydrochloric acid inorganic modulator to the reaction media. It is duly proved that acid modulators induce a random displacement of aminoterephthalate organic linkers along the fcu crystal structure of UiO-66 type frameworks.[37,54,55] Two are the side-effects of increasing the density of linker defects on the UiO-66-NH$_2$ properties: first, an increase of the overall surface area and pore volume, and second; the generation of preferential chemisorption positions for inorganic oxyanions.[56–58] Therefore, "defect-free" UiO-66-NH$_2$ and linker defective UiO-66-NH$_2$-def materials were synthesized at the same hydrothermal conditions but adding a controlled volume of HCl in the specific case of the defective sample.

Once synthesized, the quality, particle size, porosity and optical properties of the materials were fully characterized by X-ray diffraction, UV-Vis spectroscopy,

thermogravimetric analysis, transmission electron microscopy and surface area measurements.

The X-ray diffraction (XRD) patterns of the samples were analysed by a full profile pattern fitting, which confirms that the experimental data are fully consistent with the cell parameters and the symmetry of UiO-66[44] and MIL-125[46], as can be observed in Figure 3.3.
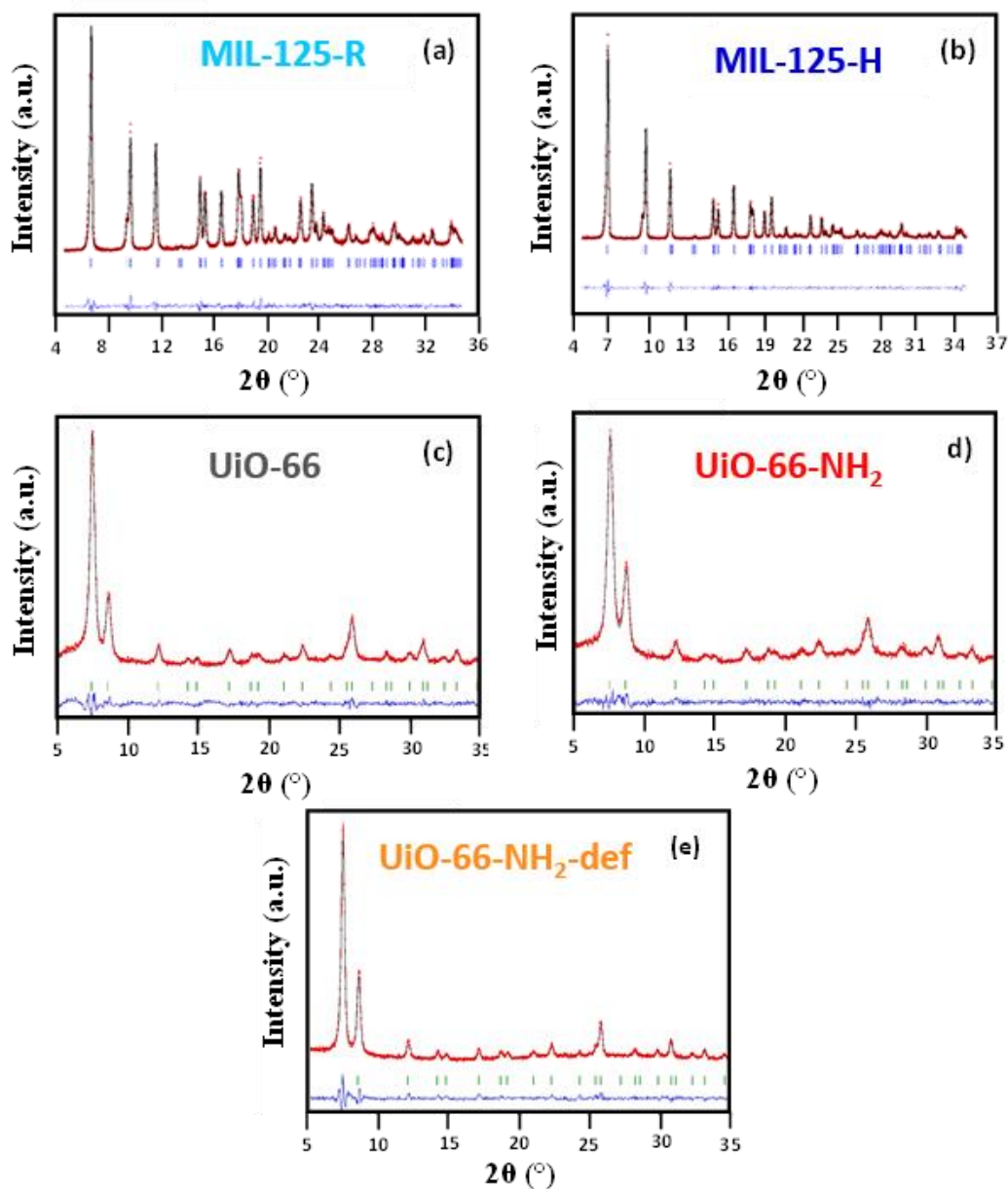
Figure 3.3. Powder X-ray diffraction profile matching analysis of: (a) MIL125-R, (b) MIL125-H, (c) UiO-66, (d) UiO-66-NH₂ and (e) UiO-66-NH₂-def samples.

The final results obtained from the XRD fittings confirmed that there are no meaningful displacements of the cell parameters due to the generation of linker defects in UiO-66-NH$_2$-def, neither associated to the particle size reduction from MIL-125-H to MIL-125-R (Table 3.1).

Table 3.1. Cell parameters obtained from the full profile analysis of the XRD patterns of the different MOF samples.

Sample	a parameter (Å)	c parameter (Å)
UiO-66	20.671 ± 0.001	---
UiO-66-NH$_2$	20.693 ± 0.002	---
UiO-66-NH$_2$-def	20.698 ± 0.001	---
MIL125-H	18.649 ± 0.003	18.136 ± 0.002
MIL125-R	18.668 ± 0.002	18.156 ± 0.003

XRD patterns (Figure 3.4a) show a significant increase of the peak width in the specific case of the samples with smaller particle size, ascribed to the reduction of the crystalline domains as a consequence of the synthesis conditions. This experimental evidence is confirmed by the micrographs obtained by means of transmission electron microscopy, shown in Figure 3.4e. Indeed, for zirconium aminoterephthalate compounds, the addition of the HCl inorganic modulator induces an increase of the crystal size from 10-20 nm in non-defective UiO-66-NH$_2$ to 50-100 nm in UiO-66-NH$_2$ defective samples. A similar particle size dependence on the crystallization conditions is found for titanium terephthalate compounds. MIL-125-H, which was synthesized at 150 °C under hydrothermal conditions, exhibits micron-size particles, whilst MIL-125-R, which was obtained from reflux conditions, crystallizes as spherical particles with diameters ranging from 100 to 400 nm.

Figure 3.4. Characterization of the MOF samples: (a) XRD patterns, (b) UV-Vis spectra, (c) CO$_2$ adsorption isotherms (d) TGA curves and (e) TEM images.

Light-harvesting capacity of the materials was studied by means of solid UV-Vis spectroscopy (Figure 3.4b). The UV-Vis spectra point that both UiO-66 and MIL-125 materials adsorb in the UV range, with optical band gaps of 3.84 eV for UiO-66, and 3.31 and 3.09 eV for MIL-125-H and MIL-125-R samples. UV-Vis spectrum of UiO-66-NH$_2$ exhibits two additional absorption bands ascribed to the visible l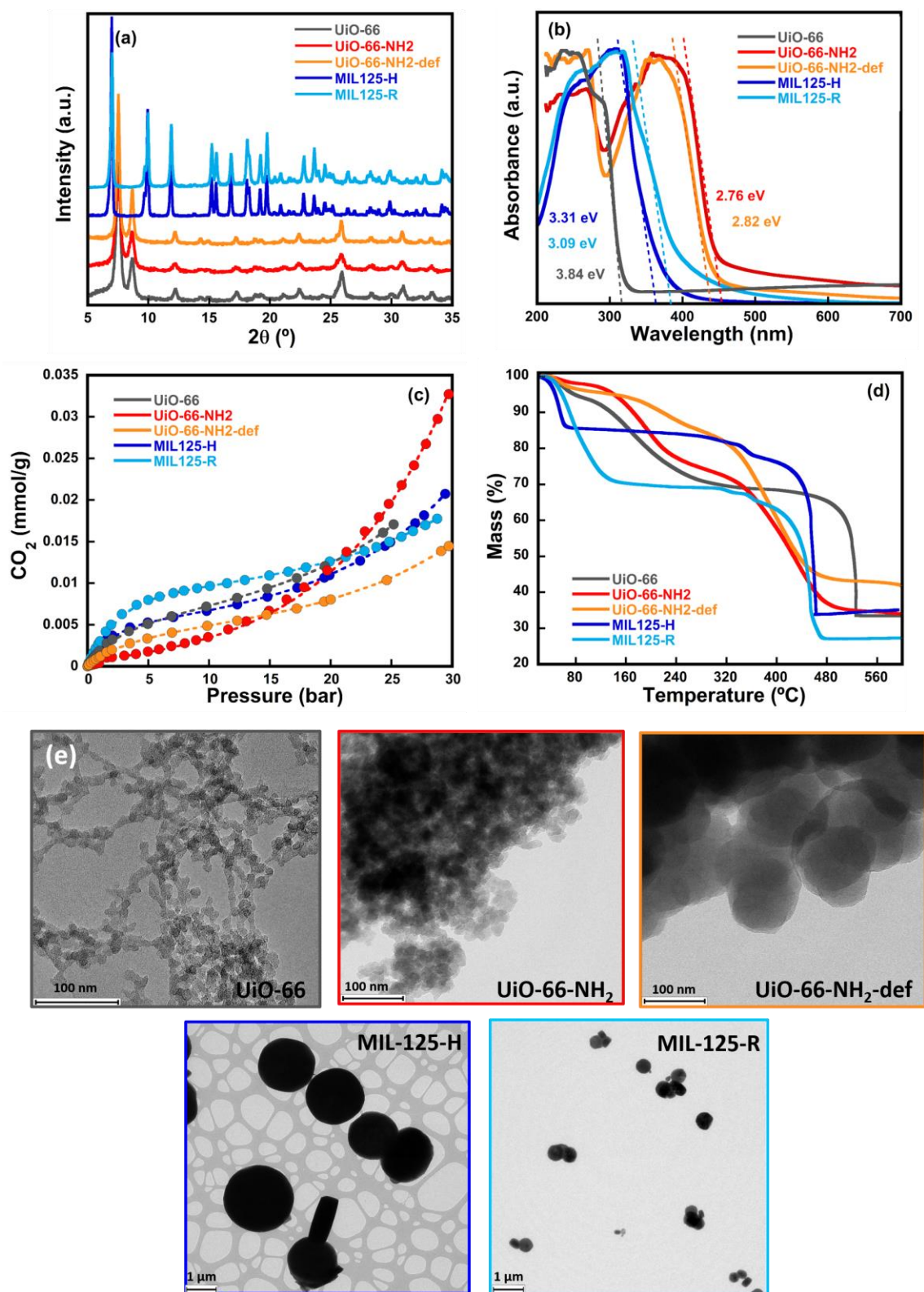ight harvesting capacity of aminoterephthalic organic linkers, whilst maintains a UV-light absorption similar to the one of the UiO-66 material, which is ascribed to the zirconium inorganic clusters. As expected, the presence of linker defects in UiO-66-NH$_2$-def induces a shift of the spectrum to blue wavelengths (UiO-66-NH$_2$ = 2.76 eV, UiO-66-NH$_2$-def = 2.82 eV). Similarly, the different synthesis conditions of MIL-125-H and MIL-125-R also induces a slight red shift to the charge-transfer absorption band associated to the titanium oxo-nuclear clusters.

The surface area and pore size distribution were determined from CO_2 adsorption isotherms at 273 K (Figure 3.4c). The Brunauer-Emmett-Teller (BET) surface area was calculated from the fitting of the linearized form of BET equation. The obtained surface areas and microporous distribution (UiO-66 = 906 m$^2\cdot$g^{-1}, UiO-66-NH$_2$ = 894 m$^2\cdot$g^{-1}, UiO-66-NH$_2$-def = 600 m$^2\cdot$g^{-1}, MIL-125-H = 872 m$^2\cdot$g^{-1}, MIL-125-R = 1346 m$^2\cdot$g^{-1}) are in good agreement with previous reports.[59,60]

Thermogravimetric analysis shown in Figure 3.4d allowed quantifying the linker defect degree of UiO-66 materials by applying the protocol described by Shearer *et al*.,[55] which can be found in section 2.2.5. In the specific case of the UiO-66-NH$_2$ and UiO-66-NH$_2$-def samples, 0.6 and 2.2 positions, over the twelve carboxyl groups per inorganic clusters present in the ideal structure, are vacant. The TGA curves of MIL-125-H and MIL-125-R compounds show two main weight loss processes associated to: (i) the release of water molecules entrapped within the pores (RT-100 °C) and (ii) the calcination of the aminoterephthalate linkers (350–480 °C). The weight percentage associated to the calcination of the organic linkers fits well with an ideal structure free of linker defects, independently on the synthesis route applied to obtain the material.

According to that initial characterization, there would be an expected improved photoreduction efficiency for the samples with lower particle size as a result of the

shorter migration path to the surface of the electron–hole pairs, which will lead to a more efficient generation of the reactive species that trigger the photoreduction. However, other parameters need to be considered in parallel. The light-harvesting capacity is also a key indicator of the photocatalytic efficiency dependence on the radiation wavelength (e.g., UV, visible…) of our materials. Finally, linker functionalities of MOFs, such as amine groups, also favour the electron transfer along the framework while improving the chromium adsorption capacity.

Adsorption kinetics of Cr^{VI} and Cr^{III} Ions

First, adsorption affinity of the samples over Cr^{VI} and Cr^{III} species was assessed by the evaluation of their adsorption kinetics at acidic conditions (pH = 3.5) (Figure 3.5). As expected from previous works,[3,41] Zr-based UiO-66-NH$_2$ materials show fast kinetics and efficiencies over 90 % to capture both hexavalent and trivalent chromium species. For hexavalent chromium, the equilibrium is reached within the first 15 min of the experiment. In agreement with previous works[3], linker defective UiO-66-NH$_2$-def shows higher chromate adsorption capacity than the non-defective UiO-66-NH$_2$ (Figure 3.5a). It is duly proved that linker defective positions in Zr-MOFs act as preferential adsorption points for anionic inorganic and organic species. For instance, hexavalent chromium is stabilized in a wide range of pH values as dichromate or hydrogen dichromate oxyanions.[61,62] On the contrary, MIL-125 materials show a negligible adsorption affinity over negative chromate anions, as expected because of the lack of defective linker positions of titanium terephthalate frameworks (Figure 3.5a).
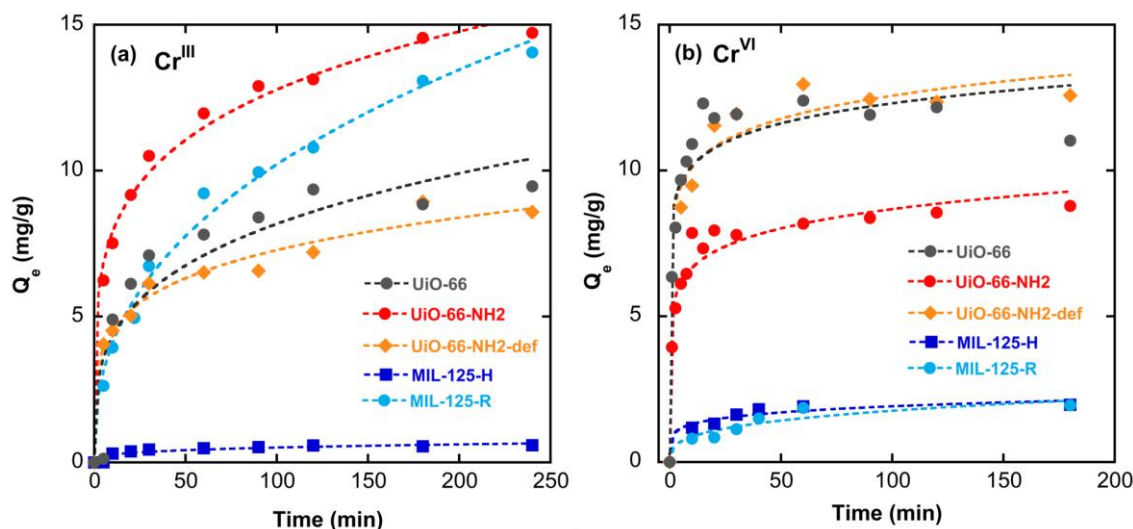
Figure 3.5. (a) Cr^{VI} and (b) Cr^{III} adsorption kinetics for UiO-66, UiO-66-NH$_2$, UiO-66-NH$_2$-def, MIL-125-R and MIL-125-H. Points: experimental data. Line: Bangham model fitting. Adsorbent concentration 0.25 mg·mL^{-1}, C$_i$=5 ppm.

Zr-UiO-66-NH$_2$ and MIL-125 compounds also exhibit adsorption affinity over trivalent chromium (Figure 3.5b), with adsorption capacities ranging from 8 to 15 mg·g^{-1} for a 5 ppm solution. It is also worthwhile to notice the great impact that the particle size reduction has on the Cr^{III} adsorption capacity of MIL-125 type materials, since nanosized MIL-125-R overperform the adsorbing capacity of its micron-size MIL-125-H homologue. Opposite, UiO-66-NH$_2$-def materials have larger particles size than that of the non-defective homologue, but their Cr^{VI} absorption capacity overperform that of the UiO-66-NH$_2$ materials. In this case, the Cr^{VI} adsorption process is driven by the inner linker defects density instead of surface defects induced by the particle size reduction. In comparison to hexavalent chromate, Cr^{III} adsorption kinetics are slower, with equilibrium times above one hour. The time dependence of Cr^{VI} and Cr^{III} adsorption is well fitted by Bangham and pseudo-second order models, while the pseudo-first-order model fails to reproduce the tendency above 60 min of adsorption, indicating that Cr^{VI} and Cr^{III} immobilization is not solely governed by diffusion processes, but also by chemisorption process into the MOF structure.

Bifunctional Photocatalytic Reduction of Cr^{VI} to Cr^{III} and adsorption of Cr ions

Once the capacity of the different MOFs to adsorb Cr^{III} and Cr^{VI} species has been assessed, their Cr^{VI} to Cr^{III} photocatalytic reduction efficiency was investigated. Thus, photoreduction curves were first measured under UV light in a 5 ppm Cr^{VI} solution and at a sorbent loading of 0.25 g·L^{-1} (Figure 3.6). The first adsorption stage in dark conditions reveals that UiO-66-NH$_2$ type materials are able to capture more efficiently Cr^{VI} ions than the MIL-125 family, in good agreement with the Cr^{VI} adsorption kinetics presented above.
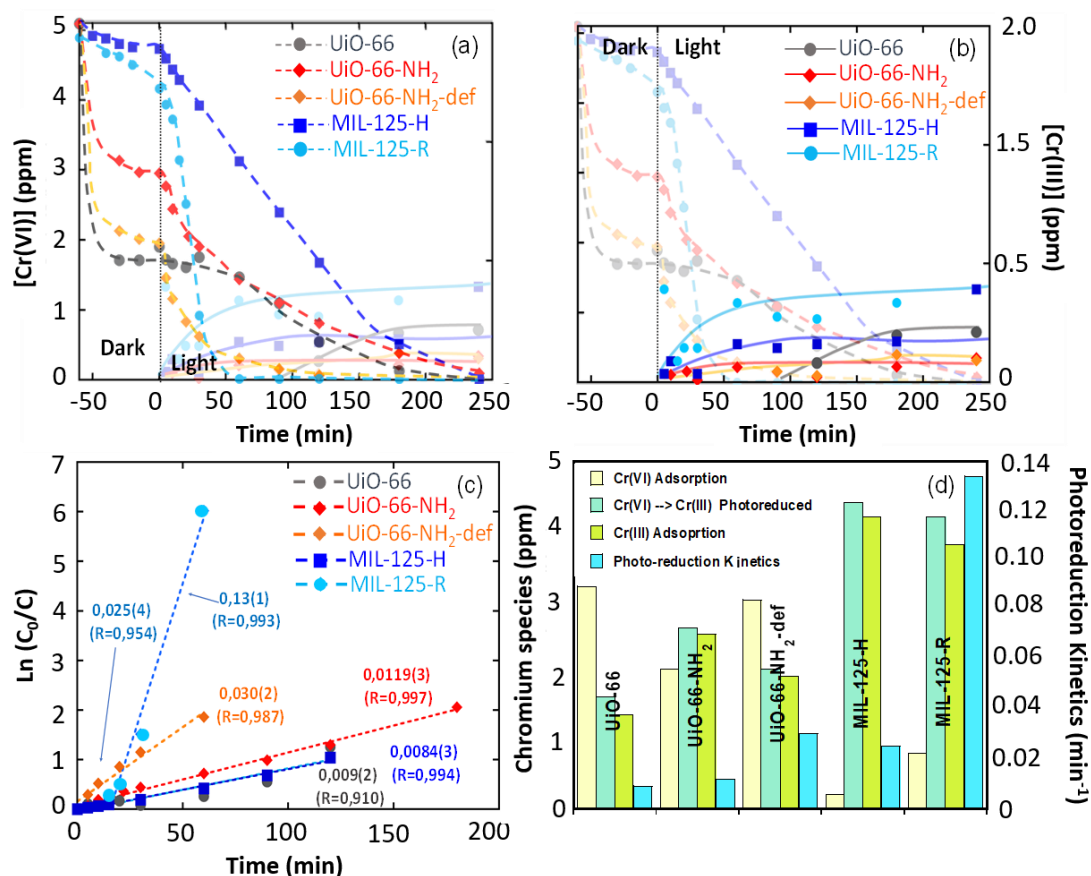
Figure 3.6. (a-b) Adsorption and photocatalytic reduction of Cr^{VI} in the different MOF samples under UV light: (a) Detail of the Cr^{VI} and (b) Cr^{III} concentration evolutions. (c) Fitting of the photoreduction kinetics with Langmuir-Hinshelwood model. (d) Summary of Cr^{VI} adsorbed at the MOF at dark conditions, the total amount of Cr^{VI} photoreduced to Cr^{III}, the amount of photoreduced Cr^{III} adsorbed at the MOF, and the photoreduction rate of the studied materials.

Nonetheless, a different trend is observed upon illumination, where MIL-125-R exhibits the most efficient photoreduction response and kinetic rate compared to UiO-66 materials (Figure 3.6c-d), which can be ascribed to its adsorption efficiency in the UV range. On the contrary, the photoreduction capacity of MIL-125-H is appreciably slower. Even if the light-harvesting capacity is quite similar for both MIL125-R and MIL-125-H variants (Figure 3.6b), the shorter migration path of the electron-hole pairs to the surface of MIL-125-R nanoparticles due to the smaller particle size, can aid to reduce their recombination, and consequently, to enhance the photoconduction and the generation of the reactive species that trigger the photoreduction process.

In addition to the good photoreduction kinetics of MIL-125 materials, they also exhibit significant Cr^{III} adsorption capacities. The Cr^{III} concentration after the photoreduction process with MIL-125-R and MIL-125-H is quite low (<0.5 ppm), but it is still higher than the observed for UiO-66-NH_2 materials (<0.1 ppm). Thus, in terms of photoreduction capacity coupled to the Cr^{III} recovery, UiO-66 materials show the best combined performance. In addition to a high Cr^{VI} initial adsorption capacity, UiO-66-NH_2 materials exhibit interesting kinetics for Cr^{VI} to Cr^{III} photoreduction, combined with a negligible release of the photogenerated Cr^{III}, due to their high adsorption capacity toward this cationic specie.

The conclusions drawn by the photocatalytic experiments opens relevant questions to properly understand the underlying processes that governs the photocatalytic and adsorptive dual function of the studied materials. In particular, it is important to address how the materials work under visible light illumination with the aim of evaluating their possible performance under solar light. In addition, the initial Cr^{VI} concentration, just before the illumination, is another key parameter to be explored in order to assess its impact on the photoreduction kinetics of the studied frameworks.

In order to gain further insights regarding the above-mentioned questions, UiO-66-type materials have been selected to continue the investigation. First, their photocatalytic capacity under visible light has been investigated. In order to enhance the photoreduction kinetics under visible light, the charge of the photocatalyst has

been increased from the 0.25 g·L^{-1} used in the previous experiments to 0.35 g·L^{-1}. All the results are shown in Figure 3.7.
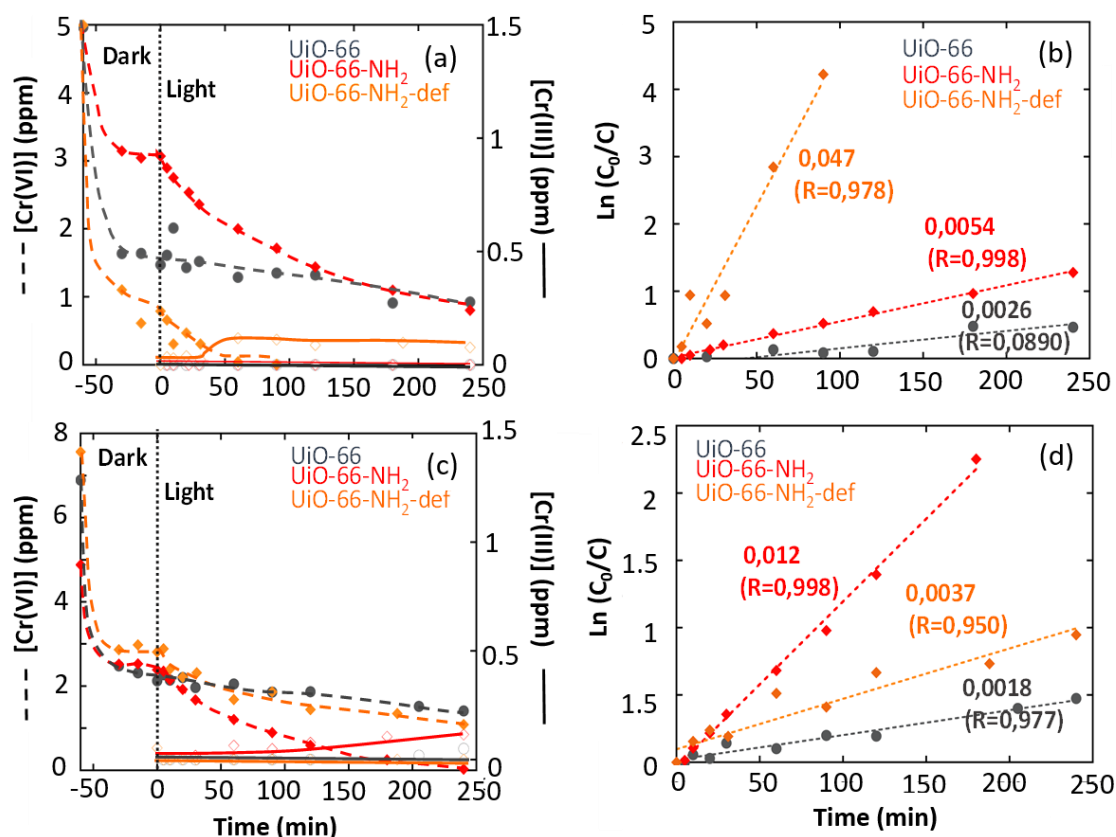
Figure 3.7. Photocatalytic reduction of Cr^{VI} in the UiO-66 samples under visible light at a sorbent concentration of 0.35 g·L^{-1} (an initial adsorption stage in dark conditions until equilibrium was performed before illumination in all the experiments). (a) Photocatalysis performed with the same initial Cr^{VI} concentration and (b) the fitting of the photoreduction kinetics with Langmuir-Hinshelwood model. (c) Starting from different Cr^{VI} concentrations to reach the same Cr^{VI} content in the solution after finalizing the adsorption in dark conditions and (d) fitting of the photoreduction kinetics with Langmuir-Hinshelwood model.

The increase on the MOF's photocatalysts loading generates a higher Cr^{VI} retention during the adsorption step in dark conditions, being the most efficient adsorbent of the UiO-66-NH$_2$-def material, followed by UiO-66 and UiO-66-NH$_2$ variants. Regarding the photocatalytic process in visible light, the amine functionalities play again an important role in the chromium photoreduction kinetics due to the more efficient light harvesting capacity of UiO-66-NH$_2$ in comparison to UiO-66. UiO-66-

NH$_2$ variants exhibit higher efficiencies and faster kinetics (Figure 3.7a-b) than UiO-66, achieving 100% (UiO-66-NH$_2$-def) and 60% (UiO-66-NH$_2$) of the Cr^{VI} photoreduction in about 1 h. This indicates the feasibility of applying these photocatalysts under solar irradiation. Regarding Cr^{III}, a small increase in the concentration of this species is observed in the solution during the photoreduction process, but it is still very low for UiO-66 and UiO-66-NH$_2$ ($\approx$0.1 ppm) when compared to the starting Cr^{VI} concentration.

Once the bi-functionality of UiO-66-NH$_2$ materials under visible light illumination was confirmed, chromium photoreduction experiments were performed starting from a similar Cr^{VI} concentration after the adsorption stage in dark conditions (Figure 3.7c). To this end, the Cr^{VI} concentration before adsorption was tuned for each material in order to get a similar concentration value of approx. 3 ppm after the initial adsorption stage in dark conditions. Thus, the photocatalytic kinetics for the three studied materials were compared starting from similar conditions. As it could be observed in Figure 3.7d, when the photoreduction process starts from a similar initial concentration, UiO-66-NH$_2$ photocatalyst presents better photoreduction kinetics than UiO-66-NH$_2$-def and UiO-66. It is important to note that the calculated photocatalytic rates (Figure 3.7d) are quite different from those obtained from the previous experiments (Figure 3.7b), where the Cr^{VI} concentration after adsorption differs significantly for the three studied compounds. Indeed, generally speaking, the higher the Cr^{VI} concentration before the illumination stage, the lower the photocatalytic rate.

The kinetic rates for Cr^{VI} photoreduction obtained from the experimental data plotted in the Figure 3.6d reveal that this parameter is affected by the particles size and the light-harvesting capacity of our dual sorbent-photocatalysts; but also, by the experimental conditions themselves. Independently of both parameters, the Cr^{III} recovery efficiencies are above 98% if the adsorption and the photocatalytic steps are jointly considered. It is important to point out that a slight increment of the Cr^{III} concentration in solution has been observed under certain experimental conditions. Further investigations are needed to elucidate the activation and reusability of the studied materials, as well as the Cr^{III} saturation point under photocatalysis experiments.

UiO–66–NH₂ Chromatographic Columns: Continuous Flux Adsorption

When designing continuous flux adsorption experiment, it is necessary to integrate the MOF in a highly permeable chromatographic column that maximizes the contact between the aqueous solution and the active MOF sorbent. First, the protocol described by Rapti *et al.*[63] was followed to assemble a UiO-66-NH₂/sand (1% w/w) based chromatographic column to test its adsorptive capacity over Cr^{VI} in a continuous flow open circuit configuration. The evolution of the chromium concentration at the output of the system has been plotted in the Figure 3.8a. The breakthrough adsorption experiment was carried out in dark conditions, with an initial Cr^{VI} concentration of 2.5 ppm and a 1 mL·min^{-1} flux. The experimental data for the adsorption stage was fitted to Thomas model.[64]

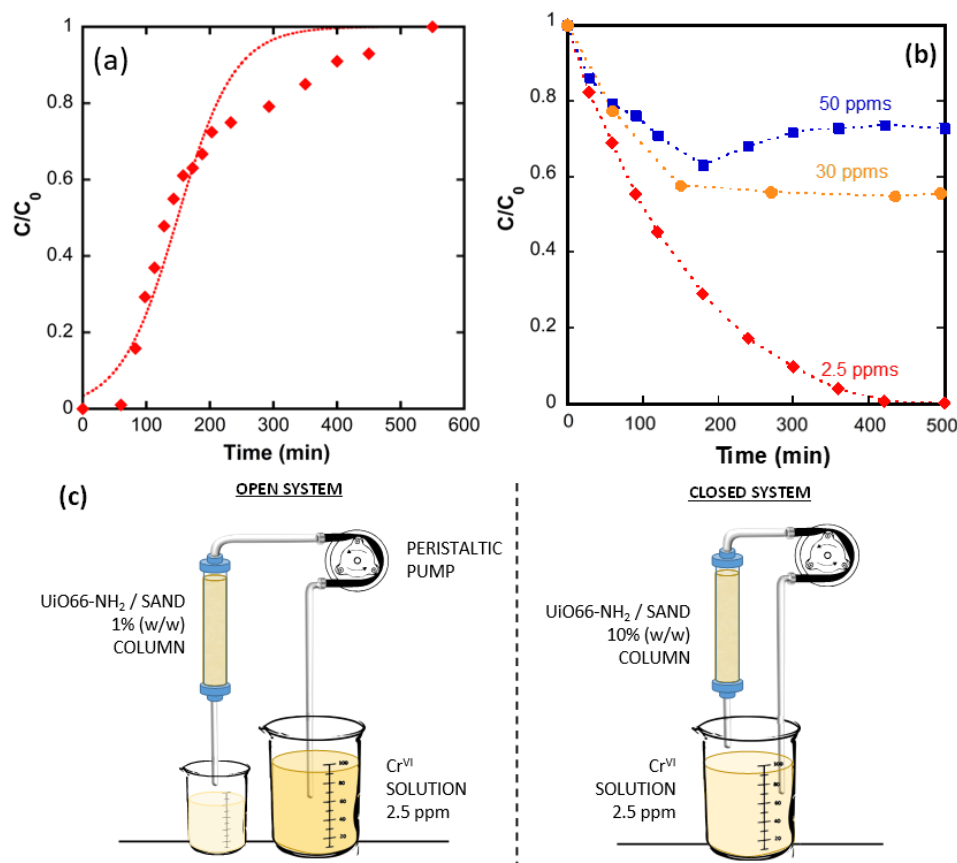**Figure 3.8**. Continuous flux Cr^{VI} adsorption and photodegradation with UiO-66-NH₂ chromatographic columns. (a) Open circuit adsorption. 1% w/w UiO-66-NH₂/Sand column, [Cr^{VI}] = 2.5 ppm, Flux = 1 mL·min^{-1}. (b) Closed circuit adsorption. 10% w/w UiO-66-NH₂/Sand column, [Cr^{VI}] = 2.5, 30 and 50 ppm, Flux = 1 mL·min^{-1}. (c) Schematic representation of the open and closed circuits.

It is important to point out that kinetics of adsorption differ significantly in static and continuous flux experiments. Indeed, in static mode, most of the Cr^{VI} adsorption occurs within the five initial minutes while in continuous adsorption experiments, the sorbent saturation point is reached after 10 hours.

Afterwards, we decided to increase the MOF content on the chromatographic column and evaluate its performance under a continuous flux process in a closed loop (see Figure 3.2 for a detailed information). By applying this strategy, the cumulative effect of the adsorption process in the long-term can be experimentally observed (Figure 3.8b). Henceforth, 10 % w/w UiO-66-NH$_2$/sand chromatographic columns were prepared, and 100 mL Cr^{VI} solutions of 2.5, 30 and 50 ppm concentrations were pumped at 1 mL·min^{-1} flux until the adsorption equilibrium was reached. For the experiment performed with a 2.5 ppm concentration, the column was able to adsorb all the Cr^{VI} content in the 100 mL pumped across the column in 400 min. In the specific case of highly concentrated 50 ppm solution, the UiO-66-NH$_2$/sand column was able to retain almost 40 % of the initial chromium in the adsorption stage. Indeed, a slight increase of the chromium content in the solution was observed after the saturation stage of the material. The color of the column changes appreciably during the experiments suggesting that the material possess certain degree to induce a chemical reduction of Cr^{VI} to Cr^{III}. Finally, for the experiment performed at an intermediate concentration (Cr^{VI} = 30 ppm), the system was able to capture near 50 % under dark conditions. It is clear that the time to reach the adsorption saturation stage is four-fold longer in the continuous flux conditions than in static adsorption experiments. The maximum adsorption capacities for the UiO-66-NH$_2$ material obtained from static sand adsorption experiments are very close. Indeed, 27 mg·g^{-1} for static experiments, and 27 and 29 mg·g^{-1} for continuous flux experiments developed with 30 and 50 ppm solutions. Therefore, just by applying a continuous flux adsorption experiment with a column containing 1 g of UiO-66-NH$_2$, 12 L of water with 2.5 ppm Cr^{VI} concentration could be depolluted in a closed system.

3.1.3. CONCLUSIONS

The dual photocatalytic and adsorptive functionality of archetypal Zr and Ti-based metal–organic frameworks over the simultaneous Cr^{VI} to Cr^{III} photoreduction and Cr^{III} immobilization has been demonstrated. The particle size reduction of Ti-based MIL-125 has been revealed as a key parameter to enhance the photoactivity of the material, whilst the linker defective chemistry of Zr-based UiO-66 compounds is detrimental for the chromium photoreduction but beneficial for the retention of the Cr^{III} phototransformed species. Considered as a whole, the bifunctional Zr and Ti-based MOFs are able to retain from 90 to 98% of the initial chromium at acidic solutions. The adsorption process can be performed efficiently on a continuous flux closed loop circuit when the MOF active material is assembled as a chromatographic column.

The experimental procedure described in this work opens the future perspective to test the bifunctional catalytic and adsorptive capacity of photoactive MOFs synthesized so far, not just applied for the specific case of chromium, but also for homologous studies such as the As^{III} to As^{V} photooxidation, or the photodegradation of emerging pollutant and the concurrent adsorption of the photogenerated intermediate products.

However, further research is needed to evaluate in a quantitative manner the economic and technical feasibility of MOFs for chromium recovery in real scenarios far from ideal laboratory models. In this regard, the chemical versatility of UiO-66 frameworks opens a window to combine different functional groups in its structure, better known as multivariate functionalization, making it possible to synthetize materials with synergic properties or coupled functions. This is the focus of the following section, where we have explored the potentials of multivariate reticular UiO-66 materials for the photocatalytic water remediation.

3.2. MULTIVARIATE FUNCTIONALIZATION OF UiO-66 FOR PHOTOCATALYTIC WATER REMEDIATION

The discovery of hydrolytically stable and chemically robust Zirconium(IV) UiO-66 (Figure 3.9a) triggered the application of MOFs for water remediation purposes.[1,52,65–70] One of the advantages of Zr-UiO-66 structure is that its defective linker sites act as preferential adsorption sites for oxoanionic species, including Cr^{VI} (Figure 3.9b).[5,71] The second advantageous feature of Zr-UiO-66 is that it functions as a semiconductor photocatalyst able to absorb UV-Vis light[72,73], which afterwards activates the metal sites by electron/hole transfer, and finally, leads to the generation of radical oxygen species (ROS) able to photoreduce the Cr^{VI} to Cr^{III}. Indeed, these three key characteristics (*i.e.* light harvesting, electron/holes generation and transport and, ROS formation efficiency), define the efficiency of a photocatalyst, whose chemical stability is incorrectly assumed.
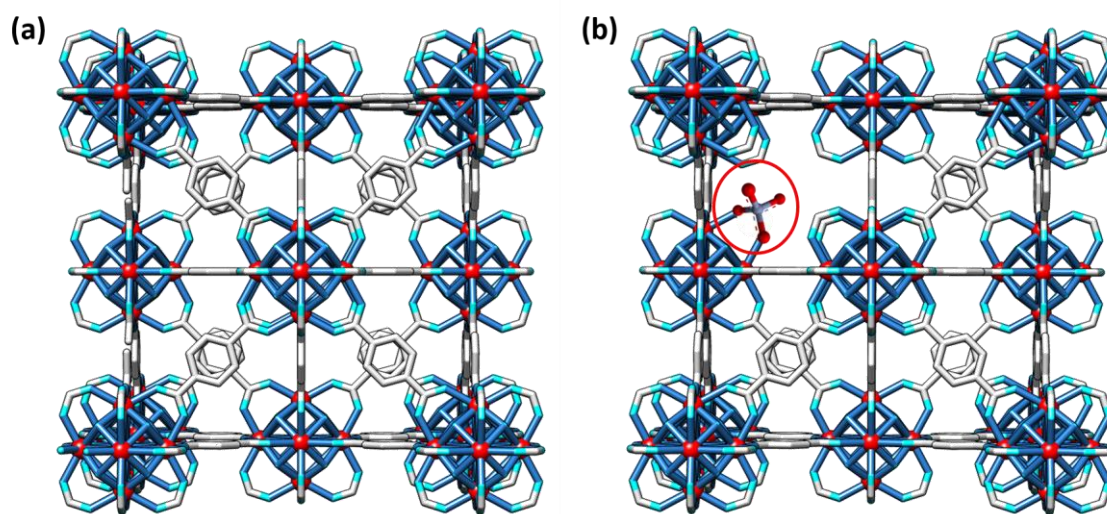
Figure 3.9. UiO-66 crystalline structure a) defectless b) with linker-defective points that act as Cr^{VI} adsorption sites.

Nowadays, there are many studies that have improved either Cr^{VI} adsorption or photocatalytic performance of pre- or post-synthetically modified Zr-UiO-66 frameworks.[74,75] For example, amino and dihydroxyl functionalization endow UiO-66 with chemical (*i.e.* –(OH)$_2$) and photocatalytic (*i.e.* -NH$_2$) capacity to reduce Cr^{VI}

to Cr$^{III[4,16]}$, as well as with the chemical affinity to adsorb both Cr^{VI} (*i.e.* -NH$_2$) and Cr^{III} (*i.e.* -(OH)$_2$). However, as concluded from X-ray diffraction data after operation, both UiO-66-NH$_2$, UiO-66-(OH)$_2$ lack the chemical robustness to work under highly acidic or caustic conditions that only the nitro functionalized UiO-66-NO$_2$ can tolerate.[76] Nevertheless, the loss of the long-range ordering of the MOF material (determined by X-ray diffraction) is not the only parameter that accounts for their overall chemical stability. The partial release of the organic linkers or metals of the framework when the MOFs are immersed under slightly acidic or basic solutions, is as well a key parameter to assess their chemical strength. For instance, the partial leaching of the MOF constituents does not preclude the structural collapse of the material, which under most of the conditions maintains its X-ray diffraction fingerprint, leading to conclusions that are not entirely precise regarding its chemical and hydrolytic stability.

Recently, multivariate functionalization strategy has emerged, offering an opportunity to tailor and balance all the targeted characteristics to achieve a fast and efficient Cr^{VI} to Cr^{III} photoreduction *via* the synergistic combination of different functional groups (Figure 3.10). Multivariate MOFs (MTV-MOFs) possess more than two functionalities randomly distributed within the framework that work together in a cooperative fashion, outperforming — as an ensemble — their homogenous and periodic counterparts.[77–86] In other words, the synergistic performance of a MTV-MOF (outperforming the homogenous and periodic counterparts) is the key criteria. However, introducing compositional variance in crystalline compounds brings new challenges, such as the exploration of the vast chemical space of functionalities variance and distribution that results in a cooperative performance and distinguishing multivariance from statistical disorder.[87,88] In practice, reticular chemistry introduces variance synthetically or post-synthetically towards optimizing for a particular function.[66,89,90] This requires the identification of a structure, its constituents, and possible compositional and structural variabilities (such as metals, organic linkers, absence of linkers, etc. that are compatible with the structure's integrity). Ideally, variants that could aid in performing a specific task are identified.[91] Furthermore, up to date, the impact of the chemical variance on the

thermal or chemical/hydrolytic stability and photocatalytic properties of MTV-MOFs are fairly unexplored.

In this second section of Chapter 3, the multivariate functionalization strategy to tune multiple chemical characteristics of UiO-66 structure has been employed, such as the light harvesting, adsorption capacity over Cr^{VI} and Cr^{III} species, photoconduction efficiency, and Cr^{VI} to Cr^{III} chemical reduction and photoreduction properties. In parallel, we have explored how the compositional variance in MTV-MOFs affects their hydrolytic stability in comparison to the one of their parent single-functionalized frameworks. To this end, we have studied the MTV space of amino, dihydroxyl and nitro functionalized single (UiO-66-NH$_2$, UiO-66-(OH)$_2$, UiO-66-NO$_2$) and multivariate (UiO-66-NH$_2$-(OH)$_2$, UiO-66-NH$_2$-NO$_2$, UiO-66-(OH)$_2$-NO$_2$ and UiO-66-NH$_2$-(OH)$_2$-NO$_2$) materials, combining aminoterephthalate (BDC-NH$_2$), 1,5-dihydroxyterephthalate (BDC-(OH)$_2$) and nitroterephtalate (BDC-NO$_2$) linkers.

From the overall performance to photoreduce and capture chromium ions, the balanced multivariate functionalization of the UiO-66-NH$_2$/-(OH)$_2$/-NO$_2$ framework has resulted in a dual sorbent/photocatalyst with: (i) efficient chemical/photoreduction of Cr^{VI} to Cr^{III}, and (ii) retention through adsorption of the resulting Cr^{III} ions (Figure 3.10c). When considering the hydrolytic stability of the MTV-frameworks, although the leaching of the organic linkers is attenuated in comparison to the single functionalized UiO-66 frameworks (specially in comparison to -NO$_2$ and -(OH)$_2$ variants), there is still a significant selective release of nitro and dihydroxyterephthalate linkers under acidic or basic conditions, even when the structural stability of the compounds is maintained, as confirmed by X-ray diffraction. Overall, this work shows the high potentials, but also the limitations in terms of thermal and chemical stability, of multivariate functionalization strategy to create synergetic properties and functions for targeted applications. Although the study is focused on the MTV-MOF application for water remediation purposes, it could be expanded to other case studies far from water remediation such as gas or vapour adsorption in humid conditions, chromatographic separation or catalysis performed in liquid media.
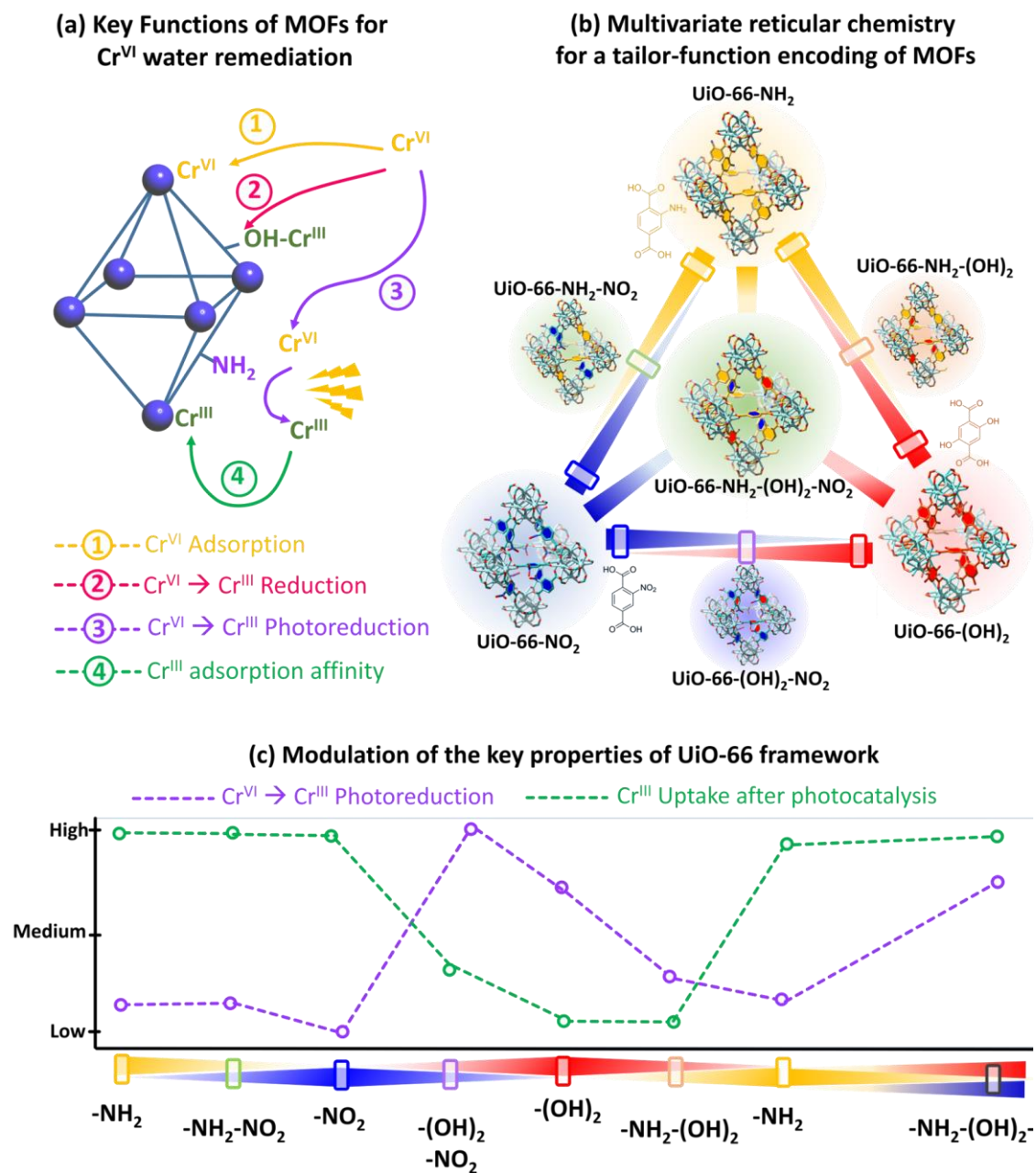
Figure 3.10. (a) Key functions needed in MOF materials for the Cr^{VI} to Cr^{III} capture and transformation. (b) Multivariate encoding strategy of the UiO-66 framework developed in this work. (c) Modulation of the key properties of the UiO-66 variants depending on their single and multivariate functionalities.

3.2.1. EXPERIMENTAL PROCEDURE

Synthesis of UiO–66 single and multivariate materials

The UiO-66 amine, dihydroxyl and nitro variants and the multivariate compounds with two or three different functionalities, were synthesized following the protocol described in the previous section 2.1.1 of this chapter. The main difference lies on the quantities of organic linker added to the reactor for the synthesis of the MTV-materials. These are summarized in the Table 3.2.

Table 3.2. Quantity of organic linkers used in multivariate UiO-66 materials.

Sample	BDC-NH$_2$ (mmol)	BDC-(OH)$_2$ (mmol)	BDC-NO$_2$ (mmol)
UiO-66-NH$_2$	2.310	----	----
UiO-66-(OH)$_2$	----	2.310	----
UiO-66-NO$_2$	----	----	2.310
UiO-66-NH$_2$-(OH)$_2$	1.155	1.155	----
UiO-66-NH$_2$-NO$_2$	1.155	----	1.155
UiO-66-(OH)$_2$-NO$_2$	----	1.155	1.155
UiO-66-NH$_2$-(OH)$_2$-NO$_2$	0.770	0.770	0.770

Sample stability assessment

In order to study the stability of the materials in different acidic or basic media, 30 mg of the samples were immersed in 15 mL of water solutions with pH 4, 7, 9 and 12. After that, they were recovered by centrifugation, washed with methanol three times, and dried at 80 ºC. XRD analysis of the powdered samples recovered after the experiment was recorded as described previously in this section. The aqueous solutions from pH 4 to 12 were recovered after the chemical stability tests and measured using a Spectronic 20 Genesys spectrophotometer, in order to follow the characteristic absorption bands that BDC linkers show (250 nm for BDC-NH$_2$, BDC-(OH)$_2$ and BDC-NO$_2$; 350 nm for BDC-NH$_2$ and BDC-(OH)$_2$).

Adsorption kinetics

The adsorption kinetics of single and multivariate UiO-66 materials over Cr^{VI} and Cr^{III} species were assessed at room temperature. Several dispersions of 6 mg of MOF adsorbent in 24 mL of 5 ppm Cr^{VI} or Cr^{III} solutions were prepared. The mixtures were agitated under magnetic stirring at 400 rpm and each of it was filtered with a hydrophilic 0.22 µm filter at a different time, from 5 to 360 min. Then solutions were acidified for its stabilization, and finally analyzed by means of ICP-AES. Adsorbents were dried and collected for future characterization after the adsorption experiments. pH of the chromium solutions was kept below 3.5 to prevent chromium oxide precipitation. The absence of chromium oxide precipitation was confirmed experimentally, monitoring the Cr^{III} concentration on the Cr^{III} stock solution over a period of two months, which remained constant. Kinetics were fitted with pseudo-first order (Equation 2.8 in section 2.3.2) and pseudo-second order (Equation 2.10 in section 2.3.2) models.

Photocatalysis for Cr^{VI} to Cr^{III} reduction

A 365 nm lamp was used to trigger the photocatalytic activity of UiO-66-R variants studied in this work. 35 mg of the samples were placed in 140 mL Cr^{VI} solution. The initial Cr^{VI} concentration was tuned between 14 and 12 ppm in order to obtain a similar Cr^{VI} concentration at the initial point of the photocatalysis experiments, and after the adsorption in dark conditions for 2 hours. After illumination, 5 mL aliquots were taken at different times of the reaction (5, 10, 15, 30, 45, 60, 120 and 240 min), and afterwards, filtered with a 0.22 µm pore filter.

The Cr^{VI} concentration was measured by a simplified methodology based on a previously reported diphenylcarbazide colorimetric protocol.[92] The overall chromium concentration of the solutions was determined by ICP-AES. Cr^{III} content of the aliquots was determined by the subtraction between the total chromium concentration obtained by ICP-AES and the Cr^{VI} concentration determined by the colorimetric method. The rates of Cr^{VI} to Cr^{III} photoreduction in the single and

multivariate samples were obtained after the fitting of the experimental data to the Langmuir-Hinshelwood model (Equation 2.12).[51]

The chemical stability of the materials after the Cr^{VI} adsorption and the Cr^{VI} to Cr^{III} photoreduction processes was studied following the same protocol described previously. The UV-Vis spectra of the chromium solutions after adsorption and photocatalysis were recorded as well in order to monitor whether a partial leached of the organic linkers from the MOFs has occurred.

3.1.1. RESULTS AND DISCUSSION

Samples characterization

Once synthesized, the quality, particle size and compositional variance of the samples was initially assessed by X-ray diffraction, IR spectroscopy and ^{1}H-NMR. The X-ray diffraction (XRD) patterns of all the single and MTV-UiO-66 materials are quite similar in terms of the diffraction maxima position and intensity ratio (Figure 3.11a). In addition, the X-ray diffraction data were analysed through a full profile pattern analysis, which confirms that they are fully consistent with the cell parameters and cubic Fm-3m space group of the UiO-66[44] structure, as can be observed in Figure 3.11b-h.

Our fittings revealed that all the samples have almost identical cell parameters (Table 3.3), with only slight variations in the values of the full width at half maximum of the patterns. As observed by scanning electron microscopy, the divergence on the full width at half maximum of the patterns for the different materials can be explained by the variation of their particle size (Figure 3.12).
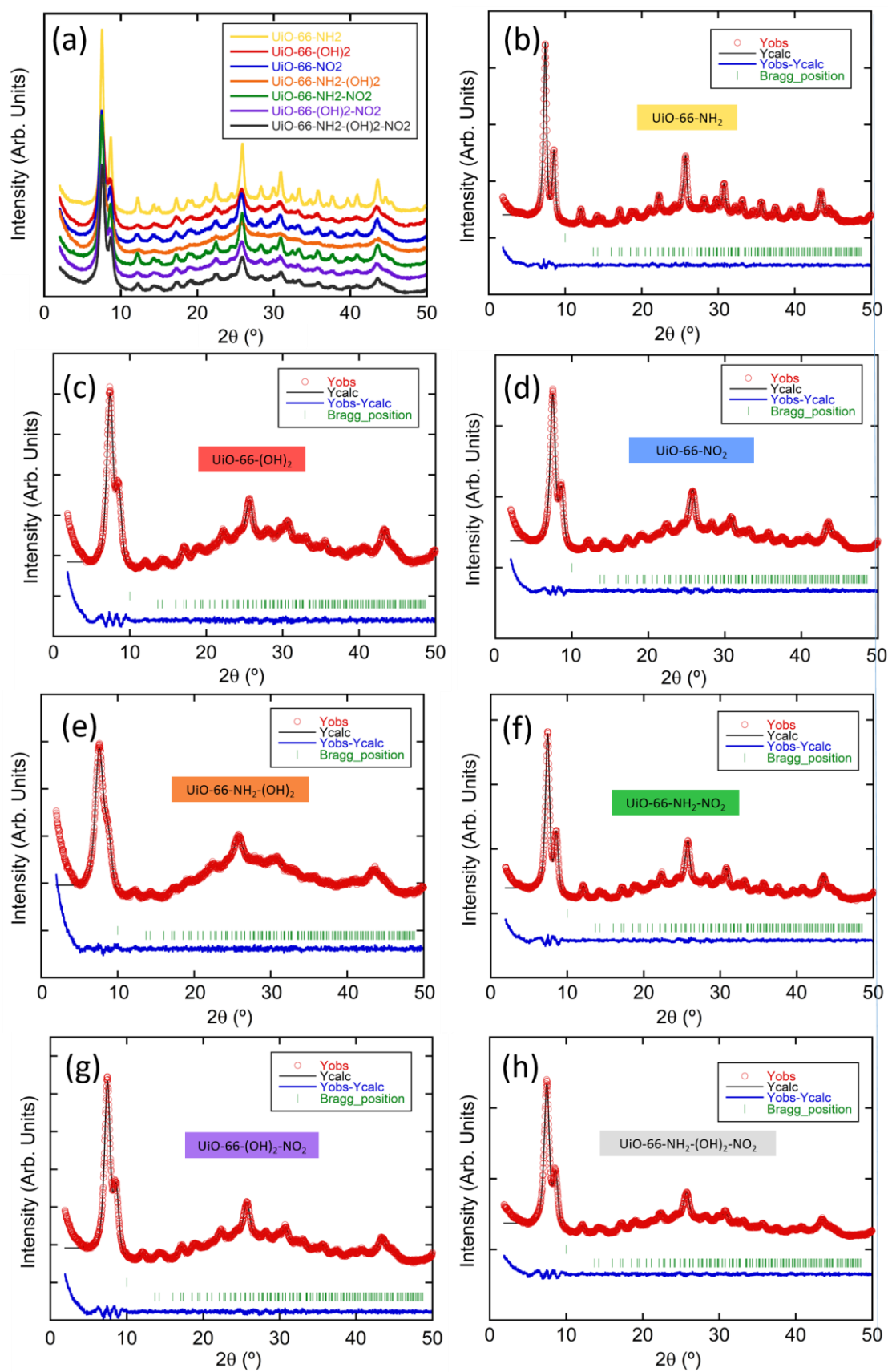
Figure 3.11. (a) XRD pattern and (b-h) pattern matching profile analysis of the UiO-66-R samples.

Table 3.3. Cell parameters obtained from the full profile analysis of the XRD patterns of the different MOF samples.

Sample	a parameter (Å)
UiO-66-NH$_2$	20.765±0.001
UiO-66-(OH)$_2$	20.778±0.003
UiO-66-NO$_2$	20.709±0.002
UiO-66-NH$_2$-(OH)$_2$	20.720±0.004
UiO-66-NH$_2$-NO$_2$	20.733±0.002
UiO-66-(OH)$_2$-NO$_2$	20.745±0.003
UiO-66-NH$_2$-(OH)$_2$-NO$_2$	20.744±0.003
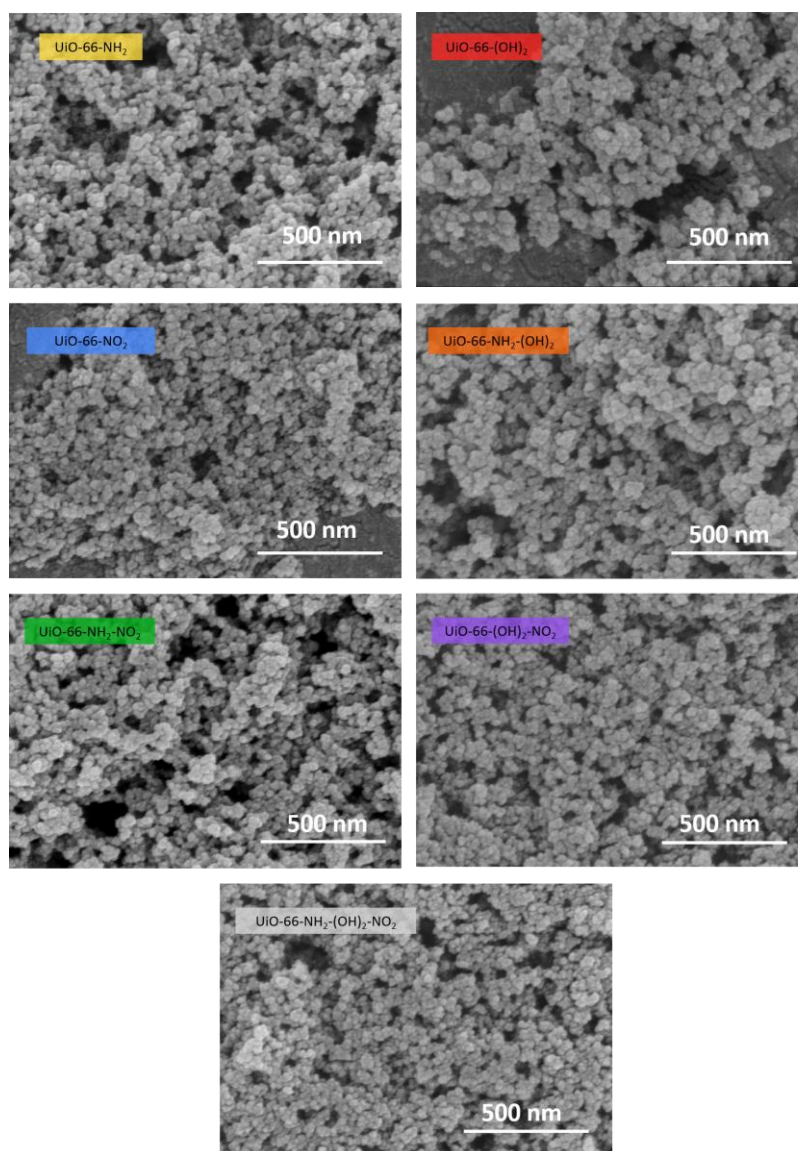
Figure 3.12. SEM images for the UiO-66-R samples.

FTIR spectra show the characteristic fingerprint bands of the UiO-66 framework, as well as those of the $-NH_2$, $-NO_2$ and $-(OH)_2$ functionalities within the single and multivariate materials (Figure 3.13). There is no significant shift in the vibrational frequencies from the single-functionalized to the multivariate frameworks. Some of the most characteristic vibrational modes common to all the UiO-66-R (R= $-NH_2$, $-(OH)_2$, $-NO_2$, $-NH_2-(OH)_2$, $-NH_2-NO_2$, $-(OH)_2-NO_2$ and $-NH_2-(OH_2)-NO_2$) frameworks studied in this work are the longitudinal and transverse vibration of the Zr-O bonds (at 745 and 660 cm^{-1})[93] and/or to the asymmetric and symmetric stretching vibrations of the carboxylate groups (1581 and 1389 cm^{-1}).[67]
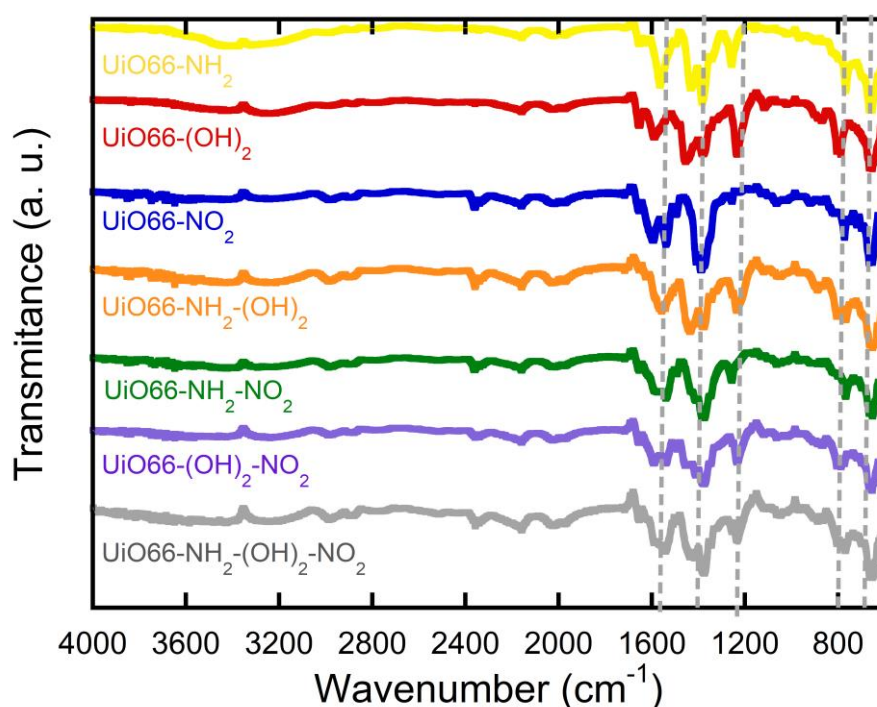
Figure 3.13. IR spectra of UiO-66-R samples.

Once the presence of the amino, nitro, and hydroxyl functional groups within the single and multivariate materials was confirmed by IR spectroscopy, the molar ratio of the organic linkers in multivariate samples was calculated by ^{1}H-NMR analysis of the dissolved samples (Figure 3.14 and Table 3.5). For the MTV-MOFs, the linkers' molar ratio (as obtained from integration of the ^{1}H-NMR data) aligns with the expected value, although there was a slight preference for the incorporation of BDC-

NO$_2$ over the BDC-NH$_2$ and BDC-(OH)$_2$, and of the BDC-NH$_2$ linkers over the BDC-(OH)$_2$ during the synthesis, as summarized in the data of the Table 3.4.
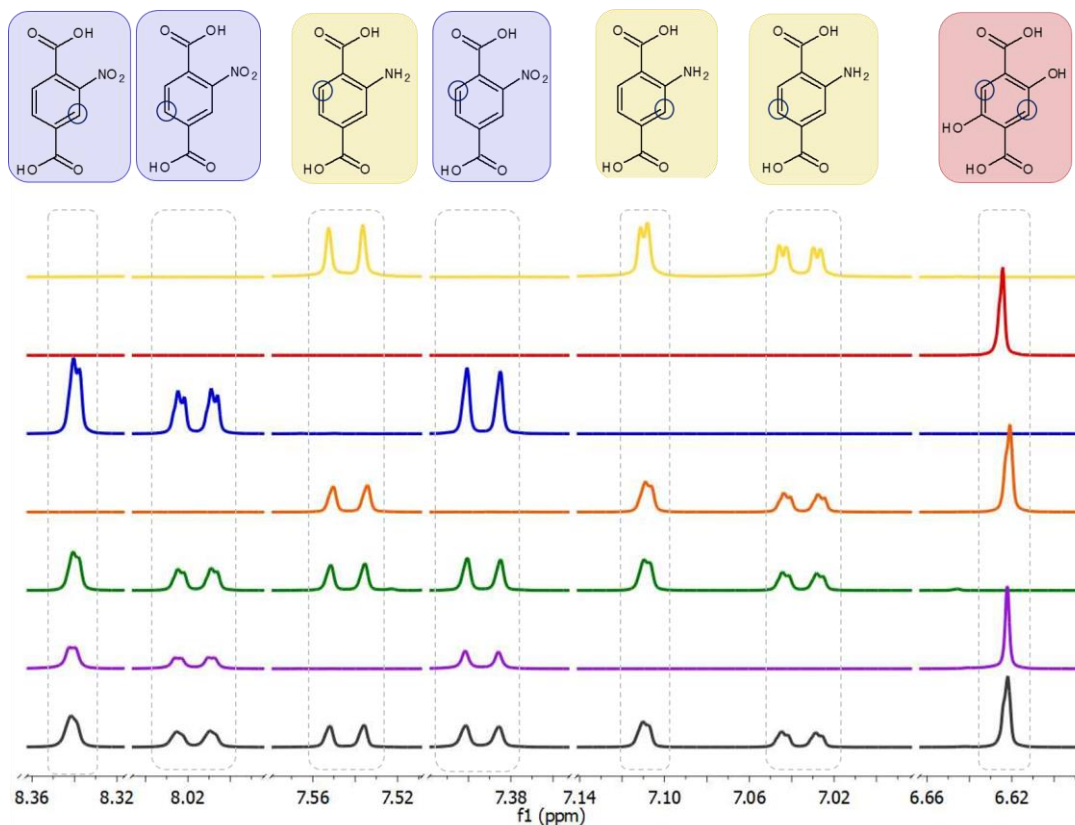
Figure 3.14. ^{1}H-NMR spectra of UiO-66-R samples.

Table 3.4. Molar ratio of BDC-NH$_2$, BDC-(OH)$_2$ and BDC-NO$_2$ linkers in single and multivariate UiO-66 frameworks.

	BDC-NH$_2$ Synthesis/Material*	BDC-(OH)$_2$ Synthesis/Material*	BDC-NO$_2$ Synthesis/Material*
UiO-66-NH$_2$	100 % / 100 %	0 % / 0 %	0 % / 0 %
UiO-66-(OH)$_2$	0 % / 0 %	100 %/ 100 %	0 % / 0 %
UiO-66-NO$_2$	0 % / 0 %	0 % / 0 %	100 % / 100 %
UiO-66-NH$_2$-(OH)$_2$	50 % / 56 %	50 % / 44 %	0 % / 0 %
UiO-66-NH$_2$-NO$_2$	50 % / 46 %	0 % / 0 %	50 % / 54 %
UiO-66-(OH)$_2$-NO$_2$	0%	50 % /41 %	50 % / 59%
UiO-66-NH$_2$-(OH)$_2$-NO$_2$	33 % / 34 %	33 % /26 %	33 % / 40 %

* Molar percentage of the linkers in the reaction media and incorporated to the UiO-66-R material.

The micropore surface areas, obtained by analysing nitrogen adsorption isotherms at low-pressure, are lower in comparison to the values reported in literature (Table 3.5). Instead, the surface area of our samples seems to be linked to the external area of the nanoparticles in the mesoporous regime (Figure 3.15).[94,95] The similarity to isotherm types I/II or I/IV is consistent with a microporous solid formed by nanoscopic particles that have meso/macro-porous-sized gaps between them. For instance, the external surface area of the particles can be qualitatively correlated with the particle size observed by scanning electron microscopy (Figure 3.12).
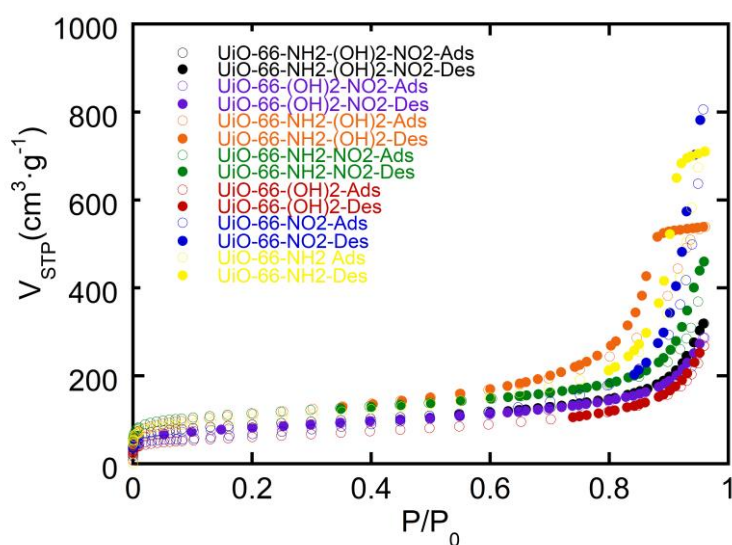
Figure 3.15. N_2 adsorption isotherm of UiO-66 materials.

Table 3.5. Micropore surface areas of UiO-66-R materials calculated by N_2 adsorption isotherms.

Sample	S_{BET} $(m^2 \cdot g^{-1})$	S_{micro} $(m^2 \cdot g^{-1})$	S_{ext} $(m^2 \cdot g^{-1})$	V_{micro} $(cm^3 \cdot g^{-1})$	V_T $(cm^3 g^{-1})$ P/P_0: 0.96 (<50nm)
UiO-66-NH$_2$	358.7	110.3	248.4	0.051	1.100
UiO-66-(OH)$_2$	217.5	69.7	147.8	0.031	0.415
UiO-66-NO$_2$	228.3	--	--	--	1.247
UiO-66-NH$_2$-(OH)$_2$	405.2	127.3	277.9	0.054	0.834
UiO-66-NH$_2$-NO$_2$	420.8	169.6	251.2	0.105	0.712
UiO-66-(OH)$_2$-NO$_2$	298.0	146.0	152.0	0.063	0.443
UiO-66-NH$_2$-(OH)$_2$-NO$_2$	323.6	177.1	146.5	0.075	0.494

As explained in the following sections, the thermal and chemical stability, light harvesting capacity and photoconduction efficiency of the single and multivariate UiO-66 frameworks are all affected by the type and amount of the functional groups. Overall, the chemical variance of MTV materials improves their efficiency to capture and photoreduce chromium species, but affects as well their hydrolytic stability, especially at highly acidic and basic conditions.

Multivariate modulation of the thermal and chemical stability

The thermal stability of the UiO-66 frameworks was evaluated through thermogravimetric analysis. The thermogravimetric profiles of MTV-UiO-66 samples are close to the average sum of the TGA signal of single-functionalized materials. Therefore, the thermal stability of MTV-UiO-66 materials is governed by the functionality with the lower thermal resistance (Figure 3.16). For the single-functionalized materials, the calcination process of the organic linker, usually associated with the thermal collapse of the framework, begins at 360 °C, 320 °C, and 295 °C for UiO-66-NH$_2$, UiO-66-(OH)$_2$, and UiO-66-NO$_2$, respectively. By contrast, in MTV materials, the thermal collapse begins at almost the same temperature as the collapse of the corresponding singly functional framework with the lower thermal stability (i.e. UiO-66-NH$_2$-NO$_2$ ≈ 320 °C, UiO-66-NH$_2$-(OH)$_2$ ≈ 300 °C, UiO-66-(OH)$_2$-NO$_2$ ≈ 300 °C, and UiO-66-(OH)$_2$-NO$_2$-NH$_2$ ≈ 310 °C).

These results confirm that the thermal resistance of MTV-MOFs is defined by one of the functionalities, that is, the weakest link in the chain is the one that marks the thermal collapse of the framework. The quantitative analysis of the thermogravimetric curves (specifically the weight loss associated with the calcination of the organic linker) display that all samples have approximately 0.5 linker defects per formula unit. This is an important structural feature, since defect chemistry promotes the adsorption of chromate anions. Therefore, having a similar density of linker-defects within the studied material assures that the differences observed in their properties (e.g. adsorption capacity and kinetics, photocatalysis, photoconduction…) arises from the single or multivariate functionalities installed in the framework.
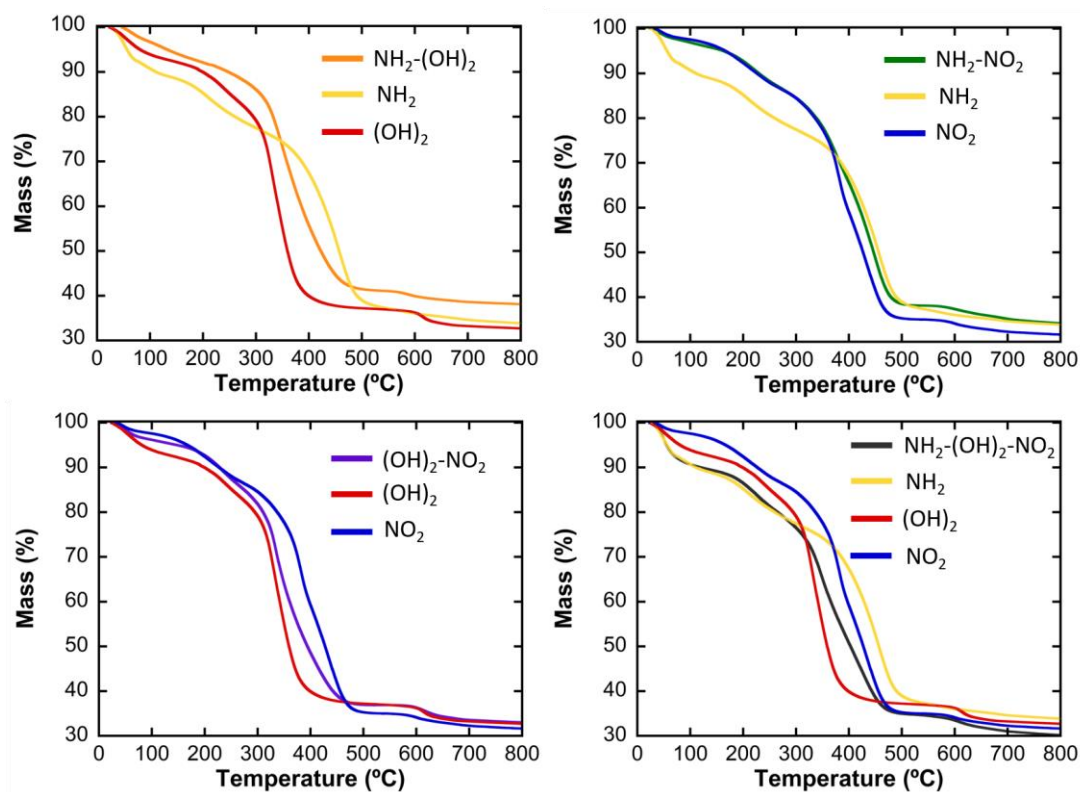
Figure 3.16. Thermogravimetric analysis of UiO-66-R materials.

The chemical stability of the single and multivariate functionalized UiO-66 materials was studied after immersing them in acidic and basic aqueous solutions. After the experiment, the solid was collected by centrifugation and studied by XRD, and the supernatant was kept for its study by UV-Vis spectroscopy. The X-ray diffraction patterns of the single and multivariate UiO-66 materials immersed at slightly acidic to basic aqueous media (pH 4 to 9) do not show significant changes in comparison to the initial ones (Figure 3.17). This is not the case for the XRD data of the samples exposed to basic solutions of pH=12, which point that the long-range ordering of the frameworks is lost during the process. These results match with expected ones, as the structural stability of the UiO-66 family in aqueous media has been corroborated in many works by X-ray diffraction.[76,96–100] However, this data cannot be used alone to positively claim that no fraction of the sample has been partially destabilized/dissolved giving rise to a leaching of the organic linkers and zirconium ions to the aqueous media.[101,102]
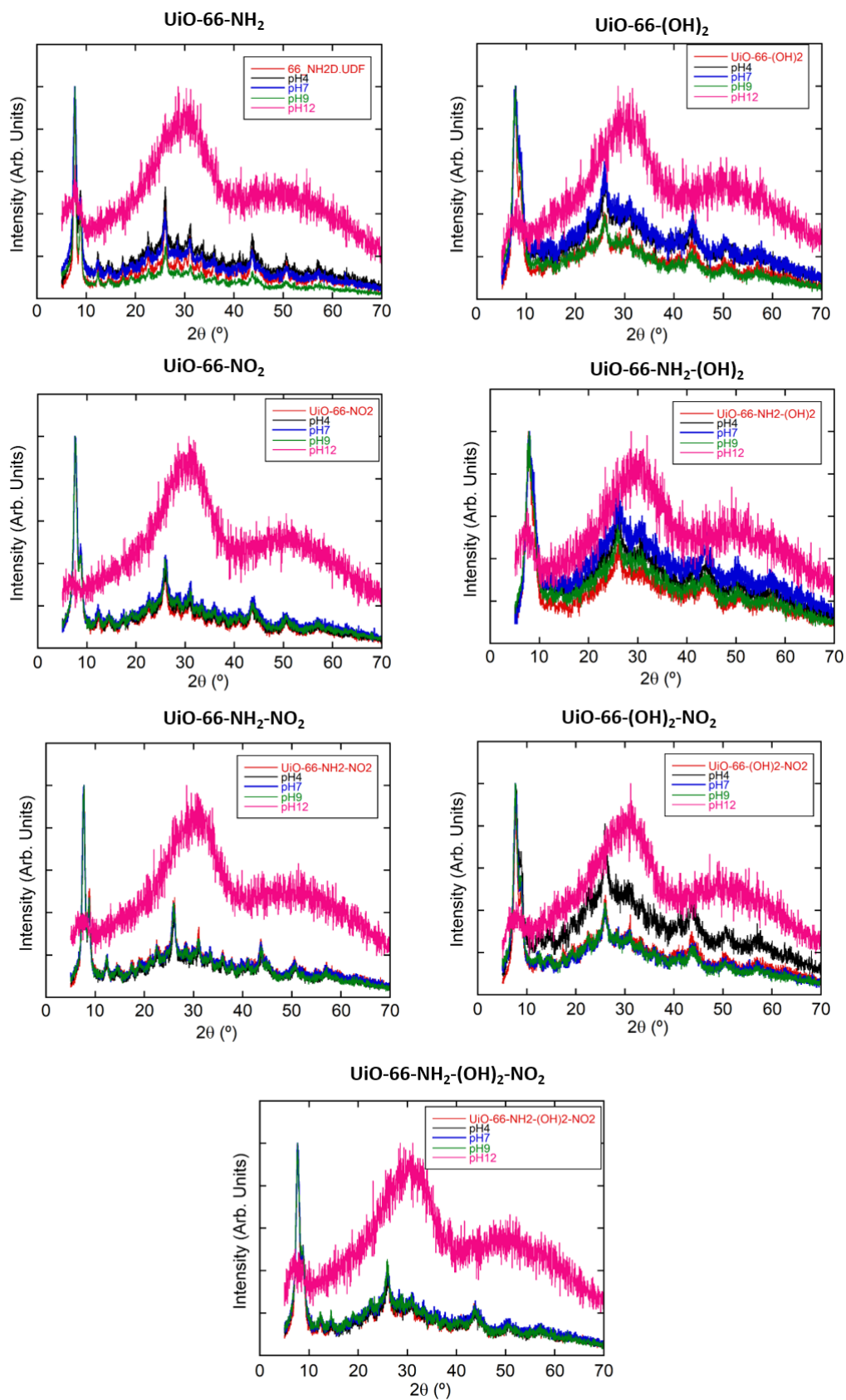
Figure 3.17. XRD patterns of UiO-66-R samples after being exposed to different acidic and basic media.

Further stability tests from pH 4 to 9 were carried out by using UV-Vis spectroscopy, in order to monitor the linker amount in the solution, as any leaching of the organic linkers to the solutions above a concentration of 1 mg·L^{-1} would be detectable *via* UV-Vis, as shown in the Figure 3.18a-c. Even though the absorbance values of the UV-Vis spectra give us only a comparative estimation of the organic linkers concentration leached from the MOF into the aqueous media, we have tried to semiquantify this information. To this end, a calibration curve was built for the BDC-NH$_2$, BDC-(OH)$_2$ and BDC-NO$_2$ aqueous solutions at 250 nm for all samples and at 350 nm in the specific case of amino and dihydroxyl linkers (Figure 3.18d-f) Therefore, on the basis of the calibration curves, we can estimate in a semiquantitative manner the concentration of the linkers leached from the single functionalized MOFs. For the single functionalized UiO-66-NH$_2$, UiO-66-(OH)$_2$ and UiO-66-NO$_2$ samples, this can be easily calculated with this calibration curve. However, for the MTV MOFs a slightly longer procedure is used.

In the specific case of MTV-MOFs having amino-nitro and dihydroxyl-nitro linkers, first the concentration of the amino or dihydroxyterephthalic linker was obtained from the 350 nm calibration curve. Afterwards, the absorbance arising from the amino or dihydroxyl linkers at 250 nm was calculated on the basis of the calibration curves obtained for this wavelength. The calculated value was subtracted to the observed experimental absorbance, and the resulting absorbance used to calculate the concentration of BDC-NO$_2$ linker. For UiO-66-NH$_2$-(OH)$_2$, as BDC-NH$_2$ and BDC-(OH)$_2$ linkers have a very similar UV-Vis fingerprint, their individual concentrations cannot be distinguished by following this experimental approach. In this case, the calculations were performed assuming that the UV-Vis absorbance was related with a 100 % release of BDC-NH$_2$ and BDC-(OH)$_2$. The average, maximum and minimum values of % of linker release from the MOF have been obtained and plotted in Figure 3.19.
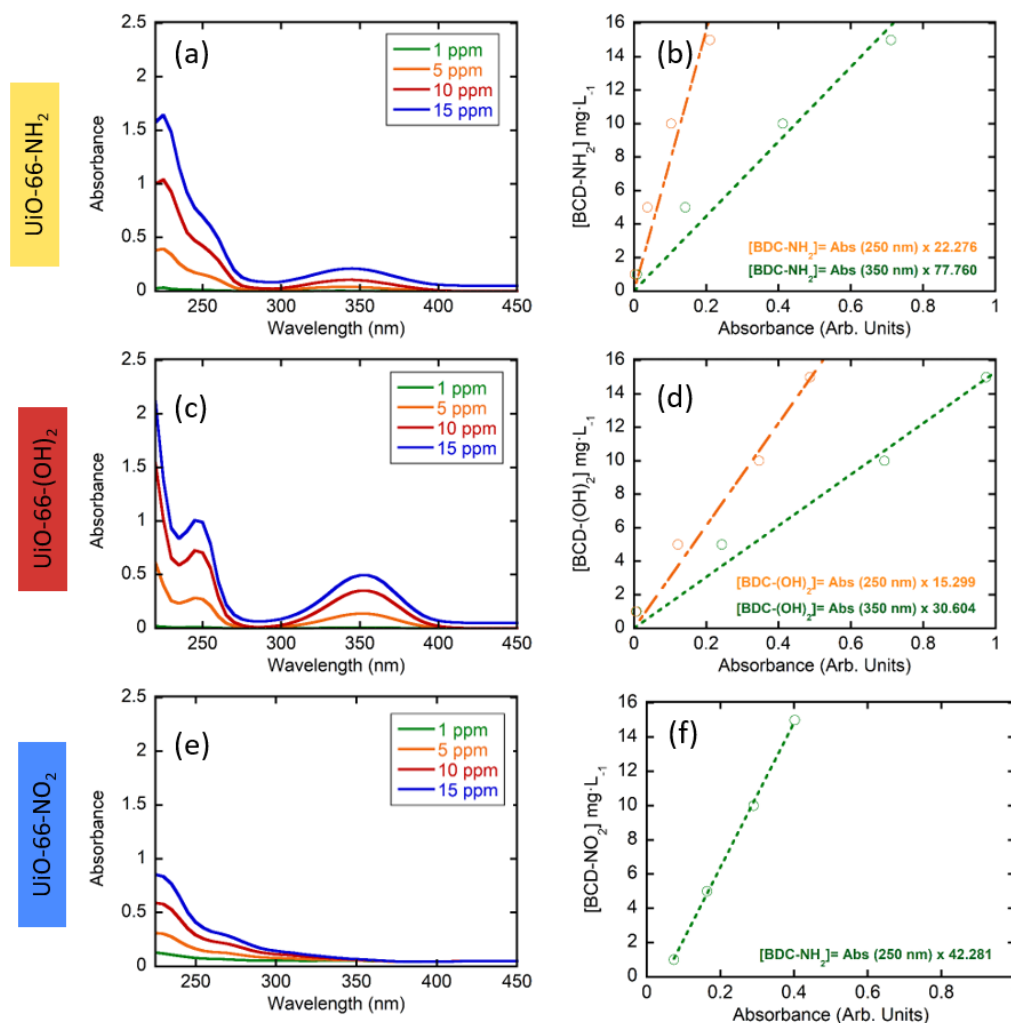
Figure 3.18. (a, c and e) UV-Vis spectra of BDC-X solutions (1, 5, 10, 15 mg·L^{-1}).and (b, d and f) concentration vs. absorbance (250 and 350 nm) calibration curves.

The percentage of the organic linkers leached from the MOF was calculated as detailed in the Equation 3.1.

$$L_{rel} = \frac{[L]_{UV-Vis}}{[L]_{total}} \times 100 \qquad (3.1)$$

where, L$_{rel}$ are the % of linkers released, [L]$_{UV-Vis}$ is the concentration of the linkers determined by UV-Vis spectroscopy, and [L]$_{total}$ stands for the concentration of the linkers calculated if all the MOF sample is dissolved in the aqueous solution.

It is important to mention that our approach is a qualitative one to estimate the chemical robustness of UiO-66 frameworks, and in general of MOF materials, which organic linkers or metals give a UV-Vis signal when dissolved in water (or other

organic solvents). This makes the methodology easily accessible for the research community working on MOF materials, although less accurate than the quantification of the linkers concentration through liquid chromatography.
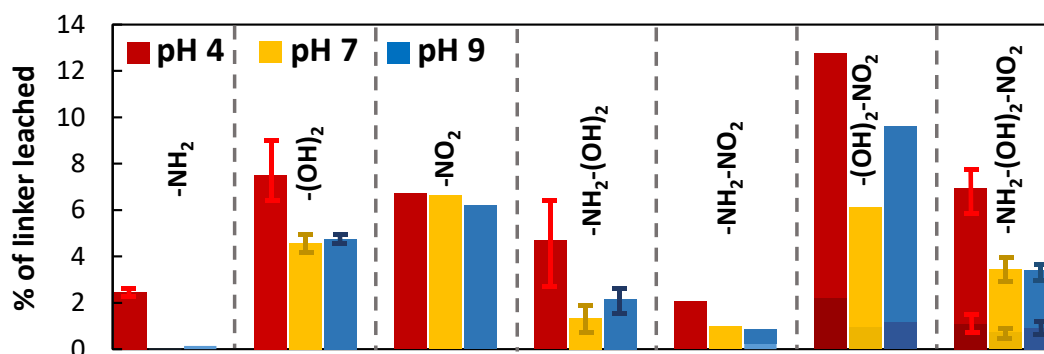
Figure 3.19. Percentage of the organic linkers dissolved when after immersing 30 mg of MOFs in 15 mL of aqueous solutions (pH= 4, 7 and 9) during 24 h.

UV-Vis spectroscopy confirms that even if the crystallinity of the samples is maintained, there is a partial leaching of the linkers into solution for all samples between pH 4 and 9, but the value of this figure is highly dependent on the functional groups presence in the frameworks. UiO-66-NH$_2$ shows the smaller release of BDC-NH$_2$ linkers into the solution (nearly negligible at pH 7 and 9, and close to 2 % at acidic conditions (i. e. pH 4)) in comparison to the ones observed for UiO-66-NO$_2$ and UiO-66-(OH)$_2$ (from 5 to 7.5 %). In contrast, UiO-66-(OH)$_2$ and UiO-66-NO$_2$ release significant amounts of their linker to the solution, especially at acidic conditions (> 6 %). For MTV-MOFs, the hydrolytic stability is approximately an average of the one reported for their single functionalized materials. The samples with amino functionalities are the ones that show the lower degree of linker release. For instance, UiO-66-NH$_2$-NO$_2$ exhibits a selective loss of BDC-NO$_2$ linkers (< 2 %) and a negligible release of BDC-NH$_2$ at acidic and neutral conditions (as concluded by the absence of the UV-Vis absorption band located at 350 nm). UiO-66-NH$_2$-(OH)$_2$ shows intermediate values between the ones observed for UiO-66-NH$_2$ and UiO-66-(OH)$_2$. The release of organic linkers in UiO-66-(OH)$_2$-NO$_2$ and UiO-66-NH$_2$-(OH)$_2$-NO$_2$ is accentuated in comparison to their single functionalized counterparts. For instance, in these two cases we were able to roughly differentiate the BDC-NO$_2$ and BDC-NH$_2$/(OH)$_2$ leaching to the media, but the final

values need to be considered carefully. Nevertheless, the overall percentage of organic linkers released to the aqueous media in after the immersion of UiO-66-(OH)$_2$-NO$_2$ and UiO-66-NH$_2$-(OH)$_2$-NO$_2$ exceeds the sum of the values obtained for the single-functionalized materials. When comparing the results obtained in this study with the tendencies reported in previous works, we found that our findings gives a complementary information. For instance, the structural stability of UiO-66-NH$_2$[103] and UiO-66-NO$_2$[104] when exposed to acidic and basic conditions have been previously corroborated, but this does not preclude that a partial release or dissolution of the MOF materials occurs during the process, as confirmed in our study. In parallel, as far as we know, this is the first time the corresponding data has been reported for the UiO-66-(OH)$_2$ homologue. Overall, it has been confirmed that the incorporation of amino functionalities to MTV-UiO-66 add chemical robustness to the frameworks by preventing amorphization but does not fully block the partial and selective release of nitro and dihydroxyl organic linker to the media.

Multivariate modulation of the light harvesting and photoconduction

The light-harvesting capacity of the materials was studied by UV-Vis spectroscopy of solid samples. The absorbance data was transformed into $(\alpha h v)^2$ *vs.* energy plots to calculate the optical band gaps of the single and multivariate MOFs (Figure 3.20a-d). Three absorption bands were observed in the UV-Vis spectra: (i) the first two were ultraviolet wavelengths, (likely from the charge transfer between the organic linkers and zirconium hexa-nuclear clusters), and (ii) the third band was located in the visible range, and therefore can be assigned to the colour of the amino and dihydroxyterephthalic linkers. As expected, the white coloured UiO-66-NO$_2$ shows the highest band gap value, 3.26 eV, demonstrating its capacity to harvest light exclusively in the ultraviolet energy range. UiO-66-NH$_2$ (2.84 eV) and UiO-66-(OH)$_2$ (2.75 eV) have smaller band gaps, suggesting that they can harvest light in the range of visible blue light. In the most cases, the MTV-MOFs exhibit band gaps slightly lower than the average value calculated from the band gaps of single-functional MOFs. UiO-66-NH$_2$-(OH)$_2$ is an exception to the general trend; it outperforms its calculated band gap of by 0.15 eV, and also the band gaps of the UiO-66-NH$_2$ and

UiO-66-(OH)$_2$ materials. Therefore, MTV chemistry allows us to tune not only the semi-conduction band by selecting the proper functional groups, but to also manipulate synergistic effects to improve the light harvesting capacity of the parent, singly functional MOFs (Figure 3.20f).
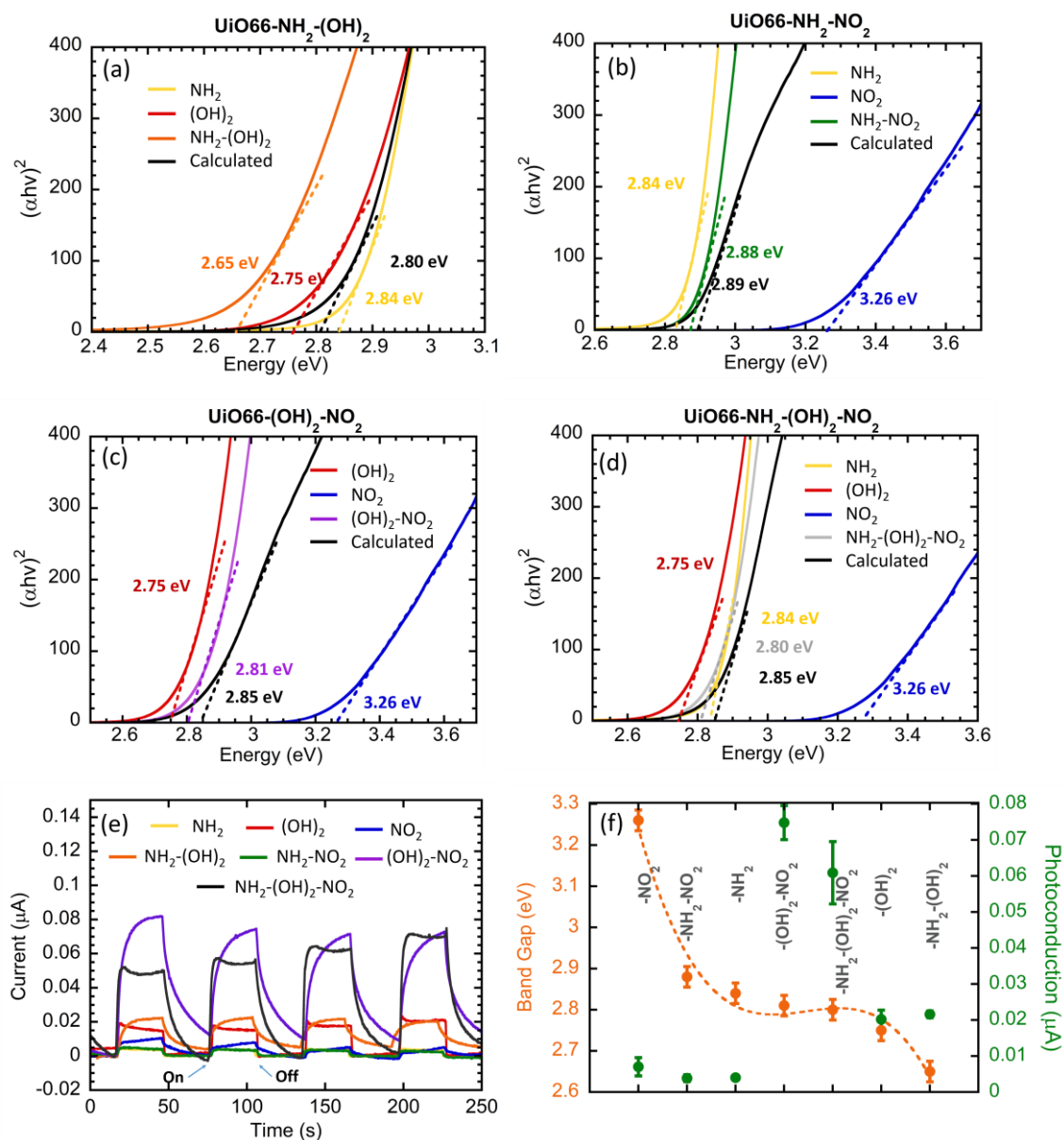
Figure 3.20. (a-d) Tauc plots and calculated band gaps for single functionalized and multivariate MOF. Black lines account for the calculated Tauc plot of the MTV-MOF from the averaged sum of the single functionalized UiO-66 frameworks. (e) Photocurrent response under intermittent light irradiation for single and multivariate encoded UiO-66 frameworks. (f) Band gap and photoconduction values for single and multivariate encoded UiO-66 frameworks.

Mott-Schottky plots were performed to investigate the flat band potential as well as Fermi energy level of the materials. As shown in Figure 3.21, the positive slopes of the Mott-Schottky plots exhibit the typical n-type semi-conduction. The flat band potentials are around -0.5 V *vs.* Ag/AgCl, which is in good agreement with previous researches.[42,105] In general, the flat band potential of n-type semi-conductor (intercept value at the x-axis) can be used to estimate the energy level of its conduction band (CB).[106] The CB potential of the UiO-66-R single and MTV materials (around -0.5 V *vs.* Ag/AgCl) is more negative compared to the $O_2/O_2^{-\cdot}$ (-0.13 V *vs.* Ag/AgCl), and thus, they can reduce the adsorbed O_2 to form $O_2^{-\cdot}$.[107], and it is also more negative than the Cr^{VI} to Cr^{III} reduction potential (+1.15 V *vs.* Ag/AgCl), allowing the material to perform this reduction process.[42]
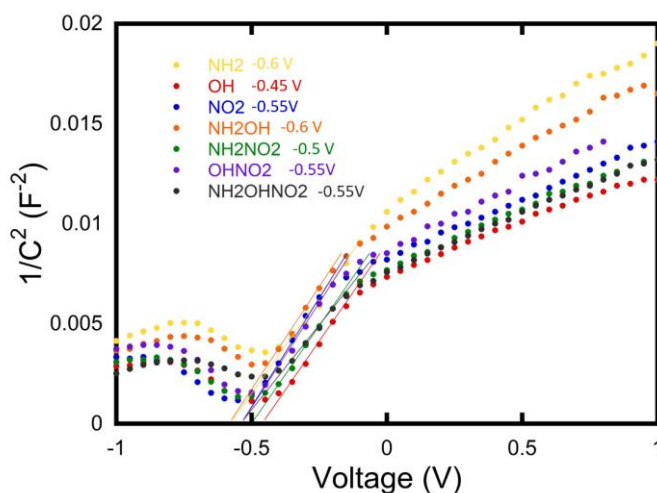
Figure 3.21. Mott-Schottky plot of UiO-66-R materials.

The photocurrent response of the materials was also measured under intermittent light irradiation (Figure 3.20e). Among the single encoded materials, UiO-66-(OH)$_2$ shows the best photoconduction as a consequence of encoding an electron-donor hydroxyl group into the structure that provides the linkers of free electrons, and thus, increases its conductivity. For the MTV-MOFs, it is noticeable than when BDC-(OH)$_2$ is combined with BDC-NO$_2$ a huge increase in the photoconductivity is observed. This can be due to the combination of electron donor and electron acceptor groups in the same structure, which increases the electron flux through the framework. Between the two materials with best photochemical response, a shape difference can be seen.

UiO-66-(OH)$_2$-NO$_2$ shows a wave-like profile, which is characteristic of materials with slower photoresponse, as it needs more time to rise its maximum photoconduction when it is illuminated. On the other hand, UiO-66-NH$_2$-(OH)$_2$-NO$_2$ exhibits a square-like shape, characteristic of a very quick photochemical response, achieving its maximum photoconduction rate in less than a second.

Modulation of the Cr^{VI} and Cr^{III} adsorption

The adsorption kinetics of single and multivariate UiO-66 materials over Cr^{VI} and Cr^{III} species were assessed with 5 ppm chromium solutions. Note that a sorbent dosage of 0.25 g·L^{-1} was used in these experiments because this value is within the operative photocatalyst dosage (0.25 – 1 g·L^{-1}) that will be used later for the Cr^{VI} to Cr^{III} photoreduction experiments. The adsorption kinetics were performed under acidic conditions (pH = 3.5) which prevents the precipitation of Cr^{III} oxides/hydroxides during dark and illumination conditions. The experimental data and its fitting with a pseudo-second order kinetic model have been plotted in Figure 3.22a-b. The Cr^{VI} and Cr^{III} adsorption capacities and kinetic rates have been summarized in the Figure 3.22c-d.

As previously mentioned, Cr^{VI} is stabilized as dichromate (Cr$_2$O$_7^{2-}$) and hydrogen-chromate (HCrO$_4^-$) anionic species at acidic pH values. All of the UiO-66 materials studied exhibit interesting Cr^{VI} adsorption capacities because of the presence of uncoordinated positions derived from linker defects. At first sight, the amino decorated MOF is the one of the UiO-66 variants that exhibits the best adsorption capacity over Cr^{VI} (Q_e = 15.5 mg·g^{-1}). This increased absorption capacity can be explained by the electrostatic interactions between the protonated NH^{3+} groups and the chromate anions, as reported previously by S. Rapti *et al.*[63] Dihydroxyl, nitro and MTV materials show similar Cr^{VI} loading values at equilibrium, ranging from Q_e = 6 to 8 mg·g^{-1} (Figure 3.22a). It is interesting to note that the kinetics of Cr^{VI} adsorption are strongly affected by the MTV chemistry, as shown by the k values obtained from the pseudo-second order modelling (dashed lines in Figure 3.22a and b) used to fit the experimental data (Figure 3.22c). For instance, single and MTV UiO-66 frameworks

encoded with hydroxyl functionalities exhibit slower kinetics, likely due to the steric and electrostatic repulsions arising from the hydroxyl groups and chromate oxyanions (Figure 3.22c). Overall, amino and/or nitro functionalized UiO-66 variants are the strongest candidates for the Cr^{VI} capture in terms of adsorption capacity and kinetics, respectively.
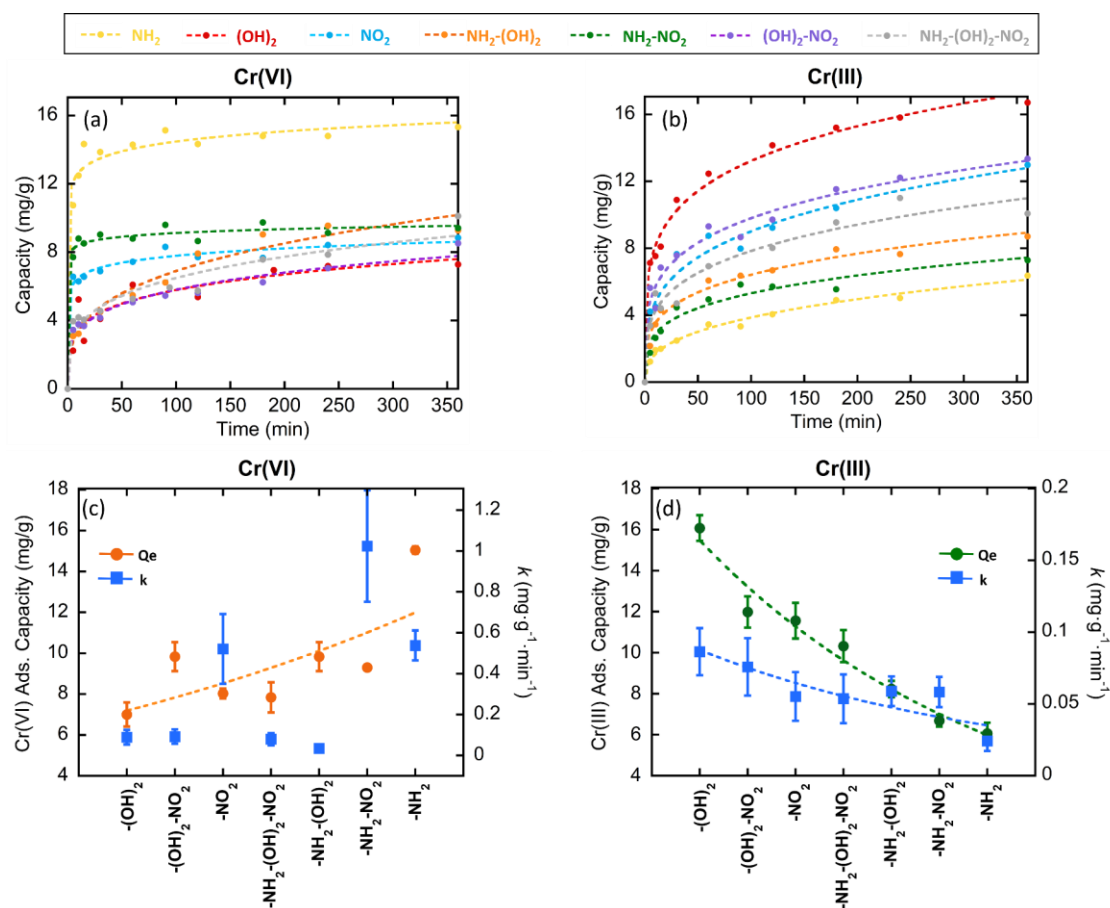
Figure 3.22. Adsorption kinetics over (a) Cr^{VI} (5 ppm) and (b) Cr^{III} (5 ppm) for UiO-66 type materials. Q_e and k values obtained by fitting the experimental data for (c) Cr^{VI} and (d) Cr^{III} adsorptions to a pseudo second order model. Dashed lines in (a) and (b) correspond to the fitting curve obtained from the application of a pseudo-second kinetic model to the experimental data (circles).

The trend is almost perfectly reversed for Cr^{III} cations. In general terms, the profiles of the kinetics of Cr^{III} adsorption suggest slower uptakes in comparison to Cr^{VI} (Figure 3.22b). Dihydroxyl (Q_e = 16.5 mg g^{-1}) and/or nitro (Q_e = 12.5 mg g^{-1}) functionalized UiO-66 variants show the best performance to capture Cr^{III} in terms of adsorption

capacity and kinetics, although k rates are at least twofold smaller than in Cr^{VI} adsorption. Most importantly, MTV chemistry opens proves to be an excellent and unique tool for fine modulation of both the capacity and kinetics of the Cr^{III} capture (Figure 3.22d).

Dual photocatalytic and adsorptive capacity

Once the ability of MTV-UiO-66 family to adsorb Cr^{VI} and Cr^{III} was assessed, their capacity to photoreduce Cr^{VI} to Cr^{III} under UV irradiation was studied (Figure 3.23a-d). First, an initial adsorption in darkness was performed with Cr^{VI} solutions of specific concentrations between 14 and 12 mg·g^{-1}. The initial point of the experiment was adapted to each material in order to obtain the most similar Cr^{VI} concentration after adsorption stage, and hence, as the starting point of the photocatalysis experiments. This point is relevant for later quantitative comparison of Cr^{VI} to Cr^{III} photocatalysis kinetics, since this parameter depends on the initial substrate concentration. Once equilibrium is reached after adsorption, the Cr^{VI} to Cr^{III} photoreduction is triggered by the illumination of the catalysts with a 365 nm UV-lamp. The experimental results of the multivariate compounds and of the UiO-66 compounds with single-functionalities are shown in Figure 3.23a-d. In experiments, the change in Cr^{VI} and Cr^{III} concentration was monitored during both the adsorption and photocatalysis steps. The rates of Cr^{VI} to Cr^{III} photoreduction in the single and multivariate samples were obtained after the fitting of the experimental data to a first-order kinetic model. The photoconduction values and the photocatalysis rates have been summarized in Figure 3.23e. In addition, the Cr^{III} release has been correlated with the hydrolytic stability of the frameworks, and especially with the release of BDC-$(OH)_2$ linker to the media, with the Cr^{III} concentration detected after the photocatalysis experiments. In order to study the effect of the initial Cr^{VI} concentration in the photoreduction rate, additional experiments were done for UiO-66-NH_2-$(OH)_2$-NO_2 at 5 and 30 mg·L^{-1} (Figure 3.23f).
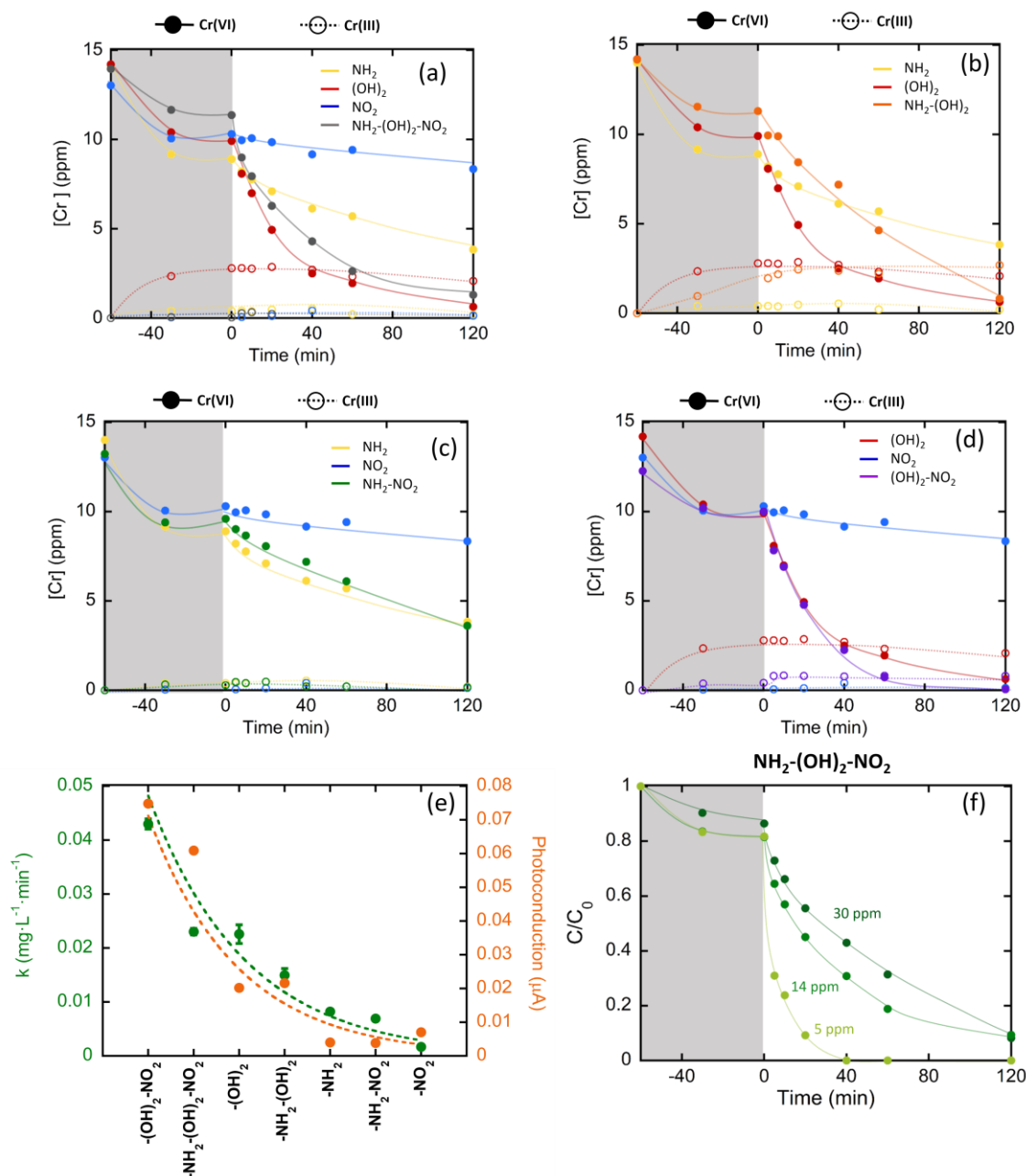
Figure 3.23. (a-d) Cr^{VI} to Cr^{III} photocatalytic reduction by single functionalized and multivariate UiO-66 materials. (e) Comparison between the Cr^{VI} to Cr^{III} photoreduction rates (calculated with Langmuir-Hinshelwood model) and band gap values for the studied materials. (f) Cr^{VI} to Cr^{III} photocatalytic reduction for UiO-66-NH$_2$-(OH)$_2$-NO$_2$ material starting at different Cr^{VI} concentrations.

First, UiO-66-NO$_2$ (Figure 3.23a) shows negligible photoreduction activity when illuminated (~10 % of Cr^{VI} → Cr^{III}). By comparison, UiO-66-NH$_2$ (Figure 3.23a) shows that 50% of the Cr^{VI} was eliminated after 2 hours of UV-illumination. The

experiments conducted with both UiO-66 variants show a negligible amount of Cr^{III} in the solution during the adsorption and photoreduction stages. Therefore, the Cr^{III} species generated during photocatalysis are retained within the MOF, and not released into the media. Photocatalysis efficiency is even better for UiO-66-$(OH)_2$ (Figure 3.23a), which reduces almost the 99% of Cr^{VI} to Cr^{III} in 2 hours. Unfortunately, UiO-66-$(OH)_2$ shows an appreciable release of Cr^{III} during adsorption step even though this UiO-66 variant has the best Cr^{III} adsorption capacity (as demonstrated in kinetic experiments). The outstanding Cr^{III} adsorption and Cr^{VI} to Cr^{III} photoreduction performance of the hydroxylated framework proves that it exhibits both photoreduction and chemical reduction functions. In return, the low hydrolytic stability of the framework gives rise to a release of dihydroxylated terephthalic molecules (and therefore also the Cr^{III} ions previously held at the hydroxyl sites) into the aqueous acidic media. However, it is clear that Cr^{III} concentration remains stable during photocatalysis, suggesting that an equilibrium between the MOF and the media is established once a certain concentration of BDC-$(OH)_2$ linkers is released. Multivariate UiO-66-NH_2-$(OH)_2$ shows a 99 % Cr^{VI} to Cr^{III} photoreduction efficiency, but with slightly slower photoreduction kinetics (Figure 3.23b) in comparison to UiO-66-$(OH)_2$. In parallel, a dual-stage Cr^{III} release has been observed during adsorption and photocatalysis. The Cr^{III} released in darkness (~ 1.2 mg$\cdot$L^{-1}) is between the negligible values obtained for UiO-66-NH_2 and the 2.5 mg$\cdot$L^{-1} observed for UiO-66-$(OH)_2$. After UV-illumination, a second Cr^{III} release occurs, plateauing at a concentration of 2.5 mg$\cdot$L^{-1}, mirroring the observations of the UiO-66-$(OH)_2$ experiment. It is still unclear whether the Cr^{III} release is related to: (i) a destabilization of the MOF, or (ii) the limited capacity of the framework to retain the Cr^{III} ions generated during the photocatalysis. Given the good Cr^{III} adsorption capacity of UiO-66 variants containing hydroxyl functions, the first hypothesis seems to be the most plausible.

The Cr^{III} release during Cr^{VI} adsorption and photocatalysis is partially blocked when BDC-NO_2 linkers are included in the multivariate MOFs. As an illustrative example, UiO-66-NH_2-NO_2 is able to retain the Cr^{III} ions generated during photocatalysis while its photoreduction kinetics and efficiency are as good as UiO-66-NH_2, but still far inferior to UiO-66-$(OH)_2$ (Figure 3.23c). Conversely,

BDC-(OH)$_2$ and BDC-NO$_2$ linkers act synergistically in the UiO-66-(OH)$_2$-NO$_2$ framework (Figure 3.23d), where photoreduction activity becomes as good as UiO-66-(OH)$_2$, but Cr^{III} retention is improved by the stabilizing BDC-NO$_2$ linkers. Even though Cr^{III} release is minimized when nitro and hydroxyl functions are encoded within the material, an appreciable 1.5 mg·L^{-1} Cr^{III} concentration is observed during the experiment. To address this, the nitro, amino and dihydroxyl functions were encoded in the same MTV-UiO-66 framework, which exhibits both excellent Cr^{VI} to Cr^{III} chemical reduction and photoreduction kinetics similar to UiO-66-(OH)$_2$, and negligible Cr^{III} release to the media as exhibited by UiO-66 variants containing nitro and/or amino functionalities.

When comparing the Cr^{III} release observed during the photocatalysis experiments to the chemical stability of the compounds, it is clear that these factors are closely correlated in the case of hydroxyl bearing linkers. For the nitro homologues, the correlation is not so evident. Despite the chemical stability studies show that there is a significant BDC-NO$_2$ release to the media, there is not a Cr^{III} concentration increase during photocatalysis. This evidence could be related with the lack of an important role of the nitro functions to adsorb Cr^{III} ions, so their release does not induce the loss of the Cr^{III} ions immobilized at the UiO-66 amino and hydroxyl functionalities. For instance, the higher the dihydroxyl and aminotherepthalate linkers leached to the media, the more accentuated the Cr^{III} release during adsorption and photocatalysis.

Multivariate chemistry of MOFs in the UiO-66 family gives rise to synergic effects in their photocatalytic performance. The photoconduction efficiency of the single and multivariate materials is closely correlated with their efficiency in transforming Cr^{VI} to Cr^{III}. For instance, these materials containing hydroxyl groups exhibit faster kinetics to photoreduce Cr^{VI} to Cr^{III}, although they exhibit significant Cr^{III} release during adsorption and photocatalysis stages. When balancing the chemical and photoreduction capacity with hydrolytic stability, tri-functional MTV UiO-66-(OH)$_2$-NH$_2$-NO$_2$ exhibits the best performance; in addition to superior photoreduction kinetic rates rivalling the dihydroxyl variant. For instance, this trifunctional MTV-variant is able to retain the phototransformed Cr^{III} species with the

same efficiency as the amino functionalized material (Figure 3.23a), even if significant leaching of nitro linkers has been observed.

In order to study how the initial Cr^{VI} concentration affects the photoreductive activity of UiO-66-NH$_2$-(OH)$_2$-NO$_2$, extra photocatalysis experiments were performed, starting at 30 ppm and 5 ppm (Figure 3.23f). The adsorption process in darkness remains similar, however, when the UV-lamp is turned-on, some differences can be observed. As it can be observed in Figure 3.24, the material shows better kinetic rates at low Cr^{VI} concentrations (5 ppm > 15 ppm > 30 ppm), as more catalytic sites per Cr^{VI} ions are accessible for their photoreduction. Starting from a Cr^{VI} 5 ppm solution, 100% of the chromium can be eliminated in only 40 minutes. This photoreductive response fits with the usual chromium concentrations found in real-water streams, usually bellow 5 ppm.
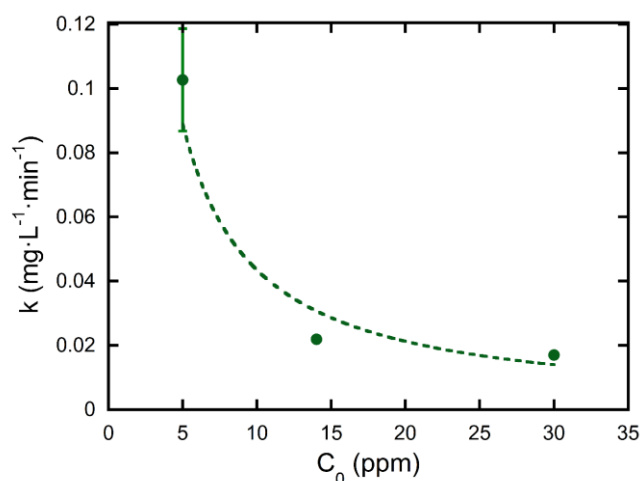
Figure 3.24. Comparison of k values of photocatalytic performance of UiO-66-NH$_2$-(OH)$_2$-NO$_2$ starting at different Cr^{VI} concentrations.

Further research is needed to fully understand the electronic properties and enhanced photocatalytic activity of the MTV-UiO-66 variants in comparison to the expected average response of single-functional materials. One of the possible hypotheses is that proton, electron, and hole transfer within the MTV-UiO-66 is enhanced due to the concurrent presence of electron donating and withdrawing groups within the framework, as initially pointed out by the photoconduction experiments.

Stabilization of chromium in MTV-MOFs

Chromium speciation after adsorption and photocatalysis was studied by means of UV-Vis and EPR spectroscopies. In order to enhance the chromium UV-Vis and EPR signals, the experiments were performed with 100 ppm Cr^{VI} solutions.

First, the color change of the samples was noted both after the adsorption step in darkness and after UV illumination (Figure 3.25). After adsorption, UiO-66-NO$_2$ and UiO-66-NH$_2$-NO$_2$ materials get the characteristic yellow colour of chromate anions. For the variants including amine and hydroxyl functionalities, the colour change after Cr^{VI} adsorption is even more drastic, especially for multivariate UiO-66-NH$_2$-(OH)$_2$ and UiO-66-NH$_2$-(OH)$_2$-NO$_2$, becoming light brown. This darkening in the colour of the solid samples is more severe under exposure to UV-radiation, which is indicative of electron transfer between Cr^{VI} and Cr^{III} mixed-valence species stabilized within the frameworks. In parallel, the colour of the Cr^{VI} solutions was monitored as well. It is interesting to point that there is an appreciable decrease in intensity of the yellow color of the solution for almost all samples after photocatalysis, i.e. the intensity of the color of the Cr^{VI} solutions can be related with the efficiency of the materials to adsorb Cr^{VI} and catalyse the Cr^{VI} to Cr^{III} reduction.

Figure 3.25. Samples after the adsorption of 100 ppm Cr^{VI} solution in darkness and under UV-Vis light.
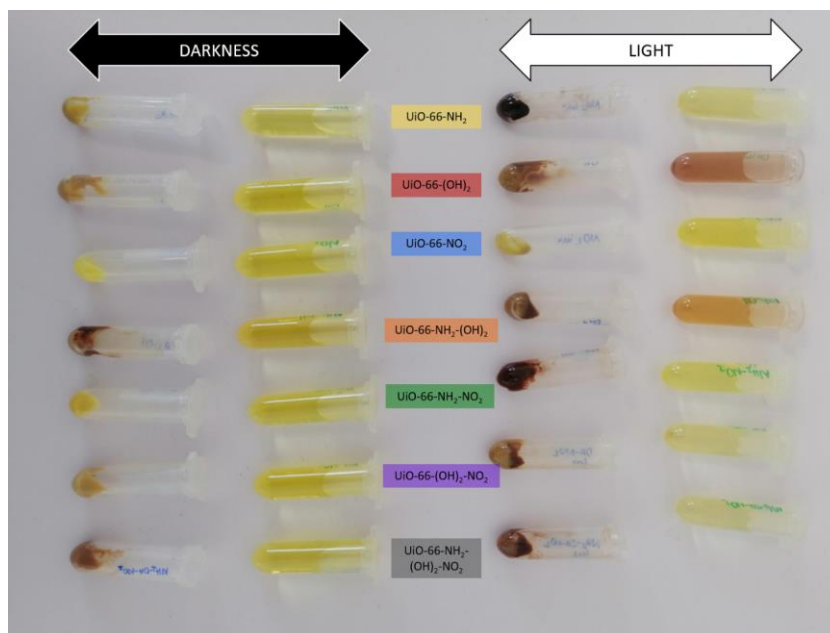
In line with previous results, the solutions after the photocatalysis with UiO-66 materials functionalized with hydroxyl groups display orange to brown dark hues, far from the yellow expected for Cr^{VI} solutions. Indeed, this deviation from the expected orange colour associated to chromate anions is explained by the BDC-(OH)$_2$ and Cr^{III} released to the solutions during photocatalysis experiments, in alignment with the previous results observed during the chemical stability assessments of UiO-66 and MTV-UiO-66 materials by UV-Vis.

In order to confirm this point, the multivariate samples were dissolved and studied by ^{1}H-NMR after their use as photocatalysts. The integration of the ^{1}H-NMR signature of hydroxyl, nitro and amino linkers indicates that there is a preferential leaching of hydroxyl linkers in comparison to amino and nitro ones; the molar percentage of the linkers in the MTV-MOFs changes considerably after their working period, as described observed in the Table 3.6. This experiment confirms the preference of hydroxyl linkers to be solubilized at acidic conditions, but does not give clues about the release of BDC-NO$_2$ struts, in contrast with the observations obtained by UV-Vis spectroscopy. Although further research is needed to fully understand this counterintuitive difference, it is important to note that the release of zirconium ions from the UiO-66 framework could give rise to an additional absorbance of the UV-Vis signal in the same wavelength range (i.e. < 250 nm) that is used in this work to estimate the BDC-NO$_2$ concentration.[108] This would lead to an overestimation of the release calculated for BDC-NO$_2$ linkers, but does not refuse the fact that even when the stability of UiO-66-NO$_2$ is studied by UV-Vis spectroscopy, a non-negligible signal is observed at 250 nm, which confirms the partial release of nitro linkers jointly with zirconium ions into the aqueous solutions. In addition, the presence of chromium ions, and the illumination during photocatalysis, can alter as well the selective release of the linkers studied under ideal conditions in the previous sections.

Table 3.6. Molar percentage of BDC-NH$_2$, BDC-(OH)$_2$ and BDC-NO$_2$ linkers in the MTV-MOFs before and after their use as photocatalysts.

Sample	BDC-NH$_2$ (%)	BDC-(OH)$_2$ (%)	BDC-NO$_2$ (%)
	(initial % / after operation)		
UiO-66-NH$_2$-(OH)$_2$	56 / 63	44 / 37	---
UiO-66-NH$_2$-NO$_2$	46 /45	---	54 / 55
UiO-66-(OH)$_2$-NO$_2$	---	41/ 35	59 / 65
UiO-66-NH$_2$-(OH)$_2$-NO$_2$	34 / 39	26 / 16	40 / 45

UV-Vis spectra of powdered UiO-66 materials after Cr^{VI} adsorption and Cr^{VI} to Cr^{III} photoreduction show the common fingerprint bands ($\sim$ 37000 cm^{-1}) attributed to the ligand-to-metal charge transfer (LMCT) (Figure 3.26). An additional band, located around 26500 cm^{-1}, is observed for the materials containing amino or dihydroxyl functionalities. This signal is associated with the electron density transfer from the dihydroxyl and amine groups to the π^* orbitals of the benzene ring; which gives the characteristic yellow colour to UiO-66-NH$_2$ and UiO-66-(OH)$_2$. After Cr^{VI} adsorption, the UV-Vis spectra show additional adsorption bands related to Cr^{VI} and Cr^{III} species. Cr^{6+}-O^{2-} charge transfer bands for mono-chromate species are found at 35000 and 27000 cm^{-1}, and in our case, they overlap significantly with the UV-Vis signals coming from the MOF materials. The absorption band located around 17000 cm^{-1} confirms the presence of Cr^{III} species even after the adsorption stage. Thus, the amine, and especially the hydroxyl functionalities incorporated within the UiO-66 frameworks, trigger the Cr^{VI} to Cr^{III} chemical reduction in dark conditions. The intensity ascribed to the Cr^{III} UV-Vis signature increases in almost all samples after photocatalysis, but especially in UiO-66-NH$_2$, UiO-66-NH$_2$-(OH)$_2$ and UiO-66-NH$_2$-(OH)$_2$-NO$_2$. This evidence further confirms that during the Cr^{VI} to Cr^{III} phototransformation, most of the Cr^{III} ions are stabilized within the porous frameworks.
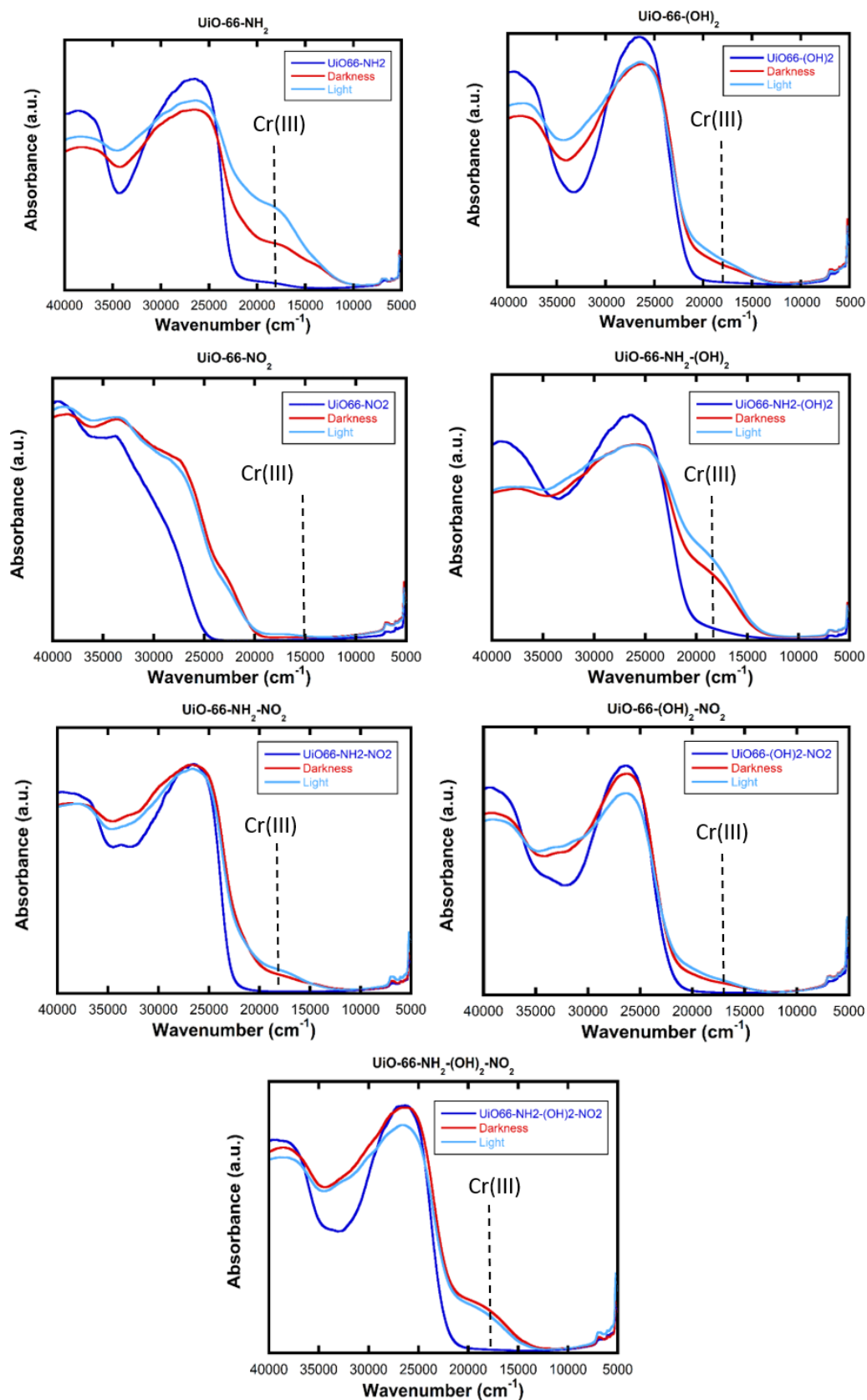
Figure 3.26. UV-Vis spectra of original samples (dark blue lines), and after Cr[VI] adsorption in dark conditions (red line) and under UV-light (light blue lines).

The results obtained from EPR spectroscopy support the conclusions drawn by UV-Vis spectroscopy (Figure 3.27). For instance, EPR can be used as a complementary tool to study the transient Cr^V and final Cr^{III} species once immobilized within the porous structures of the MOFs. Jointly with the information obtained from UV-Vis, EPR gives access to obtain a precise description of the chromium immobilization and transformation during adsorption and photocatalysis. Regarding EPR, three different signals associated with Cr^{III} and Cr^V species are observed after adsorption and photoreduction experiments, as illustrates schematically in the Figure 3.27a and b[109–111]:

1. The **ɣ-signal** is an axially symmetric intense and sharp absorption band located around 3400 G. It is usually ascribed to isolated Cr^V intermediate and highly reactive species, which usually exhibit a highly distorted octahedral or pseudo-pyramidal coordination environment. The ɣ-signal shows a characteristically sharp $g_\perp$=1.979 (~ 3390 G) and a weak somewhat diffuse g_{II} 1.961 (~ 3425 G) lines. (Figure 3.27b).

2. The **ϱ-signal** is a dispersed absorption band (~ 1350, $g_\perp$ ~ 5) associated with Cr^{III} ions immobilized as isolated species (Figure 3.27a). From an EPR perspective, isolated Cr^{III} ions are the ones that are far enough from surrounding Cr^{III} to establish strong enough ferro or antiferromagnetic interactions.

3. The **ß-signal** is a broad isotropic band related to clustered Cr^{III} ions, whose g value strongly depends on the size and shape of the chromium clusters. The presence of this characteristic EPR fingerprint indicates that the Cr^{III} ions are immobilized within the UiO-66 matrix close enough to establish magnetic interactions (i.e. Cr^{III}-O-Cr^{III} or Cr^{III}-OH$\cdots$O-Cr^{III}, (Figure 3.27a).
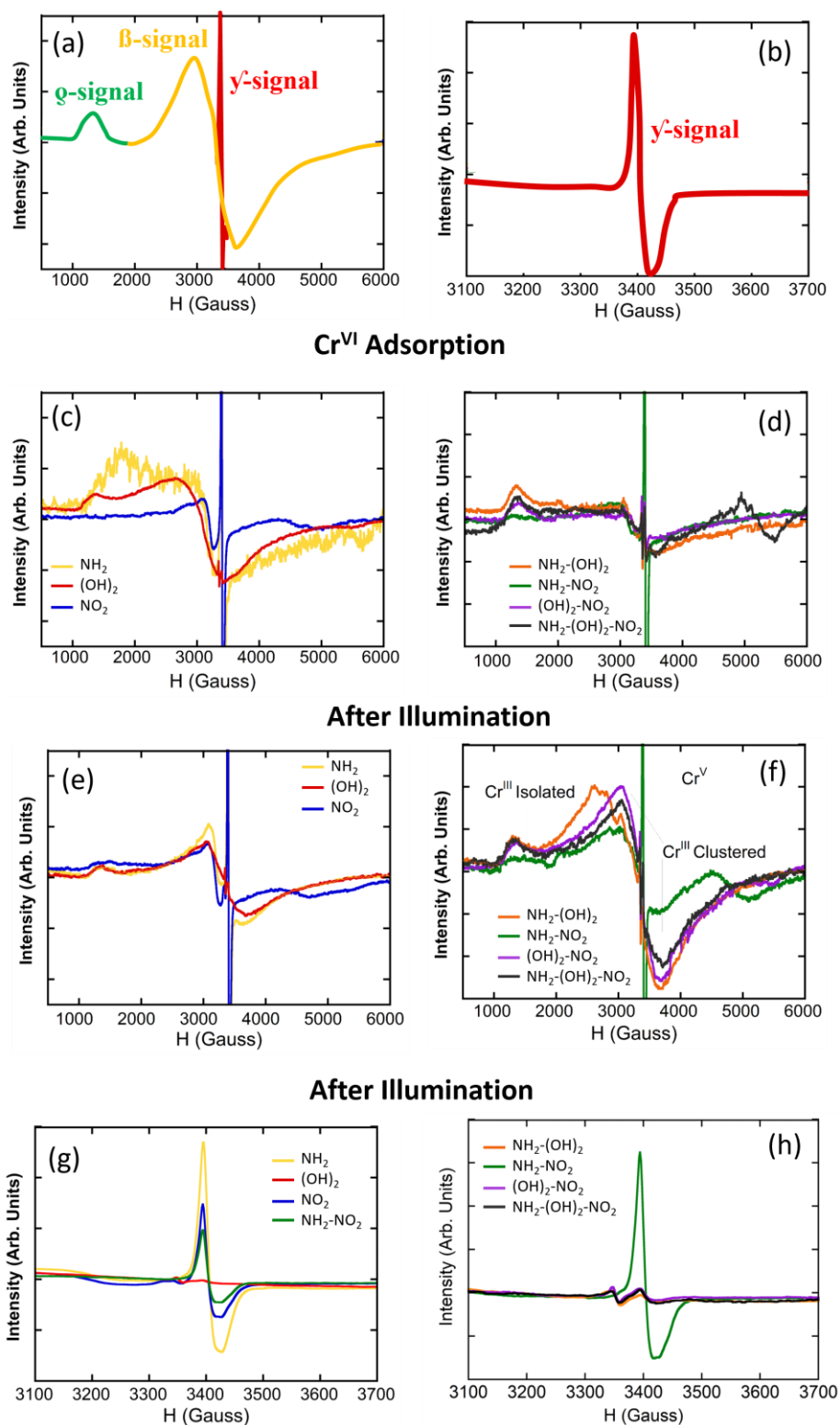
Figure 3.27. (a-b) Illustration of the ϱ, ß and ɣ-signals of the EPR spectra associated to Cr^{III} isolated and clustered ions, and intermediate Cr^V species, respectively. (c-d) Detailed ERR spectra after Cr^{VI} adsorption for (c) single and (d) multivariate frameworks. (e-f) Detailed EPR spectra after Cr^{VI} to Cr^{III} photoreduction for (e) single and (f) multivariate frameworks. (g-h) ɣ-signal associated to Cr^V after photoreduction process.

After Cr^{VI} adsorption, the EPR spectrum of single functionalized UiO-66-(OH)$_2$ shows the most intense ϱ-and ß-signals associated with the immobilization of Cr^{III} isolated and clustered species, followed by the EPR-spectra of UiO-66-NH$_2$ and UiO-66-NO$_2$ (Figure 3.27c). This evidence further points to the capacity of hydroxyl, and in less extent amine groups installed within UiO-66 framework, to induce a chemical reduction of Cr^{VI} to Cr^{III} during adsorption. Multivariate MOFs including hydroxyl functionalities also exhibit Cr^{VI} to Cr^{III} chemical reduction capacity, as derived from their EPR spectra. After adsorption, Cr^{III} ions are mainly stabilized as isolated ions within the porous framework (ϱ-signal – Figure 3.27f). Once illuminated, the intensity of the ß-signal associated with Cr^{III} clustered species increases for all the studied materials, but especially for MTV-UiO-66 exhibiting good Cr^{VI} to Cr^{III} photoreduction activity (Figure 3.27d and g). Overall, the presence of the EPR signals associated to Cr^{III} ions confirm that they are immobilized within the MOF's pore structure after photocatalysis, preventing their migration to the water media during the experiments.

Regarding the ɣ-signal associated to Cr^{V} transient species, this is mainly found in the EPR spectra at -NO$_2$ and -NH$_2$ single variants of UiO-66 (Figure 3.27e), as well as at bi-functional UiO-66-NH$_2$-NO$_2$ multivariate MOF. Although UV illumination slightly reduces the intensity of the ɣ-signal associated with Cr^{V}, it is still clearly visible after photocatalysis (Figure 3.27h). In comparison, any incorporation of hydroxyl groups within the frameworks, even in the case of the trifunctional UiO-66-NH$_2$-(OH)$_2$-NO$_2$ material, gives rise to the disappearance of the ɣ-signature associated to Cr^{V} (Figure 3.27e and h). A possible hypothesis is that the presence of electron donor functionalities (i.e. dihydroxyl or amino) destabilize the intermediate and highly reactive pentavalent chromium, quickly reducing it to Cr^{III}. This is a crucial observation when MOF materials are applied for water remediation purposes since pentavalent ions are even more reactive and hazardous than Cr^{VI}. It is important to highlight that Cr^{VI} is silent by EPR, so despite that the presence of Cr^{III} and Cr^{V} has been duly confirmed by this technique, the evidence does not preclude the fact that hexavalent chromium is concurrently stabilized with Cr^{VI} and Cr^{III} ions within the MOFs after operation, as detailed by UV-Vis analyses.

Mechanisms for the chemical and photocatalytic transformation and immobilization of Cr^{VI} to Cr^{III}

The description of the overall transformation of Cr^{VI} species immobilized within a porous matrix needs to consider that the modification of the chromium oxidation state is linked to variation in its coordination environment (Figure 3.28a). Overall, Cr^{VI}, stabilized as CrO$_4^{2-}$ chromate anions, gains three electrons and incorporates two hydroxyl or water molecules within its coordination environment during its reduction to Cr^{III}. During this process, the highly reactive and transient intermediate Cr^{V} species are formed as well, as proved by EPR. As Cr^{V} is usually stabilized as a five or six-coordinated species, during the chromate reduction to Cr^{V}, at least a water molecule needs to be incorporated within the coordination sphere of the chromium ions (Figure 3.28a).

The first step of the immobilization and transformation of Cr^{VI} to Cr^{III} into the UiO-66 frameworks is the adsorption of chromate anions (Figure 3.28b). Two possible mechanisms explain chromate adsorption capacity of the UiO-66 frameworks, their covalent immobilization to the linker defective positions located at the zirconium hexanuclear clusters, or their electrostatic interaction with hydroxyl, but especially, with amine protonated groups. Reached at this point, two possible paths for the Cr^{VI} to Cr^{III} reduction are possible: (i) photocatalysis and (ii) chemical reduction.[112] The chemical encoding of the UiO-66 frameworks determine the efficiency and combination of the separated paths.

During photocatalysis, the light harvesting capacity of the UiO-66 frameworks (i.e. band gap) promotes the electron and holes separation, but their posterior conduction and transfer to the chromium ions is governed by the photoconduction efficiency of the materials (Figure 3.28c.1). At this point, the chemical variance of MTV materials makes the difference, because the incorporation of electro donor and withdrawing groups within the same framework improves the photoconduction and fasten the Cr^{VI} to Cr^{III} phototransformation. The chromate anions stabilized within the porous scaffold are steadily reduced to Cr^{V} and Cr^{III} while are immobilized into their adsorption position (Figure 3.28c.2). As the photocatalytic transformation of Cr^{VI} to Cr^{III} evolves, the Cr^{VI} to Cr^{III} photoreduction process is repeated leading to the

clustering of Cr^{III} ions within the framework (Figure 3.28c.3). It is important to note at this point that if the single or MTV-UiO-66 lacks hydroxyl groups, transient Cr^{V} species will be stabilized within the material after operation.
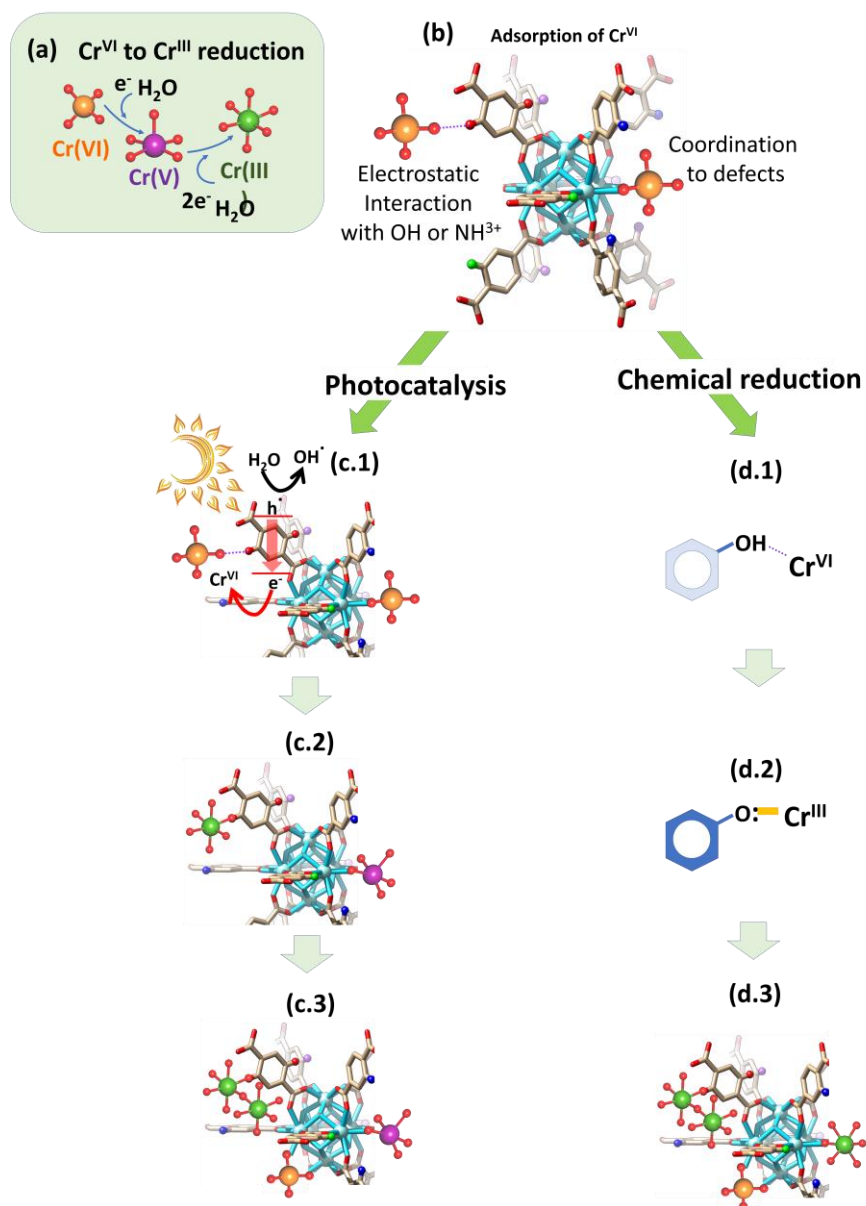
Figure 3.28. Cr^{VI} to Cr^{III} chemical and photoreduction mechanisms in MTV-UiO-66 dual sorbent/photocatalysts. (a) Overall Cr^{VI} to Cr^{III} reduction. (b) Adsorption mechanisms for Cr^{VI} oxyanions within the MTV-UiO-66 frameworks. (c.1) light triggered generation of e$^-$ and holes and the concurrent e$^-$ transfer from the UiO-66-R framework to Cr^{VI}. (c.2-c.3) Evolution of the chromium species into the porous frameworks during photocatalysis. (d.1) Electrostatic interaction between hydroxyl groups and Cr^{VI} ions. (d.2) Chemical reduction of Cr^{VI} to Cr^{III} and their stabilization into electron rich quinone groups. (d.3) Chromium speciation within the UiO-66 framework after the chemical reduction of Cr^{VI} to Cr^{III}.

In contrast, when hydroxyl functionalities are encoded in UiO-66, the Cr^{VI} adsorption process (Figure 3.28b and d.1) is coupled to its chemical reduction to Cr^{III} *via* electron rich quinone groups coming from hydroxyl functionalities (Figure 3.28d.2). For instance, in addition to the EPR maxima associated to chromium, the presence of a small EPR signal that could be tentatively ascribed to an organic quinone radical in the hydroxylated materials has been found as well. Finally, as the chemical reduction, or its combination with photocatalysis, evolves, chromium ions are stabilized as clustered Cr^{III} ions with the frameworks (Figure 3.28d.3). Regardless if photocatalysis, chemical reduction or their combination is the process that triggers the Cr^{VI} transformation to Cr^{III}, the presence of hydroxyl ions is key to destabilize Cr^{V} transient species and transform them into Cr^{III} ions. This does not preclude the presence of Cr^{VI} and Cr^{III} ions within dihydroxyl-functionalized frameworks, but the absence of highly reactive and toxic Cr^{V}.

3.2.3. CONCLUSIONS

In this work, multivariate functionalization of Zr-UiO-66 framework with $-NH_2$, $-(OH)_2$ and $-NO_2$ functional groups has been used to create a new MOF material with enhanced Cr^{VI} and Cr^{III} adsorption capacity and excellent Cr^{VI} to Cr^{III} photoreduction efficiency.

The integral functionalization of UiO-66 frameworks has given rise to a synergistic enhancement of the band gap, photoconduction and photocatalytic efficiency of the multivariate frameworks, which exceed properties of the single functionalized materials.

Trifunctional UiO-66-NH_2-$(OH)_2$-NO_2 exhibits; (i) 99% Cr^{VI} to Cr^{III} photoreduction in two hours, (ii) photocatalysis and adsorption kinetics nearly as good as the UiO-66-$(OH)_2$ framework, (iii) great capacity to retain the phototransformed Cr^{III} ions within the framework, (iv) only negligible amounts of the highly reactive and hazardous Cr^{V} intermediate species after operation.

MTV-reticular chemistry has been revealed as a limited tool to control the thermal and hydrolytic stability of UiO-66 type frameworks. Nevertheless, our findings can

open the avenue to control the selective leaching of the linkers from multivariate UiO-66 frameworks to generate defects in these materials.

Overall, multivariate reticular chemistry has shown to be an outstanding tool to tune the physico-chemical properties of UiO-66 frameworks in environmental applications, a strategy that can be easily adapted to other research fields such as controlled adsorption/desorption of target molecules i.e. drugs, modulation of optoelectronic properties, or controllable MOF degradation profiles under specific surrounding biological conditions, or multivariate catalytic pockets approaching the ones of enzymes.

3.3. REFERENCES

1   Maleki A, Hayati B, Naghizadeh M, Joo SW. Adsorption of hexavalent chromium by metal organic frameworks from aqueous solution. *Journal of Industrial and Engineering Chemistry* 2015; **28**: 211–216. [DOI: 10.1016/j.jiec.2015.02.016]

2   Rengaraj S, Venkataraj S, Yeon JW, Kim Y, Li XZ, Pang GKH. Preparation, characterization and application of Nd-TiO2 photocatalyst for the reduction of Cr(VI) under UV light illumination. *Appl Catal B* 2007; **77**: 157–165. [DOI: 10.1016/j.apcatb.2007.07.016]

3   G. Saiz, P., Iglesias, N., Gonzalez-Navarrete, B., Rosales, M., Quintero, Y. M., Reizabal, A., Orive, J., Fidalgo-Marijuan, A., Lanceros-Mendez, S., Arriortua, M. I.,& Fernandez de Luis R. Chromium speciation in zirconium-based metal – organic frameworks for environmental remediation. *Chemistry—A European Journal* 2020; **26**: 1–13. [DOI: 10.1002/chem.202001435]

4   Wang CC, Du XD, Li J, Guo XX, Wang P, Zhang J. Photocatalytic Cr(VI) reduction in metal-organic frameworks: A mini-review. *Appl Catal B* 2016; **193**: 198–216. [DOI: 10.1016/j.apcatb.2016.04.030]

5   Wang Y, Zhang N, Chen D, Ma D, Liu G, Zou X, Chen Y, Shu R, Song Q, Lv W. Facile synthesis of acid-modified UiO-66 to enhance the removal of Cr(VI) from aqueous solutions. *Science of the Total Environment* 2019; **682**: 118–127. [PMID: 31108266 DOI: 10.1016/j.scitotenv.2019.04.407]

6   Kabay N, Arda M, Saha B, Streat M. Removal of Cr(VI) by solvent impregnated resins (SIR) containing aliquat 336. *React Funct Polym* 2003; **54**: 103–115. [DOI: 10.1016/S1381-5148(02)00186-4]

7   Roy Choudhury P, Majumdar S, Sahoo GC, Saha S, Mondal P. High pressure ultrafiltration CuO/hydroxyethyl cellulose composite ceramic membrane for separation of Cr (VI) and Pb (II) from contaminated water. *Chemical Engineering Journal* 2018; **336**: 570–578. [DOI: 10.1016/j.cej.2017.12.062]

8   Wu S, Ge Y, Wang Y, Chen X, Li F, Xuan H, Li X. Adsorption of Cr(VI) on nano Uio-66-NH2 MOFs in water. *Environmental Technology (United Kingdom)* 2018; **39**: 1937–1948. [PMID: 28625105 DOI: 10.1080/09593330.2017.1344732]

9   Liu Y, Liu F, Ding N, Hu X, Shen C, Li F, Huang M, Wang Z, Sand W, Wang CC. Recent advances on electroactive CNT-based membranes for environmental applications: The perfect match of electrochemistry and membrane separation. *Chinese Chemical Letters* 2020; **31**: 2539–2548. [DOI: 10.1016/j.cclet.2020.03.011]

10   Daier V, Signorella S, Rizzotto M, Frascaroli MI, Palopoli C, Brondino C, Salas-Peregrin JM, Sala LF. Kinetics and mechanism of the reduction of cr(VI) to cr(III) by D-ribose and 2-deoxy-D-ribose. *Can J Chem* 1999; **77**: 57–64. [DOI: 10.1139/v98-210]

11   Azimi A, Azari A, Rezakazemi M, Ansarpour M. Removal of Heavy Metals from Industrial Wastewaters: A Review. *ChemBioEng Reviews* 2017; **4**: 37–59. [DOI: 10.1002/cben.201600010]

12   Unceta N, Séby F, Malherbe J, Donard OFX. Chromium speciation in solid matrices and regulation: A review. *Anal Bioanal Chem* 2010; **397**: 1097–1111. [DOI: 10.1007/s00216-009-3417-1]

13   Reizabal A, Costa CM, Saiz PG, Gonzalez B, Pérez-Álvarez L, Fernández de Luis R, Garcia A, Vilas-Vilela JL, Lanceros-Méndez S. Processing Strategies to Obtain Highly Porous Silk Fibroin Structures with Tailored Microstructure and Molecular Characteristics and Their Applicability in Water Remediation. *J Hazard Mater* 2021; **403**: 123675. [DOI: https://doi.org/10.1016/j.jhazmat.2020.123675]

14   Matos J, Rosales M, García A, Nieto-Delgado C, Rangel-Mendez JR. Hybrid photoactive materials from municipal sewage sludge for the photocatalytic degradation of methylene blue. *Green Chemistry* 2011; **13**: 3431–3439. [DOI: 10.1039/c1gc15644f]

15   Rosales M, Zoltan T, Yadarola C, Mosquera E, Gracia F, García A. The influence of the morphology of 1D TiO 2 nanostructures on photogeneration of reactive oxygen species and enhanced photocatalytic activity. *J Mol Liq* 2019; **281**: 59–69. [DOI: 10.1016/j.molliq.2019.02.070]

16   Li YH, Yi XH, Li YX, Wang CC, Wang P, Zhao C, Zheng W. Robust Cr(VI) reduction over hydroxyl modified UiO-66 photocatalyst constructed from mixed ligands: Performances and mechanism insight with or without tartaric acid. *Environ Res* 2021; **201**: 111596. [PMID: 34224713 DOI: 10.1016/j.envres.2021.111596]

17   Barrera-Díaz CE, Lugo-Lugo V, Bilyeu B. A review of chemical, electrochemical and biological methods for aqueous Cr(VI) reduction. *J Hazard Mater* 2012; **223–224**: 1–12. [PMID: 22608208 DOI: 10.1016/j.jhazmat.2012.04.054]

18   Valverde A, G.-Sainz P, Orive J, E. L, Reizabal-Para A, Tovar G, Copello G, Lazaro-Martinez JM, Rodriguez B, Gonzalez-Navarrete B, Quintero MY, Rosales M, García A, Arriortua MI, Fernandez de Luis R. Porous, lightweight, metal organic materials: environment sustainability. In: *Advanced Lightweight Multifunctional Materials*. Elsevier, 2020: 43–130.

19   Massari S, Ruberti M. Rare earth elements as critical raw materials: Focus on international markets and future strategies. *Resources Policy* 2013; **38**: 36–43. [DOI: 10.1016/j.resourpol.2012.07.001]

20   Wübbeke J. Rare earth elements in China: Policies and narratives of reinventing an industry. *Resources Policy* 2013; **38**: 384–394. [DOI: 10.1016/j.resourpol.2013.05.005]

21   Martins PM, Salazar H, Aoudjit L, Gonçalves R, Zioui D, Fidalgo-Marijuan A, Costa CM, Ferdov S, Lanceros-Mendez S. Crystal morphology control of synthetic giniite for enhanced photo-Fenton activity against the emerging pollutant metronidazole. *Chemosphere* 2021; **262**: 128300. [PMID: 33182084 DOI: 10.1016/j.chemosphere.2020.128300]

22   Torras J, Buj I, Rovira M, de Pablo J. Chromium recovery from exhausted baths generated in plating processes and its reuse in the tanning industry. *J Hazard Mater* 2012; **209–210**: 343–347. [PMID: 22326242 DOI: 10.1016/j.jhazmat.2012.01.036]

23   De Souza E Silva PT, De Mello NT, Menezes Duarte MM, Montenegro MCBSM, Araújo AN, De Barros Neto B, Da Silva VL. Extraction and recovery of chromium from electroplating sludge. *J Hazard Mater* 2006; **128**: 39–43. [PMID: 16144742 DOI: 10.1016/j.jhazmat.2005.07.026]

24   Gupta B, Deep A, Tandon SN. Recovery of chromium and nickel from industrial waste. *Ind Eng Chem Res* 2002; **41**: 2948–2952. [DOI: 10.1021/ie010934b]

25   Karagiaridi O, Bury W, Mondloch JE, Hupp JT, Farha OK. Solvent-assisted linker exchange: An alternative to the de novo synthesis of unattainable metal-organic frameworks. *Angewandte Chemie - International Edition* 2014; **53**: 4530–4540. [DOI: 10.1002/anie.201306923]

26   Khalil LB, Mourad WE, Rophael MW. Photocatalytic reduction of environmental pollutant Cr (VI) over some semiconductors under UV / visible light illumination. *Appl Catal B* 1998; **17**: 267–273.

27   Stassin T, Reinsch H, Van de Voorde B, Wuttke S, Medina DD, Stock N, Bein T, Ameloot R, De Vos D. Adsorption and Reactive Desorption on Metal–Organic Frameworks: A Direct Strategy for Lactic Acid Recovery. *ChemSusChem* 2017; **10**: 643–650. [DOI: 10.1002/cssc.201601000]

28   Ji Z, Wang H, Canossa S, Wuttke S, Yaghi OM. Pore Chemistry of Metal–Organic Frameworks. *Adv Funct Mater* 2020; **30**: 2000238. [DOI: https://doi.org/10.1002/adfm.202000238]

29   Connolly BM, Aragones-Anglada M, Gandara-Loe J, Danaf NA, Lamb DC, Mehta JP, Vulpe D, Wuttke S, Silvestre-Albero J, Moghadam PZ, Wheatley AEH, Fairen-Jimenez D. Tuning porosity in macroscopic monolithic metal-

organic frameworks for exceptional natural gas storage. *Nat Commun* 2019; **10**: 2345. [DOI: 10.1038/s41467-019-10185-1]

30 Connolly BM, Aragones-Anglada M, Gandara-Loe J, Danaf NA, Lamb DC, Mehta JP, Vulpe D, Wuttke S, Silvestre-Albero J, Moghadam PZ, Wheatley AEH, Fairen-Jimenez D. Tuning porosity in macroscopic monolithic metal-organic frameworks for exceptional natural gas storage. *Nat Commun* 2019; **10**: 2345. [DOI: 10.1038/s41467-019-10185-1]

31 Xu SC, Pan SS, Xu Y, Luo YY, Zhang YX, Li GH. Efficient removal of Cr(VI) from wastewater under sunlight by Fe(II)-doped TiO2 spherical shell. *J Hazard Mater* 2015; **283**: 7–13. [DOI: https://doi.org/10.1016/j.jhazmat.2014.08.071]

32 Feng Y, Chen Q, Cao M, Ling N, Yao J. Defect-tailoring and titanium substitution in metal-organic framework UiO-66-NH2 for the photocatalytic degradation of Cr(VI) to Cr(III). *ACS Appl Nano Mater* 2019; **2**: 5973–5980. [DOI: 10.1021/acsanm.9b01403]

33 Zhang Y, Xu M, Li H, Ge H, Bian Z. The enhanced photoreduction of Cr(VI) to Cr(III) using carbon dots coupled TiO2 mesocrystals. *Appl Catal B* 2018; **226**: 213–219. [DOI: https://doi.org/10.1016/j.apcatb.2017.12.053]

34 Costa IGF, Terra NM, Cardoso VL, Batista FRX, Reis MHM. Photoreduction of chromium(VI) in microstructured ceramic hollow fibers impregnated with titanium dioxide and coated with green algae Chlorella vulgaris. *J Hazard Mater* 2019; **379**: 120837. [DOI: 10.1016/j.jhazmat.2019.120837]

35 Saouma CT, Richard S, Smolders S, Delley MF, Ameloot R, Vermoortele F, Vos DE De, Mayer JM, Saouma CT, Richard S, Smolders S, Delley MF, Ameloot R. Bulk-to-Surface Proton-Coupled Electron Transfer Reactivity of the Metal-Organic Framework MIL-125 Bulk-to-Surface Proton-Coupled Electron Transfer Reactivity of the Metal-Organic Framework MIL-125. (e-pub ahead of print 2018; doi:10.1021/jacs.8b09120).

36 Feng Y, Chen Q, Cao M, Ling N, Yao J. Defect-tailoring and titanium substitution in metal-organic framework UiO-66-NH2 for the photocatalytic degradation of Cr(VI) to Cr(III). *ACS Appl Nano Mater* 2019; **2**: 5973–5980. [DOI: 10.1021/acsanm.9b01403]

37 Muguruza AR, de Luis RF, Iglesias N, Bazán B, Urtiaga MK, Larrea ES, Fidalgo-Marijuan A, Barandika G. Encapsulation of β-alanine model amino-acid in zirconium(IV) metal organic frameworks: Defect engineering to improve host guest interactions. *J Inorg Biochem* 2020; **205**: 110977. [DOI: 10.1016/j.jinorgbio.2019.110977]

38 Ali Akbar Razavi S, Morsali A. Linker functionalized metal-organic frameworks. *Coord Chem Rev* 2019; **399**: 213023. [DOI: 10.1016/j.ccr.2019.213023]

39   Huang L, He M, Chen B, Hu B. A mercapto functionalized magnetic Zr-MOF by solvent-assisted ligand exchange for Hg2+ removal from water. *J Mater Chem A Mater* 2016; **4**: 5159–5166. [DOI: 10.1039/c6ta00343e]

40   Karagiaridi O, Bury W, Mondloch JE, Hupp JT, Farha OK. Solvent-assisted linker exchange: An alternative to the de novo synthesis of unattainable metal-organic frameworks. *Angewandte Chemie - International Edition* 2014; **53**: 4530–4540. [DOI: 10.1002/anie.201306923]

41   Zhang Y, Xu X, Yue C, Song L, Lv Y, Liu F, Li A. Insight into the efficient co-removal of Cr(VI) and Cr(III) by positively charged UiO-66-NH2 decorated ultrafiltration membrane. *Chemical Engineering Journal* 2021; **404**. [DOI: 10.1016/j.cej.2020.126546]

42   Shen L, Liang S, Wu W, Liang R, Wu L. Multifunctional NH2-mediated zirconium metal-organic framework as an efficient visible-light-driven photocatalyst for selective oxidation of alcohols and reduction of aqueous Cr(vi). *Dalton Transactions* 2013; **42**: 13649–13657. [PMID: 23903996 DOI: 10.1039/c3dt51479j]

43   Wang Z, Yang J, Li Y, Zhuang Q, Gu J. Simultaneous degradation and removal of CrVI from aqueous solution with Zr-based metal–organic frameworks bearing inherent reductive sites. *Chemistry - A European Journal* 2017; **23**: 15415–15423. [DOI: 10.1002/chem.201702534]

44   Øien S, Wragg D, Reinsch H, Svelle S, Bordiga S, Lamberti C, Lillerud KP. Detailed structure analysis of atomic positions and defects in zirconium metal-organic frameworks. *Cryst Growth Des* 2014; **14**: 5370–5372. [DOI: 10.1021/cg501386j]

45   Wang H, Yuan X, Wu Y, Zeng G, Chen X, Leng L, Wu Z, Jiang L, Li H. Facile synthesis of amino-functionalized titanium metal-organic frameworks and their superior visible-light photocatalytic activity for Cr(VI) reduction. *J Hazard Mater* 2015; **286**: 187–194. [PMID: 25585267 DOI: 10.1016/j.jhazmat.2014.11.039]

46   Dan-hardi, M., & Serre C. A new photoactive crystalline highly porous titanium (IV) dicarboxylate. *J Am Chem Soc* 2009; **131**: 10857–10859. [DOI: 10.1021/ja903726m]

47   Gil A, Assis FCC, Albeniz S, Korili SA. Removal of dyes from wastewaters by adsorption on pillared clays. *Chemical Engineering Journal* 2011; **168**: 1032–1040. [DOI: 10.1016/j.cej.2011.01.078]

48   Rodriguez A, Ovejero G, Mestanza M, García J. Removal of Dyes from Wastewaters by Adsorption on Sepiolite and Pansil. *Ind Eng Chem Res* 2010; **49**: 3207–3216.

49 Sereshti H, Vasheghani Farahani M, Baghdadi M. Trace determination of chromium(VI) in environmental water samples using innovative thermally reduced graphene (TRG) modified SiO2 adsorbent for solid phase extraction and UV-vis spectrophotometry. *Talanta* 2016; **146**: 662–669. [PMID: 26695315 DOI: 10.1016/j.talanta.2015.06.051]

50 Rai D, Sass BM, Moore DA. Chromium(III) hydrolysis constants and solubility of chromium(III) hydroxide. *Inorg Chem* 1987; **26**: 345–349. [DOI: 10.1021/ic00250a002]

51 Zoltan T, Rosales MC, Yadarola C. Reactive oxygen species quantification and their correlation with the photocatalytic activity of TiO2 (anatase and rutile) sensitized with asymmetric porphyrins. *J Environ Chem Eng* 2016; **4**: 3967–3980. [DOI: 10.1016/j.jece.2016.09.008]

52 Cavka JH, Jakobsen S, Olsbye U, Guillou N, Lamberti C, Bordiga S, Lillerud KP. A new zirconium inorganic building brick forming metal organic frameworks with exceptional stability. *J Am Chem Soc* 2008; **130**: 13850–13851.

53 Saouma CT, Richard S, Smolders S, Delley MF, Ameloot R, Vermoortele F, Vos DE De, Mayer JM, Saouma CT, Richard S, Smolders S, Delley MF, Ameloot R. Bulk-to-Surface Proton-Coupled Electron Transfer Reactivity of the Metal-Organic Framework MIL-125 Bulk-to-Surface Proton-Coupled Electron Transfer Reactivity of the Metal-Organic Framework MIL-125. (e-pub ahead of print 2018; doi:10.1021/jacs.8b09120).

54 Øien, S., Wragg, D., Reinsch, H. , Svelle, S., Bordiga, S., Lamberti, C., & Lillerud KP. Detailed structure analysis of atomic positions and defects in Zirconium Metal − Organic Frameworks. *Cryst Growth Des* 2014; **14**: 5370–5372.

55 Shearer GC, Chavan S, Ethiraj J, Vitillo JG, Svelle S, Olsbye U, Lamberti C, Bordiga S, Lillerud KP. Tuned to perfection: Ironing out the defects in metal-organic framework UiO-66. *Chemistry of Materials* 2014; **26**: 4068–4071. [DOI: 10.1021/cm501859p]

56 Audu CO, Nguyen HGT, Chang CY, Katz MJ, Mao L, Farha OK, Hupp JT, Nguyen ST. The dual capture of AsV and AsIII by UiO-66 and analogues. *Chem Sci* 2016; **7**: 6492–6498. [DOI: 10.1039/c6sc00490c]

57 Shearer GC, Chavan S, Bordiga S, Svelle S, Olsbye U, Lillerud KP. Defect Engineering: Tuning the Porosity and Composition of the Metal-Organic Framework UiO-66 via Modulated Synthesis. *Chemistry of Materials* 2016; **28**: 3749–3761. [DOI: 10.1021/acs.chemmater.6b00602]

58 Wang C, Liu X, Chen JP, Li K. Superior removal of arsenic from water with zirconium metal-organic framework UiO-66. *Sci Rep* 2015; **5**: 1–10. [DOI: 10.1038/srep16613]

59 Sohail M, Yun Y, Lee E, Kim SK, Cho K, Kim J, Kim TW, Moon J, Kim H. Synthesis of Highly Crystalline NH 2 - MIL-125 (Ti) with S - Shaped Water Isotherms for Adsorption Heat Transformation. 2017; **125**: 2–7. [DOI: 10.1021/acs.cgd.6b01597]

60 Chavan, S. M., Shearer, G. C., Svelle, S., Olsbye, U., Bonino, F., Ethiraj, J., Lillerud, K. P., & Bordiga S. Synthesis and characterization of amine-functionalized mixed-ligand metal−organic frameworks of UiO-66 topology. *Inorg Chem* 2014; **53**: 9509–9515. [DOI: 10.1021/ic500607a]

61 Rakhunde R, Deshpande L, Juneja HD. Chemical speciation of chromium in water: A review. *Crit Rev Environ Sci Technol* 2012; **42**: 776–810. [DOI: 10.1080/10643389.2010.534029]

62 Unceta N, Séby F, Malherbe J, Donard OFX. Chromium speciation in solid matrices and regulation: A review. *Anal Bioanal Chem* 2010; **397**: 1097–1111. [DOI: 10.1007/s00216-009-3417-1]

63 Rapti S, Pournara A, Sarma D, Papadas IT, Armatas GS, Hassan YS, Alkordi MH, Kanatzidis MG, Manos MJ. Rapid, green and inexpensive synthesis of high quality UiO-66 amino-functionalized materials with exceptional capability for removal of hexavalent chromium from industrial waste. *Inorg Chem Front* 2016; **3**: 635–644. [DOI: 10.1039/C5QI00303B]

64 Torres DI, Lazaro-Martínez JM, Copello GJ, dall Orto VC. Single step synthesis of a polyhydroxy ether and its optimization to adsorption of a textile dye. *J Environ Chem Eng* 2019; : 103416. [DOI: 10.1016/j.jece.2019.103416]

65 Gropp C, Canossa S, Wuttke S, Gándara F, Li Q, Gagliardi L, Yaghi OM. Standard Practices of Reticular Chemistry. *ACS Cent Sci* 2020; **6**: 1255–1273. [DOI: 10.1021/acscentsci.0c00592]

66 Freund R, Zaremba O, Arnauts G, Ameloot R, Skorupskii G, Dincă M, Bavykina A, Gascon J, Ejsmont A, Gościańska J, Kalmutzki M, Lächelt U, Ploetz E, Diercks C, Wuttke S. The Current Status of MOF and COF Applications. *Angewandte Chemie International Edition* 2021; **60**: 23975–24001. [DOI: 10.1002/anie.202106259]

67 Wu J, Zhou J, Zhang S, Alsaedi A, Hayat T, Li J, Song Y. Efficient removal of metal contaminants by EDTA modified MOF from aqueous solutions. *J Colloid Interface Sci* 2019; **555**: 403–412. [PMID: 31398567 DOI: 10.1016/j.jcis.2019.07.108]

68 Li J, Wang X, Power E, Zhao G, Chai Z, Chen C, Alsaedi A, Hayat T, Wang X. Metal–organic framework-based materials: superior adsorbents for the capture of toxic and radioactive metal ions. *Chem Soc Rev* 2018; **47**: 2322. [DOI: 10.1039/c7cs00543a]

69   Mon M, Bruno R, Ferrando-Soria J, Armentano D, Pardo E. Metal–organic framework technologies for water remediation: towards a sustainable ecosystem. *J Mater Chem A Mater* 2018; **6**: 4912–4947. [DOI: 10.1039/C8TA00264A]

70   Freund R, Canossa S, Cohen SM, Yan W, Deng H, Guillerm V, Eddaoudi M, Madden DG, Fairen-Jimenez D, Lyu H, Macreadie LK, Ji Z, Zhang Y, Wang B, Haase F, Wöll C, Zaremba O, Andreo J, Wuttke S, Diercks CS. 25 years of Reticular Chemistry. *Angewandte Chemie International Edition* 2021; **60**: 23946–23974. [DOI: 10.1002/anie.202101644]

71   Chen Q, Feng Y, Tian R, Chen J, Wang A, Yao J. Defect Rich UiO-66 with Enhanced Adsorption and Photosensitized Reduction of Cr (VI) under Visible Light. *Ind Eng Chem Res* 2019; **58**: 21562–21568. [DOI: 10.1021/acs.iecr.9b05464]

72   Dhakshinamoorthy A, Asiri AM, García H. Metal-Organic Framework (MOF) Compounds: Photocatalysts for Redox Reactions and Solar Fuel Production. *Angewandte Chemie - International Edition* 2016; **55**: 5414–5445. [PMID: 26970539 DOI: 10.1002/anie.201505581]

73   Wang CC, Du XD, Li J, Guo XX, Wang P, Zhang J. Photocatalytic Cr(VI) reduction in metal-organic frameworks: A mini-review. *Appl Catal B* 2016; **193**: 198–216. [DOI: 10.1016/j.apcatb.2016.04.030]

74   Bedia J, Muelas-ramos V, Peñas-garzón M, Gómez-avilés A, Rodríguez JJ, Belver C. A Review on the Synthesis and Characterization of Metal Organic Frameworks for Photocatalytic Water Purification. *Catal* 2019; **9**: 52. [DOI: 10.3390/catal9010052]

75   Dhakshinamoorthy A, Asiri AM, García H. Metal-Organic Framework (MOF) Compounds: Photocatalysts for Redox Reactions and Solar Fuel Production. *Angewandte Chemie - International Edition* 2016; **55**: 5414–5445. [PMID: 26970539 DOI: 10.1002/anie.201505581]

76   Kandiah M, Nilsen MH, Usseglio S, Jakobsen S, Olsbye U, Tilset M, Larabi C, Quadrelli EA, Bonino F, Lillerud KP. Synthesis and stability of tagged UiO-66 Zr-MOFs. *Chemistry of Materials* 2010; **22**: 6632–6640. [DOI: 10.1021/cm102601v]

77   Deng H, Doonan CJ, Furukawa H, Ferreira RB, Towne J, Knobler CB, Wang B, Yaghi OM. Multiple functional groups of varying ratios in metal-organic frameworks. *Science (1979)* 2010; **327**: 846–850. [PMID: 20150497 DOI: 10.1126/science.1181761]

78   Osborn Popp TM, Yaghi OM. Sequence-dependent materials. *Acc Chem Res* 2017; **50**: 532–534. [PMID: 28945416 DOI: 10.1021/acs.accounts.6b00529]

79   Abánades Lázaro I, Wells CJR, Forgan RS. Multivariate Modulation of the Zr MOF UiO-66 for Defect-Controlled Combination Anticancer Drug Delivery. *Angewandte Chemie - International Edition* 2020; **59**: 5211–5217. [PMID: 31950568 DOI: 10.1002/anie.201915848]

80   Dong Z, Sun Y, Chu J, Zhang X, Deng H. Multivariate Metal-Organic Frameworks for Dialing-in the Binding and Programming the Release of Drug Molecules. *J Am Chem Soc* 2017; **139**: 14209–14216. [PMID: 28898070 DOI: 10.1021/jacs.7b07392]

81   Luo TY, Liu C, Gan XY, Muldoon PF, Diemler NA, Millstone JE, Rosi NL. Multivariate Stratified Metal-Organic Frameworks: Diversification Using Domain Building Blocks. *J Am Chem Soc* 2019; **141**: 2161–2168. [PMID: 30636428 DOI: 10.1021/jacs.8b13502]

82   Yuan S, Lu W, Chen Y-P, Zhang Q, Liu T-F, Feng D, Wang X, Qin J, Zhou H-C. Sequential Linker Installation: Precise Placement of Functional Groups in Multivariate Metal–Organic Frameworks. *J Am Chem Soc* 2015; **137**: 3177–3180. [DOI: 10.1021/ja512762r]

83   Hu Z, Gami A, Wang Y, Zhao D. A Triphasic Modulated Hydrothermal Approach for the Synthesis of Multivariate Metal–Organic Frameworks with Hydrophobic Moieties for Highly Efficient Moisture-Resistant CO2 Capture. *Adv Sustain Syst* 2017; **1**: 1700092. [DOI: https://doi.org/10.1002/adsu.201700092]

84   Mon M, Bruno R, Tiburcio E, Viciano-Chumillas M, Kalinke LHG, Ferrando-Soria J, Armentano D, Pardo E. Multivariate Metal–Organic Frameworks for the Simultaneous Capture of Organic and Inorganic Contaminants from Water. *J Am Chem Soc* 2019; **141**: 13601–13609. [DOI: 10.1021/jacs.9b06250]

85   Fan W, Yuan S, Wang W, Feng L, Liu X, Zhang X, Wang X, Kang Z, Dai F, Yuan D, Sun D, Zhou H-C. Optimizing Multivariate Metal–Organic Frameworks for Efficient C2H2/CO2 Separation. *J Am Chem Soc* 2020; **142**: 8728–8737. [DOI: 10.1021/jacs.0c00805]

86   Li Y-M, Yuan J, Ren H, Ji C-Y, Tao Y, Wu Y, Chou L-Y, Zhang Y-B, Cheng L. Fine-Tuning the Micro-Environment to Optimize the Catalytic Activity of Enzymes Immobilized in Multivariate Metal–Organic Frameworks. *J Am Chem Soc* 2021; **143**: 15378–15390. [DOI: 10.1021/jacs.1c07107]

87   Schrimpf W, Jiang J, Ji Z, Hirschle P, Lamb DC, Yaghi OM, Wuttke S. Chemical diversity in a metal-organic framework revealed by fluorescence lifetime imaging. *Nat Commun* 2018; **9**: 1647. [PMID: 29695805 DOI: 10.1038/s41467-018-04050-w]

88   Lyu H, Ji Z, Wuttke S, Yaghi OM. Digital Reticular Chemistry. *Chem* 2020; **6**: 2219–2241. [DOI: 10.1016/j.chempr.2020.08.008]

89 Furukawa H, Müller U, Yaghi OM. 'Heterogeneity within order' in metal-organic frameworks. *Angewandte Chemie - International Edition* 2015; **54**: 3417–3430. [DOI: 10.1002/anie.201410252]

90 Ejsmont A, Andreo J, Lanza A, Galarda A, Macreadie L, Wuttke S, Canossa S, Ploetz E, Goscianska J. Applications of reticular diversity in metal–organic frameworks: An ever-evolving state of the art. *Coord Chem Rev* 2021; **430**: 213655. [DOI: 10.1016/j.ccr.2020.213655]

91 Bitzer J, Kleist W. Synthetic Strategies and Structural Arrangements of Isoreticular Mixed-Component Metal–Organic Frameworks. *Chemistry – A European Journal* 2019; **25**: 1866–1882. [DOI: https://doi.org/10.1002/chem.201803887]

92 Sereshti H, Vasheghani Farahani M, Baghdadi M. Trace determination of chromium(VI) in environmental water samples using innovative thermally reduced graphene (TRG) modified SiO2 adsorbent for solid phase extraction and UV-vis spectrophotometry. *Talanta* 2016; **146**: 662–669. [PMID: 26695315 DOI: 10.1016/j.talanta.2015.06.051]

93 Gu Y, Xie D, Ma Y, Qin W, Zhang H, Wang G, Zhang Y, Zhao H. Size Modulation of Zirconium-Based Metal Organic Frameworks for Highly Efficient Phosphate Remediation. *ACS Appl Mater Interfaces* 2017; **9**: 32151–32160. [PMID: 28850219 DOI: 10.1021/acsami.7b10024]

94 Modena MM, Rühle B, Burg TP, Wuttke S. Nanoparticle Characterization: What to Measure? *Advanced Materials* 2019; **31**: 1–26. [DOI: 10.1002/adma.201901556]

95 Hirschle P, Preiß T, Auras F, Pick A, Völkner J, Valdepérez D, Witte G, Parak WJ, Rädler JO, Wuttke S. Exploration of MOF nanoparticle sizes using various physical characterization methods – is what you measure what you get? *CrystEngComm* 2016; **18**: 4359–4368. [DOI: 10.1039/C6CE00198J]

96 Burtch NC, Jasuja H, Walton KS. Water stability and adsorption in metal-organic frameworks. *Chem Rev* 2014; **114**: 10575–10612. [PMID: 25264821 DOI: 10.1021/cr5002589]

97 Chen SS, Hu C, Liu C-H, Chen Y-H, Ahamad T, Alshehri SM, Huang P-H, Wu KC-W. De Novo synthesis of platinum-nanoparticle-encapsulated UiO-66-NH2 for photocatalytic thin film fabrication with enhanced performance of phenol degradation. *J Hazard Mater* 2020; **397**: 122431. [DOI: https://doi.org/10.1016/j.jhazmat.2020.122431]

98 Liu Y, Lin S, Liu Y, Sarkar AK, Bediako JK, Kim HY, Yun Y. Super-Stable , Highly Efficient , and Recyclable Fibrous Metal – Organic Framework Membranes for Precious Metal Recovery from Strong Acidic Solutions. *Nano Micro Small* 2019; **1805242**: 1–9. [DOI: 10.1002/smll.201805242]

99 Leus K, Bogaerts T, De Decker J, Depauw H, Hendrickx K, Vrielinck H, Van Speybroeck V, Van Der Voort P. Systematic study of the chemical and hydrothermal stability of selected "stable" Metal Organic Frameworks. *Microporous and Mesoporous Materials* 2016; **226**: 110–116. [DOI: https://doi.org/10.1016/j.micromeso.2015.11.055]

100 G. Saiz P, Lopes AC, Eizagirre Barker S, Fernández de Luis R, Arriortua MI. Ionic liquids for the control of the morphology in poly(vinylidene fluoride-co-hexafluoropropylene) membranes. *Mater Des* 2018; **155**. [DOI: 10.1016/j.matdes.2018.06.013]

101 Bennett TD, Cheetham AK. Amorphous Metal–Organic Frameworks. *Acc Chem Res* 2014; **47**: 1555–1562. [DOI: 10.1021/ar5000314]

102 Burtch NC, Jasuja H, Walton KS. Water stability and adsorption in metal-organic frameworks. *Chem Rev* 2014; **114**: 10575–10612. [PMID: 25264821 DOI: 10.1021/cr5002589]

103 Liu Y, Lin S, Liu Y, Sarkar AK, Bediako JK, Kim HY, Yun Y. Super-Stable , Highly Efficient , and Recyclable Fibrous Metal – Organic Framework Membranes for Precious Metal Recovery from Strong Acidic Solutions. *Nano Micro Small* 2019; **1805242**: 1–9. [DOI: 10.1002/smll.201805242]

104 Howarth AJ, Liu Y, Li P, Li Z, Wang TC, Hupp JT, Farha OK. Chemical, thermal and mechanical stabilities of metal-organic frameworks. *Nat Rev Mater* 2016; **1**: 1–15. [DOI: 10.1038/natrevmats.2015.18]

105 Mu X, Jiang J, Chao F, Lou Y, Chen J. Ligand modification of UiO-66 with an unusual visible light photocatalytic behavior for RhB degradation. *Dalton Transactions* 2018; **47**: 1895–1902. [PMID: 29340397 DOI: 10.1039/c7dt04477a]

106 Iqbal S, Pan Z, Zhou K. Enhanced photocatalytic hydrogen evolution from: In situ formation of few-layered MoS2/CdS nanosheet-based van der Waals heterostructures. *Nanoscale* 2017; **9**: 6638–6642. [PMID: 28497825 DOI: 10.1039/c7nr01705g]

107 Liang Q, Cui S, Liu C, Xu S, Yao C, Li Z. Construction of CdS@UIO-66-NH2 core-shell nanorods for enhanced photocatalytic activity with excellent photostability. *J Colloid Interface Sci* 2018; **524**: 379–387. [PMID: 29660625 DOI: 10.1016/j.jcis.2018.03.114]

108 Sun X, Ma J, Chen X, Li Z, Deng C, Liu B. Sol–gel preparation of ZrC–ZrO2 composite microspheres using fructose as a carbon source. *J Solgel Sci Technol* 2018; **86**: 431–440. [DOI: 10.1007/s10971-018-4653-7]

109 Daier V, Signorella S, Rizzotto M, Frascaroli MI, Palopoli C, Brondino C, Salas-Peregrin JM, Sala LF. Kinetics and mechanism of the reduction of cr(VI)

to cr(III) by D-ribose and 2-deoxy-D-ribose. *Can J Chem* 1999; **77**: 57–64. [DOI: 10.1139/v98-210]

110   Padlyak B V., Kornatowski J, Zadrozna G, Rozwadowski M, Gutsze A. Electron paramagnetic resonance spectroscopy of chromium in CrAPO-5 molecular sieves. *Journal of Physical Chemistry A* 2000; **104**: 11842–11843. [DOI: 10.1021/jp002490n]

111   Weckhuysen BM, Schoonheydt RA, Mabbs FE, Collison D. Electron paramagnetic resonance of heterogeneous chromium catalysts. *Journal of the Chemical Society - Faraday Transactions* 1996; **92**: 2431–2436. [DOI: 10.1039/ft9969202431]

112   Wang Z, Yang J, Li Y, Zhuang Q, Gu J. Simultaneous degradation and removal of CrVI from aqueous solution with Zr-based metal–organic frameworks bearing inherent reductive sites. *Chemistry - A European Journal* 2017; **23**: 15415–15423. [DOI: 10.1002/chem.201702534]

Chapter **4**

Chapter 4
Post-synthetic Modification of MOFs for Metal-Chelator like traps design

The selective adsorption of metal ions from aqueous solutions is a pivotal process for environmental remediation,[1] but it is also a technology of paramount importance for metal separation purposes. The recovery and purification of metal ions from polluted water sources are increasingly gaining importance within the concept of a closed loop circular economy. In this sense, metal-chelating agents and adsorbents are the simplest, cost efficient and flexible (in terms of design/operation and regeneration) technologies applied for the metal ions capture, separation and purification purposes.[2]

On one hand, chelation is a type of bonding of chelating agents to metal ions that involves the formation of two or more separate coordinate bonds between a polydentate (multiple bonded) ligand and a single central metal atom.[3,4] The efficiency and selectivity of the chelation-based solvent extraction of a metal depends on the coordination chemistry behind the process and the chemical structure of the chelator itself.[5,6] Although engineering of these polydentate molecules has great flexibility, solvent extraction makes the recovery of the metal-chelator complexes time and energy consuming, and even environmentally unfriendly for specific applications. On the other hand, adsorption has attracted considerable attention due to its simplicity and cost efficiency.[7] Classic sorbents as zeolites[8], clays[9] or activated carbons[10], although easier to recover and reactivate than soluble metal-chelators, suffer from low adsorption capacity[11] and selectivity due to their limited chemical tailorability.

One of the multiple approaches to replicate the metal binding modes of organic chelators in solid porous materials is the chemical encoding of a particular class of Metal-organic frameworks (MOFs) holds enormous promise.[12–15] Thanks to their impressive porosity metrics (e.g. large surface area, a big pore volume/window…), and their versatility to be encoded with specific functionalities, the MOFs have been

successfully applied to capture or separate metal ions from different aqueous media (e.g. polluted freshwater, seawater or acid leachates).[16–19] Solvent assisted ligand exchange (SALE) and solvent assisted ligand incorporation (SALI) are two of the most facile and versatile experimental protocols to anchor metal-chelating motifs into MOFs.[20–24] In SALE, the structural linkers coordinated to the clusters are replaced with alternative linkers, while in SALI, labile, non-structural inorganic linkers are replaced with functional organic or inorganic functions.[25]

Among the varied M^{III} and M^{IV} MOFs that have stand out because of their great water stability even in acidic media, MOF-808 has opened the perspective to an easy installation of small to bulky functionalities, while preserving long range order of the backbone structure. MOF-808 has attracted considerable attention for metal adsorption in wastewater due to its strong metal-ligand bonds, the great pore diameter (18 Å), and the relatively labile formate ligands in the cluster, which allows post-synthetic modification by SALI.[20] Thanks to this technique, different functionalities can be introduced in the clusters, replacing the formate molecules without destroying the crystalline structure of the MOF, which allows creating a chelator type center (Figure 4.1). In fact, the metal ion adsorption capacity of MOFs is not only dependent on their overall porosity, but on the nature and density of the functional group decorating their interior surface.[26–28]
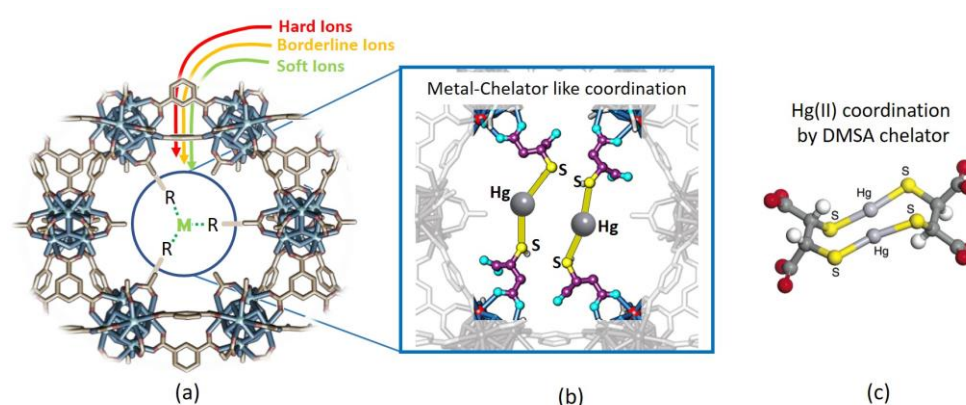

Figure 4.1. (a) Illustration of hard, borderline and soft metal-chelator like traps within the MOF-808 scaffold. (b) Illustration of a tentative placement of the mercaptosuccinic molecules into the MOF-808 pore space and their coordination to Hg^{II}. (c) Coordination modes of dimercaptosuccinic acid (DMSA) chelators over Hg^{II} ions.

4.1. AMINO ACID AND NATURAL ACID DECORATION OF MOF–808 FOR HEAVY METAL ADSORPTION

Some studies have already explored the post-synthetic modification of MOF-808 to enhance its metal adsorption properties. Just as a relevant example, Y. Peng *et al.*[7] have successfully installed the well-known ethylenediaminetetraacetic acid (EDTA) chelator into the MOF-808 structure endowing the material of impressive adsorption capacity towards a broad scope of metal-ions with varied acidities. Even though MOF-808@EDTA lacks strong selectivity over the capture of a specific ion, the adsorption experiments performed in a continuous flow with a multielement solution pointed that the breakthrough volume of the MOF-808@EDTA column was dependent on the metal acidity, suggesting that alternative encodings of the pore space of the MOF-808 may lead to a stronger column breakthrough dispersion of the metal-ions.

As a general rule, the density and the hard/soft nature of the metal binding functions encoded in the MOFs' pores determine their metal ion adsorption capacity and affinity.[26–30] Thus, in this work we have explored the pore space functionalization of MOF-808 scaffold with amino acids (*i.e.* histidine, cysteine and asparagine) and natural acids (*i.e.* malic acid, mercaptosuccinic acid, succinic acid, fumaric acid and citric acid) having residual groups of different natures in order to replicate metal-chelator like traps and fine-tune the metal-ion adsorption specificity of the parent MOF-808 material.[30,31] The MOF-808@amino acid system has been explored and expanded very recently by J. Baek *et al.* [12] and H. Lyu *et al.*[32]. The first authors studied the decoration of the MOF-808 pore space with histidine functions, metalizing the system to engineer a pseudo-enzymatic like copper oxidase. The authors were able to incorporate three histidine molecules per cluster *via* an organic solvent SALI protocol. H Lyu *et al.* have extended very recently the MOF-808@amino acid system to glycine, sarcosine, L-alanine, DL-alanine, (R)-3-aminobutanoic acid, (RS)-3-aminobutanoic acid, L-isoleucine, L-serine, L-histidine, L-threonine and DL-lysine by applying a water SALI protocol with optimized temperature and concentration conditions to achieve the higher degree of functionalization of MOF-808 as possible. H. Lyu *et al.* installed from 2 to 4 amino acid molecules per cluster (except for MOF-

808@glycine materials) by modulation the concentration of the amino acid and the temperature of the media during the SALI. These results are very similar to the one obtained in our work, but still different when comparing the four histidine molecules per cluster of this investigation with the 5 molecules per cluster incorporated in our study. These differences tell us how sensitivity could be the SALI functionalization to experimental conditions as the reactor volume or the concentration of the MOF dispersion into the media.

The chemical structure and the molecular size of the amino acids and natural acids functions have been selected in order to engineer a MOF-808 pore space able to act as a multidentate chelator for metal ions. The chemical stability of the functionalities installed by SALI has been assessed simulating the acidity and anion strength conditions that could be found in natural waters (*i.e.* arsenic polluted water of the north of Chile),[33] acid waters (*i.e.* wastewater coming from mining or industrial activities),[34] and water media with high anionic strengths (*i.e.* acid-waters from phosphor-gypsum deposits)[35]. Finally, the specificity of adsorption has been tested in batch and continuous flow conditions in single and multielement solutions. The metal-binding modes of the most promising MOF-808@cysteine variant have been identified by a combination of electron paramagnetic resonance and inelastic neutron spectroscopies.

4.1.1. EXPERIMENTAL PROCEDURE

Synthesis and post-synthetic functionalization of MOF-808

Trimesic acid (BTC) (2.1 g, 10 mmol) and $ZrOCl_2 \cdot 8H_2O$ (9.7 g, 30 mmol) were dissolved in two dimethylformamide (DMF)/formic acid solutions (225 mL/225 mL each) and mixed in a 1-L screw-capped glass jar. Afterwards, the reaction was performed at 130 °C for 48 h in an isothermal oven.[36] The white precipitate was collected by centrifugation and washed 4 times with DMF (100 mL x 2) and MeOH (100 mL x 2) over a period of 24 h. The sample was then activated at 80 °C for 24 h and stored at room conditions into a sealed vial.

Solvent assisted ligand incorporation (SALI) was performed with water solutions of eight natural acids and amino acids: L-asparagine (Asp), L-histidine (His) mercaptosuccinic acid (Msc), L-cysteine (Cys), succinic acid (Suc), fumaric acid (Fum), L-malic acid (Mal), and citric acid (Cit). Starting with L-cysteine, the concentration of the solution was screened (0.15, 0.10 and 0.05 M) at a temperature of 60 ºC monitoring the crystallinity of the XRD patterns and the trimesic acid (BTC)/cysteine molar ratio in the compounds by ^{1}H-NMR after the functionalization. We selected the following optimized conditions to achieve the higher functionalization degree as possible while maintaining the crystallinity of the MOF-808 after the SALI. A more detailed information about the post-synthetic functionalization protocol is described in the main results and discussion section.

Optimized conditions for (amino) acid functionalization of MOF-808

300 mL of 0.05 M water solutions of the (amino) acids were prepared in a 500 mL autoclave at 60 °C. MOF-808 (600 mg) was dispersed under continuous stirring during 1h in the (amino) acid solution and heated at 60 °C for 24 h in an isothermal oven. MOF-808@(amino) acid was recovered by centrifugation (x 6500 rpm), washed 3 times with 100 mL water (12 h each) and then with 100 mL methanol other 3 times (12 h each). Finally, the samples were dried at 80 °C overnight (12 h) and stored in a desiccator.

MOF-808 general characterization protocols

MOF-808@(amino) acids were characterized by X-ray diffraction, infrared spectroscopy, thermogravimetry and N_2 sorption at 77 K. The presence and quantification of the (amino) acid functionalities was performed by ^{1}H-NMR spectroscopy. To this end, 20 mg of the samples were digested in 0.7 mL of NaOH deuterated solution (1 M) overnight. The mixture was centrifugated at 7000 rpm. The solution was recovered carefully with a syringe, preventing the uptake of powdered material settled at the bottom of the centrifuge tube.

Once the ^{1}H-NMR spectra were acquired, the (amino) acid content per formula unit was calculated by integrating the signals associated to the (amino) acids, and fingerprint peak (8.26 ppm) associated to the trimesic acid molecules. The MOF functionalization and the posterior ^{1}H-NMR quantification of the BTC:(amino) acid molar ratio has been done by triplicate in order to evaluate the accuracy that can be achieved by replicating the experimental protocol.

0.08 linker defects per formula unit have been calculated for the parent MOF-808 material by the analysis of the last weight loss of the TGA curve (see Chapter 2, section 2.2.5. for detailed information). The strong overlapping of the thermal release of the (amino) acid functions and the trimesic acid calcination observed in the TGA measurements of MOF-808@(amino) acid samples, hinders elucidating if additional trimesic linker defects have been generated during the (amino) acids incorporation to the porous framework of MOF-808. It has been assumed that the trimesate defects in MOF-808@(amino) acid samples is close to the one calculates for the parent MOF-808 material, although some degree of linker displacement by (amino) acid molecules could occur during the functionalization process. The charge neutrality of the chemical formulas was achieved by balancing the (amino) acid and formate content on the basis of the data obtained from ^{1}H-NMR, and balancing the additional positive unbalanced charges arising from linker defective sites in the clusters, with one hydroxyl and one water molecule per position. For di-topic or tri-topic carboxylates as fumaric, succinic, malic, mercaptosuccinic and citric acids it has been assumed that the carboxyl groups not coordinated to the clusters are protonated.

MOF-808@(amino) acid chemical and thermal stability

The chemical stability of (amino) acid functionalities incorporated to the MOF-808 was assessed by immersing 100 mg MOF-808@(amino) acid in 100 mL water solutions with pH values of 4, 3 and 2. Afterwards, the samples were characterized by powder X-ray diffraction and ^{1}H-NMR spectroscopy in order to (i) inspect if the long-range order of the crystal structure is maintained or altered in some degree, and (ii) to quantify if the BTC:(amino) acid molar ratio varies in comparison to the one of the initial MOF-808@(amino) acid.

Thermal stability of the samples was studied by means of thermogravimetric and thermo-diffraction measurements. The experiments were performed with the same weight of sample, as well as equal heating conditions. A peak fit approach was applied to treat the X-ray diffraction data obtained from the thermo-diffraction experiments. By fitting the (311) diffraction maxima, the thermal evolution of the cell parameters, X-ray diffraction maxima broadening and intensity loss during the MOF-(amino)acid thermal collapse were monitored.

Metal adsorption screening

The adsorption affinity of the MOF-808@(amino) acid frameworks over metal ions with varied acidities (*i.e.* Z^+/r^2) was determined performing adsorption tests in single metal aqueous solutions with a concentration of 100 ppm. MOF-808@(amino) acids (10 mg) were dispersed in 5 mL - 100 ppm water solutions of Hg^{II}, Pb^{II}, Cd^{II}, Cu^{II}, Ni^{II}, Eu^{III}, Cr^{III} or Cr^{VI}. The dispersion was stirred overnight (12 h) under isothermal (21 °C) and dark conditions. After adsorption equilibrium was reached, the dispersion was centrifuged (x 700 rpm) and filtered with a nylon syringe filter (Branchia, pore: 0.22 µm, diameter: 25 mm). Finally, 3 mL aliquots were taken, acidified with 100 µL of HNO_3 and measured after dilution to the proper metal concentration range with an ICP-AES Horiba Yobin Yvon Activa.[26,37] Adsorption capacity of MOF-808@(amino) acid samples was determined on the basis of Equation 4.1:

$$Q_e = \frac{([M]_i - [M]_f) \cdot V}{m} \tag{4.1}$$

where $[M]_i$ and $[M]_f$ are the metal initial and final concentrations, V is the volume of the solution and m is the mass of adsorbent.

Competitive adsorption experiments

Competitive adsorption experiments were performed in a multielement solution of soft (Hg^{II}, Pb^{II}), intermediate (Cd^{II}, Cu^{II}, Ni^{II}) and hard metal ions (Eu^{III}, La^{III}, Y^{III}, Cr^{III}), each of them in a concentration close to 10 ppm. Although the concentration of the metals in the multielement solutions applied in competitive adsorption

experiments are usually tailored to the ones observed in the final scenarios of application (e.g. recovery of rare-earth elements (REEs) from acid polluted waters, capture of Pd-ions from radioactive wastewater…), we decided to use the same concentration for all the metals in order to confirm if the adsorption affinity observed in the metal adsorption screening experiments is maintained in a complex mixtures containing multiple ions. The metal-ion adsorption selectivity was evaluated determining the distribution coefficient K_d for each metal, as described in the Equation 4.2:

$$K_d = \frac{V}{m} \frac{(C_0 - C_e)}{C_e} \tag{4.2}$$

where, V is the volume of the solutio, m is the mass of the adsorbent and C_0 and C_e are the concentration of the metals in the solution at the initial and equilibrium points of the adsorption, respectively.

The separation factor (SF) was calculated as described by the Equation 4.3 to identify the MOF-808@(amino) acid sorbents that could be applied to separate ions from the multielement solutions with factors of at least above three between two different ions.

$$SF = \frac{K_d^A}{K_d^B} \tag{4.3}$$

where K_d^A and K_d^B are the distribution factors for the metals A and B respectively, calculated for the same adsorbent material.

Continuous flow metal-ions separation with MOF-808@(amino) acid columns

When designing continuous flux adsorption experiment, it is necessary to integrate the MOF in a highly permeable chromatographic column that at the same time maximizes the contact between the aqueous solution and the active MOF sorbent. First, the protocol described by Rapti *et al.*[38] was followed to assemble a MOF-808@(amino acid)/sand (15% w/w: 150 mg of MOF dispersed in 1500 mg of sand) based chromatographic column. The mixture was homogenized and packed in a glass

column of 0.25 cm inner diameter, and approximately 1.5 cm height. A peristaltic pump was used to control the flux of the multi-metal solution through the column at 0.5 mL per minute. The multielement solution was prepared as described in the previous section. Aliquots from the output-solution where taken approximately each 60 min of the experiment, until the complete breakthrough of the column was achieved by most of the metals of the multielement solutions. The concentration of the metal in the input and output solutions were monitored by ICP-MS. Variance of the concentration of the metals was normalized taking into account their initial concentration.

The final data was fitted to the Thomas model (Equation 2.16) described in the Chapter 2, section 2.3.2. The mathematical models such Thomas are used to describe a dynamic behavior of the pollutants capture in a fixed-bed column assuming negligible external and internal diffusion limitations.

Adsorption isotherms and kinetics

Adsorption isotherms were obtained for Pb^{II}, Cd^{II} and Hg^{II} using MOF-808@Cys and MOF-808@His samples. The experiments were conducted with 10 mg MOF-808@amino acid dispersed in 5 mL of metal solutions with different concentrations from 1 to 2000 ppm. The solutions were put under magnetic stirring overnight (12 h) until adsorption equilibrium was reached. After that, the suspension was removed with a hydrophilic 0.22 μm filter, it was acidified for its stabilization, and finally it was analyzed by means of ICP-AES.

Adsorption capacity for each point of the isotherm curve was determined on the basis of Equation 4.1. Adsorption isotherms were fitted to Langmuir and Freundlich models (Equations 2.7 and 2.8 in Section 2.3.1).[39–41] Adsorption kinetics curves were obtained as well for Pb^{II} and Hg^{II}. To this end, 10 mg of MOF-808@amino acid was dispersed in a 5 mL – 100 ppm water solution of the metal ion and further stirred under isothermal and dark conditions. The adsorption process was stopped at different time intervals (5 – 1400 min) by removing the MOF sorbent through centrifugation (6500 rpm, 3 min). The solution was further filtrated with a hydrophilic 0.22 μm filter,

acidified with 100 µL 0.1 M HNO$_3$, and analyzed by ICP-AES after its dilution (if necessary). Bangham model was applied to fit the experimental data (Equation 2.9 in Section 2.3.2).[42,43]

Metal adsorption at natural conditions

The metal adsorption efficiencies of MOF-808@(amino) acid samples for Hg^{II}, Pb^{II}, and Cd^{II} were evaluated in metal concentrations ranges close to these ones found in polluted water sources (1 ppm). In this experiment, the initial and final metal concentrations of the heavy metals were determined with ICP-MS.

4.1.2. RESULTS AND DISCUSSION

MOF-808 functionalization

Microcrystalline MOF-808 was synthesized as reported in previous works,[36] and the formate ligands exchange performed directly with an aqueous solution of the (amino) acid molecule at a moderate temperature and concentration of the solution (60 ℃, 0.05 M). L-cysteine was selected as a model amino acid to establish the SALI conditions due to its high solubility in water. The volume of the cysteine aqueous solution and the concentration of the MOF-808 dispersion into the media were fixed to the values reported in the experimental section.

In parallel, the concentration of the cysteine solution (0.05, 0.10 and 0.15 M) was varied to identify the best conditions in terms of the number of cysteine molecules installed per formula unit and the crystallinity of the MOF-808@Cys. To this end, the materials after each functionalization cycle were characterized by X-ray diffraction and ^{1}H-NMR. First, we noticed a concentration and temperature dependence for the SALI in MOF-808 up to a maximum of four cysteine molecules incorporated per formula unit.

When the cysteine-SALI ideal protocol (80 ℃ and 0.15 M cysteine solution) was applied for citric acid, it induced a structural collapse of the MOF-808 framework. Therefore, gentler conditions (60 ℃ and 0.05 M citric acid solution) are necessary to

establish a common protocol for all the amino acid functionalities selected to perform this study. This finding suggests that above a certain temperature and concentration of the (amino) acid solution the citric acid molecules are able to displace the trimesate pillars of the structure, leading to its collapse.

As revealed recently by W. Zhang and co-workers,[44] the MOF-808 post-synthetic functionalization is a pK_a-directed process, where acid groups with pK_a lower than the pK_a of the carboxyl groups of trimesic acid, induce the collapse of the framework. Nevertheless, other factors apart from the pK_a, such as the number of acid groups in the molecules incorporated to the framework, may play as well an important role during its collapse, as is the case of citric acid protocol studied in this work. Although the acidity of the carboxyl groups of citric acid (pK_{a1} = 3.13, pK_{a2} = 4.76, pK_{a3} = 6.39, 6.40) are lower than this of the cysteine (pK_a= 1.91), the same conditions induce significant degradation of MOF-808 by citric acid functionalities, while not by the cysteine. We found a similar result when more acidic sulfonic or phosphonic acids were used to encode the MOF-808 at 60 °C. If the temperature of the functionalization process was softened to 21 °C, it was possible to anchor to the MOF-808 very acidic nitrilotris(methylene)tryphosphonic acid (pK_a = 1.09) molecules, with a pK_a value of the phosphonic groups much lower than the threshold marked by the pK_a of the trimesate linkers.[44]

The samples were characterized as well by means of X-ray diffraction, IR-spectroscopy, N_2 adsorption isotherms at 77 K and thermogravimetric measurements. The successful formate substitution was confirmed by ^{1}H-NMR of the digested samples. The final formula for MOF-808@(amino) acids were obtained taking into account the BTC:(amino) acid molar ratio obtained by H[1]-NMR, and the trimesic linker defect of the parent MOF-808 determined from the weight loss processes observed in the TGA measurements. As concluded by these analysis, 3 to 5 of the six available sites per cluster where replaced by (amino) acid functionalities (Table 4.1).

Table 4.1. Chemical formula for MOF-808@(amino) acid samples.

	Formula	Cluster:AA*
MOF-808	$Zr_6O_4(OH)_{6.58}(H_2O)_{2.58}(C_9O_6H_3)_{1.92}(HCOO)_{3.5}$	--
Asp	$Zr_6O_4(OH)_{7.19}(H_2O)_{2.19}(C_9O_6H_3)_{1.92}(HCOO)_{1.25}(C_4H_7N_2O_3)_{3.40}$	1:3.4(4)
His	$Zr_6O_4(OH)_{4.44}(H_2O)_{0.44}(C_9O_6H_3)_{1.92}(HCOO)_{0.8}(C_6H_8N_3O_2)_{5.00}$	1:5.0(3)
Msc	$Zr_6O_{4.0}(OH)_{5.94}(H_2O)_{1.94}(C_9O_6H_3)_{1.92}(C_4H_5O_4S)_{4.30}$	1:4.3(4)
Cys	$Zr_6O_{4.0}(OH)_{5.89}(H_2O)_{1.89}(C_9O_6H_3)_{1.92}(HCOO)_{0.7}(C_3H_6NO_2S)_{3.65}$	1:3.7(2)
Suc	$Zr_6O_{4.0}(OH)_{6.79}(H_2O)_{2.79}(C_9O_6H_3)_{1.92}(C_4O_4H_4)_{3.45}$	1:3.5(3)
Fum	$Zr_6O_{4.0}(OH)_{6.74}(H_2O)_{2.74}(C_9O_6H_3)_{1.92}(C_4O_4H_2)_{3.36}$	1:3.4(2)
Mal	$Zr_6O_{4.0}(OH)_{5.64}(H_2O)_{1.64}(C_9O_6H_3)_{1.92}(HCOO)_{0.25}(C_4H_5O_5)_{4.60}$	1:4.6(4)
Cit	$Zr_6O_{4.0}(OH)_{7.06}(H_2O)_{3.06}(C_9O_6H_3)_{1.92}(HCOO)_{0.4}(C_6H_7O_7)_{2.78}$	1:2.8(4)

*AA= (amino) acid

X-ray diffraction data confirmed the chemical stability of the framework after its (amino) acid decoration (Figure 4.2a). Meaningful displacement of intensity variations of the diffraction maxima have not been observed. These lack of disturbance of the X-ray diffraction signal evidences that the crystal structure of MOF-808 remains mostly unaltered after SALI, and hence, that the (amino) acid molecules exhibit a large degree of disorder within the mesopores. These experimental results are in line with the single crystal X-ray diffraction study performed by Baek *et al.*[12] for the histidine modified homologue compound; where a highly dispersed electron density map could be attributed to the amino acid molecules at the pore space of the highly symmetric zirconium trimesate framework.

The IR spectra of the samples (Figure 4.2b) show the additional bands associated to the vibrational modes of the (amino) acid functionalities (*i.e.* -SH, -NH$_2$, -COOH). Particularly noteworthy is the absence of the $\upsilon_{est}(C=O)$ vibrational mode (~ 1700 cm^{-1}) for mono-carboxylate amino acids (*i.e.* His, Asp and Cys). The deprotonation of the carboxyl groups during SALI indicate that this bridging group links the amino acids to the zirconium oxo-clusters of the MOF-808 framework, as corroborated in previous studies by single crystal X-ray diffraction.[28] In contrast, di-carboxylate (*i.e.* Suc, Fum, Mal and Msc) and tri-carboxylate (*i.e.* Cit) acids are predicted to bind to the zirconium clusters only *via* one of their carboxylate groups,

while non-connected carboxyl residues will remain protonated, as confirmed by the IR absorption band associated to the $\upsilon_{est}(C=O)$ vibrational mode.[45–47]
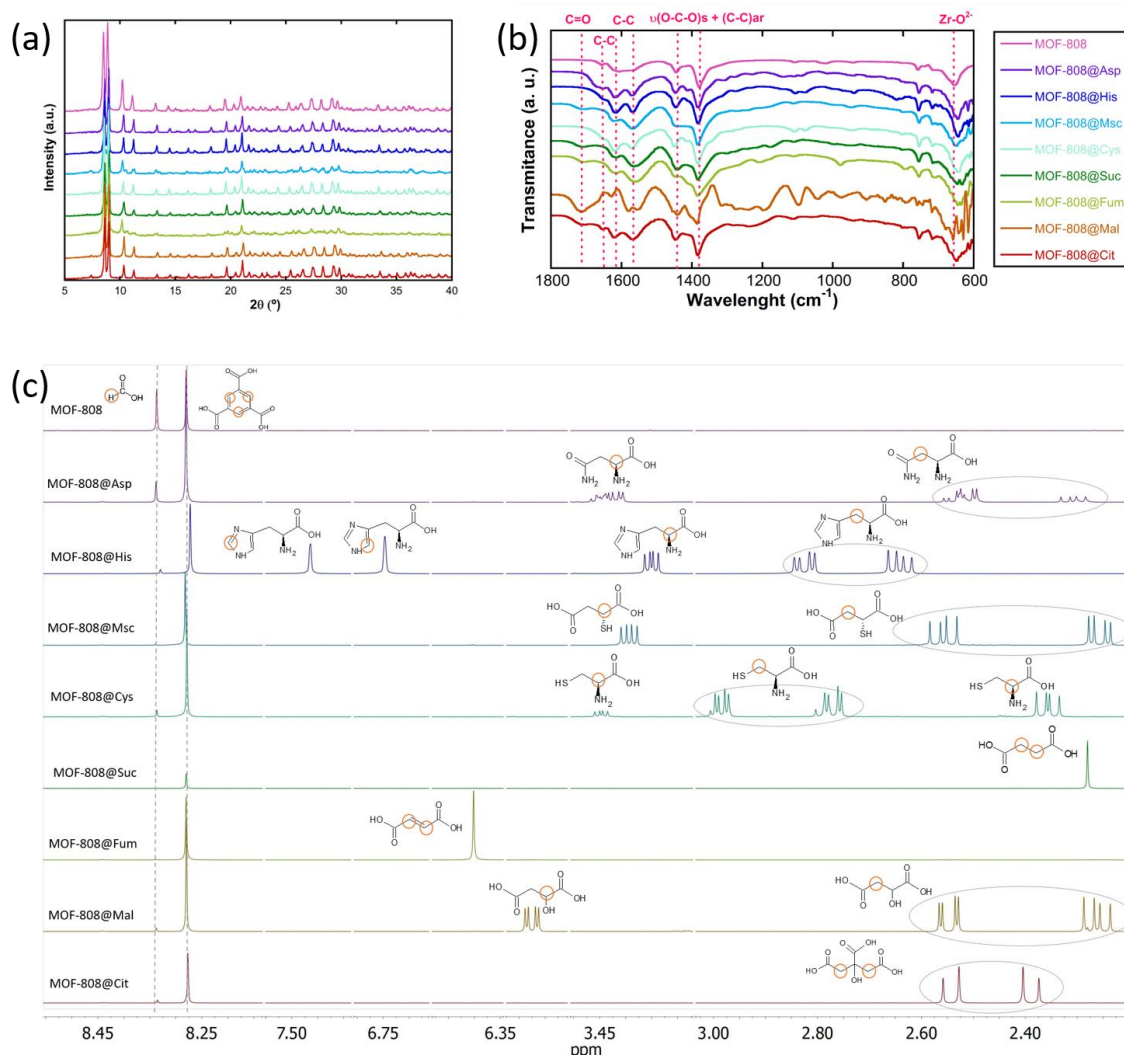

Figure 4.2. (a) IR spectra, (b) XRD patterns, and (c) ^{1}H-NMR spectra of the digested MOF-808 samples with L-asparagine, L-histidine, mercaptosuccinic acid, L-cysteine, succinic acid, fumaric acid, malic acid and citric acid functionalities.

As revealed by N$_2$ adsorption isotherms at 77 K, the porosity was preserved after the functionalization process. A reduction of the BET surface area and pore diameter is associated as a consequence of the MOF chemical encoding (Figure 4.3), but mesopore space is still highly available after the amino acid decoration of the framework.
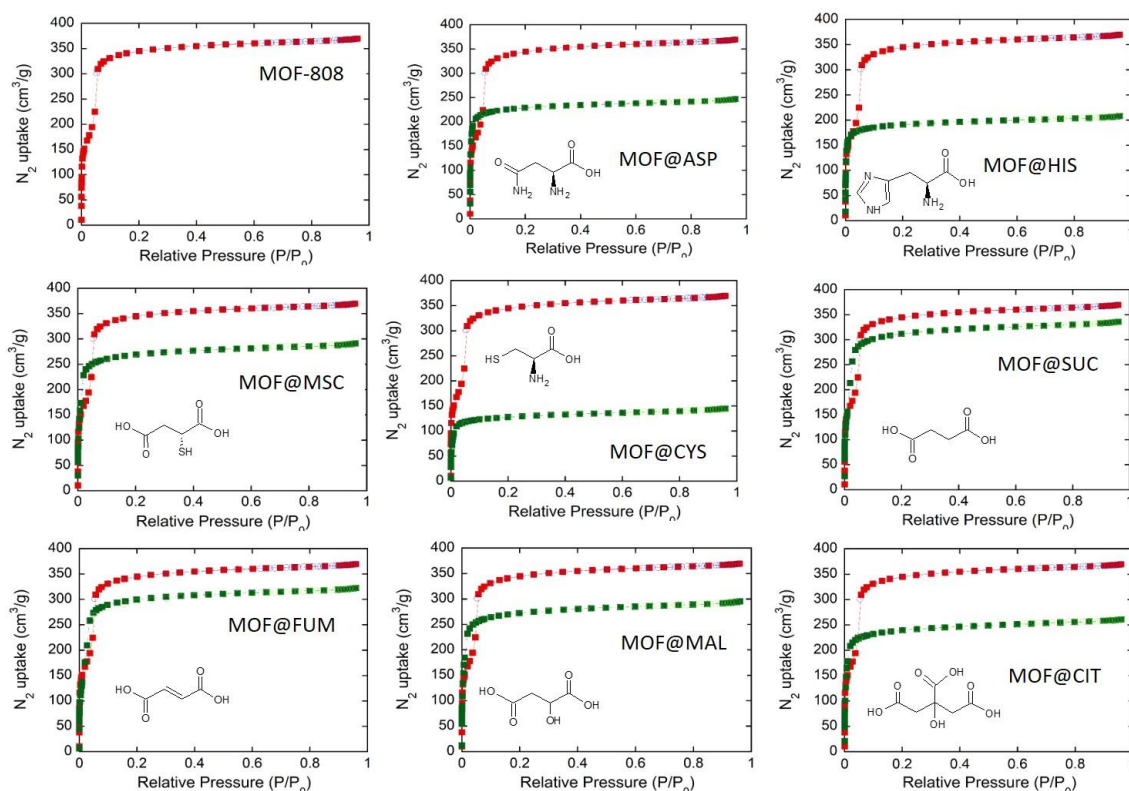
Figure 4.3. Nitrogen adsorption isotherms at 77 K.

MOF-808@(amino) acid structure

MOF-808 is built from cuboctahedron $Zr_6O_4(OH)_4(-COO)_{12}$ clusters connected to six homologue inorganic units through benzenetricarboxylate (BTC) linkers (Figure 4.4a-b).[48] The spatial arrangement of the inorganic and organic building blocks into the MOF-808 structure generates a three-dimensional framework with adamantane shaped pores of a 18 Å diameter.[7] The zirconium clusters are located at the vertices of the hexagonal shaped gates that give access to the inner space of the adamantane pores. The six equatorial plane positions of the clusters are coordinated by six formate groups that point to the center of the pore window. The metrics of the MOF-808 pore entrance are ideal to replace the formate anions and install small to medium size-molecules, as illustrated in the Figure 4.4c.[7,36,49] This is the case of the eight natural acids (*i.e.* succinic (Suc), fumaric (Fum), citric (Cit), L-malic (Mal) and mercaptosuccinic (Msc) acids), and amino acids (L-asparagine (Asp), L-histidine (His) and L-cysteine (Cys)) that we have selected to decorate the pore space of the MOF-808 in this research (Figure 4.4c).

Taking into account the bridging modes observed for carboxylate and amino acid molecules installed into the MOF-808 structure in previous works,[7] we have constructed tentative structural models for MOF-808@(amino) acid variants assuming that (i) the most acid carboxyl group of the (amino) acid is the one that binds the zirconium oxo-clusters, (ii) the (amino) acid coordinated the zirconium clusters *via* its carboxyl group, and (iii) the (amino) acids are spatially arranged (*i.e.* bond distances, angles and torsion angles) to prevent unreasonable contacts between them within the pore space.[12] Even though the models lack the backup of single crystal X-ray diffraction experimental data, they aid to visualize and analyse the possible disposition of the (amino) acids within the pore space after the SALI, and the possible distances between the functional groups of adjacent molecules that could bind the same metal-ion during adsorption.
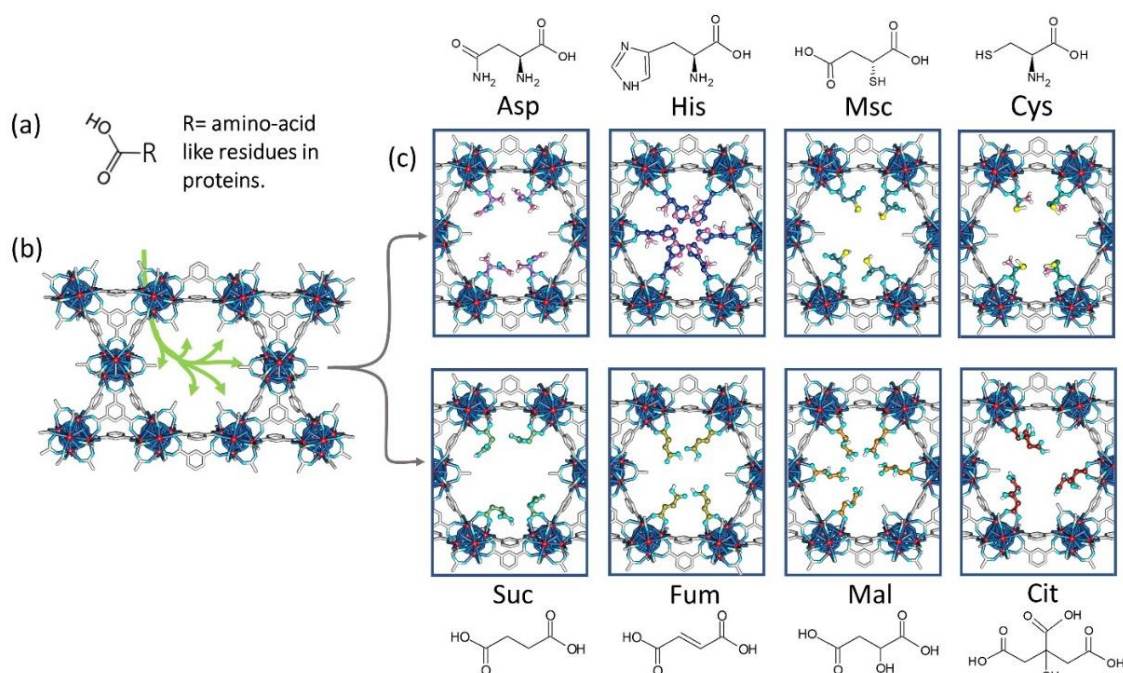

Figure 4.4. (a) Simplified structure of amino-acid like residues. (b) Installation of amino acid functionalities by solvent assisted exchange into MOF-808 scaffold. (c) Illustration of the pore environment of MOF-808 after its decoration with L-asparagine (Asp), L-histidine (His), mercaptosuccinic acid (Msc), L-cysteine (Cys), succinic acid (Suc), fumaric acid (Fum), L-malic acid (Mal), and citric acid (Cit).

It is important to point that, at a first sight, the chemical and conformational flexibility of succinic, fumaric, malic, and mercaptosuccinic molecules may lead to the impression that they could act as bidentate linkers connecting two of the open sites of the same Zr_6 clusters. Nevertheless, the geometric disposition and the distance between the uncoordinated positions at the zirconium clusters makes that even in a highly distorted configuration, these C_4 acids are far to bind the two adjacent linker-defective positions of the same zirconium cluster. Even in the case of a highly distorted C_5 molecule as citric acid, the free carboxyl molecules are far to bind two adjacent positions of the same cluster. It is important to note as well, that the same SALI process could induce to some extent the displacement of some of the trimesate linkers by amino acids or C_4 and C_5 acids used in this study without destabilizing the framework.

At a first sight, the metal capture within the (amino) acid decorated pore space of MOF-808 could occur *via* (i) a single molecule – metal coordination, or (ii) cooperatively, when two or more (amino) acid molecules binds the same metal ion. Single (amino) acids can coordinate metals in monodentate -μ_1 or bidentate -μ_2 fashions (Figure 4.5). Instead, a cooperative metal-adsorption will depend on the chemical conformation and disposition of the amino acids within the MOF-808. For example, for C_3 and C_4-molecules anchored to opposite clusters within the framework, even if they acquire a *trans* conformation, distance between the pedant groups pointing to the pores would range from 7 to 9 Å approximately. This distance is too long to generate (amino) acid-metal-(amino) acid bridges during adsorption. Contrary, the distance of the binding groups pointing to the pore space of the MOF-808 in C_3 and C_4-molecules anchored to adjacent clusters could be short enough (3-5 Å) to trap metals in a bidentate fashion (Figure 4.5d). The imidazole groups of histidine molecules installed in opposite positions within MOF-808 pore window exhibits an imidazole – imidazole distances (*i.e.* 4.5 – 5.5 Å) in the range of many metal-imidazole compounds found in the Cambridge Structural Database. A similar scenario is found for MOF-808@Cit compound, where the distance and conformational flexibility of citrate anions open the perspective to found carboxyl-carboxyl distances within the ranges of the ones found in monomeric, dimeric or trimeric metal-carboxylates.
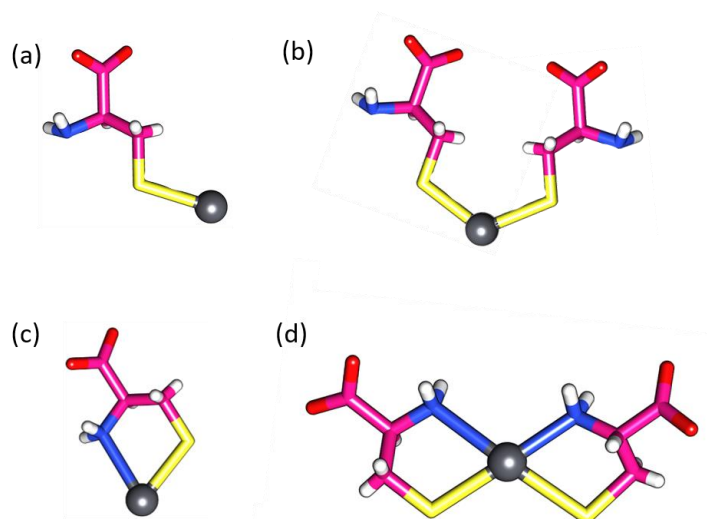
Figure 4.5. Schematic representation of (a) single cysteine and (b) two cysteine molecules coordinating metals in a monodentate fashion. (c) Single cysteine and (d) two cysteine molecules coordinating metals in a bidentate fashion.

Thermal and Chemical stability

The assessment of thermal and chemical stability of MOF-808@(amino) acids is key establishing their window of applicability. Thermogravimetric curve for MOF-808 (Figure 4.6) shows three weight loss stages associated to: (i) the water release (30 – 100 °C), (ii) the loss of formate groups and dehydration and dihydroxylation of the zirconium clusters, (125 – 300 °C) and (iii) the calcination of the trimesate bridges (425 – 550 °C). As reported by Shearer *et al.,*[50] the zirconium hexanuclear clusters of the UiO-66 structure are completely dehydrated and dehydroxylated at 400 °C. Thus, the linker deficiency of this zirconium MOF can be calculated by considering the chemical equation of the aerobic decomposition of the dehydroxylated UiO-66 (*i.e.* $Zr_6O_6(BDC)_6$). A similar approach can be applied to estimate the linker defects in MOF-808 if we assume that the zirconium clusters of the materials are fully dehydrated and dehydroxylated at 400 °C.[51–53] To this end, the theoretical weight loss associated to the linker calcination can be calculated taking into account the following reaction:

$$Zr_6O_{9+1.5x}(BTC)_{2-x} \rightarrow Zr_6O_{12} + (CO_2)_{18-2x} + (H_2O)_{6-3x};$$
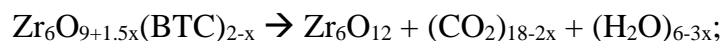
where x is the linker defects of the MOF-808 framework and compared to the experimental ones obtained from the thermogravimetric analysis.

By following this approach, 0.08 defects per formula unit has been determined. For MOF-808@(amino) acid samples, the degree of overlapping between the thermal release of (amino) acid molecules and the trimesic acid calcination is too high to clearly stablish the temperature where the dehydroxylated $Zr_6O_{9+1.5x}(BTC)_{2-x}$ is formed, and hence, to accurately calculate if the trimesate linker deficiency is enhanced as a consequence of the SALI process.

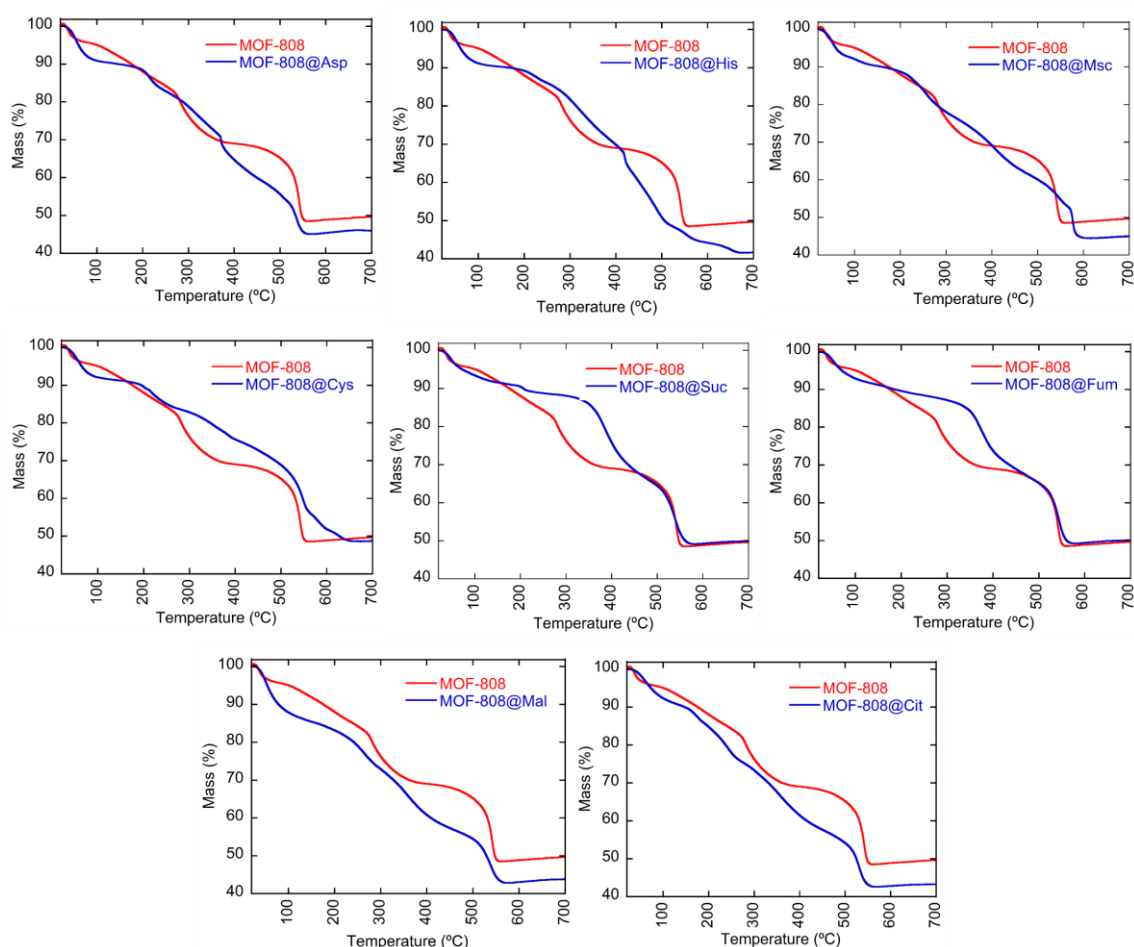**Figure 4.6.** TGA curves of parent MOF-808 and functionalized samples.

Thermodiffraction experiments confirm that the formate release induces a progressive loss of the long-range ordering of MOF-808 above 175 °C. It is important to note that during the thermal collapse, the XRD maxima do not show an appreciable displacement of their 2θ(°) position (Figure 4.7a). Henceforth, MOF-808 long-range

ordering disruption is not accompanied by a structural contraction of the framework (Figure 4.7b). Therefore, two parameters can describe the thermal resistance of the MOF-808 framework, the starting point of the thermal degradation (T_i = temperature at which an appreciable intensity loss of the XRD maxima is observed), and the crystallographic cell volume contraction occurring during the release of anionic groups attached to the zirconium oxo-clusters.[54]
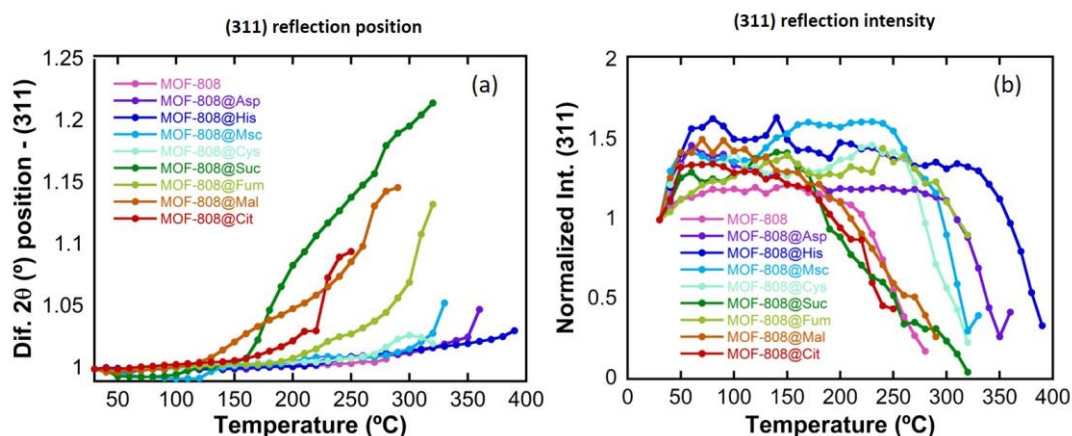

Figure 4.7. (a) Thermal displacement of (311) reflection in MOF-808@(amino)acids. (b) Normalized intensity thermal dependence for (311) reflection in MOF-808@(amino)acids.

Generally, the thermal stability of MOF-808 is improved when the scaffold is functionalized with (amino) acids as the thermal detachment starts and ends at higher temperatures than the formate anions. In fact, the thermal stability threshold can be increased by over 100 °C for some functionalities. In parallel, we have observed that the thermal collapse of MOF-808@(amino) acids can be accompanied by a structural contraction (Table 4.2). MOF-808@His, MOF-808@Asp, MOF-808@Cys, and MOF-808@Msc experience long-range ordering loss simultaneously with a slight structural contraction during the last steps of the thermal degradation (Figure 4.7a). By contrast, in MOF-808 functionalized with Cit, Fum, Suc or Mal acids, the long-range ordering loss is coupled to a progressive structural contraction that is extended in a wide range of temperatures during the thermal release of the acid functionalities (Figure 4.7b). A cell volume reduction between 30 to 40% has been observed in carboxyl acid functionalized MOF-808 before the complete collapse of its long-range structure (Table 4.2).

It is important to note, that the thermal dependence of the cell parameters and volume have been obtained both by pattern matching and peak fit analyses of the XRD data with similar results. Nevertheless, the absolute values of the structural contraction reported in the Table 4.2 need to be considered in a qualitative way, since the loss of crystallinity of the XDR patterns at high temperatures hinders an accurate determination of the diffraction maxima positions.

Table 4.2. Summary of MOF-808@(amino)acid compositions and thermal stability ranges

Sample	L/Zr$_6$ Molar Ratio	Thermal Stability* (°C)	Δ Cell Volume (%)
MOF-808	---	175	-2.4
Asp	3.5	290	-13.2
His	5.2	340	-8.7
Msc	4.5	275	-14.4
Cys	3.8	275	-6.0
Suc	3.6	160	-44.2
Fum	3.5	260	-31.2
Mal	4.8	175	-33.6
Cit	2.9	160	-23.8

*Temperature at which an appreciable loss of intensity is observed in the XRD patterns.

The chemical stability of the MOF-808@(amino) acids was studied by immersing the samples in water solution with different acidities (pH = 4, 3 and 2) during 24 h. The crystallinity and functionalization degree of the samples before and after their immersion in acidic aqueous media were studied by means of means of XRD and ^{1}H-NMR. The same experimental procedure has been applied to the MOF-808 for sake of comparison. From the structural stability point of view, all the materials, including the parent MOF-808, are robust enough to keep their diffraction signature after immersing them in acid conditions (Figure 4.8). The exception to this experimental evidence are MOF-808@His and MOF-808@Asp, which diffraction patterns show a significant broadening of the diffraction maxima. In parallel, the chemical stability of the molecules installed by SALI in the MOF-808 depends on the (amino) acid nature itself. Except MOF-808@His and MOF-808@Msc compounds, the

MOF-808@(amino) acids show good chemical stabilities, with minor release of the (amino) acid functionalities (Figure 4.8 and Figure 4.9). In addition, MOF-808@His is more sensitive to acidic media, showing an appreciable broadening of the X-ray diffraction maxima and nearly complete loss of the (amino) acid molecules when exposed to highly acidic media (pH = 3 and 2). In contrast, even if MOF-808@Msc shows an appreciable loss of the Msc molecules at acidic media, the XRD pattern maintain the crystallinity.

It is still unclear why the chemical stability of (amino) acid functions varies if similar anchoring mechanisms of the (amino) acids to the MOF structure are expected. At a first sight, the stability of the MOF-(amino) acid bridges may be defined by the pK_a of the carboxyl groups of the (amino) acid molecules. Nevertheless, no rationale can be found considering only this parameter, since pK_a values for carboxyl groups of His, Cys or Asp are quite similar, and their chemical stabilities when installed in the MOF-808 frameworks differs significantly. A possible explanation for MOF-808@His compound could be a charge-balance related destabilization triggered by a protonation of amine groups (pK_a = 6) when the pH is below 6. Still this cannot explain the chemical instability of Msc functions.
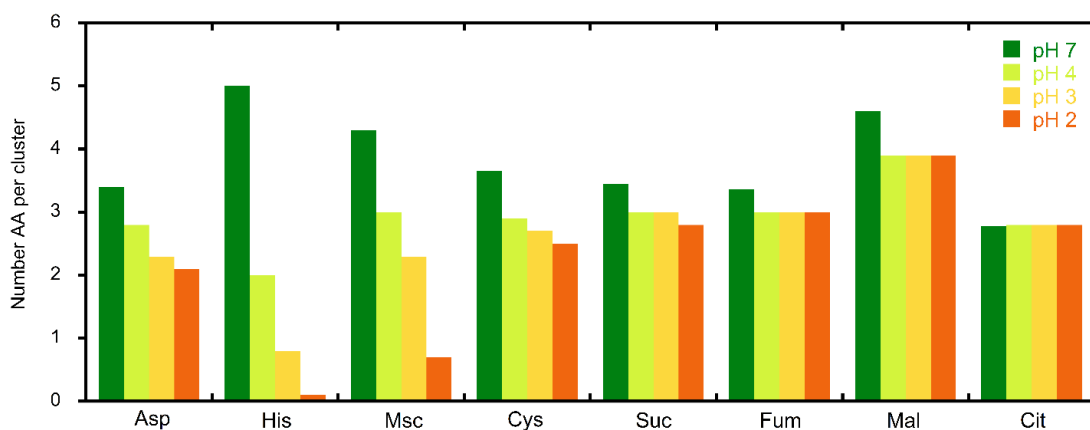

Figure 4.8. Variation of (amino) acid functionalities per formula unit after immersing MOF-808@Cys, MOF-808@His and MOF-808@Cit in water acidic solutions during 24 h.
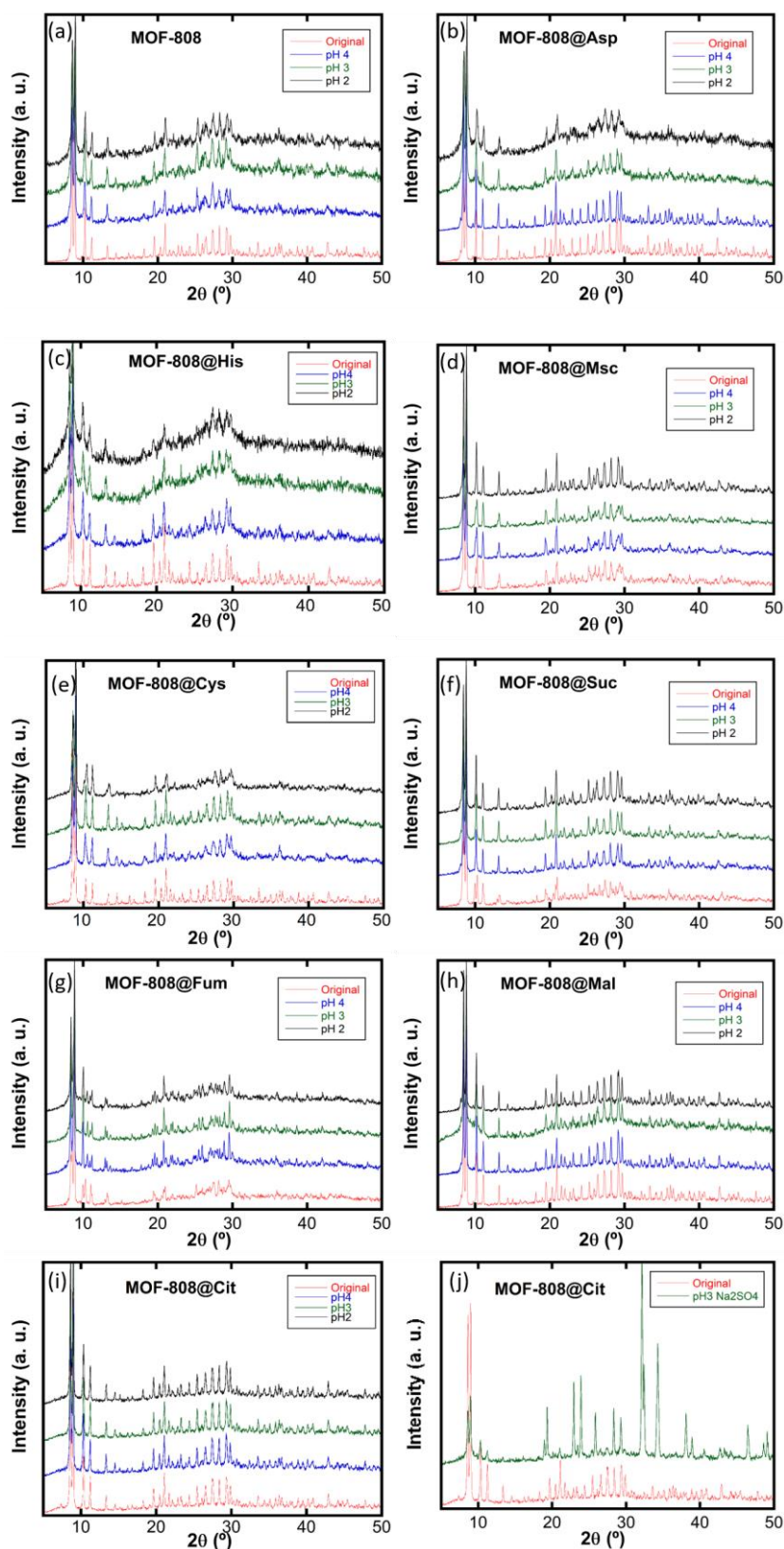
Figure 4.9. XRD analysis of MOF-808@(amino) acid samples (a-i) before and after being exposed to different acidic conditions, (j) before and after being exposed to Na_2SO_4 100 ppm solution for MOF-808@Cit sample.

The stability over the presence of highly coordinating sulphate anions was as well tested for MOF-808@Cit compound, since this variant is the one exhibiting the lower loss of crystallinity and citrate release in acidic media. MOF-808@Cit was immersed in 1 M Na_2SO_4 solution (100 ppm of sulphate concentration) of pH = 3 during 24 h. As concluded from the XRD data, the compound is partially transformed to another phase during the process (Figure 4.9j). Nevertheless, the trimesic to citric acid molar ratio obtained by ^{1}H-NMR after the transformation is very similar to the citrate molecules per zirconium cluster observed for the parent compound. So, the presence of an elevated concentrations of highly coordinating anionic species as sulphate induces the degradation of a significant weight fraction of the MOF-808@Cit framework, but the citrate groups in the MOF-808@Cit that is still crystalline after the process are stable enough to remain anchored to the framework.

The chemical stability of MOF-808@(amino) acid materials allows advancing their horizon of applicability for the recovery of metals from aqueous environments. First, the robustness of the SALI encoding opens the perspective to the application of MOF-808@(amino) acids for surface water decontamination purposes, but not for the recovery of metals from seawater (e.g. uranium adsorption), or from acid-waters derived from phospho-gypsum deposits, since the sulphate content in this media is above the stability threshold of our system. Second, the acid-stability of MOF-808@(amino) acids may enable the recovery of metals from acid leachates derived from metal-recycling or mining activities, but not if the anionic strength of highly coordinating oxyanions (e.g. sulphate, phosphate, chloride…) in the solutions is above the chemical stability limit of the MOF-808@(amino) acids.

Metal adsorption affinity

Single-ion adsorption tests were performed with MOF-808@(amino) acids in acidic solutions (pH $\approx$ 4) of 100 ppm metal concentration. To this end, 100 mg of MOF-808@(amino) acid was immersed in 50 mL of Hg^{II}, Pb^{II}, Cd^{II}, Cu^{II}, Ni^{II}, Eu^{III}, Cr^{III} or Cr^{VI} 100 ppm solutions while monitoring the metal concentration before and after the sorption equilibrium. Metal ions were selected on the basis of their acidity

$(Z/r^2$- Soft-Intermediate and Hard), coordination environment, and charge. Adsorption capacity was calculated as mmol of metal adsorbed per mol of sorbent (Figure 4.10). Except Cr^{VI}, all the metal ions are found in their cationic forms in water solutions. In the specific case of Cr^{VI}, it is stabilized as $(Cr_2O_7)^{2-}$ and $(HCrO_4)^-$ anions at the acidic conditions studied in this work.

Unmodified MOF-808 welcomes Cr^{VI} adsorption since its chromate anionic form is able to displace formate anions to bind the zirconium hexa-nuclear clusters (Figure 4.10a).[55] The mechanism of MOF-808 capture of Cu^{II} and Cr^{III} intermediate and hard ions is still unclear. Nevertheless, previous researches have installed copper and chromium oxo-aqueous species covalently bonded to the zirconium clusters through solvent vapor deposition.[56]

Once the (amino) acid functionalities are installed within the MOF-808 framework, its ability to capture metal ions changes drastically (Figure 4.10b-i). As a general rule, the adsorption affinity of the MOF-808@(amino) acid samples over cations can be explained by Pearson acid-base theory,[57] that is, soft acidic metal ions tend to interact with soft basic functional groups, and vice versa. However, this is not the unique parameter governing the adsorbing affinity of MOF-808@(amino) acid system, as the number of amino acid residues and their spatial disposition shape as well the affinity of the system to trap metal ions far from the general trends described by the Pearson Rule.

When histidine is installed at the MOF-808 framework, amino and imidazole functionalities decorate its inner pore structure enabling the capture of soft intermediate metal ions as Hg^{II}, Pb^{II} and Cd^{II} (Figure 4.10c).

Similarly, the combination of thiol-amine, and, thiol-carboxyl residues in MOF-808@Cys and MOF-808@Msc give rise to the concurrent adsorption of weak (Hg^{II}, Cd^{II} and Pb^{II}) and intermediate (Cu^{II}, Ni^{II}) metal ions (Figure 4.10d-e). In comparison to His and Asp based MOF-808, Cys and Msc homologues capture Ni^{II} ions too, which is an ion slightly more acidic than Cu^{II}. The installation of carboxyl and hydroxyl residues within the MOF-808 through its functionalization with succinic, fumaric, malic and citric acids give access to trap intermediate to hard metal ions, as Cu^{II}, Ni^{II} and Eu^{III} (Figure 4.10f-i). Indeed, complex functionalities combining several carboxyl

and hydroxyl groups (*i.e.* malic and citric acid) work more efficiently than functionalities based on single carboxyl residues (Figure 4.10h-i). On the top of that, it is important to mention that it is still a room of improvement to enhance the adsorption capacities towards these hard ions by including sulphonyl or phosphonate groups within the framework, as reported in previous works.[58]

The capture of Cr^{VI} and Cr^{III} by MOF-808@(amino) acids seems to be governed by factors beyond the general hard-soft acid-base rule. As previously mentioned, Cr^{VI} is a chromate anionic form in solution, so anion exchange by formate anions is predicted to be the preferred adsorption mechanism in non-functionalized MOF-808 (Figure 4.10a). For instance, carboxylate type functionalizations (*i.e.* Suc, Fum, Mal, and Cit) significantly reduce the adsorption capacity of MOF-808 to capture Cr^{VI} since chromate is not able to displace them and access the preferred chemisorption positions at the zirconium clusters (Figure 4.10f-i). This is especially notorious in MOF-808@Cit, as electrostatic repulsions and stearic impediments can further impede Cr^{VI} uptake. Counterintuitively, amino acid decorated MOF-808 materials exhibit similar adsorption capacities over Cr^{VI} than parent MOF-808. Chromate uptake by these functional groups can be explained on the basis of two different mechanisms, (i) the electrostatic adsorption by $-NH_3^+$ protonated groups in His, Cys and Asp functionalities,[38] and (ii) the chemical reduction of Cr^{VI} to Cr^{III} by the electron donation of thiol and amine groups.[59] This dual adsorption/chemical reduction mechanism over chromate anions has proven to be highly effective for amino and hydroxyl UiO-66 variants.[42]

The adsorption affinity of MOF-808@His and MOF-808@Asp over Cr^{III} is counterintuitive, since highly acidic ions (such as trivalent chromium) prefer to coordinate carboxyl hard functionalities (*i.e.* MOF-808@Cit and MOF-808@Mal). However, MOF-808@His and MOF-808@Asp exceeds by much the capacity to capture Cr^{III} (1600 mmol·mol^{-1} and 500 mmol·mol^{-1}) in comparison to the MOF-808 counterparts functionalized with carboxyl acid residues.
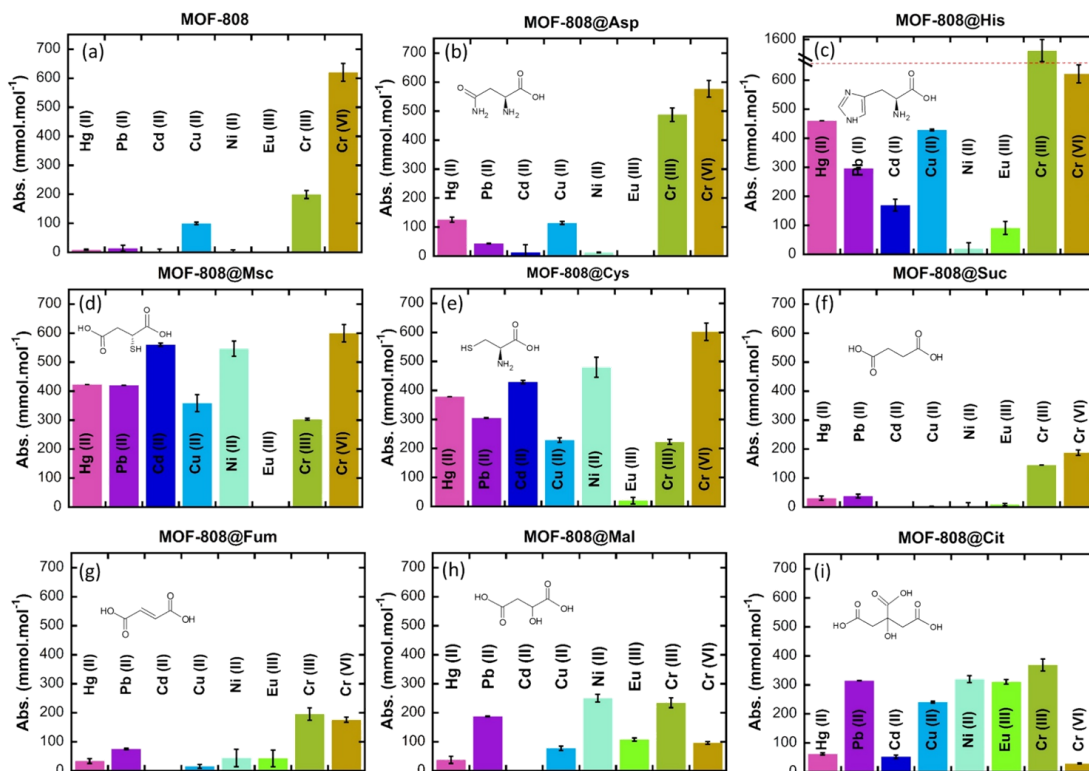
Figure 4.10. Adsorption capacity (mmol·mol^{-1}) of the different MOF-808@(amino) acid samples over Hg^{II}, Pb^{II}, Cd^{II}, Cu^{II}, Ni^{II}, Eu^{III}, Cr^{III} and Cr^{VI}. Experiments were performed with an initial metal ion concentration of 100 ppm, using 2 mg MOF·mL^{-1}.

MOF-808@Cys was also tested under static adsorption conditions to capture Hg^{II}, Cd^{II} and Pb^{II} from solutions with concentrations closer to those usually observed in polluted water sources (*i.e.* 1 ppm) (Figure 4.11). An adsorption efficiency above 99.99 % was obtained for Hg^{II}, reducing its concentration from 1 ppm to 0.002 ppm, a value below the legal limit (0.01 ppm) established by the World Health Organization (WHO).[60] The performance of MOF-808@Cys to capture Pb^{II} and Cd^{II} ions is also outstanding, with uptakes above 98% of the initial metal ions content, reaching concentrations close to 0.1 ppm after adsorption. Adsorption conditions can be easily improved by increasing the MOF loading (current = 2 mg MOF·mL^{-1}) to achieve the concentration thresholds stablished by WHO for Pb^{II} (0.001 ppm) and Cd^{II} (0.003 ppm).
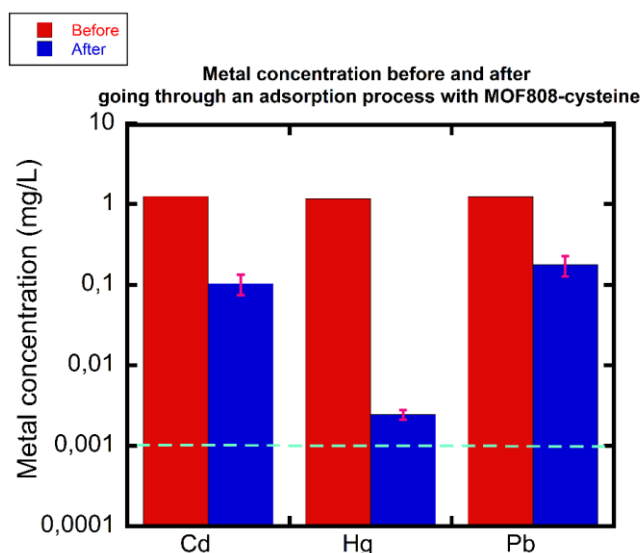
Figure 4.11. Metal concentration in water before and after the adsorption process with MOF-808@Cys. A logarithmic scale is used in Y axis. Turquoise line: legal limit established by WHO.[60]

The capacity to adsorb the same metal-ions from a multielement solution was determined for all the studied materials. The results have been plotted in terms of distribution coefficient factor (K_d) (calculated as detailed in the experimental section, Equation 4.2). K_d values of each adsorbent for each metal allows easily visualizing the efficiency of the sorbent to extract the metal from the solution. In addition, the separation factor of a sorbent can be obtained by calculating the ratio of the K_d values for different metals (Equation 4.3 in the experimental section).

The linear plot of the K_d values shown in the Figure 4.12a clearly reveals the more affine sorbent – metal pairs (*i.e.* MOF-808@Cys-Hg^{II}, MOF-808@Cys-Cu^{II}, MOF-808@His-Cr^{III} and MOF-808@Cys-Hg^{II}), all of them with K_d values above 10^5. If the data is plotted in a logarithmic scale (Figure 4.12b), these sorbent-metal pairs with K_d values below 10^5 are revealed. Although less efficient than the sorbent-metal pairs identified in the Figure 4.12a, K_d values from 10^3 to 10^5 are still interesting, especially for the later computing of separation factors.
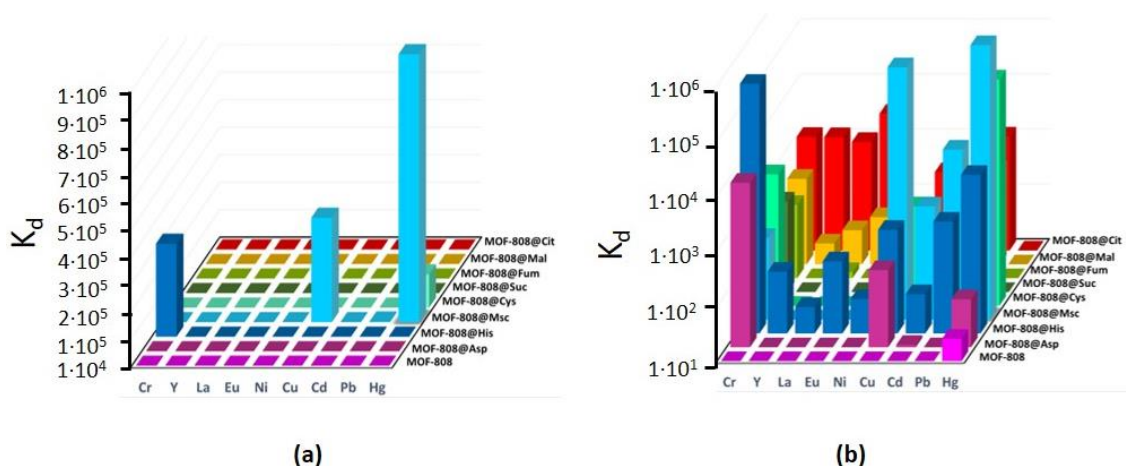
Figure 4.12. Metal distribution coefficients for MOF-808@(amino) acid samples obtained from the adsorption experiments in a multielement solution of Cr^{III}, Y^{III}, La^{III}, Eu^{III}, Ni^{II}, Cu^{II}, Cd^{II}, Pb^{II}, and Hg^{II} ions. The data have been plotted in (a) linear and (b) logarithmic scale basis. Experiments were performed with an initial metal ion concentration of 10 ppm, using 2 mg MOF·mL^{-1}.

Following the same tendency than for single-element adsorption tests, two families of MOF-808@(amino) acid materials can be distinguished, the Msc, Cys, His and Asp variants able to capture soft to intermediate metal ions, and the Cit and Mal functionalized compounds, which metal-affinity is shifted towards hard metals as the trivalent REE. Therefore, taking into account the K_d values, the first group of MOF-808@(amino) acid materials are appealing from water remediation of the three of the heavy metals (Pb^{II}, Cd^{II}, Hg^{II}) included in the big-four defined by the World Health Organization. Giving the differences in the K_d values for soft and hard metal ions, the separation of heavy metals Msc, Cys, His and Asp MOF-808 variants. Last but not least, although the K_d values of MOF-808@Cit or MOF-808@Mal for REE are low, some of the calculated separation factors between Eu^{III}, Y^{III} and La^{III} start to be interesting for individual REE separation. Nevertheless, further development of the MOF-808 pore chemistry is needed to improve them.

Breakthrough experiments

Breakthrough experiments with the multielement solution flowing over a sand-packed bed of MOF-808@(amino) acid were performed with a flow rate of 0.5 mL·min^{-1}. As expected, the metal-affinity of each MOF-808@(amino) acid alters the breakthrough volume of each metal in the column (Figure 4.13). The experimental data have been fitted to the Thomas model, and the adsorption capacity and the Thomas constant values for each Sorbent-Metal pair summarized in the Table 4.3.
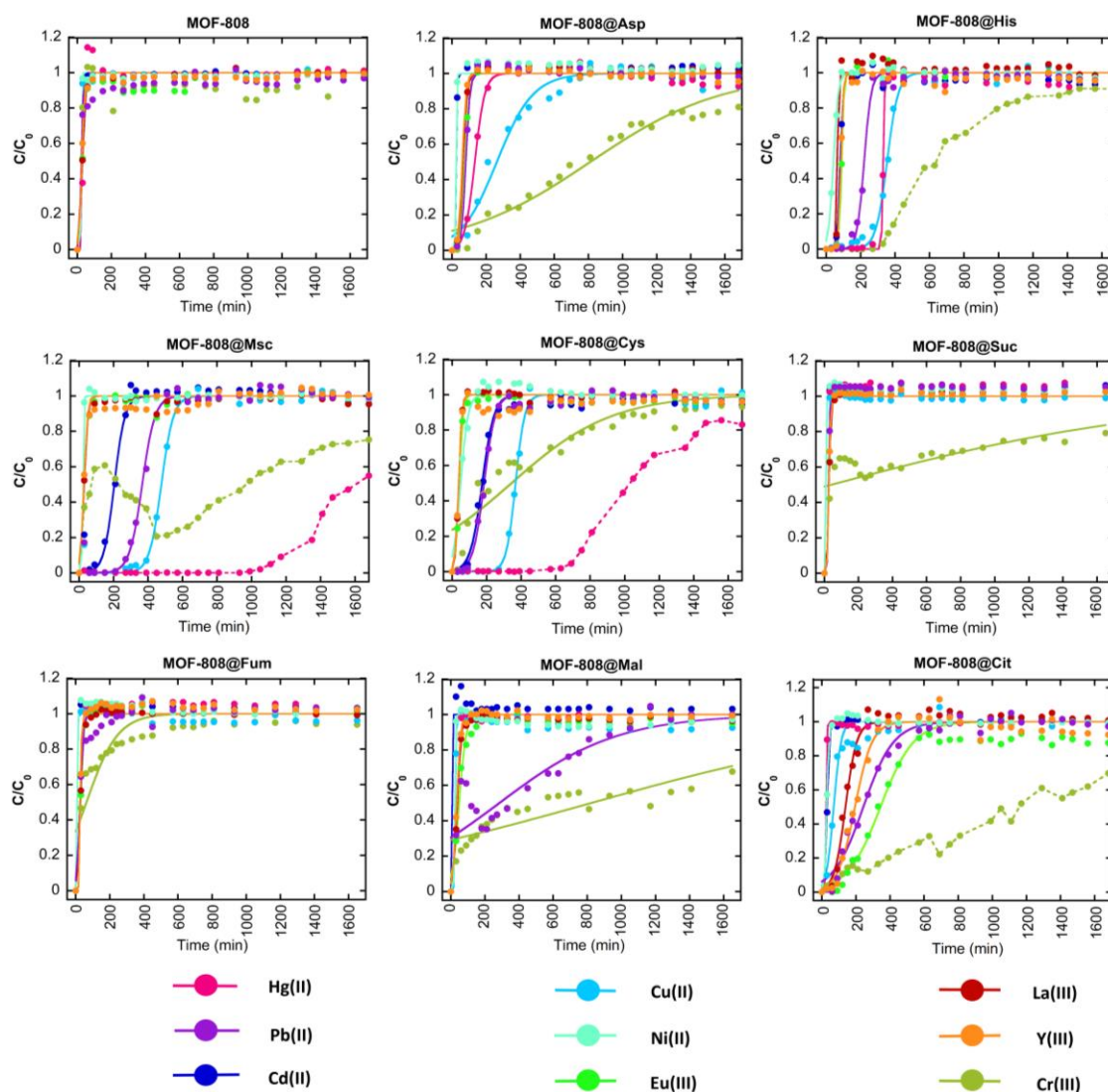

Figure 4.13. Breakthrough curves of of the different MOF-808@(amino) acid samples over a multielement mixture. Experiments were performed with an initial metal ion concentration of 10 ppm, using a packed bed column of 100 mg of MOF in 1.5 g of sand, and with a flux of 0.5 mL·min^{-1}.

Continuous flux adsorption experiments show that the parent MOF-808, Suc and Fum variants show negligible retentions times for soft to hard metal-ions, so all the studied elements cross the column without a delay time. For Cys, His, Msc and Asp materials, the breakthrough time of the soft and intermediate metals in the output of the column is delayed significantly in comparison to hard ions.

Within the intermediate and soft ions studied, the order and the volume of the column rupture for each metal varies significantly depending on the MOF-808 functionalization. For example, MOF-808@Msc and Cys columns are able to detoxify from 300 to 500 mL of a 10 ppm Hg^{II} solution lowering the mercury concentration below the legal limits stablished by WHO, but the breakthrough volumes for Cd^{II} or Pb^{II} are lower than the ones of Hg^{II}. Event though, the terminal concentrations of Cd^{II} and Pb^{II} before the rupture of the column are lower as well than the legal threshold defined by WHO as well.[60]

In parallel, the incorporation of carboxyl and hydroxyl groups in MOF-808@Mal and MOF-808@Cit variants has an opposite effect on the breakthrough experiments. In these cases, the times of column ruptures for acidic metal ions are increased, whilst the soft metal-ions pass the column without delay time. For instance, a quite interesting separation capacity for different rare earth elements is starting to be observed for MOF-808@Cit variant. It is important to note the uncommon behavior of Cr^{III} on the static adsorption and breakthrough experiments in multielement solutions that may be related to its precipitation due to its long-term stability in solution.

Table 4.3. Adsorption kinetic parameters of Thomas equation from continuous flow metal-ions separation with MOF-808@(amino) acid columns

		Hg(II)	Pb(II)	Cd(II)	Cu(II)	Ni(II)	Eu(III)	La(III)	Y(III)	Cr(III)
MOF-808	K	0.0146	0.1676	0.047	0.0359	0.0437	0.01	0.01	0.0123	0.0364
	Q	1.7252	1.1595	1.1398	1.1178	1.1127	1.5021	1.5152	1.3501	1.3075
	R	0.9912	0.8512	0.9974	0.9751	0.9901	0.924	0.9886	0.9755	0.7851
MOF-808@Asp	K	0.0034	0.0083	0.0443	0.0009	0.0447	0.0074	0.0084	0.009	0.0003
	Q	3.2237	4.0416	1.2934	13.137	1.1702	3.7498	3.2237	3.026	40.549
	R	0.9930	0.9937	0.9790	0.9688	0.9591	0.9955	0.9930	0.9951	0.9500
MOF-808@His	K	0.025	0.0049	0.01167	0.003	0.0072	0.0155	0.0295	0.0149	-
	Q	16.562	11.039	4.12	17.693	2.1065	4.5221	3.2917	4.3175	-
	R	0.993	0.9927	0.9798	0.9927	0.991	0.9933	0.98	0.9829	-
MOF-808@Msc	K	-	0.0027	0.0033	0.0029	0.0404	0.00928	0.0094	0.0097	-
	Q	-	18.31	10.233	23.85	1.1005	1.5027	1.5008	1.4372	-
	R	-	0.9885	0.9797	0.9929	0.9946	0.9743	0.9727	0.9316	-
MOF-808@Cys	K	-	0.0031	0.0029	0.0038	0.0048	0.0095	0.0109	0.0103	0.0003
	Q	-	9.269	8.6923	18.366	2.5025	2.0996	1.8918	1.8769	17.177
	R	-	0.9914	0.9834	0.9951	0.9757	0.9769	0.9919	0.926	0.8714
MOF-808@Suc	K	0.0994	0.0303	0.0982	0.053	0.0986	0.0213	0.0182	0.0235	-
	Q	0.4617	1.268	0.5005	1.0402	0.4893	1.3743	1.3583	1.3373	-
	R	0.92358	0.9464	0.9495	0.9938	0.9569	0.985	0.9936	0.9957	-
MOF-808@Fum	K	0.1049	0.0109	0.1545	0.08189	0.1384	0.0118	0.0126	0.0326	0.0011
	Q	0.44426	1.2796	0.3231	0.5684	0.3202	1.4459	1.4046	1.3987	3.1588
	R	0.9351	0.9270	0.9670	0.9683	0.9604	0.9865	0.9947	0.9678	0.7705
MOF-808@Mal	K	0.0439	0.0003	0.1123	0.0361	0.0441	0.005	0.008335	0.0089	-
	Q	1.1333	14.202	0.4319	1.3258	1.1371	2.4303	1.8952	1.7167	-
	R	0.9864	0.8182	0.9684	0.9134	0.9434	0.9646	0.9870	0.9927	-
MOF-808@Cit	K	0.037	0.0011	0.1506	0.0047	0.0169	0.001	0.003	0.002	-
	Q	1.2097	12.16	1.5429	3.474	1.4141	17.192	6.9288	9.7111	-
	R	0.9931	0.98368	0.9981	0.9526	0.9937	0.9547	0.9842	0.9800	-

Adsorption isotherms and kinetics

The feasibility of MOF-808@(amino) acids as water remediation technology against heavy metals pollution (*i.e.* Cd^{II}, Hg^{II} and Pb^{II}) was evaluated as well through kinetics and isotherm adsorption experiments for MOF-808@Cys and MOF-808@His. Adsorption kinetics studies reveal extremely fast capture with equilibrium times below 2 min (Figure 4.14). Adsorption isotherms indicate a maximum adsorption capacities up to of 40 mg·g^{-1} for Cd^{II} (MOF-808@Cys), 175 mg·g^{-1} for Pb^{II} (MOF-808@His) and over 350 mg·g^{-1} for Hg^{II} (MOF-808@Cys and MOF-808@His) (Figure 4.15). That is, at its maximum loading capacities, the MOF-808@Cys variant is able to host 1.35 Pb^{II}, 1.9 Hg^{II} and 0.55 Cd^{II} ions per formula unit.
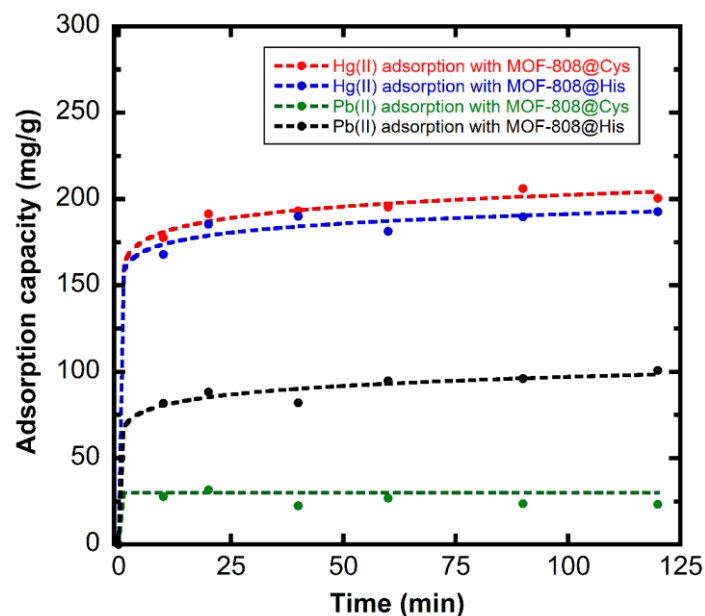

Figure 4.14. Adsorption kinetics for MOF-808@Cys and MOF-808@His with Pb^{II} and Hg^{II}. Line: Bangham model fitting. Adsorbent concentration: 1mg·mL^{-1}. C$_i$ = 100 ppm.

Langmuir and Freundlich models were applied to fit the experimental data (Equation 2.7 and 2.8 in Chapter 2) and in order to better quantify the adsorption capacity and affinity of His and Cys modified MOF-808 over Cd^{II}, Hg^{II} and Pb^{II}. The slightly better fitting of the experimental curves to the Freundlich model suggest a homogeneous binding of the metal ions to the MOF-808@amino acids functionalities.

Nevertheless, Pb^{II} and Cd^{II} capture can be related to their coordination by imidazole and amino functionalities, as it can be observed in many Pb^{II} and Cd^{II} amino acid metal complexes. In comparison, given the tendency of Hg^{II} to form Hg^{II}-S bonds, their coordination to thiol and imidazole residues of Cys and His is the most plausible mechanisms for the capture of soft ions.
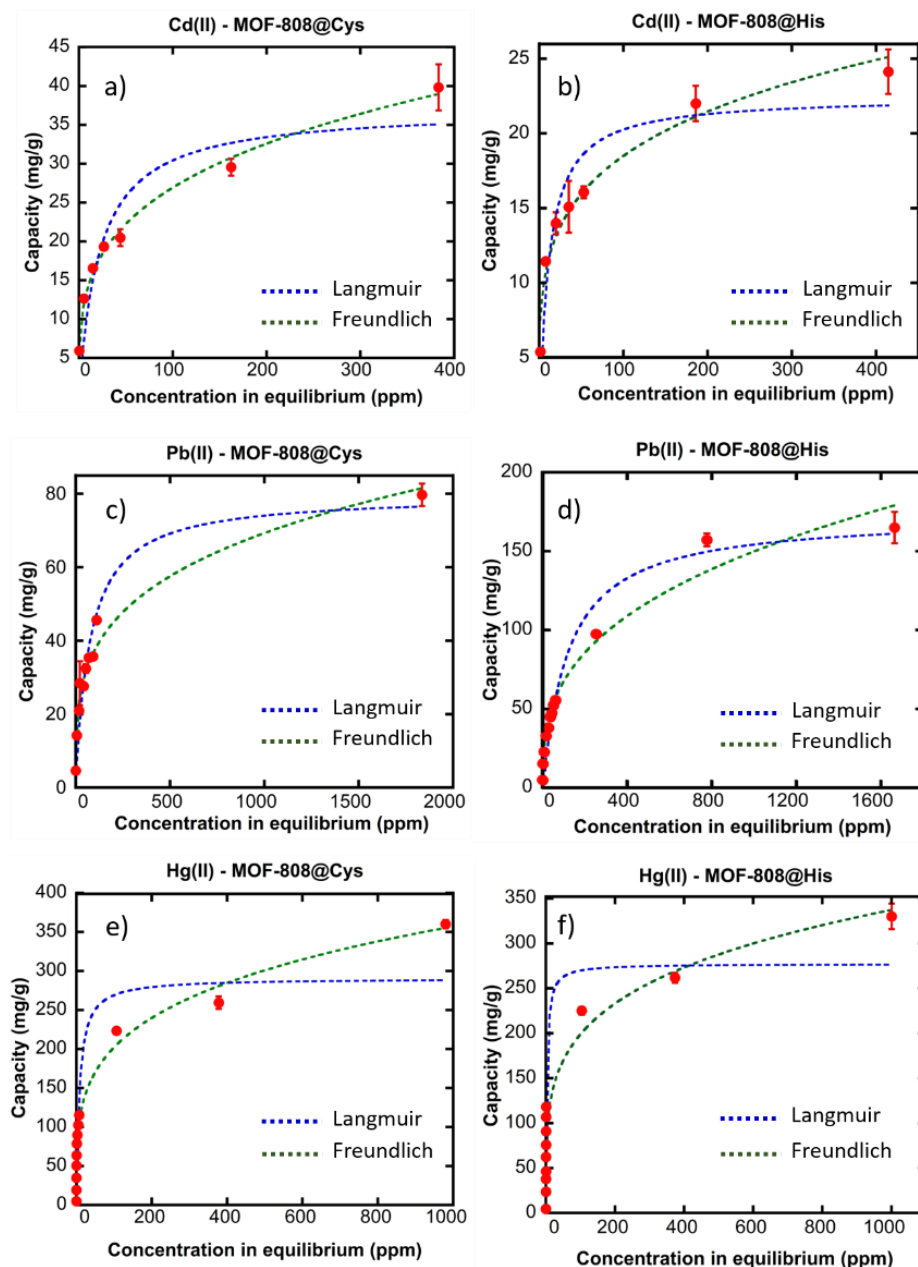

Figure 4.15. Adsorption isotherms for MOF-808@Cys and MOF-808@His over (a-b) Cd^{II}, (c-d) Pb^{II}, and (e-f) Hg^{II}. Dashed lines, blue- Langmuir fitting, green - Freundlich fitting.

The performance of MOF-808@amino acid, both in terms of adsorption kinetics and capacity, is close to the best values reported for MOFs materials so far (Figure 4.16), and rivals the values reported for sorbents as functionalized-carbon, polymers or zeolites.[40,61]
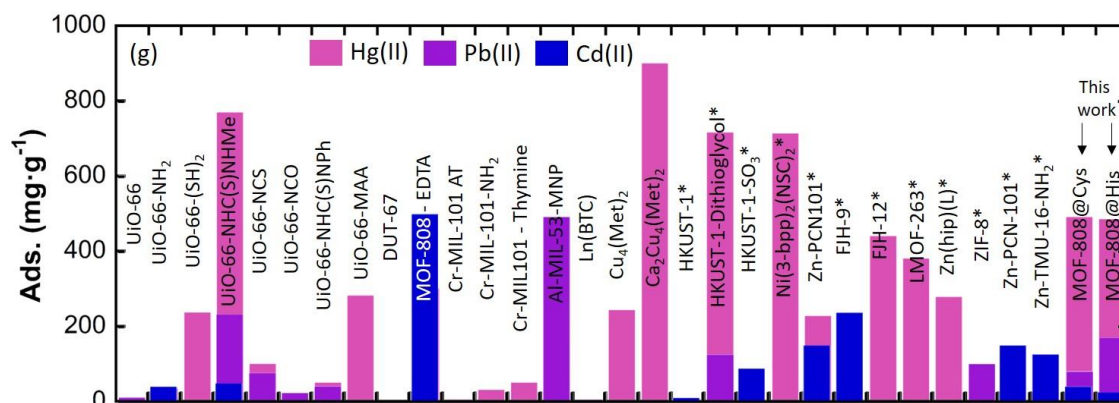

Figure 4.16. Comparison of the MOF-808@His and MOF-808@Cis maximum adsorption capacities over Hg[II], Cd[II], and Pb[II] with previously studied MOFs.

Metal speciation – the case study of MOF-808@Cys and MOF-808@His

Copper was selected as ion-probe to monitor its color and the electron paramagnetic spectroscopy fingerprints once immobilized by MOF-808@(amino) acids. Copper compounds exhibit characteristic colors that are easily linked to its coordination environment and oxidation state. First, during adsorption, the color of the MOF-808@His and MOF-808@Cys dispersions, once immersed in the $CuCl_2$ (100 ppm) solution, were monitored. A fast and drastic color change from green pale ($CuCl_2$) to pale blue and pale-brown was noted in MOF-808@His and MOF-808@Cys dispersions respectively, and 3 hours after the adsorption, MOF-808@His-Cu acquired a more intense blue color (Figure 4.17). The blue color of MOF-808@His-Cu is in good agreement with copper histidine coordination compounds.[62,63] Contrary, the pale brown suspension obtained after the addition of MOF-808@Cys suggests that the copper coordination *via* thiol groups is coupled to its partial reduction.
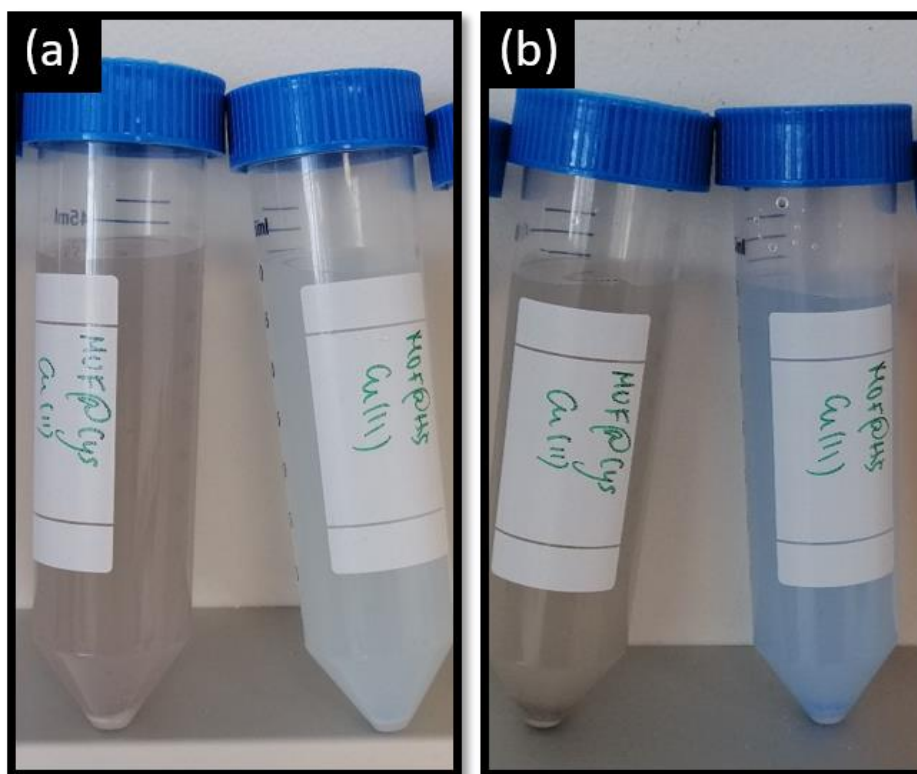
Figure 4.17. MOF-808@Cys and MOF-808@His color changes (a) seconds after adsorbing Cu^{II} and (b) 3 h after adsorbing Cu^{II}.

For sake of comparison, similar experiments were conducted with Cr^{III}, and Cr^{VI} metal ions with Cys functionalized materials. This time, the color of the MOF-808@Cys-Cr^{VI} sample in agreement with the yellow color of the potassium dichromate solution. However, the system evolved after some minutes to the characteristic pale-green color of Cr^{III}, which led us to think that Cr$^{VI}\rightarrow$ Cr^{III} reduction happened concurrently with the Cr^{VI} adsorption (Figure 4.18).[42] Just from the visual inspection of the color evolution, and considered the characteristic UV-Vis adsorption fingerprints of the studied metals (*i.e.* coordination environments, oxidation…), it can be concluded that metal immobilization in MOF-808@(amino) acid system does not only involve amino acid-metal coordination chemistry, but electron transfers processes able to reduce and oxidize the immobilized metal ions.
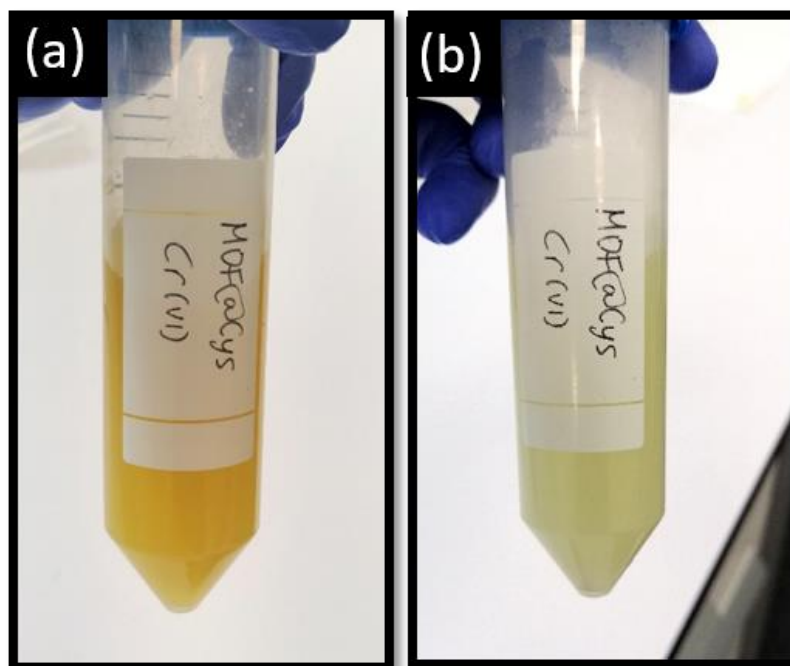
Figure 4.18. MOF-808@Cys (a) just after adsorbing Cr^{VI} and (b) 1 h later.

EPR spectroscopy help us to gain further insights about the metal coordination on MOF-808@amino acid systems. MOF-808@Cys-Cu^{II} and MOF-808@His-Cu^{II} exhibit the characteristic EPR fingerprint of magnetically isolated Cu^{II} complexes with a tetragonal ligand field environments (Figure 4.19a-b).[64] A second signal associated to Cu^{II} clustered ions is also observed jointly with the one of isolates species. The fitting of EPR spectra points to $g\perp$ values of 2.274/2.259 2.063/2.062 (His/Cys) and $g_{\parallel}$ values of 2.274/2.259 (His/Cys). The four-line hyperfine structure allows estimating the $A_{\parallel} = 175 \cdot 10^{-4}/183 \cdot 10^{-4}$ cm^{-1} (His/Cys) and $A\perp = 10 \cdot 10^{-4}/15 \cdot 10^{-4}$ cm^{-1} values too. The obtained g and A values are in good agreement with a highly symmetric equatorial square planar coordination geometry formed by two oxygen and two nitrogen atoms. While this conclusion is highly robust for the MOF-808@His-Cu^{II} sample, it is surprising when cysteine residues are considered as the chelating molecules of the copper ions in the MOF-808@Cys system. The Cu^{II} ions coordination by the thiol groups may involve its partial reduction to Cu^{I}, making Cu-S based metal centers in MOF-808@Cys silent to be detected by EPR.[65] Therefore, Cu^{II} is likely to be coordinated by amine functions. Considering the fact that cysteine amino acid only possesses one amine-group per molecule, the coordination

environment suggested by the EPR data points towards the immobilization of the copper ions *via* at least two different amino acid molecules. In addition, it is important to notice that both MOF-808@Cys-Cu^{II} and His-Cu^{II} systems exhibit clustered copper ions with g values (*i.e.* 2.10 (His), 2.12 (Cys)) that are close to the average of g⊥ and g∥ observed for the isolated species, so when clustered, the coordination environment of the square planar Cu^{II} individual ions is still maintained in the system.[66]
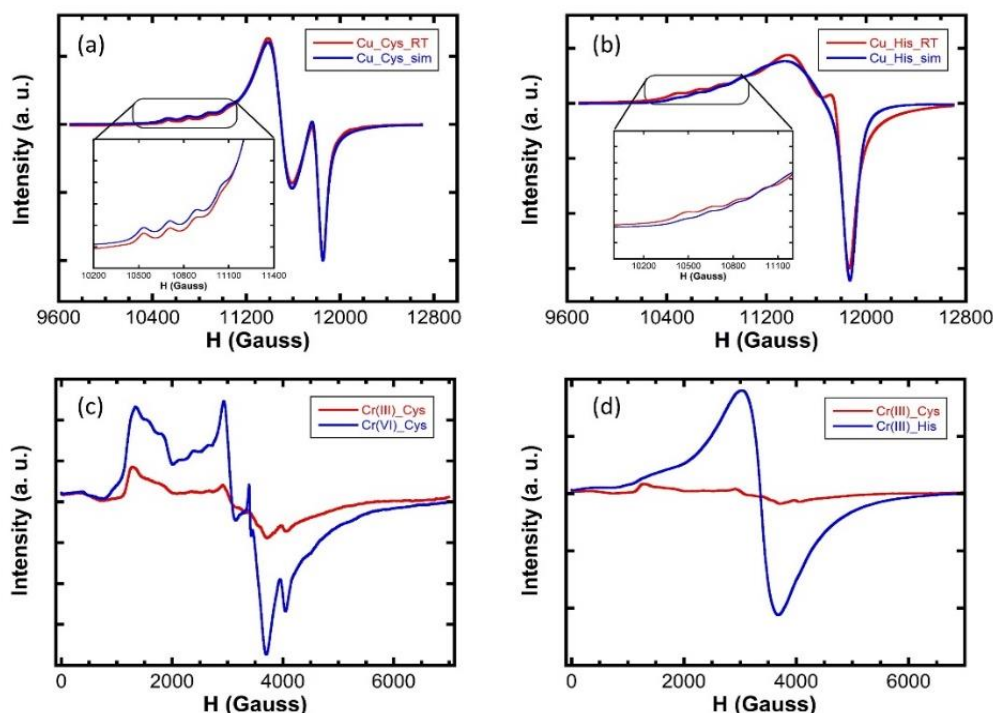

Figure 4.20. Experimental and simulated Q-band EPR spectra of (a) MOF-808@Cys-Cu, (b) MOF-808@His-Cu at room temperature, (c) MOF-808@Cys-Cr^{III}/Cr^{VI}, and (d) MOF-808@His and Cys –Cr^{III}.

A similar strategy was applied to study the metal speciation of Cr^{VI} and Cr^{III} ions in MOF-808@amino acid system by means of EPR. In order to prove the reduction capacity of MOF-808@Cys, Cr^{VI} adsorption experiments were conducted. Cr^{VI} is silent by EPR, but if it is reduced to its trivalent state, it becomes active. For instance, the presence of the characteristic EPR fingerprint of isolated Cr^{III} in MOF-808@Cys sample after the adsorption of Cr^{VI} confirms that reduction process is coupled to the metal ion capture (Figure 4.19c).[67] In fact, the Cr^{III} EPR signal is more intense in MOF-808@Cys after adsorbing/reducing Cr^{VI} in comparison to the one after the direct

Cr^{III} adsorption. This is in agreement with the MOF-808@Cys adsorption capacities for Cr^{III} and Cr^{VI} species shown in the Figure 4.10e. This trend is further accentuated for the MOF-808@His. The broad and high intense absorption band for Cr^{III} in MOF-808@His (g = 1.99) (Figure 4.19d) is indicative of the clustered Cr^{III} ions, which seems logic due to the enormous adsorption capacity that MOF-808@His shows for Cr^{III} (1600 mmol·mol^{-1} - Figure 4.10c).

Although EPR is highlight sensitive to metal coordination variation, it does not give a direct experimental evidence of the functional groups that are participating in the metal ion capture. And thus, a deeper analysis of the metal immobilization process is necessary, which will be provided in the following section thanks to the combination of Raman and Inelastic Neutron Scattering techniques.

4.1.3. CONCLUSIONS

It has been demonstrated that the installation of natural acids and amino acids within a MOF can alter significantly the adsorption capacity and affinity towards metal ions with varied characteristics. In addition, MOF-808@(amino) acids show fast kinetics and outstanding capacity to capture heavy metals even in continuous flow conditions. For instance, the adsorption capacities obtained for MOF-808@(amino) acids rival the figures of the best MOFs reported up to date for HgII, CdII and PbII adsorption. The immobilization of amino acid functions into the pore space of MOF-808 endow the material of metal-complexing mechanisms where single or cooperative metal-binding modes give rise to the stabilization of isolated, clustered, and even, partially reduced species for some specific metals such as copper. We anticipate that amino acid encoding will become an important tool in engineering artificial metal-chelator functions with improved selectivity to trap metal ions from complex mixture. Furthermore, copper doped MOF-808@(amino) acid could resemble the active core sites of some metalloproteins, and thus, in the following section, the catalytic activity of these materials is studied.

4.2. ENCODING BIOINSPIRED COPPER-SITES IN MOF-808 FOR THE WET OXIDATION OF PHENOLIC COMPOUNDS

Nature, through millions of years of evolution, has found sophisticated ways to coordinate metal ions in precise and unconventional ways in order to reach outstandingly effective and selective biocatalysts.[68–70] Through the sequential assembly of simple repetitive units, biology has built up complex three-dimensional scaffolds of metalloproteins, which deposit functional amino acid residues able to coordinate the metal catalytic site in specific spatial configurations.[71] The chemical arrangement of the amino acid residues that conforms the first and second coordination environment of the metal-sites plays a key role in defining the activity and selectivity of metalloenzymes.[72,73] Thus, a mutation or alteration of any of the amino acid residues that coordinate the metal-site placed into the heart of the metalloenzyme, affects drastically their efficiency, selectivity and function. In fact, metalloenzymes are artificially modified by surgically altering the amino acid sequence that controls their metal-site coordination environment.[74,75]

In this respect, an important example is the case of copper metalloenzymes, where the coordination of copper ions is usually completed by histidine, cysteine and carboxyl residues, or a combination of these.[76–80] Depending on the copper-biocatalyst, Cu^{II} ions are stabilized as isolated and/or clustered sites able to carry out oxidative catalytic reactions based on the activation of oxygen (e.g. laccases[81–83]) or hydrogen peroxide (e.g. peroxidase) molecules.[84,85] The overall selectivity and oxoreductive efficiency of copper-enzymes over a specific substrate is partially defined by the coordination modes of the copper sites.[64,86–90] Furthermore, the oxidative capacity of copper bio-catalysts has important technological implications in water remediation, since it can be adapted to degrade highly concerning and persistent phenolic compounds *via* Catalytic Wet Peroxide Oxidation (CWPO).[91–94] CWPO is a low-cost, low-temperature and environmentally friendly Fenton process able to drive the degradation of phenolic compounds *via* the activation of hydrogen peroxide to hydroxyl radicals [95] with the participation of a catalyst.[91,96,97]

Despite the great potentials of oxidoreductase-like biocatalysts for water remediation applications, their cost of production and low chemical stability window (*i.e.* pH, temperature, ionic strength…) still limits their practical application[68]. As an alternative and highly appealing solution, extensive research is being carried out to replicate and expand the metalloenzymes' pockets and catalytic activity to robust porous materials.[98–100] In this regard, the chemical encoding of bio-catalytic like sites into MOFs holds an enormous promise.[100–107] Once the pore space has been decorated with specific amino acid moieties, metal-sites can be easily installed by adsorbing them from aqueous or non-aqueous solutions.[108–111] Furthermore, the enzymatic-like catalytic activity dependence of the characteristic of the copper-metal ions installed into MOFs has already been studied for reactions alternative to CWPO.[12] Within these recent investigations, it is interesting to highlight the low temperature methane to methanol oxidation performed with copper decorated MOF-808@Histidine and NU-1000-Cu[112] systems, or the peroxidase oxidative degradation of phenols by copper doped UiO-67-Bpy[113] material, or copper decorated zirconium oxides derived from UiO-66.[114] In addition, MOFs directly assembled with copper ions, as copper-trimesate[115] or copper-benzene dicarboxylate,[116] also exhibit outstanding oxidative functions to degrade phenols, but their hydrolytic instability may prevent their application in water remediation processes.

In this work, we study the copper immobilization into some of the materials developed in the previous section (*i.e.* Cys, His, Msc, Mal and Cit), investigating the different coordination modes and clustering degrees they show. Moreover, the multivariate MOF-808@HisCys is synthetized, combining into the same MOF pore space the two amino acids that are most commonly found in copper metalloproteins. The efficiency and selectivity of our system to oxidize phenolic pollutants (*i.e.* phenol, 2,4,-dichlorophenol, catechol, hydroquinone, or dopamine) through CWPO have been duly assessed. The results presented in this work represent a milestone for the installation and artificial evolution of metal-amino catalytic sites into the robust architectural backbone of MOFs, which successfully mimic those oxidative functions of macromolecules such as metalloenzymes.

4.2.1. EXPERIMENTAL PROCEDURE

MOF–808 synthesis and functionalization

The MOF-808 synthesis and functionalization was performed following the same experimental protocol applied in section 4.1.1 of this chapter. For the synthesis of the multivariate MOF-808@HisCys, a solution with a 0.025 M concentration of Cys and 0.025 M of His was employed, and then the same procedure as in section 4.1.1 was followed.

MOF–808@(amino) acid copper metalation

100 mg of MOF-808@(amino) acid were immersed in 50 mL Cu^{II} solutions of 10, 50, 100 and 1000 ppm concentrations during 15 min. After that, the samples were recovered by centrifugation (x 7000 rpm) , washed with water (100 mL, 2 times) and methanol (100 mL, 2 times) over three days, and dried at RT in a desiccator for 24 h.

Catalytic Wet Peroxide Oxidation of phenolic compounds

The catalytic activity of MOF-808@His doped with a copper solution of 100 ppm (MOF-808@His-Cu100) was measured *via* a chromogenic reaction of phenolic compounds with 4-aminoantypirine (4-AP). In brief, for laccase like activity, 100 µL of an aqueous solution of the phenolic pollutant (1 mg·mL^{-1}), 500 µL of 4-AP (1 mg·mL^{-1}), 100 µL of the bioinspired catalyst (1 mg·mL^{-1}) were added. To test the CWPO capacity of the sample, 20 µL of H_2O_2 were added. When the laccase-like activity of the sample was tested, the addition of H_2O_2 was omitted. The volume of the reaction was completed with distilled water until a total of 1 mL. The reactor was shaken during specific periods of time, centrifuged at 10000 rpm during 1 min and the absorbance of the supernatant was measured by UV-Vis at 510 nm. Each of the reactions where fitted to a first order kinetic model (Equation 2.17 in Chapter 2) to obtain the k-rate of the substrate oxidation.

In order to follow the byproduct generation of the phenol substrate, an extra experiment was performed using liquid chromatography. To this end, the reaction was

scaled up to 20 mL but avoiding the addition of 4-AP co-reagent. Aliquots were taken and filtered with 0.2 μm hydrophilic PTFE syringe filter at 0, 15, 30, 60, 90, 120, 180, 240 and 1200 min. The complete mineralization of phenol through oxidative processes involves an initial step where catechol, hydroquinone or benzoquinone byproducts, whose toxicity excesses the one of phenol, are formed. At this stage, it is key that the catalysts further oxidize these byproducts until the rupture of C-C bond in benzoquinones led to the formation of environmentally friendly carboxylic acids. Further oxidation of these acids would lead to the complete mineralization of phenolic compounds.

For the study of the influence of the pollutant concentration, 100 μL of an aqueous solution of the phenolic pollutant with a concentration from 0.1 to 2 mg·mL^{-1} were used, and quantities of the rest of the materials were maintained the same. For these reactions, the K_M and V_{max} kinetic parameters were obtained from the fitting of the Michaelis-Menten plot to the model described by the Equation 2.18 in Chapter 2.

Once the laccase and CWPO activity for the MOF-808@His-Cu100 were studied, the impact of (i) the copper loading within the same host porous matrix and (ii) the coordination environment of the copper ions on the catalytic activity for the oxidation of hydroquinone and 2,4-dichlorophenol were studied. To this end, MOF-808@His with different Cu^{II} loadings and MOF-808 functionalized with various (amino) acids were used as catalysts.

The following reaction conditions were employed to compare the oxidation reactions starting from batch solutions/dispersions of 1g·L^{-1} concentration. Hydroquinone (HQ): 200 μL of catalyst, 200 μL of HQ and 500 μL of 4-AP solutions, 20 μL of H$_2$O$_2$ and 1080 μL of H$_2$O. 2,4-dichlorophenol (2,4-DCP): 150 μL of catalyst, 300 μL of 2,4-DCP and 500 μL of 4-AP solutions, 20 μL of H$_2$O$_2$ and 1030 μL of H$_2$O. The aliquots taken from the reactions at 0, 5, 10, 15, 30, 45, 60, 90 and 120 min were treated as above described for the previous reactions.

4.2.2. RESULTS AND DISCUSSION

MOF-808 functionalization

MOF-808 synthesis and (amino) acid functionalization was performed following the same procedures as in section 4.1. In order to compare the multivariate MOF-808@HisCys to the other functionalized samples, the XRD spectra and N_2 adsorption isotherms have been plotted in Figure 4.20.

As concluded from the XRD data, the crystallinity, the position, and the relative intensity of the diffraction maxima for MOF-808@(amino) acids remain similar to the ones of the parent material (Figure 4.20a). As expected, the disorder of the installed (amino) acid function does not contribute to modifying significantly the main XRD signature of the compounds. A slight reduction of the surface area after the SALI was found for MOF-808@HisCys, similar to the ones reported for the other functionalized MOFs, and in good agreement with previous post-synthetic functionalization studies (Figure 4.20b).[117]
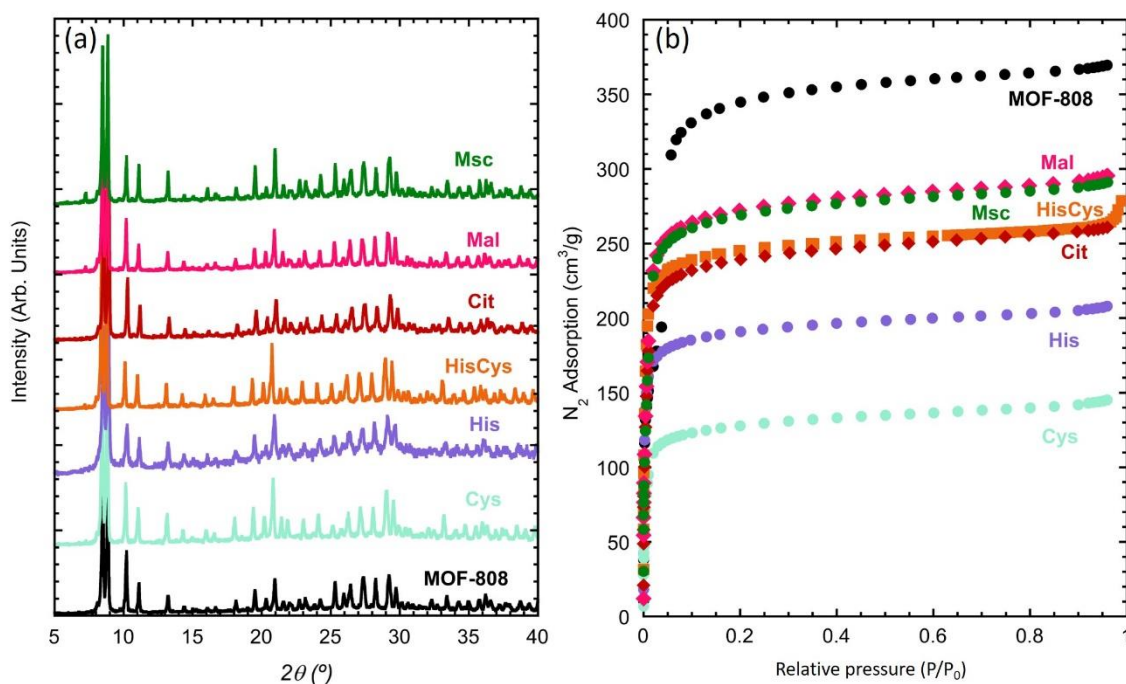

Figure 4.20. (a) X-ray powder diffraction patterns and (b) N_2 adsorption isotherms (77 K) of parent MOF-808 and MOF-808 (amino) acid functionalized materials

Similarly than for the MOF-808@(amino) acid samples, the BTC:amino acid ratio for MOF-808@HisCys multivariate material was determined from the integration of the proton signatures of BTC and amino acids in the ^{1}H-RMN spectra of the digested samples, showing an amount of 3.3 cysteine and 2.7 histidine molecules per cluster.

Copper immobilization

The metal immobilization in MOF-808 was carried out by the direct adsorption of copper ions from aqueous solutions of 10, 50, 100 or 1000 mg·L^{-1} concentration. The Cu^{II} loading into the MOF-808@His was controlled by increasing the concentration of the metalation solution. The concentration of the copper loading for the other MOF-808@(amino) acid samples studied in this work was controlled to get a final Cu^{II} doping of the material similar to the one obtained for the MOF-808@His-Cu100 sample.

Immediately after the MOF-808@(amino) acid materials contacted the copper solution, it turned an intense light blue to green color that depends on the amino acids installed into the framework. For instance, the Mal and Cit variants of MOF-808 exhibit a pale blue-greenish color, the His functionalized compound gains an intense dark blue color, whilst the Cys and Msc variants exhibit a light to dark brown coloration that suggests the existence of mixed valence Cu^{I} and Cu^{II} species after metalation. As will be alluded to later, the color of the copper coordination complexes is closely related to their electronic structure, and hence, to their spectroscopic signature.

Fluorescence X-ray spectroscopy measurements of the solid samples after copper installation have allowed the estimation of the cluster/copper and ligand/copper molar ratios of our biomimetic catalysts (Table 4.4).

Table 4.4. Summary of the catalyst composition after copper metalation

Sample	[Cu] ion in the metalation solution (mg·L^{-1})	Cu/Zr$_6$	Cu/L	Cu (%)*
His-10	10	0.18	0.04	2.02
His-50	50	0.65	0.14	6.86
His-100	100	0.89	0.22	9.16
Cys-100	100	1.18	0.42	11.77
His/Cys-100	100	1.16	0.19	11.65
Msc-100	100	2.38	0.61	21.12
Mal-1000	1000	0.40	0.10	4.36
Cit-1000	1000	0.76	0.13	7.91

*These data are obtained from the normalization of the sum of weight percentages for Zr and Cu ions to 100% in the FRX measurements.

For the samples doped with copper solutions of 100 ppm or below, the XRD patterns remain mostly unchanged after the metalation process (Figure 4.21). It is important to note as well, that Cu-adsorption in copper solutions of 1000 ppm induce a significant loss of crystallinity in the parent His and Mal based compounds (Figure 4.21b,e), but not in the other MOF-808@(amino) acid variants studied in this work. So, in general terms, the MOF-808@(amino) acid materials are robust enough to resist the copper metalation process.
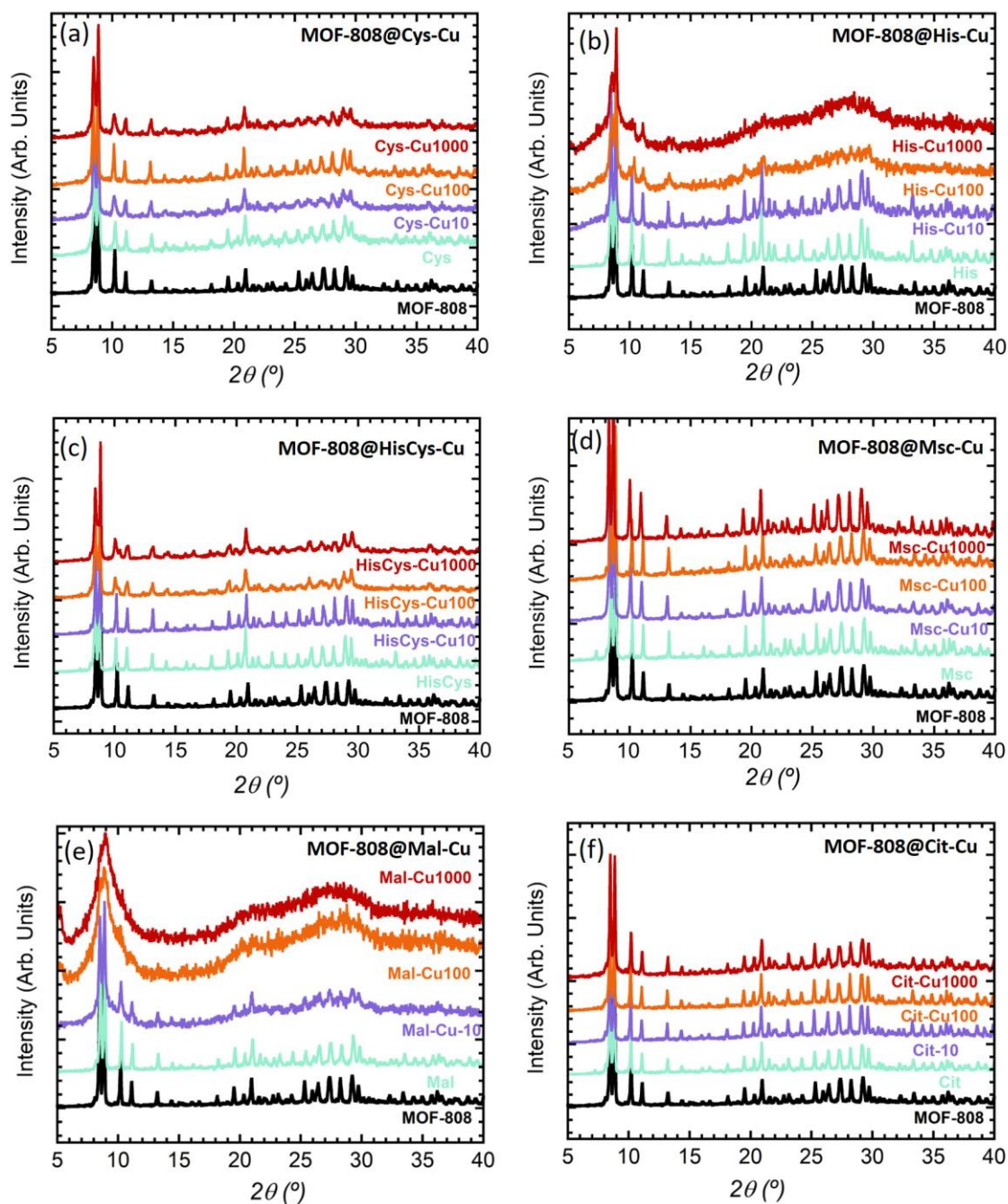
Figure 4.21. X-ray powder diffraction patterns of MOF-808 and functionalized MOF-808 materials before and after their doping with copper ions with water Cu^{II} solutions of 10, 100 and 1000 ppm concentrations.

Combined characterization of the copper catalytic sites

The copper complexation within the MOF will induce a significant tuning on the electronic structure and spectroscopic properties of the catalytic sites. The benefits of

selecting copper as the probe metal-ion is that its UV-Vis, EPR and XPS spectroscopic fingerprints are intimately linked to (i) the groups conforming its coordination sphere, and (ii) the monomeric or clustered nature of the copper-complexes formed during its binding to the (amino) acid residues installed into the pore space of MOF-808. In addition, there is a vast background on spectroscopy and magnetism of Cu-complexes that can be employed to understand such a complex and disordered system as the one studied in our bioinspired materials. Futhermore, copper adsorption also induces a variation of the spectroscopic signatures of the host MOF-808@(amino) acid matrix that are related with the copper stabilization process.

Raman spectra of the pre and post-functionalized and metalated compounds show slight but significant variations of the absorption bands involved or affected by the metal-coordination (Figure 4.22). MOF-808 decorated with di (Mal, Msc) and tricarboxylic acids (Cit), shows the characteristic absorption band associated to the C=O double bond, which indirectly indicates the presence of protonated carboxyl groups at the pore space of the material (Figure 4.22a-d). The vibrational modes associated to the C-O bonds participating in the coordination of zirconium clusters appear at lower energy values than the ones associated to the C=O protonated groups.[118] After copper adsorption, this band is drastically attenuated, indicating the deprotonation of the free-carboxyl groups, and indirectly, their coordination to copper ions.

For Msc, Cys and HisCys variants, the weak Raman bands associated to the -SH stretching vibration (~ 2500 cm^{-1}), have been identified (Figure 4.22a,f,g). However, in Cys sample the signal is almost suppressed, probably due to Cys-Cys interactions through sulphide groups. Contrary, in Msc sample, the signal corresponding to the S-H bond is clearly visible in the Raman spectra. As expected, the v_s(SH) is blocked after the absorption of copper ions by MOF-808@Msc because of the deprotonation of SH groups resulting from the formation of Cu-thiolate bridges.

Finally, the HisCys variant shows also a weak signal corresponding to v_s(SH). This band does not lose intensity after the copper adsorption, which could mean that the Cu^{II} is preferably immobilized within the imidazole or amino groups of the sample. In fact, both HisCys and His variants show significant modification of the Raman

bands associated to the stretching vibration of C-H bonds of the imidazole rings (Figure 4.22e,g). Therefore, it seems that the vibrational freedom of imidazole residues is as well attenuated after copper installation, either because they are directly or indirectly involved in the copper adsorption.
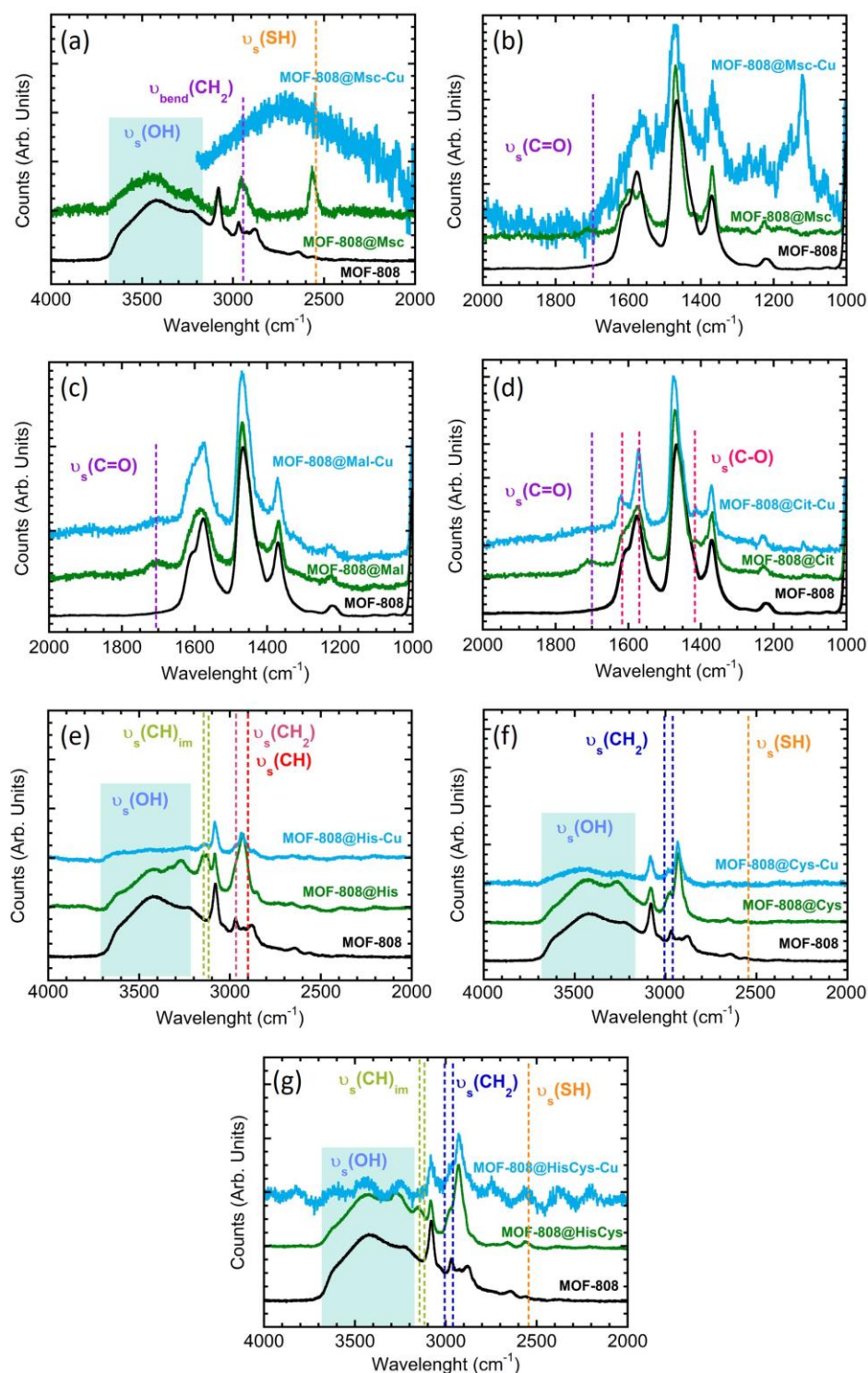

Figure 4.22. Raman spectra of MOF-808 functionalized with (a-b) Msc, (c) Mal, (d) Cit, (e) His, (f) Cys and (g) HisCys before and after copper immobilization.

Spectroscopic information obtained from Raman was completed with Inelastic neutron scattering (INS) data for the Histidine and Cysteine variants before and after the copper immobilization.

At a first step, the vibrational bands of the INS data of MOF-808, cysteine and MOF-808@Cys samples were identified on the basis of the bibliographic data (Figure 4.23a).[119] Among the differences observed between the free Cys and MOF-808@Cys spectra (Figure 4.23a), the disappearance of the INS bands associated to the COOH vibrations (CO_2 rock at ~500 cm^{-1}) is in good agreement with the anchoring of the Cys molecules to the zirconium clusters of the framework *via* the carboxyl groups. In addition, both the disappearance of the NH_3 torsion vibration (~300 cm^{-1}), together with the displacement to lower energies of the other bands associated to the Cys molecule, clearly indicate that once immobilized, the interactions of the Cys with the framework and the adjacent Cys molecules alter the vibrational modes of the molecule, blocking even some of their intramolecular vibrations. It is important to note that the assignment of the NH_3 torsion vibrational mode to the INS band located at 300 cm^{-1} is not fully clear, since some of the bibliographic data indicate that this vibration is usually located at slightly higher wavelength values around 400 to 500 cm^{-1}. Indeed, the vibration of the cysteine skeleton could as well be related to this signal. In order to clarify this point, Density Functional Theory (DFT) calculations of the isolated molecules: free cysteine, and a model of two cysteine molecules coordinating a Cu^{II} ion in a bidentate fashion were performed (Figure 4.24), and then the calculated INS spectra were obtained. In this calculations, the NH_3 torsion vibration is located at 300 cm^{-1}. Although the intensity of the INS signal for these simplified models is not representative of the one that would be obtained in an ordered crystal environment, the energy values associated to the vibrations are accurate enough to stablish qualitative comparisons. Two are the main spectral variations observed when the cysteine is anchored to the MOF: (i) the vibrational modes of COOH and NH_3 disappear, and (ii) the bands associated to the CH, CH_2, and the bending and rocking modes of SH and NH_3 groups, respectively, gain intensity in comparison to the ones of the free cysteine. It is important to note that the signals associated to the bending and rocking modes of SH (~ 975 cm^{-1}) and NH_3

(~ 990 cm^{-1}) groups in free cysteine molecules seem to be shifted to the same position in the MOF-808@Cys compound (~ 975 cm^{-1}).
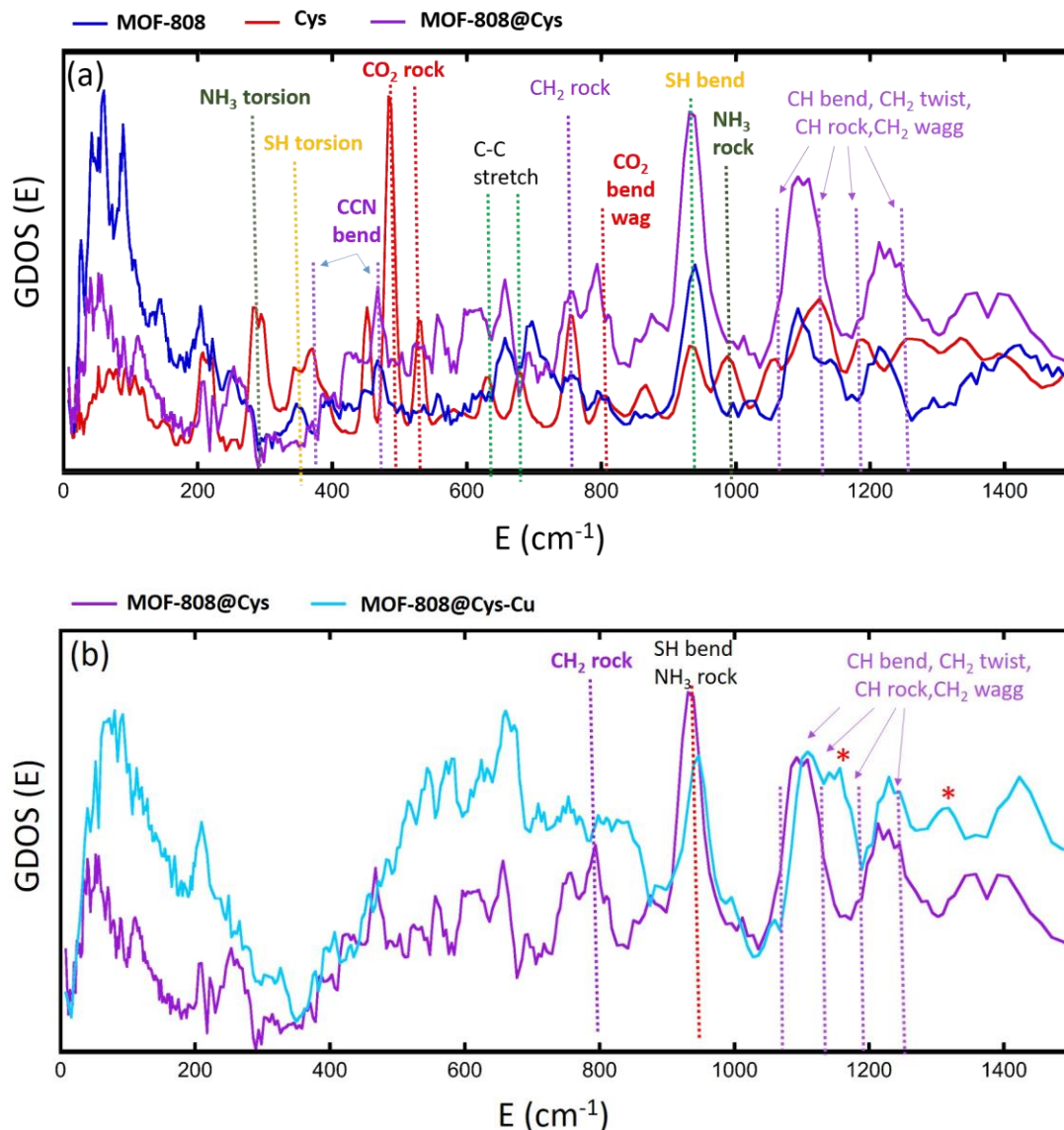

Figure 4.23. Inelastic scattering spectra of (a) MOF-808, L-cysteine and MOF-808@Cys and (b) MOF-808@Cys after and Cu^{II} adsorption.

Among the INS bands affected by the metal adsorption (Figure 4.23b), the intensity of the signal located at 950 cm^{-1} energy is slightly reduced in comparison to the initial MOF-808@Cys. The band was initially assigned to the combination of the bending vibration of SH and the rocking vibration of NH$_3$ groups. This band assignment was

done taking into account the work performed by Stewart F. Parker *et al.*,[119] as well as the INS spectra calculated from the vibrational modes of free Cys molecules. In addition to the subtle intensity loss, Cu^{II} adsorption induces a slight displacement of the signal to higher energy values. The metal coordination of sulfide groups by Cu^{II} ions would induce a deprotonation to S^- anions, and thus, to a reduction of the INS signals associated to the SH vibrational modes (~ 950 cm^{-1}).

In contrast, as revealed by many metal-coordination complexes found in the CSD database, the coordination of NH_3 groups to Cu^{II} usually induces a deprotonation of the ammonium to amine, so the vibrational modes associated to NH_2 functions are still active after the metal complexation, although maybe displaced to a slightly different energy values. Thus, revisiting our first assignment of the band located at 950 cm^{-1}, it seems that the SH's vibrational modes contribution is not so relevant as the one of NH_3 rocking vibrational mode to this signal of the INS spectra. This conclusion is based on an active participation of the -SH groups to the metal-chelation of Cu^{II} ions, that finally would lead to a significant reduction of the intensity of the band.

In parallel, the suppression or the variation of the -CH_2 rocking vibrational mode after Cu^{II} adsorption, as well as the appearance of two new INS signals (1150 and 1325 cm^{-1}), marked with asterisks in the Figure 4.23b, within energy region of CH bend, CH_2 twist, CH rock and CH_2 wagg vibrational modes for Cu^{II} loaded MOF-808@Cys variant, offer the keys to further understand the Cu^{II} uptake mechanisms. Considering that the Cys-Cu^{II} complex could be similar to the Cys-Pb^{II} complex proposed by F. Jalilehvand *et al.*,[120] a bidentate coordination of the SH and NH_3 groups to the Cu^{II} could give rise to the complete blocking of the CH_2 rocking mode, since its vibrational freedom would be severely restricted if the metal ion is linked to both SH and NH_3 terminal groups of the cysteine molecules. This binding mode, where SH groups are involved, explain the slight reduction the INS band at 950 cm^{-1}. Copper complexation by cysteine seems to be governed by its preferential binding to the thiol groups. A Cu-S-Cysteine monodentate binding mode (Figure 4.5a), or even a dual coordination of the copper ions by two adjacent cysteine molecules *via* S-Cu-S bridges (Figure 4.5d), would suppress the CH_2 rocking

vibrational mode, but also would give rise to the modification of the CH bend, CH_2 Twist, CH rock and CH_2 wagg vibrational modes. For instance, in addition to the main population of copper ions stabilized as Cu^{II} and Cu^{I} within the MOF-808@Cys *via* cysteine groups, it is important to take into account that there is a population of copper ions that are coordinated as well *via* amine groups, as revealed by EPR spectroscopy in the section 4.1.[121] This dual stabilization mode of copper could explain the complexity of the INS region CH bend, CH_2 Twist, CH rock and CH_2 wagg vibrational modes in comparison to the initial MOF-808@Cys compound.
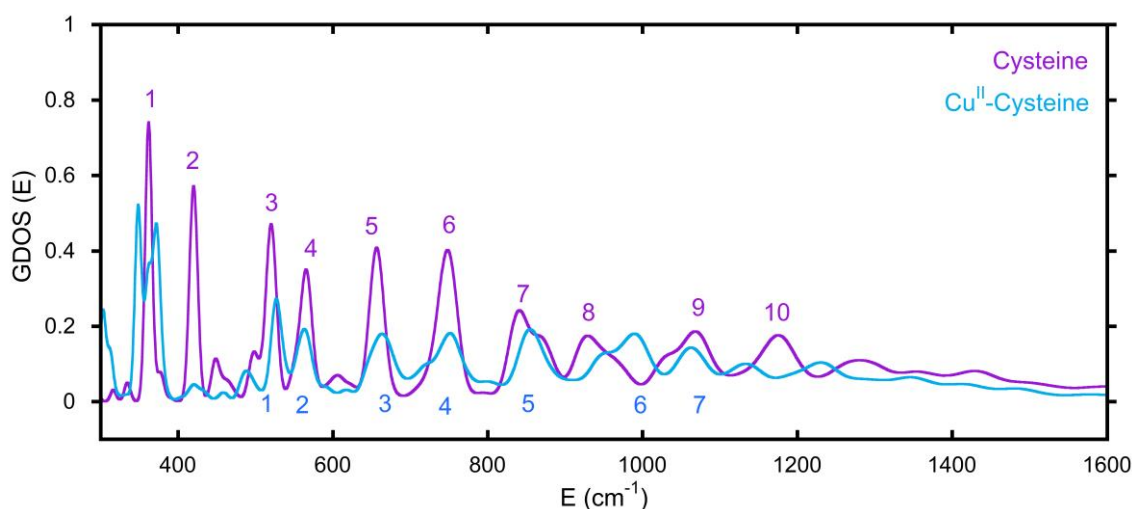

Figure 4.24. INS spectra simulated from the free cysteine model and the Cu-Cys2 bidentate complex shown in the Figure 4.5d.

Table 4.5. Inelastic scattering bands assignation of the simulated spectra of Cysteine and Cu^{II}-Cysteine complex of Figure 4.24.

Cysteine main INS signals (cm⁻¹)		Cu^{II}-Cysteine main INS signals (cm⁻¹)	
1 - 363	NH_3		
2 - 418	$NH_3 + SH$		
3 - 506	$NH_2 + CH$	1.- 526	$CH + NH$
4 - 581	All	2.- 561	All
5 - 661	Stretch SC + rocking CH	3.- 664	All
6 - 750	$SH + CH_2$	4.- 750	NH_2 (no SH)
7 - 869	SH + All bending	5.- 856	CH_2
8 - 928	NH + SH	6.- 989	NH_2
9 - 1067	$SH + CH_2 + NH_2$	7.- 1061	CH_2

A similar study was performed to gain information from the INS spectra obtained for MOF-808@His and MOF-808@His-Cu system. The vibrational bands of the INS data for these samples were identified on the basis of the bibliographic data based on the combination of experimental and computational studies (De Sousa *et al.*[122] and Freire *et al.*[123]). In addition the band asigment of the MOF-808@Cys sstem studied before has been taken into account too. The bands assignation for the MOF-808@His compounds have been summarized in Figure 4.25 and Table 4.6.

Table 4.6. Inelastic scattering bands assignation for MOF-808@His. The number assigned to each vibrational modes are related with the number depicted in the INS spectra shown in the Figure 4.25. In the INS column, the position of the bands before and after the metalation has been detailed.

Band	IR	Raman	INS	Assignment
1	1416	1449 1416	1416 →1435	Ustr. (CN)$_{im}$ + Ustr.(CN)$_{im}$
2	1337	1334-	1330 → 1315	δ(NH)im + Ustr.(CN)im
3	---	1262	1225 →1240	CH_2 + NH_3 bend
4	1144	1143	1160 →1160	Twist (NH_2) + bend (CH) + str. (NC)$_{im}$
5	1120	---	1095 →1110	wag.(NH_3) + bend (CH)
6	959	977	996 →998	r(NH_3) + δ(CH)
7	875-1000		940 → 945	Ʊ(CC) MOF + His
8	868	874	860 →860	Mixed vibr. NH_3 + δ(CH)
9	---	803	817 →810	Def. (Im) + δ(NH_3) δ(CH)
10	696	694	660→660	δ-ofp (CH)im
11	631	645	630 →639	δ-ofp (CH)im
12	---	604	--- →580	def.(Im) + δ (CCN)
13	528	540	--- →552	def.(Im) + δ (CH_2)
14	---	---	475 →475	δ(COH)
15	---	----	350 → ---	Skeletal vibrations of His+ t(NH_3)

Firstly, the incorporation of histidine molecules into the MOF induces the disappearance of the INS bands associated to the -COOH vibrations of the amino acid. Although in this study we could not measure the base histidine sample, it is well known that the CO_2 rocking and COH bending modes of amino acids are usually located around 530 and 500 cm^{-1} respectively. However, these bands are not observed in the MOF-808@His, due to the anchoring of the amino acid to the cluster from the carboxyl group (Figure 4.25).
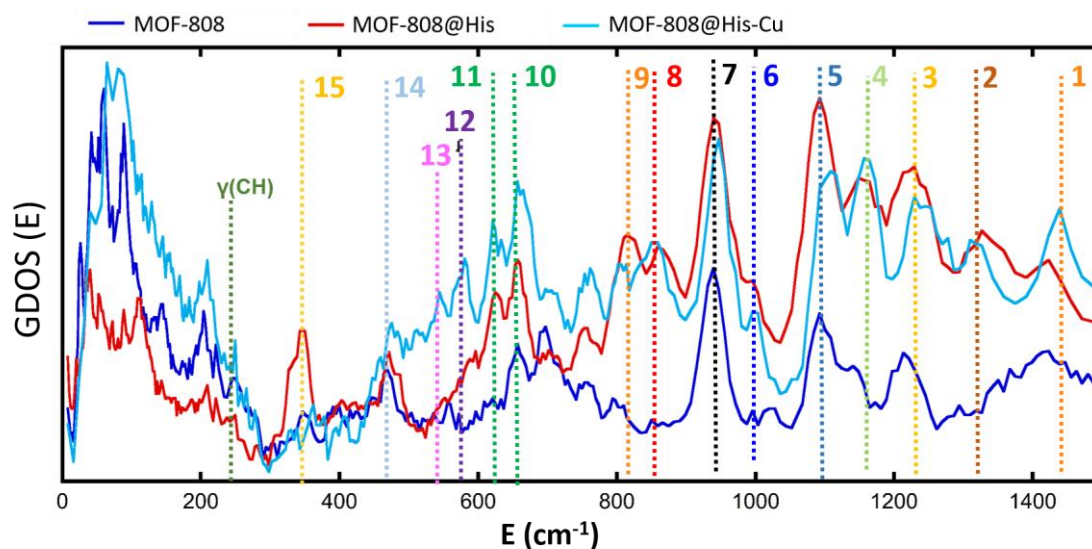
Figure 4.25. Inelastic Neutron Scattering spectra of MOF-808@His sample before and after its copper metalation. . The bands have been identified by a number code. The code is used in the table 4.5 to identify the vibrational mode assigned to each INS signal.

It is important to highlight the variation of the band located at ~350-400 cm^{-1}, which can be tentatively ascribed to two possible vibrational modes: (i) the torsion vibration of NH_3^+ and (ii) the skeletal vibration of the histidine molecule. In contrast to the MOF-808@Cys homologue studied previously, the NH_3^+ torsion or the skeletal vibration of histidine molecules are not attenuated after its incorporation into the MOF. Thus, strong intermolecular interactions between His molecules are not expected within the MOF pore space. This vibrational mode located at 375 cm^{-1} is one of the most affected by the copper installation. This can be easily understood, since independently from the single or cooperative mechanisms of the histidine molecules to coordinate copper ions, the mobility of the molecules incorporated within the MOF-808 pore space may be severely restricted once copper ions are directly linked to them. In parallel, as observed in many copper-coordination compounds, amino functions are prompt to form part of the coordination sphere of copper ions forming Cu-N bonds. Therefore, any coordination of the His molecules to the copper ions through the amino groups is likely to suppress some of the vibrational modes associated to associated to it ($\tau(NH_3)$, but also to restrict the overall skeletal vibration of the hole molecule ($\upsilon(sk)$).

In parallel, there are several signals of the INS spectra that do not disappear during metalation, but that experiences a slight attenuation or a shift of their positions. These are the cases of the bands 1, 2, 3 and 5. Indeed, the bands 1 and 2 are closely related to the stretching vibrational modes of the C-N bonds within the imidazole groups. In parallel, the bands 3 and 5 are linked to the bending and wagging vibrations of NH_3. Although all these slight variations do not give a direct evidence of the copper coordination to the imidazole or the amino groups in the histidines, it is clear that the metalation process induces some adaptation of their vibrational freedom. As the copper coordination by imidazole molecules would imply the deprotonation of the imidazole rings, this need to be reflected in the vibrational modes involving the N-H bond within this group. In contrast, we do not observe any intensity reduction of the band 2, which is directly related to the deformation vibration of the NH group within the imidazole rings. This does not discard that the vibrational modes of the imidazole rings are not altered after the copper installation into the material, as is reflected in the intensity gain of the out of plane vibration of C-H bonds within the ring (bands 10 and 11), and the appearance of the 12 and 13 bands, also related with the deformation of the imidazole rings.

All in all, it can be concluded that not all the imidazole rings participate in the coordination of copper ions. This does not preclude that the coordination of copper ions by the NH_3^+ affected the vibrational energy of imidazole rings, as observed in the displacement of the bands associated to this group. Since the coordination of the copper ions by the NH_3^+ groups of His does not involve their deprotonation, a complete disappearance of the INS vibrational modes after the metalation of the MOF-808@His is not expected. For instance, the slight variations on the relative intensities of the rocking vibration of NH_3^+ and stretching vibration of CN bonds further indicate that amino groups have an active role during the immobilization of copper ions within the material.

Copper is most usually stabilized in biocatalysts as Cu^{II} paramagnetic ions with a ($3d^9$) electronic configuration. Nevertheless, it is important to note that cysteine rich peptides or metalloenzymes can isolate it in its reduced intermediate form, as $3d^{10}$ Cu^I diamagnetic centers. More specifically, Cu^{II} prefers tetragonally distorted

(compressed or elongated) octahedral, tetra- and penta-coordination environments showing the well-known Jahn-Teller effect.[124] In addition to this, the nature of the amino acid residues forming part of the copper coordination sphere significantly alters the electronic structure of this 3d^9 ion, and hence, its UV/Vis and EPR spectra. For example, the $[Cu(H_2O)_6]^{2+}$ ideal complex exhibits three electronic transitions that collapse into a single UV-Vis absorption band located approximately at 780 nm. The replacement of coordinated water molecules in $[Cu(H_2O)_6]^{2+}$ by stronger electron donors, as peptide N > NH$_2$ > imide > COO$^-$ > H$_2$O, displaces the UV-Vis absorption maximum of copper complexes to higher energy wavelengths, as is the case of our MOF-808@(amino) acid biomimetic systems.

The UV-Vis spectra of copper doped MOF-808@(amino) acids showed absorption maxima associated to the metal to ligand charge transfer bands (< 350 nm), and to the ^2E_g → $^2T_{2g}$ transition of copper ions (800 – 600 nm) (Figure 4.26a). Copper ions stabilized by citric (770 nm) and malic (795 nm) acid functionalities exhibit a UV-Vis maximum slightly displaced to the blue and the red in comparison to the $[Cu(H_2O)_6]^{2+}$ ideal ion (780 nm), respectively. Cysteine molecules induce a significant red-shift of the UV-Vis absorption maxima to 670 nm; whilst His/Cys multivariate material and His variant further displace the absorption to 630 and 620 nm, respectively.

Overall, the position of the copper UV-Vis absorption maxima (λ_{max}) can be qualitatively calculated based on the nature and the number of the groups forming part of the coordination environment of the copper ions if the empirical equation obtained by Sigel and Martin is applied.[125] The λ_{max} for Mal (795 nm) and Cit (770 nm) compounds fits with copper's equatorial plane formed by two coordinated water molecules and two carboxyl groups (calc λ_{max} = 790 nm). When analyzing the UV-Vis signature of the Cys variant (λ_{max} = 690 nm), the equatorial coordination mode of the copper ions seems to consist of two amine groups and a couple of water molecules (calc λ_{max} 663 nm). At first sight, this conclusion seems counterintuitive given the great chemical affinity of thiol groups for copper thiolate bonds. Nevertheless, the increase of the overall UV-Vis background signal for Cys and Msc variants suggests the co-existence of Cu^{II} and Cu^{I} mixed species that lead to electron-transfer processes. That is, when thiol groups are involved in the coordination of Cu^{II} ions, they induce

its partial reduction to Cu^I. This conclusion is as well in agreement with the Cu^{II}/Cu^I mixed valence speciation found in many copper-thiolates. In the specific case of His and multivariate His/Cys variant, the displacement of the UV-Vis λ_{max} to higher energies suggests the participation of at least an imidazole and an amino group (calc λ_{max} 648 nm) or of two imidazole groups (calc λ_{max} 634 nm) in the copper coordination.

The configuration of the copper ions within the MOF-808@(amino) acid systems is not only shaped by the type of coordinating groups, but by the degree of copper loading. When a low concentrated solution is used to install the copper ions within MOF-808@His, the UV-Vis absorption maxima is located at 620 nm (Figure 4.26b). This value fits better with a coordinated mode involving two imidazole rings. If the concentration of the copper solution is increased, the λ_{max} shifts to 640 nm, a value that suggests the participation of amine groups in the copper-coordination. Therefore, copper ions first occupy preferential adsorption sites at imidazole rings, and once saturated are stabilized by amine groups. This copper stabilization mechanism does not only have implications into the spectroscopic signature of the ion, but on its EPR signal too (Figure 4.26d).

The MOF-808@His-Cu10 (doped with a 10 ppm copper solution) exhibits the characteristic EPR fingerprint of magnetically isolated Cu^{II} complexes with tetragonal ligand field environments consisting of a central EPR absorption signal of (g⊥ = 2.274 and g$_{\parallel}$ = 2.063) completed by four less intense signals associated to the hyperfine structure lines (A$_{\parallel}$ = 175·10^{-4} and A⊥ = 10·10^{-4} cm^{-1}) (Figure 4.26d). Given the g-values obtained for the fitting of the EPR spectra, the copper ions are stabilized in an axially highly elongated system that could involve a square-planar coordination, or an octahedral or pyramid-square coordination with long Cu-H$_2$O bonds (> 2.3-2.4 Å). When the concentration of the copper solution employed to immobilize the ions is increased to 50 ppm (MOF-808@His-Cu50), the EPR spectrum shows the presence of two copper ions with slightly different g values, and hence, a slight variation on the distortion of the coordination environment. This tendency is further accentuated for the MOF-808@His-Cu100, where the EPR spectrum fits with the usual signature observed for copper magnetically clustered systems. The g values estimated by EPR for the MOF-808@His-Cu systems agree with a highly symmetric equatorial square

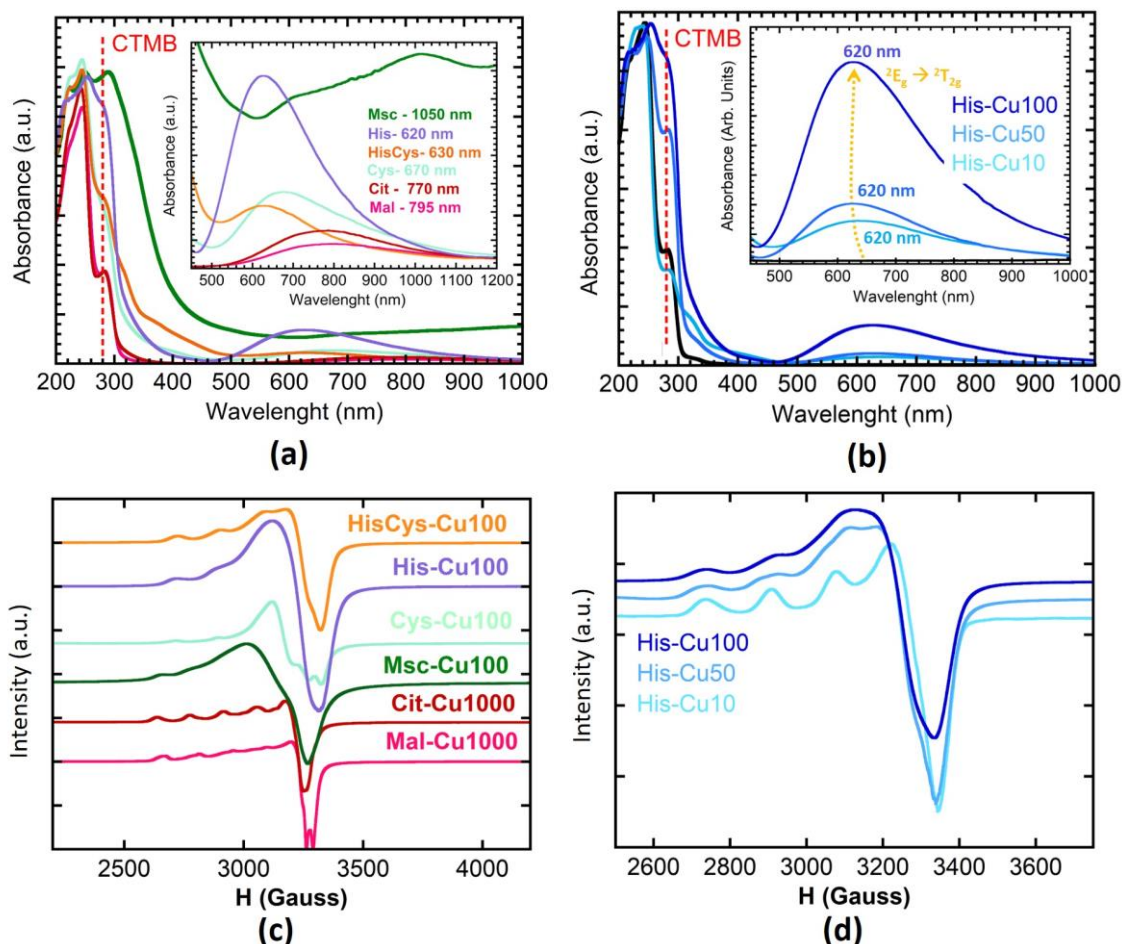planar coordination geometry for copper ions formed by two oxygen and two nitrogen atoms.

Figure 4.26. UV-Vis spectra of (a) MOF-808@His variant with increasingly copper content and (b) MOF-808@(amino) acid compounds with similar copper loadings. EPR spectra of (c) MOF-808@His variant with increasingly copper content and (d) MOF-808@(amino) acids with similar copper loadings. CTMB is the abbreviation for Charge Transfer Metal Bands.

EPR was employed as well to study the MOF-808@(amino) acid materials decorated with similar copper loadings (Figure 4.26c). It is clear that Cit and Mal variants stabilize copper ions as magnetically isolated species. In the case of MOF-808@Cit-Cu1000 only one type of copper is observed by EPR, whilst MOF-808@Mal-Cu1000 exhibits two types of magnetically isolated copper ions stabilized in slightly different coordination environments. For Msc and Cys functionalizations, copper ions are stabilized as magnetically clustered species, or as a mixture of

different magnetically isolated ions with different coordination environments. This occurs as well when a multivariate combination of His and Cys functions are included within the framework (Figure 4.26c).

This clustering of copper centers could be even more accentuated than as suggested by EPR, since in addition to the Cu^{II} species detected by this technique, XPS spectra of Msc, Cys and HisCys variants confirm the additional existence of Cu^{I} ions stabilized within the MOF-808@(amino) acid matrix (Figure 4.27). In fact, the bimodal peaks of the XPS spectra, which are related to copper binding energies, can be fitted to two contributions centered at 952.6/953.0 eV (Cu^{II}) and 951.0/950.8 eV (Cu^{I}) for the $Cu1p_{1/2}$ electronic level in Cys/Msc variants.[126] In parallel, the same splitting of the signal is observed for Cu2p2/3 binding energies of Cu^{II}/Cu^{I} in Msc (933.0/931.0 eV) and Cys (933.4/931.1 eV) (Figure 4.27). These values agree as well with the binding energies reported for Cu^{II} oxides and coordination compounds and Cu^{I} thiolates. From the intensity of each contribution, it can be concluded that the ¼ and ½ of the copper ions stabilized within the Cys and Msc variants have been reduced to Cu^{I}.
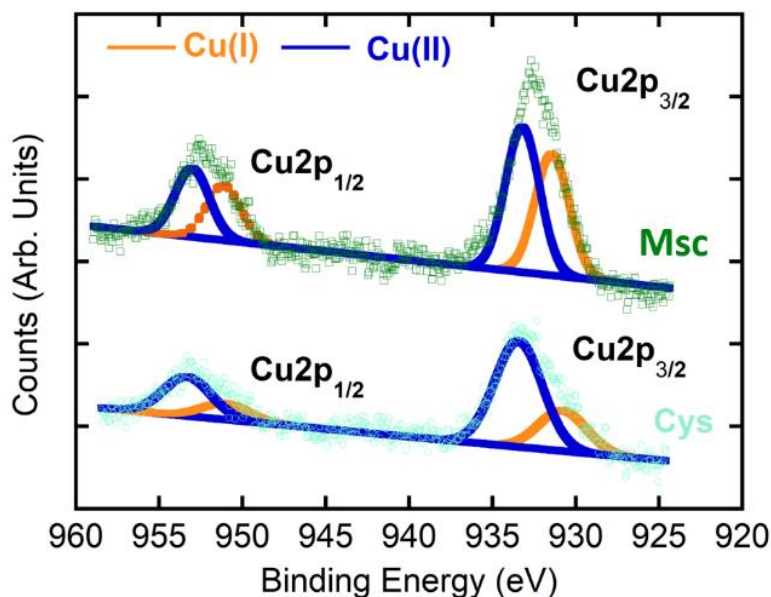

Figure 4.27. Fitting of the XPS spectra for MOF-808@Cys and MOF-808@Msc materials.

Voltamperometric measurements confirm the reversibility of the $Cu^{II} \longleftrightarrow Cu^{0}$ redox pairs, and the influence of the (amino) acid coordination on the redox potentials

observed for each of the studied materials (Figure 4.28). This modulation of the redox characteristics of metal-sites is also observed in metalloenzymes when the amino acid residues participating in the coordination of the metal-sites are altered.[127]

Overall, the amino acid functionalization of MOF-808 and the copper doping process does not only enable controlling the coordination environment of the copper ions immobilized within the framework, but their clustering degree and mixed oxidation state. All these features of the catalytic sites are foreseen to significantly affect the catalytic activity and affinity of the system.
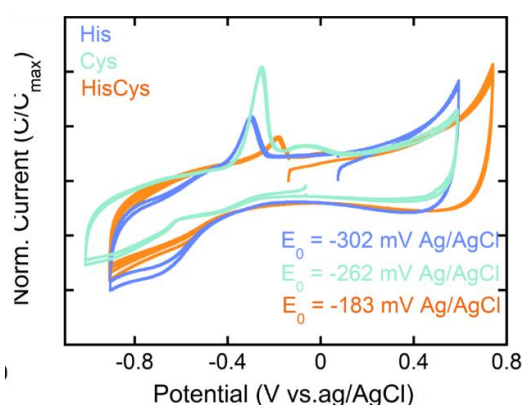

Figure 4.28. Cyclic voltammetry of MOF-808@His-Cu, MOF-808@Cys-Cu and MOF-808@HisCys-Cu.

Catalytic Wet Peroxide Oxidation (CWPO) of phenolic pollutants by MOF-808@His-Cu

This section assesses the performance of the biomimetic systems studied for the Catalytic Wet Peroxide Oxidation (CWPO) of phenolic pollutants as phenol, catechol, hydroquinone, dopamine and 2,5-dichlorophenol. Due to the similarity with copper-histidine metal-sites of laccases, the MOF-808@His-Cu100 catalyst was selected as the starting point for the study.

By applying the chromogenic reaction between the model 2,4-DCP substrate and the 4-AP marker,[128] the laccase-like capacity of MOF-808@His-Cu to catalyze the oxidation of 2,4-DCP without the addition of an oxidant was firstly confirmed (Figure 4.29a). The efficiency of MOF-808@His-Cu, both in terms of 2,4-diclhlorophenol

overall conversion and kinetics, was similar to reported laccase-like catalysts. When adding a co-oxidant as hydrogen peroxide to the reaction, MOF-808@His-Cu catalysts are able to activate the model 2,4-DCP substrate by performing a biomimetic peroxidase like oxidation (Figure 4.30a). Moreover, the MOF-808@His-Cu enhances the reaction rate by close to one order of magnitude, if compared with the one developed in the absence of hydrogen peroxide (Figure 4.30a). Although hydrogen peroxide is able to catalyze the wet oxidation of 2,4-DCP, the reaction rate and conversion values are negligible in comparison to the studied biomimetic system. In addition, the catalyst is able to oxidize phenol, catechol and hydroquinone, or more complex emerging phenolic pollutants as the dopamine hormone (Figures 4.29b and 4.30b).
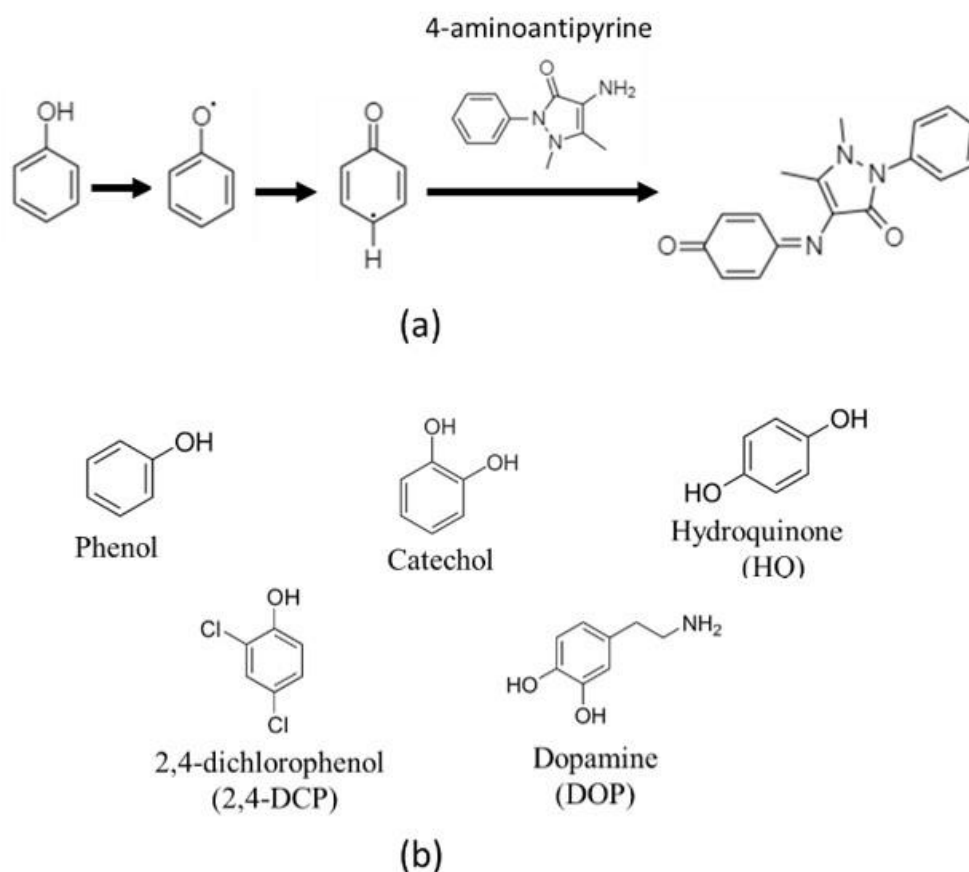

Figure 4.29. (a) Chromogenic reaction for phenols oxidations with 4-aminoantipyrine. (b) Chemical structure of the phenolic pollutants employed in this work..

From the UV-Vis absorbance value recorded at 510 nm and the rate of conversion after 2 hours of reaction, it can be concluded that the His-Cu variant of MOF-808 has a specific affinity to oxidize catechol and hydroquinone molecules, but predominantly dopamine. For instance, the kinetics and conversion efficiency of the CPWO for this substrate far exceeds the ones obtained for the other phenolic compounds (Figure 4.30b).
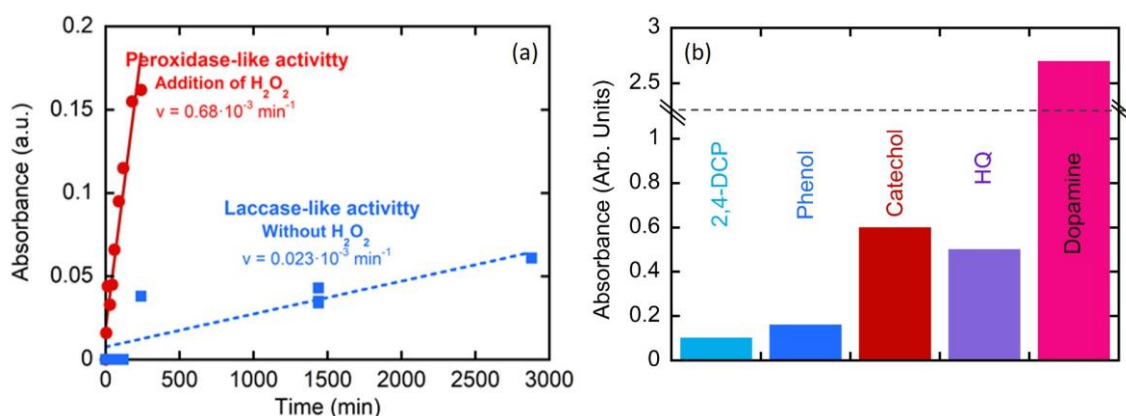

Figure 4.30. (a) Evolution of the absorbance during the 2,4-dichlorophenol oxidation without and with the addition of hydrogen peroxide to the media. (b) Absorbance value at 510 nm for the CWPO of different model pollutants at 100 µg·mL^{-1}.

The response of our biomimetic catalyst system was also studied for 2,4,-dichlorophenol, phenol, catechol, hydroquinone and dopamine oxidations at varying concentrations. First, it is interesting to observe how the reaction kinetics to oxidize phenol (Figure 4.31a) or 2,4-DCP (Figure 4.31b) are slower than the ones obtained for the transformation of catechol (Figure 4.31c), hydroquinone (Figure 4.31d) and dopamine (Figure 4.31e) substrates. In addition, the sigmoidal profile of the kinetic curve for the hydroquinone oxidation suggests that there is a negative allosteric effect due to the substrate binding to the copper-metal sites. Therefore, the activity of MOF-808@His-Cu depends on the number and position of the hydroxyl groups within the aromatic ring of the studied substrates, but it is influenced as well by the existence of other substituent groups (as is the case of dopamine or 2,4-DCP substrates). Overall, the MOF-808@His-Cu exhibits enzymatic like kinetics, as

concluded from the Michaelis-Menten plot and the fitting of the experimental data shown in the Figure 4.32. For instance, the K_M and V_{max} values obtained from the Michaelis-Menten fit (Equation. 2.18 in Chapter 2) confirm that our biomimetic systems are more efficient for the oxidation of catechol or hydroquinone substrates in comparison to phenolic based ones (Table 4.5).
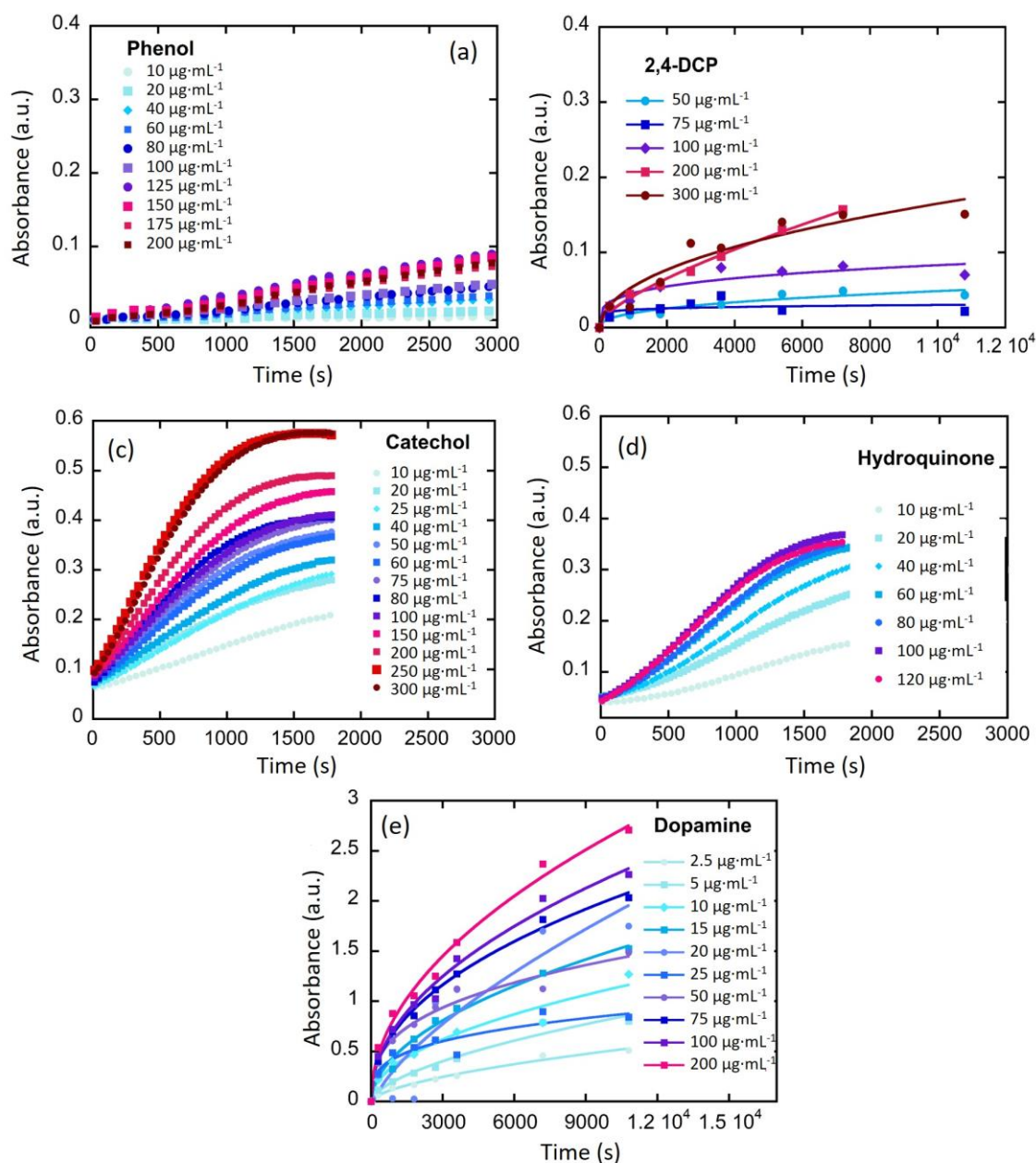

Figure 4.31. (a-e) Concentration dependence on the CWPO of the different phenolic pollutants.
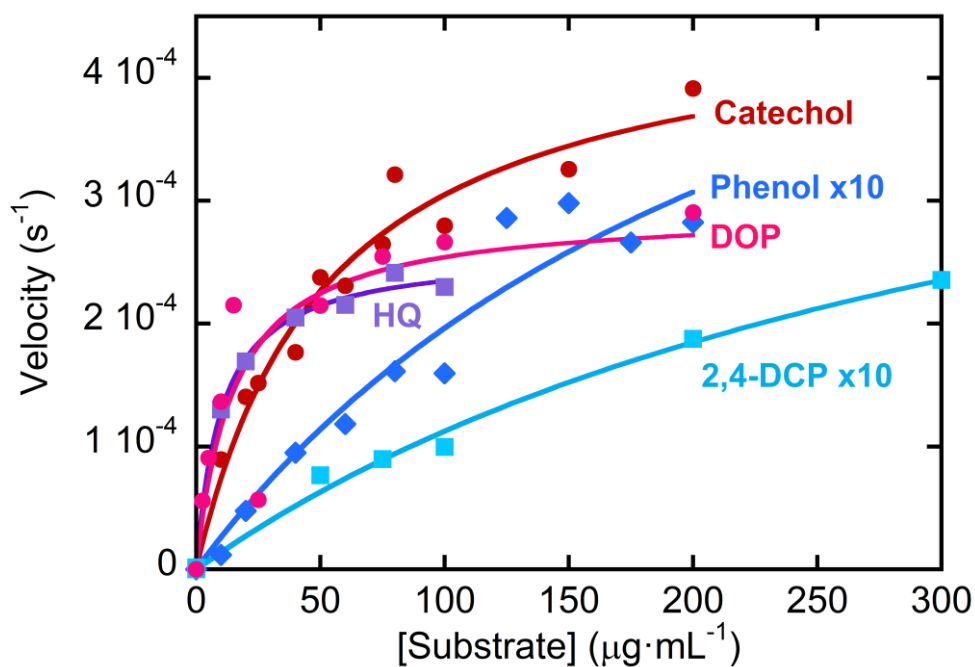
Figure 4.32. Michaelis-Menten plot for the CWPO of Catechol, Phenol, 2,4-dichlorophenol, Hydroquinone and Dopamine with MOF-808@His-Cu100.

Table 4.5. Kinetic parameters of the reactions catalyzed by MOF-808@His-Cu at 21 °C.

Substrate	K_M (mg·mL^{-1})	V_{max} (sec^{-1}·10^6)
2,4-Dichlorophenol	361 ± 86	519 ± 80
Phenol	258 ± 144	704 ± 257
Catechol	53 ± 10	466 ± 34
Hydroquinone	10 ± 1	258 ± 6
Dopamine	15 ± 8	290 ± 5

Even if the CWPO is a green and highly appealing approach to face the mineralization of phenolic compounds in polluted waters, the oxidative routes for phenol can accelerate the generation of catechol, hydroquinone and benzoquinone products at the first stage of the reaction. These intermediates exhibit even higher

environmental risks than the parent pollutant. So, as reported by A. Azizi *et al.*,[129] an efficient oxidation of these intermediates is necessary to induce the aromatic ring opening, and the subsequent generation of linear carboxylic acids until their mineralization is completed. Thus, it is important to follow up the oxidation process to identify the intermediate products generated during the reaction.

Although the chromogenic protocol employed in the initial stage of this work allows a rapid and easy experimental access to evaluate the CWPO activity, liquid chromatography is necessary to monitor the catechol and hydroquinone generation during the catalytic wet oxidation of phenol. The results of the experiment have been plotted in the Figure 4.33. First, it is important to note that the MOF-808@His-Cu100 is able to oxidize nearly 75 % of the phenol in less than three hours, reaching an 87.5% conversion in 20 h at RT. Nearly half of the amount of by-products generated during the first 4 h cannot be retained by the chromatographic column employed for catechol and hydroquinone. This fraction of the reaction was tentatively ascribed to the carboxyl groups generated after the ring-opening stage of the reaction. Interestingly, the oxidation of phenol to catechol is slightly more favorable than the one for hydroquinone. Nevertheless, after 4 h, the catalyst is still able to degrade hydroquinone and phenols, whilst the concentration of catechol remains unaltered. At this point, it is important to note that higher catalyst loadings or H_2O_2 concentrations could contribute to further displace the oxidation into non-environmentally hazardous by-products as carboxyl acids, preventing the generation of highly-concerning hydroquinone or catechol intermediates.

Further research is needed to endow this biomimetic systems with higher chemical stability, since a partial leakage of copper ions to the medium has been detected after the phenol oxidation experiment performed with the MOF-808@His-Cu100 variant. Indeed, the XRF spectra indicates that nearly 40% of the copper ions are lost during the catalytic tests.
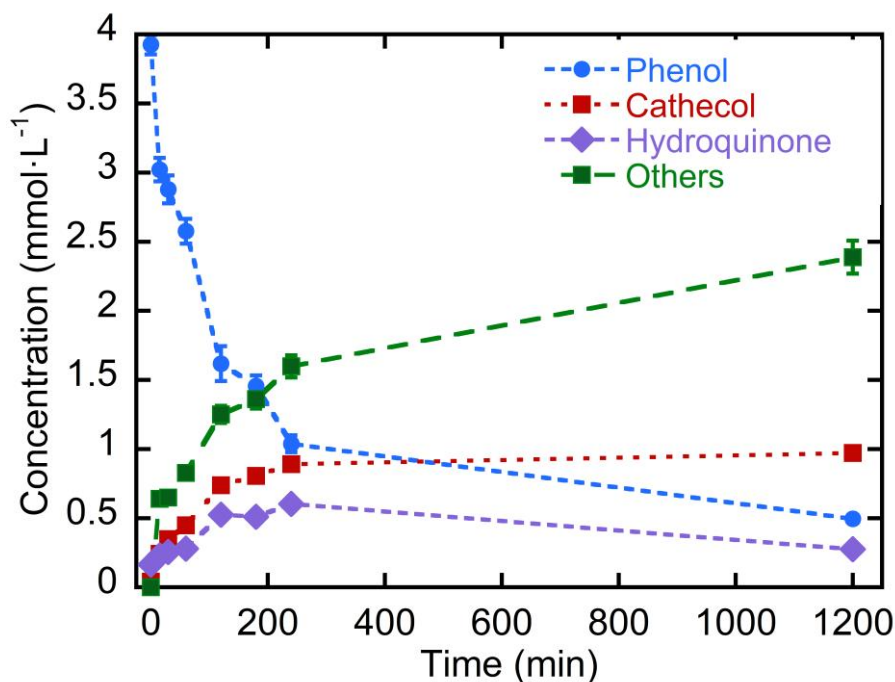
Figure 4.33. Kinetics of the catalytic wet oxidation of phenol and of its degradation products with MOF-808@His-Cu100 followed by liquid chromatography.

Catalytic activity and selectivity dependence on the Copper–active center

Once the biomimetic activity of the MOF-808@His-Cu system has been confirmed, the influence on the catalytic activity of the (i) clustering degree and (ii) coordination sphere of the copper metal sites stabilized within MOF-808@(amino) acid system was studied. To this end, the CWPO reactions of 2,4-DCP and Hydroquinone were carried out at the same conditions for all the developed catalysts. In addition, the UV-Vis absorbance of the reaction media was normalized to the copper content of the different catalysts listed in the Table 4.4. In general terms, the higher copper loadings in the MOF-808@(amino) acid system lead to faster kinetics and higher conversion efficiency. Figure 4.34 shows an analogue of turnover frequency (TOF) per copper ion, allowing to assess the activity of each single catalytic site.

It is important to remember that as revealed by EPR, the clustering degree of the copper ions immobilized into the MOF-808@His matrix can be controlled by

performing its metalation with solutions with increasing metal-concentration. Therefore, the clustering of the copper ions installed into MOF-808@His increases progressively for Cu-10, Cu-50 and Cu-100 variants of the material. The kinetics of 2,4-DCP oxidation strongly depends on the presence of single-copper metal-sites in the catalysts, since the TOF per copper is significantly greater for MOF-808@His-Cu10 than for Cu50 and Cu100 variants (Figure 4.34a). That is, the activity per catalytic site seems inversely related to the copper clustering. In contrast, for the CWPO of hydroquinone some degree of copper-clustering is beneficial, since the conversion for MOF-808@His-Cu50 is better than for Cu-10 and Cu-100 catalysts (Figure 4.34b).

In a second attempt, the effect of the coordination environment of the copper ions installed into MOF-808@(amino) acids on their catalytic activity was studied for the abovementioned two reactions. In agreement with the results obtained for MOF-808@His-Cu, the MOF-808@(amino) acid materials featuring less copper clustering (*i.e.* Cit > His ~ His/Cys > Mal > Cys > Msc) exhibit better efficiencies for the 2,4-DCP oxidation (Figure 4.34c). Even if the MOF-808@(amino) acid catalysts show similar degree of copper clustering in the active sites, small variations of their coordination environment induces significant changes on their oxidative activity, as is the case of His, His/Cys and Cys variants studied in this work. The tendency observed for the 2,4-DCP oxidation is reversed when studying the CPWO of hydroquinone (Figure 4.34d). In this case, the best conversion is achieved by the Cys-Cu variant, followed by the Cys/His and His based compounds. It is interesting to note the significant differences observed in transformation rate of hydroquinone. His, Cys, HisCys and Msc variants show a fast transformation of the substrate in the first 20 minutes until the evolution is frozen, whilst Mal and Cit based compounds exhibit slower kinetics but a constant hydroquinone oxidation along the 120 min of the experiment. This fact points out that the coordination sphere of copper ions does not only modulate its overall efficiency to oxidize hydroquinone, but also the kinetics of the transformation at the initial stages of the reaction.
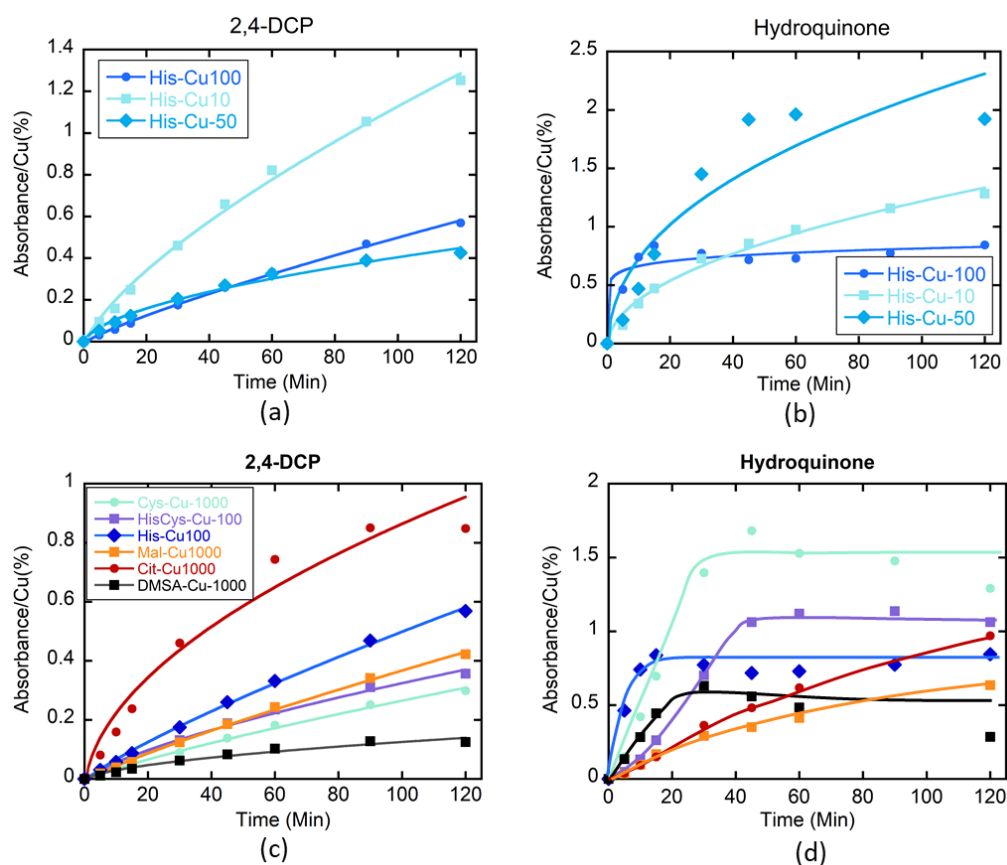
Figure 4.34 Kinetics of CWPO of 2,4-dichlorophenol and hydroquinone of (a) MOF-808@His-Cu system with increasing doping of copper, and (b) MOF-808@(amino) acid-Cu catalysts exhibiting Cu-catalytic sites stabilized by different amino acid and acid residues. For all the reactions, the absorbance value recorded at 510 nm was normalized to the copper content of each material to obtain the turnover frequency (TOF).

Mechanisms of CWPO in MOF-808@(amino) acid–Cu systems

Based on the kinetic evidence shown earlier, two key features need to be considered when proposing a possible oxidative mechanisms: (i) the coordination modes of the copper ions stabilized within the MOF-808@(amino) acid materials and (ii) the activity shown by the individual catalysts studied in contrast with the possible mechanistic pathways shown by the reported copper coordination complexes in solution.[95,130,131] The tentative structural models constructed for the MOF-808@(amino) acid materials allow to qualitatively evaluate the distance between the potential metal-coordination groups within the pore space of the material.

It is well known that the anchoring mechanism of the (amino) acid molecules to MOF-808 is mainly given through their coordinative binding to the equatorial plane of the $Zr_6O_4(OH)_4$ secondary building units (Figure 4.35a.3). In fact, starting from the crystal and chemical structures of the MOF-808 and of the (amino) acid molecules employed in this study, a qualitative description of their disposition within the pore space of the material can be done by building up tentative structural models where the (amino) acid molecules are coordinated to the defective positions of the zirconium clusters of the MOF-808 framework (Figure 4.35a.1-3). Overall, after SALI,[22] the side chains of (amino) acids are foreseen to point towards the center of the 12 Å pore-window that give access to the adamantane 18 Å pores of MOF-808. Hence, (amino) acid functionalized MOF-808 will show a decoration of its pore space with imidazole, thiol, amine or carboxyl groups (or their combination) able to bind copper ions in a cooperative manner. Our qualitative structural models enable evaluating the distances between the metal-coordination groups decorating the pore space of the MOF-808@(amino) acids (Figure 4.35b.1-b.2). In general terms, the distance between R1 and/or R2 groups of amino acid molecules installed in adjacent zirconium clusters (*i.e.* defined as d2 in the Figure 4.35b.2) is ≥ 4 Å, whilst the separation between the R2 groups of (amino) acid molecules anchored to adjacent clusters of the crystal structure (*i.e.* defined as d1 in the Figure 4.35b.2) is ≥ 7 Å. The histidine variant is an exception to this general rule where d1 could be ≥ 4 Å.

Cu-O and Cu-N bonds usually show lengths close to 2 Å if they form part of the equatorial plane of copper's coordination sphere. Therefore, a R1-Cu-R1 direct linkage (~ 4 Å) could fit with the separation between the R1 groups of (amino) acid molecules attached to adjacent zirconium clusters into the MOF-808 structure. In contrast, the connection of the R2 group of (amino) acids placed at opposite sides of the pore-window need to involve at least two copper ions linked by an intermediate water, hydroxyl or oxygen specie (R2-Cu-O-Cu-R2, $d_{R2-R2} \sim 8$ Å).
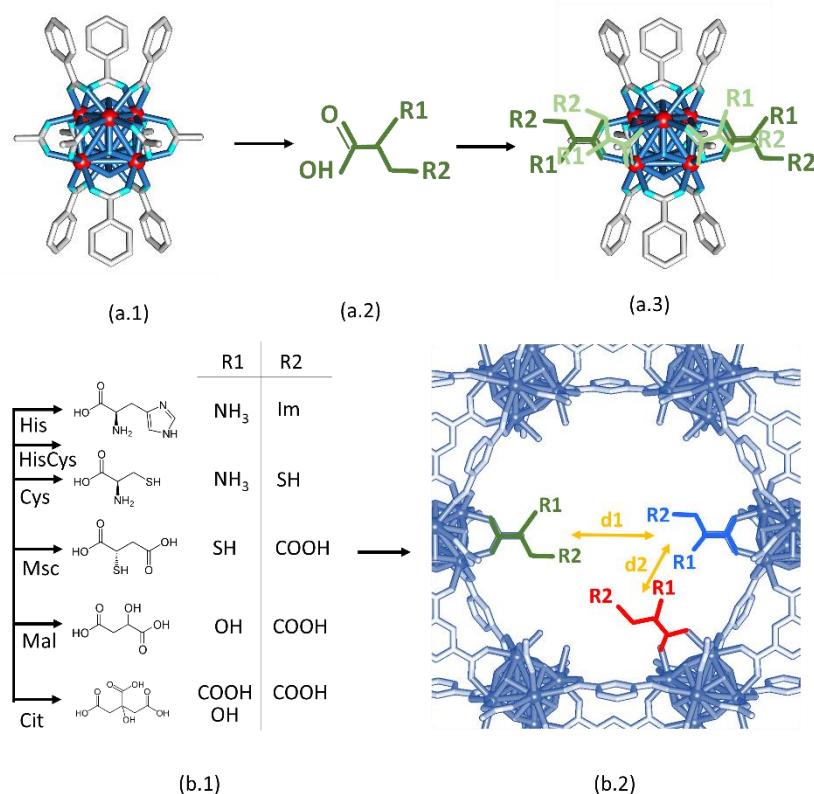
Figure 4.35. (a.1) Local structure of zirconium hexanuclear clusters in MOF-808. (a.2) Simplified chemical structure of (amino) acid molecules. (a.3) Tentative local structure of zirconium hexanuclear clusters after their functionalization. Color code: Red – Zirconium. Light blue – Oxygen. Grey- Carbon. (b.1) Chemical structure and metal coordination groups of (amino) acid functions installed into MOF-808. (b.2) Simplification of the pore structure of MOF-808 once functionalized with (amino) acids.

In addition to the distances between the copper coordination groups, many of the (amino) acid molecules employed to decorate the MOF-808 pore space can also act as multidentate linkers able to coordinate one or several copper ions. In order to illustrate this point, a search for copper-(amino) acid complexes was performed in the Cambridge Structural Database[132,133] to evaluate the possible coordination modes of the copper-(amino) acid system in detail. Considering this information, various possible coordination modes are identified for copper ions within the MOF-808@(amino) acid system: (i) Monodentate or bidentate coordination of a single Cu^{II} ion by a single (amino) acid (Figure 4.36a1-a3),[134–136] (ii) bidentate coordination of clustered Cu^{II} ions by a single (amino) acid (Figure 4.36a4), and (iii) cooperative

coordination of single and clustered ions by two of the (amino) acid molecules installed within the MOF-808 in adjacent (Figure 4.36b1-2) and/or opposite zirconium cluster units (Figure 4.36c1-2).[137–141] In addition to this, it is important to consider that Cys and Msc functionalities can stabilize the copper ions as Cu^I. Thus, if catalytic sites are formed by clustered species, both Cu^{II} and Cu^I ions could be found in the same system.

The activation of hydrogen peroxide by copper-metal complexes has been widely applied to chemical synthesis, environmental control, effluent treatment and sterilization.[142] The activation of the hydrogen peroxide by transition metal-ions, and specifically by copper-complexes, follows two possible routes: (i) Metal-H_2O_2-complexation: its direct complexation with the copper metal-centers as hydroxoperoxo, peroxo, or oxo species that trigger the substrate oxidation (Figure 4.36d, and (ii) Fenton route: *via* its conversion to hydroxyl radical ($^\bullet$OH) coupled to a redox reaction of the copper center (Figure 4.36d).[143,144] Today, it is still unclear if the reaction in copper complexes studied in solution proceeds *via* a single reaction path or *via* the combination of both possible routes.[145] In addition, the identification of the active oxidative species coordinated to the copper ions (*i.e.* oxo, peroxo or hydroxoperoxo) is as well challenging due to their transient nature.

In contrast, our biomimetic copper system seems to preferentially catalyze the peroxo complexation route, since in MOF-808@(amino) acid variants with stabilized Cu^I, the catalytic activity per site is significantly lower than for catalyst where copper is mainly stabilized as Cu^{II} (Figure 4.36e). This preference is not given by the redox-unfeasibility of the copper-sites installed with the MOF-808@(amino) acid system, as demonstrated by the cyclic voltammetry measurements. In addition, the efficiency of the hydroquinone transformation by clustered Cu^{II} centers in comparison to the isolated-copper ones also provides a valuable mechanistic information. It is important to note that for hydroquinone oxidation an important negative allosteric effect was observed for several catalysts, a fact that is usually ascribed to the coordination of the substrate to the active site. In copper-clustered catalyst, the formation of the copper-peroxo active species in a position of the catalytic-site could aid to unlock the copper-ions blocked by substrate species nearby the first ion (Figure 4.36e).
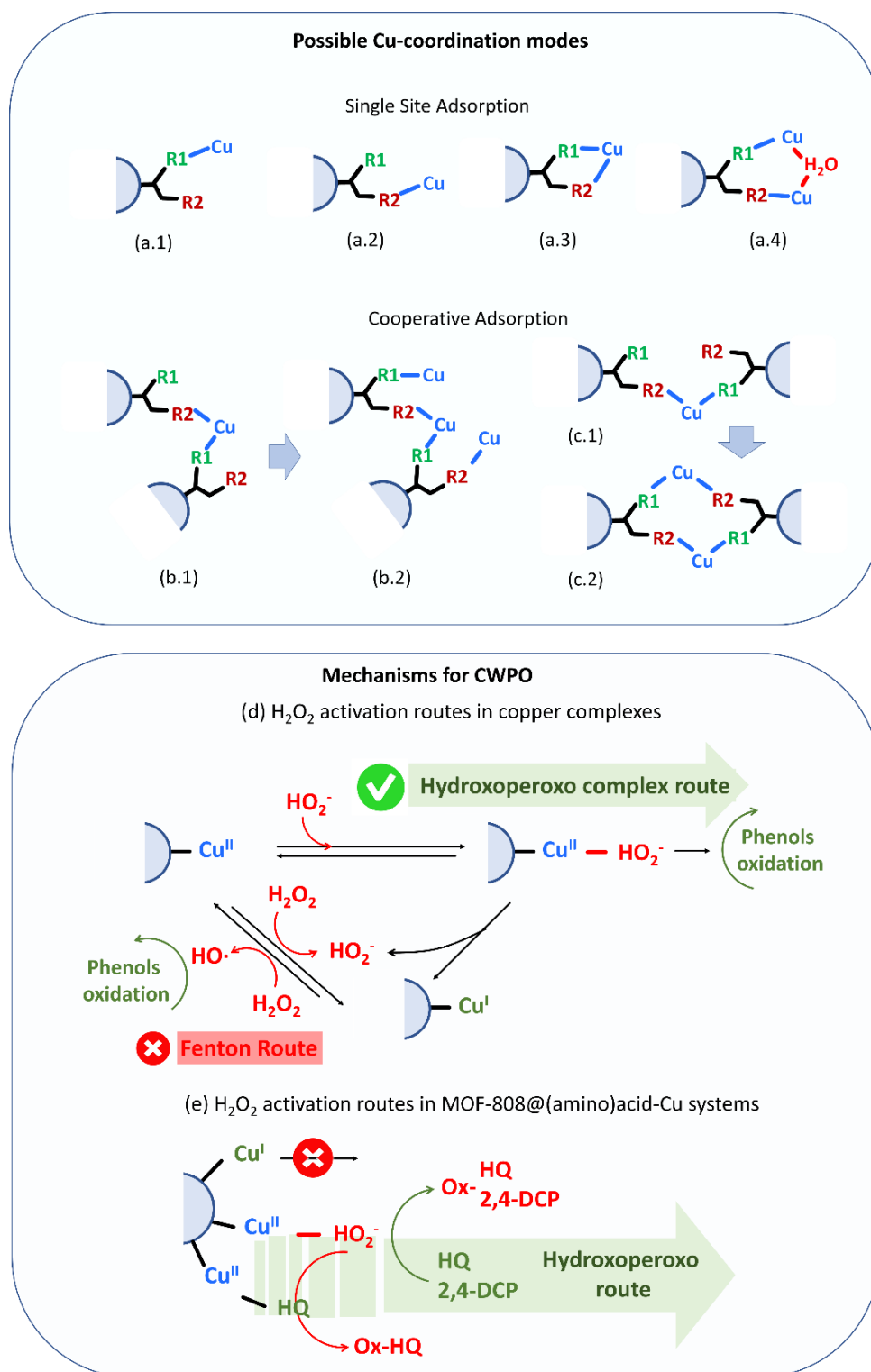
Figure 4.37. Tentative coordination modes of copper (Cu) ions within MOF-808 *via* (a.1-a.4) single site adsorption or (b.1, b.2, c.1-c.2)) cooperative adsorption. Mechanisms of H$_2$O$_2$ activation in (d) copper complexes and (e) copper metal sites in MOF-808@(amino) acid system.

4.2.3. CONCLUSIONS

The chemical encoding of MOFs with amino acid and acid functions enables the subsequent adsorption-driven immobilization of copper sites with controlled coordination environments and clustering degrees within these porous and ordered materials. The engineered heterogeneous biomimetic copper-catalysts show laccase and peroxidase like enzymatic activities over model and real phenolic pollutants. Similarly than metalloenzymes, the catalytic activity and selectivity of our biomimetic systems depend on: (i) the amino acid and acid residues coordinating the copper metal sites and (ii) the clustering degree of the copper catalytic centers installed within the pore space of MOF-808. Further research is needed to fully understand the activation of hydrogen peroxide by the copper-sites, and the evolution of the oxidation state and of the coordination environments of the catalytic centers, especially for reactions where a negative allosteric effect has been observed during the first stage of the phenolic wet oxidation. In return, this work open the perspective of copper enzyme mimicking and fine tuning in MOFs, as well as for their future application in added value enantioselective catalysis.

4.3. REFERENCES

1   Tchounwou PB, Yedjou CG, Patlolla AK, Sutton DJ. Heavy Metal Toxicity and the Environment. In: *Molecular, Clinical and Envirnmental Toxicology.*2012: 133–164.

2   Dinu MV, Dragan ES. Heavy metals adsorption on some iminodiacetate chelating resins as a function of the adsorption parameters. *React Funct Polym* 2008; **68**: 1346–1354. [DOI: 10.1016/j.reactfunctpolym.2008.06.011]

3   Henry WD, Zhao D, SenGupta AK, Lange C. Preparation and characterization of a new class of polymeric ligand exchangers for selective removal of trace contaminants from water. *React Funct Polym* 2004; **60**: 109–120. [DOI: 10.1016/j.reactfunctpolym.2004.02.016]

4   Baraka A, Hall PJ, Heslop MJ. Preparation and characterization of melamine-formaldehyde-DTPA chelating resin and its use as an adsorbent for heavy metals removal from wastewater. *React Funct Polym* 2007; **67**: 585–600. [DOI: 10.1016/j.reactfunctpolym.2007.01.015]

5   Chen Y, Tang J, Wang S, Zhang L. Facile preparation of a remarkable MOF adsorbent for Au(III) selective separation from wastewater: Adsorption, regeneration and mechanism. *J Mol Liq* 2022; **349**: 118137. [DOI: 10.1016/j.molliq.2021.118137]

6   Tang J, Zhao J, Wang S, Zhang L, Zhao M, Huang Z, Hu Y. Pre-modification strategy to prepare a novel Zr-based MOF for selective adsorption of Palladium(II) from solution. *Chemical Engineering Journal* 2021; **407**: 127223. [DOI: 10.1016/j.cej.2020.127223]

7   Peng Y, Huang H, Zhang Y, Kang C, Chen S, Song L, Liu D, Zhong C. A versatile MOF-based trap for heavy metal ion capture and dispersion. *Nat Commun* 2018; **9**. [DOI: 10.1038/s41467-017-02600-2]

8   Lu X, Wang F, Li X, Shih K, Zeng EY. Adsorption and Thermal Stabilization of Pb 2+ and Cu 2+ by Zeolite. *Ind Eng Chem Res* 2016; **55**: 8767–8773. [DOI: 10.1021/acs.iecr.6b00896]

9   Seliman AF, Lasheen YF, Youssief MAE, Shehata FA. Removal of some radionuclides from contaminated solution using natural clay: bentonite. *J Radioanal Nucl Chem* 2014; **300**: 969–979. [DOI: 10.1007/s10967-014-3027-z]

10   Krukowska J, Thomas P, Kołodyn D. Comparison of sorption and desorption studies of heavy metal ions from biochar and commercial active carbon. *Chemical Engeneering Journal* 2017; **307**: 353–363. [DOI: 10.1016/j.cej.2016.08.088]

11   Li J, Wang X, Power E, Zhao G, Chai Z, Chen C, Alsaedi A, Hayat T, Wang X. Metal–organic framework-based materials: superior adsorbents for the capture of toxic and radioactive metal ions. *Chem Soc Rev* 2018; **47**: 2322. [DOI: 10.1039/c7cs00543a]

12   Baek J, Rungtaweevoranit B, Pei X, Park M, Fakra SC, Liu YS, Matheu R, Alshmimri SA, Alshehri S, Trickett CA, Somorjai GA, Yaghi OM. Bioinspired Metal-Organic Framework Catalysts for Selective Methane Oxidation to Methanol. *J Am Chem Soc* 2018; **140**: 18208–18216. [DOI: 10.1021/jacs.8b11525]

13   Ding C-W, Luo W, Zhou J-Y, Ma X-J, Chen G-H, Zhou X-P, Li D. Hydroxo Iron(III) Sites in a Metal–Organic Framework: Proton-Coupled Electron Transfer and Catalytic Oxidation of

Alcohol with Molecular Oxygen. *ACS Appl Mater Interfaces* 2019; **11**: 45621–45628. [DOI: 10.1021/acsami.9b15311]

14   Sun Q, Aguila B, Ma S. Metalloenzyme Mimicry at the Nodes of Metal-Organic Frameworks. *Chem* 2018; **4**: 2736–2738. [DOI: 10.1016/j.chempr.2018.11.017]

15   Chiong JA, Zhu J, Bailey JB, Kalaj M, Subramanian RH, Xu W, Cohen SM, Tezcan FA. An Exceptionally Stable Metal-Organic Framework Constructed from Chelate-Based Metal-Organic Polyhedra. *J Am Chem Soc* 2020; **142**: 6907–6912. [PMID: 32223143 DOI: 10.1021/jacs.0c01626]

16   Maleki A, Hayati B, Naghizadeh M, Joo SW. Adsorption of hexavalent chromium by metal organic frameworks from aqueous solution. *Journal of Industrial and Engineering Chemistry* 2015; **28**: 211–216. [DOI: 10.1016/j.jiec.2015.02.016]

17   Wang C, Liu X, Chen JP, Li K. Superior removal of arsenic from water with zirconium metal-organic framework UiO-66. *Sci Rep* 2015; **5**: 1–10. [DOI: 10.1038/srep16613]

18   Howarth AJ, Katz MJ, Wang TC, Platero-Prats AE, Chapman KW, Hupp JT, Farha OK. High Efficiency Adsorption and Removal of Selenate and Selenite from Water Using Metal-Organic Frameworks. *J Am Chem Soc* 2015; **137**: 7488–7494. [PMID: 26000611 DOI: 10.1021/jacs.5b03904]

19   De Decker J, Rochette J, De Clercq J, Florek J, Van Der Voort P. Carbamoylmethylphosphine Oxide-Functionalized MIL-101(Cr) as Highly Selective Uranium Adsorbent. *Anal Chem* 2017; **89**: 5678–5682. [DOI: 10.1021/acs.analchem.7b00821]

20   Healey K, Liang W, Southon PD, Church TL, D'Alessandro DM. Photoresponsive spiropyran-functionalised MOF-808: Postsynthetic incorporation and light dependent gas adsorption properties. *J Mater Chem A Mater* 2016; **4**: 10816–10819. [DOI: 10.1039/c6ta04160d]

21   Karagiaridi O, Bury W, Mondloch JE, Hupp JT, Farha OK. Solvent-assisted linker exchange: An alternative to the de novo synthesis of unattainable metal-organic frameworks. *Angewandte Chemie - International Edition* 2014; **53**: 4530–4540. [DOI: 10.1002/anie.201306923]

22   Deria P, Bury W, Hod I, Kung CW, Karagiaridi O, Hupp JT, Farha OK. MOF functionalization via solvent-assisted ligand incorporation: Phosphonates vs carboxylates. *Inorg Chem* 2015; **54**: 2185–2192. [DOI: 10.1021/ic502639v]

23   Kalaj M, Cohen SM. Postsynthetic Modification: An Enabling Technology for the Advancement of Metal-Organic Frameworks. *ACS Cent Sci* 2020; **6**: 1046–1057. [DOI: 10.1021/acscentsci.0c00690]

24   al Danaf N, Schrimpf W, Hirschle P, Lamb DC, Ji Z, Wuttke S. Linker Exchange via Migration along the Backbone in Metal-Organic Frameworks. *J Am Chem Soc* 2021; **143**: 10541–10546. [PMID: 34228932 DOI: 10.1021/jacs.1c04804]

25   Islamoglu T, Goswami S, Li Z, Howarth AJ, Farha OK, Hupp JT. Postsynthetic Tuning of Metal–Organic Frameworks for Targeted Applications. *Acc Chem Res* 2017; **50**: 805–813. [DOI: 10.1021/acs.accounts.6b00577]

26   Reizabal A, Costa CM, Saiz PG, Gonzalez B, Pérez-Álvarez L, Fernández de Luis R, Garcia A, Vilas-Vilela JL, Lanceros-Méndez S. Processing Strategies to Obtain Highly Porous Silk Fibroin Structures with Tailored Microstructure and Molecular Characteristics and Their Applicability in Water Remediation. *J Hazard Mater* 2021; **403**: 123675. [DOI: https://doi.org/10.1016/j.jhazmat.2020.123675]

27   Wang K, Gu J, Yin N. Efficient Removal of Pb(II) and Cd(II) Using NH2-Functionalized Zr-MOFs via Rapid Microwave-Promoted Synthesis. *Ind Eng Chem Res* 2017; **56**: 1880–1887. [DOI: 10.1021/acs.iecr.6b04997]

28   Muguruza AR, de Luis RF, Iglesias N, Bazán B, Urtiaga MK, Larrea ES, Fidalgo-Marijuan A, Barandika G. Encapsulation of β-alanine model amino-acid in zirconium(IV) metal organic frameworks: Defect engineering to improve host guest interactions. *J Inorg Biochem* 2020; **205**: 110977. [DOI: 10.1016/j.jinorgbio.2019.110977]

29   Zha M, Liu J, Wong YL, Xu Z. Extraction of palladium from nuclear waste-like acidic solutions by a metal-organic framework with sulfur and alkene functions. *J Mater Chem A Mater* 2015; **3**: 3928–3934. [DOI: 10.1039/c4ta06678b]

30   Mon M, Bruno R, Ferrando-Soria J, Armentano D, Pardo E. Metal–organic framework technologies for water remediation: towards a sustainable ecosystem. *J Mater Chem A Mater* 2018; **6**: 4912–4947. [DOI: 10.1039/C8TA00264A]

31   Custelcean R, Moyer BA. Anion Separation with Metal – Organic Frameworks. *Eur J Inorg Chem* 2007; **2007**: 1321–1340. [DOI: 10.1002/ejic.200700018]

32   Lyu H, Chen OIF, Hanikel N, Hossain MI, Flaig RW, Pei X, Amin A, Doherty MD, Impastato RK, Glover TG, Moore DR, Yaghi OM. Carbon Dioxide Capture Chemistry of Amino Acid Functionalized Metal-Organic Frameworks in Humid Flue Gas. *J Am Chem Soc* 2022; **144**: 2387–2396. [PMID: 35080872 DOI: 10.1021/jacs.1c13368]

33   Becker FG, Cleary M, Team RM, Holtermann H, The D, Agenda N, Science P, Sk SK, Hinnebusch R, Hinnebusch A R, Rabinovich I, Olmert Y, Uld DQGLQ, Ri WKHU, Lq V, Frxqwu WKH, Zklfk E, Edvhg L V, Wkh RQ, Becker FG, Aboueldahab N, Khalaf R, De Elvira LR, Zintl T, Hinnebusch R, Karimi M, Mousavi Shafaee SM, O 'driscoll D, Watts S, Kavanagh J, Frederick B, Norlen T, O'Mahony A, Voorhies P, Szayna T, Spalding N, Jackson MO, Morelli M, Satpathy B, Muniapan B, Dass M, Katsamunska P, Pamuk Y, Stahn A, Commission E, Piccone TED, Annan MrK, Djankov S, Reynal-Querol M, Couttenier M, Soubeyran R, Vym P, Prague E, World Bank, Bodea C, Sambanis N, Florea A, Florea A, Karimi M, Mousavi Shafaee SM, Spalding N, Sambanis N, ح فاطمی. Reviews of Environmental Contamination and Toxicology. Volume 196. Springer

34   Azimi A, Azari A, Rezakazemi M, Ansarpour M. Removal of Heavy Metals from Industrial Wastewaters: A Review. *ChemBioEng Reviews* 2017; **4**: 37–59. [DOI: 10.1002/cben.201600010]

35   León R, Macías F, R. Cánovas C, Pérez-López R, Ayora C, Nieto JM, Olías M. Mine waters as a secondary source of rare earth elements worldwide: The case of the Iberian Pyrite Belt. *J Geochem Explor* 2021; **224**. [DOI: 10.1016/j.gexplo.2021.106742]

36 Jiang J, Gándara F, Zhang YB, Na K, Yaghi OM, Klemperer WG. Superacidity in sulfated metal-organic framework-808. *J Am Chem Soc* 2014; **136**: 12844–12847. [DOI: 10.1021/ja507119n]

37 Rosales M, Orive J, Espinoza-González R, Fernández de Luis R, Gauvin R, Brodusch N, Rodríguez B, Gracia F, García A. Evaluating the bi-functional capacity for arsenic photo-oxidation and adsorption on anatase TiO2 nanostructures with tunable morphology. *Chemical Engineering Journal* 2021; **415**: 128906. [DOI: https://doi.org/10.1016/j.cej.2021.128906]

38 Rapti S, Pournara A, Sarma D, Papadas IT, Armatas GS, Hassan YS, Alkordi MH, Kanatzidis MG, Manos MJ. Rapid, green and inexpensive synthesis of high quality UiO-66 amino-functionalized materials with exceptional capability for removal of hexavalent chromium from industrial waste. *Inorg Chem Front* 2016; **3**: 635–644. [DOI: 10.1039/C5QI00303B]

39 Allen SJ, Mckay G, Porter JF. Adsorption isotherm models for basic dye adsorption by peat in single and binary component systems. *J Colloid Interface Sci* 2004; **280**: 322–333. [DOI: 10.1016/j.jcis.2004.08.078]

40 Valverde A, G.-Sainz P, Orive J, E. L, Reizabal-Para A, Tovar G, Copello G, Lazaro-Martinez JM, Rodriguez B, Gonzalez-Navarrete B, Quintero MY, Rosales M, García A, Arriortua MI, Fernandez de Luis R. Porous, lightweight, metal organic materials: environment sustainability. In: *Advanced Lightweight Multifunctional Materials*. Elsevier, 2020: 43–130.

41 Peralta Ramos ML, González JA, Albornoz SG, Pérez CJ, Villanueva ME, Giorgieri SA, Copello GJ. Chitin hydrogel reinforced with TiO2 nanoparticles as an arsenic sorbent. *Chemical Engineering Journal* 2016; **285**: 581–587. [DOI: 10.1016/j.cej.2015.10.035]

42 G. Saiz P, Valverde A, Gonzalez-Navarrete B, Rosales M, Quintero YM, Fidalgo-Marijuan A, Orive J, Reizabal A, Larrea ES, Arriortua MI, Lanceros-Méndez S, García A, Fernández de Luis R. Modulation of the Bifunctional CrVI to CrIII Photoreduction and Adsorption Capacity in ZrIV and TiIV Benchmark Metal-Organic Frameworks. Catalysts. 2021; **11**: 51–60.

43 Gil A, Assis FCC, Albeniz S, Korili SA. Removal of dyes from wastewaters by adsorption on pillared clays. *Chemical Engineering Journal* 2011; **168**: 1032–1040. [DOI: 10.1016/j.cej.2011.01.078]

44 Zhang W, Bu A, Ji Q, Min L, Zhao S, Wang Y, Chen J. pKa-directed incorporation of phosphonates into mof-808 via ligand exchange: Stability and adsorption properties for uranium. *ACS Appl Mater Interfaces* 2019; **11**: 33931–33940. [PMID: 31409065 DOI: 10.1021/acsami.9b10920]

45 Du Y, Fang HX, Zhang Q, Zhang HL, Hong Z. Spectroscopic investigation on cocrystal formation between adenine and fumaric acid based on infrared and Raman techniques. *Spectrochim Acta A Mol Biomol Spectrosc* 2016; **153**: 580–585. [PMID: 26436846 DOI: 10.1016/j.saa.2015.09.020]

46 Mesu JG, Visser T, Soulimani F, Weckhuysen BM. Infrared and Raman spectroscopic study of pH-induced structural changes of L-histidine in aqueous environment. *Vib Spectrosc* 2005; **39**: 114–125. [DOI: 10.1016/j.vibspec.2005.01.003]

47 Hargreaves MK, Stevinson EA. The infra-red spectra of fumaramic and maleamic acids and their sodium salts. *Spectrochimica Acta* 1965; **21**: 1681–1689. [DOI: 10.1016/0371-1951(65)80079-0]

48 Furukawa H, Gándara F, Zhang YB, Jiang J, Queen WL, Hudson MR, Yaghi OM. Water adsorption in porous metal-organic frameworks and related materials. *J Am Chem Soc* 2014; **136**: 4369–4381. [DOI: 10.1021/ja500330a]

49 Wu J, Zhou J, Zhang S, Alsaedi A, Hayat T, Li J, Song Y. Efficient removal of metal contaminants by EDTA modified MOF from aqueous solutions. *J Colloid Interface Sci* 2019; **555**: 403–412. [PMID: 31398567 DOI: 10.1016/j.jcis.2019.07.108]

50 Shearer GC, Chavan S, Ethiraj J, Vitillo JG, Svelle S, Olsbye U, Lamberti C, Bordiga S, Lillerud KP. Tuned to perfection: Ironing out the defects in metal-organic framework UiO-66. *Chemistry of Materials* 2014; **26**: 4068–4071. [DOI: 10.1021/cm501859p]

51 Hardian R, Dissegna S, Ullrich A, Llewellyn PL, Coulet MV, Fischer RA. Tuning the Properties of MOF-808 via Defect Engineering and Metal Nanoparticle Encapsulation. *Chemistry - A European Journal* 2021; **27**: 6804–6814. [PMID: 33586233 DOI: 10.1002/chem.202005050]

52 Basu O, Mukhopadhyay S, Laha S, Das SK. Defect Engineering in a Metal – Organic Framework System to Achieve Super-Protonic Conductivity. *Chemistry of Materials* 2022; **34**: 6734–6734. [DOI: 10.1021/acs.chemmater.2c00654]

53 Ardila-Suárez C, Perez-Beltran S, Ramírez-Caballero GE, Balbuena PB. Enhanced acidity of defective MOF-808: Effects of the activation process and missing linker defects. *Catal Sci Technol* 2018; **8**: 847–857. [DOI: 10.1039/c7cy02462b]

54 Fernández De Luis R, Urtiaga MK, Mesa JL, Larrea ES, Iglesias M, Rojo T, Arriortua MI. Thermal response, catalytic activity, and color change of the first hybrid vanadate containing Bpe guest molecules. *Inorg Chem* 2013; **52**. [DOI: 10.1021/ic302662x]

55 G. Saiz, P., Iglesias, N., Gonzalez-Navarrete, B., Rosales, M., Quintero, Y. M., Reizabal, A., Orive, J., Fidalgo-Marijuan, A., Lanceros-Mendez, S., Arriortua, M. I.,& Fernandez de Luis R. Chromium speciation in zirconium-based metal – organic frameworks for environmental remediation. *Chemistry—A European Journal* 2020; **26**: 1–13. [DOI: 10.1002/chem.202001435]

56 Li Z, Peters AW, Bernales V, Ortuño MA, Schweitzer NM, Destefano MR, Gallington LC, Platero-Prats AE, Chapman KW, Cramer CJ, Gagliardi L, Hupp JT, Farha OK. Metal-Organic Framework Supported Cobalt Catalysts for the Oxidative Dehydrogenation of Propane at Low Temperature. *ACS Cent Sci* 2017; **3**: 31–38. [DOI: 10.1021/acscentsci.6b00290]

57 Pearson RG. Hard and Soft Acids and Bases. *J Am Chem Soc* 1963; **85**: 3533–3539.

58 Zhang W, Dong X, Mu Y, Wang Y, Chen J. Constructing adjacent phosphine oxide ligands confined in mesoporous Zr-MOFs for uranium capture from acidic medium. *J Mater Chem A Mater* 2021; **9**: 16685–16691. [DOI: 10.1039/D1TA03972E]

59 Ifthikar J, Zhao M, Shahzad A, Shahib II, Wang J, Wang H, Sellaoui L, Chen Z, Chen Z. Recyclable process modeling study of hexavalent chromium elimination by thiol-based

electron donor: Implications for practical applicability. *J Environ Chem Eng* 2021; **9**: 105645. [DOI: 10.1016/j.jece.2021.105645]

60   Kinuthia GK, Ngure V, Beti D, Lugalia R, Wangila A, Kamau L. Levels of heavy metals in wastewater and soil samples from open drainage channels in Nairobi, Kenya: community health implication. *Sci Rep* 2020; **10**: 1–13. [PMID: 32439896 DOI: 10.1038/s41598-020-65359-5]

61   Mon M, Lloret F, Ferrando-Soria J, Marta-Gastaldo C, Armentano D, Pardo E. Selective and Efficient Removal of Mercury from Aqueous Media with the Highly Flexible Arms of a BioMOF. *Angewandte Chemie - International Edition* 2016; **55**: 11167–11172. [DOI: 10.1002/anie.201606015]

62   Gala L, Lawson M, Jomova K, Zelenicky L, Congradyova A, Mazur M, Valko M. EPR Spectroscopy of a Clinically Active (1:2) Copper(II)-Histidine Complex Used in the Treatment of Menkes Disease: A Fourier Transform Analysis of a Fluid CW-EPR Spectrum. Molecules . 2014; **19**. DOI:10.3390/molecules19010980

63   Krupa K, Korabik M, Kowalik-Jankowska T. Coordination properties of Cu(II) ions towards the peptides based on the His-Xaa-His motif from Fusobacterium nucleatum P1 protein. *J   Inorg   Biochem*   2019;   **201**:   110819.   [DOI: https://doi.org/10.1016/j.jinorgbio.2019.110819]

64   Holm RH, Kennepohl P, Solomon EI. Structural and Functional Aspects of Metal Sites in Biology. *Chem Rev* 1996; **96**: 2239–2314. [DOI: 10.1021/cr9500390]

65   Maiti BK, Maia LB, Moro AJ, Lima JC, Cordas CM, Moura I, Moura JJG. Unusual Reduction Mechanism of Copper in Cysteine-Rich Environment. *Inorg Chem* 2018; **57**: 8078–8088. [PMID: 29956539 DOI: 10.1021/acs.inorgchem.8b00121]

66   Bennett B, Kowalski JM. Chapter Thirteen - EPR Methods for Biological Cu(II): L-Band CW and NARS. In: Qin PZ, Warncke KBT-M in E, editors. *Electron Paramagnetic Resonance Investigations of Biological Systems by Using Spin Labels, Spin Probes, and Intrinsic Metal Ions, Part A*. Academic Press, 2015: 341–361.

67   Saiz PG, Iglesias N, González Navarrete B, Rosales M, Quintero YM, Reizabal A, Orive J, Fidalgo Marijuan A, Larrea ES, Lopes AC, Lezama L, García A, Lanceros-Mendez S, Arriortua MI, Fernández de Luis R. AAAAAA. *Chemistry - A European Journal* 2020; **26**: 13861–13872. [DOI: 10.1002/chem.202001435]

68   Davis HJ, Ward TR. Artificial Metalloenzymes: Challenges and Opportunities. *ACS Cent Sci* 2019; **5**: 1120–1136. [DOI: 10.1021/acscentsci.9b00397]

69   Thompson Z, Cowan JA. Artificial Metalloenzymes: Recent Developments and Innovations in Bioinorganic Catalysis. *Small* 2020; **16**: 2000392. [DOI: https://doi.org/10.1002/smll.202000392]

70   Yu Y, Liu X, Wang J. Expansion of Redox Chemistry in Designer Metalloenzymes. *Acc Chem Res* 2019; **52**: 557–565. [DOI: 10.1021/acs.accounts.8b00627]

71   Wang VCC, Maji S, Chen PPY, Lee HK, Yu SSF, Chan SI. Alkane Oxidation: Methane Monooxygenases, Related Enzymes, and Their Biomimetics. *Chem Rev* 2017; **117**: 8574–8621. [PMID: 28206744 DOI: 10.1021/acs.chemrev.6b00624]

72 Li Y-M, Yuan J, Ren H, Ji C-Y, Tao Y, Wu Y, Chou L-Y, Zhang Y-B, Cheng L. Fine-Tuning the Micro-Environment to Optimize the Catalytic Activity of Enzymes Immobilized in Multivariate Metal–Organic Frameworks. *J Am Chem Soc* 2021; **143**: 15378–15390. [DOI: 10.1021/jacs.1c07107]

73 Eom H, Song WJ. Emergence of metal selectivity and promiscuity in metalloenzymes. *Journal of Biological Inorganic Chemistry* 2019; **24**: 517–531. [PMID: 31115763 DOI: 10.1007/s00775-019-01667-0]

74 Zastrow ML, Pecoraro VL. Designing functional metalloproteins: From structural to catalytic metal sites. *Coord Chem Rev* 2013; **257**: 2565–2588. [DOI: 10.1016/j.ccr.2013.02.007]

75 Lu Y, Yeung N, Sieracki N, Marshall NM. Design of functional metalloproteins. *Nature* 2009; **460**: 855–862. [PMID: 19675646 DOI: 10.1038/nature08304]

76 Fontecave M, Pierre JL. Oxidations by copper metalloenzymes and some biomimetic approaches. *Coord Chem Rev* 1998; **170**: 125–140. [DOI: 10.1016/S0010-8545(98)00068-X]

77 Quist DA, Diaz DE, Liu JJ, Karlin KD. Activation of dioxygen by copper metalloproteins and insights from model complexes. *JBIC Journal of Biological Inorganic Chemistry* 2017; **22**: 253–288. [DOI: 10.1007/s00775-016-1415-2]

78 Fontecave M, Pierre JL. Oxidations by copper metalloenzymes and some biomimetic approaches. *Coord Chem Rev* 1998; **170**: 125–140. [DOI: 10.1016/S0010-8545(98)00068-X]

79 Snyder BER, Bols ML, Schoonheydt RA, Sels BF, Solomon EI. Iron and Copper Active Sites in Zeolites and Their Correlation to Metalloenzymes. *Chem Rev* 2018; **118**: 2718–2768. [PMID: 29256242 DOI: 10.1021/ACS.CHEMREV.7B00344/ASSET/IMAGES/MEDIUM/CR-2017-00344F_0069.GIF]

80 Rumo C, Stein A, Klehr J, Tachibana R, Prescimone A, Häussinger D, Ward TR. An Artificial Metalloenzyme Based on a Copper Heteroscorpionate Enables sp3C-H Functionalization via Intramolecular Carbene Insertion. *J Am Chem Soc* 2022; **144**: 11676–11684. [PMID: 35749305 DOI: 10.1021/JACS.2C03311]

81 Alcalde M. Laccases: Biological functions, molecular structure and industrial applications. *Industrial Enzymes: Structure, Function and Applications* 2007; : 461–476. [DOI: 10.1007/1-4020-5377-0_26]

82 Liang H, Lin F, Zhang Z, Liu B, Jiang S, Yuan Q, Liu J. Multicopper laccase mimicking nanozymes with nucleotides as ligands. *ACS Appl Mater Interfaces* 2017; **9**: 1352–1360. [PMID: 28004568 DOI: 10.1021/ACSAMI.6B15124/ASSET/IMAGES/LARGE/AM-2016-151242_0007.JPEG]

83 Hernández-Monjaraz WS, Caudillo-Pérez C, Salazar-Sánchez PU, Macías-Sánchez KL. Influence of iron and copper on the activity of laccases in Fusarium oxysporum f. sp. lycopersici. *Brazilian Journal of Microbiology* 2018; **49**: 269–275. [PMID: 30145263 DOI: 10.1016/J.BJM.2018.06.002]

84 Mirts EN, Bhagi-Damodaran A, Lu Y. Understanding and Modulating Metalloenzymes with Unnatural Amino Acids, Non-Native Metal Ions, and Non-Native Metallocofactors. *Acc Chem Res* 2019; **52**: 935–944. [PMID: 30912643 DOI: 10.1021/acs.accounts.9b00011]

85 Dawson J. Probing structure–function relations in heme-containing oxygenases and peroxidases. *Science (1979)* 1988; **240**: 433–439.

86 Solomon EI, Heppner DE, Johnston EM, Ginsbach JW, Cirera J, Qayyum M, Kieber-Emmons MT, Kjaergaard CH, Hadt RG, Tian L. Copper Active Sites in Biology. *Chem Rev* 2014; **114**: 3659–3853. [DOI: 10.1021/cr400327t]

87 Poulos TL. Heme Enzyme Structure and Function. *Chem Rev* 2014; **114**: 3919–3962. [DOI: 10.1021/cr400415k]

88 Farha OK, Shultz AM, Sarjeant AA, Nguyen ST, Hupp JT. Active-Site-Accessible, Porphyrinic Metal–Organic Framework Materials. *J Am Chem Soc* 2011; **133**: 5652–5655. [DOI: 10.1021/ja111042f]

89 Balasubramanian R, Smith SM, Rawat S, Yatsunyk LA, Stemmler TL, Rosenzweig AC. Oxidation of methane by a biological dicopper centre. *Nature* 2010; **465**: 115–119. [PMID: 20410881 DOI: 10.1038/nature08992]

90 Solomon EI, Chen P, Metz M, Lee SK, Palmer AE. Oxygen binding, activation, and reduction to water by copper proteins. Angewandte Chemie - International Edition. 2001; **40**: 4570–4590.

91 Inchaurrondo NS, Massa P, Fenoglio R, Font J, Haure P. Efficient catalytic wet peroxide oxidation of phenol at moderate temperature using a high-load supported copper catalyst. *Chemical Engineering Journal* 2012; **198–199**: 426–434. [DOI: 10.1016/J.CEJ.2012.05.103]

92 Yang XF, Wang A, Qiao B, Li J, Liu J, Zhang T. Single-atom catalysts: A new frontier in heterogeneous catalysis. *Acc Chem Res* 2013; **46**: 1740–1748. [DOI: 10.1021/AR300361M/ASSET/IMAGES/LARGE/AR-2012-00361M_0009.JPEG]

93 Wang C, Xie Z, Dekrafft KE, Lin W. Doping MetalÀOrganic Frameworks for Water Oxidation, Carbon Dioxide Reduction, and Organic Photocatalysis. *J Am Chem Soc* 2011; **133**: 13445–13454. [DOI: 10.1021/ja203564w]

94 Ray K, Pfaff FF, Wang B, Nam W. Status of Reactive Non-Heme Metal–Oxygen Intermediates in Chemical and Enzymatic Reactions. *J Am Chem Soc* 2014; **136**: 13942–13958. [DOI: 10.1021/ja507807v]

95 Elwell CE, Gagnon NL, Neisen BD, Dhar D, Spaeth AD, Yee GM, Tolman WB. Copper-Oxygen Complexes Revisited: Structures, Spectroscopy, and Reactivity. *Chem Rev* 2017; **117**: 2059–2107. [PMID: 28103018 DOI: 10.1021/ACS.CHEMREV.6B00636/ASSET/IMAGES/MEDIUM/CR-2016-00636B_0043.GIF]

96 Liou RM, Chen SH. CuO impregnated activated carbon for catalytic wet peroxide oxidation of phenol. *J Hazard Mater* 2009; **172**: 498–506. [PMID: 19640643 DOI: 10.1016/J.JHAZMAT.2009.07.012]

97 Maduna K, Kumar N, Aho A, Wärnå J, Zrnčević S, Murzin DY. Kinetics of Catalytic Wet Peroxide Oxidation of Phenolics in Olive Oil Mill Wastewaters over Copper Catalysts. *ACS Omega* 2018; **3**: 7247–7260. [DOI: 10.1021/ACSOMEGA.8B00948/ASSET/IMAGES/LARGE/AO-2018-00948M_0010.JPEG]

98 Charles Dismukes G, Brimblecombe R, Felton GAN, Pryadun RS, Sheats JE, Spiccia L, Swiegers GF. Development of bioinspired Mn4O4-cubane water oxidation catalysts: Lessons from photosynthesis. *Acc Chem Res* 2009; **42**: 1935–1943. [PMID: 19908827 DOI: 10.1021/AR900249X/ASSET/IMAGES/LARGE/AR-2009-00249X_0006.JPEG]

99 Chen B, Xiang S, Qian G. Metal-organic frameworks with functional pores for recognition of small molecules. *Acc Chem Res* 2010; **43**: 1115–1124. [DOI: 10.1021/AR100023Y/ASSET/IMAGES/LARGE/AR-2010-00023Y_0002.JPEG]

100 Zhao M, Ou S, Wu C de. Porous metal-organic frameworks for heterogeneous biomimetic catalysis. *Acc Chem Res* 2014; **47**: 1199–1207. [PMID: 24499017 DOI: 10.1021/AR400265X/ASSET/IMAGES/LARGE/AR-2013-00265X_0010.JPEG]

101 Wang X, Lan PC, Ma S. Metal-Organic Frameworks for Enzyme Immobilization: Beyond Host Matrix Materials. *ACS Cent Sci* 2020; **6**: 1497–1506. [DOI: 10.1021/ACSCENTSCI.0C00687/ASSET/IMAGES/LARGE/OC0C00687_0006.JPEG]

102 Deuss PJ, Denheeten R, Laan W, Kamer PCJ. Bioinspired Catalyst Design and Artificial Metalloenzymes. *Chemistry – A European Journal* 2011; **17**: 4680–4698. [PMID: 21480401 DOI: 10.1002/CHEM.201003646]

103 Bour JR, Wright AM, He X, Dincă M. Bioinspired chemistry at MOF secondary building units. *Chem Sci* 2020; **11**: 1728–1737. [DOI: 10.1039/C9SC06418D]

104 Doonan C, Riccò R, Liang K, Bradshaw D, Falcaro P. Metal-Organic Frameworks at the Biointerface: Synthetic Strategies and Applications. *Acc Chem Res* 2017; **50**: 1423–1432. [PMID: 28489346 DOI: 10.1021/ACS.ACCOUNTS.7B00090/ASSET/IMAGES/LARGE/AR-2017-000906_0005.JPEG]

105 Hartmann M. Ordered mesoporous materials for bioadsorption and biocatalysis. *Chemistry of Materials* 2005; **17**: 4577–4593. [DOI: 10.1021/CM0485658/ASSET/IMAGES/LARGE/CM0485658F00023.JPEG]

106 Ji Z, Wang H, Canossa S, Wuttke S, Yaghi OM, Ji Z, Wang H, Yaghi OM, Canossa S, Wuttke S. Pore Chemistry of Metal–Organic Frameworks. *Adv Funct Mater* 2020; **30**: 2000238. [DOI: 10.1002/ADFM.202000238]

107 Landaluce N, Perfecto-Irigaray M, Albo J, Beobide G, Castillo O, Irabien A, Luque A, Méndez ASJ, Platero-Prats AE, Pérez-Yáñez S. Copper(II) invigorated EHU-30 for continuous electroreduction of CO2 into value-added chemicals. *Scientific Reports 2022 12:1* 2022; **12**: 1–7. [PMID: 35595765 DOI: 10.1038/s41598-022-11846-w]

108 Valverde A, Payno D, Lezama L, Laza JM, Wuttke S, Fernández de Luis R. Multivariate Functionalization of UiO-66 for Photocatalytic Water Remediation. *Adv Sustain Syst* 2022; **6**: 2200024. [DOI: 10.1002/adsu.202200024]

109 Hong AN, Kusumoputro E, Wang Y, Yang H, Chen Y, Bu X, Feng P, Hong AN, Kusumoputro E, Wang Y, Chen Y, Feng P, Yang H, Bu X. Simultaneous Control of Pore-Space Partition

and Charge Distribution in Multi-Modular Metal–Organic Frameworks. *Angewandte Chemie International Edition* 2022; **61**: e202116064. [PMID: 35098623 DOI: 10.1002/ANIE.202116064]

110   Evans JD, Bon V, Senkovska I, Lee HC, Kaskel S. Four-dimensional metal-organic frameworks. *Nature Communications 2020 11:1* 2020; **11**: 1–11. [PMID: 32483346 DOI: 10.1038/s41467-020-16527-8]

111   Feng L, Day GS, Wang KY, Yuan S, Zhou HC. Strategies for Pore Engineering in Zirconium Metal-Organic Frameworks. *Chem* 2020; **6**: 2902–2923. [DOI: 10.1016/J.CHEMPR.2020.09.010]

112   Ikuno T, Zheng J, Vjunov A, Sanchez-Sanchez M, Ortuño MA, Pahls DR, Fulton JL, Camaioni DM, Li Z, Ray D, Mehdi BL, Browning ND, Farha OK, Hupp JT, Cramer CJ, Gagliardi L, Lercher JA. Methane Oxidation to Methanol Catalyzed by Cu-Oxo Clusters Stabilized in NU-1000 Metal-Organic Framework. *J Am Chem Soc* 2017; **139**: 10294–10301. [PMID: 28613861 DOI: 10.1021/JACS.7B02936/SUPPL_FILE/JA7B02936_SI_001.PDF]

113   Yi Hu C, Wei Jiang Z, Zhi Huang C, Fang Li Y. Cu 2+-modified MOF as laccase-mimicking material for colorimetric determination and discrimination of phenolic compounds with 4-aminoantipyrine. *Microchimica Acta* 2021; **188**: 272. [DOI: 10.1007/s00604-021-04944-5/Published]

114   Pan Y, Jiang S, Xiong W, Liu D, Li M, He B, Fan X, Luo D. Supported CuO catalysts on metal-organic framework (Cu-UiO-66) for efficient catalytic wet peroxide oxidation of 4-chlorophenol in wastewater. *Microporous and Mesoporous Materials* 2020; **291**: 109703. [DOI: 10.1016/J.MICROMESO.2019.109703]

115   Shams S, Ahmad W, Memon AH, Wei Y, Yuan Q, Liang H. Facile synthesis of laccase mimic Cu/H 3 BTC MOF for efficient dye degradation and detection of phenolic pollutants. *RSC Adv* 2019; **9**: 40845–40854. [DOI: 10.1039/C9RA07473B]

116   Gholipoor O, Hosseini SA. Phenol removal from wastewater by CWPO process over the Cu-MOF nanocatalyst: process modeling by response surface methodology (RSM) and kinetic and isothermal studies. *New Journal of Chemistry* 2021; **45**: 2536–2549. [DOI: 10.1039/D0NJ04128A]

117   Valverde A, Tovar GI, Rio-López NA, Torres D, Rosales M, Wuttke S, Fidalgo-Marijuan A, Porro JM, Jiménez-Ruiz M, Sakai VG, García A, Laza JM, Vilas-Vilela JL, Lezama L, Arriortua MI, Copello GJ, Luis RF de. Designing Metal-Chelator-like Traps by Encoding Amino Acids in Zirconium-Based Metal–Organic Frameworks. *Chemistry of Materials* 2022; **34**: 9666–9684. [DOI: 10.1021/ACS.CHEMMATER.2C02431]

118   Hadjiivanov KI, Panayotov DA, Mihaylov MY, Ivanova EZ, Chakarova KK, Andonova SM, Drenchev NL. Power of Infrared and Raman Spectroscopies to Characterize Metal-Organic Frameworks and Investigate Their Interaction with Guest Molecules. *Chem Rev* 2021; **121**: 1286–1424. [DOI: 10.1021/acs.chemrev.0c00487]

119   Parker SF. Assignment of the vibrational spectrum of l-cysteine. *Chem Phys* 2013; **424**: 75–79. [DOI: 10.1016/j.chemphys.2013.04.020]

120 Jalilehvand F, Sisombath NS, Schell AC, Facey GA. Lead(II) complex formation with L-cysteine in aqueous solution. *Inorg Chem* 2015; **54**: 2160–2170. [PMID: 25695880 DOI: 10.1021/IC5025668/SUPPL_FILE/IC5025668_SI_001.PDF]

121 Dokken KM, Parsons JG, McClure J, Gardea-Torresdey JL. Synthesis and structural analysis of copper(II) cysteine complexes. *Inorganica Chim Acta* 2009; **362**: 395–401. [DOI: 10.1016/j.ica.2008.04.037]

122 de Sousa GP, Freire PTC, Filho JM, Melo FEA, Lima CL. Low-Temperature Raman Spectra of l-Histidine Crystals. *Brazilian Journal of Physics* 2013; **43**: 137–144. [DOI: 10.1007/S13538-013-0132-3/FIGURES/6]

123 Freire PTC, Barboza FM, Lima JA, E.A. Melo F, Filho JM, Freire PTC, Barboza FM, Lima JA, E.A. Melo F, Filho JM. Raman Spectroscopy of Amino Acid Crystals. In: *Raman Spectroscopy and Applications*. IntechOpen, 2017 DOI:10.5772/65480

124 Sturge MD. The Jahn-Teller Effect in Solids. *Solid State Physics - Advances in Research and Applications* 1968; **20**: 91–211. [DOI: 10.1016/S0081-1947(08)60218-0]

125 Sigel H, Martin RB. Coordinating Properties of the Amide Bond. Stability and Structure of Metal Ion Complexes of Peptides and Related Ligands. *Chem Rev* 1982; **82**: 385–426. [DOI: 10.1021/CR00050A003/ASSET/CR00050A003.FP.PNG_V03]

126 Ivanova TM, Maslakov KI, Sidorov AA, Kiskin MA, Linko R v., Savilov S v., Lunin V v., Eremenko IL. XPS detection of unusual Cu(II) to Cu(I) transition on the surface of complexes with redox-active ligands. *J Electron Spectros Relat Phenomena* 2020; **238**: 146878. [DOI: 10.1016/J.ELSPEC.2019.06.010]

127 Alessandrini A, Corni S, Facci P. Unravelling single metalloprotein electron transfer by scanning probe techniques. *Physical Chemistry Chemical Physics* 2006; **8**: 4383–4397. [PMID: 17001404 DOI: 10.1039/B607021C]

128 Wang J, Huang R, Qi W, Su R, Binks BP, He Z. Construction of a bioinspired laccase-mimicking nanozyme for the degradation and detection of phenolic pollutants. *Appl Catal B* 2019; **254**: 452–462. [DOI: 10.1016/J.APCATB.2019.05.012]

129 Azizi A, Abouseoud M, Amrane A. Phenol Removal by a Sequential Combined Fenton-Enzymatic Process Nature Environment and Pollution Technology An International Quarterly Scientific Journal Open Access. *Nature Environment and Pollution Technology* 2017; **16**: 321–330. www.neptjournal.com. Accessed 28 November 2022

130 Ray K, Pfaff FF, Wang B, Nam W. Status of reactive non-heme metal-oxygen intermediates in chemical and enzymatic reactions. *J Am Chem Soc* 2014; **136**: 13942–13958. [PMID: 25215462 DOI: 10.1021/JA507807V/ASSET/IMAGES/LARGE/JA-2014-07807V_0012.JPEG]

131 Nosaka Y, Nosaka AY. Generation and Detection of Reactive Oxygen Species in Photocatalysis. *Chem Rev* 2017; **117**: 11302–11336. [PMID: 28777548 DOI: 10.1021/acs.chemrev.7b00161]

132 Groom CR, Allen FH. The Cambridge Structural Database in Retrospect and Prospect. *Angewandte Chemie International Edition* 2014; **53**: 662–671. [DOI: 10.1002/ANIE.201306438]

133   Allen FH. The Cambridge Structural Database: A quarter of a million crystal structures and rising. *Acta Crystallogr B* 2002; **58**: 380–388. [PMID: 12037359 DOI: 10.1107/S0108768102003890/HTTPS://JOURNALS.IUCR.ORG/SERVICES/TERMSOFUSE. HTML]

134   Yoshinari N, Igashira-Kamiyama A, Konno T, Yoshinari N, Igashira-Kamiyama A, Konno T. Polar 2D Sheet versus Nonpolar 1D Helix Metallosupramolecular Architectures Based on M6M'8 (M=PdII, NiII; M'=CuI, AgI) Cage Clusters with D-Penicillaminate. *Chemistry – A European Journal* 2010; **16**: 14247–14251. [DOI: 10.1002/CHEM.201001886]

135   OnoTaizo, SasadaYoshio. Crystal Structures of Mixed Ligand Copper(II) Complexes Containing L-Amino Acids. II. (L-Alaninato)aqua(L-histidinato)copper(II) Trihydrate. *https://doi.org/101246/bcsj5490* 2006; **54**: 90–93. [DOI: 10.1246/BCSJ.54.90]

136   Fleck M, Tillmanns E, Bohatý L, Held P. On racemic and L-malates: A comparison of their crystal structures. *Zeitschrift fur Kristallographie* 2004; **219**: 101–111. [DOI: 10.1524/ZKRI.219.2.101.26323/MACHINEREADABLECITATION/RIS]

137   Al-Dajani MTM, Abdallah HH, Mohamed N, Yeap CS, Fun HK. Tetraguanidinium bis-[citrato(3-)]cuprate(II) dihydrate. *Acta Crystallogr Sect E Struct Rep Online* 2009; **65**: m1540–m1541. [DOI: 10.1107/S1600536809046170/CI2960ISUP2.HKL]

138   Lane RH, Pantaleo NS, Farr JK, Coney WM, Newton MG. A Structural Model for Type 3 Copper in Multicopper Oxidases. *J Am Chem Soc* 1978; **100**: 1610–1611. [DOI: 10.1021/JA00473A052/ASSET/JA00473A052.FP.PNG_V03]

139   Gudavarthy R v., Burla N, Kulp EA, Limmer SJ, Sinn E, Switzer JA. Epitaxial electrodeposition of chiral CuO films from copper(II) complexes of malic acid on Cu(111) and Cu(110) single crystals. *J Mater Chem* 2011; **21**: 6209–6216. [DOI: 10.1039/C0JM03423A]

140   Evertsson B, IUCr. The crystal structure of bis-l-histidinecopper(II) dinitrate dihydrate. *Acta Crystallographica Section B* 1969; **25**: 30–41. [DOI: 10.1107/S0567740869001737]

141   HoriFumio, KojimaYoshitane, MatsumotoKeiji, OoiShun'ichiro, KuroyaHisao. The Synthesis and Crystal Structure of Bis(cyclo-L-histidyl-L-histidyl)copper(II) Perchlorate Tetrahydrate. *http://dx.doi.org/101246/bcsj521076* 2006; **52**: 1076–1079. [DOI: 10.1246/BCSJ.52.1076]

142   Lin TY, Wu CH. Activation of hydrogen peroxide in copper(II)/amino acid/H2O2 systems: effects of pH and copper speciation. *J Catal* 2005; **232**: 117–126. [DOI: 10.1016/J.JCAT.2005.01.038]

143   Robbins MH, Drago RS. Activation of Hydrogen Peroxide for Oxidation by Copper(II) Complexes. *J Catal* 1997; **170**: 295–303. [DOI: 10.1006/JCAT.1997.1754]

144   Banu KS, Chattopadhyay T, Banerjee A, Bhattacharya S, Zangrando E, Das D. Catechol oxidase activity of dinuclear copper(II) complexes of Robson type macrocyclic ligands: Syntheses, X-ray crystal structure, spectroscopic characterization of the adducts and kinetic studies. *J Mol Catal A Chem* 2009; **310**: 34–41. [DOI: 10.1016/J.MOLCATA.2009.05.016]

145   Langerman M, Hetterscheid DGH. Mechanistic Study of the Activation and the Electrocatalytic Reduction of Hydrogen Peroxide by Cu-tmpa in Neutral Aqueous Solution. *ChemElectroChem* 2021; **8**: 2783–2791. [DOI: 10.1002/CELC.202100436]

Chapter 5

Chapter 5
Polymer@MOF composites for water remediation

Metal-organic frameworks (MOFs) have shown to be highly efficient sorbents to recover metal ions from wastewater. However, there are three main drawbacks that hinders the MOF's applicability as heavy metal remediation systems. The first one is related to their powder nature, which makes their recovery from water time and energy consuming, as filtration or centrifugation techniques are usually needed.[1] Second, MOFs exhibit limited processability to shape them as millimetre to macrometre size objects like filters or membranes. Last but not least, even if MOFs exhibit record surface areas, most of them are microporous, and thus, their adsorption capacity is limited to small elements as ions or molecules as dyes or drugs.

In this regard, the hybridization of active sorbents such as MOFs with mechanically robust polymeric matrixes stands out as one of the most appealing strategies to solve the abovementioned handicaps. Polymeric composites bring the opportunity to merge the functions of the MOF microporous sorbents with the easy manipulation of filter or membrane technologies. In addition, the polymeric matrixes can be processed to endow them of meso to a macroporous interconnected structure.[2] What is more, the variety of possible polymers and sorbents combinations,[3,4] and the control over the final macro to micropore structure of the composite membranes, opens up the perspective to obtain easily recoverable, reactivable, and function/pollutant-tailored filter or membrane devices for water remediation purposes.[5–9] However, MOF-polymer hybridization remains a challenge since involves merging two types of materials, each with their unique intrinsic characteristics.

It is important to note that, among several parameters, the properties and functionalities of a polymeric nano-composite is highly dependent on (i) the dispersion and distribution of the nano-material in the polymeric matrix and (ii) the interfacial interaction between the surface of the nanomaterial and the matrix.[10] Nevertheless, these two features of polymeric composites systems have been scarcely

studied, being the interface between the polymer and the MOF a specially unexplored point of these complex materials. This elusive region of the composite systems requires of quite advanced experimental approaches, as small angle scattering techniques, to unravel its characteristics. Considering all the landscape, several challenges arise when polymer@MOF composites are synthetized:

- To obtain a good dispersion and a stable integration of the MOF particles into the polymeric matrix.
- To achieve the MOF immobilization at the surface of the membrane's pores instead inside the polymer matrix to enhance the accessibility of MOF to the water media migrating across the composite system.
- To integrate the MOF without affecting the processing of the polymer.
- To obtain a highly interconnected macro-meso structure in the polymer.
- To engineer a composite without altering the individual MOF's or polymer's properties for water remediation.

As it is difficult to cover the entire spectrum of the research opportunities in the timespan of a thesis project, we have focused our efforts on two case-studies. First, we have investigated how the nano-structuration of PVDF-HFP@MOF composites impacts their adsorption performance. Second, we have evaluated the meso to nanoporous nature of Chitin@MOF system as wide range adsorbent for small to large size inorganic and organic pollutants.

5.1. UNRAVELLING THE MICRO TO NANOSTRUCTURE OF PVDF-HFP@MOF WATER REMEDIATION MEMBRANES BY SMALL ANGLE SCATTERING

Poly (vinylidene fluoride-co-hexafluoropropylene) (PVDF-HFP), is a chemical, thermal and mechanical robust polymer widely employed for water remediation purposes (*i.e.* removal or separation of organic and inorganic pollutants,[11] organic matter,[12] ions (desalination)[13,14] and heavy metals).[15] In addition to this, PVDF-HFP has an easy and widely-studied processability, which opens the perspective to shape it as water-filters and membranes with outstandingly varied porous structures.[16]

Generally speaking, the properties of PVDF-HFP membranes for water remediation are based on the size exclusion methodology provided by their porous structure. That is, depending on their porosity and structure, they can be used as membranes from microfiltration to nanofiltration, or even, reverse osmosis.[15,17] However, the permeability and adsorbing capacity of these membranes is drastically limited because of their overall hydrophobicity. The integration of nanomaterials, and especially of porous Metal-Organic Framework nanomaterials, into the polymeric porous structure of the PVDF-HFP membranes, has arisen as a smart and straightforward strategy to improve the hydrophilicity of membranes or filters based on this per-fluorinated polymer.[18,19] In parallel, the engineering of PVDF-HFP@MOF composites can endow these systems of a multifunctionality, easy recoverability, reactivation and reusability that the individual elements lack.

Among all the processing routes that PVDF and its co-polymers offer, phase inversion techniques are ones of the most employed to obtain a PVDF membrane with an interconnected porous structure suitable for water remediation applications. Phase transformations of PVDF involves the transition from a homogeneously dissolved polymeric units in a liquid media to their conformation as a porous interconnected solid with the desired micrometric shape (*i.e.* membrane). The process can be achieved by following different routes as: thermally induced phase separation (TIPS), non-solvent induced phase separation (NIPS), vapour-induced phase separation (VIPS) and evaporation induced phase separation (EIPS).[16,20] The type and

conditions of the phase separation have great influence on the PVDF micro to macrometer pore structuration, as well as on the fillers homogeneous or heterogeneous integration and/or segregation on the PVDF-matrix.

Moreover, the processing of the PVDF is key to: (i) avoid the full encapsulation of the MOFs within the polymeric matrix, (ii) enhance their surface exposure into the interconnected pore-space of the polymeric matrix, and (iii) prevent their detachment during working and activation conditions.[21] Overall, these characteristics are closely related to the structuration of the composites from the macroscopic to the nanoscopic perspectives. Even if several PVDF-HFP composites have been profoundly studied from macro to microscopic regimes, the investigations aiming to unravel the nanostructure of these composites *via* small angle scattering techniques (*i.e.* small angle X-ray (SAXS) and neutron (SANS) scattering) are still limited.[22] This point is far to be trivial, since SAXS and SANS can give access to unravel key aspects of these composites, such as (i) the disposition of the MOF particles into the PVDF structure, (ii) the interconnexion of their pore-space or (iii) the interface between the MOF and the PVDF components.[23,24] All these features may have a great impact in the functionality of the composite membranes to capture the target pollutants.

In this work, the templating effect of the MIL-125, UiO-66-NH$_2$ and MOF-808 fillers in the porous structure and physicochemical properties of PVDF-HFP@MOF composites processed by TIPS and NIPS has been investigated. The macro, meso and microporous structure of the PVDF-HFP@MOF composites has been characterized by a combination of specific experimental techniques such as scanning electron microscopy and mercury intrusion porosimetry. The study has been extended to small angle neutron and X-ray scattering experiments, which provide a complete insight of the interphase and structuration of PVDF-HFP@MOF composites at the nanoscale. Finally, the performance of the MOF particles immobilized in the PVDF-HFP membranes to adsorb hexavalent chromate oxyanions (CrO$_4^{2-}$) has been evaluated. The encapsulation degree of the MOF particles within the membrane has been determined comparing their adsorption capacity over Cr^{VI} before and after their immobilization. In parallel, the post-synthetic functionalization of the MOF-808 immobilized into the PVDF-HFP has been carried out in order to adapt its adsorption

affinity to soft metal cations as Hg^{II}. Overall, the adsorption performance of the MOFs immobilized in the composite membranes over cationic and anionic species have been correlated with the macro to nano-structural features of the system.

5.1.1. EXPERIMENTAL PROCEDURE

Synthesis of MIL-125

MIL125-R was synthetized by reflux adapting the protocol described previously by Wang *et al.*[25] BDC (7.70 g) was dissolved in 100 mL of DMF under reflux and continuous stirring at 100 °C for 1 h. Then, 28 mL of methanol was added to the solution and further stirred for 1 h. Afterwards, 8.4 mL of Titanium isopropoxide $(Ti(iPrO)_4)$ was added drop by drop to prevent the formation of agglomerates. The reaction was refluxed for three days, recovered by centrifugation, and thoroughly washed with DMF (100 mL, three times) and methanol (100 mL, three times) over the period of three days to remove the non-reacted reagents. Finally, it was dried at 80°C during one day.

Synthesis of UiO-66-NH$_2$

A slightly modified solvothermal synthesis was employed to prepare a UiO-66-NH$_2$ nanometric sample as previously reported[26]. Zirconium chloride (ZrCl$_4$, 0.5418 g) was dissolved in 60 mL of dimethylformamide (DMF) under stirring in a Pyrex® autoclave. Afterwards, aminoterephthalic acid (BDC-NH$_2$ 0.185 g) and distilled water (1.5 mL) were dropwise added to the zirconium chloride solution. The reactor was heated in an isothermal oven at 80 °C for one day. The material was recovered by centrifugation, washed with DMF (100 mL, three times) and methanol (100 mL, three times) over a period of three days. Finally, it was dried at 80 °C during one day.

Synthesis of MOF-808

Trimesic acid (BTC, 2.1 g, 10 mmol) and zirconium dichloride oxide octahydrate ($ZrOCl_2 \cdot 8H_2O$, 9.7 g, 30 mmol) were dissolved in two DMF/formic acid solutions (225 mL/225 mL each), that later on were mixed in a 1 L screw-capped glass jar. Afterwards, the reaction was performed at 130 °C for 48 h in an isothermal oven.[27] The white precipitate was collected by centrifugation and washed with DMF (100 mL, three times) and methanol (100 mL, three times) over a period of three days. Finally, the sample was dried at 80 °C for one day.

Functionalization of MOF-808 particles

Solvent assisted ligand incorporation (SALI)[28] was performed into water solutions of cysteine (Cys). To this end, 300 mL of a 0.05 M water solution of cysteine was prepared in a 500 mL autoclave at 60 °C. MOF-808 (600 mg) was dispersed under continuous stirring during 1h in the cysteine solution and heated at 60 °C for 24 h in an isothermal oven. MOF-808@Cys was recovered by centrifugation and washed with water (100 mL, three times) (12 h each) and then with 100 mL methanol other 3 times (12 h each). Finally, the samples were dried at 80 °C overnight (12 h) and stored in a desiccator.

Membrane preparation and in-situ functionalization

PVDF-HFP@MOF membranes were prepared through two different phase inversion methods: thermal induced phase separation (TIPS) and non-solvent induced phase separation (NIPS).

For both procedures, the first step is the preparation of the PVDF-based solution. For the samples without MOF particles, 1 g PVDF-HFP was dissolved in 6 mL of DMF (15 % wt solution) and stirred magnetically until a homogeneous solution was obtained. For the membranes prepared with different MOF loadings, first, the MOF particles were dispersed *via* sonication in the DMF, and then the PVDF-HFP was

added until a homogeneous mixture was obtained. A resume of the quantities used for each composite can be found in Table 5.1.

Table 5.1. Quantities of PVDF-HFP and MOFs used for the preparation of the membranes

Sample	PVDF-HFP (g)	MOF(g)	DMF (mL)
PVDF-HFP	1.00	0.00	6
PVDF-HFP@MIL-125 10%	0.90	0.10	6
PVDF-HFP@UiO-66-NH$_2$ 10%	0.90	0.10	6
PVDF-HFP@MOF-808 10%	0.90	0.10	6
PVDF-HFP@MOF-808 30%	0.70	0.30	6

Once a homogeneous PVDF-HFP solution and PVDF-HFP/MOF dispersions were obtained, two different methodologies were followed to process the composites. For TIPS membranes (Figure 5.1a), the solution/dispersion was spread on a glass substrate by doctor blade with a selected thickness of 250 µm. Then, the film was placed in an air oven at 25 °C for three days to evaporate the DMF solvent. For NIPS membranes (Figure 5.1b), the solution was also spread on a glass substrate by doctor blade, but the film was immediately placed in a water bath at 75 °C temperature for 30 minutes. Then, the film was immersed in clean water at room temperature for 5 minutes to remove traces of the solvent, and finally it was allowed to dry at room temperature for 24 hours.

For the functionalization of the PVDF-HFP@MOF-808 membranes with cysteine, the procedure was similar to the one applied for the MOF-808 particles functionalization. 100 mg membrane were immersed in 100 mL of a 0.05 M cysteine solution and heated at 60 °C for 24 h. Then, the membranes were washed with water two times and dried at room temperature for 24 h.
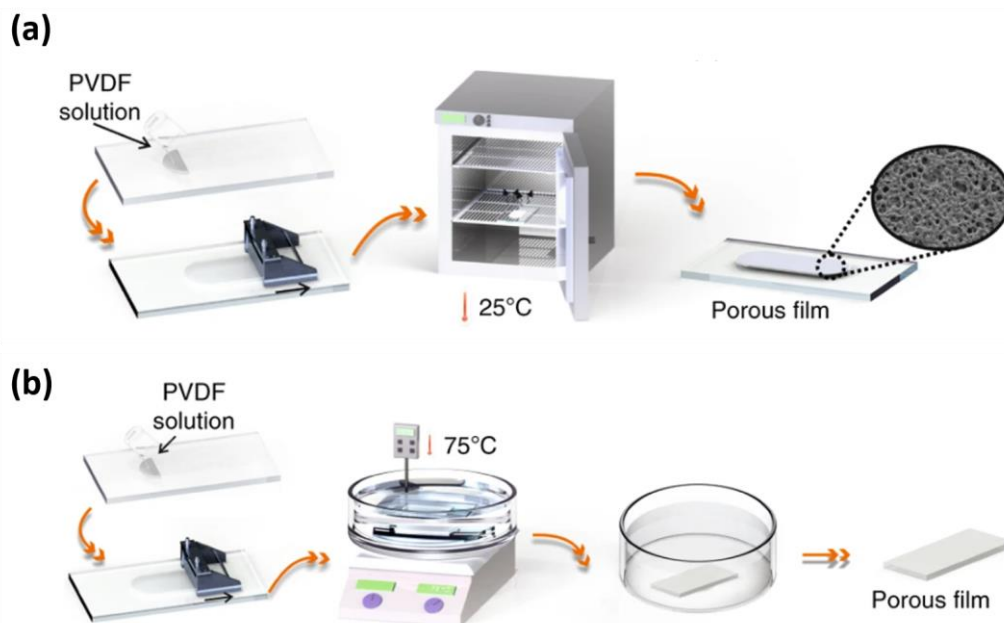
Figure 5.1. Schematic representation of PVDF-HFP film preparation methods: (a) TIPS and (b) NIPS. Reproduced with permission from Ribeiro *et al.*[16]

Cr^{VI} adsorption experiments

The adsorption capacity over Cr^{VI} of the free MOFs (MIL-125, UiO-66-NH$_2$ and MOF-808) and of the PVDF-HFP@MOF composites processed by TIPS and NIPS was studied in parallel and employing the same MOF: solution ratio for both the free materials and the membranes. For the adsorption experiments using free MOF particles, 5 mg of MOF were dispersed in 50 mL of a 5 ppm heavy metal solution and stirred overnight. Then, they were filtrated with nylon filters (0.22 µm) and the metal concentration was analysed. For the adsorption experiments using the membranes, 10 mg of the membrane was introduced in 10 mL Cr^{VI} solution at 5 ppm. The membrane was recovered after the adsorption, and the Cr^{VI} concentration of the solution was quantified through UV-Vis spectroscopy by applying the previously reported diphenyl carbazide (DPC) colorimetric methodology (see Chapter 2, section 2.3.3). Triplicate experiments were performed at the same conditions in order to determine the uncertainty of the protocol.

Hg^{II} adsorption experiments

The PVDF-HFP@MOF-808 composite membranes were in situ functionalized with cysteine in order to study the modulation of the adsorption affinity of the MOF-808 immobilized into the polymeric matrix for cationic species as Hg^{II}. To this end, Hg^{II} punctual adsorption experiments were performed in cysteine functionalized and non-functionalized membranes. As previously reported in this thesis, the encoding of MOF-808 with cysteine shifts the adsorption affinity of the materials towards soft cations such as Hg^{II}.

The adsorption experiments were performed following the same procedure used for Cr^{VI} adsorption. Hg^{II} concentrations were quantified by means of ICP-AES. Similarly than for Cr^{VI} adsorption experiments, triplicate experiments were performed at the same conditions in order to determine the uncertainty of the protocol.

5.1.2. RESULTS AND DISCUSSION

MOF characterization

As mentioned before, the Metal-Organic Frameworks employed in this work were selected due to their (i) good water stability, (ii) affinity towards adsorption of metal oxyanions, and (iii) chemical functionalizability to modulate their adsorption properties. Once synthesised, solvent exchanged and activated, a full characterization of the MOFs and PVDF-HFP@MOF membranes was performed by XRD, IR, CO_2 adsorption and TGA.

The visual comparison between the experimental and simulated X-ray diffraction patterns of the MOF-808, UiO-66-NH$_2$ and MIL-125 materials reveals a full agreement among them. The absence of additional maxima discards the existence of secondary impurities in the samples. Full profile matching fitting further confirms the initial analysis of the XRD data (Figure 5.2). As expected, a slight broadening of the diffraction maxima is observed due to the nanometer-scale size of the MOF crystals, especially for MOF-808 and UiO-66-NH$_2$. As confirmed by SEM, these MOFs show

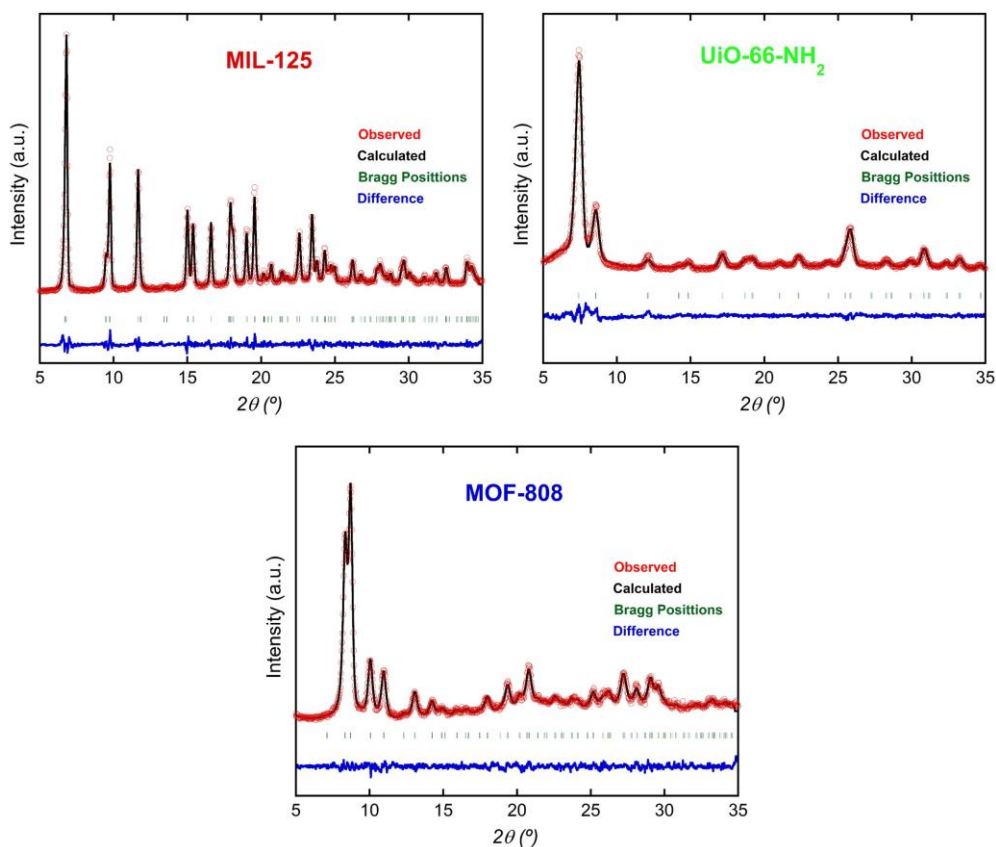a smaller particle size (50-200 nm) in comparison to the one of MIL-125 (100-500 nm) (Figure 5.3).

Figure 5.2. Full profile matching analysis of the XRD-patterns of MIL-125, UiO-66-NH$_2$ and MOF-808 samples.

The SEM images (Figure 5.3) show that UiO-66-NH$_2$ crystalizes as spherical particles of approximately 50-100 nm of diameter. Nevertheless, it is worthy to point out that an important agglomeration between the UiO-66-NH$_2$ particles has been observed by scanning electron microscopy. MOF-808 shows particles of around 150-200 nm, but less agglomerated than the ones observed for the UiO-66-NH$_2$ samples. Finally, MIL-125 is the most heterogeneous material in terms of particle size distribution. With diameters that go from 100 nm to 500 nm, MIL-125 crystallizes as cylindrical crystals that show a negligible agglomeration, as perceived in the SEM images.
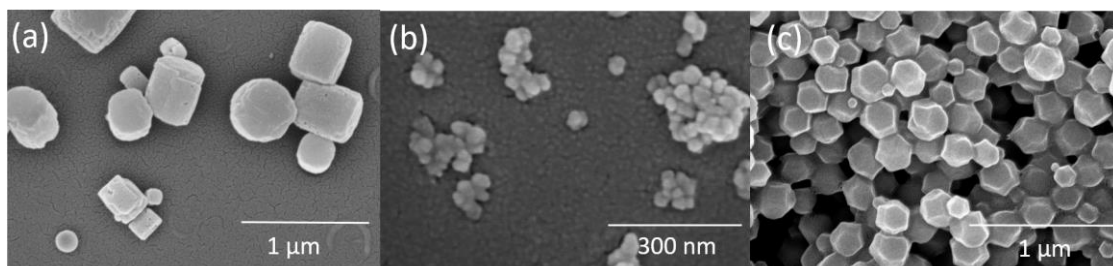
Figure 5.3. SEM images of (a) MIL-125, (b) UiO-66-NH$_2$ and (c) MOF-808 samples.

Thermogravimetric curves of the three studied MOFs (Figure 5.4a) are similar to the ones reported in previous studies.[26,29] In general, the thermal processes associated to the loss of solvent molecules (30 - 120 ºC), coordinated species (120 - 350 ºC) and calcination of the organic linkers (350 - 600 ºC) are observed in the thermogravimetric curves. In addition, the type I CO$_2$ adsorption isotherms (Figure 5.4b) confirm the microporous nature of the compounds. The surface area, calculated from the linearized fitting of the adsorption isotherm, is in the usual ranges reported in previous investigations for these materials (MIL-125[30] = 785 m$^2\cdot$g^{-1}, UiO-66-NH$_2$[31] = 922 m$^2\cdot$g^{-1}, MOF-808[32] = 1037 m$^2\cdot$g^{-1}).
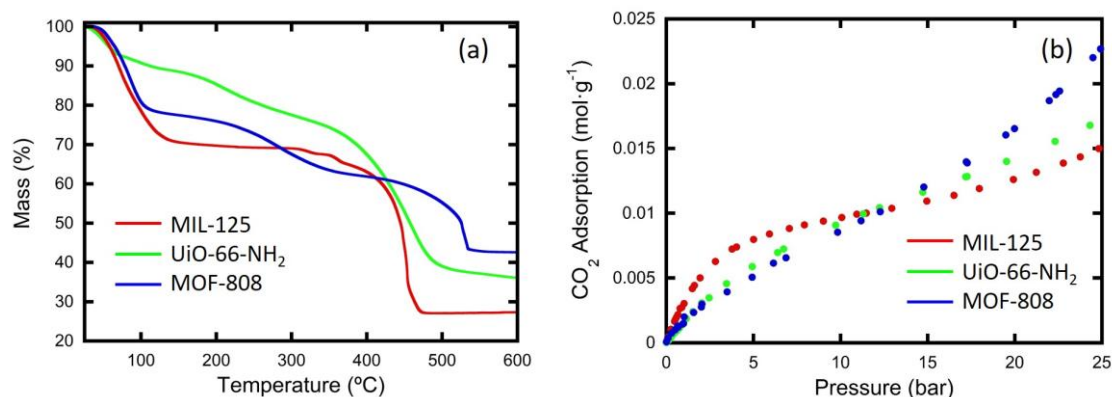

Figure 5.4. (a) Thermogravimetric analysis and (b) CO$_2$ adsorption isotherms acquired at 0 ºC for the three MOFs.

Macro to microporous structure of PVDF-HFP@MOF composites

The presence of the MOF in the PVDF-HFP composites was confirmed by infrared spectroscopy (Figure 5.5a-b) and powder X-ray diffraction (Figure 5.5c-d). Infrared spectra point out that PVDF-HFP@MOF membranes are stabilized as both α and β phases. The bands corresponding to β phase are found at 1234 and 840 cm⁻¹, while the bands corresponding to α phase are located at 976 and 763 cm⁻¹.[33] It is not fully clear if a minor content of the γ-PVDF phase is also present in the composites, as it's characteristic signal (833 cm⁻¹) is located next to the one corresponding to the β phase. The inclusion of the MOFs does not seem to modify the crystallization phase of the polymeric matrix, with the exception of the band located at 763 cm⁻¹ that corresponds to α phase, which gains intensity in TIPS membranes after the incorporation of the particles.
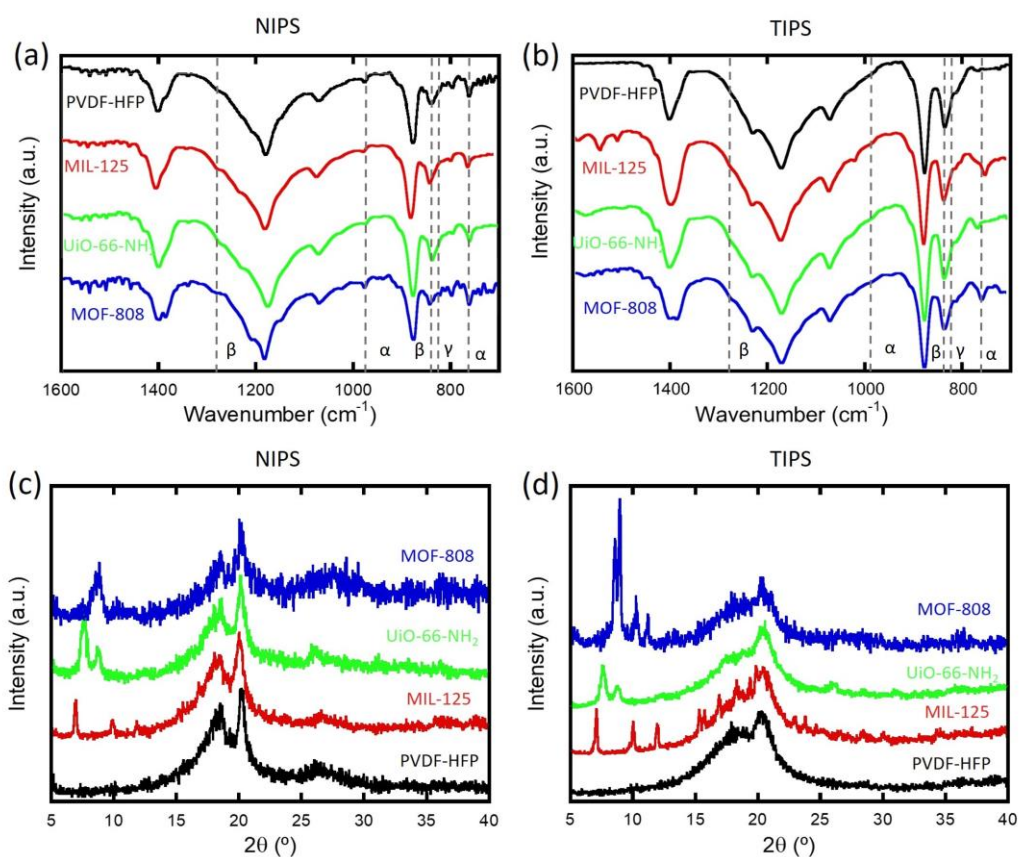

Figure 5.5. (a-b) FTIR spectra and (c-d) X-ray diffraction patterns for neat PVDF-HFP and different PVDF-HFP@MOF composites.

XRD patterns of the composites confirm the presence of MOF materials after their integration within the PVDF-HFP polymeric matrix (Figure 5.5c-d). The characteristic diffraction maxima of the MOFs can be easily recognized in the XRD patterns of all the membranes. It is important to note, that even if the MOF loading in the polymeric matrixes is the same for NIPS and TIPS membranes, the intensity of the diffraction peaks associated to the MOFs are quite different. This could be related with a heterogeneous distribution of the MOF in the polymer, being the TIPS membranes the ones that seem to have a higher density of MOF particles near the surface of the membrane.

The processing method also induces a change in its X-ray diffraction signal coming from the polymeric matrix. Both membranes present the diffraction maxima and their relative intensity expected for the alpha phase of the material. However, the mean height width of the maxima in the membranes processed by TIPS and by NIPS is different. In general terms, the composites processed by TIPS present more defined and narrow diffraction maxima, and therefore, a higher crystallinity in comparison to the NIPS homologues.

Thermogravimetric data of PVDF-HFP@MOF composites point out that the integration of the MOF particles reduces the thermal stability of the polymeric support (Figure 5.6a-b). The thermal collapse of the PVDF-HFP matrix consists of two overlapped weight losses from 425 to 450 °C and 450 to 600 °C. This weight losses are related to PVDF carbon-hydrogen and carbon-fluoride bond scission, and occur in two partially overlapped steps due to the difference in the bond strength of C–H compared with C–F (410 and 460 kJ·mol^{-1}, respectively).[21,34–36] MOF particles reduce the degradation temperature as well as the percentage of weight loss associated to the initial step, which is ascribed to the thermal collapse of the polymer. This trend has also been reported for PVDF composites including other inorganic and organic fillers.[33,37,38]

In line with the thermogravimetric analyses, the DSC measurements of the PVDF-HFP and PVDF-HFP@MOF samples (Figure 5.6c-d) exhibit the characteristic endothermic peak corresponding to the melting temperature of the polymer (~140 °C), but also an endothermic process (60–90°C) related to the dehydration of the MOF

compounds. On the other hand, during the cooling process, the crystallization of the polymer is detected approximately at ~100 °C.
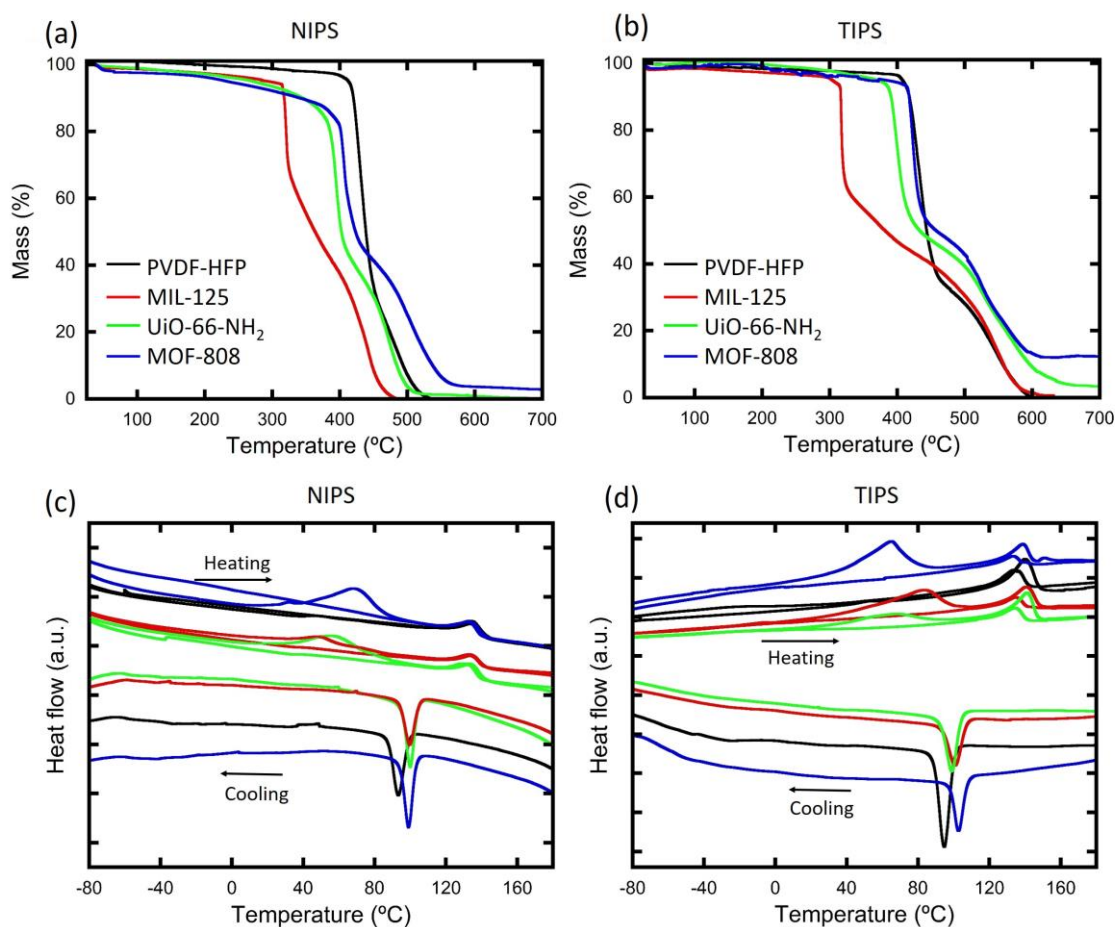

Figure 5.6. (a-b) Thermogravimetric analysis and (c-d) differential scanning calorimetry for neat PVDF-HFP and different PVDF-HFP@MOF composites.

As revealed by scanning electron microscopy, TIPS processing generates PVDF-HFP-composites with a slightly heterogeneous porous structure composed of interconnected macro-pores. This structuration is similar both in the cross-section and at the surface of the membranes, as suggested by SEM micrographs (Figure 5.7). The SEM images of composites' surface show a heterogeneous pore distribution ranging from 5 to 10 µm, suggesting a highly accessible interphase for the pollutants' migration into the membrane.
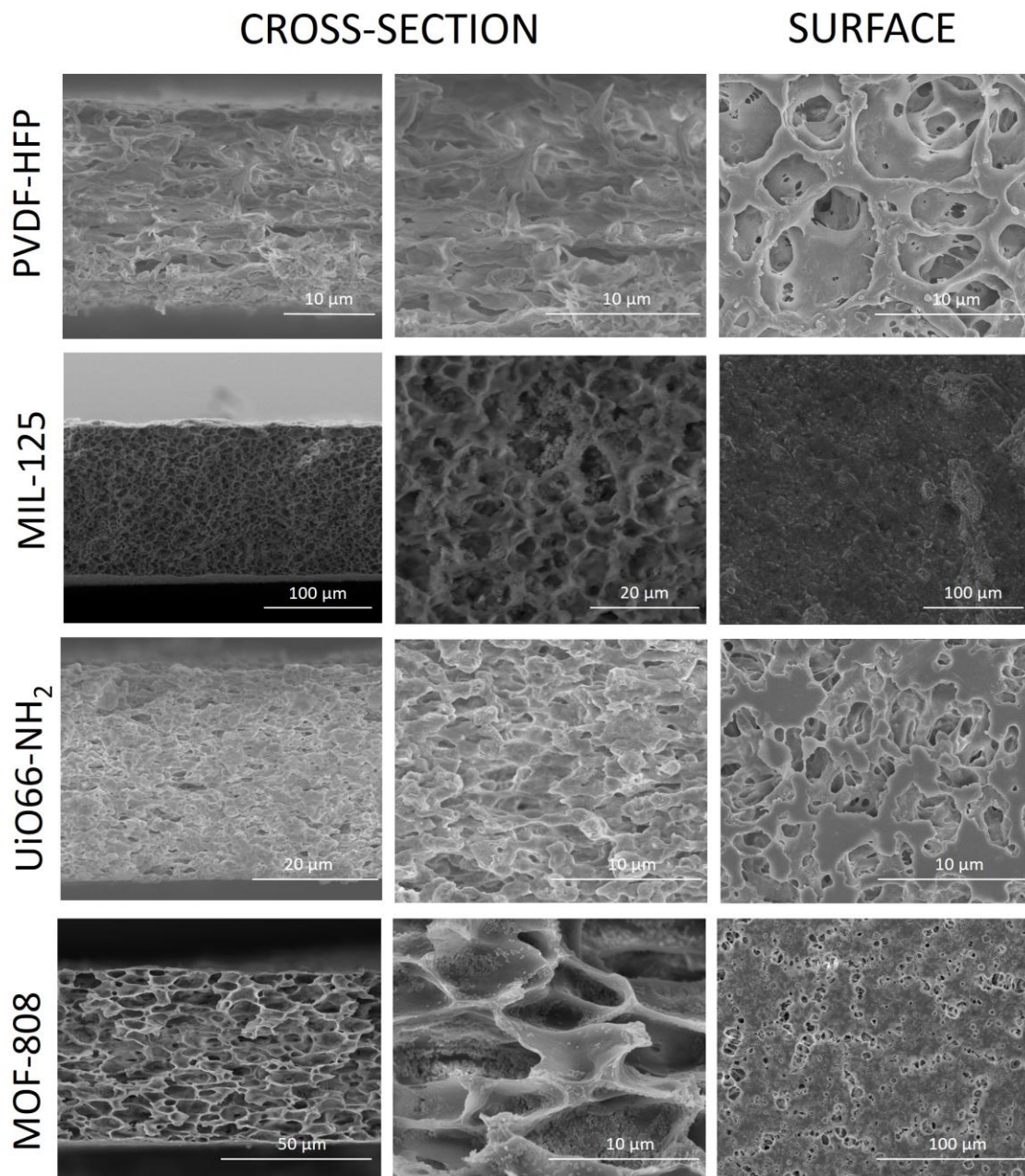
Figure 5.7. SEM images of TIPS membranes.

The inclusion of MOF particles at the PVDF-HFP porous matrix slightly alters the geometry and pore size of the membrane at its surface and inner structure. Moreover, depending on the MOF integrated within the polymer, the change in the morphology differs. The inclusion of MIL-125 induces a homogenization of the PVDF-HFP inner structure, while it slightly increases the average pore size of the PVDF-HFP structure until ~ 10 µm. In contrast, the porosity on the surface of the composite is significantly

reduced in comparison to the one of the bare PVDF-HFP. When UiO-66-NH$_2$ is introduced into the membrane, the main diameter of the pores at the inner structure and at the surface of the composite is slightly reduced, but in general terms, a well-interconnected pore-network is maintained. Finally, the inclusion of MOF-808 is the one that alters most the porosity. On one hand, the size of the surface pores is maintained, but they show a heterogeneous distribution that leads to the generation of highly-porous and non-porous domains at the surface of the membrane. On the other hand, the inner pores of the membrane are significantly elongated and better defined than in the parent PVDF-HFP membrane. The macro-pores at the body of the membrane have an average size close to 10 µm, but they are well interconnected by narrower pore windows. In addition, the MOF-808 particles are homogeneously placed decorating the inner surface of the pore structure. In the case of the MIL-125 or UiO-66-NH$_2$ based composites, in addition to MOF particles located at the surface of the PVDF-HFP structure, significant agglomerates of MOF particles have been detected as well within the pores of the PVDF-HFP matrix.

At this stage, it is difficult to conclude by SEM if all the MOF components of the composites (*i.e.* single particles or agglomerates) are fully accessible to the water media that will permeate the system, or a fraction of them is partial or fully encapsulated within the polymer structure. In any case, MOF-808 particles seem to be better dispersed and homogeneously disposed along the surface of the PVDF-HFP's pores in comparison to the ones of UiO-66-NH$_2$ and MIL-125. This homogeneous covering of the PVDF-HFP's pores by the MOF-808 particles led us to think that they may have a better accessibility, and hence performance, to adsorb metal ions.

On the other hand, NIPS method generates PVDF-HFP-based composite membranes with an anisotropic structure and pore distributions (Figure 5.8). Big pores of about 10 µm of diameter appear near to the surface of the composite, while smaller, anisotropic and elongated pores of about 2-3 µm of diameter are generated at the bulk of the membrane. In addition, the surface of the NIPS membrane exhibits a thin layer with a compact structure with isolated pores. It is important to point that the diameter of the pores generated within this thin layer of the NIPS membranes are considerably smaller (*i.e.* 300 nm of diameter) than the ones observed for TIPS homologues. In

addition, the pores are isolated from each other. The structure of the thin film at the surface of the membrane is generally maintained when the MOFs are incorporated into the polymer, with the exception of MOF-808, where its insertion causes a curious change in its porosity (diameter and density of pores at the surface). In addition, the MOF particles modulate as well the anisotropic structuration within the body of the NIPS membranes, so, their incorporation makes the pore structure more homogeneous by preventing the formation of the larger macro-pores located closer to the surface's thin-film layer in pure PVDF-HFP NIPS membrane.
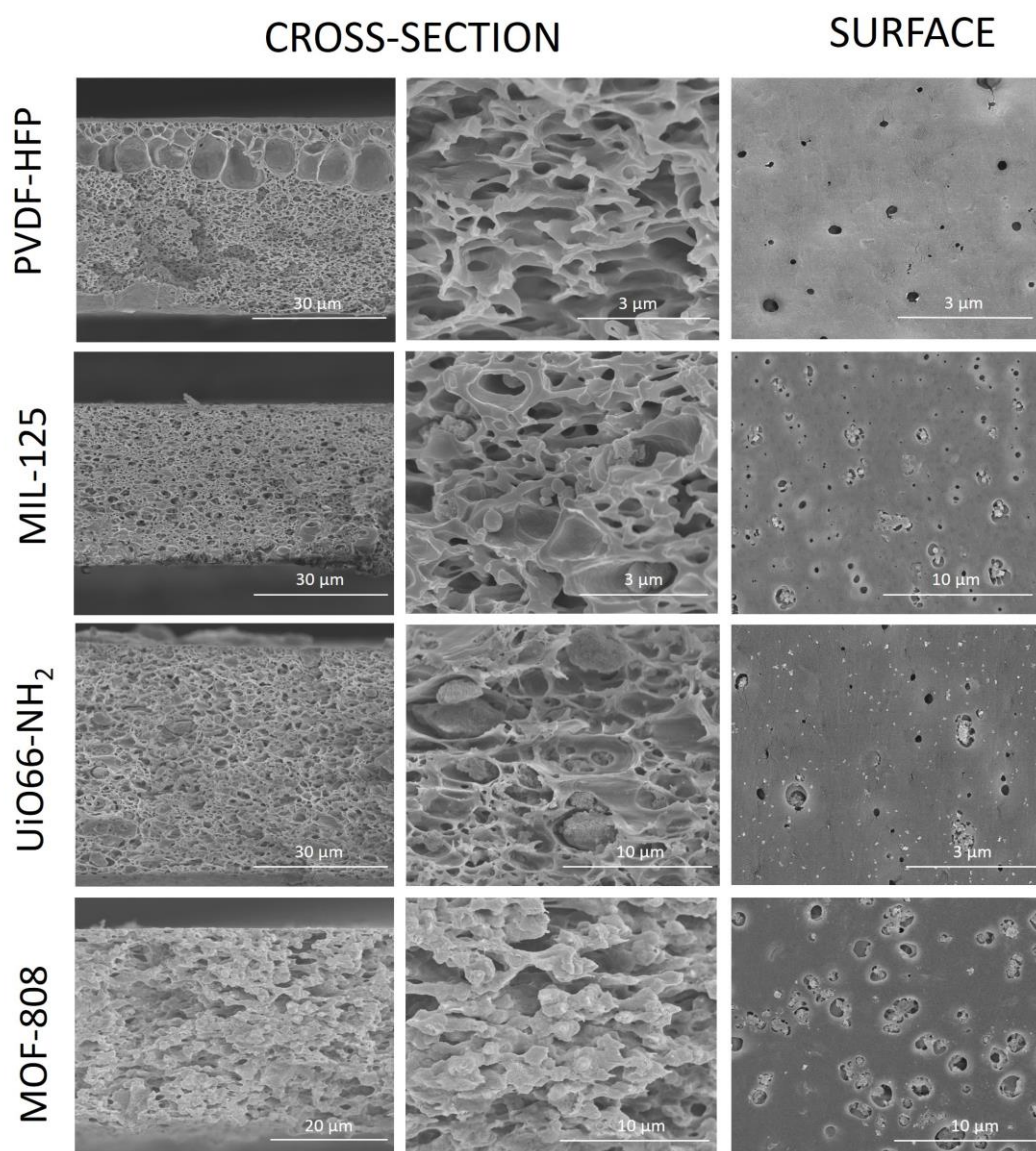

Figure 5.8. SEM images of NIPS membranes.

Given the location-disposition of the MOF particles revealed by SEM, the accessibility of the water-solutions and heavy metals may be favoured in TIPS membranes. The interconnectivity of the pores in this type of membranes together with the disposition of the MOF particles in the surface of the macropores of the PVDF-HFP structure are factors within the structuration of the membrane that foresee to increase their efficiency for heavy metals capture from water.

The template effect of the MOF fillers on the micrometre range structure of the PVDF-HFP matrix was further investigated by means of mercury porosimetry. Figure 5.9 shows the empty volume fraction per gram of material associated with each pore diameter. PVDF-HFP TIPS membranes accumulate most of the volume of their accessible-pores for those with a 1.5 µm pore diameter. In contrast with the main pore size observed in the SEM images (~ 10 µm of diameter), mercury porosimetry indicates that most of the surface area of the membrane lies within the pores with a smaller diameter of approximately one micron. A similar trend is found for the composites based on MIL-125 and MOF-808, with most of the accessible volume located at the cavities from 1 to 1.5 µm of pore diameter. In contrast, PVDF-HFP@UiO-66-NH$_2$ shows a bimodal pore distribution with mean diameters of 2.9 and 4.6 µm.

On the other hand, PVDF-HFP NIPS membranes accumulate most of their free space volume within the pores with a 0.25 µm diameter. The inclusion of UiO-66-NH$_2$ and MIL-125 MOFs does not alter this distribution. However, when MOF-808 is integrated within the PVDF-HFP matrix, a bimodal distribution, with mean pore diameters of 0.21 and 0.45 µm, is found for the composite membrane.

It is important to note that although the most of the free-pore volume into the membranes is ascribed to the pore diameters described above, this does not preclude the existence of certain porosity related with macro and mesopores below and above the main value obtained from the mercury porosimetry measurements.
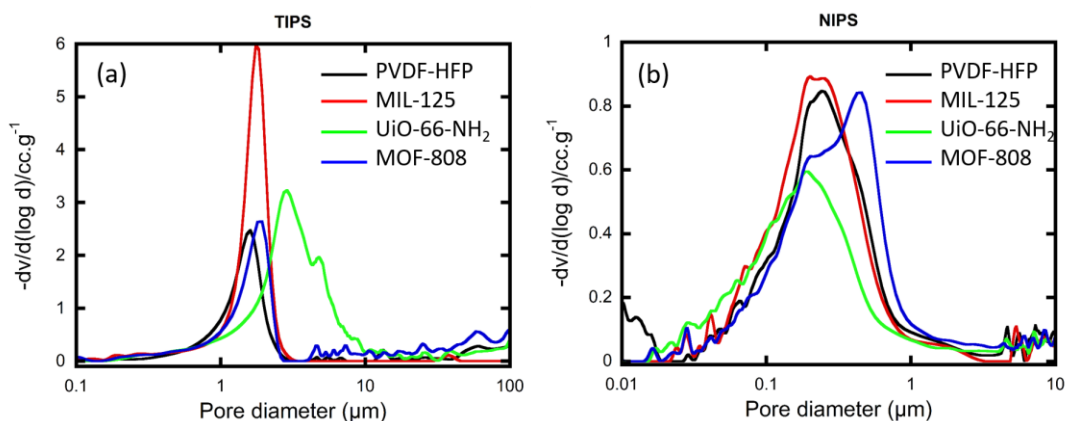
Figure 5.9. Cumulative pore volume dependence of the pore size for PVDF-HFP polymer membrane and composites with MOFs addition.

In order to get a deeper insight into the internal morphology of the composites at the nanometric scale, SANS and SAXS measurements were conducted. The variations at the nanoscale of the structure of the PVDF-HFP membranes, and of the three PVDF-HFP@MOF composites (*i.e.* UiO-66-NH$_2$, MIL-125 and MOF-808) processed *via* TIPS and NIPS were studied.

Small angle scattering is widely applied to characterize all type of materials at the nanometre scale. Indeed, the typical interval of the conventional small angle scattering is 1-200 nm,[39] which gives access to a size-scale regime below the macro to micrometre ones observed by SEM or mercury porosimetry. In general, the SANS and SAXS data are plotted as the scattering intensity versus the scattering vector q. The q vector is inversely proportional to the size of the particles or the inhomogeneities, and thus, objects/inhomogeneities with different sizes from 1 to 200 nm give different scattering signals in various q regions.

In general terms, three SANS and SAXS features have been observed for the PVDF-HFP and PVDF-HFP@MOF composites: (i) the scattering arising from the nanoinhomogeneities generated within the membranes due to the phases/domains structuration of the polymer itself (8-12 nm), (ii) the interparticle space created due to the MOF particles agglomeration within the polymer (30-20 nm) and (iii) the power low decay of the scattering data that is related to the mass or surface fractal structures

of the composites. All these heterogeneities reflected in the SAXS and SANS spectra can be fitted if the proper model is applied.

At sufficiently small q-values (qRg < 1), the scattered intensity related with the inhomogeneities at the polymer or nanoparticles included within the polymer levels, can be described by the Guinier approximation (Equation 5.1).[40]

$$I(q) = I(0)\exp\left(\frac{-(qRg)^2}{3}\right) \tag{5.1}$$

where I(0) is proportional to the concentration; square of the contrast in scattering length density between matrix and inhomogeneity; and square of the particles volume and Rg is the radius of gyration, related to the characteristic size of the scattering objects within a given matrix or media. That is, at low q-values, the inhomogeneities arising form the polymeric matrix and the MOF-MOF and MOF-polymer interphases will be detected.

On the other hand, the power law decay of the SANS and SAXS data, associated to the fractal structuration of the systems, was fitted by the Equation 5.2.

$$I(q) = B \cdot q^{-P} \tag{5.2}$$

where B is the normalization constant and the value of the P exponent reflects the inner structure of the scattering units. In addition, P exponent characterizes the type of the mass or surface organization of the aggregates according to the following classification[41]:

1 < P < 3; mass fractal with fractal dimension, Dm = P

3 < P < 4; surface fractal with fractal dimension, Ds = 6 – P

Just to give an easy viewing of the different possible-fractals that can arise from the P values described above, we have summarized them in the Figure 5.10.

When our system shows only single polydisperse objects with no agglomeration (Figure 5.10a), there is no fractal organization, and the initial part of the curves can be fitted by Guinier approximation (Equation 5.1). When the system shows mass fractal aggregations (Figure 5.10b), it means that an agglomeration of inhomogeneities is happening, and the bigger the value of the P exponent is, the more

agglomeration (or more particles inside an aggregate) we have in the same volume. On the other hand, when the P value is above 3.0, a surface fractal organization of our composites is occurring. The surface fractals refer to the roughness of a surface or to the aggregation of the particles on the surface, as for example the MOF nanoparticles decorating the pore space of the PVDF-HFP (Figure 5.10c). In this case, the higher the P value, the smoother the surface of the inhomogeneity.
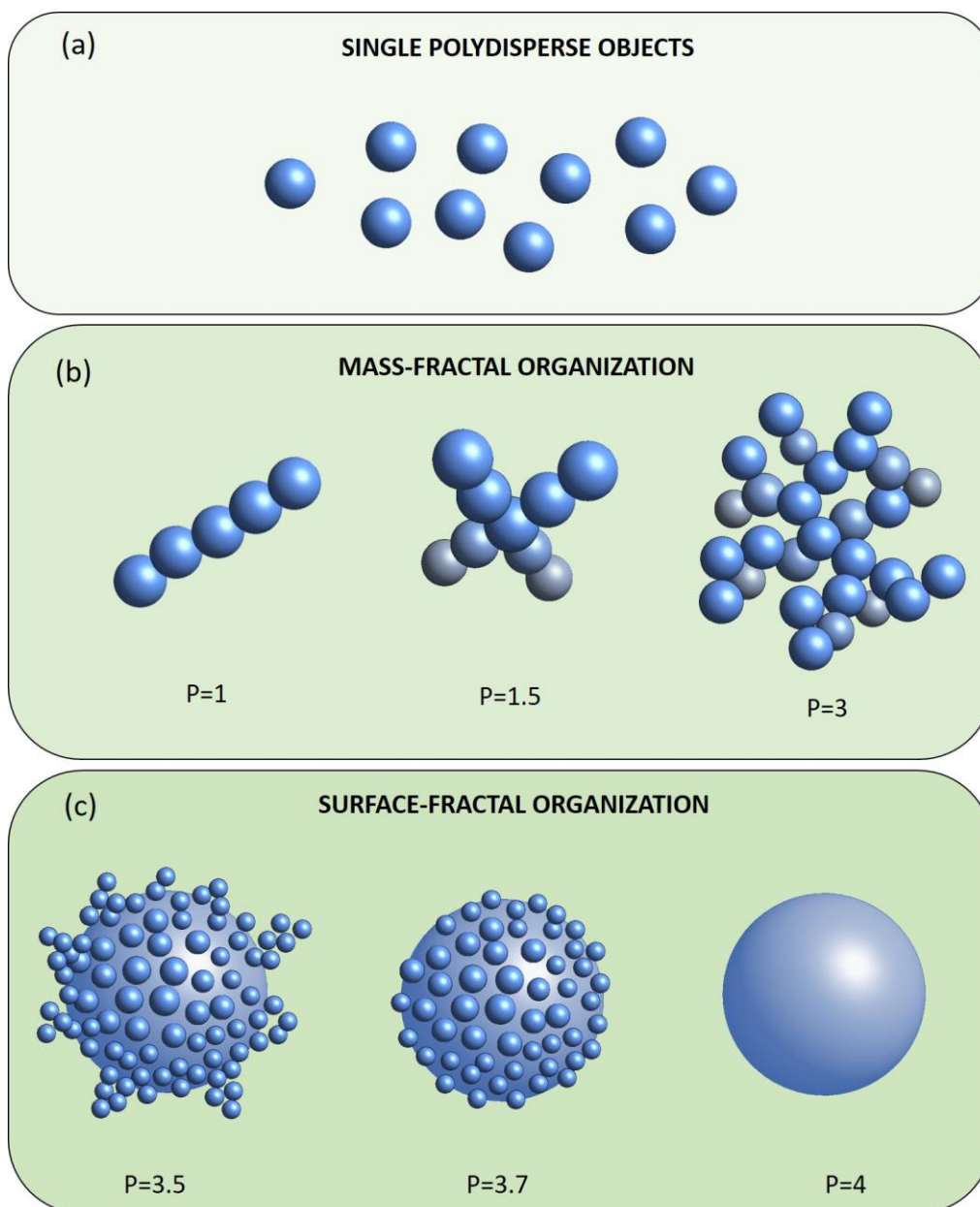

Figure 5.10. Different inhomogeneity organizations that can be studied with small angle scattering. (a) Single polydisperse objects, (b) mass-fractal organization of the aggregates with corresponding P exponents and (c) surface-fractal organization with corresponding P exponents.

According to the information described above, three parameters can be extracted from the SAXS and SANS data of our membranes: (i) the value or the power law decay that is related with the nature of the fractal nano-structuration of the system, (ii) the size of the inhomogeneities or Rg within a given matrix observed at low q values, and finally, (iii) the diffraction signal coming from the crystal structure of the MOF particles included within the polymeric matrixes.

Experimental SANS and SAXS curves for PVDF-HFP@MOF composites are presented in Figure 5.11. Scattering objects for all samples are highly polydisperse, as concluded from the smoothed nature of the SANS and SAXS data. This experimental signal is typical for polydisperse systems, since a highly symmetric system of monodisperse particles will give rise to the characteristic oscillations of the SANS and SAXS profiles.[40] In the specific case of PVDF-HFP@MOFs composites, scattering objects can arise from the MOF particles dispersed into the polymeric matrix, or due to heterogeneities in the polymer itself.
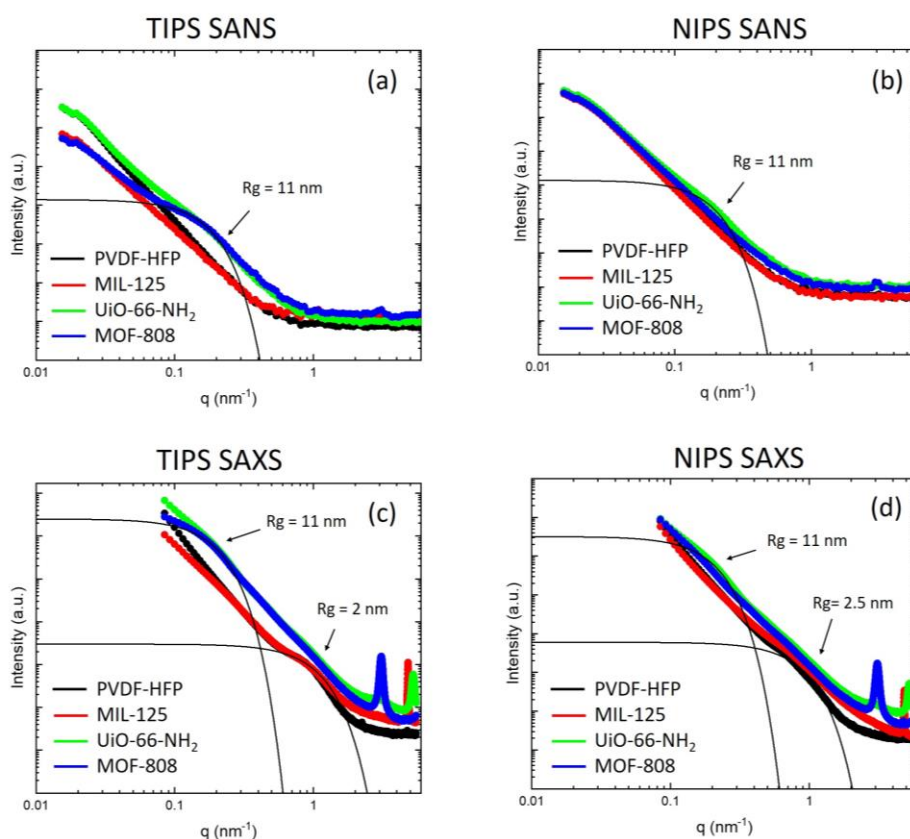

Figure 5.11. SANS data for (a) TIPS and (b) NIPS membranes. SAXS data for (c) TIPS and (d) NIPS membranes

PVDF-HFP membranes processed by TIPS and NIPS show similar nanostructures, with surface fractals of about 3.8-3.9 obtained for both SANS and SAXS measurements. We have tentatively ascribed these fractal-structuration to the surface and internal organization of the PVDF-HFP around the pore structure of the membranes. The arrangement of the pore-space could be replicated in a fractal manner from the macro to the mesopores observed in the porosimetry measurements. That is, big pores with the PVDF-HFP matrix are interconnected by channels to mid-size pores, and mid-size pores interconnected at the same time with small-pores, giving rise to a surface fractal with an interconnected structure, as illustrated in the Figure 5.12.

When MOF particles are introduced into the PVDF-HFP matrix, the nanometric differences observed between the membranes processed by the NIPS and TIPS methods increase. TIPS composites show different fractal structures depending on the MOF incorporated into the membrane. For instance, bare PVDF-HFP and PVDF-HFP containing UiO-66-NH$_2$ show surface fractals of 3.9 and 3.7 respectively (Ds = 2.1 and 2.3, respectively). Composites containing MIL-125 show also surface fractal, but with a value of 3.3 (Ds = 2.7), which is indicator of a higher roughness of the surface, probably due to the big size of MIL-125 particles. Finally, PVDF-HFP@MOF-808 sample has the most complex of the fractal structures studied in the system. The SANS data shows a mass fractal of Dm = 2.8, which corresponds to quite dense agglomerations of significant size within the polymeric matrix. However, SAXS data of the same membrane reveals two different fractals: one corresponding to a mass fractal with Dm = 1.7, and other one corresponding to a surface fractal of P=3.5 (Ds = 2.5). Overall, the SANS and SAXS data led us to think that we can find a branched and interconnected fractal structure formed from anisotropic elongated pores. The nanostructuration seems to be clearly related with the interconnected porosity of the membrane revealed by SEM and mercury porosimetry measurements. The decrease of the surface-fractal structuration of the PVDF-HFP@MOF-808 composite can be easily understood by the decoration of the surface of the pore space in the PVDF-HFP with MOF-808 particles, which increases the roughness of the surface. In addition, the values of the mass fractals obtained from the SAXS and

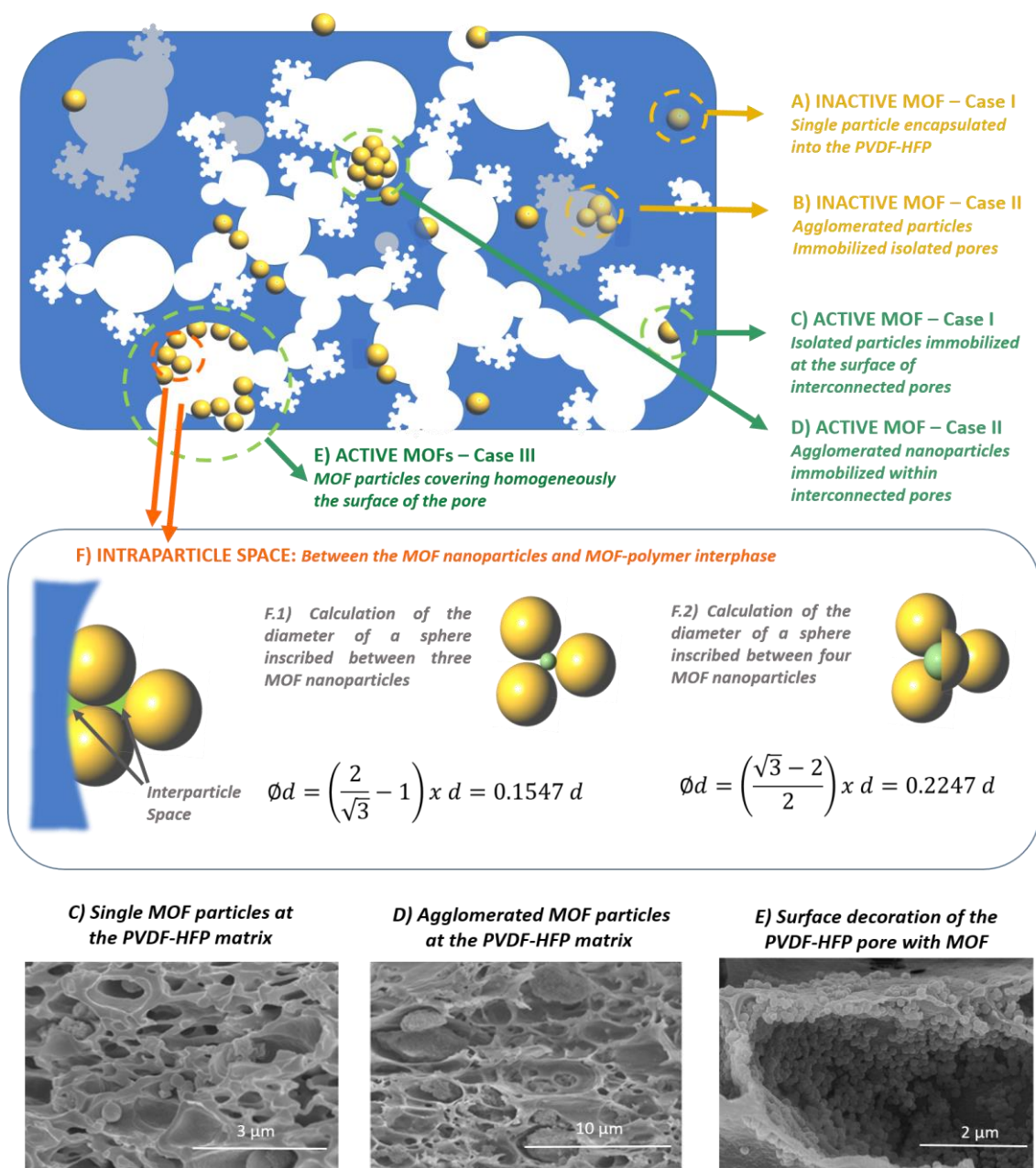SANS data fitting can be closely related with the entrapment of MOFs agglomerates into the PVDF-HFP pores.

Figure 5.12. Schematic representation of the overall structuration of PVDF-HFP@MOF composites. (a-e) Schematic illustration of the of the fractal pore interconnected structure of the PVDF-HFP matrix, the MOF immobilization possibilities within the membrane, and (f) the mathematic description of the interparticle space between MOF particles, and at the polymer-MOF interphase. Bottom of the figure: SEM images of the different cases.

Altogether, it is clear that the surface fractals arising from the empty pore-space of the PVDF-HFP membrane are significantly modulated when MOF particles are included within the system. Therefore, this modulation gives rise to different P values when fitting the power-law decay of the SANS and SAXS data of the composites. In addition, if the MOF particles are agglomerated within the pores, or decorate the surface of the pores of the PVDF-HFP matrix, this induces the appearance of a SANS/SAXS signal decay associated to the mass fractal structuration of the PVDF around these objects within the membranes.

Contrary to TIPS, NIPS composite membranes exhibit power laws with mass fractals of about 3.7, very similar to the bare PVDF-HFP membranes, and therefore the nanostructuration of the polymeric matrix is not almost affected by the inclusion of the MOF particles. Considering the information coming from the scanning electron microscopy, and the once obtained by SANS and SAXS, we have proposed the branched fractal structuration of the porosity in PVDF-HFP membranes shown in the Figure 5.12. It is important to consider that the pore-geometry, size, heterogeneity and anisotropy for each of the studied PVDF-HFP@MOF systems can modulate the branched fractal structuration both at the body and at the surface of the composites.

When studying the nano-inhomogeneities of the systems, SANS data does not show inhomogeneities for bare polymeric membranes usually observed at higher q values. In contrast, SAXS data reveal slight inhomogeneities with Rg values of 2 and 2.5 nm for TIPS and NIPS membranes, respectively. We have ascribed these inhomogeneities to the structuration of the PVDF-HFP per-fluorinated chains at the amorphous and crystalline domains of the different phases of the polymeric matrix. For instance, a size of 2 to 2.5 nm would correspond to a polymeric chain of approximately 20-22 carbons, which is much below the molecular weight of the polymer.

When the MOFs are incorporated to the membrane, these inhomogeneties observed for the bare PVDF-HFP seem to disappear, with the exception of MIL-125 particles. It is difficult to directly relate this SANS signal with a specific feature of the polymeric chains' structuration at the nanoscale, but given the size of the inhomogeneity, MOF-808 and UiO-66-NH$_2$ could alter the crystalline and amorphous domain structuration of the PVDF-HFP. In fact, it is well known that the inclusion of

nanoobjects within PVDF-HFP can alter significantly its crystallization as one of its polymeric phases.

What is more, additional inhomogeneities with a Rg value of 11 nm are found in both SANS and SAXS data for the TIPS samples containing MOF-808 and UiO-66-NH_2, but not for MIL-125. According to this value, these inhomogeneities could correspond to the interparticle space created by the MOF's when they are agglomerated within the membrane, since the inhomogeneity is too small to be related with the MOF nanoparticles themselves. Indeed, in a perfect packing of MOF spherical particles, the diameter of the spheres enclosed within three particles in a triangular configuration, or within four particles in a tetrahedral disposition, can be calculated applying the equations summarized in the Figure 5.12e. Therefore, for MOF particles with diameters ranging from 50 to 200 nm, interparticle inhomogeneities ranging from 7.8 to 31 nm and 11 to 45 nm could be found enclosed within a triangle or a tetrahedron of MOF particles, respectively. It is important to note that these calculations have been performed considering a perfect sphere packing. As the packing of the MOF particles into the membrane is foreseen to deviate from the ideal, the size of the interparticle size could variate significantly from the ideal minimum (7 nm) and maximum (44 nm) values. Even though, the experimental evidences point in this direction, since this inhomogeneities with a Rg value close to 11 nm are only appreciable in UiO-66-NH_2 and MOF-808 based samples. In both cases, the diameter of the MOF particles is of 50 and 100-200 nm for UiO-66-NH_2 and MOF-808, respectively. Our hypothesis is further confirmed by the lack of this nanometer range inhomogeneity in MIL-125 based membranes. In fact, MIL-125 has a particle diameter of about 500 nm, a size that would give rise to an average interparticle pore space of 110 nm. This range of size is above the usual limits studied by SAXS.

On the other hand, NIPS membranes barely show the inhomogeneities corresponding to the interparticle space that we could observe in TIPS membranes. In these samples, only the membrane containing UiO-66-NH_2 shows a slight inhomogeneity in both SANS and SAXS data that corresponds to a size of about 12 nm. These results, together with the information obtained from SEM images (Figures

5.7 and 5.8), point out that the interparticle space generated because of the agglomeration of MOF particles is significantly smaller in NIPS membranes, probably due to a smaller agglomeration of the particles in these membranes.

Overall, the experimental data points towards a higher percentage of isolated MOF particles stabilized at the surface or at the inner body of the PVDF-HFP membrane. In the last case, the MOF would be inaccessible to act as adsorption points of the membrane. The observed P and Rg values are summarized in Table 5.2.

Table 5.2. Obtained P and Rg values for the different composites.

		P	Rg
TIPS	PVDF-HFP	3.9	2 nm (SAXS)
	PVDF-HFP@MIL125	3.3	2 nm (SAXS)
	PVDF-HFP@UiO-66-NH$_2$	3.7	11 nm (SAXS and SANS)
	PVDF-HFP@MOF-808	2.8 // 1.7 and 3.5	11 nm (SAXS and SANS)
NIPS	PVDF-HFP	3.85	2.5 nm (SAXS)
	PVDF-HFP@MIL125	3.7	2.5 (SAXS)
	PVDF-HFP@UiO-66-NH$_2$	3.7	11 nm (SAXS)
	PVDF-HFP@MOF-808	3.7	-

Additional SANS measurements were performed for samples wetted with deuterated methanol in order to increase the neutron scattering contrast between the interconnected porosity and the isolated nano-inhomogeneities of the PVDF-HFP@MOF systems (Figure 5.13). In NIPS membranes (Figure 5.13a-d), the power law related with the fractal-structure of the composites does not decrease when deuterated methanol is included within the pore space. However, there is a general decrease of the scattering signal due to the incorporation of the d-solvent in the pores of the polymeric matrix. PVDF-HFP@UiO-66-NH$_2$ processed by NIPS (Figure 5.13c) was the only membrane showing an inhomogeneity of about 11 nm, a signal that disappears when the membrane is wetted with deuterated methanol. Similar

happens in TIPS membranes, where composites including MOF-808 and UiO-66-NH$_2$ loss the signal corresponding to the interparticle space of the MOF agglomerates (Figure 5.13g-h).

This variation is attributed to the decrease of the neutron scattering contrast between the MOF and the interparticle space when the deuterated solvent is placed in the interphase of the MOF particles. In fact, both MOF-808 and UiO-66-NH$_2$ have a scattering length density (SLD) of about $2.7 \cdot 10^{10}$ cm^{-2}, and the SLD of the air is 0. As a consequence, the contrast between the two objects in an air-filled membrane is of $2.7 \cdot 10^{10}$ cm^{-2}. However, when the composite is wetted with d-methanol, the SLD of the MOF with d-methanol in its pores increases to $3.32 \cdot 10^{10}$ cm^{-2} (taking into account that the porosity of the MOF is 38% in volume fraction), while the SLD of the d-methanol located at the MOF interparticle space is of $5.16 \cdot 10^{10}$ cm^{-2}. Overall, a contrast of $1.84 \cdot 10^{10}$ cm^{-2} is obtained, a value almost two-fold smaller than the initial one for the as-synthesized composites. Therefore, this loss of contrast when the pore space of the membrane is filled with deuterated methanol, can explain the loss of the SANS signal associated to the heterogeneity ascribed to the MOF interparticle space.

Finally, it is important to note that a new inhomogeneity appears in all TIPS membranes after their wetting with d-methanol, except in the composite containing MIL-125. This heterogeneity has an approximate size of 2-3 nm, and has being tentatively ascribed to an increase of the contrast due to the preferential uptake of d-methanol by some of the phases or amorphous/crystalline domains of the PVDF-HFP matrix. Although this initial hypothesis needs further experimentation to be fully corroborated, some hypothesis points that several processes as ionic diffusion can be favored in the amorphous domains regions of the PVDF-HFP. In parallel, a 2-3 nm inhomogeneity cannot be ascribed to the MOF particles (their size > 50 nm), neither to their interparticle porosity or interphase with the polymer (> 11 nm), since after their filling with d-methanol, they should loss contrast instead of gaining it.
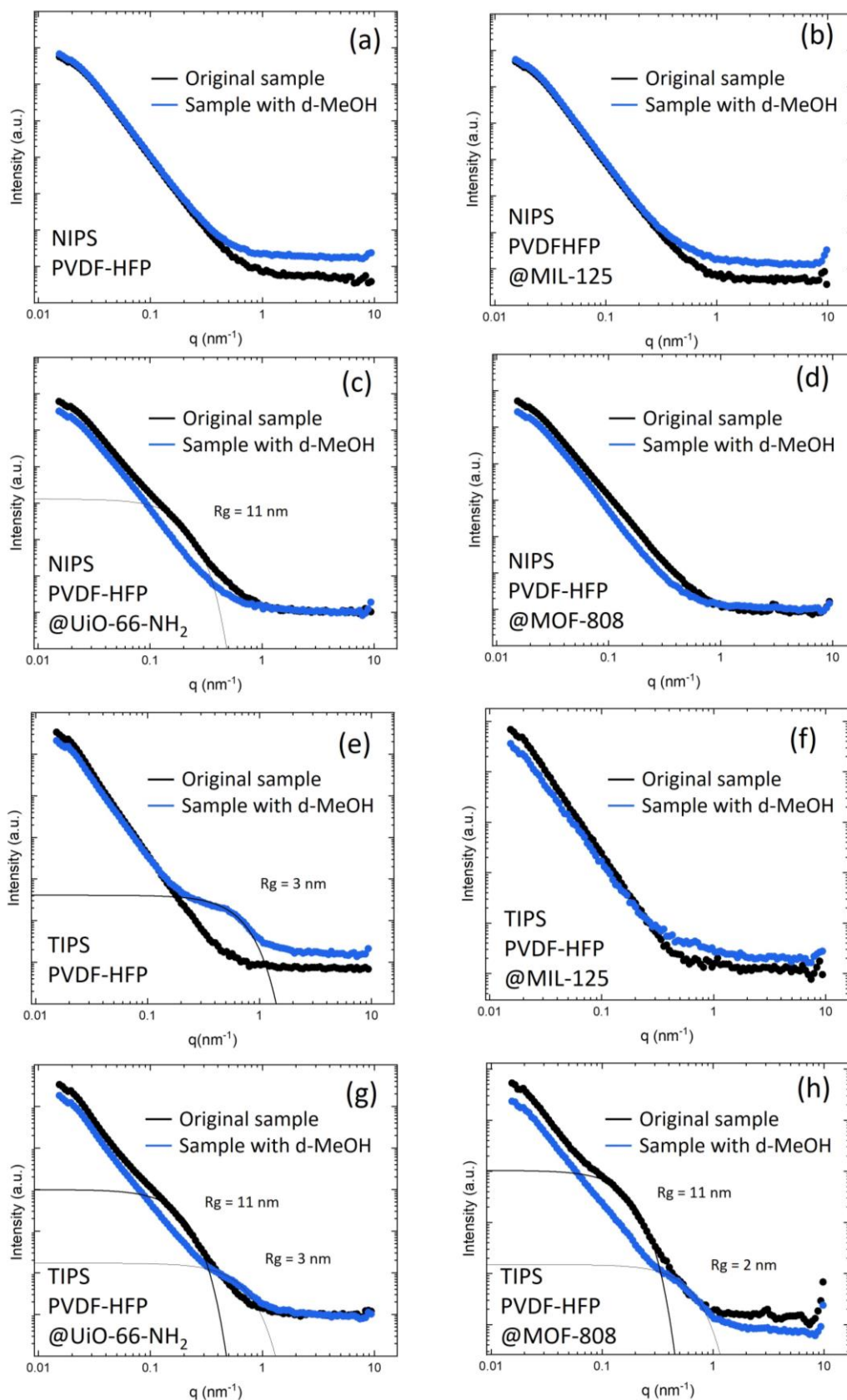
Figure 5.13. Small angle neutron scattering experiments.

Last but not least, we have focused on the NIPS PVDF-HFP@MOF-808 system to preliminary explore by SANS and SAXS: (i) if the MOF loading degree alters the nanostructure of the composites, (ii) if the functionalization of the MOF-808 with cysteine before and after its incorporation into the PVDF-HFP matrix can alter somehow the nanostructuration of the polymer and (iii) if the adsorption of Cr^{VI} generates new inhomogeneities into the composites.

Regarding the MOF-loading degree parameter, it is interesting to note how the power law decay of the SANS signal is lowered with the inclusion of the MOF-808 particles in the system from 3.9 in pure PVDF-HFP to 3.8 and 3.5 in composites with a 10 and 30 % of weight loadings (Figure 5.14a-b). In addition, the MOF-loading induces the disappearance of the 2.5 nm size inhomogeneity that has been ascribed to the phase or crystalline/amorphous domains of the PVDF-HFP matrix. This evidence is not surprising as there are many reports that have confirmed that the inclusion of fillers as MOF into PVDF-HFP matrix alters significantly its crystalline/amorphous ratio, as well as the crystallization of specific PVDF-HFP phases.[42–45]

On the other hand, the functionalization process does not seem to have an effect on the nanostructuration of the PVDF-HFP matrix (Figure 5.14c-d). In fact, there are no significant changes on the SANS and SAXS data when the introduced MOF-808 particles that have been functionalized with cysteine before their inclusion in the PVDF-HFP matrix. It seems that surface chemistry related with the cysteine decoration does not affect drastically the NIPS process. Moreover, the nanostructuration of the PVDF-HFP@MOF-808 system is neither altered if the MOF-808 is functionalized after being inserted to the membrane.

More interesting, the SANS remains unaltered after Cr^{VI} adsorption by the membranes, so the metal loading does not enhance the nanoinhomogeneities already present in the system or generate new ones (Figure 5.14e-f).
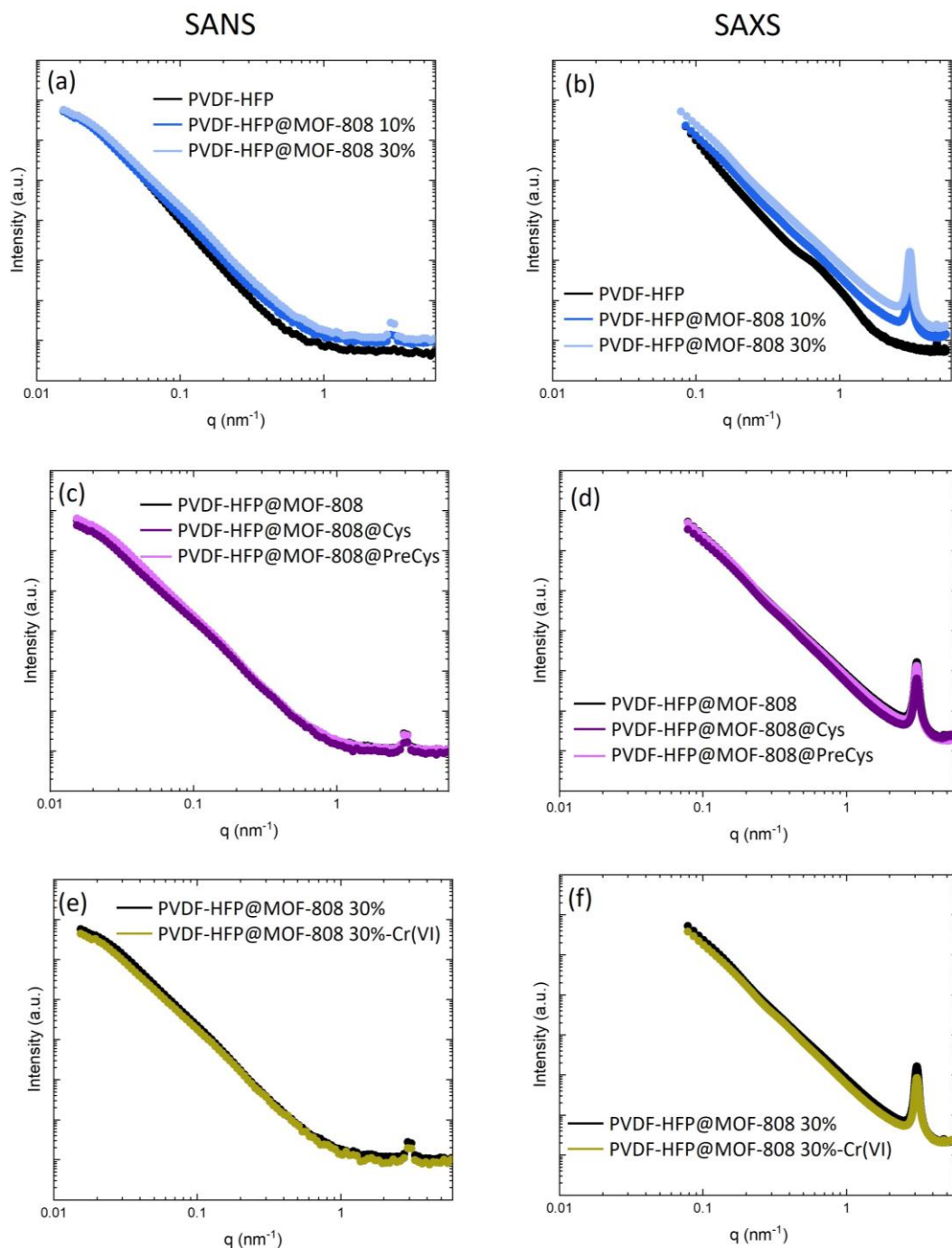
Figure 5.14. SANS and SAXS data for (a-b) PVDF-HFP@MOF-808 NIPS membranes with different MOF loadings, (c-d) PVDF-HFP@MOF-808 NIPS membranes before and after the functionalization process with Cysteine and (e-f) PVDF-HFP@MOF-808 NIPS membranes before and after the adsorption process with Cr^{VI}.

Cr^{VI} and Hg^{II} adsorption experiments

Once the macro to nanometric structuration of the composites is better understood, metal adsorption experiments were performed in order to correlate the efficiency of the membranes with their structure (Figure 5.15). Two different case-studies were tackled.

In a first one, the Cr^{VI} adsorption capacity of the membranes was evaluated in order to determine the accessibility of the MOF particles in the polymer (Figure 5.15a). That is, as PVDF-HFP lacks any capacity to adsorb hexavalent chromium, the overall capacity of the membranes to capture chromate anions will arise from the MOF particles that are not encapsulated within the polymeric matrix. Thus, first the capacity of powdered MOF samples to capture Cr^{VI} was determined in order to compare this value with the one obtained for the MOFs which are immobilized in the membrane. This way, if the MOF is completely accessible, a similar adsorption capacity should be obtained in both cases. On the other hand, if part of the MOF is occluded within the polymer, the reduction of the adsorption capacity will let us to quantify the encapsulation degree of the MOF, by comparing the adsorption capacity of the MOFs in the membrane with the value obtained for the powdered MOF.

In a second approach, the Hg^{II} adsorption capacity of the membranes was evaluated before and after the *in-situ* post-synthetic cysteine functionalization of the MOF-808 immobilized within the NIPS composites (Figure 5.15b). Moreover, the comparison between de adsorption capacities of PVDF-HFP@MOF-808@Cys samples has been done depending if the functionalization process of the MOF was done before (denoted as PVDF@MOF@PreCys in Figure 5.15b) or after the immobilization of the particles in the polymeric matrix (denoted as PVDF@MOF@Cys in Figure 5.15b).

First, it is important to note that adsorption of pure PVDF-HFP membranes is near 0 mg·g^{-1} for Cr^{VI}, so the polymeric matrix is inactive for adsorption purposes. From the studied MOFs, UiO-66-NH$_2$ shows the higher Cr^{VI} adsorption capacity (23.88 mg·g^{-1}) thanks to its linker-defective sites and the protonated amino groups, which act as adsorption points for CrO$_4^{2-}$ oxyanions. Indeed, as reported in Chapter 3, UiO-66-NH$_2$ exhibits as well certain capacity to chemically reduce the Cr^{VI} to Cr^{III}.

MOF-808 shows an adsorption capacity for Cr^{VI} of 11.3 mg·g^{-1}. This adsorption capacity is ascribed to the replacement of the labile formate modulators linked to the zirconium clusters of its framework by the CrO_4^{2-} oxyanions. Finally, MIL-125 shows the smaller adsorption capacity, of 5.73 mg·g^{-1}, tentatively ascribed to weak hydrogen interactions between the MOF framework and the chromate anions.

The MOFs immobilized into TIPS membranes show similar adsorption capacities over Cr^{VI} that the powdered samples. The comparison between the adsorption capacity of immobilized and non-immobilized materials indicates an accessibility of 80-100% of the MOF particles in the polymer. On the other hand, MOFs immobilized within NIPS membranes show only half of the capacity of the powdered samples. This adsorption values point out that only the 45-55% of the MOF immobilized within the membrane is accessible for Cr^{VI}. In perspective, the small porosity that the surface of the NIPS membrane shows, hinder the mobility of the chromate ions, but also isolate some of the MOF particles from the media. The encapsulation degree observed through adsorption is related with a nanostructuration of the membrane that lacks the inhomogeneities coming from the agglomeration of the MOF particles and MOF-polymer interphase space.

At this point, we decided to evaluate if an *in-situ* functionalization of the MOF-808 immobilized within the membrane *via* the water based SALI protocols described in the Chapter 4 was possible. As it was described in the previous chapter, the incorporation of cysteine functions with –SH groups into the MOF-808 pore space shifts drastically its adsorption affinity to capture soft metal ions such as Hg^{II}. Because of this, MOF-808 into the PVDF-HFP NIPS membranes has been functionalized with cysteine in order to increase the affinity of the composite to capture Hg^{II}. The cysteine SALI encoding of MOF-808 particles has been performed as well for sake of comparison.

We have selected PVDF-HFP@MOF-808 NIPS membrane for this study because it shows a higher degree of encapsulation of the MOF-808 particles in comparison to its TIPS homologue. So, it will enable evaluating if there is any unblocking of the MOFs encapsulated within the membrane during the *in-situ* cysteine functionalization of system, or if the MOF-encapsulation is reduced if the particles have been

functionalized with cysteine before their incorporation to the membrane. In addition, it is important to remember that NIPS membranes are much quicker and environmentally friendly to produce than TIPS homologues, as they only need 30 minutes to eliminate the DMF from the structure, and they can be dried without special extraction systems. Thus, a method to improve their affinity towards cationic heavy metals capture would be highly interesting both from the fundamental and application perspectives.

First, as revealed by ^{1}H-NMR, the SALI process in MOF-808 nanomaterial give rise to an average functionalization of 1.7 cysteine molecules per zirconium cluster, whilst 0.9 cysteine molecules per cluster are incorporated into the MOF-808 immobilized within the membrane after the SALI. That is, only the 53 % of the MOF-808 particles within the membrane are accessible to the SALI process, a value that is similar to the 60 % accessibility obtained from the Cr^{VI} adsorption experiments. Therefore, as expected, SALI process does not de-block the access to the MOF particles encapsulated within the polymer.

Regarding the Hg^{II} adsorption performance (Figure 5.15b), first, an adsorption study of the powdered MOF-808 and MOF-808@Cys samples was performed to determine their capacity in the applied experimental conditions. MOF-808 shows an acceptable adsorption towards Hg^{II} (11.3 mg·g^{-1}). When the MOFs are functionalized with cysteine, the adsorption capacity is multiplied by four, reaching a value of 42.4 mg·g^{-1}.

Regarding the polymeric composites, NIPS PVDF-HPF membrane shows negligible adsorption capacity towards Hg^{II}. When non-functionalized MOF-808 is introduced in the membrane, PVDF-HFP@MOF-808 NIPS membrane rises its capacity up to 7 mg·g$_{MOF}^{-1}$. According to the Hg^{II} adsorption capacity of the bare MOF, this means an accessibility of a 62% to the MOF integrated within the membrane. Similarly, the adsorption capacities over Hg^{II} of the composites functionalized with cysteine directly in the NIPS membrane, point out towards a 70% accessibility degree of the MOF in the 10 % loaded membrane. This accessibility decays to the 43 % for the 30 % wt. MOF-808 loaded membrane that has been functionalized within cysteine molecules. Thus, increasing the MOF loading,

increases as well the encapsulation degree of the MOF particles into the system. This issue is not solved if MOF-808 is pre-functionalized before its inclusion into the PVDF-HFP (denoted as PVDF@MOF@PreCys in Figure 5.15b), since both 10 % and 30 % wt. loaded PVDF-HFP membranes show accessibilities close to 35%, much lower than the ones reported for the *in-situ* modified composites.
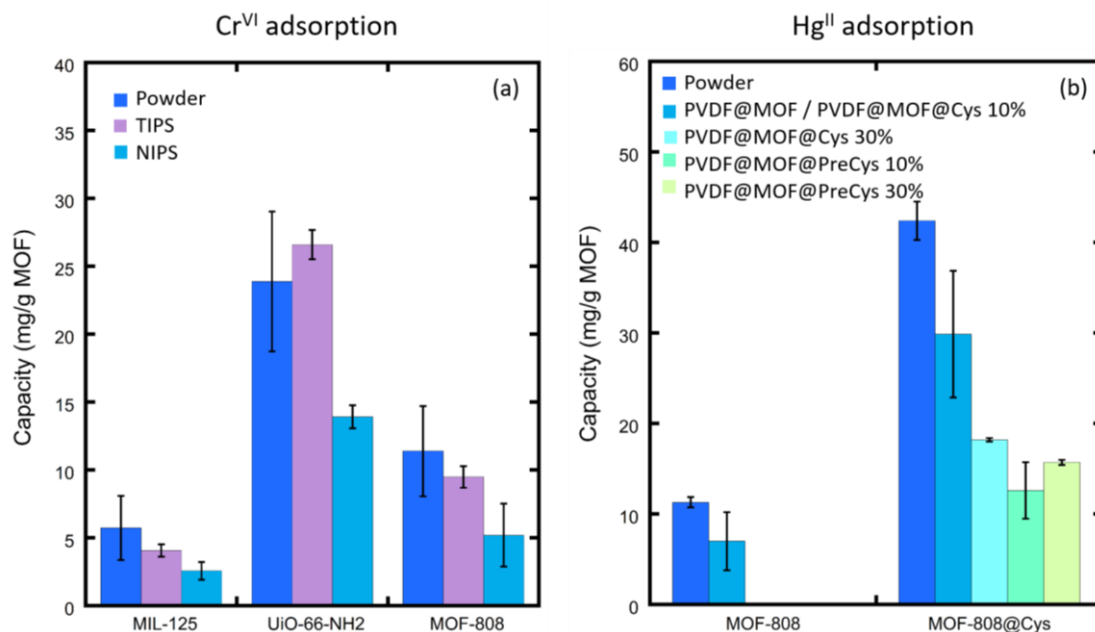

Figure 5.15. (a) Cr^{VI} adsorption experiments for TIPS and NIPS membranes and (b) Hg^{II} adsorption experiments NIPS membranes with and without Cysteine functionalization.

5.1.3. CONCLUSIONS

The combined and complementary experimental characterization protocols that have been applied into this study have allowed to understand the structuration of the PVDF-HFP@MOF membranes processed by TIPS and NIPS from macro to nanometric point of views.

It is clear that the main structure of the composite is governed by the TIPS and NIPS phase separation, but the inclusion of the MOF particles in the process disturbs it until different extent, and hence, provokes a significant differentiation of the PVDF-HFP@MOF composites in comparison to the parent PVDF-HFP NIPS and TIPS membranes.

MOF particles induces significant changes on surface and inner the macrometric structure of the membranes, as concluded by the scanning electron microscopy micrographs. In parallel, they have as well some modulation effect to shape the microscale pores that are responsible of the main empty pore volume of the system, as revealed by the mercury porosimetry data. Overall, the surface and mass fractal pore structure of the PVDF-HFP is as well altered when MOFs are included within the system. Indeed, SANS and SAXS exhibits additional features related to the MOF particles organization into the polymeric system.

Overall, the macro to nanometric characterization of the composites has allowed to unravel specific features of this complex systems not reported before. As a small drawback, the combination of the experimental techniques applied in this study does not give access to quantify to which extent the MOF particles included within the system are active for adsorption. To this end, comparative Cr^{VI} adsorption experiments have allowed estimating that the accessibility degree of the MOF particles installed into TIPS membranes is higher than the one observed for NIPS homologues. Even within the same kind of membranes, the nature of the MOF modulates as well the encapsulation degree of the particles in the polymeric system. For instance, the encapsulation-degree governs as well these MOF fraction that is accessible to be *in-situ* modified by SALI once immobilized in the membrane.

It is important to note that, as far as we know, this is the first time that a SALI direct functionalization of a polymeric-MOF composite system has been performed, and that this strategy has been fully effective to modulate the adsorption affinity of the system towards cationic soft species as Hg^{II}. *In-situ* modification of polymer-MOF systems opens the perspective to improve the processing of the composites until the proper accessibility, porosity, permeability and MOF-loading features are achieved, and later on, modify the inner chemistry of the system to tailor-adapt it to the capture or separation of specific metal ions.

5.2. CHITIN@METAL–ORGANIC FRAMEWORK COMPOSITES AS WIDE–RANGE ADSORBENTS

Any pollution input within the natural water cycle impacts on the base of the trophic chain in the short term, reaching in the long term to affect all its scales. The challenge of the current water remediation lies in the pollution heterogeneity, since in addition to heavy metal cations or oxyanions derived from natural geologic environments, human activities incorporate uncountable types of inorganic and organic long-term persistent chemicals to the water cycle. Today, highly persistent pollutants such as antibiotics, endocrine disruptors, heavy metals, particles, organic dyes, and pesticides can be found in wastewater streams. [46–48] The wide range of chemical characteristics of these pollutants make cleaning such a complex aqueous matrix an enormous challenge beyond the capabilities of a single technology or material. The development of efficient and broadly applicable water remediation technologies is an urgent need and must consider the fundamental properties of these hazardous molecules, such as their size, shape, charge, and potential binding groups.

Heavy metals, for example, are found as aquo-oxo-metal species up to 4.5 Å in dynamic diameter. These inorganic species can be positive, negative or neutral, and they show degrees of acidity that depend on their charge density (Z/r^2). The size, charge and chemical variety of organic pollutants is even higher. They range from small, angstrom-scale molecules (e.g., drugs, endocrine disruptors or organic dyes), to nano (e.g., nanoparticles) and even micron-scale pollutants (e.g., enzymes, hormones, proteins or microplastics). Therefore, multi-use water remediation technology must be able to remove a large variety and size-range of pollutants, from small ions to large macromolecules, with any number of different chemical functionalities or charged binding groups.[49–51]

Of the current wastewater treatment technologies, adsorption has emerged as a green, efficient, selective and reusable option.[52] Many types of different sorbents have been developed and tested to recover single specific pollutants. Nevertheless, this "one adsorbent/one pollutant" strategy does not address the challenge of cleaning real water samples that often contain multiple types of hazardous chemicals.

To achieve broad-scope sorption of sizes from angstroms to microns the sorbent materials should comply with at least two requirements. First, it is necessary to synergistically combine porous materials having micro-, meso- and macropores. Second, functionalization of the porous scaffold is needed, as this enables to introduce key-lock mechanisms to trap neutral, anionic and cationic compounds.[53] Encompassing these characteristics in one type of sorbent is not easy, since well-ordered microporous materials lack the capacity to adsorb large size molecules; whilst macro and mesoporous polymers usually fail to retain selectively small metal ions.[54,55]

Therefore, the development of hybrid materials has the potential to be one of the most flexible approaches to create porous materials that can retain molecules across the micro to the macroscale. After considering the many possible combinations of meso/macroporous polymers and microporous sorbents, Chitin (CH) [56–59] and Metal-Organic Frameworks[60–68] (MOFs) have been selected to develop a functional composite with multiple porosities and chemical functionalities[69,70] (Figure 5.16)

Chitin (CH) is the second most abundant natural polymer, formed by polymeric chains of N-acetylglucosamine units. The presence of acetamido and hydroxyl groups at the CH's molecular chains makes this natural polymer highly effective in interacting with organic pollutants.[71,72] In addition, CH is easy handled and processed as macro/mesoporous gels,[73–76] which enables their use as sorbents for macromolecules (e.g. enzymes and proteins).[77–80] Nevertheless, CH usually lacks of adsorption affinity for cationic and anionic inorganic species at the microporous scale.[81]

To overcome this problem, Zr-based MOF-808 particles have been included as fillers within the CH matrix.[27,82] MOF-808 has been specifically selected because in addition to its water and acid resistance, it exhibits a wide pore window and high surface area (~2000 to 1000 $m^2 \cdot g^{-1}$) that facilitates the pollutant migration into the structure, together with a six linker defect positions at the inorganic hexa-nuclear clusters that welcome negatively charged inorganic oxyanions and molecules. These structural features make MOF-808 particles highly efficient to retain negatively charged arsenate, chromate or selenite species, a function that the CH matrix

lacks.[83–85] In the following, the potential of CH@MOF-808 based composites as broad scope adsorbents will be exhaustively demonstrated.
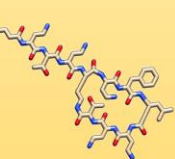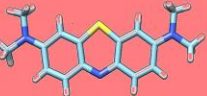

Figure 5.16. Representative examples of organic and inorganic components that can be found in a wastewater stream as well as their possible adsorption by the developed CH@MOF-808 composites at the micro, meso and macropores.

5.2.1. EXPERIMENTAL PROCEDURE

Synthesis of MOF-808

MOF-808 particles were synthesized using a slightly modified version of the protocol described by Jiang *et al.*[27] $ZrCl_4$ (0.1234 g, 0.5295 mmol), 1,3,5-benzenetricarboxylic acid (H_3BTC, 0.1237 g, 0.5887 mmol), formic acid (12 mL), water (0.5 mL) and N,N-dimethylformamide (DMF, 12 mL) were mixed, stirred at room temperature, sealed in a 25 mL glass autoclave (Schott, Duran®) and then placed in an oven at 120 °C for 48 h. After the reaction, the vessel was cooled naturally

to room temperature in the oven. The white precipitate was centrifuged and washed with methanol three times. Subsequently, the obtained precipitate was dried at 80 °C for one day.

Synthesis of CH and CH@MOF-808 composites

Chitin gels were synthesized according to the protocol described by González *et al.*[86] Firstly, calcium solvent was prepared suspending $CaCl_2$ $2H_2O$ (42.5 g, 0.288 mol) in 50 mL of methanol and refluxed for 30 min at 92 °C to a state of near-dissolution. Then, 1 g of CH was refluxed in the calcium solvent for 2 h at 92 °C under constant stirring. For the preparation of the composites, 50, 100 or 150 mg of MOF-808 were added to the above solution at this point. The process is illustrated in Figure 5.17. The mixtures were stirred in methanol until they gelled. Finally, the gel composites were washed three times with methanol overnight. The gel of chitin will be denoted as CH and the obtained composites as CH5, CH10, and CH15, respectively.
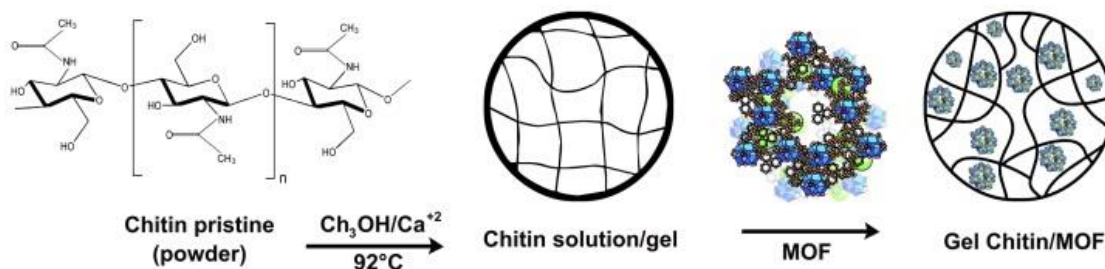
Figure 5.17. Schematic illustration of the fabrication of CH@MOF-808 composites.

Punctual pollutant adsorption tests

Adsorption experiments with CH, MOF-808, and CH@MOF-808 were conducted at 20 °C, using 10 mg adsorbent dispersed in 1·mL pollutant model solutions/dispersions contained in a conical flask. The flasks were agitated in vibrator shaker at 180 rpm during 12 h until adsorption equilibrium was reached. After that, the suspension was centrifuged at 6000 rpm for 10 min, filtrated with a hydrophilic 0.22 μm filter, and finally analysed by means of UV-Vis or ICP-AES depending on

the analyte. Erythrosine (ERY, λ_{max} = 491 nm), Methyl Orange (MO, λ_{max} = 465 nm), Methylene Blue (MB, λ_{max} = 610 nm), Gold nanoparticles (Au(0), λ_{max} = 400 nm) Lysozyme (LYS, λ_{max} = 280 nm), and Polymyxin B antibiotic (POL-B, λ_{max} = 280 nm) concentrations were analysed by UV-Vis spectroscopy. ICP-AES was used to determine the concentration of As^V and Cr^{VI}.

Synthesis of gold nanoparticles

13.8 nm diameter gold nanoparticles (Au(0)) were synthesized by standard citrate reduction method. Briefly, 5 mL of 1 wt % sodium citrate aqueous solution was added under continuous stirring to a boiling aqueous solution of $HAuCl_4$ (100 mL, 0.5 mM) and allowed to react. After 15 min, the solution was cooled down to room temperature and then stored at 4 °C for long-term storage.

Adsorption kinetic curves

For As^V and some of the organic dyes, the full kinetic and curves were determined by separating the adsorbent and adsorbate solutions at different equilibrium times. To this end, a 1 mL solution of 1 ppm As^V and 100 ppm organic dyes was added to Eppendorf tubes. Afterwards, 10 mg CH15 was added to the solutions. The Eppendorf tube was shaken at room temperature and filtrated at given times of the adsorption process. Measurements were performed in triplicate.

Adsorption isotherm curves

The same experimental protocol was used to determine the adsorption isotherms, but using the same equilibrium time (4 h) and different concentrations of the pollutants in the initial solutions. The adsorbent concentration and volume of the initial solutions were kept as previously described.

5.2.2. RESULTS AND DISCUSSION

Synthesis and characterization of materials

CH and CH@MOF materials were synthetized as described previously. Three CH@MOF-808 samples were obtained varying the MOF-808 weight content from 5% (CH5), 10% (CH10) to 15% (CH15). XRD analyses of the MOF-808 nanoparticles confirm the correlation between the experimental and calculated patterns obtained from the structural model of MOF-808 (Figure5.18).[87,88]
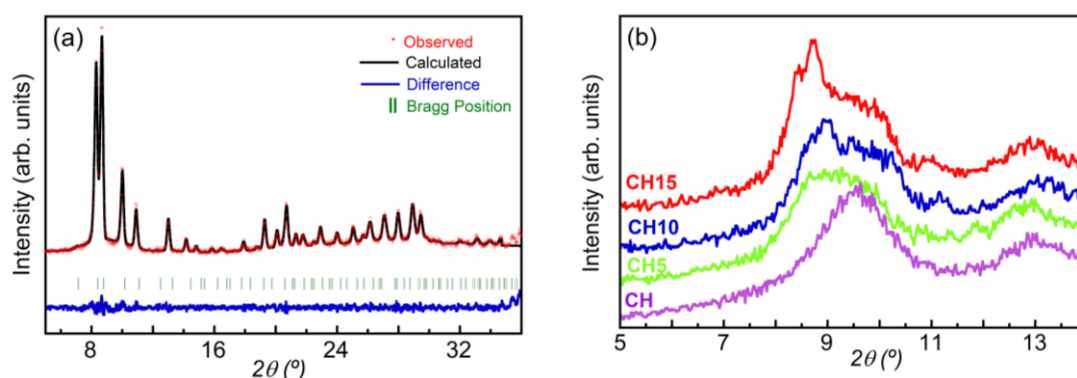
Figure 5.18. (a) Pattern matching analysis of MOF-808. (b) XRD patterns of CH, CH5, CH10 and CH15.

As shown in the TEM images (Figure 5.19a-b), the presence of water in the synthesis media reduces the MOF-808 particle size from the micron to the nanoscale (20 ± 4 nm in diameter). No morphological or particle size changes of MOF-808 nanoparticles are produced due to their incorporation into the chitin matrix (Figure 5.19c-d).
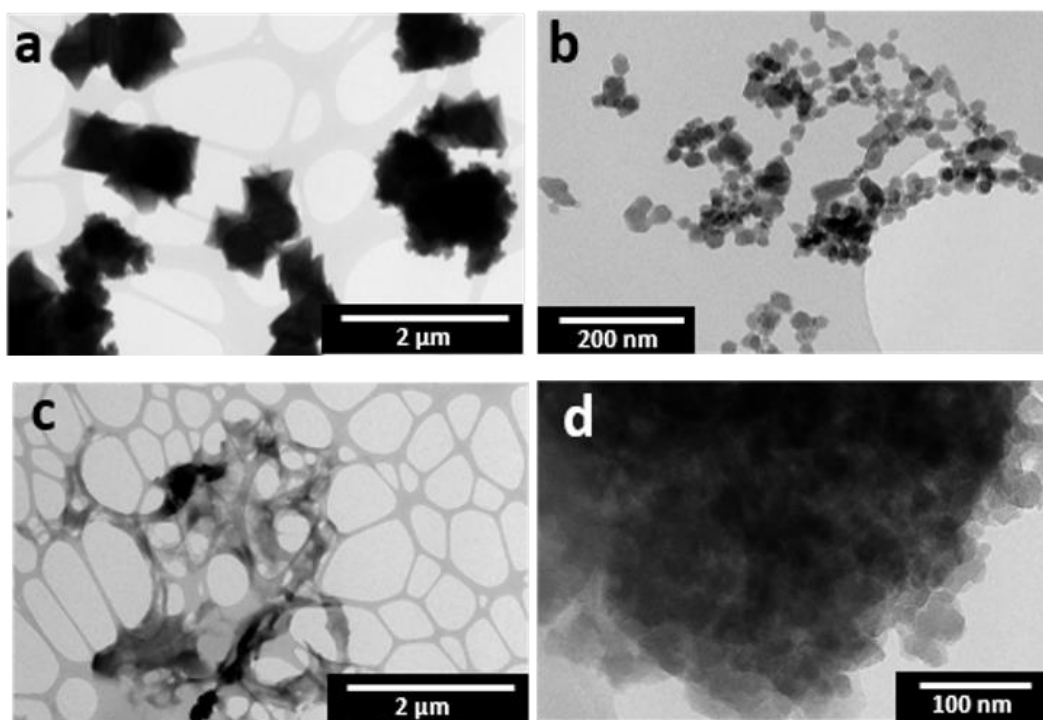
Figure 5.19. TEM micrographs of (a) micrometric MOF-808 particles, (b) MOF-808 nanoparticles, (c) CH and (d) CH15.

The morphology and structure of CH@MOF-808 composites were also studied by SEM (Figure 5.20). CH shows a macro porous structure with average pore diameters of 18 ± 2 µm (Figure 5.20a). The first consequence of the incorporation of MOF808 nanoparticles is the CH pores compartmentalization to 7 ± 2 µm in CH5 (Figure 5.20b), 2.3 ± 1.3 µm and 640 ± 160 nm for CH10 (Figure 5.20c) and 1.6 ± 0.7 µm and 450 ± 140 nm for CH15 (Figure 5.20d). Compositional mapping of carbon, oxygen and zirconium content in CH@MOF-808 composites (Figure 5.20e-h) indicates a uniform MOF-808 distribution within the CH structure.
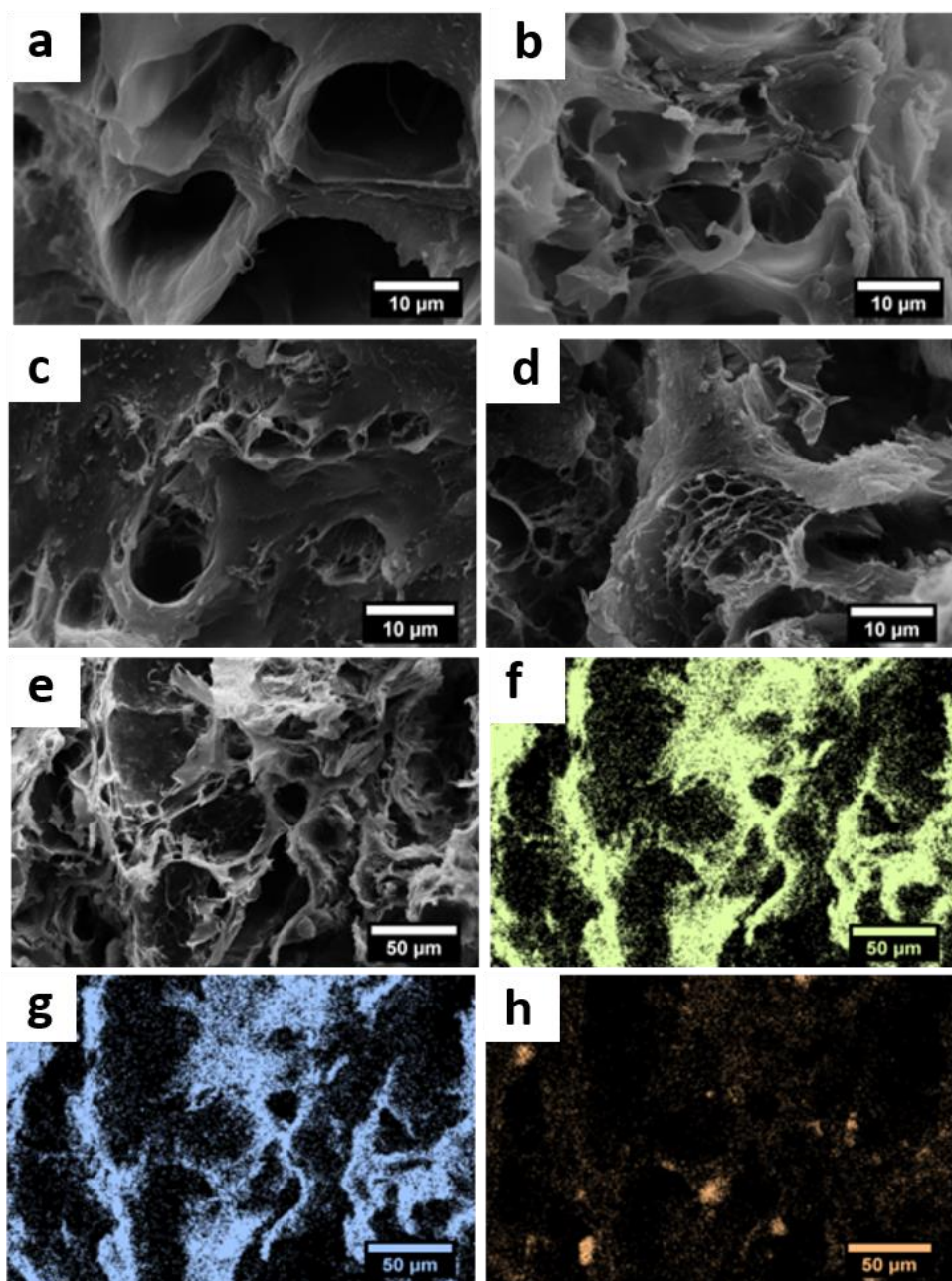
Figure 5.20. SEM micrographs of the samples: (a) CH; (b) CH5; (c) CH10; (d) CH15. €
SEM-EDS mapping zone of CH15 sample for C, O and Zr (f, g and h, respectively).

Mercury porosimetry (Figure 5.21a-b) and room temperature CO_2 adsorption (Figure 5.21c-d) measurements were carried out in order to study the porosity of CH@MOF-808 samples from the macro to the micro-porous regimes.[89,90] The macro-pores compartmentalization directed by the template effect of MOF-808

nanoparticles increases the total porosity (%) and surface area ($m^2 \cdot g^{-1}$) of the samples from 49.8 % and 34 $m^2 \cdot g^{-1}$ in CH, to 72.9 % and 275 $m^2 \cdot g^{-1}$ in CH15 (Table 5.3).[91]

Table 5.3. Total porosity and surface area values.

Sample	Total macro- meso- porosity (%)	Exp. BET macro- meso-porosity ($m^2 \cdot g^{-1}$)	Exp. BET microporosity ($m^2 \cdot g^{-1}$)
MOF-808	---	475	1416,78
CH	49.8	34.5	15,94
CH5	62.1	151.3	167,39
CH10	63.0	222.0	307,01
CH15	72.9	275.3	317,61

In order to gain further insights into the interaction between the polymeric CH matrix and the MOF nanoparticles, the CH@MOF-808 composites were studied by Raman spectroscopy (Figure 5.21e). In MOF-808, the characteristic bands are ascribed to the vibrational modes of inorganic Zr-O bonds (644 cm^{-1}). C−H out-of-plane bending of ring, symmetric stretch (C=C), benzene ring, symmetric stretching (COO) and asymmetric stretch (COO) of trimesate organic linkers have been also identified at 808, 1008, 1370 and 1473 cm^{-1}, respectively. Spectra for CH@MOF-808 composites reveal predominantly the adsorption bands related to the vibrational modes of the CH matrix. Specifically, Amide I (1630 and 1660 cm^{-1}), Amide III (1200-1350 cm^{-1}), C–O–C and C–O stretching vibration region (1200–950 cm^{-1}), and β-glycosidic bonds (890 cm^{-1}) have been identified as the main Raman fingerprints of CH. The intensity of the 1008 cm^{-1} adsorption band in CH@MOF-808 composites is correlated to the degree of MOF-808 loading. No meaningful wavenumber displacements or new vibration modes were observed in the Raman signals of the separate components that form the composites, suggesting that the blending of MOF-808 and CH is not based on strong chemical interactions.

The DSC-TGA thermograms of pure CH and CH@MOF-808 composites are illustrated in Figure 5.21f and g. The TGA curves of CH@MOF-808 show the first

weight loss at low temperatures (RT-100 ℃); associated with the release of adsorbed water molecules. After dehydration, the TGA and DSC curves show a decrease in the temperature of the CH exothermic transition from 250 (CH) to 220 ℃ (CH15). This effect is attributed to a reduction of the interactions between carbon chains (*i.e.* increase of the disorder degree) rather than to new chemical interactions with MOF-808 nanoparticles.[92] At higher temperatures, the CH exothermic deacetylation process starts around 320 °C, which is not altered by the presence of the MOF-808 nanoparticles.

The dielectric relaxation spectra for all CH@MOF-808 composites show a loss factor (tan δ) peak between 250-350 kHz (Figure 5.21h). The tan δ peak shifts to lower frequencies upon the addition of MOF-808, indicating a slowing-down of the relaxation dynamics of CH chains. The embedding of MOF-808 within the CH matrix can induce both a (i) disorder in the CH polymeric chains and (ii) CH chain - MOF-808 electrostatic interactions, both leading to a decrease the polymer relaxation dynamics.[93]
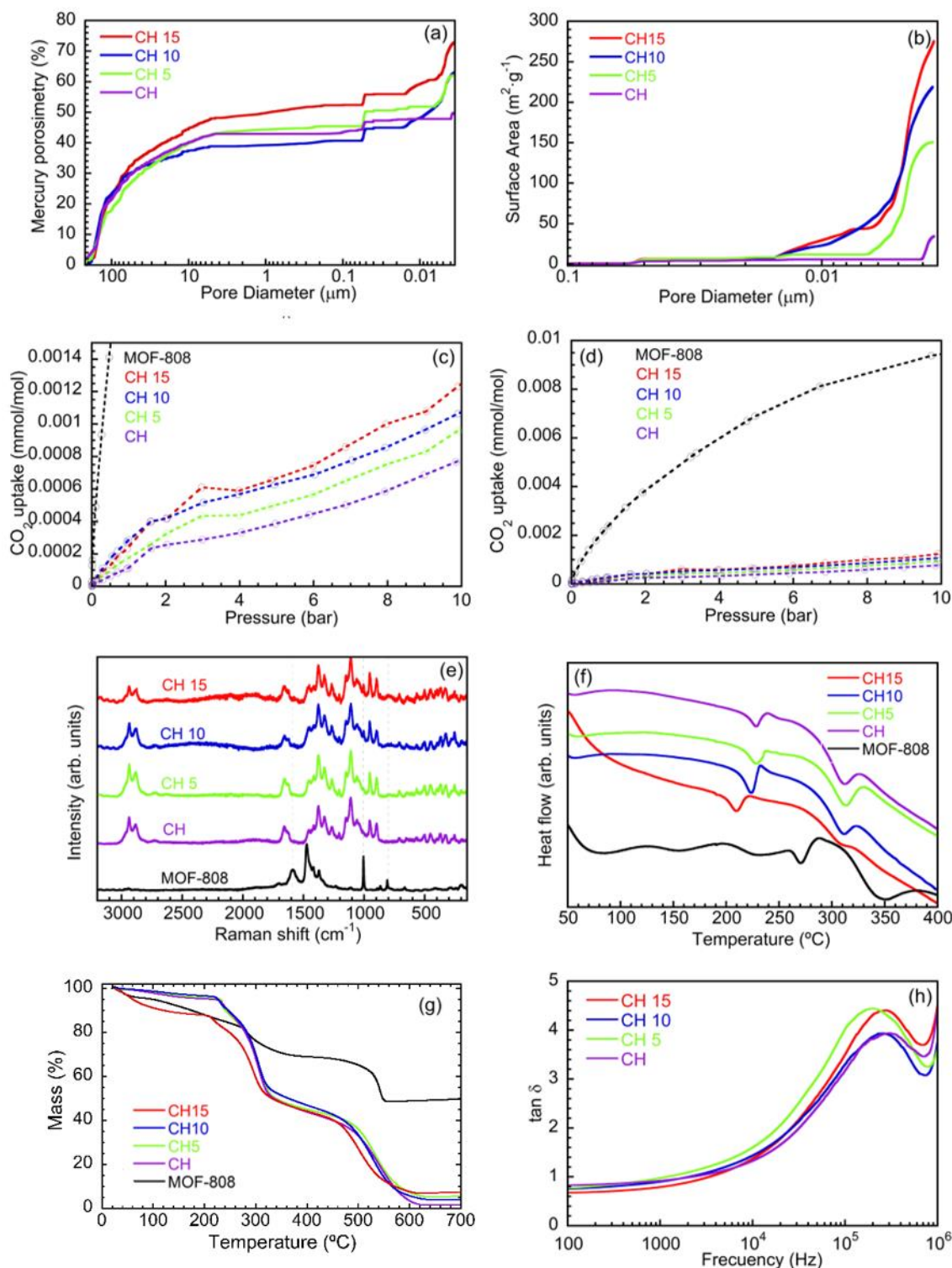
Figure 5.21. (a) Cumulative porosity variation determined by mercury porosimetry, (b) Cumulative surface area determined by mercury porosimetry (c) and (d) CO_2 adsorption isotherms, (e) Raman spectra, (f) DSC (g) TGA and (h) dielectric relaxation spectra of CH, MOF-808 and composite CH5, CH10 and CH15 samples

Pollutant adsorption tests

Initial adsorption screening tests have been performed with CH, MOF-808 and CH@MOF-808 composites over cationic, anionic and neutral pollutants with sizes ranging from nanometre to the angstrom scales. To this end, CH@MOF-808 adsorption efficiency over aqueous solutions of lysozyme (LYS, 5000 ppm), gold nanoparticles (AuNP, 50 ppm), polymyxin B (POL-B, 50 ppm), erythrosine (ERY, 50 ppm), methylene blue (MB, 50 ppm), methyl orange (MO, 50 ppm), hexavalent chromium (Cr^{VI}, 50 ppm) and pentavalent arsenic (As^{V}, 40 ppm) has been quantified. Figure 5.22a shows the adsorption efficiency in % adsorption of CH@MOF-808 composites, CH and MOF-808 materials. In order to uncover whether the assembly of CH@MOF-808 composites synergistically combines the individual MOF-808 and CH components, the experimental adsorption efficiency values for CH5, CH10 and CH15 have been compared with those calculated in the plots of Figure 5.22b, c and d, respectively.

The calculated adsorption efficiencies have been obtained from the sum of the weight average adsorption capacities of the MOF-808 and CH in CH5, CH10 and CH15 composites. The difference in adsorption % between the calculated and experimental values of CH@MOF-808 composites is defined by the Equation 5.3.

$$\Delta SE = (SE_{CH@MOF-808}) - ((SE_{MOF-808})WP + (SE_{CH})(100 - WP) \qquad (5.3)$$

where ΔSE is the difference in adsorption capacity (%), WP is the weight percentage of MOF-808 on CH@MOF-808 samples, $(SE_{CH@MOF-808})$ and (SE_{CH}) are the experimental sorption capacities of separate MOF-808 and CH components.
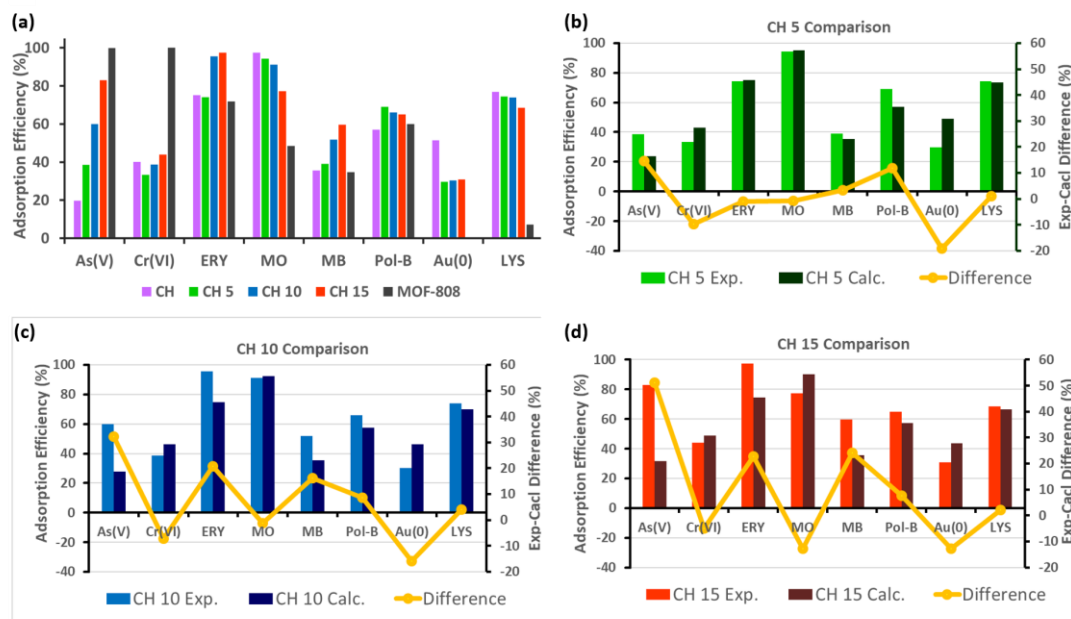
Figure 5.22. (a) Removal efficiency of CH, CH5, CH10 and CH15 over different pollutants. Comparison between experimental (light columns) and calculated (dark columns) adsorption efficiencies for (b) CH5, (c) CH10 and (d) CH15 CH@MOF-808 composites.

The discussion of the results derived from the adsorption tests will be performed in the following order: metal oxyanions, organic dyes, large molecules, and nanoparticles.

Regarding their chemical properties, inorganic cations and oxyanions are the smallest pollutant species, and their adsorption is highly dependent on the presence of attractive charged groups in the adsorbent structure.[94–96] As demonstrated by previous researches,[27,84,88] MOF-808 shows an As^V removal capacity of near 99 % for As^V 40 ppm solution (Figure 5.22a), while CH exhibits a much lower performance (20 %). CH@MOF-808 composites show intermediate efficiencies, highly dependent on the MOF-808 content. When comparing experimental and calculated adsorption efficiencies, CH@MOF-808 composites outperform the averaged sum of the capacities of CH and MOF-808 components (Figure 5.22b-d).

The immobilization of hexavalent chromium anions in MOF-808,[97,98] CH@MOF-808 composites, and CH matrixes is governed by two factors: (i) adsorption at the CH@MOF-808 structure,[26,99,100] and (ii) reduction from Cr^{VI} to Cr^{III} due to the electron donor groups of CH matrix[101,102]. MOF-808 nanoparticles have a near 100% capacity for the removal of Cr^{VI} species from water; whilst CH and CH@MOF-808 show just a 40% removal. Contrary to the expected tendency, the CH@MOF-808 composites do not show an increase of the chromate anions removal in comparison to CH matrix. In order to gain further insights chromium speciation after operation was studied by means of EPR spectroscopy. As revealed by EPR, MOF-808 immobilizes chromium mainly as hexavalent chromate; and also, as highly reactive and hazardous pentavalent chromium (Figure 5.23a,b). Although CH is less efficient in adsorbing Cr^{VI}, it is highly effective in immobilizing it as trivalent chromium (Figure 5.23c,d). Similar Cr^{VI} to Cr^{III} reduction capacity is found for CH@MOF-808 composites. It seems that the Cr^{VI} to Cr^{III} reduction in CH composites is the process that governs the final chromate removal capacity of the system, prevailing over, or even blocking, the Cr^{VI} adsorption process on the MOF-808 nanoparticles. Even though CH and CH@MOF-808 composites are less efficient than MOF-808, and lower than the expected average sum of their capacities (Figure 5.22b–d), they immobilize the chromium in its less toxic, reactive, and mobile trivalent ion form.
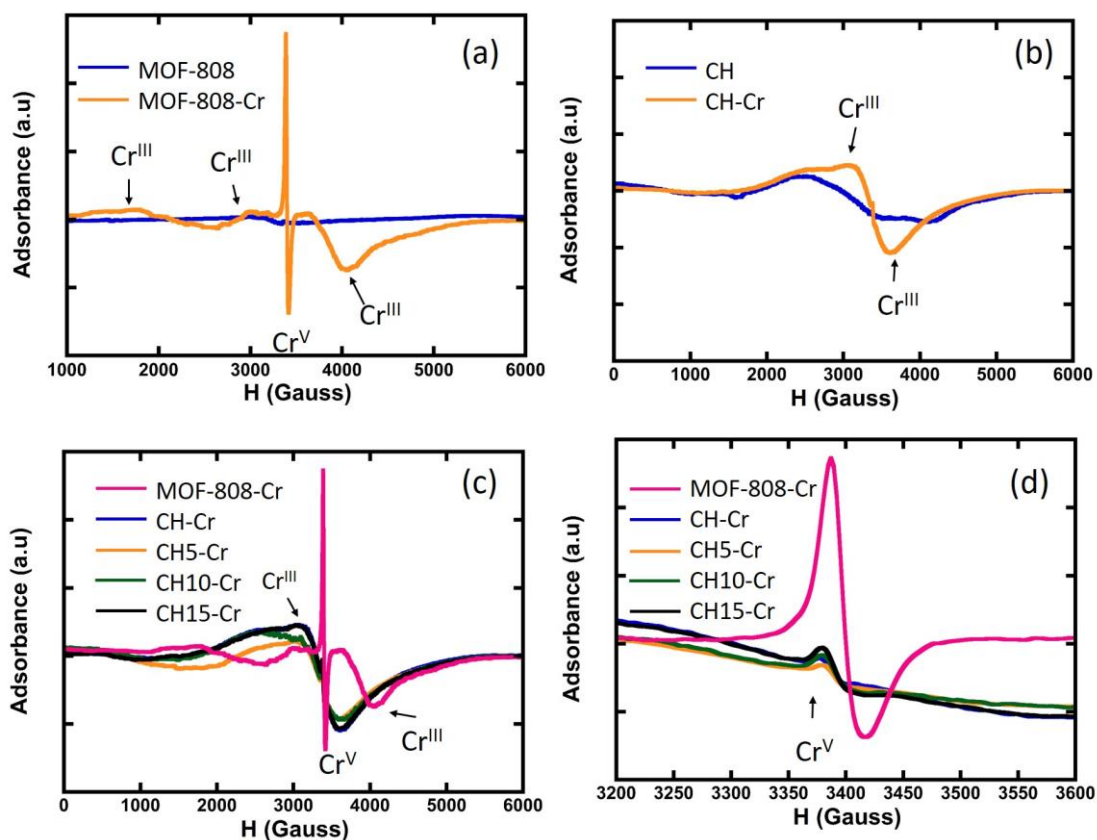
Figure 5.23. (a) EPR spectra of MOF-808 before and after the Cr^{VI} adsorption. (b) Comparison between EPR spectra of CH and CH after Cr^{VI} adsorption. Broad signal at 3600 Gauss is assigned to Cr(III) ions. (c) EPR spectra of MOF-808, CH and CH@MOF-808 composites. (d) Detail of the Cr(V) signal intensity.

Further, the possibility of removing larger organic molecules was also evaluated for CH@MOF-808 composites. Several organic dyes were first selected with shapes and average dimensions suitable matching MOF's pores;[103] but also having charged groups prone to interact with the CH and CH@MOF-808 surface (Figure 5.16).[104] A screening of the CH@MOF-808 adsorption over cationic MB, anionic ERY, and MO dye molecules was carried out (Figure 5.22). For MO, CH shows higher adsorption capacity (100 %) than MOF-808 (50%), and the performance of the CH@MOF-808 composites simply averaged the performances of the individual materials. (Figure 5.22b-d). Surprisingly, the results obtained for cationic and anionic MB and ERY indicate that CH@MOF-808 composites adsorb them more efficiently than the corresponding MOF-808 or CH components (Figure 5.22b-d). Two factors could

explain this synergetic effect that leads to enhances adsorption of CH@MOF-808 composites: (i) the increase of the active total porosity due to the compartmentalization of the CH's macro-pores into mesopores (*i.e.*, the increase of available surface area) and (ii) the role of the CH@MOF-808 interface.

In addition, the behaviour of CH@MOF-808 was investigated with respect to the adsorption of larger molecules able to enter the meso and macroporous structure of CH, but not into the pore system of the MOF-808 nanoparticles. It is worth noting that even if the pore window of the MOF-808 nanoparticles impedes the access of bulky macromolecules within its structure, their outer surface also represents an important adsorption region, since under-coordinated inorganic clusters and organic linkers can act also as interacting points for adsorbates. This is in fact observed for the absorption of POL-B.[105] Nearly 60% of POL-B molecules are retained at the surface of MOF-808 nanoparticles; a capacity slightly higher than the one observed for the CH macro-porous matrix (58%) (Figure 5.22a). Again, CH@MOF-808 composites outperform the adsorption capacity of the separate CH and MOF-808 components. This behaviour further confirms the relevance of the compartmentalization and interface chemistry of CH@MOF-808 porous structure on its adsorption capacity (Figure 5.22b-d). It is worth noting that POL-B is a natural antibiotic agent used in this work as a model pollutant, since its chemical structure and molecular size resembles the ones of medium molecular size pollutants found in current wastewater, such as hormones or antibiotics.[106,107]

Due to the meso- and macro-porous structure of CH and CH@MOF-808 composites, they are also able to retain larger adsorbates, such as lysozyme[108,109] protein (30 x 50 Å) or gold nanoparticles with 13.6 ± 1.4 nm average diameters. The estimation of an adsorbent system to retain large proteins is also interesting, since despite proteins are not a pollutants *per se*, they are involved in the selectively recognition of endocrine disruptor hormones, a property that could lead to future development of CH@MOF-protein system able to retain them.

MOF-808 is not generally useful in LYS or AuNPs capture, the adsorption capacity for both adsorbates being negligible. In these two cases, the CH macro- and meso-porous structure is the active component, retaining a 50 and 70% of gold and LYS,

respectively (Figure 5.22a). For LYS, CH@MOF sorbents show efficiencies slightly lower than CH (Figure 5.22a), which can be understood as the average sum of CH and MOF-808 (Figure 5.22b-d). In the case of AuNPs, CH@MOF-808 composites underperform in comparison to their components (Figure 5.22b-d). For these two case studies, the compartmentalization of the CH's macro-pores into mesopores impede the migration of LYS and AuNPs through the structure of the CH@MOF-808 matrix, reducing the area accessible to the adsorbate. Therefore, compartmentalization of CH macro-pore structure is beneficial to certain limit in terms of pollutant molecular size. Despite this limitation, it has been duly proved that the synergistic combination of CH and MOF-808 give access to the adsorption of a wide variety of pollutants from the angstrom to nanoregimes.

CH15 composite performance was fully studied for the specific case of pentavalent arsenic oxyanion. It is important to note that arsenic natural pollution is a worldwide issue affecting large geographical areas of many countries (e.g. USA, India, Chile, Argentina, Europe…). As^V adsorption was studied at a 1 ppm initial concentration, which is a level of arsenate contamination common in many river basins worldwide, in particular in those ones crossing bedrocks containing arsenic-rich minerals. Full kinetic and isotherm adsorption of As^V for the CH15 composite are shown in the Figure 5.24. The adsorption capacity of the CH15 matrix at 1 ppm arsenic concentration is 33%, far from the 82% value obtained when using a 40 ppm As^V concentration (Figure 5.24a). Nevertheless, at this low concentration, the inclusion of MOF-808 fillers continue to enhance the CH matrix with the affinity for negative species that the CH polymer solely lacks.

The CH15 adsorption kinetic profile for As^V (Figure 5.24b) is similar to that previously reported for zirconium-based MOFs, with most of the adsorption occurring at the first stage of the experiment.[110] The Elovicth model (Equation 2.4 in Chapter 2), used to fit the experimental data (orange line of Figure 5.24b), indicates that the arsenate is chemisorbed into CH15. This observation is in agreement with previously reported adsorption mechanisms on Zr-MOFs over oxyanions, since it has been experimentally proven that oxyanions uptake occurs through direct coordination of arsenate to the zirconium hexa-nuclear clusters.[111]
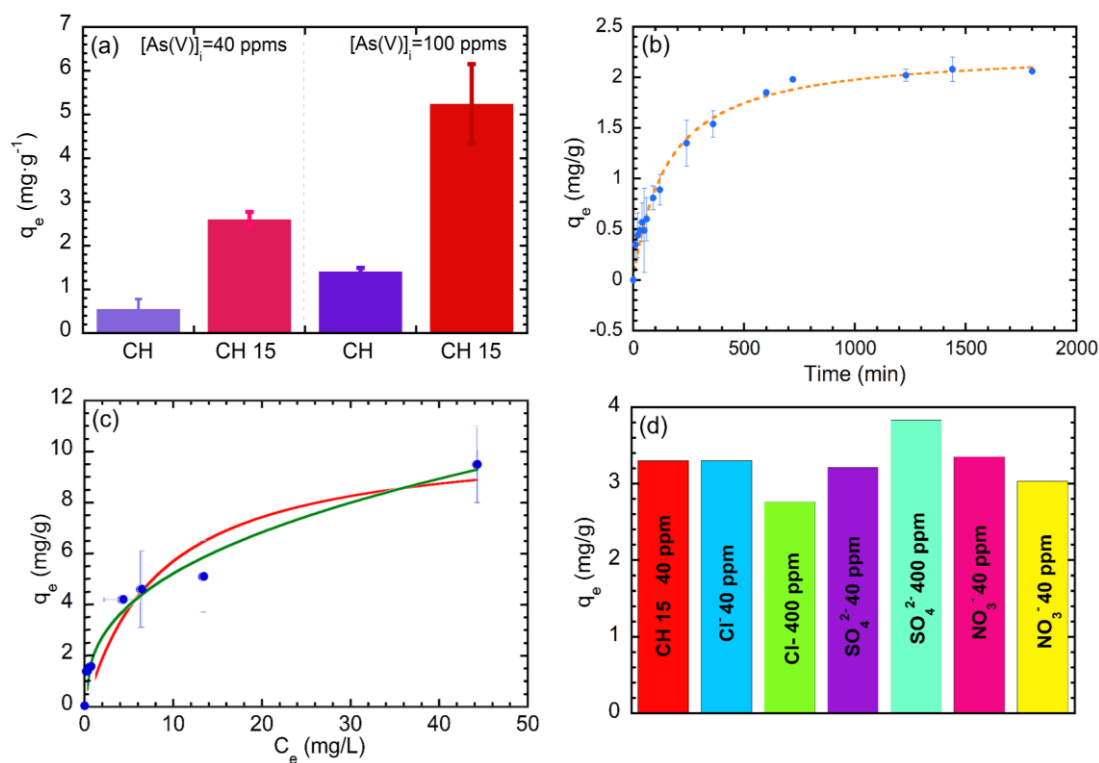
Figure 5.24. (a) Adsorption capacities over As^V at 40 and 100 ppm for CH and CH15. (b) Adsorption kinetics of As^V at 1 ppm for CH15 composite. (c) Adsorption isotherm over As^V for CH15 (red line: fitting obtained with a Langmuir model, green line: fitting obtained with a Freundlich model). (d) Adsorption capacity over As^V (C_0=40 ppm) of CH15 in the presence of competitor anions at 40 and 400 ppm. The first red colored bar of the Fig d is the adsorption capacity of CH15 over As^V ($C_0 = 40$ ppm). This data has been depicted as a reference. All the adsorption studies were performed with the addition of 10 mg of CH and CH@MOF composites to 10 mL of arsenic solution

Figure 5.24c shows the adsorption isotherms for CH15 over arsenate. The data can be fitted with the Freundlich and Langmuir models resulting in slightly better agreement factors for Freunlich model, (Freunlich, R = 0.991; Langmuir, R = 0.958). The values of the q_{max} and k constants (related to the adsorption capacity of the CH15) calculated from the fittings are of 10.6 ± 1.7 mg·g^{-1} and 2.2 ± 0.2 mg·L^{-1} respectively.[112] More interesting is that the n Freundlich parameter value of 0.39(2) further confirms that a chemisorption mechanism is responsible for arsenate retention within the CH15 composite, overriding the inter-particle interaction effects among the arsenate oxyanions and the CH matrix.

The adsorption capacity of CH15 over As^V (C$_0$ = 40 ppm) was also tested in the presence of 40 and 400 ppm sulphate, nitrate and chloride anions (Figure 5.24d). The competition of these anions for the adsorption sites does not strongly affect the performance of CH15. Indeed, the observed deviation is correlated with slight differences of the As^V initial concentration found for the solions containing different competitor species. In the worst-case scenario, a slight reduction of the retention capacity is observed in the presence of 400 ppm of Cl$^-$ and NO$_3^-$ species

In the specific case of organic dyes, CH15 adsorption kinetics for larger molecules is faster than those reported for arsenate oxyanions (Figure 5.25). Indeed, the system reaches equilibrium in 60 min for MB and MO and in 100 min for ERY. The charge of the organic dyes is a key factor in an electrostatic interaction driven adsorption process. In comparison to As^V, here the CH plays also a very active role during adsorption, since it is able to retain the same quantity of target dye as MOF-808 (Figure 5.22a).
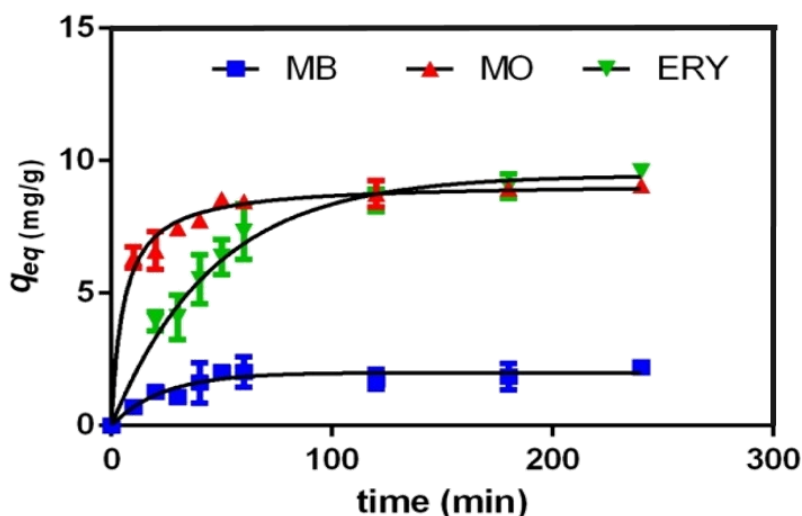

Figure 5.25. Experimental kinetic adsorption profiles for methylene blue (MB), methyl orange (MO) and erythrosine (ERY) dyes

5.2.3. CONCLUSIONS

MOF-808 nanoparticles incorporation into chitin gel polymeric matrix develop micro-, meso- and macro-porous composites that can be used as broad scope adsorbents. This is possible because MOF-808 nanoparticles compartmentalize into the macroporous structure of CH polymeric matrix, endowing the composite with the inherent micro-porosity of the MOF-808 material itself, and additionally increasing the surface area available for absorption.

Due to their micro, meso and macroporous structure, the CH@MOF-808 composites are able to work efficiently for the adsorption of a large variety of pollutants ranging from small ions and molecules to large proteins or nanoparticles. CH@MOF-808 composites exhibit the chemical affinity of their separate components; but in some cases (e.g. As^V, methylene blue, erythrosine and Polymyxin B), the material benefits from the synergistic interactions of its components, outperforming both MOF-808 and CH efficiency. This synergetic effect is attributed to (i) the compartmentalization of the CH macro-pores when including MOF-808 nanoparticles within its structure, and (ii) the active role of the interface between MOF-808 and CH during adsorption. CH@MOF-808 composites are also able to work efficiently in terms of capacity and kinetics over As^V capture in solutions mimicking real polluted waters. As concluded from the fittings of adsorption isotherms and kinetic curves, As^V is captured through chemisorption at the MOF-808 nanoparticles.

Considering the performance of the CH@MOF-808 systems, it can be concluded that we have achieved a broad adsorption technology able to work in the present of complex variety of pollutants that can be found in current water streams. Moreover, the MOF structural diversity and designability at the molecular levels, combined with the easy processability and biocompatibility of CH polymers, makes the developed materials suitable for applications where available surface area, pore size and pore chemistry become a relevant issue.

5.3. REFERENCES

1   Salazar H, Martins PM, Santos B, Fernandes MM, Reizabal A, Sebastián V, Botelho G, Tavares CJ, Vilas-Vilela JL, Lanceros-Mendez S. Photocatalytic and antimicrobial multifunctional nanocomposite membranes for emerging pollutants water treatment applications. *Chemosphere* 2020; **250**: 126299–126314. [PMID: 32113095 DOI: 10.1016/j.chemosphere.2020.126299]

2   Choi H, Zakersalehi A, Al-Abed SR, Han C, Dionysiou DD. Nanostructured Titanium Oxide Film- and Membrane-Based Photocatalysis for Water Treatment. In: *Nanotechnology Applications for Clean Water*.2014: 123–132.

3   Gupta K, Joshi P, Gusain R, Khatri OP. Recent advances in adsorptive removal of heavy metal and metalloid ions by metal oxide-based nanomaterials. *Coord Chem Rev* 2021; **445**: 214100. [DOI: 10.1016/j.ccr.2021.214100]

4   Zhang S, Wang J, Zhang Y, Ma J, Huang L, Yu S, Chen L, Song G, Qiu M, Wang X. Applications of water-stable metal-organic frameworks in the removal of water pollutants: A review. *Environmental Pollution* 2021; **291**: 118076. [PMID: 34534824 DOI: 10.1016/j.envpol.2021.118076]

5   Grandcolas M, Lind A. 3D-printed polyamide structures coated with TiO2 nanoparticles, towards a 360-degree rotating photocatalytic reactor. *Mater Lett* 2022; **307**: 131044. [DOI: 10.1016/j.matlet.2021.131044]

6   Martins PM, Ribeiro JM, Teixeira S, Petrovykh DY, Cuniberti G, Pereira L, Lanceros-Méndez S. Photocatalytic microporous membrane against the increasing problem of water emerging pollutants. *Materials* 2019; **12**. [DOI: 10.3390/ma12101649]

7   Ng LY, Mohammad AW, Leo CP, Hilal N. Polymeric membranes incorporated with metal/metal oxide nanoparticles: A comprehensive review. *Desalination* 2013; **308**: 15–33.

8   Salazar H, Nunes-Pereira J, Correia DM, Cardoso VF, Gonçalves R, Martins PM, Ferdov S, Martins MD, Botelho G, Lanceros-Méndez S. Poly(vinylidene fluoride-hexafluoropropylene)/bayerite composite membranes for efficient arsenic removal from water. *Mater Chem Phys* 2016; **183**: 430–438. [DOI: 10.1016/j.matchemphys.2016.08.049]

9   Vinothkumar K, Shivanna Jyothi M, Lavanya C, Sakar M, Valiyaveettil S, Balakrishna RG. Strongly co-ordinated MOF-PSF matrix for selective adsorption, separation and photodegradation of dyes. *Chemical Engineering Journal* 2022; **428**: 132561. [DOI: 10.1016/j.cej.2021.132561]

10   Joshi P, Kumar D. The role of polymer nanocomposite-based membranes for environmnental remediation. In: *New Polymer Nanocomposites for Environmental remediation*.2018: 437–456.

11   da Silva RJ, Mojica-Sánchez LC, Gorza FDS, Pedro GC, Maciel BG, Ratkovski GP, da Rocha HD, do Nascimento KTO, Medina-Llamas JC, Chávez-Guajardo AE, Alcaraz-Espinoza JJ, de Melo CP. Kinetics and thermodynamic studies of Methyl Orange removal by polyvinylidene fluoride-PEDOT mats. *J Environ Sci (China)* 2021; **100**: 62–73. [PMID: 33279054 DOI: 10.1016/j.jes.2020.04.034]

12   Zhao S, Tao Z, Chen L, Han M, Zhao B, Tian X, Wang L, Meng F. An antifouling catechol/chitosan-modified polyvinylidene fluoride membrane for sustainable oil-in-water emulsions separation. *Front Environ Sci Eng* 2021; **15**. [DOI: 10.1007/s11783-020-1355-5]

13   Hou D, Wang J, Qu D, Luan Z, Ren X. Fabrication and characterization of hydrophobic PVDF hollow fiber membranes for desalination through direct contact membrane distillation. *Sep Purif Technol* 2009; **69**: 78–86. [DOI: 10.1016/J.SEPPUR.2009.06.026]

14   Fan H, Peng Y. Application of PVDF membranes in desalination and comparison of the VMD and DCMD processes. *Chem Eng Sci* 2012; **79**: 94–102. [DOI: 10.1016/J.CES.2012.05.052]

15   Bahrami S, Yaftian MR, Najvak P, Dolatyari L, Shayani-Jam H, Kolev SD. PVDF-HFP based polymer inclusion membranes containing Cyphos® IL 101 and Aliquat® 336 for the removal of Cr(VI) from sulfate solutions. *Sep Purif Technol* 2020; **250**. [DOI: 10.1016/J.SEPPUR.2020.117251]

16   Ribeiro C, Costa CM, Correia DM, Nunes-Pereira J, Oliveira J, Martins P, Gonçalves R, Cardoso VF, Lanceros-Méndez S. Electroactive poly(vinylidene fluoride)-based structures for advanced applications. *Nat Protoc* 2018; **13**: 681–704. [DOI: 10.1038/nprot.2017.157]

17   Liu F, Hashim NA, Liu Y, Abed MRM, Li K. Progress in the production and modification of PVDF membranes. *J Memb Sci* 2011; **375**: 1–27. [DOI: 10.1016/j.memsci.2011.03.014]

18   Salazar H, Martins PM, Valverde A, Fernández De Luis R, Luis Vilas-Vilela J, Ferdov S, Botelho G, Lanceros-Mendez S. Reusable Nanocomposite Membranes for Highly Efficient Arsenite and Arsenate Dual Removal from Water. *Adv Mater Interfaces* 2021; **9**: 2101419. [DOI: 10.1002/admi.202101419]

19   Queirós JM, Salazar H, Valverde A, Botelho G, Fernández de Luis R, Teixeira J, Martins PM, Lanceros-Mendez S. Reusable composite membranes for highly efficient chromium removal from real water matrixes. *Chemosphere* 2022; **307**. [PMID: 35940413 DOI: 10.1016/J.CHEMOSPHERE.2022.135922]

20   Lalia BS, Kochkodan V, Hashaikeh R, Hilal N. A review on membrane fabrication: Structure, properties and performance relationship. *Desalination* 2013; **326**: 77–95. [DOI: 10.1016/j.desal.2013.06.016]

21   Barbosa JC, Gonçalves R, Valverde A, Martins PM, Petrenko VI, Márton M, Fidalgo-Marijuan A, Fernández de Luis R, Costa CM, Lanceros-Méndez S. Metal organic framework modified poly(vinylidene fluoride-co-hexafluoropropylene) separator membranes to improve lithium-ion battery capacity fading. *Chemical Engineering Journal* 2022; **443**: 136329. [DOI: 10.1016/J.CEJ.2022.136329]

22   Petrenko VI, Fernandes LC, Ivankov OI, Tubio CR, Tariq M, Esperança JMSS, Correia DM, Lanceros-Mendez S. Structural organization of ionic liquids embedded in fluorinated polymers. *J Mol Liq* 2022; **360**: 119385. [DOI: 10.1016/J.MOLLIQ.2022.119385]

23   Saiki E, Nohara Y, Iwase H, Shikata T. Evidence of Long Two-Dimensional Folding Chain Structure Formation of Poly(vinylidene fluoride) in N-Methylpyrrolidone Solution: Total Form Factor Determination by Combining Multiscattering Data. *ACS Omega* 2022; **7**: 22825–22829. [DOI: 10.1021/ACSOMEGA.2C02483/ASSET/IMAGES/LARGE/AO2C02483_0004.JPEG]

24   Cuscito O, Clochard MC, Esnouf S, Betz N, Lairez D. Nanoporous β-PVDF membranes with selectively functionalized pores. *Nucl Instrum Methods Phys Res B* 2007; **265**: 309–313. [DOI: 10.1016/J.NIMB.2007.08.089]

25   Wang H, Yuan X, Wu Y, Zeng G, Chen X, Leng L, Wu Z, Jiang L, Li H. Facile synthesis of amino-functionalized titanium metal-organic frameworks and their superior visible-light photocatalytic activity for Cr(VI) reduction. *J Hazard Mater* 2015; **286**: 187–194. [PMID: 25585267 DOI: 10.1016/j.jhazmat.2014.11.039]

26   G. Saiz P, Valverde A, Gonzalez-Navarrete B, Rosales M, Quintero YM, Fidalgo-Marijuan A, Orive J, Reizabal A, Larrea ES, Arriortua MI, Lanceros-Méndez S, García A, Fernández de Luis R. Modulation of the Bifunctional CrVI to CrIII Photoreduction and Adsorption Capacity in ZrIV and TiIV Benchmark Metal-Organic Frameworks. Catalysts. 2021; **11**: 51–60.

27   Jiang J, Gándara F, Zhang YB, Na K, Yaghi OM, Klemperer WG. Superacidity in sulfated metal-organic framework-808. *J Am Chem Soc* 2014; **136**: 12844–12847. [DOI: 10.1021/ja507119n]

28   Healey K, Liang W, Southon PD, Church TL, D'Alessandro DM. Photoresponsive spiropyran-functionalised MOF-808: Postsynthetic incorporation and light dependent gas adsorption properties. *J Mater Chem A Mater* 2016; **4**: 10816–10819. [DOI: 10.1039/c6ta04160d]

29   Valverde A, Gonçalves R, Silva MM, Wuttke S, Fidalgo-Marijuan A, Costa CM, Vilas-Vilela JL, Laza JM, Arriortua MI, Lanceros-Méndez S, Fernández de Luis R. Metal–Organic Framework Based PVDF Separators for High Rate

Cycling Lithium-Ion Batteries. *ACS Appl Energy Mater* 2020; **3**: 11907–11919. [DOI: 10.3390/catal11010051]

30 Song JL, Huang ZQ, Mao J, Chen WJ, Wang B, Yang FW, Liu SH, Zhang HJ, Qiu LP, Chen JH. A facile synthesis of uniform hollow MIL-125 titanium-based nanoplatform for endosomal esacpe and intracellular drug delivery. *Chemical Engineering Journal* 2020; **396**. [DOI: 10.1016/j.cej.2020.125246]

31 Shearer GC, Chavan S, Bordiga S, Svelle S, Olsbye U, Lillerud KP. Defect Engineering: Tuning the Porosity and Composition of the Metal-Organic Framework UiO-66 via Modulated Synthesis. *Chemistry of Materials* 2016; **28**: 3749–3761. [DOI: 10.1021/acs.chemmater.6b00602]

32 Dai S, Simms C, Dovgaliuk I, Patriarche G, Tissot A, Parac-Vogt TN, Serre C. Monodispersed MOF-808 Nanocrystals Synthesized via a Scalable Room-Temperature Approach for Efficient Heterogeneous Peptide Bond Hydrolysis. *Chemistry of Materials* 2021; **33**: 7057–7066. [DOI: 10.1021/acs.chemmater.1c02174]

33 Martins P, Lopes AC, Lanceros-Mendez S. Electroactive phases of poly(vinylidene fluoride): Determination, processing and applications. *Prog Polym Sci* 2014; **39**: 683–706. [DOI: 10.1016/J.PROGPOLYMSCI.2013.07.006]

34 Madorskaya LY, Loginova NN, Panshin YA, Lobanov AM. Role of end groups in polyvinylidene fluoride. *Polymer Science USSR* 1983; **25**: 2490–2496. [DOI: 10.1016/0032-3950(83)90186-7]

35 Zulfiqar S, Zulfiqar M, Rizvi M, Munir A, McNeill IC. Study of the thermal degradation of polychlorotrifluoroethylene, poly(vinylidene fluoride) and copolymers of chlorotrifluoroethylene and vinylidene fluoride. *Polym Degrad Stab* 1994; **43**: 423–430. [DOI: 10.1016/0141-3910(94)90015-9]

36 Costa CM, MacHiavello MNT, Ribelles JLG, Lanceros-Méndez S. Composition-dependent physical properties of poly[(vinylidene fluoride)-co-trifluoroethylene]-poly(ethylene oxide) blends. *J Mater Sci* 2013; **48**: 3494–3504. [DOI: 10.1007/S10853-013-7141-Z/FIGURES/6]

37 Thakur P, Kool A, Bagchi B, Das S, Nandy P. Effect of in situ synthesized Fe2O3 and Co3O4 nanoparticles on electroactive b phase crystallization and dielectric properties of poly(vinylidene fluoride) thin films. *Physical Chemistry Chemical Physics* 2015; **17**: 1368. [DOI: 10.1039/c4cp04006f]

38 Lopes AC, Correia Neves I, Lanceros Mendez S. Ion Exchange Dependent Electroactive Phase Content and Electrical Properties of Poly(vinylidene fluoride)/Na(M)Y Composites. *The Journal of Physical Chemistry C* 2015; **119**: 5211–5217. [DOI: 10.1021/acs.jpcc.5b00271]

39 Steriotis TA, Stefanopoulos KL, Mitropoulos AC, Kanellopoulos NK. Membrane Characterisation by Combination of Static and Dynamic Techniques. *Membrane Science and Technology* 2000; **6**: 1–34. [DOI: 10.1016/S0927-5193(00)80003-0]

40 Feigin LA, Svergun DI. Structure Analysis by Small-Angle X-Ray and Neutron Scattering. Springer.

41 Schmidt PW. Small-angle scattering studies of disordered, porous and fractal systems. *J Appl Crystallogr* 1991; **24**: 414–435. [DOI: 10.1107/S0021889891003400]

42 Guo F, Zhao J, Li F, Kong D, Guo H, Wang X, Hu H, Zong L, Xu J. Polar crystalline phases of PVDF induced by interaction with functionalized boron nitride nanosheets. *CrystEngComm* 2020; **22**: 6207–6215. [DOI: 10.1039/D0CE01001D]

43 Bodkhe S, Rajesh PSM, Kamle S, Verma V. Beta-phase enhancement in polyvinylidene fluoride through filler addition: Comparing cellulose with carbon nanotubes and clay. *Journal of Polymer Research* 2014; **21**: 1–11. [DOI: 10.1007/S10965-014-0434-3/FIGURES/7]

44 Elashmawi IS. Effect of NaCl filler on ferroelectric phase and polaron configurations of PVDF films. *Crystal Research and Technology* 2007; **42**: 389–393. [DOI: 10.1002/CRAT.200610833]

45 Elashmawi IS. Effect of LiCl filler on the structure and morphology of PVDF films. *Mater Chem Phys* 2008; **107**: 96–100. [DOI: 10.1016/J.MATCHEMPHYS.2007.06.045]

46 Sanganyado E, Gwenzi W. Antibiotic resistance in drinking water systems: Occurrence, removal, and human health risks. *Science of the Total Environment* 2019; **669**: 785–797. [DOI: 10.1016/j.scitotenv.2019.03.162]

47 Tursi A, Chatzisymeon E, Chidichimo F, Beneduci A, Chidichimo G. Removal of endocrine disrupting chemicals from water: Adsorption of bisphenol-a by biobased hydrophobic functionalized cellulose. *Int J Environ Res Public Health* 2018; **15**. [DOI: 10.3390/ijerph15112419]

48 Burkhardt-Holm P. Endocrine disruptors and water quality: A state-of-the-art review. *Int J Water Resour Dev* 2010; **26**: 477–493. [DOI: 10.1080/07900627.2010.489298]

49 Zoltan T, Rosales MC, Yadarola C. Reactive oxygen species quantification and their correlation with the photocatalytic activity of TiO2 (anatase and rutile) sensitized with asymmetric porphyrins. *J Environ Chem Eng* 2016; **4**: 3967–3980. [DOI: 10.1016/j.jece.2016.09.008]

50 Rosales M, Zoltan T, Yadarola C, Mosquera E, Gracia F, García A. The influence of the morphology of 1D TiO 2 nanostructures on photogeneration of

reactive oxygen species and enhanced photocatalytic activity. *J Mol Liq* 2019; **281**: 59–69. [DOI: 10.1016/j.molliq.2019.02.070]

51   Matos J, Rosales M, García A, Nieto-Delgado C, Rangel-Mendez JR. Hybrid photoactive materials from municipal sewage sludge for the photocatalytic degradation of methylene blue. *Green Chemistry* 2011; **13**: 3431–3439. [DOI: 10.1039/c1gc15644f]

52   Prasad R, Karchiyappan T. Advanced Research in Nanosciences for Water Technology. Springer DOI:10.1007/978-3-030-02381-2

53   Dong Z, Sun Y, Chu J, Zhang X, Deng H. Multivariate Metal-Organic Frameworks for Dialing-in the Binding and Programming the Release of Drug Molecules. *J Am Chem Soc* 2017; **139**: 14209–14216. [PMID: 28898070 DOI: 10.1021/jacs.7b07392]

54   Liu Q, Song Y, Ma Y, Zhou Y, Cong H, Wang C, Wu J, Hu G, O'Keeffe M, Deng H. Mesoporous Cages in Chemically Robust MOFs Created by a Large Number of Vertices with Reduced Connectivity. *J Am Chem Soc* 2019; **141**: 488–496. [DOI: 10.1021/jacs.8b11230]

55   Reizabal A, Costa CM, Saiz PG, Gonzalez B, Pérez-Álvarez L, Fernández de Luis R, Garcia A, Vilas-Vilela JL, Lanceros-Méndez S. Processing Strategies to Obtain Highly Porous Silk Fibroin Structures with Tailored Microstructure and Molecular Characteristics and Their Applicability in Water Remediation. *J Hazard Mater* 2021; **403**: 123675. [DOI: https://doi.org/10.1016/j.jhazmat.2020.123675]

56   González JA, Villanueva ME, Piehl LL, Copello GJ. Development of a chitin/graphene oxide hybrid composite for the removal of pollutant dyes: Adsorption and desorption study. *Chemical Engineering Journal* 2015; **280**: 41–48. [DOI: 10.1016/j.cej.2015.05.112]

57   Villanueva ME, Diez AMDR, González JA, Pérez CJ, Orrego M, Piehl L, Teves S, Copello GJ. Antimicrobial Activity of Starch Hydrogel Incorporated with Copper Nanoparticles. *ACS Appl Mater Interfaces* 2016; **8**: 16280–16288. [DOI: 10.1021/acsami.6b02955]

58   González JA, Villanueva ME, Peralta Ramos ML, Pérez CJ, Piehl LL, Copello GJ. Chitin based hybrid composites reinforced with graphene derivatives: A nanoscale study. *RSC Adv* 2015; **5**: 63813–63820. [DOI: 10.1039/c5ra13563j]

59   Villanueva ME, Salinas A, Díaz LE, Copello GJ. Chitin nanowhiskers as alternative antimicrobial controlled release carriers. *New Journal of Chemistry* 2015; **39**: 614–620. [DOI: 10.1039/c4nj01522c]

60   Reinsch H, Waitschat S, Chavan SM, Lillerud KP, Stock N. A Facile "Green" Route for Scalable Batch Production and Continuous Synthesis of Zirconium

MOFs. *Eur J Inorg Chem* 2016; **2016**: 4490–4498. [DOI: 10.1002/ejic.201600295]

61 Baumann AE, Burns DA, Liu B, Thoi VS. Metal-organic framework functionalization and design strategies for advanced electrochemical energy storage devices. *Commun Chem* 2019; **2**: 1–14. [DOI: 10.1038/s42004-019-0184-6]

62 Maurin G, Serre C, Cooper A, Férey G. The new age of MOFs and of their porous-related solids. *Chem Soc Rev* 2017; **46**: 3104–3107. [PMID: 28561090 DOI: 10.1039/c7cs90049j]

63 Yuan S, Qin JS, Lollar CT, Zhou HC. Stable Metal-Organic Frameworks with Group 4 Metals: Current Status and Trends. *ACS Cent Sci* 2018; **4**: 440–450. [PMID: 29721526 DOI: 10.1021/acscentsci.8b00073]

64 Denny MS, Cohen SM. In Situ Modification of Metal-Organic Frameworks in Mixed-Matrix Membranes. *Angewandte Chemie - International Edition* 2015; **54**: 9029–9032. [PMID: 26073065 DOI: 10.1002/anie.201504077]

65 Feng D, Wang K, Wei Z, Chen YP, Simon CM, Arvapally RK, Martin RL, Bosch M, Liu TF, Fordham S, Yuan D, Omary MA, Haranczyk M, Smit B, Zhou HC. Kinetically tuned dimensional augmentation as a versatile synthetic route towards robust metal-organic frameworks. *Nat Commun* 2014; **5**. [DOI: 10.1038/ncomms6723]

66 Wang C, Liu X, Keser Demir N, Chen JP, Li K. Applications of water stable metal-organic frameworks. *Chem Soc Rev* 2016; **45**: 5107–5134. [DOI: 10.1039/c6cs00362a]

67 Yaghi OM, O'Keeffe M, Ockwig NW, Chae HK, Eddaoudi M, Kim J. Reticular synthesis and the design of new materials. *Nature* 2003; **423**: 705–714. [PMID: 12802325 DOI: 10.1038/nature01650]

68 G. Saiz P, Gandia D, Lasheras A, Sagasti A, Quintana I, Fdez-Gubieda ML, Gutiérrez J, Arriortua MI, Lopes AC. Enhanced mass sensitivity in novel magnetoelastic resonators geometries for advanced detection systems. *Sens Actuators B Chem* 2019; **296**: 126612. [DOI: 10.1016/j.snb.2019.05.089]

69 Illes B, Wuttke S, Engelke H. Liposome-coated iron fumarate metal-organic framework nanoparticles for combination therapy. *Nanomaterials* 2017; **7**: 1–11. [DOI: 10.3390/nano7110351]

70 Steinborn B, Hirschle P, Höhn M, Bauer T, Barz M, Wuttke S, Wagner E, Lächelt U. Core-Shell Functionalized Zirconium-Pemetrexed Coordination Nanoparticles as Carriers with a High Drug Content. *Adv Ther (Weinh)* 2019; **2**: 1900120. [DOI: 10.1002/adtp.201900120]

71   Zhou D, Zhang L, Zhou J, Guo S. Cellulose/chitin beads for adsorption of heavy metals in aqueous solution. *Water Res* 2004; **38**: 2643–2650. [DOI: 10.1016/j.watres.2004.03.026]

72   Torres DI, Lazaro-Martínez JM, Copello GJ, dall Orto VC. Single step synthesis of a polyhydroxy ether and its optimization to adsorption of a textile dye. *J Environ Chem Eng* 2019; : 103416. [DOI: 10.1016/j.jece.2019.103416]

73   Jayakumar R, Prabaharan M, Sudheesh Kumar PT, Nair S V., Tamura H. Biomaterials based on chitin and chitosan in wound dressing applications. *Biotechnol Adv* 2011; **29**: 322–337. [PMID: 21262336 DOI: 10.1016/j.biotechadv.2011.01.005]

74   Jayakumar R, Menon D, Manzoor K, Nair S V., Tamura H. Biomedical applications of chitin and chitosan based nanomaterials - A short review. *Carbohydr Polym* 2010; **82**: 227–232. [DOI: 10.1016/j.carbpol.2010.04.074]

75   Shen X, Shamshina JL, Berton P, Gurau G, Rogers RD. Hydrogels based on cellulose and chitin: Fabrication, properties, and applications. *Green Chemistry* 2015; **18**: 53–75. [DOI: 10.1039/c5gc02396c]

76   Araki J, Yamanaka Y, Ohkawa K. Chitin-chitosan nanocomposite gels: Reinforcement of chitosan hydrogels with rod-like chitin nanowhiskers. *Polym J* 2012; **44**: 713–717. [DOI: 10.1038/pj.2012.11]

77   Ruckenstein E, Zeng X. Albumin separation with Cibacron Blue carrying macroporous chitosan and chitin affinity membranes. *J Memb Sci* 1998; **142**: 13–26. [DOI: 10.1016/S0376-7388(98)00025-8]

78   Brown AH, Walsh TR. Elucidating Polymorph-Selective Bioadsorption on Chitin Surfaces. *ACS Biomater Sci Eng* 2019; **5**: 594–602. [DOI: 10.1021/acsbiomaterials.8b01260]

79   Yahyaei M, Mehrnejad F, Naderi-manesh H, Rezayan AH. Protein adsorption onto polysaccharides: Comparison of chitosan and chitin polymers. *Carbohydr Polym* 2018; **191**: 191–197. [DOI: 10.1016/j.carbpol.2018.03.034]

80   Taylor P, Tharanathan RN, Kittur FS. Critical Reviews in Food Science and Nutrition Chitin — The Undisputed Biomolecule of Great Potential Chitin — The Undisputed Biomolecule of Great Potential. *Crit Rev Food Sci Nutr* 2003; **43**: 61–87.

81   Felse PA, Panda T. Studies on applications of chitin and its derivatives. *Bioprocess Engineering* 1999; **20**: 505–512. [DOI: 10.1007/s004490050622]

82   Lin S, Zhao Y, Bediako JK, Cho C, Sarkar AK, Lim C, Yun Y. Structure-controlled recovery of palladium (II) from acidic aqueous solution using metal-organic frameworks of MOF-802 , UiO-66 and MOF-808. *Chemical Engineering Journal* (e-pub ahead of print 2019; doi:10.1016/j.cej.2019.01.044).

83   Wang C, Liu X, Chen JP, Li K. Superior removal of arsenic from water with zirconium metal-organic framework UiO-66. *Sci Rep* 2015; **5**: 1–10. [DOI: 10.1038/srep16613]

84   Li ZQ, Yang JC, Sui KW, Yin N. Facile synthesis of metal-organic framework MOF-808 for arsenic removal. *Mater Lett* 2015; **160**: 412–414. [DOI: 10.1016/j.matlet.2015.08.004]

85   Stassin T, Reinsch H, Van de Voorde B, Wuttke S, Medina DD, Stock N, Bein T, Ameloot R, De Vos D. Adsorption and Reactive Desorption on Metal–Organic Frameworks: A Direct Strategy for Lactic Acid Recovery. *ChemSusChem* 2017; **10**: 643–650. [DOI: 10.1002/cssc.201601000]

86   González JA, Villanueva ME, Peralta Ramos ML, Pérez CJ, Piehl LL, Copello GJ. Chitin based hybrid composites reinforced with graphene derivatives: A nanoscale study. *RSC Adv* 2015; **5**: 63813–63820. [DOI: 10.1039/c5ra13563j]

87   Furukawa H, Gándara F, Zhang YB, Jiang J, Queen WL, Hudson MR, Yaghi OM. Water adsorption in porous metal-organic frameworks and related materials. *J Am Chem Soc* 2014; **136**: 4369–4381. [DOI: 10.1021/ja500330a]

88   Baek J, Rungtaweevoranit B, Pei X, Park M, Fakra SC, Liu YS, Matheu R, Alshmimri SA, Alshehri S, Trickett CA, Somorjai GA, Yaghi OM. Bioinspired Metal-Organic Framework Catalysts for Selective Methane Oxidation to Methanol. *J Am Chem Soc* 2018; **140**: 18208–18216. [DOI: 10.1021/jacs.8b11525]

89   Valekar AH, Lee SG, Cho KH, Lee UH, Lee JS, Yoon JW, Hwang YK, Cho SJ, Chang JS. Shaping of porous metal-organic framework granules using mesoporous ρ-alumina as a binder. *RSC Adv* 2017; **7**: 55767–55777. [DOI: 10.1039/c7ra11764g]

90   Doan H V., Amer Hamzah H, Karikkethu Prabhakaran P, Petrillo C, Ting VP. Hierarchical Metal–Organic Frameworks with Macroporosity: Synthesis, Achievements, and Challenges. Springer Singapore DOI:10.1007/s40820-019-0286-9

91   Modena MM, Rühle B, Burg TP, Wuttke S. Nanoparticle Characterization: What to Measure? *Advanced Materials* 2019; **31**: 1–26. [DOI: 10.1002/adma.201901556]

92   Zhang H, Zhao Y. Preparation , characterization and evaluation of tea polyphenol e Zn complex loaded b -chitosan nanoparticles. *Food Hydrocoll* 2015; **48**: 260–273. [DOI: 10.1016/j.foodhyd.2015.02.015]

93   Suhailath K, Jayakrishnan P, Naufal B, Periyat P, Jasna VC, Ramesan MT. Synthesis by In Situ-Free Radical Polymerization, Characterization, and Properties of Poly (n-butyl methacrylate)/Samarium-Doped Titanium Dioxide

Nanoparticles Composites. *Advances in Polymer Technology* 2018; **37**: 1114–1123. [DOI: 10.1002/ADV.21770]

94   Xie D, Ma Y, Gu Y, Zhou H, Zhang H, Wang G, Zhang Y, Zhao H. Bifunctional NH2-MIL-88(Fe) metal-organic framework nanooctahedra for highly sensitive detection and efficient removal of arsenate in aqueous media. *J Mater Chem A Mater* 2017; **5**: 23794–23804. [DOI: 10.1039/c7ta07934f]

95   Luo J, Xu F, Hu J, Lin P, Tu J, Wu X, Hou X. Preconcentration on metal organic framework UiO-66 for slurry sampling hydride generation-atomic fluorescence spectrometric determination of ultratrace arsenic. *Microchemical Journal* 2017; **133**: 441–447. [DOI: 10.1016/j.microc.2017.03.056]

96   Sarker M, Song JY, Jhung SH. Adsorption of organic arsenic acids from water over functionalized metal-organic frameworks. *J Hazard Mater* 2017; **335**: 162–169. [DOI: 10.1016/j.jhazmat.2017.04.044]

97   Maleki A, Hayati B, Naghizadeh M, Joo SW. Adsorption of hexavalent chromium by metal organic frameworks from aqueous solution. *Journal of Industrial and Engineering Chemistry* 2015; **28**: 211–216. [DOI: 10.1016/j.jiec.2015.02.016]

98   Of A, Of A. Iron Based Metal Organic Frameworks as Photocatalysts for Chromium (VI) Degradation in Partial Fulfillment of the Requirement for the Degree of Iron Based Metal Organic Frameworks as Photocatalysts for Chromium (VI) Degradation.

99   de Decker J, de Clercq J, Vermeir P, van der Voort P. Functionalized metal-organic-framework CMPO@MIL-101(Cr) as a stable and selective rare earth adsorbent. *J Mater Sci* 2016; **51**: 5019–5026. [DOI: 10.1007/s10853-016-9807-9]

100   Lin ZJ, Zheng HQ, Zheng HY, Lin LP, Xin Q, Cao R. Efficient Capture and Effective Sensing of Cr2O72-from Water Using a Zirconium Metal-Organic Framework. *Inorg Chem* 2017; **56**: 14178–14188. [DOI: 10.1021/acs.inorgchem.7b02327]

101   Wang Z, Yang J, Li Y, Zhuang Q, Gu J. Simultaneous degradation and removal of CrVI from aqueous solution with Zr-based metal–organic frameworks bearing inherent reductive sites. *Chemistry - A European Journal* 2017; **23**: 15415–15423. [DOI: 10.1002/chem.201702534]

102   G. Saiz, P., Iglesias, N., Gonzalez-Navarrete, B., Rosales, M., Quintero, Y. M., Reizabal, A., Orive, J., Fidalgo-Marijuan, A., Lanceros-Mendez, S., Arriortua, M. I.,& Fernandez de Luis R. Chromium speciation in zirconium-based metal – organic frameworks for environmental remediation. *Chemistry—A European Journal* 2020; **26**: 1–13. [DOI: 10.1002/chem.202001435]

103   Lu F, Astruc D. Nanocatalysts and other nanomaterials for water remediation from organic pollutants. *Coord Chem Rev* 2020; **408**. [DOI: 10.1016/J.CCR.2020.213180]

104   Gallardo-Godoy A, Hansford KA, Muldoon C, Becker B, Elliott AG, Huang JX, Pelingon R, Butler MS, Blaskovich MAT, Cooper MA. Structure-Function Studies of Polymyxin B Lipononapeptides. *Molecules* 2019; **24**: 553–566. [DOI: 10.3390/molecules24030553]

105   Gallardo-Godoy A, Hansford KA, Muldoon C, Becker B, Elliott AG, Huang JX, Pelingon R, Butler MS, Blaskovich MAT, Cooper MA. Structure-function studies of polymyxin B lipononapeptides. *Molecules* 2019; **24**. [DOI: 10.3390/molecules24030553]

106   Gallardo-Godoy A, Hansford KA, Muldoon C, Becker B, Elliott AG, Huang JX, Pelingon R, Butler MS, Blaskovich MAT, Cooper MA. Structure-function studies of polymyxin B lipononapeptides. *Molecules* 2019; **24**. [DOI: 10.3390/molecules24030553]

107   Burkhardt-Holm P. Endocrine disruptors and water quality: A state-of-the-art review. *Int J Water Resour Dev* 2010; **26**: 477–493. [DOI: 10.1080/07900627.2010.489298]

108   Wang K, Li N, Hai X, Dang F. Lysozyme-mediated fabrication of well-defined core-shell nanoparticle@metal-organic framework nanocomposites. *J Mater Chem A Mater* 2017; **5**: 20765–20770. [DOI: 10.1039/c7ta06419e]

109   Liang K, Ricco R, Doherty CM, Styles MJ, Bell S, Kirby N, Mudie S, Haylock D, Hill AJ, Doonan CJ, Falcaro P. Biomimetic mineralization of metal-organic frameworks as protective coatings for biomacromolecules. *Nat Commun* 2015; **6**: 4–11. [DOI: 10.1038/ncomms8240]

110   Sarker M, Song JY, Jhung SH. Adsorption of organic arsenic acids from water over functionalized metal-organic frameworks. *J Hazard Mater* 2017; **335**: 162–169. [DOI: 10.1016/j.jhazmat.2017.04.044]

111   Howarth AJ, Katz MJ, Wang TC, Platero-Prats AE, Chapman KW, Hupp JT, Farha OK. High Efficiency Adsorption and Removal of Selenate and Selenite from Water Using Metal-Organic Frameworks. *J Am Chem Soc* 2015; **137**: 7488–7494. [PMID: 26000611 DOI: 10.1021/jacs.5b03904]

112   Allen SJ, Mckay G, Porter JF. Adsorption isotherm models for basic dye adsorption by peat in single and binary component systems. *J Colloid Interface Sci* 2004; **280**: 322–333. [DOI: 10.1016/j.jcis.2004.08.078]

Chapter 6
Conclusions and Future Trends

6.1. CONCLUSIONS

In this thesis, the potentials for water remediation of chemically robust Metal-Organic Frameworks and their composites have been assessed. Considering all the work developed in perspective, it can valued that the general objective of the thesis has been accomplished. In detail, the pros and cons of the different pre and post-synthetic functionalization pathways that can be applied to water stable MOFs to enhance their performance for the capture, separation and degradation of specific pollutants as heavy metals and phenolic compounds have been determined succesfully.

More concretely, the following conclusions arise from the thesis work considered as a whole:

- The dual photocatalytic and adsorptive functionality of the archetypical Zr-based UiO-66(-NH$_2$) over the simultaneous Cr^{VI} to Cr^{III} photoreduction and immobilization is based on a balanced combination of defective chemistry and inner functionalization of the pore space of the frameworks.

- The particle size reduction of the Ti-based MIL-125 has been revealed as a key parameter to enhance the photoactivity to reduce hexavalent chromium.

- Multivariate reticular chemistry has shown to be a versatile tool to tune the physico-chemical properties of UiO-66 frameworks and enhance their adsorption and photoreduction abilities.

- A synergistic enhancement of the band gap, photoconduction and photocatalytic efficiency of the MTV-UiO-66, which exceeds the average sum of the single-functionalized materials in some cases, is observed when -NH$_2$, -(OH)$_2$ and -NO$_2$ functional groups are encoded within its framework.

- The combination of linkers with electron-donor and electron-acceptor groups is key to improve the photoconduction in MTV-UiO-66 frameworks.

- Multivariate reticular chemistry has shown to be a limited tool to control the thermal and hydrolytic stability of UiO-66 frameworks, since both parameters are dictated by the Zr-linker bridges with the lower chemical resistance.

- The inner functionalization of the MOFs pore space with amino acids and natural acids alters significantly the chemical and thermal stability of the frameworks, as well as their adsorption capacity and affinity towards metal ions with varied acidities.

- The incorporation of these molecules endows the MOF-808 pore space of metal-complexing mechanisms where single or cooperative metal-binding modes operate to stabilize isolated, clustered and even partially reduced metal ions such as copper or chromium.

- As a consequence, the metal immobilization in MOF-808@(amino) acid system does not only involve amino acid-metal coordination chemistry, but electron transfers processes able to reduce and oxidize the immobilized metal ions.

- The metal affinity of MOF-808@(amino)acid system determined in static conditions is well correlated to the one observed in the breakthrough experiments with multielement solutions.

- The coordination environment and clustering degree of Cu^{II} metal ions immobilized within the pore space of MOF-808 can be partially controlled by selecting the proper (amino) acid encoding, in parallel to the copper adsorption conditions.

- The coordination environment and the clustering degree of the Cu^{II} ions stabilized into the MOF-808@(amino) acid system modulate both their efficiency and their selectivity to oxidize phenolic compounds.

- The multivariate combination of cysteine and histidine in the pore structure of the MOF-808 does not have a synergic effect on its catalytic properties when decorated with copper ions.

- The immobilization of MOF particles into polymeric membranes is an effective, easy and cost-effective solution to recover these materials after their use.

- The processing method of the PVDF-HFP membranes have a direct effect in their micro to nanometre scale structure.

- As concluded from small angle X-ray and neutron scattering experiments, the inclusion of the MOFs into the PVDF-HFP significantly alters its micrometre to nanometre structure inducing a change in the fractal structuration of the polymer, and generating new nanometric inhomogeneities in the membrane ascribed to the MOF-MOF, MOF-polymer and polymer-polymer interphases.

- The accessibility of the MOF particles in the membranes can be calculated *via* metal adsorption tests, comparing the adsorption capacity of the MOF immobilized in the membrane with the capacity of the MOF determined *via* its dispersion in a water solution.

- The processing methodology of the PVDF-HFP membranes influence drastically their structure, and hence, the accessibility of the MOF nanoparticles to capture the target pollutant.

- The encapsulation degree of the MOFs increases when the MOF content is increased.

- The post-synthetic modification of the MOF-808 *via* SALI can be performed when the MOF is already immobilized in the membrane.

- MOF-808 nanoparticles incorporation into chitin gel polymeric matrix develop micro, meso and macroporous composites that work efficiently for the adsorption of a large variety of pollutants ranging from small ions and molecules to large proteins or nanoparticles.

- CH@MOF-808 composite benefits from the synergistic interactions of its components, outperforming both MOF-808 and CH efficiency, mainly because of the active role of the interface between MOF-808 and CH during adsorption.

6.2. FUTURE TRENDS

The advances made throughout this work have opened the room for the future improvement of reticular materials, and especially of Metal-Organic Frameworks, not only for water remediation purposes, but for environmental prevention, monitoring and revalorization processes too. Below, there are listed some of the points that we have considered highly interesting in order to expand our research in the coming future.

- In the short term, as direct future work closely related with the efforts developed within this thesis, understanding the key processes enabling the activation and reutilization of MOFs will be key to expand their use for real-life application. Now that we have stablished the main strategies to improve their performance, the reactivation and reusability for pre- and post-synthetically encoded MOFs should be deeply studied in order to fully regenerate their functions without altering/degrading their initial crystallinity, porosity and quality.

Furthermore, in the mid-term, it would be interesting to focus the future work in the research points directly related with environmental remediation purposes detailed below:

- The photoreduction capacity towards Cr^{VI} that multivariate UiO-66 materials have shown could be extended to photooxidation of As^{III} to As^{V}. This approach is of high-environmental and societal relevance since many countries as Chile, show natural levels of arsenic in drinking and wastewater that surpass by far the legal limits stablished by WHO. In addition, As^{III} is more dangerous and difficult to capture through adsorption than As^{V}, making its photooxidation with MTV-UiO-66 with amino, nitro, thiol or bromine functional groups highly appealing. Indeed, multivariate reticular chemistry can open the room to a fast and efficient capture and phototransformation of arsenic from water at ppm concentration levels.

- The redox chemistry that the metals immobilized within the MOFs have shown opens the window to explore the electrochemical sensing capacity of these materials, not just to monitor heavy metals concentration in a solution, but to adapt the features of the redox-catalytic centres to detect complex organic pollutants such as drugs or hormones.

- In line with the possibility depicted above, the oxidative degradation that copper-doped MOF-808@(amino) acids have shown over phenolic compounds could be extended to complex pollutants as common drugs or endocrine disruptors.

- Among the innumerable possibilities to assemble PVDF-HFP and Chitin@MOF composites, this work has studied a narrow window within of the compositional parameter space. In fact, there are many factors that can be studied yet from a small angle scattering techniques perspective. As an example, the effect that the temperature has during the nanostructuration of the membranes processed by NIPS, or the effect of the colloidal dispersibility of the surface-chemistry of the MOF nanoparticles in their stabilization within the polymeric matrixes are still open questions to investigate.

- In addition, how to precisely study and describe the nanostructure of the composites, of their pore interconnectivity, or the specific accommodation of MOF nanoparticle in this space need to be further investigated.

- Moreover, the effect of the thickness of the membranes, as well the PVDF-HFP functionalization process to increase its hydrophilicity, are of high interest and there is plenty of room to explore them.

- The expansion of the polymer@MOF composites engineering to carboxyl-rich natural polymers could be of high interest to stalely anchor the MOF nanoparticles to the polymeric matrix either *via* their surface-defective points or through their direct crystallization into the polymeric matrix.

In addition to the future-possibilities related with the main focus of this thesis work, many fundamental questions have arisen from the materials engineering and advanced applications:

- From a more fundamental point of view, it would be highly interesting to unravel whether the generation of reactive-oxygen species when illuminating the MOF-photocatalyst is a process driven through the whole material or preferably at their surface.

- In parallel, it would be highly interesting to investigate if the chemical instability of specific linkers installed within MTV-MOFs could open the possibility to generate defects in the materials through their acid selective leaching.

- In fact, given the chiral nature of amino acid functions installed within the MOFs, these amazing bioinspired systems could be adapted and tested for the enantioselective separation or catalysis of highly added value chemicals.

- In line with the previous point, unravelling the oxygen and hydrogen peroxide activation mechanisms by the chiral-metal sites installed into the MOFs, and the posterior evolution of these highly reactive centres would be a highly challenging by rewarding point to clear up.

Annex
Results Dissemination
and Training Courses

A.1. PUBLICATIONS

Part of the thesis

- A. Valverde, E. Alkain, N.A. Rio-López, L. Lezama, A. Fidalgo-Marijuan, J. Manuel Laza, S.Wuttke, I. Oyarzabal, M. Jiménez-Ruiz, V. García-Sakai, J. L. Vilas-Vilela, P. L. Arias, J. M. Porro, I. Agirrezabal-Telleria and R. Fernández-de Luis. Enzyme-mimicking of copper-sites in Metal-Organic Frameworks for oxidative degradation of phenolic compounds. - *Manuscript in preparation.*

- A. Valverde, R. Fernández-de Luis, H. Salazar, B. Gonçalves, S. King, P. M. Martins, S. Lanceros-Mendez, J. M. Porro, V. I. Petrenko. Unravelling the micro to nanostructure of PVDF-HPF@MOF water remediation membranes by small angle scattering. - *Manuscript in preparation.*

- A. Valverde, G.I. Tovar, N. A. Río-López, D. Torres, M. Rosales, S. Wuttke, A. Fidalgo-Marijuan, J. M. Porro, M. Jiménez-Ruiz, V. Garcia-Sakai, A. García, J. M. Laza, J. L. Vilas-Vilela, L. Lezama, M. I. Arriortua, G. J. Copello and R. Fernández-de Luis. Designing Metal-Celator-like Traps by Encoding Amino Acids in Zirconium-based Metal-Organic Frameworks. *Chemistry of Materials* (2022), 34, 9666-9684. DOI: 10.1021/acs.chemmater.2c02431

- A. Valverde, D. Payno, L. Lezama, J. M. Laza, S. Wuttke and R. Fernández-de Luis. Multivariate Functionalization of UiO-66 for Photocatalytic Water Remediation. *Advanced Sustainable Systems* (2022), 6, 2200024. DOI: 10.1002/adsu.202200024

- G. I. Tovar, A.Valverde, C. Mendes-Felipe, S. Wuttke, A. Fidalgo-Marijuan, E. S. Larrea, L. Lezama, F. Zheng, J. Reguera, S. Lanceros-Méndez, M. I. Arriortua, G. Copello and R. Fernández-de Luis. Chitin/Metal-Organic

Framework Composites as Wide-Range Adsorbent. *ChemSusChem* (2021), 14, 2898-2901. DOI: 10.1002/cssc.202100675

- P. G. Saiz, A. Valverde, B. Gonzalez-Navarrete, M. Rosales, Y. M. Quintero, A. Fidalgo-Marijuan, J. Orive, A. Reizabal, E. S. Larrea, M. I. Arriortua, S. Lanceros-Méndez, A. García and R. Fernández-de Luis. Modulation of the Bifunctional Cr^{VI} to Cr^{III} Photoreduction and Adsorption Capacity in Zr^{IV} and Ti^{IV} Benchmark Metal-Organic Frameworks. *Catalysts* (2021), 11, 51. DOI: 10.3390/catal11010051

Other publications

- A. Garcia, B. Rodriguez, M. Rosales, Y. M. Quintero, P. G. Saiz, A. Reizabal, S. Wuttke, L. Celaya, A. Valverde and R. Fernández-de Luis. A state-of-the-art of Metal-Organic Frameworks for chromium photoreduction vs. photocatalytic water remediation. *Nanomaterials* (2022), 12, 4263.
  DOI: 10.3390/nano12234263

- J. C. Barbosa, R. Gonçalves, A. Valverde, P. M. Martins, V. I. Petrenko, M. Márton, A. Fidalgo-Marijuan, R. Fernández-de Luis, C. M. Costa and S. Lanceros-Méndez. Metal Organic Framework modified poly(vinylidene fluoride-co-hexafluoropropylene) separator membranes to improve lithium-ion battery capacity fading. *Chemical Engineering Journal* (2022), 443, 136329.
  DOI: 10.1016/j.cej.2022.136329

- J. M. Queirós, H. Salazar, A. Valverde, G. Botelho, R. Fernández-de Luis and J. Teixeira. Reusable composite membranes for highly efficient chromium removal from real wáter matrixes. *Chemosphere* (2022), 307, 135922.
  DOI: 10.1016/j.chemosphere.2022.135922

- H. Salazar, P. M. Martins, A. Valverde, R. Fernández-de Luis, J. L. Vilas-Vilela, S. Ferdov, G. Botelho and S. Lanceros-Méndez. Reusable Nanocomposite Membranes for Highly Efficient Arsenite and Arsenate Dual Removal from Water. *Advanced Materials Interfaces* (2022), 9, 2101419.
  DOI: 10.1002/admi.202101419

- A. Valverde, P. G. Saiz, J. Orive, E. S. Larrea, A. Reizabal-Para, G. I. Tovar, G. Copelo, J. M. Lázaro-Martinez, B. Rodriguez, B. Gonzalez-Navarrete, Y. Quintero, M. Rosales, A. García, M. I. Arriortua and R. Fernández-de Luis. Chapter Three – Porous, lightweight metal organic materials: environment sustainability. Chapter in *Advanced Lightweight Multifucntional Materials* (2021), 43-129.

- A. Valverde, R. Gonçalces, M. M. Silva, S. Wuttke, A. Fidalgo-Marijuan, C. M. Costa, J. L. Vilas-Vilela, J. M. Laza, M. I. Arriortua, S. Lanceros-Méndez and R. Fernández-de Luis. Metal-Organic Framework Based PVDF Separators for High Rate Cycling Lithium-Ion Batteries. *Applied Energy Materials* (2020), 3, 11907-11919. DOI: 10.1021/acsaem.0c02044

A.2. CONTRIBUTION TO CONFERENCES

- Seventh Internatonal Conference on Multifunctional, Hybrid and Nanomaterials. Genova, Italy (19th-22nd of October, 2022) – Oral Presentation. *Metal-Organic Framework Advanced Adsorbents for Heavy Metal Recovery in Wastewater.* A. Valverde, G. I. Tovar, D. Torres, M. I. Arriortua, G. Copello, J. M. Laza, J. L. Vilas-Vilela and R. Fernández-de Luis.

- 1st IKUR Neutrionics Workshop. Donostia-San Sebastian, Spain (29th of September, 2022) – Oral Presentation. *MOF-based materials for energy and environmental remediation.* A. Valverde, G. I. Tovar, N. A. Rio-López, B. Gonçalves, M. Jiménez-Ruiz, V. García-Sakai, S. King, J. M. Laza, J.M. Porro, V. Petrenko and R. Fernández-de Luis.

- 8th International Conference on Metal-Organic Framework Compounds. Dresden, Germany (4th-7th of September, 2022) – Poster Contribution. *Multivariate Functionalization of UiO-66 for Photocatalytic Water Remediation.* A. Valverde, D. Payno, L. Lezama, J. M. Laza and R. Fernández-de Luis.

- International Conference on Neutron Scattering. Buenos Aires, Argentina – Online (21st-25th of August, 2022) – Poster Contribution.

Direct post-synthetic encoding of Metal-Organic Framework/PVDF composites for enzymatic-like capture and degradation of inorganic and organic pollutants.
A. Valverde, N. A. Río-López, J. M. Porro, V, Petrenko, V. García-Sakai, M. Jiménez-Ruiz, L. Almasy, J. M. Laza and R. Fernández de Luis.

- 1st International Meeting on Challenges and Opportunities for HICANS. Leioa. Spain (20th-22nd of June, 2022) – Poster Contribution.
Direct post-synthetic encoding of Metal-Organic Framework/PVDF composites for enzymatic-like capture and degradation of inorganic and organic pollutants.
A. Valverde, N. A. Río-López, J. M. Porro, V, Petrenko, V. García-Sakai, M. Jiménez-Ruiz, L. Almasy, J. M. Laza and R. Fernández de Luis.

- B&B 2021: BCMaterials – University of Bourdeaux symposium on bilateral copperation in advanced materials and applications. Leioa, Spain – Online (22th of June, 2021) – Poster Contribution.
Amino Acid Encoded Metal-Organic Framework adsorbents for heavy metals.
A. Valverde, G. I. Tovar, D. Torres, M. I. Arriortua, G. Copello, J. M. Laza, J. L. Vilas-Vilela and R. Fernández-de Luis.

- New Materials for a Better Life: Advanced Multifunctional Materials and Devices. Leioa, Spain (8th of October, 2020). – Poster Contribution.
Metal-Organic Framework advanced adsorbents for metal ions recovery from polluted water sources.
A. Valverde, G. I. Tovar, D. Torres, M. I. Arriortua, G. Copello and R. Fernández-de Luis.

A.3. TRAINING COURSES

- ISIS SANS Training course. Harwell, United Kingdom – Online (1st-10th of February, 2022). 32 hours.
- 14th Central European Training School on Neutron Techniques. Budapest, Hungary. (4th-8th and 25th-28th of October, 2021). 30 hours.
- 6th European Crystallographic School. Budapest, Hungary – Online (4th-10th of July, 2021). 40 hours.

- Introducción a la caracterización de adsorbentes y catalizadores. Jarandilla de la Vera, Spain (8th-11th of June, 2021). 20 hours.

- HERCULES: Higher European Research Course for Users of Large Experimental Systems. Grenoble, France – 2 weeks presential and then turned online because of Covid-19 (2nd of March to 3rd of April, 2020). 118 hours.

- 16th Oxford School on Neutron Scattering. Oxford, United Kingdom (2nd-12th of September, 2019). 46 hours.

- Bilbao Neutron School on Science and Instrumentation for Compact Accelerator-driven Neutron Sources (CANS). Leioa, Spain (17th-19th of June, 2019). 30 hours.

- Difracción y Fluorescencia de Rayos X: Aplicación en materiales geologicos y afines. Leioa, Spain (27th-31st of May, 2019). 20 hours.

- Buenas Prácticas en el Laboratorio: Gestión de Residuos. Leioa, Spain – Online (1st-9th of November, 2018). 25 hours.

A.4. GRANTS AND AWARDS

- Predoctoral grant from the Basque Government in the specific area of Neutron Science. (PREB_2018_1_004).

- Best poster award in the 1st International Meeting on Challenges and Opportunities for HICANS Leioa. Spain (20th-22nd of June, 2022).

- Best poster award in the HERCULES training course. Grenoble, France (2nd of March to 3rd of April, 2020).

- Best proposal award in the 16th Oxford School on Neutron Scattering. Oxford, United Kingdom (2nd-12th of September, 2019).

A.5. RESEARCH STAYS

- Research stay in the University of Buenos Aires (Facultad de Farmacia y Bioquímica) in the frame of the INDESMOF project from Marie Curie RISE action from the 1st of October to the 27th of December, 2019.